Transactions of the ASME

Journal of Fluids Engineering

Contents (continued)

Review—Mechanisms of Cavitation Inception

E. P. Rood

Office of Naval Research,
Fluid Dynamics Program,
Arlington, VA 22217

A review is made of progress in research during the period 1979–1989 on the fundamental physical mechanisms of hydrodynamic cavitation inception. During that decade identification of the physical phenomena has been made, and techniques have been developed to reproduce on laboratory scale selected forms of full scale cavitation inception. Understanding of the mechanisms remains shallow, and analytical/numerical prediction methods are nonexistent except for the restricted case of travelling bubble cavitation inception in a passive pressure field. The control of inception is seen to be related in part to control of the underlying viscous flow features. A growing body of experimental evidence points to microscale vortex cavitation as a primal inception event.

I Why a Review?

Cavitation for most engineering purposes degrades performance. Engineering designs are aimed at producing geometries and operating conditions that resist cavitation. From an applied scientist's point of view, it is desirable to identify, understand, predict, and control the physical mechanisms leading to cavitation inception. There is a large amount of empirical information on the phenomena of inception, and many empirical rules have been formulated to guide engineering design. The rules are generally based on correlations between measurements on model scale and observations of full scale characteristics and performance. Because there is a need to better understand the model scale phenomena, and in fact to develop prediction techniques, investigations during the past twenty years have focused on real fluid and environmental effects on idealized cavitation inception. The result of those investigations has been the identification of complex bubble and viscous flow interactions leading to cavitation inception. The goal for future cavitation research is to understand and control those complex processes.

During the past twenty years research on cavitation inception has been characterized by progressive development. The decade of the 1970's chiefly produced research directed at uncovering and classifying real fluid (viscous) effects in the cavitation inception process, such as laminar separation and turbulence. In the early 1980's those processes were examined closely and found to be more complex than previously assumed. However, the major thrust of research in the 1980's was directed at uncovering the effects of both size distribution and concentration of active nuclei, an aspect of the inception process that was also found to be more complex than previously assumed. This review addresses principally the results from recent research on real fluid effects and active nuclei, and encourages future research on uncovering the microscale physics of the

local cavitation inception "event." Among other results, this review demonstrates that the two separate (in the past) topics of *cavitation inception* and *turbulent flow structures* are in fact inseparable in many situations of cavitation inception.

The need for this review originates in a perception that new scientific opportunities are available to obtain a significant increase in knowledge about cavitation inception, and that this review will help set the stage for future scientific thrusts.

II Scope of Review

This review of cavitation inception is limited to fluids in which the cavitation is produced by hydrodynamic pressures. In this case, cavitation inception occurs most often when gas- and vapor-filled microbubbles experience critical pressures with subsequent explosive growth in their volume. This review addresses the physical mechanisms initiating the rapid bubble growth; it does not consider the subsequent growth and evolution of the bubble other than as a possible qualifier as to whether the bubble results in cavitation. The exception is when the bubble interacts with the underlying flow structure to alter subsequent inception events.

This paper demonstrates that there is an important interaction between expanding nuclei and the underlying flow structures that must be understood to explain the mechanisms of cavitation inception. The literature provides numerous instances that by inference demonstrate this connection. A full explanation of the interaction is hindered by the lack of knowledge about the dynamics of the underlying flow structures in the single-phase flow. Although a considerable research effort has gone into this area, the results remain inconclusive (Lian, 1990), and there is no attempt in this paper to report on the findings because that would require a substantial addition to the length of the paper.

Cavitation has been a research topic at least since 1873 when Reynolds investigated cavitation in constrictions. The literature is bountiful, and includes an authoritative textbook (Knapp et al., 1970). This paper is written on the assumption that the

reader is familiar with the fundamentals of cavitation as described in that text. A longer version of this paper is given by Rood (1989), and the reader may find the additional information helpful although the essential information is presented here. Another recent comprehensive review of cavitation inception is presented by Arndt (1981a), which is distinguished from a similar article on cavitation (Arndt, 1981b) that appeared around the same time. It summarizes the cumulative knowledge about cavitation inception as of approximately the year 1978, and was used for a starting point for the present review. Since then, there have been many notable contributions to the understanding of cavitation inception, particularly with respect to the role of microscale fluid structures and the importance of active nuclei.

In this review, state-of-the-art material is collated and discussed in a format intended to describe the current notions about cavitation inception. There is much more to this review, however. The look toward the future is based on numerous substantial discussions with investigators involved in current research on cavitation inception. There is expectation for new insights and understanding resulting from the use of new research tools which will provide the means to answer many questions regarding the fundamental physical mechanisms leading to cavitation inception. Those tools include supercomputers for numerical experiments (including direct Navier-Stokes computation of complex two-phase flows), and optical measurement systems capable of obtaining and digitally processing information from instantaneous whole flow fields including liquid velocities and bubble deformations.

III Definition of Cavitation Inception

An imprecise but useful definition for cavitation inception is the initial rapid growth of vapor- and gas-filled bubbles as a consequence of hydrodynamic forces. This definition implies instabilities resulting from mechanical forces (principally inertia), and distinguishes cavitation from rapid growth caused by thermal instabilities (boiling). It is presumed that very small gas and vapor filled voids (microbubbles) exist in the fluid, either in the interior or on a boundary, and that they become unstable at inception. The role of solid particles and organisms in producing tensile weakness in the fluid is recognized, but not considered dominant in most flows of interest. Implicit in this description is the presence of some inhomogeneity to produce a local "weakness" in the liquid; pure liquid would not cavitate at the tensile pressures associated with cavitation inception in either the laboratory or the field.

Rapid growth of a microbubble that remains stable is called gaseous cavitation. Gaseous cavitation may or may not involve significant mass transfer of gas between the liquid and the bubble. The mass transfer is a relatively slow process, observed perhaps in tip vortices but probably not significant for gaseous bubble expansion in processes of shorter duration. Dreyer (1987) used the term "pseudo cavitation" for gaseous cavitation due to volumetric changes in a constant gas mass. He reserved the term "gaseous cavitation" for processes where there is significant mass transfer. For both vaporous and gaseous cavitation, inception refers to the individual *event*, the growth of a single microbubble however short the lifetime of that microbubble.

These scientific definitions of cavitation inception are appropriate for understanding and describing microscale processes, but must be modified for engineering and practical purposes. An engineering definition applies when cavitation inception is determined indirectly through visual or acoustic techniques, in which case a notion of *events per unit time* is often required. Cavitation inception occurs when the measurement detects events above a predefined threshold. The limited cavitation at this threshold is usually more developed than the scientific event of inception, but less developed than full

cavitation (Billet and Holl, 1979). The threshold is sufficiently low that the cavitation is certain, but does not necessarily affect the performance of the device under investigation.

There are practical complications in determining the actual cavitation event, and the precise notion of cavitation inception as a practically observed phenomenon in contrast to a mathematical consequence of an equation is a subject for discussion. Peterson (1972) found that visual determination of cavitation inception correlated with acoustic determination in a towing tank with a small nuclei concentration, but that visual determination indicated premature inception in comparison to the acoustic determination in a water tunnel with a large nuclei concentration. The discrepancy can be explained by contrasting the dynamic gaseous growth of bubbles, in which the growth and collapse occur slowly yet are observed visually, and the vaporous growth due to bubble instability, in which the collapse is acoustically violent. According to the definition of cavitation inception given above, only the unstable growth is cavitation inception. However, much of the laboratory research on cavitation inception appears to actually be directed towards gaseous travelling bubble dynamics (Ling et al., 1982). Therefore this paper includes gaseous cavitation as an ancillary cavitation inception, where the "event" is usually defined by bubble growth to a threshold size. As evidenced by the above investigation (Peterson, 1972) and by others (Dreyer, 1987), there is a need to develop consistent and adequate definition of the cavitation inception event to be used in experiments.

Initial conditions and real fluid effects lead to a complex description of cavitation inception. In an attempt to understand the underlying features of this complex phenomenon, the process has been greatly simplified in a mathematical model which illustrates the basic processes involved for a passive spherical bubble in a known pressure field. The various equations (Rayleigh-Plesset; Johnson-Hsieh; Hsieh-Plesset; see Arndt, 1981a) are useful within their assumptions, but the actual process is complicated by random pressure fluctuations and by bubble deformation and bubble/flow structure interactions. These complications have been known for a long time; they have not been adequately incorporated into understanding and prediction of cavitation inception.

IV Forms of Limited Cavitation Inception

The type of cavitation known as hydrodynamic cavitation can take many physical forms, or geometric shapes, at inception. Experimental observation has shown that there may be several distinct forms of smooth body cavitation for the same geometrical body under nominally identical conditions (Johnsson, 1969). Although it is now known that subtle differences in those conditions as well as in facility characteristics and measurement techniques are responsible for the resulting forms of cavitation, there is also an implication that the inception process may interact with the final form of the cavitation (Holl and Carroll, 1979; Xu et al., 1986).

An experimental definition for the form of cavitation inception requires practical applicability. As discussed above, the actual microscopic inception process is difficult to observe. On the other hand, extensive cavitation itself may alter the flow sufficiently that the inception features are no longer revealed. Therefore, limited cavitation, the intermediate state of cavitation marking the initial stage of permanently appearing cavitation, is used to classify inception types in experiments. From an engineering perspective, there is general agreement on the forms of cavitation inception and on the association of inception with the underlying viscous flow characteristics and the nuclei environment (Arakeri and Acosta, 1979; Holl and Carroll, 1979; Acosta and Parkin, 1980).

Holl and Carroll (1979) conducted an experiment to sort the forms of cavitation according to viscous flow condition on the body and the water tunnel velocity and air content. By meas-

uring ambient conditions and conducting the experiments in one facility they were able to remove some of the uncertainty as to why different results are obtained for the same body in different facilities. They examined three axisymmetric bodies, or headforms, with known viscous flow characteristics: a hemispherical nose with laminar separation at all velocities, the Schiebe body with nonseparated flow at all velocities, and the DTNSRDC body with separation at low velocities and nonseparation at high velocities. The experiment both confirmed and organized the diverse results from preceding experiments: limited cavitation on smooth bodies appears in two broad classes, which were named *transient* and *attached* depending, respectively, on whether or not the cavity is convected by the flow.

The transient cavitation appeared in three forms: travelling bubble, travelling patch, and bubble ring. Travelling bubble and bubble ring were distinguished, in part, by the shapes of the bubbles. The travelling bubble cavities were nearly spherical whereas the bubble ring cavities were irregularly shaped. The concentration of bubbles in the bubble ring was dense, and the bubbles only appeared in the short width of the ring. Travelling bubble and travelling patch cavitation appeared to be manifestations of the same form of cavitation. Spherical travelling bubbles were observed to develop twin tails which elongated and separated from the spherical front part of the bubble as it was dragged along the body. The resulting cavitation had the appearance of the macroscopically observed travelling patch cavitation. The indication is that inception is in the form of the travelling bubble and the limited cavitation is in the form of the travelling patch. The conclusion then is that all three forms of transient cavitation (travelling bubble, travelling patch, and bubble ring) are related through their origin as discrete microbubbles. The final form of the limited cavitation depends on the evolution of those microbubbles.

The attached cavitation also appeared in three forms: bubble band, fixed patch, and developed. There are associations between the transient and attached forms of limited cavitation. The association between the travelling patch and fixed patch is obvious. There is also an association between bubble ring cavitation and bubble band cavitation, both of which only occur in the presence of laminar separation. The distinguishing features between the two forms is that discrete bubble cavities appear and disappear in a limited area for ring cavitation whereas band cavitation is characterized by a transparent surface at the leading edge of the laminar separation. The form of cavitation depends on the ambient pressure, with a small decrease transforming the form from bubble ring cavitation to bubble band cavitation.

Figure 1 shows the cavitation inception number for each form of cavitation as a function of flow speed for all three headforms, and demonstrates an association between the physical form of the cavitation and the cavitation inception number. The cavitation numbers for travelling bubble and travelling patch cavitation decrease with flow speed whereas the cavitation numbers for the other forms increase with flow speed. (The speed effects are often equated to Reynolds number effects, but it will be discussed later that changes in speed are associated with changes in other parameters as well as the Reynolds number in actual facilities.)

Figure 2 schematically associates the various forms of limited cavitation suggested by Holl and Carroll (1979). In this figure the underlined forms are transient and the italicized forms are attached. Holl and Carroll provide working definitions for transient and attached cavitation:

> "Transient cavitation is characterized by cavities which grow and collapse very rapidly when nuclei are subjected to pressure fluctuations due to turbulence and/or when traversing the low pressure region of a body. Because of its short life, transient cavitation
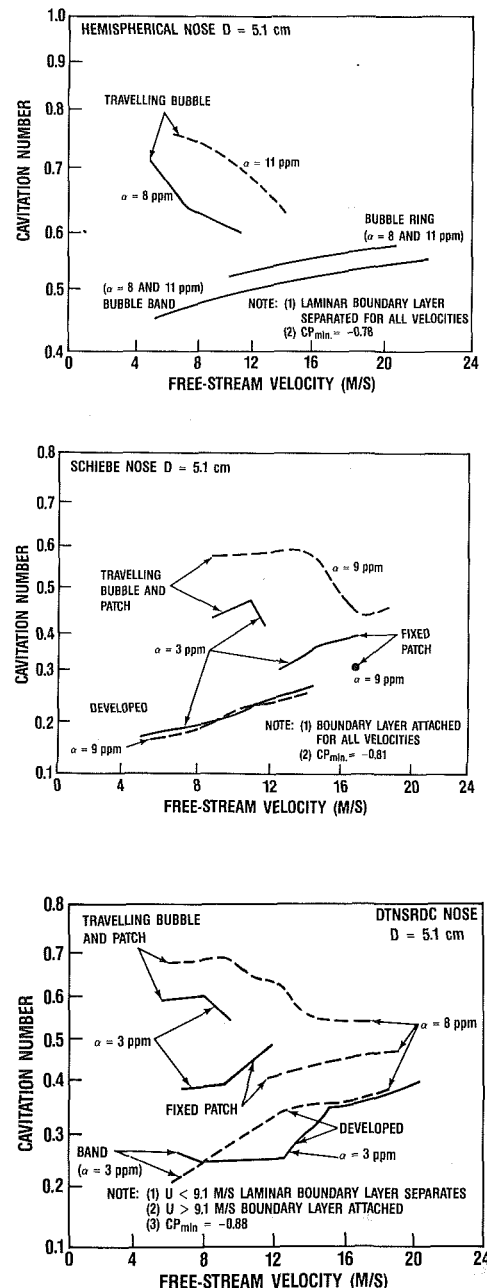
Fig. 1 Cavitation inception number for forms of cavitation inception (Holl & Carroll, 1979)

travelling bubble	$\Rightarrow$	travelling patch
$\Downarrow$		$\Downarrow$
bubble ring		*fixed patch*
$\Downarrow$		$\Downarrow$
bubble band	$\Rightarrow$	*developed*

Fig. 2 Forms of limited cavitation

is very difficult to observe under normal lighting conditions. The cavities generally appear as blurred streaks giving no indication of actual shape. On the other hand, attached cavitation usually occurs as a quasi-steady cavity which appears fixed to the body and is readily observable under normal lighting conditions."

The inference of Fig. 2 is that cavitation inception is a process by which individual microbubbles progress to the various forms of limited cavitation as the instantaneous cavitation number is decreased.

The classification schemes discussed above are directed at descriptions of limited cavitation, which is a post-inception feature of the flow. Kuiper (1985) distinguished between *micro*-cavitation and *macro*-cavitation in an attempt to isolate the actual inception event. The concept introduced by Kuiper does not modify the forms of cavitation described above as much as it describes the connection between the primitive initiation of cavitation (micro-scale event) and the visible evidence of inception (macro-scale feature). Apparently the macro-scale feature as described by Kuiper is equivalent to the limited cavitation concept described above. One significance of the perception introduced by Kuiper is an explanation of the transition from travelling bubble cavitation to sheet cavitation. He describes a process in which the bubble density increases to produce a "cloud" which then merges on the microscale level to produce an attached volume of cavitation visible on the macroscale level.

The classifications described above apply to inception on smooth axisymmetric bodies. In practice one is interested in inception for such devices as propellers, in which case more than one form of cavitation may appear simultaneously because of the different flow characteristics on the pressure and suction sides of the blades and over the tip. An absence of laminar separation on propellers reduces the number of forms the cavitation can exhibit. Billet and Holl (1979) and Ball (1984) observed only two cavitation forms on the blade faces for model propellers: travelling bubble and sheet. The three-dimensional flow produced an additional form of cavitation named tip vortex, which is related to the travelling bubble form of cavitation. The low pressures within a vortex core lead to cavitation of the core. Because the developed cavitation is evident in a "line" extending relatively far downstream, tip vortex cavitation is characterized by long time duration for the low pressures. Thus the slow process of gaseous diffusion can significantly contribute to the growth of the cavity.

The literature is predominantly concerned with classifying the various forms of cavitation inception for smooth bodies, and investigations of the underlying flow characteristics for filament cavitation in shear and other vortical flows has not been as extensive. Kuiper (1985) hypothesized a very basic micro-scale form of cavitation, described above. He based his description on observations of the cavitation inception produced by roughness elements in the leading edge regions of propellers. His description is consistent with observations of inception in flow separations (Katz, 1984). Clearly there is much to be learned about the form of cavitation inception in its first stage, before it is manifested as limited cavitation. This topic is further discussed below in the context of bubble dynamics.

V Real Fluid Bubble Dynamics

Cavitation inception is the result of a complex interplay of physical phenomena only indirectly and incompletely represented by the cavitation inception number, $C_p = (p_0 - p_v)/1/2\rho U^2$, which specifies the pressure (relative to the vapor pressure), velocity, and density conditions for the onset of cavitation in potential flow. Although travelling bubble cavitation is the most amenable form for calculation because of the assumption of discrete and noninteracting nuclei, there are many unexplained phenome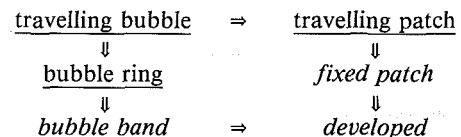na not captured in the calculations. Viscous effects in regions of high shear in the flow lead to mean pressures downstream not predicted accurately by potential flow theory, and produce local pressure minima within the flow not predicted at all by potential theory. Furthermore, the growth of a microbubble nucleus can affect the local flow

so that there is an interaction between the bubble growth and the flow conditions producing that growth. A comprehensive analytic or numerical predictive method is prohibited by the complexity of the solution to the complete Navier-Stokes equations for two-phase flow. Hence the investigations of real fluid effects have been limited to experiments.

Although it is clear from the literature that viscous effects are important for cavitation inception, it is difficult to separate the effects of viscosity, equated to changes in the Reynolds number, from the effects of nuclei availability. Most studies of cavitation inception scale effects were made with variations in velocity to obtain viscous effects. However, the critical bubble radius is a function of velocity and pressure, and hence the likelihood of cavitation even without a change in the underlying viscous flow may be changed as the critical radius of the ambient bubble size spectrum changes with the velocity.

Cavitation inception has been studied for several classes of flows to develop an understanding of the fundamental phenomena. Those flows are, in order of increasing physical complexity, around axisymmetric bodies (external and internal flows), two-dimensional non-lifting cylinders, two-dimensional hydrofoils, three-dimensional hydrofoils, and rotating propellers. Axisymmetric bodies, or headforms, have been subjected to numerous investigations to uncover fundamental viscous flow effects. On the other hand, experiments with propellers have been designed primarily to develop techniques to force a relationship between model and full scale inception numbers, and have not been used to examine closely the physical mechanisms underlying the inception process. The important advances that have been made for each of the classes of flow in the past decade are discussed in the following.

Axisymmetric Bodies. Huang (1979) conducted a comprehensive investigation of six axisymmetric headforms exhibiting either natural transition without separation or transition downstream from laminar separation. He observed the effects of Reynolds number (actually velocity) on the cavitation inception number for both travelling bubble and attached band cavitation. Travelling bubble cavitation on the naturally transitioning bodies, with no laminar separation, originated immediately downstream from the location of minimum pressure. Explosive growth was observed further downstream in the region of transition, where very large pressure fluctuations were measured on the body, and the collapse of the cavities occurred at the downstream end of the transition region. Inception for the bodies with laminar separation fell into two groups: attached band cavitation originating in the laminar separation region was produced by bodies with a large critical Reynolds number, while both travelling bubble cavitation and attached band cavitation with the latter originating at or upstream from the separation region were produced on bodies with a small critical Reynolds number. This investigation confirmed and extended the findings of Arakeri and Acosta (1973).

The location of minimum pressure is not always on the body for a viscous flow. Separations with accompanying shear layers produce local minima in the flow away from the body, and particularly in microscale vortices associated with turbulence. For example, Arakeri et al. (1978) observed bubble cavitation in the shear flow away from the surface of an axisymmetric body characterized by a long separation region on the body. At higher Reynolds numbers the shorter separation region was associated with bubble ring cavitation. The travelling bubble cavitation in the shear layer and the bubble ring cavitation were possibly the same in origin with the distinction produced by the geometry of the recirculation region.

It is concluded from the above experiments in the absence of information about the nuclei spectra, that viscous effects are factors in the determination of both the form of cavitation and the inception conditions. Features of the viscous flow that determine cavitation inception are the presence of laminar

separation, and the geometry of the separation region. Other features such as the surface roughness and bubble/flow-structure interaction contribute to real fluid effects. These features are discussed in the following.

The Laminar Separation Region. The established importance of viscous effects in determining cavitation inception led to investigations attempting to isolate the physics associated with the laminar separation region. This was done by producing recirculating flows exaggerating the separation characteristics. Specifically, separated axisymmetric flow regions were generated by backward facing steps, and measurements were made of the form of inception and the flow conditions at low ($<5 \times 10^5$) values for the Reynolds number. Arakeri (1979) investigated a headform (external flow); Ito and Oba (1984) subsequently investigated a venturi (internal flow). There were significant differences in perspective for the headform and venturi backward facing step experiments. Arakeri investigated the macroscale phenomena associated with laminar separation, whereas Ito and Oba incorporated new awareness of the effect of nuclei size to concentrate on the details of the effect of the shear on the cavitation formation. The headform and the venturi tests show that larger separations with smaller recirculation region heights are associated with smaller cavitation numbers. This result is consistent with observations of bubble ring inception associated with natural separation on hemispherical bodies (Holl and Carroll, 1979; Keller, 1979), and provides verification that the inception mechanisms are identical.

The headform and venturi backward facing step experiments produced similar forms for the cavitation inception. The observed inception for the headform was in the form of bubbles, with the origin of the inception in the shear layer whether it was close to the body (bubble ring cavitation) or far from the body (travelling bubble cavitation). The venturi produced three forms of cavitation inception described by the authors as travelling bubble, bubble "bead", and "streamer bubbles". The latter two are probably related to the bubble ring cavitation described for the headform.

The bubble beads appeared near the reattachment point, and the streamer bubbles occurred near the separation point. From the description of the bubble bead concentrations, it appears that first bubble ring then bubble band cavitation occurred as the cavitation number was reduced. The streamer bubble characteristics were more complex. Streamer bubble cavitation inception appeared in two guises: type "a," a large nucleus within the separation region with its downstream end distorted in the streamwise direction and eventually broken into microscopic bubbles, and type "b," characterized by a cloud of micron-sized bubbles in the region of separation reattachment. Somewhat confusing is the fact the the type "b" inception seems to be associated at times with a high bubble density bead cavitation and at other times with the break up of the type "a" cavitation. However, it is perfectly clear that the bubbles do in fact break up into clouds. The existence of type "a" streamer bubble cavitation was hypothetically explained by rectified diffusion causing bubble growth to the critical radius.

Roughness. Laboratory scale models characteristically feature laminar flow separation whereas the corresponding full scale prototype is operated at supercritical Reynolds numbers. The addition of surface roughness is a common method employed to stimulate transition, and has been successfully used to model cavitation inception. The reason for that success is not fully understood because the roughness is believed to be a source of nuclei as well as stimulation for flow instabilities.

At least two early experiments have demonstrated the potential importance of roughness in determining the form of cavitation inception and the cavitation inception number. Holl and Carroll (1979) observed an increase in fixed patch cavi-

tation inception number with roughness Reynolds number for axisymmetric headforms at high speeds. Billet and Holl (1979) experimentally observed that sheet cavitation originating near the leading edge of model hydrofoils may be dependent on local roughness characteristics. They based their conclusion on several factors: the increase in cavitation inception number with decreasing model chord length, the origination of cavitation near the leading edge where the boundary layer is thin, and the long streams of cavitation originating from what appeared to be point sources on the surface.

Later, Huang (1984) comprehensively investigated the effects of various turbulence stimulators on three headforms. The objective of the investigation was to determine if turbulence stimulators could effectively cause reproduction of full scale transition and produce a cavitation number equal to the negative of the minimum pressure coefficient. Huang successfully demonstrated the potential usefulness of roughness in simulating full scale cavitation inception numbers, and in comparisons with previous results from smooth headforms he showed consistency between the effect of roughness on axisymmetric headforms and the results reported by Kuiper (1979) for propellers.

Bubble/Flow Structure Interactions. Another real fluid effect is that the inception event itself may modify the flow. For example, Holl and Carroll (1979) observed that bubble band cavitation for a hemispherical headform was sensitive to the presence of travelling bubble cavitation. If a sufficient number of travelling bubbles were present, band cavitation did not occur even for lower cavitation numbers. The implication is that travelling bubble cavitation caused premature transition since it was observed that band cavitation did not occur for bodies without laminar separation. A similar characteristic was observed by Xu et al. (1986): the appearance of travelling bubble cavitation on the M-6 body caused the disappearance of the band cavitation.

Holl et al. (1987) observed apparent bubble interaction effects alleged to have caused changes in the pressure on the body such that bubble growth was limited. These apparent effects occurred when the flow was seeded with nuclei to produce an order of magnitude increase in the microbubble concentration. It is not known if the modified pressure in turn altered the underlying flow structure. However, numerical calculations by D'Agostino et al. (1988) indicate that a high density of nuclei would be expected to delay the occurrence of the minimum pressure in the flow around the body. Hence laminar separation may be delayed by the modified pressure.

Chahine (1989) calculated the interaction between a growing bubble and a tip vortex flow, and found that the initially spherical growth soon developed into an elongation followed by a tearing of the bubble. These calculations assumed that the bubble dynamics could be described by potential flow, whereas the basic flow was described by the Navier-Stokes equation. Analysis of the numerical predictions is continuing to explore the effect of the bubble growth on the vorticity distribution in the vortex.

Two-Dimensional Non-Lifting Cylinder. Ihara and Murai (1984) extended the body of empirical data for simple flows to include the two dimensional cylinder. The flow around a cylinder is more complicated than that for axisymmetric bodies because of the adverse pressure gradient on the back side. Nevertheless, the forms of cavitation inception were similar to those observed on axisymmetric bodies.

Microscale Vortex Cavitation. The results described above show that real fluid effects for cavitation inception in shear layers are not captured in a simple model of spherical bubbles passively convected by the mean flow. One deficiency in the model is that the actual nuclei grow nonspherically and in fact are often torn apart. These observations led to experiments

tempting to uncover the microscale mechanisms associated with the fine scale inception.

Arndt (1981a) reviewed results which showed that nuclei became unstable in the boundary layer while the pressures on the wall were higher than the critical pressure. The nuclei were trapped in vortices in the middle of the boundary layer. During the past decade there has been a significant effort to isolate the role of such microscale cavitation in the inception process. Keller (1979) photographically recorded cavitation inception on several axisymmetric headforms with flow separation for a range of Reynolds numbers for two levels of ambient turbulence. Cavitation inception was observed to always appear at the centers of vortices within the boundary layer. This vortex description of the cavitation inception process contrasts with the bubble description put forth by Holl and Carroll (1979) for headforms. Holl and Carroll describe travelling bubble cavitation to appear as nearly spherical cavities, and they describe bubble ring cavitation to consist of irregularly shaped bubbles that are visible briefly in the narrow region of reattachment. It is of interest to note these two contrasting descriptions (vortex vs. bubble) were developed from similar but separate experiments using hemispherical bodies of comparable diameters (3 and 5 cm) which were examined over overlapping speed ranges. Clearly there is significant information to be learned about the inception process. Ling et al. (1982) conducted a systematic investigation of the form of microscale vortex cavitation on a blunt axisymmetric headform by gradually reducing the ambient pressure to reveal the various complexities of the cavitation relative to the underlying flow structure. The initial inception was "in the form of thin cavity lines that appeared like hairs originating near the wall...the cavity lines streamed away from the wall at an angle of approximately 45 degrees." Although the severely separated flow produced by the blunt headform is not representative of flows around properly designed machinery, the experiment illustrated the physical processes probably involved in many forms of cavitation inception.

The difficulty is in isolating those processes for investigation when they are subtle yet critical for ordinary flows. During the 1980's extensive investigations were carried out at by Katz (1984) and O'Hern (1987) to identify the role of microscale vortices associated with separation in the cavitation inception process. Katz focused his investigation on the microscale cavitation processes in flows characterized by laminar separation with free shear layer transition and subsequent flow reattachment. O'Hern conducted a large scale investigation into the role of transverse and streamwise vorticity in cavitation inception in shear layers. These two studies are scientifically connected through a vaguely postulated cavitation inception mechanism associated with microbubbles and vortex/flow-structure interactions. The investigation by O'Hern had an objective similar to that of the investigation by Ling et al. (1982) discussed above: to exaggerate the flow separation to more visibly expose the fundamental cavitation inception process.

Using holography and Schlieren photography, Katz found that the origin of cavitation was in the turbulent part of the separated flow very near or in the reattachment region and that there may have been a subsequent migration of bubbles into the separation zone, momentarily filling the zone with a cloud, or into the freestream. The transition from microscopic bubble inception to band cavitation was found to occur rapidly, spreading immediately around the body. Measurements of the instantaneous pressure in the reattachment zone were consistent with observations of cavitation inception very near the zone, and indicated that the flow was in tension.

Katz' results apparently stimulated O'Hern (1987) to further experimentally isolate the physics of cavitation inception in the coherent flow structures of the sheared mixing layer. O'Hern used a sharp-edged plate normal to the flow in a water tunnel

to produce a massive separated flow region bounded by a strongly sheared mixing layer. The large size of the experiment permitted examination of the details of the inception process. The flow downstream from the plate was characterized by two distinct types of vortices: the primary spanwise vortices and the secondary streamwise vortices "connecting" the spanwise vortices. Whereas the primary vortices were the larger features in the underlying flow, cavitation inception occurred in the smaller and more intense streamwise vortices.

The interaction of the microbubble nuclei and the underlying viscous flow may be quite complex if the underlying flow is dynamic. Pauley (1988) has computationally shown that "steady" two-dimensional laminar separation experiments may actually be unsteady. Her research identifies periodic shedding from the separation detachment location such that if a bubble were present the flow periodicity and the bubble oscillation could couple in motion. Kuiper (1985) has commented on the possibility of unsteady circulation within the cavity, causing pressure gradients leading to cavitation inception.

Two-Dimensional Hydrofoils. The above discussion was concerned with nonlifting bodies. Many cavitation problems are associated with lifting surfaces on rotating machinery such as propellers. The literature in the area of propeller cavitation is very extensive, and there will be no attempt here to review this specialized topic. However, in the past decade Van der Meulen (1980) and Van der Muelen and Yuan-Pei (1982) identified the fundamental cavitation inception phenomena on two-dimensional hydrofoils and related them to observations of cavitation inception for axisymmetric headforms. This research is appropriately included here.

Van der Meulen (1980) proposed to classify forms of cavitation according to observations with hydrofoils rather than with axisymmetric bodies on the grounds that cavitation is most often in practice associated with lifting surfaces. The Reynolds numbers of the model hydrofoils, based on chord length, were approximately the same as for the axisymmetric bodies, based on diameter. Therefore it was expected that viscous effects should be of the same order of magnitude. In general the examined hydrofoils exhibited four forms of cavitation, which were named travelling bubble, sheet, band, and cloud cavitation. All four forms of inception were strongly dependent on the angle of incidence of the hydrofoil, and were associated with the viscous characteristics of the flow. The underlying viscous flow changed from laminar attached to turbulent detached with increasing angle of incidence. Travelling bubble cavitation occurred for laminar flow, sheet cavitation for the laminar separation flow, and band cavitation for the turbulent separation shear layer. Cloud cavitation occurred when the turbulent separation shear layer completely detached from the hydrofoil without subsequent reattachment. The cavitation inception number and the slope of the inception number as a function of Reynolds number generally increased as the form of cavitation changed from travelling bubble to cloud. On the one hand, travelling bubble cavitation had the lowest inception number and was independent of Reynolds number, and on the other hand, cloud cavitation at large incidence angles (where the cavitating structures appeared thread-like) exhibited an inception number increasing without bound as a function of the Reynolds number. The fact that bubble cavitation inception was independent of speed contrasts with the results, discussed above, for axisymmetric bodies in which case it decreased with increasing speed. The appearance and speed dependency of cloud cavitation is consistent with observations for axisymmetric bodies with very blunt noses or with backward facing steps.

The cloud cavitation was associated with transition to turbulence in the shear layer away from the hydrofoil. Vortices appeared as a consequence of the transition, and their cores served as low pressure sites for cavitation inception. The phys-
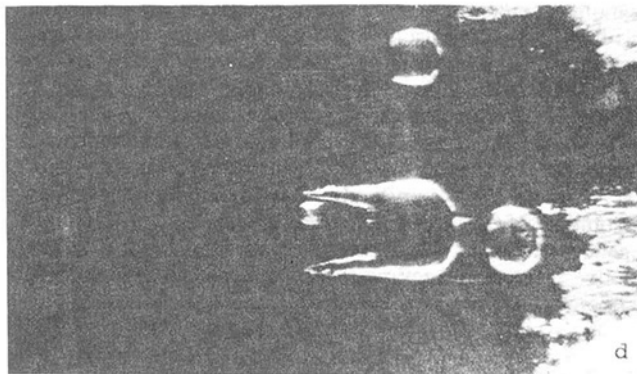
Fig. 3   Photograph of distorted bubble with twin tails (Van der Meulen, 1980)

ical form of the inception is described as sometimes having a thread-like appearance. These observations are similar to those obtained with axisymmetric bodies (Keller, 1979; Ling et al. 1982). For both two-dimensional hydrofoils and axisymmetric bodies, the mechanism of inception of reattaching flow seems to include greatly distorted bubbles, whereas the apparently more intense vorticity associated with nonreattaching flow leads to vortical cavities.

Van der Meulen sometimes observed bubble distortion for travelling bubble cavitation in which bubbles exhibited twin tails streaming from the bubbles (see Fig. 3). This type of distortion was also observed by Holl and Carroll (1979) for axisymmetric bodies and by Ito and Oba (1984) for a backward-facing step on an axisymmetric body. The distortion of the bubble is visually consistent with the presence of horseshoe, or necklace, vortices in the flow, with the bubble in the loop and the tails entrained in the vortex legs. Distortion may also be caused as the bubble is dragged through the boundary layer by the higher velocity outer flow, producing trailing vortices entraining the bubble as the boundary layer vorticity is rolled up and turned in the streamwise direction.

Van der Meulen also observed streak and transient spot cavitation on the two-dimensional hydrofoils at high speeds and low angles of incidence. He attributed these to roughness elements and to flow anomalies, or structures, such as bursts. These observations are consistent with findings for axisymmetric bodies described earlier in this paper.

Later, Van der Meulen and Yuan-Pei (1982) investigated the use of roughness to reduce scale effects for cavitation inception on model hydrofoils. They found that distributed roughness stimulated early transition to turbulence but had no effect on the cavitation inception number or the form of cavitation unless the roughness elements themselves produced nuclei through microscale cavitation. Van der Meulen raised the possibility that transition to turbulence may not be sufficient to modify cavitation inception, and that it is necessary that small nuclei exist inside the boundary layer. He observed that cavitation on the roughness elements would produce the required nuclei.

Kuiper (1979) had already uncovered what appeared to be the role of roughness in producing nuclei. This striking finding at once provided the clue for valid model testing techniques of prototypes and at the same time greatly compounded the physical complexity of the cavitation inception process since a new length scale corresponding to the roughness was introduced. Huang and Shen (1986) review the literature on roughness to stimulate turbulence and conclude that a critical roughness Reynolds number is required to minimize the difference between the cavitation inception number and the negative of the computed minimum pressure coefficient.

Van der Meulen and Yuan-Pei (1982) also found in their experiment that vortices shed from a wire upstream from the hydrofoil penetrated the boundary layer and promoted pre-

mature cavitation. The significance of this finding is in the mechanism of microscale cavitation inception. Keller (1979) found that free stream turbulence (vortices) produced earlier cavitation inception on axisymmetric headforms; however, he attributed the mechanism to a change in the underlying viscous flow characteristics rather than to cavitation inception in the turbulence element itself.

Three-Dimensional Hydrofoils. The underlying viscous flow on a three-dimensional hydrofoil is more complex than that on a two-dimensional hydrofoil. The most obvious distinguishing feature is the presence of the tip vortex, formed at one end of the hydrofoil by the spanwise roll-up of the boundary layer. The spanwise flow in addition produces numerous complex laminar and turbulent separation characteristics not present on the two-dimensional hydrofoil. Some of those characteristics are most evident at the attached end of the hydrofoil.

Billet and Holl (1979) investigated cavitation inception on three families of finite span hydrofoils. Within each family there were four geometrically similar hydrofoils of different chord lengths, and separate effects of speed and size were investigated in varying the Reynolds number. Speed and size determine not only the viscous characteristics of the flow, but also may affect the bubble dynamics in different ways as discussed above. Some trends were observed, but they were not common to all three families, and there is a need to obtain additional data. The separate effects of size and speed in the Reynolds number, and the indirect effects on critical radius and bubble growth duration, remain an issue.

Rotating Propellers. The flow around a propeller blade is complex not only because of the three-dimensional effects produced by the finite span described above, but also because of the induced centripetal forces. General analytical or numerical techniques have not been developed and hence predictions of full scale cavitation are necessarily extrapolated from model propeller tests. Because model propellers are tested at low Reynolds numbers, viscous effects are dominant and the features described above for the flow around simple axisymmetric bodies and two-dimensional hydrofoils appear in complex three-dimensional forms.

Kuiper (1979) studied bubble and sheet cavitation inception on two specially designed model propellers. He conducted his experiment in the NSMB depressurized towing tank where microbubble nuclei were essentially nonexistent. Using roughness particles attached to the leading edge of the blades to trip the boundary layer, and an electrolysis system for microbubble nuclei generation he was able to examine both viscous and nuclei effects on cavitation inception. Kuiper found that the quiescent tank water contained insufficient nuclei to cause either bubble or sheet cavitation. By injecting nuclei, sheet cavitation inception was produced on the propeller blades providing the flow was separated and the bubbles not so large as to be deflected by pressure gradient screening effects. The application of roughness produced sheet cavitation for a local pressure close to the vapor pressure, implying an early transition with large pressure fluctuations and hence insignificant scale effects. Roughness also produced bubble cavitation by the self-generation of susceptible nuclei. The appearance of these two forms of cavitation inception is consistent with observations for axisymmetric bodies. A principal difference is found in the relationship of the cavitation inception number to the model forward speed. For axisymmetric bodies the attached cavitation inception number increased with speed, whereas for the propeller it decreased. As discussed above, there are other than viscous effects when speed alone is used to change the Reynolds number. One of those is a change in the finite time duration of the bubble in the propeller blade pressure gradient. This effect may have been a factor in the propeller experiments.

Weitendorf (1979) compared cavitation results for a full scale propeller and a model of that propeller. He found that the full scale propeller was more susceptible to cavitation, and explained the difference by considering the higher negative pressures and longer time duration of the nuclei in the low pressure region for the full scale propeller. The higher negative pressures lower the critical bubble radius, and the longer time duration permit greater likelihood of growth to instability. This explanation implicitly assumes the same nuclei size spectrum for full scale and model tests; usually the model scale environment consists of a less abundant spectrum than that observed full scale.

Tip Vortices. Tip vortex cavitation is a feature of lifting surfaces related to the circulation associated with the lift force distribution. Hub vortex cavitation and blade-shroud gap vortex cavitation are also to be included in this form of cavitation. Tip vortex cavitation is little understood notwithstanding the enormous effort that has been expended to understood it. The underlying flow is complex, exhibiting viscous three-dimensional separations and undoubtedly significant unsteadiness. Platzer and Souders (1979) conducted a literature survey in which they found that most research efforts were directed at the wake of the vortex from an aeronautical perspective that excluded cavitation. Later, Souders and Platzer (1981) conducted experiments in which roughness on the body was found to be effective in suppressing tip vortex cavitation.

A comprehensive series of experiments was conducted at the St. Anthony Falls Hydraulic Laboratory to measure the tip vortex velocity field and cavitation characteristics for an elliptic planform wing. The results (Arndt et al., 1985; Arndt et al., 1986) showed effects of angle of incidence on the vortex core growth and demonstrated vortex size reduction with increasing Reynolds number. Bubble growth in the boundary layer roll-up process, and in some cases the dependence of the cavitation number on angle of incidence and Reynolds number were explained by any one of several ad hoc empirical models.

Billet and Holl (1979) have observed a steady increase in the tip vortex cavitation inception number with increasing Reynolds number for both rectangular and elliptic planform hydrofoils. In a more comprehensive investigation, Arakeri et al. (1986) conducted extensive tip cavitation inception experiments with an elliptic planform wing, found three Reynolds number regimes for the dependence, and postulated that the regimes were distinguished by the sources for critical nuclei. At low Reynolds number the cavitation inception number decreased with increasing Reynolds number, and at high Reynolds number the cavitation inception number increased with Reynolds number. These opposing trends were identified with the source of available nuclei, attributed to gas coming out of solution for low Reynolds numbers (and low cavitation inception numbers) and to micron-sized free stream nuclei at high Reynolds numbers (and high cavitation numbers). These observations are consistent with those of Billet and Holl (1979) where there was overlap in the Reynolds numbers.

Galdo and Katz (1988) used flow visualization and surface pressure measurements to identify the detailed formation of the tip vortex for a blunt tip hydrofoil. Multiple vortex structures were observed in the region of the blunt tip. The effect of surface roughness had a small effect on the vortex size and location, yet produced substantial reduction in the vortex strength.

Observations of multiple vortices have also been made with elliptic planform hydrofoils. Higuchi et al. (1989) report a measured asymmetry in the tip vortex velocities that is explained by the presence of a secondary vortex presumed to be produced by the laminar separation region near the tip. In the same experiment the observation was made that the axial velocity of the vortex core was less than free stream for low Reynolds numbers and greater than free stream for large Reynolds numbers. The reasons for this difference were not determined because of the limited measurements made. These recent results demonstrate the complexity of the underlying flow in which the cavitation inception process occurs.

Very recent three-dimensional holographic measurements of the vortex core velocity field by Green and Acosta (1989) show that the vortex core is unsteady. This finding complicates understanding of the inception process and its control. The time-dependent features will have to be determined from the perspective of low frequency quasi-deterministic unsteadiness with a superimposed random turbulence unsteadiness.

VI Nuclei and Inception

Although nuclei are thought to consist of microbubbles, solid particles, and organisms, it is believed that microbubbles are by far the dominant source of nuclei in natural waters such as rivers and oceans (Billet, 1985). Furthermore, efforts to increase nuclei in the laboratory are directed at techniques that increase the microbubble content of the fluid. Therefore this review is concerned principally with microbubbles as nuclei. It will be shown that nuclei spectra are a determinant of the form as well as the conditions of cavitation inception.

The nuclei spectrum is the *distribution*, according to size, of the concentration of nuclei, where the concentration is expressed in number per unit volume. One parameter that governs the spectrum is the air content of the water, which technically consists of the sum of the dissolved air content and the undissolved, or free, air content. Clearly the free air content is related to the total volume of the nuclei, and the dissolved air can come out of solution to form free air if the ambient pressure is lowered. Instruments that measure total air content, such as the van Slyke manometer, are ineffective in determining the amount of free air. Statements concerning the total air content in experiments generally lack information critical for determining the free air or, more importantly, the nuclei content.

Although much of the research into the sources for the inconsistent cavitation results obtained worldwide for the ITTC body (Johnson, 1969) concentrated on viscous flow effects, there was evidence that nuclei characteristics were also a significant source for the discrepancies. The decade of the 80's was a period of concentrated effort to characterize the importance of nuclei characteristics, and specifically the bubble size spectrum, to the cavitation inception process. Nevertheless, understanding of the relationship between the nuclei size spectrum and the dynamics of cavitation inception remains rudimentary.

The potential importance of nuclei characteristics is found in bubble dynamics theory. For a spherical microbubble there is a strongly nonlinear relationship between the original bubble size in the ambient fluid and its ultimate growth as it passes through a pressure field. Examination of the bubble dynamics equation shows that there may be other nuclei characteristics in addition to size affecting inception, such as nonspherical geometry, surfactant, and gas and vapor transport, as well as the internal flow inside the bubble.

A graphic example of the effect of nuclei is found in the results of studies conducted in two water tunnels at the California Institute of Technology (Katz, 1978). In those studies, the Low Turbulence Water Tunnel (LTWT) was characterized by an ample supply of nuclei, whereas the High Speed Water Tunnel (HSWT) used a deaerator and a resorber resulting in very few nuclei. Characteristically, cavitation numbers in the HSWT were lower than those in the LTWT, indicating that a certain concentration or quality of nuclei was required to obtain cavitation inception. Furthermore, the form of cavitation differed between two tunnels. Travelling bubble cavitation was observed in the LTWT whereas attached cavitation was observed in the HSWT. This difference in both the cavitation

inception number and the form of cavitation has been attributed to the relatively small number of free stream bubbles in the HSWT. This result is consistent with other observations that many nuclei are required for transient cavitation but only a few are required to initiate attached cavitation (Kuiper, 1985).

Facility Characteristics. Different facilities can be characterized by substantially and significantly different nuclei size spectra. In water tunnels the spectrum can be affected by the use of a deaerator to remove air and a resorber to dissolve free air. On the other hand, the recirculating flow in a water tunnel containing remnants of cavitation increases the nuclei concentration. With quiescent towing tanks the saturated liquid contains relatively few nuclei (Peterson, 1972). This is especially true of tanks where the free surface pressure has been reduced below atmospheric to stimulate cavitation.

Ling et al. (1982) used a light-scattering technique to measure the nuclei content in three water tunnels at David Taylor Research Center. The 12-inch tunnel had a by-pass deaeration system, the 24-inch tunnel had an on-line free surface vacuum deaeration system, and the 36-inch tunnel had both a deaerator to pull air out of the water and a resorber to drive remaining free air into solution. Nuclei concentration was found to increase with increasing air content and to decrease with increasing static pressure. The use of the resorber significantly depleted the available nuclei and had the effect of reducing the cavitation inception number.

The nuclei size spectrum in a given facility is also dependent on the facility operation procedure. Keller (1979) experimentally investigated the effect of facility operation procedure in a recirculating water tunnel. Two measurement procedures were considered, both of which are reasonable techniques for water tunnel cavitation inception studies. In procedure A cavitation was maintained on the model for a short period of time prior to conducting the cavitation inception test. In procedure B the tunnel was pressurized to remove bubbles and to force air into solution prior to conducting the cavitation inception test. Procedure A maximized the number of nuclei, whereas procedure B minimized the number of nuclei. Keller found that the increase in the cavitation inception number from procedure B to procedure A for travelling bubble inception on axisymmetric bodies with flow separation was as much as a factor of two, depending partly on the turbulence level in the ambient flow. It appears that additional nuclei produced by facility operation procedure couple with increased turbulence (vortices) to increase cavitation susceptibility.

Air Content and Nuclei Spectra. The relationship between air content and nuclei size spectrum is not well defined, but there have been rules applicable to water tunnels established from observations that seen to be reliable at least for a given facility. An enlightening investigation of the effect of free air content and total air content on travelling bubble cavitation was conducted by Peterson (1972). He found that the free gas content as determined by holographic measurement of bubble sizes increased with the total air content. Furthermore, both the concentration and the mean size of the microbubbles increased with total air content even as the liquid became supersaturated with air. These important findings established a relationship that seemed to indicate that total air content, easily measured with a van Slyke manometer apparatus, could be a single parameter specifying the nuclei size spectra. However, many investigations since then have shown that other parameters need also to be controlled (Katz and O'Hern, 1983; Billet, 1984; Shen et al., 1984; Pan and Zhang, 1986).

It is concluded from these results from various facilities that the spectrum is related to the air content, with an increase in content producing larger bubble concentrations, that the exact relationship between facility operation parameters and the nuclei content appears to be unique to each facility, and that there is inconsistency in the reported effects of pressure on the nuclei spectrum.

Nuclei Control. Implied in the wide variations in the effect of total air content on the nuclei spectra observed for different facilities and operation conditions is the possibility of controlling the nuclei spectrum both to measure the effects of changes and to produce experimental repeatability. Nuclei control requires independent variability in both the size-spectrum concentration and distribution. Lecoffre (1987) discussed practical methods to control water quality in hydrodynamic facilities. He stated that it is necessary to control both the dissolved air and the free air, and thus it is necessary to first degas the water and then to inject "artificial" nuclei.

Facilities incorporating a quiescent body of water in which cavitation is produced by lowering the free surface pressure are characterized by a dearth of microbubble nuclei. In this case various methods are incorporated to locally produce sufficient nuclei to initiate cavitation. For example, Kuiper (1979, 1985) uses roughness elements and bubble generation by electrolysis to produce nuclei. Facilities in which resorbers are used to force air into solution, e.g., the 36-in water tunnel at David Taylor Research Center and the High Speed Water Tunnel at The California Institute of Technology, are also characterized by very low nuclei concentrations and a spectrum with a small mean bubble radius. An advantage of such facilities is that there is an opportunity to experimentally control the nuclei size spectrum by injection of air.

Nuclei Measurement and Water Quality. Measurements of nuclei size spectra require that individual bubbles be counted according to size. At least part of the problem in assessing nuclei content is attributed to the different methods of measurement. Billet (1985, 1986) recently reviewed the various devices and techniques used to measure nuclei.

The need to discriminate between the nuclei size spectrum and the cavitation susceptibility follows from the recognition that the cavitation event is a dynamic result of passing the nuclei spectrum through a pressure field. D'Agostino (1987) investigated the requirements for, and the operational characteristics of, a venturi cavitation susceptibility meter. One problem in interpreting results is that the cavitation is the result of the prescribed flow through the venturi; that flow may not be an accurate representation of the flow for other situations. Shen and Gowing (1986) discuss the relative importance of the venturi characteristic time and the bubble characteristic response time. They explain the practical difference between static and dynamic bubble response to a venturi pressure field, and are led to assume cavitation inception when the gaseous bubble has grown to 10 times its original size. Their analysis concludes that the venturi excites only a portion of the nuclei spectrum. These results lead to a need to define a standard venturi cavitation susceptibility measurement. More importantly, the results demonstrate a need to understand in any flow the selection process by which the underlying hydrodynamics excites the nuclei spectrum.

Keller (1984) proposed a different device that produces a vortex in which the cavitation event takes place. The rationale for this device is that inception often occurs in vortical fluid elements and therefore it better reproduces actual cavitation inception dynamics. Keller argued that predictions of cavitation inception require exact knowledge of the tensile strength of the water which he refers to as water quality. He conducted experiments with axisymmetric bodies and compared results using vapor pressure and then critical pressure in calculations of the cavitation inception number. The critical pressure was determined using a calibrated vortex flow to simulate real fluid mechanisms in the production of cavitation inception. The cavitation inception numbers computed with the actual critical pressure exhibited much less scatter than those computed using

vapor pressure. This experiment underscores the necessity of knowing the details of the cavitation process, especially if real fluid effects are significant.

Given the nuclei size spectrum and the cavitation susceptibility, it still cannot be determined for certain which nuclei are associated with the inception in the flow under study. In fact, it is not easy to discern whether the particle is bubble, solid, or organism. Pan and Zhang (1986) found in their holographic measurements of the nuclei spectrum in the Cavitation Mechanism Loop at the China Ship Scientific Research Center that a particulate filter reduced the concentrations in the nuclei spectrum by two orders of magnitude. Similarly, Billet (1985) reported that nuclei measurements for a lake showed very large concentrations of solid particles. However, employment of a venturi cavitation susceptibility meter determined that the active nuclei had a concentration several orders of magnitude smaller, and it was concluded that the solid particle nuclei did not appear active. O'Hern (1987) used holography to measure the population of nuclei in the ocean and obtained similar results: the number of solid particles and organisms greatly outnumbered the number of microbubbles. O'Hern discussed the need to understand the dependence of cavitation inception on the specific kind of nucleus, with special focus on the role of solid particles and gas-generating organisms. This problem of identification of the active nuclei is persistent, having been underscored much earlier by Peterson (1972).

Dynamic Nuclei. The ambient nuclei size spectrum responds nonlinearly to, and sometimes interactively with, the pressure field. The very characteristics of the bubble response to the pressure depend on the initial bubble conditions. Small changes in those initial conditions can produce startlingly different responses in the bubble growth (Parkin and Baker, 1986). Gaseous growth becomes unstable to vaporization of the liquid under certain conditions depending in part on the nucleus size. The inertial growth of the bubble produces a delay in the actual nonlinear growth of the bubble. Prediction techniques have for the most part concentrated on the evolution of individual bubbles contributing to travelling bubble cavitation. For example, Jiandong et al. (1989) have integrated the spherical bubble dynamics equation to show that the critical pressure and its duration select portions of the nuclei spectrum for inception. The dynamics of travelling bubble cavitation inception are best described in terms of the passive underlying flow, either nonseparating or characterized by a laminar separation region.

Nonseparating Flow. Peterson (1972), working with an axisymmetric body exhibiting inception upstream from the location of separation, found that the number of nuclei visually undergoing cavitation inception, as determined by bubble size, increased proportional to the total air content. As described above, the concentration and mean size of the bubble spectrum increased with the total air content, indicating that more and larger bubbles were potentially available for inception. However, cavitation inception as determined at the same time by the rate of acoustic events generated by bubble collapse in the downstream pressure recovery region was independent of total air content above approximately 0.8 saturation. Since gaseous bubbles do not implosively collapse, the indication was that the large bubbles present near saturation were mostly gaseous. The vaporous growths were apparently limited to a finite portion of the bubble size spectrum. The message is that large rapidly growing bubbles do not necessarily indicate cavitation inception.

Analytic prediction techniques for travelling bubble cavitation inception, assuming spherical bubbles dynamically convected in a passive potential flow, have reached a high level of maturity. Ling et al. (1982) comprehensively provided a mathematical technique for gaseous cavitation for p_v much

smaller than p_∞, in which case cavitation inception is a fast process attributable to the direct expansion of the air filled microbubbles. They found that surface tension and time duration of the low pressure are strong controls for the cavitation inception event. For very small microbubbles the condition for inception is very distinct and bubbles below a critical size will not blow up. Large bubbles, which have a slower rate of growth than do small bubbles, will not blow up if the low pressure duration is too small for their reaction. A conclusion from the study is that models operated at low velocity will be selective of a narrow range of bubble sizes of cavitation inception, whereas a full scale prototype with large dimensions and operated at high velocity, will cavitate over the whole spectrum of bubbles. The applicability of the technique developed by Ling et al. is limited by the constraint of mechanical expansion of the gas microbubble, a constraint which ignores the presence of vapor and, in effect, excludes explosive growth of the bubble due to vaporous instability.

Dreyer (1987) found in both experimental observations of travelling bubble growth and predictions of the dynamic growth using the Rayleigh-Plesset equation, that the maximum growth is insensitive to the initial diameter of the bubble. Consequently a large portion of the ambient microbubble size spectrum was found to contribute to the cavitation inception events. On the other hand, there may be size limitations attributable to gas bubble concentrations. Numerical calculation of the dynamics of a bubble cloud undergoing pressure changes due to spatial convection have shown that the growth of individual bubbles is related to the bubble concentration (D'Agostino et al., 1988). The calculations revealed a substantial reduction in the maximum bubble size as the concentration was increased, the implication being that there may be an upper growth limit for a high density of nuclei convected into the headform low pressure region. This numerical result is consistent with the experimental results of Dreyer (1987).

Laminar Separation. The discussion above implies that the travelling bubble cavitation inception is characterized by at most a deformation of the gas- and vapor-filled bubble, and this is the characterization under some conditions. But under conditions of laminar separation the bubble is torn apart, often disintegrating into a cloud of micron-sized remnants. For example, Ito and Oba (1984), interpreting experimental results, postulated a process in which the small nuclei grow by gaseous diffusion until they are stretched and broken apart by the shear at the edge and the fluctuating pressures in the reattachment region of the separation. They postulated that rectified diffusion caused gaseous growth of critical-sized bubbles in separations with large heights, with subsequent vaporous growth and the appearance of large cavitation bubbles. On the other hand, laminar separations with small heights were believed not to permit large gaseous bubble growth, resulting in lower cavitation inception numbers and the appearance of a bubble cloud as the bubble was torn apart. A significant finding of those studies was that the details of cavitation inception in a strong shear are more complex, due to bubble break up, than can be represented by a passive travelling bubble model. Brennen and Ceccio (1989) have photographically recorded bubble break-up on the side of the bubble nearest the surface and downstream from the laminar separation on an ITTC headform. The cause and process of the break-up are being pursued.

Parkin and Baker (1986) attempted to analytically and parametrically describe the cavitation inception event. Although the objective was to account for cavitation inception in the form of bubble ring cavitation, the analysis concentrated on the nonlinear growth of the microbubble upstream from laminar separation. In the hypothetical process the bubble grows to an unstable size immediately prior to entering the laminar separation where it is enlarged, possibly by rectified diffusion,

and subsequently torn apart by the shear layer at the edge of separation.

Arakeri et al. (1984) discussed evidence that the nucleus in a laminar separation region may respond such that the effective spectrum is quite different than that in the free stream. They cite investigations in which liquid that readily cavitates in the flow separation region did not cavitate under strong tension in the absence of the separation. Katz (1984) holographically measured a larger concentration of bubbles in the separation region than in the free stream.

Effects of Nuclei on Cavitation. Numerous experiments have shown that the nuclei size spectrum strongly affects the cavitation inception number (Huang, 1979; Holl and Carroll, 1979; Billet, 1984; Tsai et al. 1989). The conclusion from these experiments is that air content seems to have a small mixed effect on attached and ring cavitation inception, but has a significant effect on transient (except ring) cavitation inception with the cavitation inception number increasing with air content.

Additional investigations have shown that the nuclei content can affect the form of cavitation inception as well as the cavitation inception number. Kuiper (1985) observed that there is always a requirement, even with attached flow, for a minimum concentration of nuclei for inception to occur. In some instances, it is necessary to generate the nuclei using roughness on the body surface. Kuiper speculated that a sparse concentration of nuclei can delay inception so that when it does occur, the flow separation is no longer present. In this manner the form of the inception is bubble cavitation rather than the sheet cavitation otherwise expected. There are several reports of bubble concentration affecting the form of inception (Huang, 1979; Ling et al. 1982; Xu et al. 1986).

Attempts have been made to relate the nuclei size spectrum to the cavitation inception using simple approximations. Holl and Carroll (1979) employed the critical radius calculation for spherical bubbles to estimate the original radius of the bubbles in the ambient flow for cavitation inception on a nonseparating (Schiebe) body. They found that increasingly smaller bubbles initiated cavitation as flow velocity was increased; that is, the size of the measured ambient bubble that eventually cavitated was found to be smaller than predicted from a gas law correction accounting for ambient static pressure changes. It is not clear if this trend is attributed to properties of the nuclei or to interactions of the nuclei with the flow around the body. This result indicates that a larger portion of the spectrum is available for inception (see Ling et al., 1982) than predicted from simple theory. The discrepancy may be found in some growth-limiting constraint on the bubbles.

Dreyer (1987) conducted a detailed investigation of the Schiebe headform following the work by Holl et al. (1987). Dreyer's focus was on the growth of the cavitation bubble for various nuclei concentrations and tunnel speeds. His objective was to provide a link between the ambient microbubble spectrum, the resulting travelling bubble size spectrum, and the cavitation inception number. The significant findings of the investigation were that air content is an important parameter determining travelling bubble cavitation inception, and that there is a level of air content above which the cavitation inception number is insensitive to total air content.

Experimental investigations have also been directed at the effect of air content on microscale vortex cavitation. Keller (1979) conducted experiments in which the gas content played a minor role in increasing the cavitation inception number. The effect of the gas content increased with the bluntness of, and the severity of flow separation on, the headform. However, the effect of air content on the detailed inception process could not be determined because the nuclei concentration and size spectrum were not measured.

It has been described above that tip vortex cavitation may be strongly dependent on gas content because of the long duration times for the characteristic low pressures. Billet and Holl (1979) observed a steady increase in the cavitation inception number as the air content was increased from 2.8 to 9.9 ppm. Arakeri et al. (1986) observed the tip vortex cavitation inception was associated with low inception numbers for low Reynolds numbers and with high cavitation inception numbers for high Reynolds numbers. The low cavitation inception numbers were postulated to be associated with nuclei produced by gas coming out of solution. Support for this explanation was obtained by calculations. In this case the cavitation inception number increased with increasing air content. On the other hand, air content had little effect on the cavitation inception number for high cavitation inception numbers (high Reynolds numbers). These results leave unclear the actual state of the tip vortex as to whether it is dominantly gaseous or vaporous. Detailed measurements or observations of the inception mechanics were not obtained, and those details remain not understood.

Bubble Generation by Roughness. A sparse concentration of ambient nuclei and the effects of bubble screening, especially in the absence of laminar separation, can lead to the necessary use of surface roughness to generate nuclei (Kuiper, 1979, 1985; Van der Meulen and Yuan-Pei, 1982). The rationale is that the roughness elements locally produce nuclei by perhaps gaseous growth. This mechanical process is related to the observed increase in cavitation inception number as a function of Reynolds number by speculation that a thinner boundary layer increases the bubble generation effectiveness of the roughness elements.

VII Perspective on Pressure

The dynamic interaction between the incoming nuclei, with a wide range of sizes, and the underlying viscous flow is potentially significant because of modifications both of the local pressure forcing bubble growth and of the local shear flow producing bubble deformation. In the context of bubble dynamics, the "local" pressure is the Lagrangian pressure associated with the travelling nucleus. Knowledge of the spatial distribution of pressure statistics such as the time average and the root mean square may not be sufficient to predict the microscale cavitation event.

Arndt (1981a) presented clear arguments supporting the need to understand the relationship between turbulent pressure fields and cavitation inception. He identified two basic factors, the turbulence frequency spectrum and the amplitude probability density as they relate to bubble dynamic response and bubble critical radius. He noted that both factors are expected to change as the scale of the flow increases. That is, larger Reynolds numbers produce a wider frequency spectrum with more likelihood of a negative pressure threshold, and should be associated with flows more likely to cavitate for a given nuclei spectrum. Arndt reported that there is little information relating cavitation inception and turbulent pressure field data. The situation has changed some since Arndt's review, but there remains much to be learned.

There have been three notable investigations during the past decade attempting to uncover pressure fluctuation phenomena relevant to cavitation inception. Huang (1979) measured unsteady surface pressures associated with cavitation inception at transition. Holl and Carroll (1979) observed underlying flow instabilities associated with transition in the laminar separation shear layer. And O'Hern (1987) measured the Lagrangian pressure leading to cavitating vortex structures in free shear flows. Each of these investigations probed an aspect of the effects of unsteady pressure, but understanding of the physical processes associated with bubble growth remains rudimentary.

The fact that turbulent flow structures cause cavitation in-

ception in the flow field rather than on the body surface (as predicted by potential flow theory) was reported as early as 1968 according to Arndt (1981a). Katz (1984) measured instantaneous pressures on the surface of cavitating headforms and determined for the configurations he investigated that inception occurred in the flow and not immediately adjacent to the body surface. This finding means that the instantaneous pressure in the flow away from the body was less than vapor pressure sufficiently long to produce an instability in bubble growth, at the same time that the fluid was not under tension on the headform surface. This finding underscores the importance of the instantaneous pressure fluctuations in producing cavitation inception, at least in some cases.

A novel technique utilizing small bubbles as Lagrangian pressure sensors has been employed by Ooi and Acosta (1983) and by O'Hern (1987) to measure fluctuating pressures in a jet and in a mixing layer, respectively. The method apparently requires refinement to solve details of the flow, and has not been adapted to measurements of the time duration of pressure fluctuations. It does, however, indicate the local pressure deviation with very high spatial resolution. Instantaneous pressures in the jet were up to 1.6 times the dynamic pressure with root mean square pressures a little more than 0.6 times the dynamic pressure. The fluctuations in the mixing layer were even larger: the peak values were up to 3 times the dynamic pressure with the root mean square fluctuation about 1.5 times the dynamic pressure. Green (1989) has extended the method to the measurement of unsteady pressures in a tip vortex in which he found peak pressures equal to the dynamic pressure and root mean square pressures equal to 20 percent of the dynamic pressure.

In this section, the discussion has been about the statistics of the unsteady pressure distribution acting on the microbubble. In the previous section the discussion was on the statistics of the susceptible bubble size spectrum. One wonders, then, if it is necessary to consider a joint probability of the occurrence of an eligible nucleus and the required pressure signature. O'Hern and Acosta (1986) made this observation from the results of their investigation of cavitation inception in the turbulent shear layer downstream of a sharp-edged plate placed across the flow. They found the major contribution to the scatter in the data to be the "inherent variability of the inception process, requiring the presence of a suitable cavitation nucleus at an instantaneously occurring low pressure point in the flow." A similar conclusion was reached by Lin and Katz (1986) upon investigating cavitation inception for jets. Their largely inconsistent findings indicate that jet flows are significantly affected by minor disturbances in flow and geometry which affect the turbulent pressure field in the jet and hence have a role in the onset of cavitation.

An eligible nucleus would have the necessary dynamic characteristics to experience unstable growth in the presence of a pressure with sufficient amplitude and time duration to produce that growth. These criteria are difficult to apply to the model of full scale phenomena or to the extrapolation of laboratory findings to full scale. For example, pressure spectra on model scale would be expected to have predominantly higher frequencies than those for full scale. This has obvious implications for the required bubble size spectra relative to the required pressure spectra to reproduce cavitation inception.

VIII Trends: The Future, The Opportunities

The physical mechanisms of cavitation inception remain to a great extent unexplained notwithstanding a long history of intensive investigation. The phenomena are governed by seemingly intractable mathematics, rich in nonlinear behavior. Observation and measurement techniques are challenged by the three-dimensionality and short time duration of the event. The microscale process of inception is only beginning to be iden-

tified and understood. The decade of the 70's saw understanding of the role of viscosity, and the decade of the 80's brought forth an awareness of the role of the dynamic nuclei spectrum. Almost surely leading-edge research in the 90's will elaborate on the interactions between the viscous flow and the nuclei content to reveal the very process of cavitation inception.

There are reasons for this expectation. There is an established scientific background in the identification of the inception phenomena. Whole flow field measurement systems such as holography and particle displacement image velocimetry are making possible the observation of three-dimensional flow interactions. Video resolution will make the detailed inception event recordable, and supercomputers will enable the number crunching required to analyze the large volume of imagery data. Lagrangian pressures are being measured, and techniques to calibrate and interpret the data will become available. Methods of direct simulation, now common for turbulent boundary layers, will be developed to numerically observe the cavitation inception event.

This wedding of the physical experiment and the numerical experiment, enhanced and made useful through supercomputer technology, gives the opportunity for discovery and understanding of the microscale inception event, and for the ability to predict and hence control that event.

There are many aspects of the inception event to be studied. Differentiation of bubble and vortex inception over the range of Reynolds numbers from laboratory scale to field scale should be high on the list of objectives. Developing methods to control boundary layer flow structures should be modified, as they become available, for the control of cavitation inception.

References

Acosta, A. J., and Parkin, B. R., 1980, "Report of the ATTC Cavitation Inception Committee," *Nineteenth Meeting of the American Towing Tank Conference*.

Arndt, R. E. A., 1981a, "Recent Advances in Cavitation Research," *Advances in Hydroscience*, Vol. 12, Academic Press.

Arndt, R. E. A., 1981b, "Cavitation in Fluid Machinery and Hydraulic Structures," *Annual Review of Fluid Mechanics*, Vol. 13.

Arndt, R. E. A., Higuchi, H., and Ikohagi, T., 1986, "Tip Vortex Cavitation," see Editorial Office of Shipbuilding of China (1986).

Arndt, R. E. A., Higuchi, H., and Quadrelli, C. J., 1985, "Tip Vortex Cavitation," *Cavitation and Multiphase Flow Forum-1985*, ASME.

Arakeri, V. H., 1979, "Inception of Cavitation from a Backward Facing Step," see Morgan and Parkin (1979).

Arakeri, V. H., and Acosta, A. J., 1973, "Viscous Effects in the Inception of Cavitation on Axisymmetric Bodies," ASME JOURNAL OF FLUIDS ENGINEERING, Vol. 95, No. 4.

Arakeri, V. H., and Acosta, A., 1979, "Viscous Effects in the Inception of Cavitation," see Morgan and Parkin (1979).

Arakeri, V. H., Carroll, J. A., and Holl, J. W., 1978, "A Note on the Effect of Short and Long Laminar Separation Bubbles on Desinent Cavitation," *Proceedings of the Symposium on Measurement in Polyphase Flows*, ASME.

Arakeri, V. H., Higuchi, H., and Arndt, R. E. A., 1986, "Analysis of Recent Tip Vortex Cavitation Inception Data," *Twenty First Meeting of the American Towing Tank Conference*, Washington.

Arakeri, V. H., Milton, S. G., and Sharma, S. D., 1984, "Role of Unsteady Pressure Fields in Cavitation Inception," see Parkin and Morgan (1984).

Ball, W. E., 1984, "The Influence of Ship Wake on Propeller Cavitation," see Parkin and Morgan (1984).

Billet, M. L., 1984, "Cavitation Nuclei Measurements," see Parkin and Morgan (1984).

Billet, M. L., 1985, "Cavitation Nuclei Measurements—A Review," *Cavitation and Multiphase Flow Forum—1985*, ASME.

Billet, M. L., 1986, "The Importance and Measurement of Cavitation Nuclei," *Advancements in Aerodynamics, Fluid Mechanics and Hydraulics*, Minneapolis.

Billet, M. L., and Holl, J. W., 1979, "Scale Effects on Various Types of Limited Cavitation," see Parkin and Morgan (1979).

Brennen, C. E., and Ceccio, S. L., 1989, "Recent Observations on Cavitation and Cavitation Noise," *Third Symposium on Cavitation Noise*, ASME, San Francisco.

Chahine, G. L., 1989, "A Numerical Model for Three-Dimensional Bubble Dynamics in Complex Flow Configurations," *Twenty Second Meeting of the American Towing Tank Conference*, St. John's Newfoundland.

D'Agostino, L., 1987, "Experiment and Theoretical Study on Cavitation Inception and Bubbly Flow Dynamics," California Institute of Technology Report No. Eng. 183.16 (PhD Dissertation).

D'Agostino, L., Brennen, C. E., and Acosta, A. J., 1988, "Linearized Dynamics of Two-Dimensional and Cavitating Flows Over Slender Surfaces," *Journal of Fluid Mechanics,* Vol. 192.

Dreyer, J. J., 1987, "Free-Stream Microbubble Effects on Travelling Bubble Cavitation Inception of a Schiebe Headform," ARL/PSU Technical Memorandum 87-205.

The Editorial Office of Shipbuilding of China, 1986, *Proceedings of the International Symposium on Propeller and Cavitation,* Wuxi, China.

Galdo, J. B., and Katz, J., 1988, "The Effect of Surface Roughness on the Rollup Process of Tip Vortices on a Rectangular Hydrofoil," *1st National Fluid Dynamics Congress,* Cincinnati.

Green, S. I., 1989, "Tailored Air Bubble Determinations of Trailing Vortex Core Pressures," *Cavitation and Multiphase Flow Forum,* San Diego, ASME FED-Vol. 79.

Green, S. I., and Acosta, A. J., 1989, "Relating Trailing Vortex Cavitation Inception to Single Phase Flow Measurements," *Twenty Second Meeting of the American Towing Tank Conference,* St. John's, Newfoundland.

Higuchi, H., Arndt, R. E. A., Arakeri, V. H., and Killen, J. M., 1989, "The Structure of Tip Vortices Over a Range of Cavitation Number," *Twenty Second Meeting of the American Towing Tank Conference,* St. John's, Newfoundland.

Holl, J. W., and Carroll, J. A., 1979, "Observations of the Various Types of Limited Cavitation on Axisymmetric Bodies," see Morgan and Parkin (1979).

Holl, J. W., et al., 1987, "Effect of Microbubble Seeding on Cavitation Inception," *Cavitation and Multiphase Flow Forum—1987,* ASME FED-Vol. 50.

Huang, T. T., 1979, "Cavitation Inception Observations on Six Axisymmetric Headforms," see Morgan and Parkin (1979).

Huang, T. T., 1984, "The Effects of Turbulence Stimulators on Cavitation Inception of Axisymmetric Headforms," see Parkin and Morgan (1984).

Huang, T. T., and Shen, Y. T., 1986, "Application of Turbulence Stimulator to Reduce Scale Effect on Cavitation Inception," see Editorial Office of Shipbuilding of China (1986).

Ihara, I., and Murai, H., 1984, "Cavitation Inception on a Circular Cylinder at Critical Supercritical Flow Range," see Parkin and Morgan (1984).

Ito, Y., and Oba, R., 1984, "A Limited Role of Separation Bubble in Desinent Cavitation," see Parkin and Morgan (1984).

Jiandong, Y., Rongqiao, W., and Jianzhi, C., 1989, "Analytical and Experimental Investigations of Cavitation Inception," *Cavitation and Multiphase Flow Forum,* San Diego, ASME FED-Vol. 79.

Johnson, V. E., and Hsieh, T., 1966, "The Influence of Trajectories of Gas Nuclei on Cavitation Inception," *Sixth Symposium on Naval Hydrodynamics,* Washington, D. C.

Johnsson, C. A., 1969, "Cavitation Inception on Head Forms, Further Tests," *Proceedings of the 12th International Towing Tank Conference,* Rome.

Katz, J., 1978, "Determination of Solid Nuclei and Bubble Distribution in Water by Holography," Report No. Eng. 183-3, California Institute of Technology.

Katz, J., 1984, "Cavitation Phenomena Within Regions of Flow Separation," *Journal of Fluid Mechanics,* Vol. 140.

Katz, J., and O'Hern, T. J., 1983, "Holographic Observations of Cavitating Flows Within Regions of Flow Separation," *Eighth Symposium on Turbulence,* University of Missouri-Rolla.

Keller, A. P., 1979, "Cavitation Inception Measurement and Flow Visualization on Axisymmetric Bodies at Two Different Free Stream Turbulence Levels and Test Procedures," see Morgan and Parkin (1979).

Keller, A. P., 1984, "Scale Effects at Beginning Cavitation Applied to Submerged Bodies," see Parkin and Morgan (1984).

Knapp, R. T., Daily, J. W., and Hammitt, F. G., 1970, *Cavitation,* McGraw-Hill, New York.

Kuiper, G., 1979, *Some Experiments With Distinguished Types of Cavitation on Ship Propellers,* see Morgan and Parkin (1979).

Kuiper, G., 1985, "Reflections on Cavitation Inception," *Cavitation and Multiphase Flow Forum—1985,* ASME.

Lecoffre, Y., 1987, "Procedures and Instrumentation for Monitoring Gas Content in Cavitation Test Loops," *International Symposium on Cavitation Research Facilities and Techniques,* ASME FED-Vol. 57.

Lian, Q. X., 1990, "A Visual Study of the Coherent Structure of the Turbulent Boundary Layer in Flow With Adverse Pressure Gradient," *Journal of Fluid Mechanics,* Vol. 215.

Lin, H. J., and Katz, J., 1986, "Cavitation Phenomena in Jets," *Twenty First Meeting of the American Towing Tank Conference,* Washington.

Ling, S. C., Gowing, S., and Shen, Y. T., 1982, "The Role of Microbubbles on Cavitation Inception on Head Forms," *Fourteenth Symposium on Naval Hydrodynamics,* Ann Arbor, MI.

Morgan, W. B., and Parkin, B. R., eds., 1979, *International Symposium on Cavitation Inception,* collection of papers presented at the ASME Winter Annual Meeting, New York.

Murai, H., ed., 1986, *Proceedings of the International Symposium on Cavitation,* Institute of High Speed Mechanics, Sendai, Japan.

O'Hern, T., 1987, "Cavitation Inception Scale Effects," California Institute of Technology Report No. Eng. 183.15 (PhD Dissertation).

O'Hern, T. J., and Acosta, A. J., 1986, "Cavitation Observations in a Turbulent Shear Flow," *Twenty First Meeting of the American Towing Tank Conference,* Washington.

Ooi, K. K., and Acosta, A. J., 1983, "The Utilization of Specially Tailored Air Bubbles as Static Pressure Sensors in a Jet," ASME Paper No. 83-FE-34.

Pan, S., and Zhang, Y., 1986, "Notes of Gas Nuclei: Spectrum, Similarity Law and Equilibrium Problem, see Murai (1986).

Parkin, B. R., and Baker, B. B., 1986, "Bubble Dynamics and Cavitation Inception Theory," see Murai (1986).

Parkin, B. R., and Morgan, W. B., eds., 1984, *International Symposium on Cavitation Inception—1984,* papers presented at the ASME Winter Annual Meeting, New Orleans.

Pauley, L., 1988, "A Numerical Study of Unsteady Boundary Layer Separation at Low Reynolds Number," Department of Mechanical Engineering, Stanford University (PhD Dissertation).

Peterson, F. B., 1972, "Hydrodynamic Cavitation and Some Considerations of the Influence of Free Gas Content," *Ninth Symposium on Naval Hydrodynamics,* Paris.

Platzer, G. P., and Souders, W. G., 1979, "Tip Vortex Cavitation Delay With Application to Marine Lifting Surfaces, A Literature Survey," DTNSRDC Report No. 79/051.

Rood, E. P., 1989, "Mechanisms of Cavitation Inception," *International Symposium on Cavitation Inception—1989,* San Francisco, ASME FED Vol. 89.

Shen, Y. T., and Gowing, S., 1986, "Cavitation Susceptibility of Ocean and Laboratory Water," *Twenty First Meeting of the American Towing Tank Conference,* Washington.

Shen, Y. T., Gowing, S., and Pierce, R., 1984, "Cavitation Susceptibility Measurements by a Venturi," see Parkin and Morgan (1984).

Shen, Y. T., and Peterson, F. B., 1983, "Cavitation Inception: A Review of Progress Since 19th ATTC," *Twentieth Meeting of the American Towing Tank Conference,* Hoboken.

Souders, W. G., and Platzer, G. P., 1981, "Tip Vortex Cavitation Characteristics and Delay of Inception on a Three-Dimensional Hydrofoil," DTNSRDC-81/0078.

Tsai, J. F., Hwang, J.-L., and Chen, Y.-N., 1989, "Air Content Effects on the Cavitation Inception of Two Axisymmetric Noses," *Cavitation and Multiphase Flow Forum,* San Diego, ASME FED-Vol. 79.

Van der Meulen, J. H. J., 1980, "Boundary Layer and Cavitation Studies of NACA 16-012 and NACA 4412 Hydrofoils," *Thirteenth Symposium on Naval Hydrodynamics,* Tokyo.

Van der Meulen, J. H. J., and Yuan-Pei, Y., 1982, "Cavitation Inception Scaling by Roughness and Nuclei Generation," *Fourteenth Symposium on Naval Hydrodynamics,* Ann Arbor, MI.

Weitendorf, E. A., 1979, "Conclusions From Full Scale and Model Investigations of the Free Air Content and of the Propeller Excited Hull Pressure Amplitudes Due to Cavitation," see Morgan and Parkin (1979).

Xu, W., Chen, G., and Pan, S., 1986, "The Influence of Cavitation Nuclei on Cavitation Inception on the Smooth Axisymmetric Bodies," see Editorial Office of Shipbuilding of China (1986).

Laminar Flow Past Colinear Spheres With Fluid Injection

H. Chiang

C. Kleinstreuer
Mem. ASME

Department of Mechanical and Aerospace
Engineering,
North Carolina State University,
Raleigh, NC 27695-7910

A validated computer simulation model has been developed for the analysis and design of colinear porous sphere systems in a convective stream. Using a modified and extended finite element software package, the steady-state Navier-Stokes equations have been solved describing laminar axisymmetric flow past closely spaced monodisperse spheres with fluid injection. Of interest are the coupled nonlinear interaction effects on the fluid flow patterns and ultimately on the drag coefficient of each sphere for different free stream Reynolds numbers ($20 \le Re \le 200$) and intersphere spacings ($1.5 \le d_{ij} \le 6.0$) in the presence of fluid injection ($0 \le v_b \le 0.1$). At small spacings and low Reynolds numbers, fluid injection causes earlier flow separation while for $Re \ge 100$ surface blowing is more influential in altering the recirculation zones between spheres and thickening the boundary layers. As a result, the total drag of each sphere decreases with increasing blowing intensity although the pressure or form drag of the first sphere may increase at small spacings.

1 Introduction

Interaction effects of multiple spheres with or without blowing determine largely the fluid dynamics and hence the optimal design of system components related to dense sprays, particle suspension flows, fluidized/packed beds, or closely spaced spherical structures. At low to moderate freestream Peclet numbers, nonlinear upstream/downstream effects due to the proximity of neighboring spheres and the intensity of surface blowing, alter significantly the effective drag coefficient and separation angle of each participating sphere when compared with a solitary solid sphere. For certain critical spacings of monodisperse (colinear) spheres, particle pairing, conditions of imminent collision and unique recirculation zones can be observed. Although the fluid dynamics of actual dense fluid-particle fields is much more complex, the present study of steady laminar flow, $20 \le Re \le 200$, past closely spaced spheres, $1.5 \le d_{ij} \le 6$, with blowing, $0 \le v_b \le 0.10$, is an important advancement over previous investigations.

Single sphere/droplet analyses are now well documented. For example, Conner and Elghobashi (1987) employed the control volume method to solve the Navier-Stokes equations for flow past a sphere ($Re \le 100$) with surface mass transfer. Similarly, Cliffe and Lever (1984) considering uniform blowing, showed that the pressure drag first increases with increasing blowing and then slightly decreases. However, the friction drag and ultimately the total drag consistently decrease with increasing surface mass transfer. One of the earliest numerical solutions of flow past a solitary sphere was presented by Hamielec et al. (1967) who assumed a functional distribution for the normal surface velocity with uniform fluid injection being the limiting case. Numerous relevant boundary-layer type analyses have been published over the last two decades, where the representative study by Kleinstreuer and Wang (1988) con-

sidered also sphere rotation, non-Newtonian fluids, heat transfer and fluid suction at the surface.

Multi-particle systems, typically two-spheres or droplets at low Reynolds numbers, have been studied in recent years by a number of researchers. Zaprynov and Toshev (1986) solved the Navier-Stokes equations and the energy equation numerically for steady laminar flow past two spheres in tandem for $Re_d \le 40$, as Tal et al. (1984) had done earlier using bispherical coordinates. Raju and Sirignano (1987) employed a finite-difference code (cf. Dwyer and Sanders, 1984) with mesh generator (cf. Thompson et al., 1977) to solve the unsteady Navier-Stokes equations ($Re \le 100$) for two vaporizing droplets. They again confirmed earlier observations that (close) particle spacings affect fluid flow parameters significantly. A patched boundary-layer approach for the approximate, but computationally very efficient analysis of multiple (vaporizing) spherical droplets has been proposed by Kleinstreuer and Wang (1990).

Relevant experimental work is limited to flow visualization, as well as measurements of the effective drag coefficients and flow separation angles of two-sphere systems. For example, Rowe and Henwood (1961) plotted the axial and transverse interaction/drag forces for a two-dimensional array of spheres. Tsuji et al. (1982) measured the interaction effects for two spheres in tandem at high free-stream Reynolds numbers. Mulholland et al. (1988) considered a two-dimensional trajectory of non-evaporating drops and "measured" a global C_D (Re, L)-curve where L is a lumped parameter distance between any two drops.

The present study is an extension of our previous work (cf. Ramachandran et al., 1991), focusing on the effects of fluid injection at various wall Reynolds numbers. Three-dimensional and transient effects, such as vortex shedding, are safely ignored for $Re \le 200$ (cf. Nakamura, 1976 and Tsuji et al., 1982). The steady-state Navier-Stokes equations for flow past three closely spaced porous spheres are numerically solved
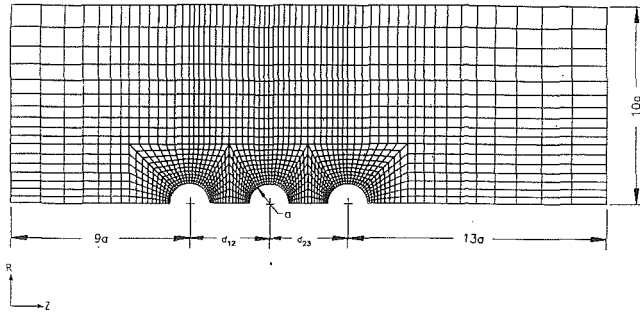
Fig. 1 Representative finite element mesh for axisymmetric flow past three colinear monodisperse spheres

using the Galerkin finite element technique (cf. Cuvelier et al., 1986). Changes due to uniform surface blowing in boundary-layer thickness, flow separation, recirculation regions, as well as friction and pressure forces are depicted and discussed. New correlations for the drag/interaction coefficients $C_{D,k} = C_{D,k}(\text{Re}, d_{ij}, v_b)$ are proposed based on computer experiments varying the freestream Reynolds number, the dimensionless spacing, and the blowing velocity. In an earlier paper it was shown that a three-sphere system is quite relevant for analyzing interaction effects of multiple particles (cf. Ramachandran et al., 1987).

2 Analysis

It is assumed that the flow past three colinear-spheres is steady laminar and axisymmetric. The steady (attached) wakes are laminar in the Reynolds number range of interest (cf. Nakamura, 1976). A representative finite element mesh, which changes in density and extent with the free stream Reynolds number, is depicted in Fig. 1. With the stated assumptions, the nondimensional equations and associated boundary conditions are:

(Continuity)

$$\nabla \cdot \mathbf{v} = 0 \qquad (1)$$

(Momentum)

$$(\mathbf{v} \cdot \nabla)\mathbf{v} = -\nabla p + \text{Re}^{-1}\nabla^2 \mathbf{v} \qquad (2)$$

where $\mathbf{v} = (v_R, v_Z)$ with $v_R = v$, $v_Z = u$ and $\nabla = \hat{\delta}_R(\partial/\partial R) + \hat{\delta}_Z(\partial/\partial Z)$.

The boundary conditions are:

(i) at the inlet

$$u = 1, \ v = 0 \qquad (3a)$$

(ii) along the centerline

$$v = 0, \ \partial u/\partial r = 0 \qquad (3b)$$

(iii) at the solid-gas interfaces (three spheres)

$$\mathbf{v} = v_b \hat{\delta}_r \qquad (3c)$$

At all Reynolds numbers, the computational domain is large enough that all appropriate gradients are zero on the upper boundary and at the outlet of the region.

The dimensionless variables are defined as

$$u = \frac{u^*}{u_\infty}, \ v = \frac{v^*}{u_\infty}, \ v_b = \frac{v_b^*}{u_\infty}, \ p = \frac{p^*}{\rho u_\infty^2}, \ \text{and Re} = \frac{u_\infty d^*}{\nu} \qquad (4)$$

3 Numerical Method

The governing equations (1) and (2) subject to the conditions (3a–c), are solved using a widely accepted finite element software package (cf. Engleman, 1990). Actually, the penalty function approach is used where the continuity requirement is weakened by replacing equation (1) with $\nabla \cdot \mathbf{v} = \epsilon p$. The penalty parameter is very small, i.e., $\epsilon = \mathcal{O}(10^{-6})$. As the finite elements, isoparametric quadrilaterals with nine nodes and biquadratic velocity and linear pressure approximations have been chosen (Cuvelier et al., 1986). The solution is started from a low Reynolds number, say, Re = 10, and then with the converged steady-state solution, the freestream Reynolds number and surface blowing are gradually increased. Specifically, a quasi-Newton algorithm is used for solving the nonlinear equations with a reformation of the Jacobian matrix every five steps. In order to facilitate convergence, a slower but more robust successive substitution method is applied for the first three steps to bring the solution within the radius of convergence of the quasi-Newton method. Subsequently, the faster converging quasi-Newton scheme is invoked. Convergence was achieved when the error criterion $\epsilon = |(\mathbf{v}^{\text{new}} - \mathbf{v}^{\text{old}})/\mathbf{v}^{\text{new}}| \leq 10^{-5}$ was fulfilled. A typical computer run requiring six iterative steps takes about one minute of CPU-time on a CRAY Y-MP.

A mesh of variable density is required for cost-effective computer runs. Very small elements are placed at the interface and large elements near the domain boundaries. A smooth transition from fine to coarse mesh regions has been provided. The overall computational domain and hence the mesh size increases dramatically with lower Reynolds numbers, i.e., Re < 50. In order to avoid crowding, the mesh shown in Fig. 1 does not contain several layers of finite elements along the spherical interface. Independence of the simulation results from

--- **Nomenclature** ---

a	= radius of sphere	u, v	= cylindrical velocity components	σ	= normal stress
$a_{1,2,3}$	= constants	$\forall$	= variable	γ	= surface tension
$b_{1,2,3}$	= constants	u_∞	= characteristic or free stream velocity	**Subscripts**	
$c_{1,2}$	= constants			b	= surface blowing, i.e., uniform fluid injection
C_{Ds}	= total drag coefficient of single sphere without blowing	Z	= axial cylindrical coordinate	d	= based on diameter
		α	= drag coefficient ratio	D	= total drag
$C_{D,k}$	= total drag coefficient of sphere k	ϵ	= error	i	= index for particle spacing $(i = 1,2)$
C_p	= form drag coefficient	$\hat{\delta}$	= unit vector		
d_{ij}	= intersphere distances	ν	= kinematic viscosity	j	= index for particle spacing $(j = i + 1)$
d	= sphere diameter	ρ	= density		
f	= function	θ	= angular spherical coordinate	k	= index for particle identification $(k = 1,2,3)$
L	= representative droplet spacing	$\Delta\theta$	= difference in separation angles, $(\Delta\theta_{\text{sep}} = \theta_{\text{sep}} - \theta_{\text{sep},s})$		
p	= pressure	θ_{sep}	= separation angle measured from forward stagnation point	s	= single sphere
r	= radial spherical coordinate			sep	= flow separation
R	= radial cylindrical coordinate			∞	= at infinity
Re	= Reynolds number	ψ	= stream function		
$\mathbf{v}$	= velocity vector	τ	= tangential stress	**Superscript**	
v_b	= uniform blowing velocity	ζ	= vorticity function	$*$	= dimensional quantities

Table 1 Comparison of drag coefficients for single sphere

Re	C_{Ds} (solitary sphere)		$C_{Ds,b}/C_{Ds}$ (blowing effect, $v_b = 0.1$)		
	Clift et al.* (1978)	Present work	Hamielec et al. (1967)	Cliffe and Lever (1984)	Present work
10	4.38	4.37	—	—	—
40	1.79	1.80	0.873	0.83	0.86
100	1.09	1.09	0.850	0.81	0.84
200	0.77	0.77	—	—	—

$$^*C_{Ds} = \frac{24}{Re}(1 + 0.1935 Re^{0.6305})$$

Fig. 2(a)

Fig. 2(b)

Fig. 2 Streamlines for Re = 20 with v_b = 0, 0.1 (d_{12} = 2, d_{23} = 4 and Pr = 0.7). A = −0.10; B = −0.05; C = −0.001; D = 0.0; E = 0.05; F = 0.10; G = 0.25; H = 0.50; I = 0.75 and J = 1.00.

Fig. 3(a)

Fig. 3(b)

Fig. 3 Streamlines for Re = 200 with v_b = 0, 0.1 (d_{12} = 2, d_{23} = 4 and Pr = 0.7). A = −0.10; B = −0.05; C = −0.001; D = 0.0; E = 0.05; F = 0.10; G = 0.25; H = 0.50; I = 0.75 and J = 1.00.

the mesh density has been successfully tested based on repeat calculations with finer meshes.

With the given post-processing capabilities, stress calculations, velocity vector graphs as well as plots of streamlines, vorticity contours and pressure profiles can be conveniently executed.

4 Results and Discussion

The numerical code has been verified with published data sets for a solitary sphere and a single porous sphere with blowing (Table 1). Clift et al. (1978) examined numerous empirical and semi-empirical correlations and proposed the one given below for a solitary sphere without blowing as the best fit using least-squares analysis. The blowing single sphere data has been obtained from numerical studies (cf. Hamielec et al. 1967). Successful two-sphere comparisons are given in Ramachandran et al. (1991).

For a linear array of three spheres, the freestream Reynolds number ($10 \leq u_\infty d^*/\nu \leq 200$), the dimensionless uniform blowing velocity ($0 \leq v_b^*/u_\infty \leq 0.1$), and the intersphere distances ($1.5 \leq d_{ij}^*/d^* \leq 6$) between the first and second sphere
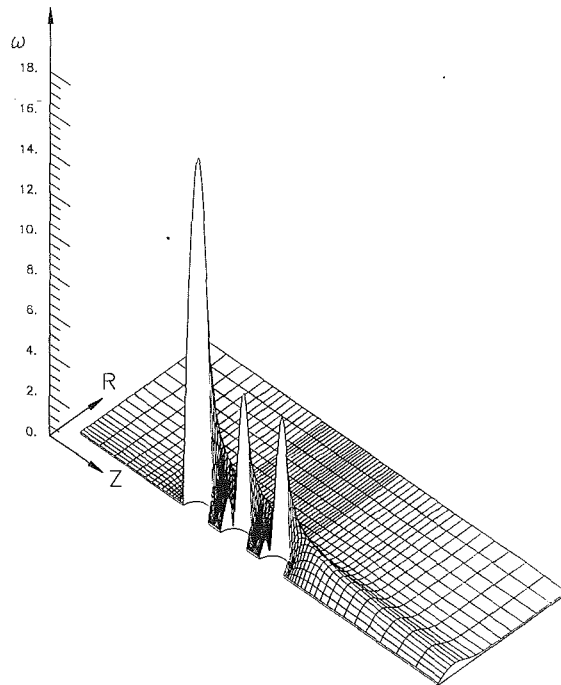
Fig. 4(a) Vorticity surface plot for closely-spaced spheres (Re = 100, d_{12} = d_{23} = 1.5; v_b = 0 and Pr = 0.7)
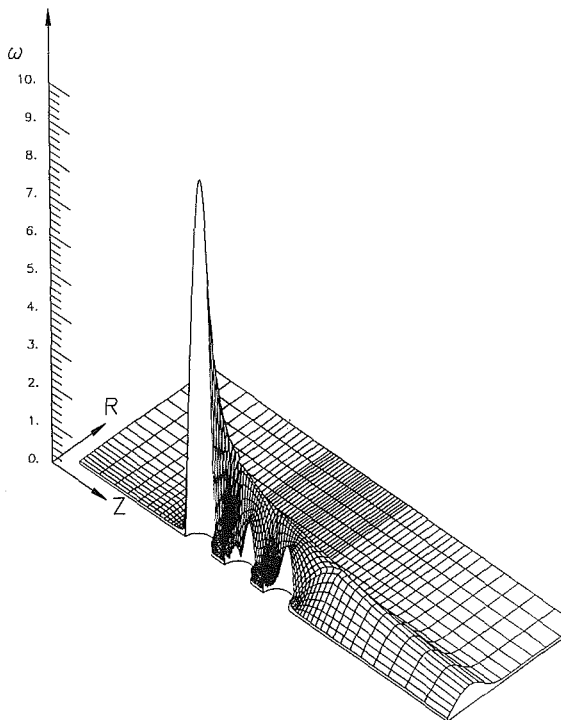
Fig. 4(b) Vorticity surface plot for closely-spaced spheres with blowing (Re = 100, d_{12} = d_{23} = 1.5; v_b = 0.1 and Pr = 0.7)

and between the second and third sphere have been systematically varied.

4.1 Streamlines and Velocity Contours. Streamlines are shown in Figs. 2(a, b) and 3(a, b) for the sphere arrangement d_{12} = 2 and d_{23} = 4 with freestream Reynolds numbers Re = 20 and 200, respectively. The effects of blowing are twofold. At low Reynolds numbers and close sphere spacings, flow separation off the first sphere occurs earlier because of fluid injection (Figs. 2(a) and 2(b)). At higher Reynolds numbers (Re ≥ 100), surface blowing effects are even more significant; recirculation zones are strongly altered and the

Fig. 5(a)
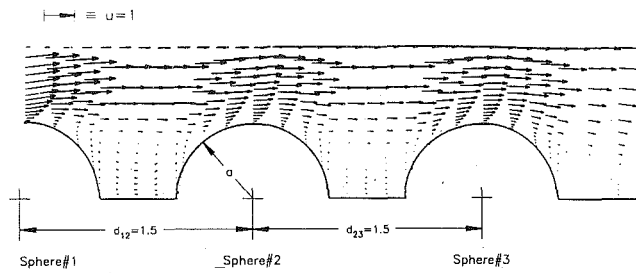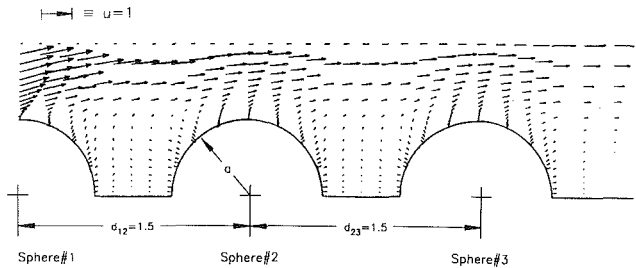

Fig. 5(b)

Fig. 5(a, b) Velocity vector plots for Re = 100 with v_b = 0, 0.1 (d_{12} = d_{23} = 1.5 and Pr = 0.7)
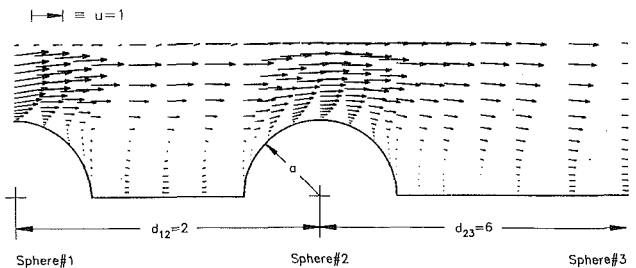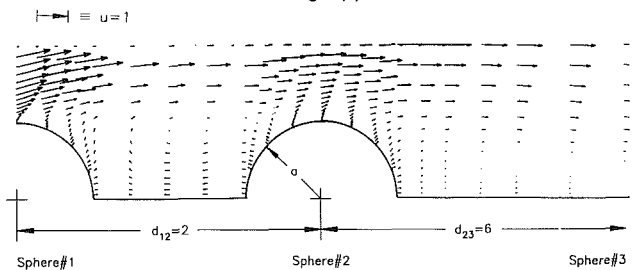

Fig. 5(c)

Fig. 5(d)

Fig. 5(c, d) Velocity vector plots for Re = 100 with v_b = 0, 0.1 (d_{12} = 2; d_{23} = 6 and Pr = 0.7)

streamlines are shifted outwards, resulting in thicker boundary layers and milder velocity gradients (cf. Figs 3(a) and 3(b)).

Figure 4(b) relative to 4(a) depicts the blowing effects in terms of vorticity surfaces for close spacings (i.e., d_{12} = d_{23} = 1.5) and a moderate freestream Reynolds number of Re = 100. Again, because of fluid injection, the affected flow region or penetration depth is larger, and flow separation and reattachment "points" are shifted, causing larger recirculation zones.

4.2 Velocity and Pressure Plots. Figures 5(a) to 5(d) depict the strong influences of surface blowing intensity and intersphere spacing on the flow field. With fluid injection, the boundary layer thickens, flow reattachment on spheres in a wake is delayed and flow separation occurs earlier. At small spacings, "cavities" are formed in which flow patterns change drastically because of surface blowing (cf. Figs. 5(a) versus Fig. 5(b)).

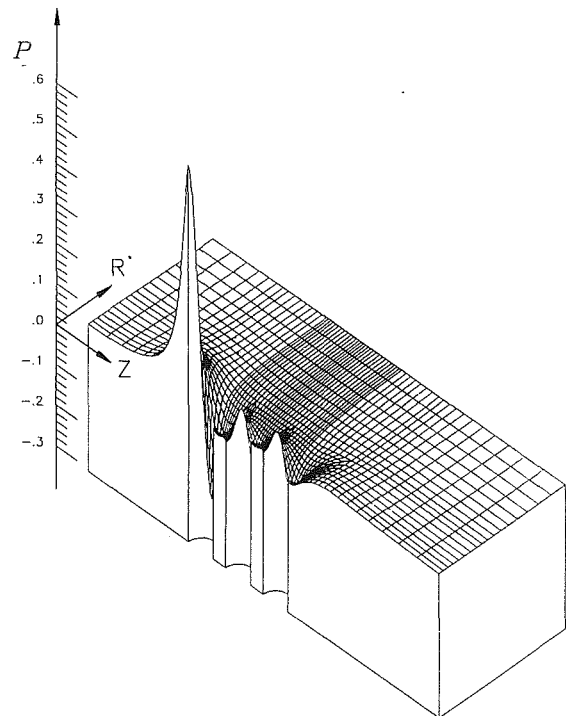Surface blowing effects on the pressure field around the spheres at Re = 100 are detectable from Fig. 6(a) versus 6(b)

Fig. 6(a) Pressure surface plot for Re = 100 with v_b = 0 and d_{12} = d_{23} = 1.5 (p_{max} = 0.562 and p_{min} = −0.245)
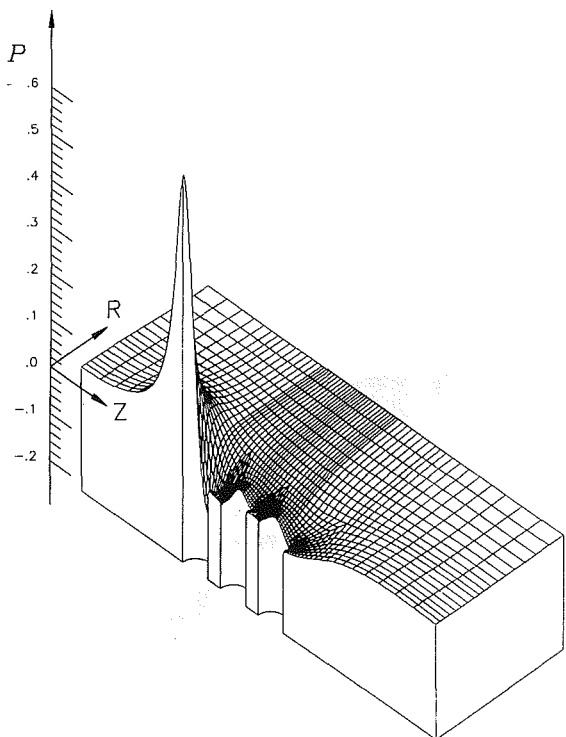

Fig. 6(b) Pressure surface plot for Re = 100 with v_b = 0.1 and d_{12} = d_{23} = 1.5 (p_{max} = 0.558 and p_{min} = −0.133)

for d_{12} = d_{23} = 1.5 and from Fig. 7(a) versus 7(b) for d_{12} = d_{23} = 6. As expected, a large pressure peak appears in each case at the stagnation point of the first sphere. For closely spaced spheres, the second and third pressure peaks occur past the front stagnation points because of the delay in flow reattachment (cf. Figs. 4(a) and 6(a)). Surface blowing reduces the maximum pressures on the second and third sphere surfaces and diminishes pressure recovery at higher Reynolds numbers. For the first sphere, the pressure or form drag always increases
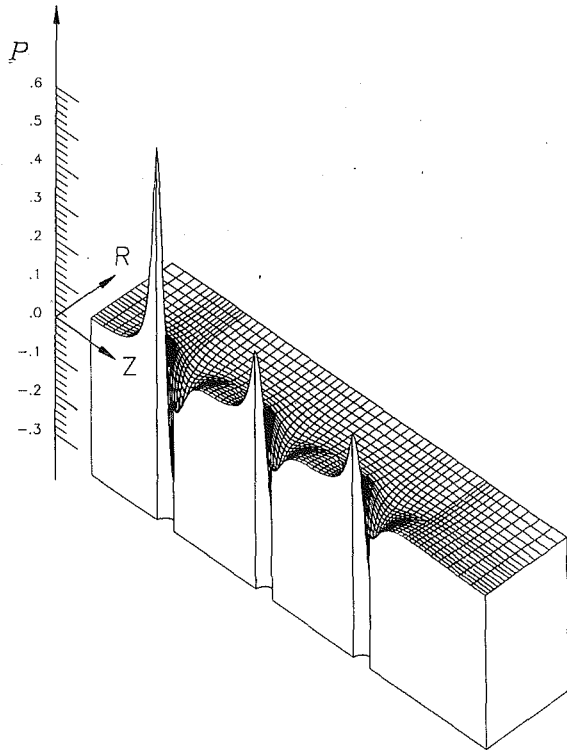
Fig. 7(a) Pressure surface plot for Re = 100 with v_b = 0 and d_{12} = d_{23} = 6 (p_{max} = 0.563 and p_{min} = −0.291)
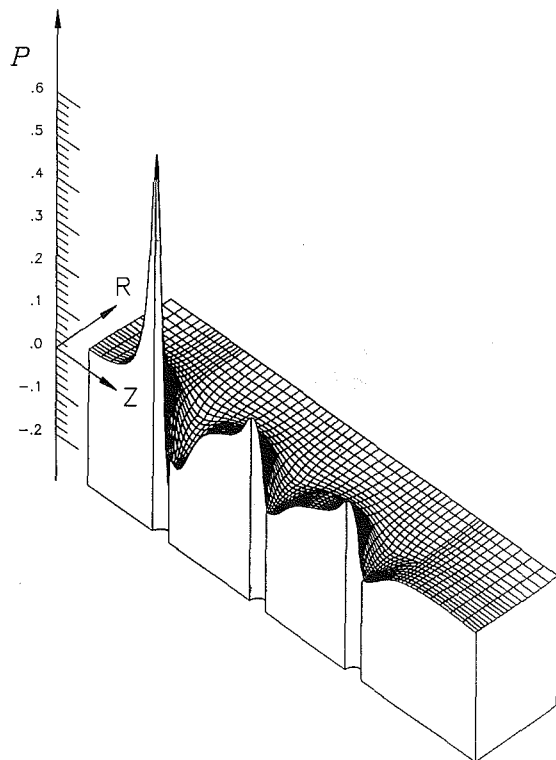

Fig. 7(b) Pressure surface plot for Re = 100 with v_b = 0.1 and d_{12} = d_{23} = 6 (p_{max} = 0.561 and p_{min} = −0.195)

with larger blowing velocities as shown in more detail below (cf. Sect. 4.3). As the intersphere spacing increases, the interaction effects have almost vanished for the nonblowing case (Fig. 7(a)) but persist when the Reynolds number and the surface blowing are relatively high (Fig. 7(b)).

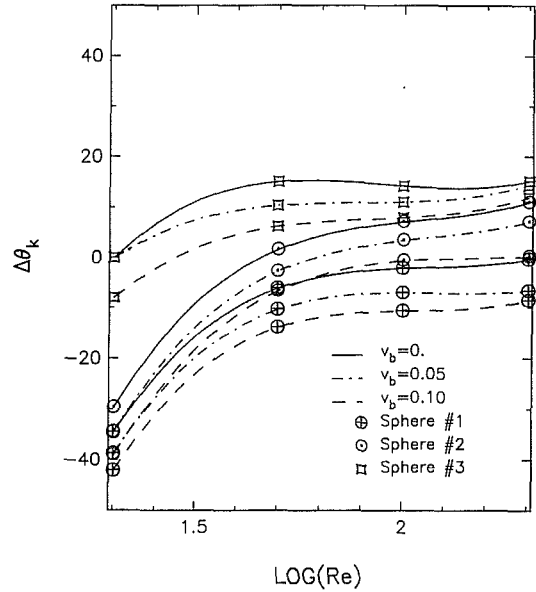**4.3 Separation Angles and Drag Coefficients.** Figures 8(a)

Fig. 8(a) Difference in separation angle $\Delta\theta_k$(Re, v_b) for three interacting spheres with fluid injection (d_{12} = d_{23} = 1.5)
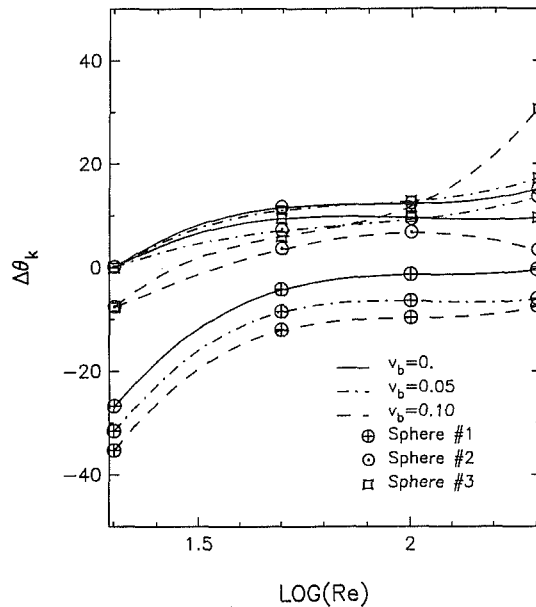

Fig. 8(b) Difference in separation angle $\Delta\theta_k$(Re, v_b) for three interacting spheres with fluid injection (d_{12} = 2 and d_{23} = 4)

and 8(b) depict $\Delta\theta_k$ (Re, v_b, d_{ij}) which is the difference between the actual separation angle for sphere k = 1, 2, 3 and the separation angle for a solitary, nonblowing sphere at the corresponding Reynolds number. Thus $\Delta\theta_k$ < 0 indicates earlier flow separation and $\Delta\theta_k$ > 0 means a delay in flow separation.

Small spacings (cf. Fig. 8(a)) promote for spheres 1 and 2 earlier separation especially for porous spheres with fluid injection. Pairing of spheres together with surface blowing generate extended cavities of slowly circulating fluid which prevents free stream fluid to penetrate. Such an enclosure does not exist behind the last sphere for which $\Delta\theta_k$ > 0 except at very low Reynolds numbers and strong surface blowing. As the intersphere distances increase, the differences in separation angles decrease (Fig. 8(b)). Fluid injection causes earlier flow separation while the presence of the first sphere may delay separation for spheres 2 and 3 because of weakening of the inertia force by the leading sphere at higher Reynolds numbers.

The individual drag/interaction coefficients, $C_{D,k}$(Re, v_b, d_{ij}) are shown in Figs. 9(a) and 9(b) for d_{12} = d_{23} = 1.5. At low
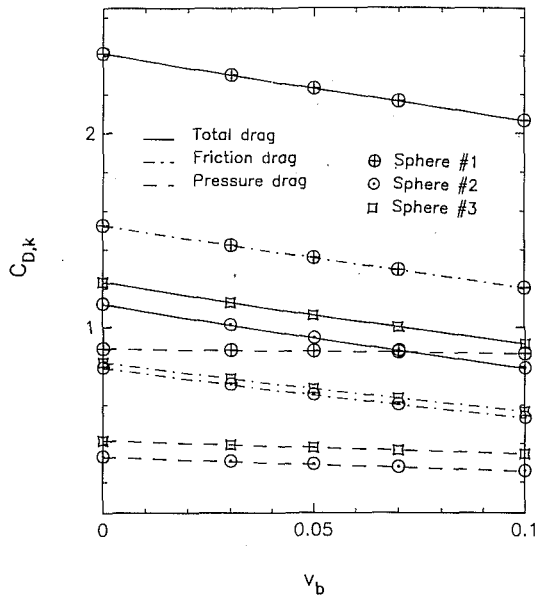
Fig. 9(a) Friction, form and total drag coefficients as a function of surface blowing (Re = 20; $d_{12} = d_{23} = 1.5$)
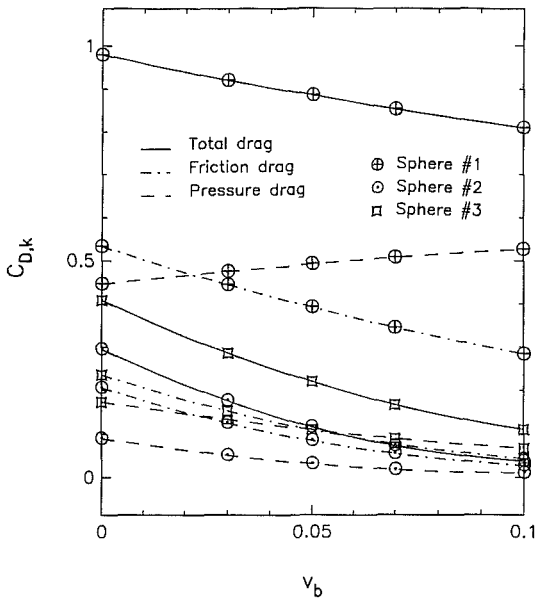

Fig. 9(b) Friction, form and total drag coefficients as a function of surface blowing (Re = 100; $d_{12} = d_{23} = 1.5$)

Reynolds numbers (cf. Fig. 9(a)), friction drag is the largest contributor whereas for higher Reynolds numbers (cf. Fig. 9(b)), the pressure or form drag becomes dominant because of the increasing wake effect. In general, the friction drag decreases with stronger surface blowing due to thicker boundary layers and hence milder velocity gradients at the spheres' surfaces. As already indicated in Fig. 7(b), the pressure drag of spheres 2 and 3 is almost independent of the blowing intensity, while the pressure drag of the leading sphere always increases with increasing blowing velocity because of the form losses due to the lack of pressure recovery.

4.4 Total Drag Coefficient Ratios. Reliable drag correlations for interacting spheres with or without blowing are most desirable for the analysis and design of multiple particle systems. For a solitary sphere, the drag coefficient C_{Ds} is a function of the Reynolds number only. It can be expected from the discussions on flow patterns, surface blowing effects, sep-

Table 2 Coefficients for equation (6)

Sphere (k)	b_1	a_1	b_2	a_2	b_3	a_3	c_1	c_2	Avg. error %
1	0.032	0.069	1.572	1.580	0.247	1.192	10.0	0.740	2.64
2	0.141	0.200	1.659	1.331	0.193	1.502	4.487	0.972	3.21
3	0.195	0.179	−0.244	1.179	1.210	1.380	3.200	0.920	2.73

aration angles and friction/form drag coefficients given in the previous sections for three spheres with fluid injection, that

$$\alpha_k \equiv \frac{C_{D,k}}{C_{Ds}} = \frac{f_1(\mathrm{Re},\, v_b,\, d_{12},\, d_{23})}{f_2(\mathrm{Re})}$$

$$= f_3(\mathrm{Re},\, v_b,\, d_{12},\, d_{23}); \quad k = 1, 2, 3 \quad (5)$$

Considering that the interaction effects, including surface blowing, are highly nonlinear and their influences cause drag reduction when compared with a single sphere, α_k should have the following functional form:

$$\alpha_k = 1 - b_1 \mathrm{Re}^{a_1} \left(1 + \frac{b_2}{d_{12}^{a_2}} + \frac{b_3}{d_{23}^{a_3}}\right)(1 + c_1 v_b^{c_2}); \quad k = 1, 2, 3 \quad (6)$$

where $a_1 - a_3$, $b_1 - b_3$ and c_1 and c_2 are constants for each sphere. Although other functional forms are permissible, equation (6) reflects the facts that (i) the interaction effect is inversely proportional to the intersphere distances, (ii) the surface blowing intensity is directly proportional to the Reynolds number, and (iii) at large spacings d_{ij} as well as small blowing velocities v_b, α_k becomes a function of the Reynolds number only.

Previously (cf. Ramachandran et al., 1991), we employed the least-square technique. However, the two additional unknowns c_1 and c_2, the extended postulate for α_k, and our goal of higher accuracy, all required the use of a robust nonlinear optimization code such as VMCON1 (cf. Crane et al., 1980), a software package which is in the public domain. Thus, based on computer experiments, the following coefficients for the α_k-correlations have been obtained using VMCON1 as summarized in Table 2.

The associated ranges of application for equation (6) are:

$$20 \leq \mathrm{Re} \leq 200, \quad 1.5 \leq d_{ij} \leq 6.0 \quad \text{and} \quad 0 \leq v_b \leq 0.07$$

At high Reynolds numbers and high blowing intensities, the rather simple functional form of equation (6) generates unacceptable local errors, especially for the second sphere, so that uniform blowing was restricted to 7 percent of the freestream velocity. The average error for each sphere was computed as

$$\hat{\epsilon}_k = \sum_1^n \sqrt{(\alpha_{k,\text{correl}} - \alpha_{k,\text{actual}})^2}/n \quad (7)$$

where n is the number of data points ($n = 200$), $\alpha_{k,\text{correl}}$ is the ratio α_k obtained from the correlation (6), and $\alpha_{k,\text{actual}}$ is the actual (directly computed) ratio of drag coefficients. For the given ranges of application, the maximum error is below 10 percent.

Equation (6) indicates that even for the largest spacing and zero surface blowing the first sphere is somewhat influenced by the spheres 2 and 3. This wake effect is, however, more pronounced at strong surface blowing and large Reynolds numbers. Specifically, Figs. 10(a) to 10(c) show a few correlations $\alpha_k(\mathrm{Re})$ for different wall Reynolds numbers, $0 \leq v_b \leq 0.1$. As expected, the leading sphere exhibits a special α_k signature where the influence of the proximity of the other spheres diminishes as the freestream Reynolds number increases. Surface blowing decreases α_k, an effect which is partially offset at higher Reynolds numbers (Re $\geq$ 100). At larger spacings (cf. Fig. 10(c)), $\alpha_1 \approx 1$ whereas α_2 and α_3 reflect the prevailing wake effects. In summary, the sequence of graphs (10a–c) indicates that the interaction effects caused by the free stream,
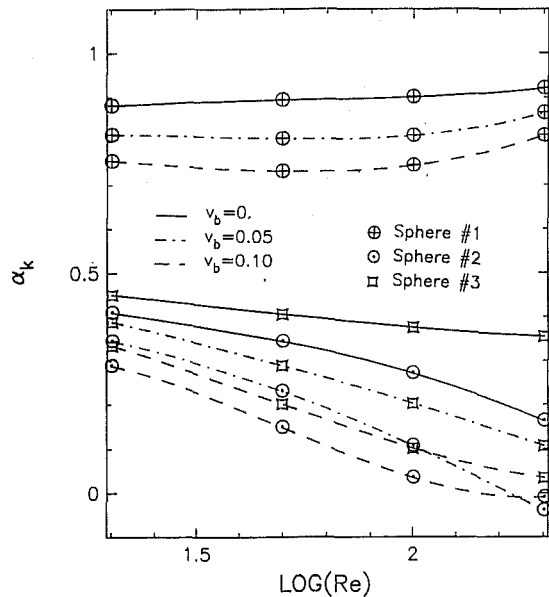
Fig. 10(a) Total drag coefficient ratio α_k(Re, v_b) for three interacting spheres with fluid injection ($d_{12} = d_{23} = 1.5$)

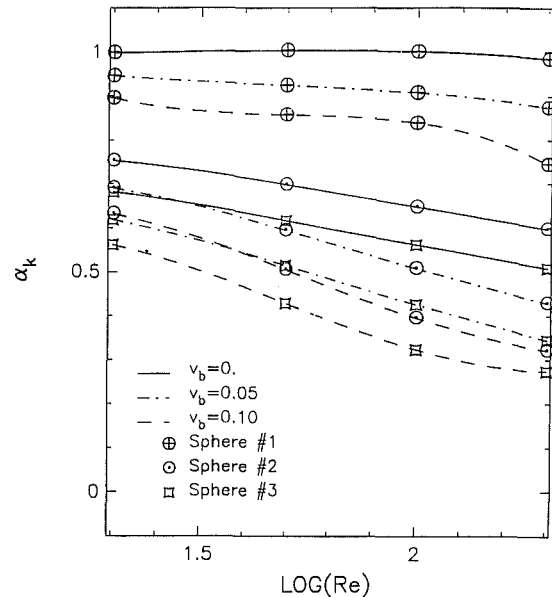

Fig. 10(c) Total drag coefficient ratio α_k(Re, v_b) for three interacting spheres with fluid injection ($d_{12} = d_{23} = 6$)
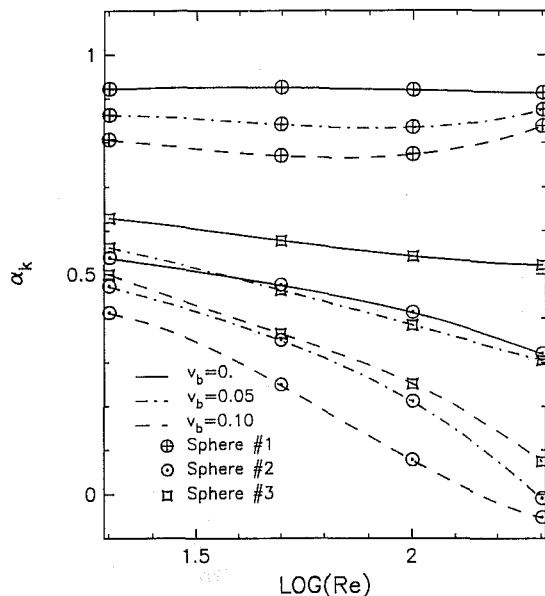

Fig. 10(b) Total drag coefficient ratio α_k(Re, v_b) for three interacting spheres with fluid injection ($d_{12} = 2$ and $d_{23} = 4$)

surface blowing and small intersphere spacings are strongly coupled and highly nonlinear. Specifically, the changes in inertia forces, the intensity of fluid injection and the sizes of cavities (i.e., spacings) with recirculating fluid, cause unique (skin) friction and (pressure) from drag distributions.

Acknowledgments

References

Cliffe, K. A., and Lever, D. A., 1984, "The Effects of Mass Efflux and Temperature-dependent Fluid Properties on Droplet Drag Coefficients," Conf. Proceedings, AIChE Heat Transfer, Niagara Falls, NY.

Clift, R., Grace, J. R., and Weber, M. E., 1978, Bubbles, Drops and Particles, Academic Press, New York.

Conner, J. M., and Elghobashi, S. E., 1987, "Numerical Solution of Laminar Flow Past a Sphere with Surface Mass Transfer," Numerical Heat Transfer, Vol. 12, pp. 57–82.

Crane, R. L., Hillstrom, K. E., Minkoff, M., 1980, "Solution of the General Nonlinear Programming Problem with Subroutine VMCON," Argonne Natl. Lab. Report ANL-80-64. NTIS, Springfield, VA. Also: Powell, M. J. D., 1978, "Algorithms for Nonlinear Constraints that Use Lagrangian Functions," Math. Programming, Vol. 14, pp. 224–248.

Cuvelier, C., Segal, A., and Van Steenhoven, A. A., 1986, Finite Element Methods and Navier-Stokes Equations, D. Reidel Publishing Company, Dordrecht, Holland.

Dwyer, H. A., and Sanders, B. R., 1984, "Detailed Combustion of Unsteady Droplet Dynamics," Twentieth Symposium on Combustion, The Combustion Institute, Pittsburgh, PA.

Engleman, M. S., 1990, "FIDAP Manuals Volumes 1 to 3," FDI, Evanston, Illinois.

Hamielec, A. E., Hoffman, T. W., and Ross, L. L., 1967, "Numerical Solution of the Navier-Stokes Equation for Flow Past Spheres," AIChE Journal, Vol. 13, No. 2, pp. 212–219.

Kleinstreuer, C., and Wang, T-Y, 1990, "Approximate Analysis of Interacting Vaporizing Fuel Droplets," Int. J. Multiphase Flow, Vol. 16, No. 2, pp. 295–304.

Kleinstreuer, C., and Wang, T-Y, 1988, "Heat Transfer Between Rotating Spheres and Flowing Power-Law Fluids with Suction and Injection," Heat and Fluid Flow, Vol. 9, No. 3, pp. 328–333.

Mulholland, J. A., Srivastava, R. K., and Wendt, J. O. L., 1988, "Influence of Droplet Spacing on Drag Coefficient in Nonevaporating Monodisperse Streams," AIAA Journal, Vol. 26, No. 10, pp. 1231–1237.

Nakamura, I., 1976, "Steady Wake Behind a Sphere," Physics of Fluids, Vol. 19, No. 1, pp. 5–8.

Raju, M. S., and Sirignano, W. A., 1987, "Unsteady Navier-Stokes Solution for Two Interacting Vaporizing Droplets," AIAA 25th Aerospace Science Meeting, Reno, Nevada.

Ramachandran, R. S., Wang, T.-Y., Kleinstreuer, C., and Chiang, H., 1991, "Fluid Flow Characteristics of Three Closely-Spaced Monodisperse Spheres on Nonevaporating Drops at Low to Moderate Reynolds Numbers," AIAA Journal, Vol. 29, No. 1, pp. 43–51.

Ramachandran, R. S., Kleinstreuer, C., and Altwicker, E. R., 1987, "Mass Transfer to an Accelerating Multidrop System," Int. J. Heat Mass Transfer, Vol. 30, No. 3, pp. 607–612.

Rowe, P. N., and Henwood, G. A., 1961, "Drag Forces in a Hydraulic Model of a Fluidized Bed—Part I," Trans. Inst. Chem. Engr., Vol. 39, pp. 43–56.

Tal, R., Lee, D. N., and Sirignano, W. A., 1984, "Heat and Momentum Transfer Around a Pair of Spheres in Viscous Flow," Int. J. Heat Mass Transfer, Vol. 27, No. 11, pp. 1953–1962.

Thompson, J. F., Thames, F. C., and Mastin, C. W., 1977, "TOMCAT—A Code for Numerical Generation of Boundary-Fitted Curvilinear Coordinate Systems on Fields Containing Any Number of Arbitrary Two-Dimensional Bodies," Journal of Computational Physics, Vol. 24, pp. 274–302.

Tsuji, Y., Morikawa, Y., and Terashima, K., 1982, "Fluid-dynamic Interaction Between Two Spheres," Int. J. Multiphase Flow, Vol. 8, pp. 71–82.

Zaprynov, Z. D., and Toshev, E. T., 1986, "Hydrodynamics and Heat Transfer Around Two Separated Spherical Particles," Proceedings of the Eighth International Conference on Heat Transfer, San Francisco, Vol. 5, pp. 2549–2553.

An Optimum Suppression of Fluid Forces by Controlling a Shear Layer Separated From a Square Prism

H. Sakamoto
Professor,
Department of Mechanical Engineering,
Kitami Institute of Technology,
Kitami, 090, Japan

K. Tan
Associate Professor,
Department of Mechanical Engineering,
Kushiro National College of Technology,
Kushiro, 084, Japan

H. Haniu
Associate Professor,
Department of Mechanical Engineering,
Kitami Institute of Technology,
Kitami, 090, Japan

This paper deals with the suppression of the fluid forces by controlling a shear layer on one side separated from a square prism. The control of the separated shear layer was established by setting up a small circular cylinder (the control cylinder) in it on one side. Experimental data were collected to examine the effects on the fluid forces and vortex shedding frequency due to variation of the position and diameter of the control cylinder. The results show that (i) the maximum reduction of the time-mean drag and fluctuating lift and drag occurred when the control cylinder was located near what would ordinarily be considered the outer boundary of the shear layer; (ii) the control of the separated shear layer by means of a small cylinder appeared to be effective in suppressing the fluctuating lift and drag rather than the time-mean drag; (iii) in the case of the control cylinder of 6 mm in diameter, the time-mean drag was reduced to about 30 percent, and the fluctuating lift and drag were reduced to approximately 95 and 75 percent, respectively; (iv) the fluid forces and the frequency of vortex shedding of the square prism were mainly dependent on the characteristics of a very thin region near the outer boundary of the shear layer.

1 Introduction

Various methods have been developed to reduce the fluid forces acting on a bluff body on which the flow separates from its surface. Methods to reduce the fluid forces acting on the bluff body can be roughly classified into the following three categories in accordance with the phenomenological mechanism of vortex shedding (Zdravkovich, 1981): (i) the control of the boundary layer on the surface with a tripping wire, fin, or blowing nozzle installed on the surface (Fage and Warsap, 1923; James and Truong, 1972; Lockwood, 1960; Waka and Yoshino, 1987), (ii) the control of the entrainment layers that supply irrotational fluid necessary for the growth of vortices by enclosing the body with a porous flexible plate or multiple rod (Wootton and Yates, 1970; Price, 1956; Knell; 1969), (iii) the control of the wake with a splitter plate, guidevane, or base-bleed (Roshko, 1954; Bearman, 1965; Apelt et al., 1973; Wood, 1967). Basically, all the above methods are designed to reduce the fluid forces by changing the position of the vortex formation region and suppressing the strength of the vortex (circulation) by controlling the separated shear layer. Recently, Strykowski and Sreenivasan (1985) made an interesting report in which the vortex shedding can be suppressed almost completely by a simple method which is to set up a small cylinder in the separated shear layer on one side. The work of Stry-

kowski and Sreenivasan is done in the range of low Reynolds number less than Re = 120 where the shear layer separating from the circular cylinder is thin, and the alternative vortex shedding is very stable with regular mode. However, the formation mechanism of vortices formed by the alternating rolling-up of the separated layer is substantially considered to be the same for any bluff body and any Reynolds number. Therefore, it is assumed that the reduction of fluid forces by suppressing the vortex shedding in the same manner as done by Strykowski and Sreenivasan is quite possible even for bluff bodies at the high Reynolds numbers. Quite recently, Igarashi and Tsutsui (1989) investigated the reduction of the time-mean drag acting on a circular cylinder by means of using a small cylinder in a manner similar to Strykowski and Sreenivasan's method, and found that the time-mean drag was reduced considerably (20 ~ 30 percent) by forcibly reattaching the separated shear layer on the surface of the circular cylinder. They also measured the fluctuating pressure on the surface of the circular cylinder, and then stated that the fluctuating fluid forces would be reduced. Thus, it is assumed that the vortex shedding from the body, and steady and unsteady fluid forces acting on the body can be fully suppressed by controlling the separated shear layer using a circular cylinder, which is fairly small compared to the body itself.

The aim of the present work is to reduce the fluid forces acting on a square prism, which is considered to represent the typical shape of a two-dimensional bluff body, by means of

setting up a circular cylinder (hereafter called the control cylinder) with small diameter in a shear layer on one side of the square prism. Measurements were carried out to change the position and size of the control cylinder systematically, and then the steady and unsteady fluid forces were examined to estimate the magnitude of the reduction themselves and to identify the optimum position of the control cylinder in order to reduce the fluid forces. Furthermore, such matters as the deformation of the shear layer, namely, the position and the strength of the rolling-up of the separated shear layers, are discussed in detail based on the results of measurement of the fluid forces and the Strouhal number.

2 Experimental Arrangement and Procedures

The experiments were carried out in a low speed, closed-circuit wind tunnel. The test section of the tunnel has a rectangular shape with a height of 0.43 m, a width of 0.4 m, and a length of 4 m. Two types of square prisms were used for the experiment; one prism with two load cells installed inside was used for the measurement of fluid forces, and another prism with a semiconductor pressure transducer installed inside was used for the measurement of the static and fluctuating pressures. Both prisms had a length of 400 mm, in order to span width of the test section. The prism for the measurement of fluid forces was composed of two parts, as shown in Fig. 1, namely, an active cylinder and a dummy cylinder, and a load cell on which four semiconductor strain gauges were attached was installed inside each cylinder. The load cell was developed by Sakamoto and Oiwake (1984) and had a high linearity in the load/output relation and a very high natural frequency of the load cell. The load cell installed inside the active cylinder measured the combination of the fluid forces and the force due to the vibration transmitted through the dummy cylinder. The load cell installed inside the dummy cylinder measured the forces due to the vibration of the dummy cylinder itself and to the vibration transmitted from outside. Hence, by subtracting the output of the load cell in the active cylinder from that of the load cell in the dummy cylinder, the fluid forces acting on the active cylinder could be measured exclusively. The diameter d of the control cylinder adopted in the present experiment was 3, 4, 5, and 6 mm. The control cylinder was set up with full tension at one side of the square prism, as shown in Fig. 1.
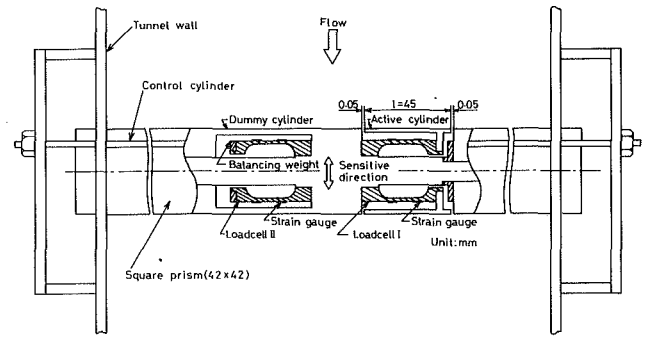

Fig. 1 Arrangement of load cells of 42 × 42 mm prism

The experiments were carried out at a constant free-stream velocity U_0 of 15 m/s. The position of the control cylinder was varied in the range of $S/W = 0 \sim 2.0$ (S is the longitudinal distance) and $T/W = 0 \sim 2.0$ (T is the lateral distance). All the analog signals were digitized and then processed by a microcomputer. The Reynolds number Re ($= U_0 W/\nu$) employed in the experiment was 4.2×10^4. The important symbols and the definition of the coordinate system used in the present study are shown in Fig. 2. The blockage effect of the prism at the test section was 9.8 percent, and no corrections were made for the blockage.

3 Results and Discussions

3.1 Position of the Separated Shear Layer. The main purpose of this study is to reduce the fluid forces by controlling the separated shear layer that dominates the fluid forces acting on the square prism. It is therefore first necessary to identify the time-averaged position of the separated shear layer. However, since the shear layer has some width and diffuses rapidly as it goes downstream, it is difficult to pinpoint the position. Fage and Johansen (1927) traversed a hot-wire probe at right angles to the direction of the undisturbed flow in the shear layer and defined a position of the outer and inner boundary in which the time-averaged velocity becomes greatest and least, respectively. Sasaki and Kiya (1984) measured the turbulence intensity in the shear layer and indicated that a position with the largest strength of turbulence is the approximate center of the shear layer.

———— Nomenclature ————

A = projected area of the active cylinder

C_D = time-mean drag coefficient $= D/(0.5 \rho U_0^2 A)$

C_{Df} = r.m.s. drag coefficient $= \sqrt{\overline{D_f^2}}/(0.5\rho U_0^2 A)$

C_L = time-mean lift coefficient $= L/(0.5\rho U_0^2 A)$

C_{Lf} = r.m.s. lift coefficient $= \sqrt{\overline{L_f^2}}/(0.5\rho U_0^2 A)$

C_p = time-mean pressure coefficient $= (p - p_0)/(0.5\rho U_0^2)$

C_{pf} = r.m.s. pressure coefficient $= \sqrt{\overline{p_f^2}}/(0.5\rho U_0^2)$

$(C_D)_{min}$ = minimum time-mean drag coefficient on each section S/W

$(C_L)_{max}$ = maximum time-mean lift coefficient on each section S/W

$(C_{Df})_{min}$ = minimum r.m.s. drag

coefficient on each section S/W

$(C_{Lf})_{min}$ = minimum r.m.s. lift coefficient on each section S/W

D = time-mean drag acting on the active cylinder

D_f = fluctuating drag acting on the active cylinder

L = time-mean lift acting on the active cylinder

L_f = fluctuating lift acting on the active cylinder

S = longitudinal distance of control cylinder from leading edge of the prism (see control cylinder coordinate defined in Fig. 2)

S_t = Strouhal number of vortex shedding $= f_c W/U_0$

T = lateral distance of control cylinder from leading edge of the prism (see control

cylinder coordinate defined in Fig. 2)

U_0 = free-stream velocity

W = width of the prism

d = diameter of the control cylinder

f_c = frequency of vortex shedding

p = time-mean pressure acting on the prism

p_0 = static pressure of free-stream

p_f = fluctuating pressure acting on the prism

u = time-mean longitudinal velocity

u' = fluctuating longitudinal velocity

x, y = cartesian coordinate system (see Fig. 1)

x_s, y_s = position of piezometric holes on surface of the prism
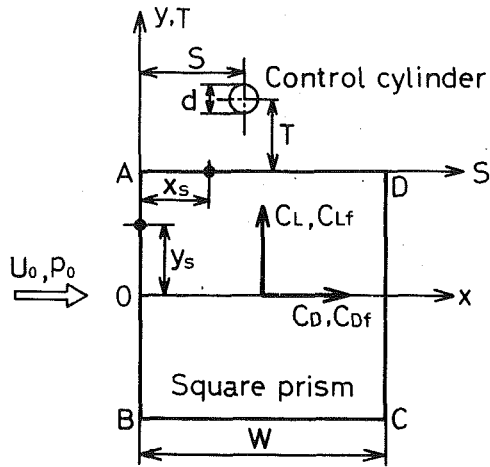
ρ = density of the fluid

Fig. 2   Definition sketch and coordinate system

Fig. 3   Distribution of the time-mean and the r.m.s. longitudinal velocity in the shear layer. (Uncertainty in u/U_0: less than ± 2 percent, in $\sqrt{u'^2}/U_0$: less than ± 2 percent, in S/W and T/W: less than ± 0.5 percent.)

Fig. 4   Equi-line diagram of the time-mean drag coefficient. (Uncertainty in C_D: less than ± 3 percent.)

Fig. 5   Equi-line diagram of the time-mean lift coefficient. (Uncertainty in C_L: less than ± 3 percent.)

Figure 3 shows the position indicating the maximum time-mean velocity and maximum degree of turbulence intensities obtained by moving the hot-wire probe along the direction of T/W on each section S/W (see Fig. 2) in the same manner as above mentioned. Generally, the fluid forces on the bluff bodies are dependent on the characteristics of the outer boundary of the shear layer representing the maximum velocity rather than at the center of the shear layer where the strength of turbulence intensity becomes the largest (Bearman and Trueman, 1972). Figure 3 also shows the position of the control cylinder with a diameter of 3 mm where the fluid forces on each section S/W becomes least, as will be discussed in detail later. It can be seen that the position of the control cylinder suppressing most the fluid forces coincides with the outer boundary of the shear layer representing the maximum velocity. Thus it is considered most effective to set the control cylinder near the outer boundary of the shear layer as shown in Fig. 3 for suppressing the fluid forces.

3.2 Control of Time-Mean Drag and Lift. Figures 4 and 5 show the values of the time-mean drag coefficient C_D and lift coefficient C_L when the position of the control cylinder with a diameter of 3 mm ($d/W = 0.07$) is changed. Each result is shown as equi-line diagrams which were obtained by interpolation between the measured values. Also, each result of C_D is expressed as a ratio of the drag coefficient to $C_D = 2.30$, the value for the square prism without the control cylinder presents in order to quantify the effect of control.

First, from the result shown in Fig. 4, it can be seen that the time-mean drag coefficient C_D is most suppressed when the control cylinder is located along the outer boundary of the shear layer (indicated by symbol o in this figure). Generally, the base pressure dominating the time-mean drag is dependent on the degree of the concentration of the vortices (strength of vortices) flowing out along the shear layer and the position of the rolling-up of the shear layer. As this pressent method, if the control cylinder is set up in the shear layer, the turbulent diffusion of the vortices flowing out from the leading edge of the square prism and the change of the radius of curvature of the shear layer are induced, as a result, a decrease in base pressure and a reduction in C_D are caused because of the recession of the position of the rolling-up of the shear layer and the weakening of the concentration of the vortices. Also, since C_D is most suppressed when the control cylinder is located in a limited region near the outer boundary of the shear layer, it is considered that the vortices flowing out from the leading edge of the square prism are not conveyed while being distributed widely in the shear layer but most of them are conveyed along a very thin layer near the outer boundary of the shear layer.
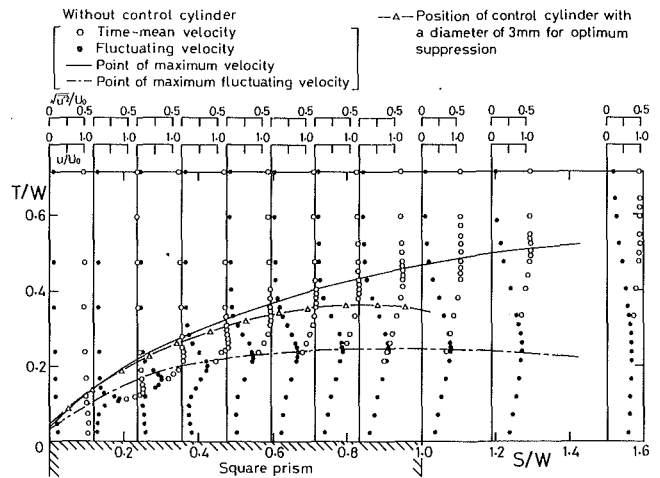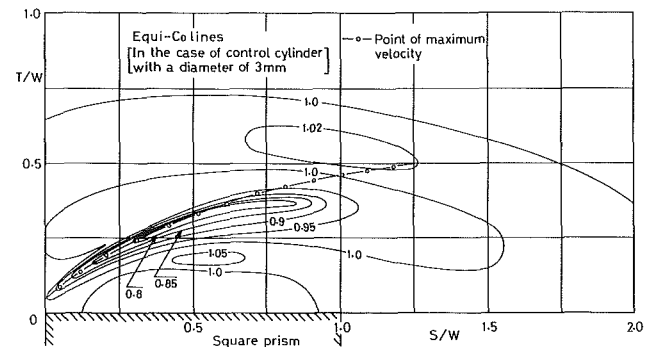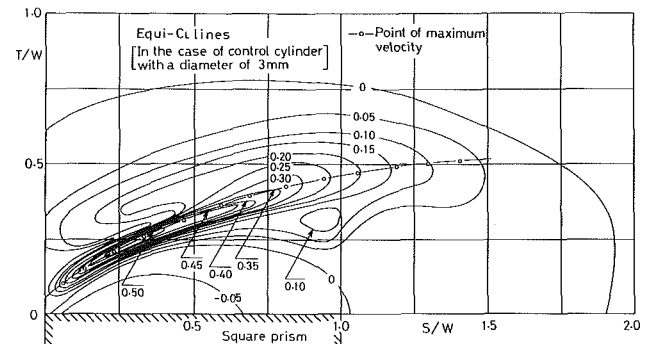
Then it is indicated that the time-mean lift coefficient C_L becomes the largest when the control cylinder is located along the outer boundary of the shear layer. This is probably due to the following reason: when the control cylinder is located along the outer boundary of the shear layer, the flow near the outer boundary of the shear layer dominating mainly the fluid forces bends toward the square prism (between the square prism and the control cylinder), so that the velocity on the bent shear layer increases due to the interference with the wake of the control cylinder. As a result, the negative pressure on the upper side (AD side) of the square prism becomes larger than that on the bottom side (BC side), causing upward lift. Figure 6 shows the distribution of the time-mean pressure coefficient C_P at the positions (x_s, y_s) on the surface of the square prism, as shown in Fig. 2, when the control cylinder

with a diameter $d = 3$ mm is placed in the position of $S/W = 0.36$ and $T/W = 0.27$. As seen from the figure, the negative pressure on the upper side AD is substantially larger than that on the bottom BC. Also, it is noticed that the pressure on the bottom side of the square prism is substantially smaller than that without the control cylinder. This indicates that the change of the characteristics in the wake caused by controlling the shear layer on one side, namely, the base pressure, the reverse flow and the concentration and counterbalance of the vortices, would be changed that of the shear layer on other side in a manner like feedback.

Figure 7 shows that relation between the minimum time-mean drag coefficient $(C_D)_{min}$ and the longitudinal position of the control cylinder S/W when the diameter of the control cylinder is changed from 3 mm to 6 mm in 1 mm increments. As the longitudinal distance of the control cylinder S/W increases, $(C_D)_{min}$ decreases rapidly and the control effect is fairly large up to about $S/W = 1$. However, when the control cylinder is located near the leading edge of the square prism or in the region over $S/W = 1$, the control effect is not so remarkable. Generally, the process of the vortex shedding is as follows: laminar shear layer separated from the prism $\Rightarrow$ transition $\Rightarrow$ turbulent shear layer $\Rightarrow$ concentration of vortices $\Rightarrow$ shedding of vortex. Therefore, when the control cylinder is located near the leading edge, since only the transition from laminar to turbulent shear layer is promoted, the strength and position of rolling-up of shear layer do not change greatly.
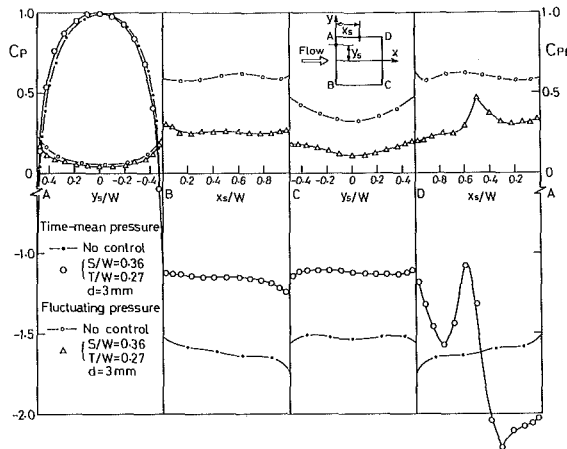
Moreover, in the region over $S/W = 1$, since the rolling-up of the shear layer to form large-scale vortices has already begun, the control cylinders with small diameters employed in this study cannot prevent the rolling-up of that into the vortex formation region. Also, the maximum reduction rate of the time-mean drag of the square prism caused when the control cylinder with the diameter of $d = 6$ mm is located at $S/W = 0.84$ and $T/W = 0.44$ is reached to about 30 percent.

Figure 8 shows the relation between the maximum lift coefficient $(C_L)_{max}$ and the longitudinal position of the control cylinder S/W when the diameter of the control cylinder is changed from 3 mm to 6 mm in 1 mm increments. When the control cylinder exists in a region where S/W is smaller than 1.0 except near the leading edge of the square prism, a large upward lift is generated. For example, fairly large lift which is a maximum value of $(C_L)_{max} = 1.0$ is generated in the case of the control cylinder with a diameter of 6 mm. For the body with symmetrical shape, a method to cause lift by boundary layer control employing a tangential blowing from surface slot or surface protrusions has been established (James and Truong, 1972; Lockwood, 1960; Wake and Yoshino, 1987). When only the generation of lift is considered, the method employed in this study in which relatively large lift can be obtained by simply placing a cylinder, which is considerable small compared to the square prism, is also worth consideration.

In Fig. 9, the positions of the control cylinder for the optimum suppression are plotted. As the diameter of the control cylinder becomes larger, its position somewhat moves in towards the direction of T/W. In the region of S/W smaller than 1.0, the positions of the control cylinder where the time-mean drag is the smallest coincide with that where the time-mean lift is the largest. However, in the region of larger than $S/W = 1$, these are different (indicated in oblique lines because of scatter of data). It is assumed that this is because the change of the drag is caused by the strength and the position of the rolling-up of the shear layer, while the lift is caused by the increase of the velocity due to the interference of the wake of the control cylinder and the outer boundary the shear layer of the square prism. Also, we can obtain the lateral distance T/W in direction normal to the flow from Fig. 9.

3.3 Control of Fluctuating Lift and Drag. Figures 10 and 11 show the r.m.s. values of the fluctuating lift coefficient C_{Lf} and drag coefficient C_{Df} when the position of the control cylinder with a diameter of 3 mm is changed. Each result is indicated as a ratio to $C_{Lf} = 1.12$ and $C_{Df} = 0.168$ of the square prism without the control cylinder. As can be seen from

Fig. 6 Distribution of the time-mean and the r.m.s. pressure coefficient. (Uncertainty in C_p: less than ±2 percent, in C_{pf}: less than ±2 percent, in x_s/W, y_s/W: less than ±0.5 percent.)
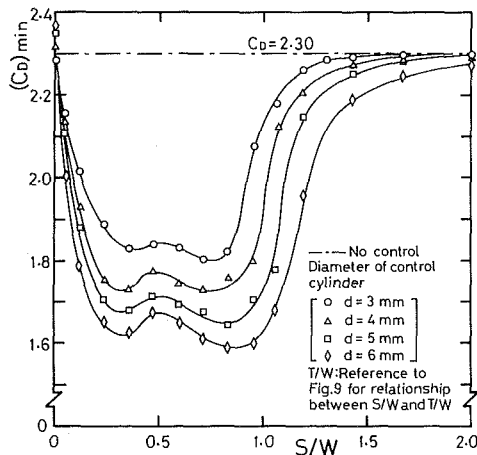

Fig. 7 Minimum values of time-mean drag coefficient at each section S/W for change in diameter of the control cylinder. (For further information see the caption of Fig. 4.)
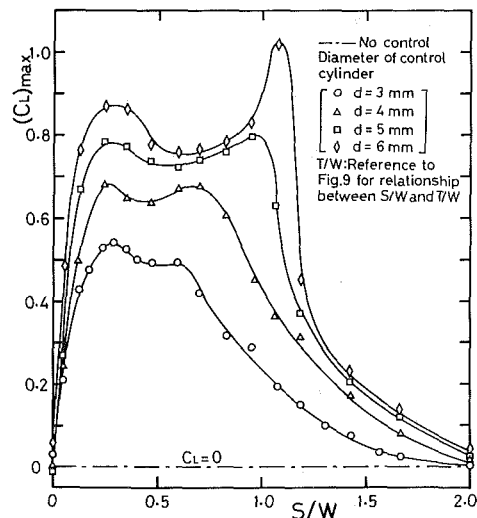

Fig. 8 Maximum values of time-mean lift coefficient at each section S/W for change in diameter of the control cylinder. (For further information, see the caption of Fig. 5.)
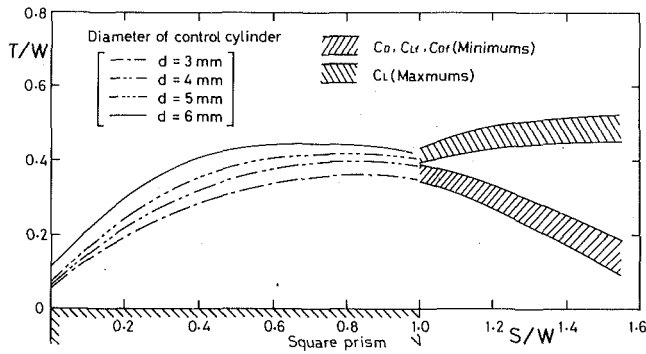
Fig. 9 Position of the control cylinder for the optimum suppression of fluid forces. (Uncertainty in *S/W* and *T/W*: less than ±0.5 percent.)
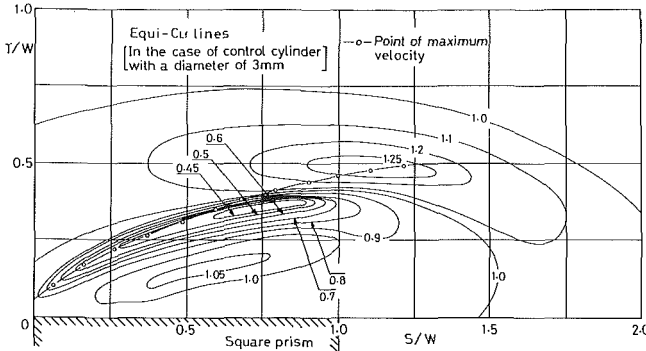

Fig. 10 Equi-line diagram of the fluctuating lift coefficient. (Uncertainty in C_{Lf}: less than ±3 percent.)
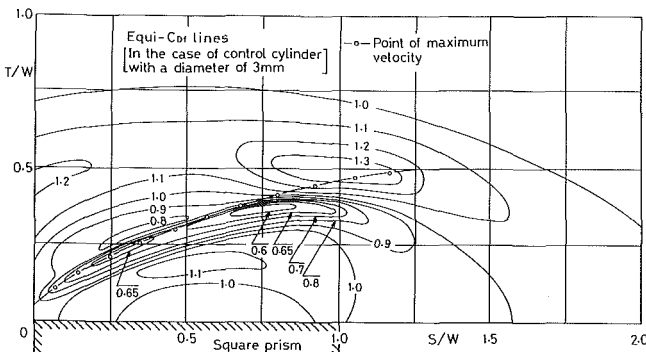

Fig. 11 Equi-line diagram of the fluctuating drag coefficient. (Uncertainty in C_{Df}: less than ±3 percent.)

the figures, C_{Lf} and C_{Df} are most suppressed as in the case of the time-mean drag when the control cylinder is located near the outer boundary of the shear layer representing the maximum velocity. However, unlike the case of the time-mean drag, when the control cylinder is located on the outside of the outer boundary of the shear layer in vicinity of the rear end of the square prism, C_{Lf} and C_{Df} show a larger value compared to the value without the control cylinder. This is most likely due to the fact that the shear layer is forcibly bent by the control cylinder and rolls up strongly into the vortex formation region, so that the concentration of vortices is intensified. In general, the change in characteristics of the flow in the vortex formation region also affects the base pressure which dominates the drag. However, as indicated in Fig. 4 in section 3.2, when the control cylinder is located in these positions, no considerable increase is recognized in C_D. The reason for this is not clear at the present time since the relation between the base pressure and characteristics of the flow in the vortex formation region remains unclear. But, it can be concluded that the time-mean drag is less sensitive to the change of the characteristics of the

flow in the vortex formation region compared with the fluctuating fluid forces.

The distribution of r.m.s. values of the fluctuating pressure coefficient C_{pf} on the surface of the square prism when the control cylinder with a diameter of d = 3 mm is placed in the position of $S/W = 0.36$ and $T/W = 0.27$ is shown in Fig. 6, together with the time-mean pressure coefficient already discussed in section 3.2. Despite the control of the shear layer only on one side, the fluctuating pressure not only on the side where the control cylinder exists (AD side) but on the opposite side (BC side) is greatly reduced as compared to values without the control cylinder. The strength of the vortex (strength of circulation) dominated the fluctuating pressure on the surface of the square prism is determined by the magnitude of the counterbalance of the vortices with opposite rotation to each other carried into the vortex formation region by the shear layers on two sides. In other words, it is necessary to equalize the strength of circulation of two vortices with opposite rotation to each other shed from the vortex formation region in order to form a stable vortex street. Therefore, it can be concluded that the suppression of the concentration of the vortices in the vortex formation region based on the control of the shear layer on one side changes the characteristics of the shear layer on other side.

Figure 12 shows the waveforms and the power spectrum distribution of the fluctuating lift in the cases of three patterns, which are (a) uncontrolled, (b) decrease in the fluctuating lift, and (c) increase in the fluctuating lift, with regard to the control cylinder of the diameter $d = 5$ mm. As can be seen from Fig. 12(b), it is noticed that the lift fluctuates almost regularly with time-averaged value of $C_L = 0.76$ corresponding the time-mean lift despite the control of the shear layer on one side. Accordingly, from this result, it can be concluded that the vortices with equal circulation of opposite rotation to each other are alternately shed from the vortex formation region. Also, the other notable feature of the waveforms of the fluctuating lift is that two kinds of fluctuating lift, which are a large and small values, are generated intermittently as shown in Fig. 13. Such phenomenon exists for each control cylinder, for example, in case of the control cylinder with $d = 5$ mm, it is generated when the control cylinder is located at the limited position of $S/W = 0.60$, $T/W = 0.24$ and $S/W = 1.07$, $T/W = 0.42$, respectively. Thus, there exists a bistable phenomenon when the control cylinder is located at such positions. As can be seen clearly from Fig. 13, two kinds of the fluctuating lift are generated with different magnitude lasting a certain length of time, clearly indicating the existence of a bistable flow. Such a bistable phenomenon results in a small fluctuating lift when the shear layer bends between the control cylinder and square prism and a large fluctuating lift when the shear layer bends outside the control cylinder. The bistable phenomeneon is also recognized with the two square prisms and circular cylinders with the same dimensions are arranged in tandem (Sakamoto and Haniu, 1988; Arie et al., 1983). However, the fact that the bistable flow is generated despite the considerable difference in size between the square prism and the control cylinder and the staggered arrangement as in the present study is noteworthy. From this result, it is considered that the fluid forces of the bluff body with the separated flow are mainly dependent on the characteristics of a very thin region in the shear layer. Thus, some methods that have been presented to evaluate the fluid forces by representing the separated shear layer as one free-streamline (Parkinson, 1970) are considered to be adequate.

Figures 14 and 15 show the distributions of the minimum values $(C_{Lf})_{min}$ and $(C_{Df})_{min}$ at each section S/W when the diameter of the control cylinder is changed. From these results, when the control cylinder exists in the vicinity of $S/W = 0.8 \sim 1.0$ where the shear layer is supposed to start the rolling-up into the vortex formation region, the fluctuating lift and
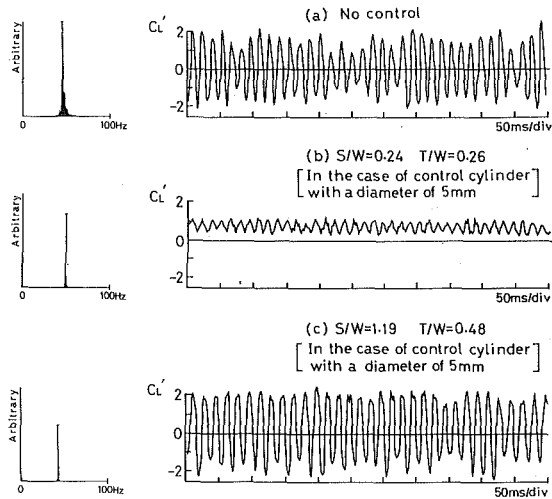
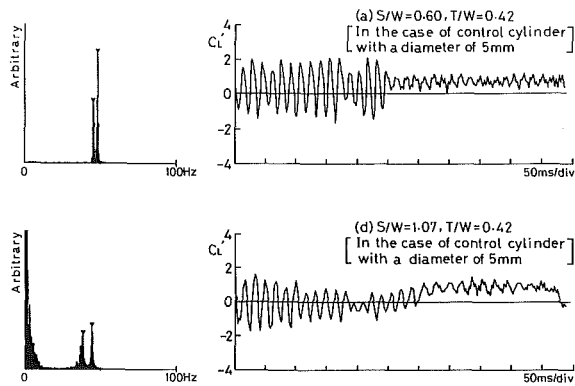Fig. 12 Waveform and power spectrum of the fluctuating lift

Fig. 13 Waveform and power spectrum of the fluctuating lift for bistable flow

Fig. 14 Minimum values of the fluctuating lift coefficient at each section S/W for change in diameter of the control cylinder. (For further information, see the caption of Fig. 10.)

Fig. 15 Minimum values of the fluctuating drag coefficient at each section S/W for change in diameter of the control cylinder. (For further information, see the caption of Fig. 11.)

drag are suppressed most. In the case of the control cylinder with a diameter of 6 mm, for example, the maximum reduction rate of C_{Lf} and C_{Df} of the square prism caused at $S/W = 0.95$ and $T/W = 0.44$ are reached to about 95 and 75 percent, respectively. Therefore, it is possible almost to suppress the fluctuating forces completely by setting the control cylinder with the diameter $d = 6$ mm ($d/W = 0.14$) on one side of the square prism. It is also indicated that the control of the shear layer is more effective to the unsteady fluid forces rather than the steady fluid forces. Furthermore, the positions of the control cylinder for optimum suppression of the fluctuating lift and drag are the same the time-mean drag. Accordingly, the lateral distance T/W of the control cylinder in direction normal to the flow can be estimated from Fig. 9.

3.4 Strouhal Number and Classification of Flow Pattern. Figure 16 show the Strouhal number St ($=fcW/U_0$, fc: frequency of vortex shedding) obtained by the spectrum analysis of the fluctuating lift as a ratio to St $= 0.128$ for the uncontrolled square prism in the form of equi-Strouhal-number lines. When the control cylinder is located along the outer boundary of the shear layer where the fluid forces are most reduced, the Strouhal number increases. This is because the growth of the shear layer is prevented, so that the rolling-up of the shear layer weakens. Namely, since the rolling-up of the shear layer is weakened, the width of the wake decreases, so that the Strouhal number increases eventually. Also, when the control cylinder is located outside the outer boundary of the shear layer where the fluid forces are large, the width of the wake increases because the rolling-up of the shear layer is intensified, so that the Strouhal number decreases.
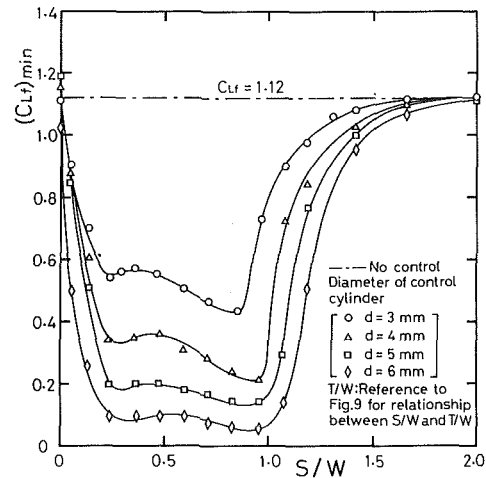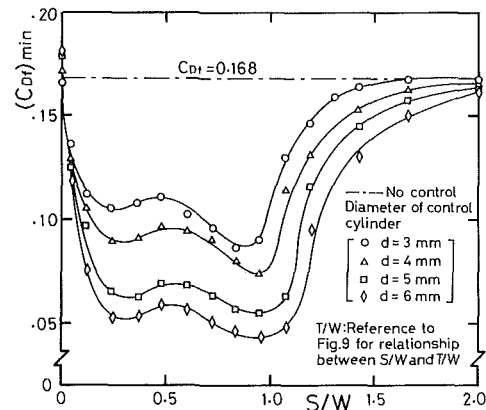
Based on the Strouhal number mentioned above and the change in fluid forces mentioned in section 3.2 and 3.3, the change in position of the shear layer, i.e., its deformation due to the difference in position of the control cylinder, is roughly classified into three patterns shown in Fig. 17. Namely, Pattern A is that the shear layer behaves like that observed for the uncontrolled square prism owing to the fact that the control cylinder is located inside the outer boundary of the shear layer where there is no effect of the control cylinder, Pattern B is that the position of the rolling-up of the shear layer recedes downward, so that the width of the wake becomes more narrow owing to the fact that the control cylinder is now located along the outer boundary of the shear layer, and Pattern C is that the shear layer is forcibly bent by the control cylinder when it is located outside the outer boundary of the shear layer, so that the strength of the rolling-up of the shear layer is intensified.

4 Conclusions

The objective of this paper is to investigate the suppression of fluid forces on a square prism by controlling the separated shear layer on one side of the square prism. The control of the separated shear layer is established by means of a small circular cylinder. The main results of the present study may be summarized as follows:

(1) The maximum reduction of the time-mean drag and the fluctuating lift and drag is found to be induced when the control
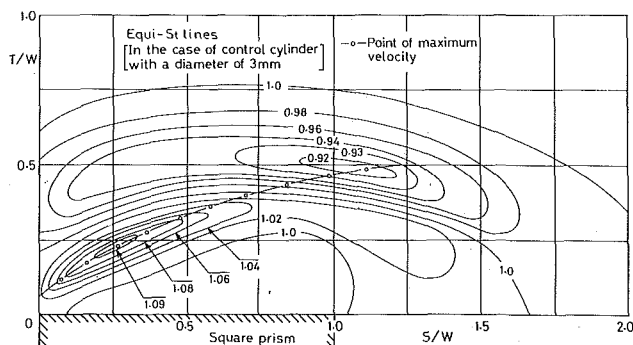
Fig. 16 Equi-line diagram of the Strouhal number. (Uncertainty in S_t less than ±3 percent.)

——— Locus of shear layer
(With a control cylinder)
- - - Locus of shear layer
(Without a control cylinder)
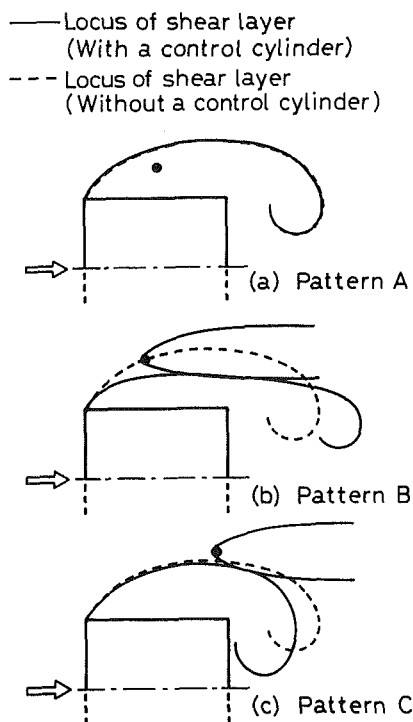

(a) Pattern A

(b) Pattern B

(c) Pattern C

Fig. 17 Locus of the shear layer (maximum velocity positions) due to the change in position of the control cylinder

cylinder is located near what would ordinarily be considered the outer boundary of the shear layer.

(2) Since the control of the shear layer is more effective in suppressing the unsteady fluid forces rather than the steady fluid forces, the unsteady fluid forces are more sensitive to the change of the position and strength of the rolling-up of the shear layer into the vortex formation region compared with the steady fluid forces.

(3) When the control cylinder with the diameter of d = 6 mm, which is considerable small compared to the size of the square prism, is located at the outer boundary of the shear layer, it is found that the maximum reduction of the time-mean drag is 30 percent, and the maximum reductions in the fluctuating lift and drag are approximately 95 and 75 percent, respectively.

(4) Based on the results of the observation of the waveforms and the spectrum analysis of the fluctuating lift, it is found that vortices with equal circulation and opposite rotation to one another are alternately shed from the vortex formation region despite the control of the shear layer on one side.

(5) Since the fluid forces are most suppressed when the control cylinder is located in a limited region near the outer boundary of the shear, it can be concluded that the fluid forces acting on the square prism are mainly dependent on the characteristics of a very thin region in the shear layer.

Acknowledgment

References

Apelt, B. J., West, G. S., and Szewczyk, A. A., 1973, "The Effects of Wake Splitter Plates on the Flow Past a Circular Cylinder in the Range $10^4 < R < 5 \times 10^4$," Journal of Fluid Mechanics, Vol. 61, Part 1, pp. 187–198.

Arie, M., Kiya, M., Moriya, M., and Mori, H., 1983, "Pressure Fluctuations on the Surface of Two Circular Cylinders in Tandem Arrangement," ASME JOURNAL OF FLUIDS ENGINEERING, Vol. 105, No. 2, pp. 161–167.

Bearman, P. W., 1965, "Investigation of the Flow Behind a Two-Dimensional Model with a Blunt Trailing Edge and Fitted with Splitter Plates," Journal of Fluid Mechanics, Vol. 21, Part 2, pp. 241–255.

Bearman, P. W., and Trueman, D. M., 1972, "An Investigation of the Flow Around Rectangular Cylinders," Aeronautical Quarterly, Vol. 23, pp. 229–237.

Fage, A., and Johansen, F. C., 1927, "On the Flow of Air Behind Inclined Flat Plate of Infinite Span," ARC R.&M., No. 1143.

Fage, A., and Warsap, J. H., 1923, "The Effects of Turbulence and Surface Roughness on the Drag of a Circular Cylinder," ARC R.&M., No. 1283.

Igarashi, T., and Tsutsui, T., 1989, "Flow Control Around a Circular Cylinder by a New Method," Transaction of JSME, Vol. 55, No. 511, pp. 701–713.

James, D. F., and Truong, Q. S., 1972, "Wind Load on Cylinder with Span-wise Protrusion," Proc. ASCE, J. Eng. Mech., Vol. 98, No. EM6, pp. 1573–1589.

Knell, B. J., 1969, "The Drag of a Circular Cylinder Fitted with Shrouds," Natl. Phys. Lab. (U.K.), Aero. Rep., No. 1297.

Lockwood, V. E., 1960, "Lift Generation on a Circular Cylinder by Tangential Blowing from Surface Slots," NASA, Tech. Note, No. D-244.

Parkinson, G. V., and Jandali, T., 1970, "A Wake Source Model for Bluff Body Potential Flow," Journal of Fluid Mechanics, Vol. 40, Part 3, pp. 577–594.

Price, P., 1956, "Suppression of the Fluid-Induced Vibration of Circular Cylinder," Proc. ASCE, J. Eng. Mech., Vol. 82, No. EM3, pp. 1030–1042.

Roshko, A., 1954, "On the Drag and Shedding Frequency of Two-Dimensional Bluff Bodies," NACA, Tech. Note, No. 3169.

Sakamoto, H., and Haniu, H., 1988, "Effect of Free-Stream Turbulence on Characteristics of Fluctuating Forces Acting on Two Square Prisms in Tandem Arrangement," ASME JOURNAL OF FLUIDS ENGINEERING, Vol. 110, No. 2, pp. 140–146.

Sakamoto, H., and Oiwake, S., 1984, "Fluctuating Forces on a Rectangular Prism and a Circular Cylinder Placed Vertically in a Turbulent Boundary Layer," ASME JOURNAL OF FLUIDS ENGINEERING, Vol. 106, No. 2, pp. 160–166.

Sasaki, K., and Kiya, M., 1984, Transaction of JSME, Vol. 50, No. 456, pp. 1842–1846.

Strykowski, P. J., and Sreenivasan, K. R., 1985, "The Control of Vortex Shedding Behind Circular Cylinders at Low Reynolds Numbers," Fifth Symp. on Turb. Shear Flows, Cornell University.

Waka, R., and Yoshino, F., 1987, "The Forced Reattachment of the Separated Shear Layer of a Circular Cylinder with Tangential Blowing," Transaction of JSME, Vol. 53, No. 490, pp. 1704–1710.

Wood, C. J., 1967, "Visualization of an Incompressible Wake with Base Bleed," Journal of Fluid Mechanics, Vol. 29, Part 2, pp. 259–272.

Wootton, L. R., and Yates, D., 1970, "Further Experiments on Drag of Perforated Shrouds," Nath. Phys. Lab. (U.K.), Aero. Rep., No. 1321.

Zdravkovich, M. M., 1981, "Review and Classification of Various Aerodynamic and Hydrodynamic Means for Suppressing Vortex Shedding," J. Wind Eng. and Ind. Aerodyn., Vol. 7, No. 2, pp. 145–189.

Ying-Jong Hong
Graduate Student.

Shou-Shing Hsieh
Professor and Chairman.
Mem. ASME

Huei-Jan Shih
Graduate Student.

Department of Mechanical Engineering,
National Sun Yat-Sen University,
Kaohsiung, Taiwan 80424

Numerical Computation of Laminar Separation and Reattachment of Flow Over Surface Mounted Ribs

Numerical results are presented concerning the fluid characteristics of steady-state laminar flow over surface mounted ribs. Computations are carried out using a false transient stream function-vorticity form. The effects of the aspect ratios (width-to-depth) of the ribs and Reynolds numbers as well as initial boundary-layer thickness on entire flow field, separated region, and reattachment length are presented and discussed. The computed reattachment distance compares reasonably well with those data reported by previous studies. A correlation is provided in terms of the rib aspect ratio, Reynolds number, and the ratio of boundary-layer thickness and rib height. The pressure drop is excessive along the upstream vertical step face and it recovers thereafter, which agrees qualitatively with those of the previous studies for the flow over backward-facing steps.

Introduction

This paper concerns numerical computations of a type of separated and reattached flow that is associated with the plane laminar flow over surface mounted ribs. Such a flow field is complicated because two and possibly three separated regions exist. The first region starts from the upstream wall near the rib and reattaches on the front wall of the rib, which is often located below that corner; the second region separates from the rear wall and reattaches on the downstream wall. A third recirculating region, attached to the top of the rib, may exist under certain conditions. After the last region, the flow reattaches, the boundary layer redevelops, and the flow is laminar thereafter. Furthermore, the pressure gradient across the rib is extremely large and the Nusselt number increases rapidly to a high value. The objective of the present study is to explore the details of the flow field, including separated as well as reattached length and the rapid change in pressure.

The work is motivated from recent development in the cooling of electronic equipment and gas cooled reactors, as well as in high performance heat exchanger where more quantitative information on pumping requirements in separated/reattached flow regions is needed (see, for example, Buller and Kilburn (1981), Wirtz and Dykshoorn (1984), and Hsieh (1988)). Studies of the topic in the literature are very few, especially for the laminar case. More recently, Hsieh and Huang (1987a,b) computed laminar flow field over an isolated rib using finite-difference formulation for primitive variables. The rapid change

in pressure and the heat transfer characteristic were reported. The pressure was found to drop rapidly immediately downstream of the front face of the rib followed by a steady recovery. The heat transfer coefficients were obtained for a rib aspect ratio (width/height) of $w/s = 1$, 2, and 4 at different Reynolds numbers covering the range $63.5 \leq Re_s \leq 254$. However, details of the flow field such as pressure distribution across the rib as well as the separated and reattached length for the upstream separation region were not presented in Hsieh and Huang (1987a). Moreover, the effect of the initial boundary layer thickness was not examined.

In the present study, we consider the fully laminar situation in which not only the flow approaching the rib is laminar, but the flow in both separated as well as in the reattached, redeveloping boundary layers is laminar. In addition, the plate upstream of the rib is assumed to have a finite length so that the boundary-layer thickness at the rib becomes a parameter that must be reckoned with.

In the present computation, the finite difference scheme using a false transient stream function/vorticity form is adopted. This choice is made in view of numerical difficulties reported by Baker (1977), who applied the primitive variable approach to turbulent flow over the forward step. Numerical difficulties could be understood in view of large pressure gradient in the field and the way by which the pressure and the continuity equation are treated. This treatment introduces first order errors, which may seriously affect the process of convergence. Large vorticity gradients are also expected near the convex corners. The vorticity equation, however, is of second order and no first order errors will be introduced in the computations.

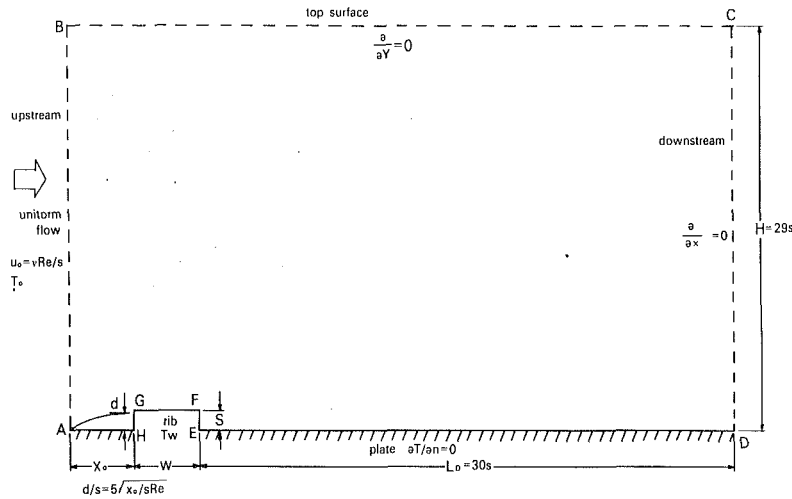It was suggested by Baron et al. (1986) that the power law

Fig. 1 Schematic of domain of calculation

scheme with a new wall-vorticity boundary condition to be described later can be applied to a forward facing step problem with success. This combination would give stable results for various Reynolds numbers, the convergence criterion (β) for all unknowns being set to 0.001. The scheme is therefore used for the present computation.

Mathematical Formulation

In this study, the two-dimensional, steady, laminar incompressible Navier-Stokes equations are solved numerically in terms of vorticity ω and stream function ψ. The false transient stream function equation is written as

$$\frac{\partial \psi}{\partial t} = \frac{\partial^2 \psi}{\partial x^2} + \frac{\partial^2 \psi}{\partial y^2} + \omega \tag{1}$$

and the conservation equation for vorticity is

$$\frac{\partial \omega}{\partial t} + u \frac{\partial \omega}{\partial x} + v \frac{\partial \omega}{\partial y} = \frac{1}{Re} \left(\frac{\partial^2 \omega}{\partial x^2} + \frac{\partial^2 \omega}{\partial y^2} \right) \tag{2}$$

The normalizing factors for length, velocity, and time are the height of the rib s, the uniform approaching velocity U_0, and s/U_0, respectively. The velocity is related to the stream function by

$$u = \frac{\partial \psi}{\partial y}, \quad v = - \frac{\partial \psi}{\partial x} \tag{3}$$

The transient term ($\partial \psi / \partial t$) appearing in equation (1) is a fictitious one, i.e., the intermediate results can by no means be considered as a transient solution. Detailed discussion on this false transient approach is provided by Mallinson and Davis (1973).

The surface pressure can be found by applying the nonslip boundary condition at the wall to the Navier-Stokes equations. They become

$$\frac{\partial \bar{p}}{\partial x} = - \frac{1}{Re} \frac{\partial \omega}{\partial y}, \quad \frac{\partial \bar{p}}{\partial y} = \frac{1}{Re} \frac{\partial \omega}{\partial x} \tag{4}$$

where $\bar{p} = (p - p_0)/\rho U_0^2$ is the pressure coefficient. Traditionally (see Roache (1972)), this requires the solution of a Poisson equation for the pressure with Neumann boundary conditions evaluated from the velocity solution. However, the pressure is often required only on the surface of the rib considered which forms the boundary of the computational domain (see, for example, Roache (1972), Fletcher and Srinivas (1983), Baron et al. (1986)). The surface pressure can thus be obtained by integrating equation (4), with respect to x and y which gives

$$\bar{p} = - \frac{1}{Re} \int_{x_0}^{x} \frac{\partial \omega}{\partial y} \, dx + \bar{p}(x_0)$$

$$\bar{p} = \frac{1}{Re} \int_{y_0}^{y} \frac{\partial \omega}{\partial x} dy + \bar{p}(y_0)$$

$$\tag{5}$$

The boundary conditions are prescribed for the computational region indicated in Fig. 1. The approaching flow is of uniform velocity U_0. The distance from leading edge to the rib front face, x_0, is a parameter controlling the thickness of the approaching boundary-layer on the separation regions; the boundary-layer thickness, d, is calculated from the relation for laminar boundary layer on a flat plate

$$d/s = 5\sqrt{x_0/s/Re_s} \tag{6}$$

Nomenclature

d = boundary layer thickness at the location of the rib computed in its absence (equation (6)), cm

G_n = the value of a function and the subscripts refer to iteration number

H = height of top boundary, cm

L_D = length of downstream boundary, cm

$Lr4$ = dimensionless reattachment length

P_0 = freestream pressure, N/m^2

$\bar{p}$ = dimensionless pressure, $(p - p_0)/\rho U_0^2$

Re, Re_s = Reynolds number based on rib depth

s = rib depth, cm

T_w = rib wall temperature, °C

T_o = freestream temperature, °C

U_0 = freestream velocity, m/s

u, v = velocity in x and y directions, respectively, m/s

w = rib width, cm

x_0 = distance of leading edge from the rib, cm

ρ = density, kg/m^3

ω = dimensionless vorticity

ψ = stream function

β = maximum residual

α = the ratio of two adjacent grid size

Subscript

D = distance

s = step height

The downstream boundary is situated far from the rib ($L_D = 30s$), so the gradients of the variables along the streamwise direction can be considered to be negligible. The upper free-stream surface is also away from the plate ($H = 29s$), so the region is sufficiently large to give computational results that are size independent. On the solid walls of plate and rib, the non-slip condition applies.

As stated in Baron et al. (1986), it is critical to approximate the boundary condition for vorticity at solid wall especially for solving the gradients of pressure and vorticity in the vicinity of the rib. To avoid the numerical instability contributed by these great gradients, a method developed by Baron et al. (1986) based on an accurate description of non-slip wall condition to improve the traditional wall vorticity boundary condition has been utilized. Consider three grid points near the wall (see Fig. 2), the wall vorticity at the point closest to the wall can be computed from the continuity equation

$$\nabla^2\psi_2 = -\omega_2 \qquad (7)$$

On the wall, the non-slip condition must be satisfied, i.e., $(\partial\psi/\partial y)_1 = 0$. Practically, this is done by a three-point backward finite difference scheme for the first derivatives. For Fig. 2 one can select,

$$\left(\frac{\partial\psi}{\partial y}\right)_1 = \frac{1}{\alpha(1+\alpha)\Delta y}\{-\psi_1\alpha(2+\alpha)$$
$$+\psi_2(1+\alpha)^2-\psi_3\}+0(\Delta y^2)=0 \qquad (8)$$

where α is the ratio of two adjacent grid size.

The computing process proceeds as follows: ψ and ω are calculated by iteration in the regular manner all the way down to point 3 (see Fig. 2). The value of ψ_2 is obtained by solving equation (8) with ψ_1 given on the boundary and ψ_3 from the last iteration. Finally, with the new value of ψ_2 available, ω_2 is obtained from equation (7). In this procedure, the nonslip condition is forced on the system to the extent of the accuracy of the expression given in equation (8). No wall vorticity ω_1 is really needed. To omit the term $\partial\omega/\partial y$ from the Taylor's expansion in deriving the traditional wall vorticity boundary conditions does not force the nonslip condition on the system. In this way the use of the value of ω at the corner was avoided and the true singular character of variation of ω around the corner was maintained.

Numerical Procedure

The alternating-direction-implicit (ADI) method was used. The ADI formulation of the governing equations is a tridiagonal matrix that can be solved readily using the Thomas algorithm. ADI was preferred over other methods because it allows relatively larger time steps. Furthermore, it has second-order accuracy and its weak stability conditions are easier to satisfy. The instabilities are caused by convection terms of equation (2). In order to improve the instability, the nonlinear
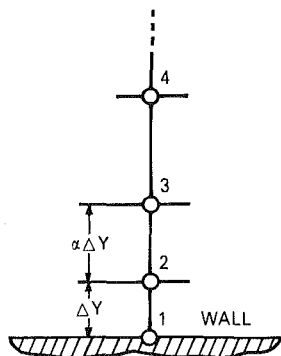
terms were evaluated using the power law scheme provided by Patankar (1980). There is an additional point that should be mentioned about the numerical procedure. With the grid structure used, the external corner points, points G and F in Fig. 1, of the rib are grid points and the vorticity is singular there. Although the corner points H and E are also grid points, the vorticity is not singular there and in any case the value of the vorticity at these points does enter the calculation.

It is found that the numerical solutions are sensitive to the size of the region A'BCDEFGH (see Fig. 1), as well as to the grid distribution. Several region sizes are tested using a given grid distribution. The final size is selected after no significant change is observed in the solution. Next, tests of various non-uniform grid systems are made for 70×50, 75×55, 85×60, 90×65, and 95×70, respectively, and a choice of the final grid distribution, 85×60 is sufficient to provide a surface pressure at sharp corner (F and G in Fig. 1) that is independent of the grid size (less than 3 percent difference between 85×60 and 90×65), and which can be seen from Fig. 3(a). The finest grid, of dimension 0.02s, is located adjacent to the wall, and the sizes of other grids are chosen such that each is within 125
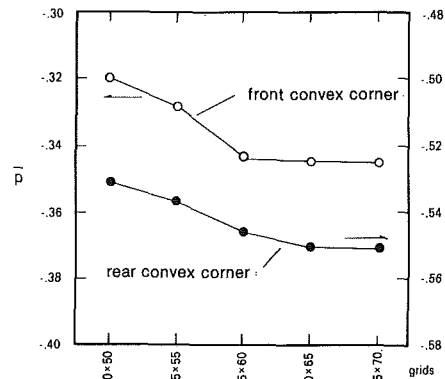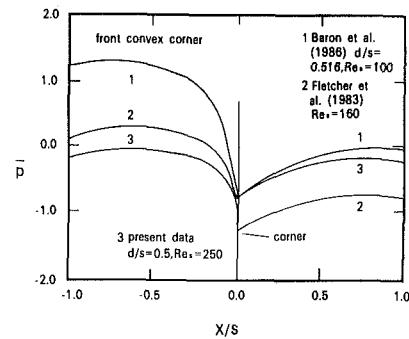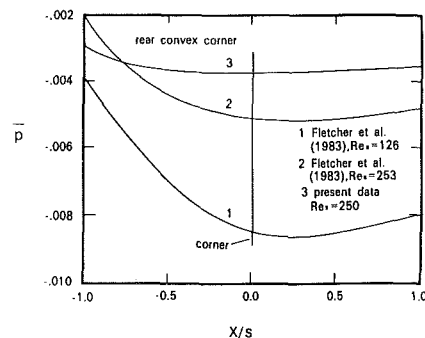
Fig. 3 (a) Computed surface pressure at sharp corner for various grid systems (b) comparison with Baron et al. and Fletcher et al. results (c) comparison with Fletcher et al. results

Fig. 2 Node details for the boundary

percent of the next grid in order to avoid abrupt changes and to obtain convergence. In 85×60 grid system, the ratio of two adjacent grid size (α) is 1.239. Figure 3(b) shows that the surface pressure distribution at the neighborhood of the front convex corner of present data (at $d/s = 0.5$, $\text{Re}_s = 250$) and those of Baron et al. ($d/s = 0.516$, $\text{Re}_s = 100$, forward-facing step) and those of Fletcher et al. (at $\text{Re}_s = 160$, forward-facing step). Figure 3(c) shows that the surface pressure distribution at the neighborhood of the rear convex corner of the present data (at $\text{Re}_s = 250$) and those of Fletcher et al. (at $\text{Re}_s = 126$ and 253).

The effect of the sharp corner vorticity singularity on the pressure solution is very important (also it is quite sensitive to the normal vorticity gradient term in equation (5)). To obtain the vorticity at the sharp corner F and G (see Fig. 1), several averaging methods using the value of its neighboring node are tested. The calculated surface pressure value varies within 5 percent. A comparison with other articles as shown in Fig. 3(b) and (c) shows that the present results behave very well. The final choice of the computation is based on the linear relation with the node north next to the sharp corner.

A variable G is said to be convergent if its residual is smaller than a pre-assigned value. The residual is defined as

$$\beta = \left| \frac{G_n - G_{n-1}}{G_n} \right|_{\substack{\max \\ i, j}} \quad (9)$$

when n refers to the nth iteration and i, j stands for the node position. In the above expression, the residual β represents the maximum value throughout the computational region. the preassigned maximum residual value is 0.001 for all cases. It was found that the first guess of the flow field is not of an essential importance as described in the literature. The relaxation parameters were set to 0.3 and the false time increment to 0.52. No internal iterations were performed. The present numerical calculations were performed on a CDC Cyber 840A at the computer center of National Sun Yat-Sen University.

Results and Discussion

The computational results for the region ABCDEFGH in Fig. 1 are presented in this section. The assumption of steady flow was tested first. It was found that for a Reynolds number over 400 no steady solution could be achieved. The values of the various dimensions and boundary conditions as well as the relevant parameters are given in Table 1. For the total 48 cases studied herein, Table 2 gives the salient features regarding the flow over a surface mounted rib. The physical interpretations of the relevant parameters are illustrated in Fig. 4. In general, it is found that both Lf1 and Lf2 are really independent of w/s; both Lu1 and Lu2 are solely dependent on d/s. Furthermore, separation bubble exists on the top of the rib only for boundary-layer thickness less than 40 percent of the rib height. Lr4 increases as Reynolds number and d/s increase. However, it decreases as w/s increases. Detail physical explanation of the aforementioned findings will be given in the forthcoming section.

The Flow Field and Surface Pressure. Figure 5 shows typical contour plots of the dimensionless stream function for the case of $d/s = 0.4$ and $w/s = 4$ and at the different Reynolds number 200, 250, 300, and 400. It is seen from the figure for $\text{Re}_s = 250$ that the approaching flow streamlines are curved

Table 1 Geometry parameters and boundary conditions

parameters	s	height of the rib, 1.27 cm
	w	width of the rib, 1.27, 2.54, 3.81, 5.08 cm
	H	29s
	L_D	30s
	x_0	1.6 ~ 29.3 (cm)
	Top boundary	Free
	d/s	0.4, 0.5, and 1.2
	w/s	1, 2, 3, and 4
	Re_s	200, 250, 300, and 400
boundary conditions	plate surface	$\psi = 0$, $\omega = -\partial^2 \psi / \partial y^2$
	rib surface	$\psi = 0$, $\omega = -\partial^2 \psi / \partial n^2$
	upstream	$\psi = y$, $\omega = \partial^2 \psi / \partial x^2$
	downstream	$\partial^2 \psi / \partial x^2 = 0$, $\partial \omega / \partial x = 0$
	free surface	$\partial^2 \psi / \partial y^2 = 0$, $\omega = 0$

Table 2 Tabulated calculated results of relevant parameters

Re	d/s	w/s	Lf1	Lf2	Lu1	Lu2	Lr1	Lr2	Lr3	Lr4
200	0.4	1	0.3304	0.2109	0.2077	–	–	0.1198	0.1227	10.1899
		2	0.3300	0.2106	0.2451	1.3988	1.0110	0.0892	0.0903	9.2671
		3	0.3298	0.2104	0.2739	1.1891	0.9919	0.0752	0.0771	8.0901
		4	0.3299	0.2105	0.2519	1.2975	0.9823	0.0677	0.0675	7.3400
	0.5	1	0.4801	0.2772	0.4561	–	–	0.1099	0.1129	12.7902
		2	0.4789	0.2766	–	–	1.0054	0.0843	0.0856	11.8720
		3	0.4784	0.2763	–	–	0.9975	0.0748	0.0767	10.6898
		4	0.4785	0.2765	–	–	0.9862	0.0674	0.0671	9.7093
	1.2	1	1.1769	0.5372	–	–	0.9961	0.0757	0.0771	15.1714
		2	1.1643	0.5350	–	–	0.9903	0.0670	0.0666	13.8845
		3	1.1622	0.5345	–	–	0.9870	0.0590	0.0595	12.9269
		4	1.1643	0.5350	–	–	0.9838	0.0556	0.0561	12.1524
250	0.4	1	0.4097	0.2473	0.2316	–	–	0.1261	0.1291	11.2756
		2	0.4091	0.2466	0.2658	1.4294	1.0182	0.0977	0.0983	10.5908
		3	0.4088	0.2463	0.2947	1.1980	0.9969	0.0794	0.0812	9.4676
		4	0.4088	0.2465	0.2716	1.2891	0.9844	0.0742	0.0760	8.5754
	0.5	1	0.5866	0.3232	0.5519	0.8411	1.0000	0.1139	0.1170	13.7911
		2	0.5854	0.3227	–	–	1.0053	0.0892	0.0903	13.0930
		3	0.5849	0.3225	–	–	0.9997	0.0780	0.0798	12.0041
		4	0.5850	0.3226	–	–	0.9877	0.0737	0.0755	11.0271
	1.2	1	1.3333	0.5686	–	–	0.9948	0.0785	0.0798	16.0800
		2	1.3180	0.5652	–	–	0.9902	0.0731	0.0749	14.8959
		3	1.3150	0.5644	–	–	0.9872	0.0652	0.0652	13.9606
		4	1.3171	0.5649	–	–	0.9842	0.0604	0.0606	13.1955
300	0.4	1	0.4927	0.2716	0.2411	–	–	0.1344	0.1373	12.3485
		2	0.4922	0.2713	0.2752	1.5057	1.0248	0.1070	0.1085	11.8382
		3	0.4919	0.2711	0.3080	1.2506	1.0003	0.0841	0.0858	10.8437
		4	0.4920	0.2712	0.2877	1.3293	0.9868	0.0773	0.0790	9.8999
	0.5	1	0.7290	0.3757	0.4538	–	–	0.1192	0.1222	16.0760
		2	0.7265	0.3743	–	–	1.0114	0.0967	0.0972	15.5515
		3	0.7255	0.3737	–	–	1.0010	0.0821	0.0837	14.6155
		4	0.7256	0.3739	–	–	0.9928	0.0766	0.0783	13.6662
	1.2	1	1.4925	0.6016	–	–	0.9996	0.0860	0.0869	17.2317
		2	1.4725	0.5997	–	–	0.9928	0.0772	0.0789	16.0650
		3	1.4665	0.5991	–	–	0.9887	0.0737	0.0756	14.9662
		4	1.4680	0.5993	–	–	0.9853	0.0705	0.0699	14.2859
400	0.4	1	0.6292	0.3225	0.2482	–	–	0.1506	0.1578	14.0149
		2	0.6280	0.3223	0.2835	1.6575	1.0397	0.1149	0.1158	13.7816
		3	0.6274	0.3219	0.3202	1.3711	1.0014	0.0954	0.9650	13.0499
		4	0.6275	0.3219	0.2995	1.4289	0.9913	0.0840	0.0856	12.1548
	0.5	1	0.8975	0.4198	0.4802	–	–	0.1317	0.1349	16.8633
		2	0.8938	0.4188	–	–	1.0103	0.1081	0.1116	16.5136
		3	0.8919	0.4184	–	–	1.0010	0.0895	0.0908	15.7691
		4	0.8920	0.4184	–	–	0.9935	0.0818	0.0834	14.9530
	1.2	1	1.9325	0.6476	–	–	0.9924	0.0894	0.0904	18.1335
		2	1.9034	0.6445	–	–	0.9897	0.0801	0.0818	17.1781
		3	1.8966	0.6438	–	–	0.9875	0.0764	0.0783	16.3414
		4	1.8986	0.6441	–	–	0.9848	0.0745	0.0763	15.6010
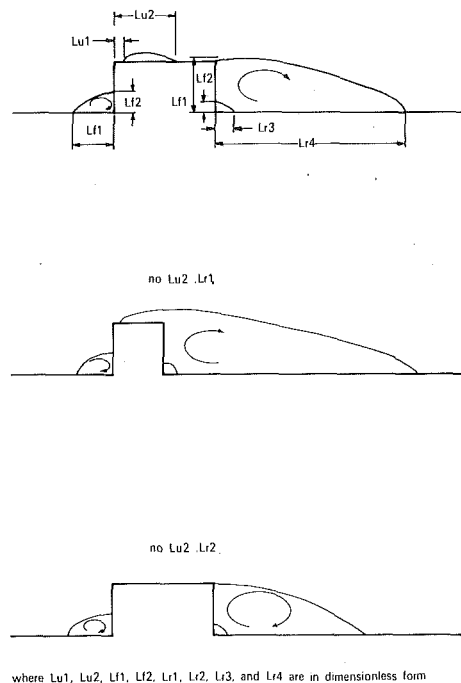
Fig. 4 Different separated flow illustration and relevant parameters

Fig. 5 Streamlines distributions at $d/s = 0.4$ and $w/s = 4.0$ for $Re_s = 200, 250, 300,$ and 400

and densely packed near the upstream protruding corner of the rib. One can treat the streamline $\psi = 0$ as the dividing streamline, this boundary separating the main flow and recirculating region. Because of the adverse pressure gradient, the flow is not able to follow the solid surface and three separation regions result. The one on the rib top, short and shallow, bounded by a dividing streamline and the upper surface of the rib, starts at a distance of $Lu1 = .2716$ (see Table 2) and ends at reattachment point $Lu2 = 1.2891$ (see Table 2). The second separation bubble located at the upstream front corner has a smaller size, extending a short separation distance $Lf1 = 0.4088$ (see Table 2) and short reattachment distance $Lf2 = 0.2465$ (see Table 2). The third separation bubble just right after the corner of the rear rib is larger in size, extending a long reattachment length $Lr4 = 8.5754$ (see Table 2). In the separation regions the stream function assumes negative values, most smaller than -1.0×10^{-4}, and its value is zero on the dividing streamline and on the solid surface. Results for these cases are illustrated by the stream function contours for $d/s = 0.4$ and $w/s = 4$ at $Re_s = 200, 250, 300,$ and 400, which also show that the streamwise length of the third separation eddy appears to increase linearly with Re_s.

Figure 6(a) shows the dimensionless vorticity distribution for $Re_s = 250$, $d/s = 1.2$, and $w/s = 4$. It is seen that the vorticity which is very strong near the corners of the rib is swept and transported into the recirculation region. In addition, the decay of vortex strength in the transverse direction is rather fast compared with that in the streamwise direction. Within the recirculation regions, the value of the vorticity changes sign when one follows a closed streamline. The vorticity contours originated near upper corners of the rib for the up/downstream of the rib which agrees well with those of previous studies for a backward facing step (Aung et al., 1985) and a forward facing step (Baron et al., 1986). It appears that, for a fixed rib size, an increase in Reynolds number would lead to an increase in the vortex strength (not shown here). This is because the Reynolds number increase designates an increase in the velocity, which in turn implies a smaller initial boundary layer thickness at the rib. Thus, a smaller initial thickness gives rise to higher vorticity values in the separated
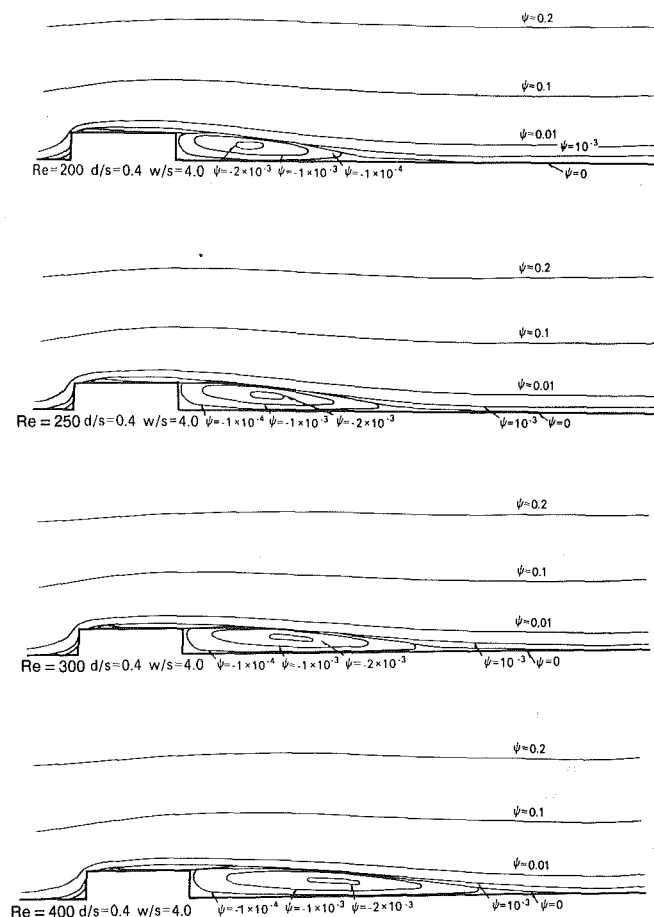
region. This can be roughly seen in Fig. 6(b) from vorticity distribution when the flow passed over the rib at $d/s = 0.5$ and $w/s = 1$ for different Reynolds numbers. Figure 7 shows that the values around external corners (points G and F of Fig. 1) have been found singular there. On the other hand, the values around internal corners (points H and E of Fig. 1) are not singular which also confirms the results of the previous studies for flow over cavities and backward facing steps (Fletcher and Srinivas (1983)).

Figure 8(a) is the surface pressure for cases $Re_s = 250$, $w/s = 3$ for different values of d/s. In the pressure distribution, $x/s = 0$ is the lower corner of front face of the rib. From the leading edge, the pressure drops rapidly to a certain level. For $d/s = 0.4$ and 0.5, as the front face approaches in separated flow regions, the pressure rises to a local maximum. This occurs at the reattachment point of the upstream separated flow on the front surface. A steep drop in the remaining of the front face follows. The minimum pressure exists at the upper corner of the front face, where the velocity is the largest. On the upper surface, the pressure increases. Further downstream, over the separated flow region behind the rear face, the surface pressure changes little until it approaches the reattachment point. Near the reattachment point, the pressure raises and then no obvious changes occur thereafter. This change becomes moderate as d/s increases. This is because the approaching boundary layer carries less momentum as d/s gets larger. The plot of Fig. 8(b) shows that the surface pressure changes little between upstream and downstream of the rib for $w/s = 1, 2, 3,$ and 4. This strongly suggests that the rib width induces no significant changes to the flow for $d/s = 1.2$ in which the boundary layer embraces the rib. In addition, the pressure distribution along
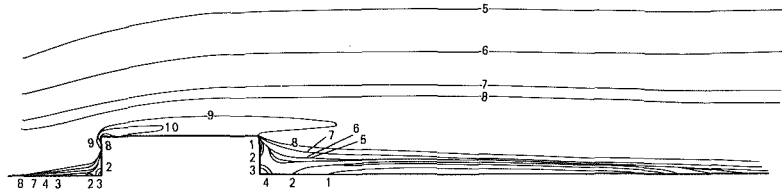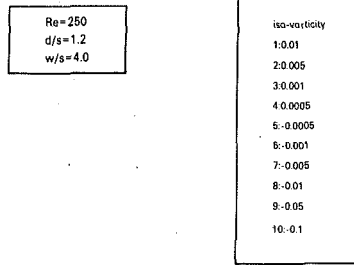
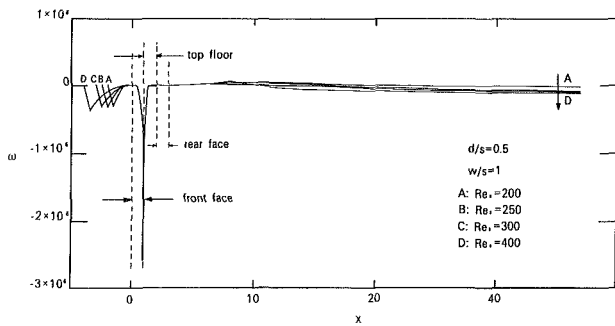Fig. 6(a) Isvorticity distributions at Re_s = 250, d/s = 1.2, w/s = 4.0

Fig. 6(b) Vorticity distributions along rib surface at d/s = 0.5, w/s = 1 for different Reynolds numbers

Fig. 7 Values of vorticity around external/internal corners (points H, G, F and E of Fig. 1)

the rib surface at d/s = 0.4 was plotted for different Reynolds numbers (Fig. 8(c)). As expected, the trend of the pressure distribution is similar to those of Figs. 8(a) and 8(b). it was also found that the Reynolds number would not affect the pressure distribution upstream as significantly as downstream of the rib.

The Size of Separated Regions. The ratio d/s is an important parameter that influences the size of the separated regions. For d/s = 0.4, w/s = 1, 2, 3, 4, the upper separated region exists; for d/s = 0.5, it exists only for w/s = 1, and there is no upper separated regions for d/s = 1.2 from Table 2. The trend may be explained using the surface pressure distribution illustrated in Fig. 8(a). For d/s = 0.4, the approaching boundary layer carries somewhat less momentum and is not able to negotiate the pressure force, resulting in an additional separated region on the top of the rib. However, in the case of d/s = 1.2, the pressure gradient at the protruding corner of the front face becomes so mild that the upper separated region on the top of the rib vanishes, leaving two lower separated regions upstream and downstream of the rib, respectively. For w/s = 1, it is found that the upper separated flow combines with the rear face downstream reattached flow. It forms a negative stream function region covering the rear face and most of the upper face which indicates that w/s is important to the shape of the downstream separated flow.

The quantity w/s has no effect on the upstream flow field. Consequently, the upstream separated flow size seems to be depended solely on the Reynolds number and initial boundary layer thickness. Figures 9(a) and 9(b) show the typical plots of separation and the reattachment point location for the upstream separated flow, respectively, for w/s = 3. In Fig. 9(a), the separated flow size increases with both Reynolds number and initial boundary layer thickness. Figure 9(b) shows the same trend as Fig. 9(a) but the Lf2 value of the corresponding Reynolds number becomes smaller a bit. Most existing literature (e.g., Baron et al. (1986) and Fletcher et al. (1983)) on forward/backward facing steps indicates that the reattachment distance is related to the system and flow parameters in a rather complicated way.

Figure 10(a)-(c) shows the changes of the reattachment length of the downstream bubble at d/s = 0.4, 0.5 and 1.2 for different w/s. The reattachment length increases by increasing Reynolds number and decreasing w/s. As expected, the calculated results can not be represented by a single curve. Fur-
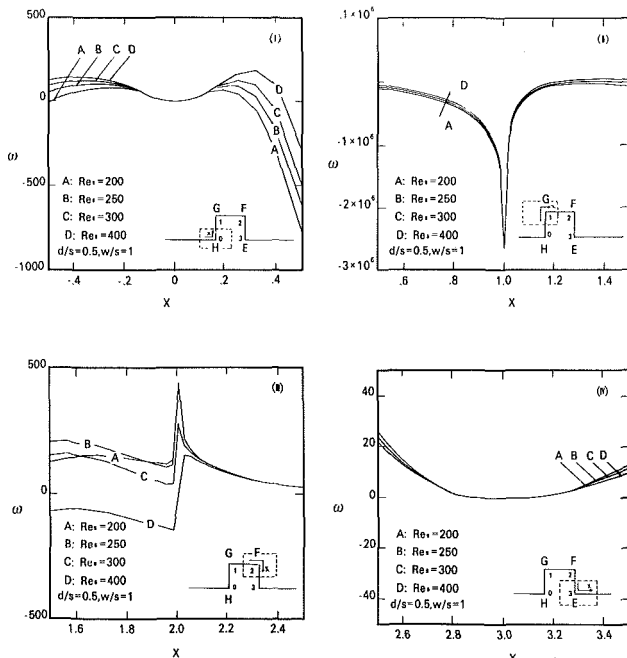
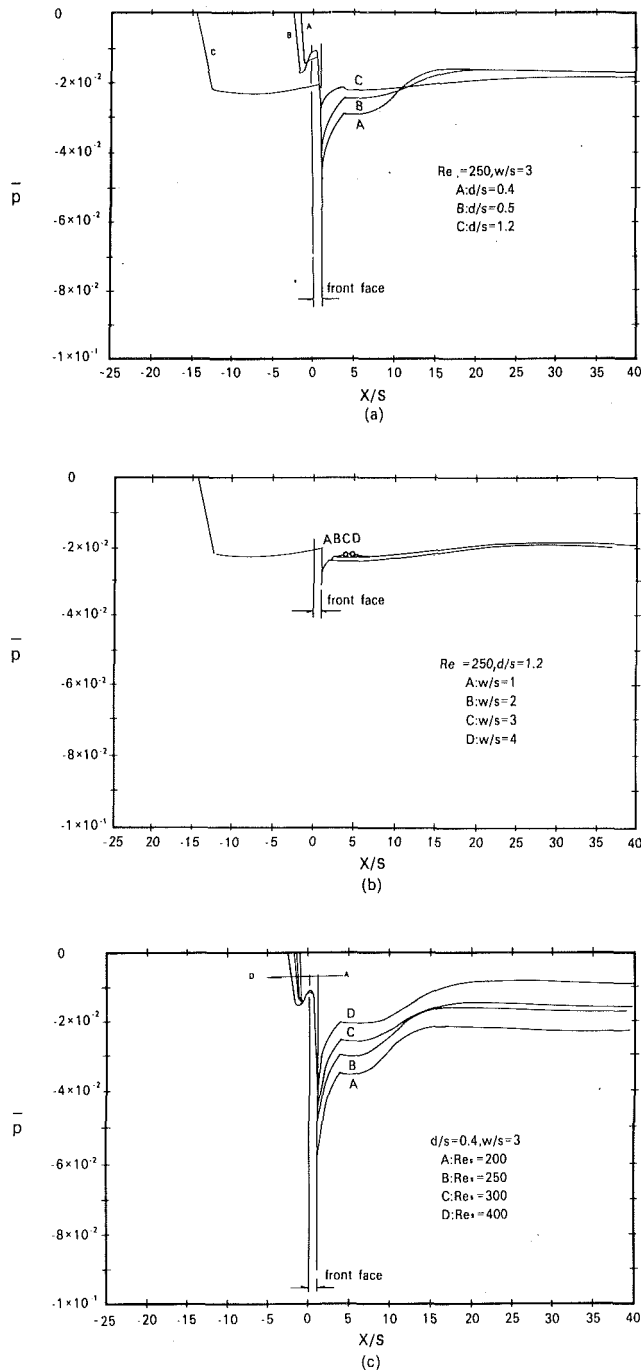Fig. 9(a) Lfl versus Re_s at w/s = 3 (b) Lf2 versus Re_s at w/s = 3

Fig. 8 Pressure distributions along rib surface (a) w/s = 3 and Re_s = 250 (b) Re_s = 250 and d/s = 1.2 (c) d/s = 0.4 and w/s = 3

thermore, the relationship between Lr4 and Re_s is nearly a linear one for any given rib shows in Fig. 10(c). Figures 10(a)-(b) present the reattachment distances versus Re_s at different d/s for w/s = 1 and w/s = 4, respectively, in which it is found that the rate of increase of the dimensionless reattachment length is nearly the same for the Reynolds number and d/s investigated. it also indicates that, for greater d/s, the flow is so slow in the vicinity of the rib that the reattachment length is increased. Those are quite different from the case of Aung et al. (1985) for the backward facing step. They indicated that the curves seem (not shown here) to intersect in the extrapolated Reynolds number in their study. However, this phenomenon did not occur here. This is because the rate of increase of the dimensionless reattachment length is greater at lower values
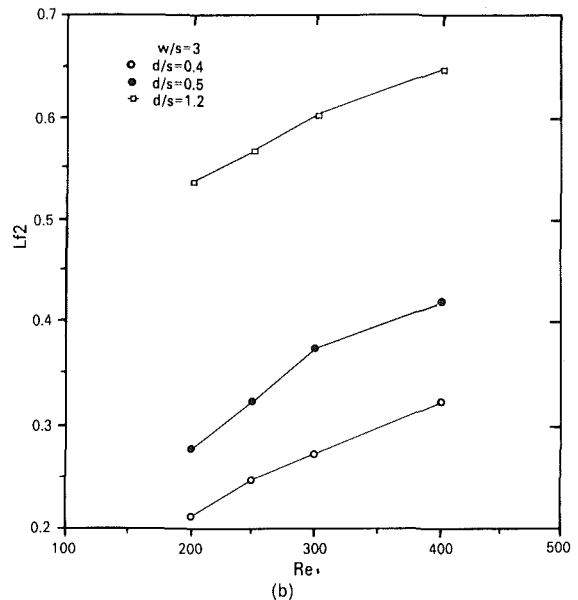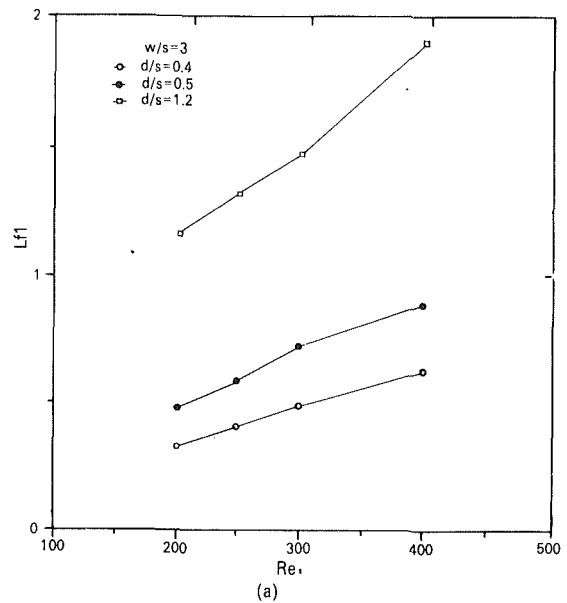
of the Reynolds number and at higher values of d/s for Aung's paper.

Figure 10(a) and 10(b) also display the data of Hsieh and Huang (1987a) for d/s = 0.5. In general, the present results are in good agreement with those of Hsieh and Huang (1987a) at low Reynolds numbers. On the other hand, Hsieh and Huang predicts lower results than the present results at higher Reynolds number. It is also found (Fig. 10(a)), that the present computation yields results of reattachment length that are higher than those of Hsieh and Huang (1987a). The influence of the approaching boundary layer thickness on the reattachment distance was investigated by plotting the dimensionless Lr4 against d/s as shown in Fig. 11. The influence of the boundary layer thickness is most pronounced at the highest Reynolds number and at the smallest w/s. As the Reynolds number is reduced, so is the slope of the curve. An increase of the approaching boundary-layer thickness results in an increase of the axial extent of the downstream bubble. For practical applications the aspect ratio of the rib is a very important
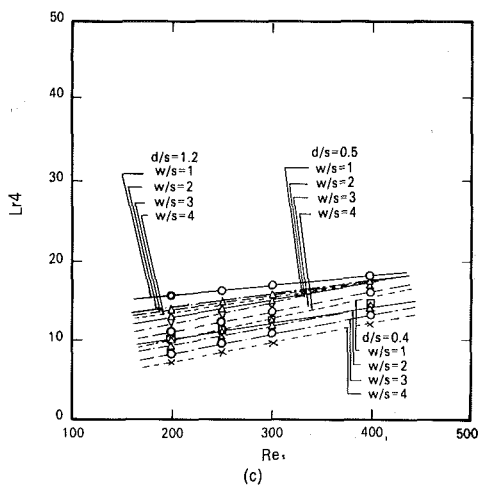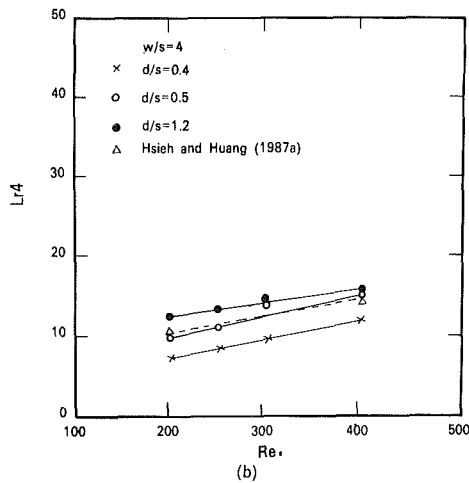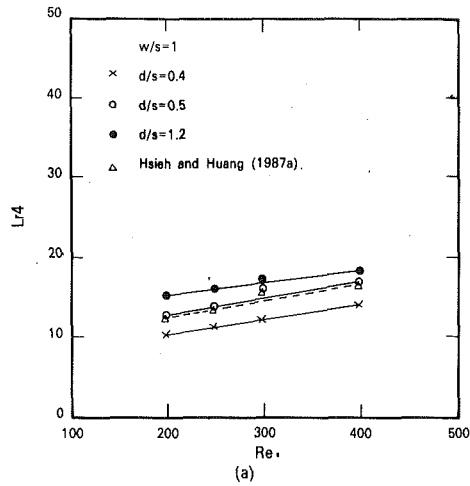
(a)

(b)

(c)

Fig. 10   Lr4 versus Re_s and comparison with Hsieh and Huang (1987a)

Fig. 11   Relationship of Lr4 and *d/s*
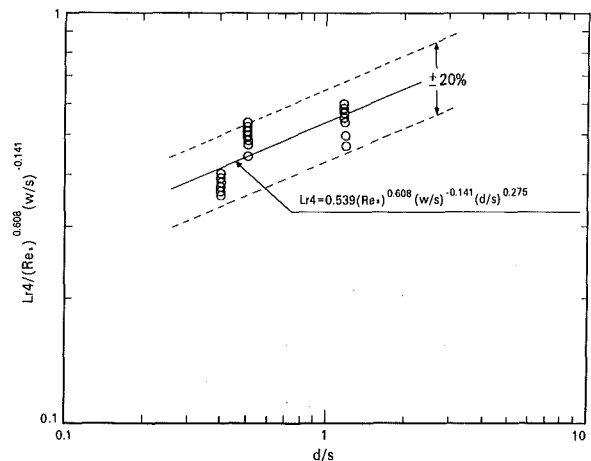
Fig. 12   Analytical correlation of Lr4

parameter which should be taken into consideration. It is found that Lr4 would be reduced as *w/s* increases for all cases studied (see Table 2). No fully satisfactory explanation is forthcoming at this stage.

Correlation of Reattachment length With Parameter (Re_s, *d/s*, *w/s*). It can also be found in Fig. 10(*c*) that the curves exhibit a definite distribution and the slope of each curve approximately the same. This indicates that there exists at least a length scale, either *d/s* or *w/s*. Keeping *d/s* constant, the relationship between $Lr4/(Re_s)^{0.608}$ and *w/s* can be found. As
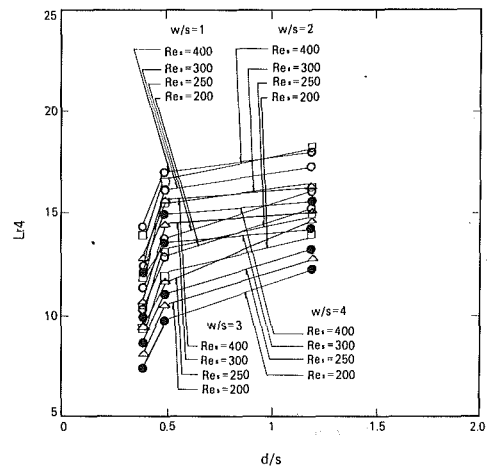
expected, the slope of the present four curves for *w/s* = 1, 2, 3, and 4 are nearly the same within the ± 9.95 percent to the raw numerical data (not shown here). This again suggests that the three curves may collapse into a curve as long as the length scale *w/s* is carefully chosen. Fig. 12 shows that results of which the Lr4 can be directly correlated with three parameters of Re_s, *d/s* and *w/s* in the following form

$$Lr4 = 0.539(Re_s)^{0.608} (w/s)^{-0.141} (d/s)^{0.275}$$

Each power dependence on the parameter strongly suggests that the downstream reattachment length (Lr4) is mainly affected by these parameters.

Conclusion

The present theoretical analysis of laminar flow over surface mounted ribs has made it possible to examine for the first time the effect of a number of parameters. The influence of Reynolds number, initial boundary-layer thickness, and the aspect ratio (width-to-height ratio) of the rib to the flow field over a surface mounted rib as well as to the changes of the surface pressure was examined and discussed. It was found that increasing the Reynolds number means the velocity is increased (if viscosity keeps constant) which makes the separated flow region expand and the separation flow strength gets stronger. Increasing *d/s* indicates boundary-layer being thicker and the velocity becoming smaller in the vicinity of the rib. This makes the separated flow region expand, but the strength of vorticity small.

The ratio *w/s* does not influence the upstream flow field, but it is an important parameter to the shape of the separated flow and it appears that there have a lot to be further discussed. For instance, the relation exists between separation bubbles and *w/s* as well as in what range of Reynolds number there is a third separation bubble on the top of rib.

References

Aung, W., Baron, A., and Tsou, F. K., 1985, "Wall Independency and Effect of Initial Shear-Layer Thickness in Separation Flow and Heat Transfer," *Int'l J. Heat Mass Transfer*, Vol. 28, No. 9, pp. 1757–1770.

Baker, S., 1977, "Regions of Recirculating Flow Associated with Two-Dimensional Steps," Ph.D. thesis, University of Surrey, Great Britain.

Baron, A., Tsou, F. K., and Aung, W., 1986, "Flow Field and Heat Transfer Associated with Laminar Flow Over a Forward-Facing Step," The 8th International Heat Transfer Conference, San Francisco, pp. 22–29.

Buller, M. L., and Kilburn, R. F., 1981, "Evaluation of Surface Heat Transfer Coefficients for Electronic Module Packages," *Heat Transfer in Electronic Equipment*, HTD, ASME Winter Annual Meeting, 20, pp. 15–20.

Fletcher, C. A. J., and Srinivas, K., 1983, "Stream Function Vorticity Revisited," *Computer Methods in Applied Mechanics and Engineering*, Vol. 41, pp. 297–322.

Hsieh, S. S., and Huang, D. Y., 1987a, "Flow Characteristics of Laminar Separation on Surface-Mounted Ribs," *AIAA Journal*, Vol. 25, pp. 819–823.

Hsieh, S. S., and Huang, D. Y, 1987b, "Numerical Computation of Laminar Separated Forced Convection on Surface-Mounted Ribs," *Numerical Heat Transfer*, Vol. 12, pp. 335–348.

Hsieh, S. S., 1988, "Thermal Characteristics of Annular Flow with Asymmetrically Roughened Surfaces," *Int'l Journal of Heat and Fluid Flow*, Vol. 9, No. 1, pp. 78–82.

Mallison, G. D., and Davis, G. D. V., 1973, "The Method of the False Transient for the Solution of Coupled Elliptic Equation," *J. Computational Physics*, No. 12, pp. 435–461.

Patankar, S. V., 1980, *Numerical Heat Transfer and Fluid Flow*, Hemisphere Publishing Corp. New York.

Roache, P. J., *Computational Fluid Dynamics*, Hermosa, Albuquerque, NM, 1972.

Wirtz, R. A., and Dykshoorn, D., 1984, "Heat Transfer from Arrays of Flat Packs in a Channel Flow," *Proceedings 4th International Electronics Packaging Society*, Baltimore, Md., pp. 318–326.

A Numerical Analysis of Pulsating Laminar Flow Through a Pipe Orifice

E. H. Jones Jr.

Chevron Oil Field Research Company,
La Habra, Calif. 90633-0446

R. A. Bajura

Energy and Water Research Center,
West Virginia University,
Morgantown, WV 46506-6064

A· study of laminar pulsating flow through a 45 degree bevel pipe orifice was performed using finite-difference approximations to the governing stream function and vorticity transport equations. The distance from ($-\infty$) to ($+\infty$) was transformed into the region from (-1) to ($+1$) for the streamwise coordinate. Solutions were obtained for orifice bore/pipe diameter ratios of 0.2 and 0.5 for bore Reynolds numbers in the range from 0.8 to 64 and Strouhal numbers from 10^{-5} to 10^2. Stream and vorticity function plots were generated for all cases and the time-dependent discharge coefficient waws computed and averaged over a cycle of pulsation. The numerical solutions agree closely with available experimental data for steady flow discharge coefficients. The results show that the effects of pulsation on the discharge coefficient can be correlated by using the product of the orifice bore Reynolds and Strouhal numbers.

Introduction

Orifice meters are used in a number of flow measurement applications. These applications include liquid, vapor, and some multiphase flow measurements. Many of these flows are unsteady or pulsating. A pulsating flow has a repetitive flow rate variation over a small time interval. Pulsation affects the performance of the orifice meter since it causes a pressure differential across the orifice which differs from the pressure differential which would be observed for the same steady flow rate. The pressure differential across the orifice is important in the measurement of the flow and also in the design and analysis of a fluid system that has an orifice as one of its components. The prediction of the pressure differential due to pulsation is both of academic and practical, interest as it advances the understanding of the orifice and extends its operating range to meter flows that cannot be measured or controlled with confidence using steady state operational characteristics.

This paper describes a numerical solution for laminar pulsating flow through a pipe orifice and summarizes the results obtained for various Reynolds and Strouhal number flows for the two different beta-ratio, β, orifices. These results show the relationship between increasing pulsation frequency and the differential pressure across the orifice.

System Description

A schematic of a pipe orifice is presented in Fig. 1. The orifice is a restriction in the pipe that causes a pressure differential proportional to the square of the flow rate. This pressure differential is due to the energy required to accelerate

the fluid through the orifice bore and the losses due to friction. Variations in the velocity profile and density of the flow affect the pressure differential through the orifice. Additionally, for a given pipe diameter more energy is dissipated for a small diameter orifice than for a large one. Other factors that affect the energy loss in the device include surface roughness, dents in the edge of the orifice, eccentricities in locating the orifice in the pipe, and other mechanical variations.

A complete study of how pulsation affects the orifice in combination with all other factors is beyond the scope of this paper. In order to limit the number of parameters, only the effects of frequency, Reynolds number, and the orifice-to-pipe diameter ratio (beta ratio) were varied in the present study. Unless otherwise noted in this paper the numeric Reynolds and Strouhal numbers are used. These numbers were obtained when the scaling parameters were applied to the basic flow equations.

In keeping with industrial standards, the orifice studied had a 45 deg bevel on the downstream side, with the bevel extending only 50 percent of the thickness of the plate. The plate thickness was fixed at 0.2 times the pipe radius; the pipe radius was used

Contributed by the Fluids Engineering Division for publication in the JOURNAL OF FLUIDS ENGINEERING. Manuscript received by the Fluids Engineering Division April 28, 1989.
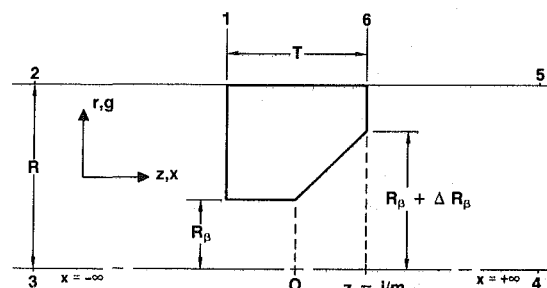
Fig. 1 Orifice plate schematic

Journal of Fluids Engineering

JUNE 1991, Vol. 113 / **199**

Downloaded 02 Jun 2010 to 171.66.16.104. Redistribution subject to ASME license or copyright; see http://www.asme.org/terms/Terms_Use.cfm

Copyright © 1991 by ASME

as the length scale. Both the orifice plate and the pipe were taken as being circular in cross section, uniform and smooth. The numerical solution assumed axisymmetric flow.

Governing Equations

The basic equations used in this model are the Navier–Stokes equations. Since angular symmetry was assumed, only the radial and axial equations were included (equations (1) and (2), respectively). Equations (1) and (2) may be combined to yield equation (3), the vorticity transport equation. The definition of vorticity, ξ, is given by equation (4). It is convenient to work with the vorticity transport equation since pressure is eliminated from the problem formulation.

$$\frac{D\bar{v}_r}{D\bar{t}} = -\frac{1}{\rho}\frac{\partial \bar{p}}{\partial \bar{r}} + \bar{\nu}\left(\frac{\partial^2}{\partial \bar{r}^2} + \frac{1}{\bar{r}}\frac{\partial}{\partial \bar{r}} - \frac{1}{\bar{r}^2} + \frac{\partial^2}{\partial \bar{x}^2}\right)\bar{v}_r \quad (1)$$

$$\frac{D\bar{v}_x}{D\bar{t}} = -\frac{1}{\rho}\frac{\partial \bar{p}}{\partial \bar{x}} + \bar{\nu}\left(\frac{\partial^2}{\partial \bar{r}^2} + \frac{1}{\bar{r}}\frac{\partial}{\partial \bar{r}} + \frac{\partial^2}{\partial \bar{x}^2}\right)\bar{v}_x. \quad (2)$$

$$\frac{D\bar{\xi}}{D\bar{t}} = \bar{\nu}\left[\frac{\partial^2\bar{\xi}}{\partial \bar{r}^2} + \frac{1}{\bar{r}}\frac{\partial \bar{\xi}}{\partial \bar{r}} + \frac{\partial^2\bar{\xi}}{\partial \bar{x}^2} - \frac{\bar{\xi}}{\bar{r}^2}\right] \quad (3)$$

$$\bar{\xi} = -\frac{\partial \bar{v}_x}{\partial \bar{r}} + \frac{\partial \bar{v}}{\partial \bar{x}} \quad (4)$$

The stream function, ψ, is defined by equations (5) and (6). The vorticity can be defined in terms of the stream function as in equation (7). From this formulation equations (3), (5), (6), and (7) define the set of basic equations required to solve the flow problem.

$$\bar{v}_r = -\frac{1}{\bar{r}}\frac{\partial \bar{\psi}}{\partial \bar{x}} \quad (5)$$

$$\bar{v}_x = +\frac{1}{\bar{r}}\frac{\partial \bar{\psi}}{\partial \bar{r}} \quad (6)$$

$$\bar{\xi} = \frac{1}{\bar{r}}\left(-\frac{\partial^2\bar{\psi}}{\partial \bar{r}^2} + \frac{1}{\bar{r}}\frac{\partial \bar{\psi}}{\partial \bar{r}} - \frac{\partial^2\bar{\psi}}{\partial \bar{x}^2}\right) \quad (7)$$

Nondimensionalization of the equations is accomplished by applying the scaling parameters listed below.

$$v_x = \bar{v}_x/\bar{V}_{\text{ref}} \qquad v_r = \bar{v}_r/\bar{V}_{\text{ref}}$$
$$x = \bar{x}/\bar{R} \qquad r = \bar{r}/\bar{R}$$
$$\xi = \bar{\xi}/(\bar{V}_{\text{ref}}/\bar{R}) \qquad t = 2\pi \bar{t}\,\bar{f}$$
$$\psi = \bar{\psi}/(\bar{V}_{\text{ref}}\,\bar{R}^2)$$

Applying these definitions to equations (3), (5), (6), and (7) yields the nondimensional equations (8)–(11), respectively.

$$\text{St}_n\frac{\partial \xi}{\partial t} + V_r\frac{\partial \xi}{\partial r} + V_x\frac{\partial \xi}{\partial x} - \xi\frac{V_r}{r} = \frac{1}{\text{Re}_n}\left[\frac{\partial^2\xi}{\partial r^2} + \frac{1}{r}\frac{\partial \xi}{\partial r} + \frac{\partial^2\xi}{\partial x^2} - \frac{\xi}{r^2}\right] \quad (8)$$

$$v_r = -\frac{1}{r}\frac{\partial \psi}{\partial x} \quad (9)$$

$$v_x = +\frac{1}{r}\frac{\partial \psi}{\partial r} \quad (10)$$

$$\xi = \frac{1}{r}\left[\frac{-\partial^2\psi}{\partial r^2} + \frac{1}{r}\frac{\partial \psi}{\partial r} - \frac{\partial^2\psi}{\partial x^2}\right] \quad (11)$$

Boundary Conditions

The solution of this set of equations requires knowledge of the boundary conditions at the wall, the centerline, and $\pm$ infinity (see Fig. 1). The variables to be defined at these locations are the two velocity components, v_x and v_r, the stream function, ψ, and the vorticity, ξ. The velocity vectors at any solid boundary are zero due to the no-slip condition. This condition along with equations (9) and (10) prescribe that the stream function value along a solid boundary must be a constant, although this value may fluctuate with time due to pulsations in the flow rate. For convenience, the value of the reference velocity was chosen to force the wall stream function value to be unity for a parabolic fully developed velocity profile corresponding to the average Reynolds number of the pulsating flow rate.

The condition of radial symmetry provides the information to determine the boundary values of variables on the centerline of the pipe. Symmetry, along with equation (4), determine that the vorticity at the centerline is zero. The radial velocity vector must also be zero due to symmetry. As was the case for the solid boundary, the stream function at the centerline must be a constant. However, its value will be zero. The centerline axial velocity vector has an unknown value which varies in space and time, but its derivative with respect to the radial direction must be zero.

The axial velocity at $\pm\infty$ is determined by equation (12), an analytical solution to fully developed pulsating pipe flow, Schlichting (1968).

Nomenclature

		Units[+]
a	= a constant in equation 13	none
C_D	= orifice discharge coefficient	none
C	= a constant in equation (14)	none
CSF_{1-5}	= constants in the stream function equation, equation (26)	none
$\bar{D}$	= pipe diameter	inches
$\overline{D1}$	= orifice plate diameter	inches
E	= a constant in equation (14)	none
F	= a constant in equation (14)	none
$\bar{f}$	= frequency	$T^{-1}*$
g	= transformed coordinate in the radial direction	none
H	= a constant in equation (14)	none
i	= coordinate index in the computational grid in the radial direction, and $\sqrt{-1}$	none
j	= coordinate index in the computational grid in the axial direction	none
KAA	= a constant	none
KVT_{1-5}	= constants in the vorticity transport equation	none

m	= number of grid lines between $z=0$ and $z=1$	none
P_p	= pulsation index or product $\text{ST}_\beta\text{Re}_\beta$, equation (30)	none
$\bar{P}$	= pressure	$ML^{-1}T^{-2}*$
$\bar{Q}$	= volume flow rate	$L^3T^{-1}*$
$\bar{R}$	= pipe radius	$L*$
$\bar{r}$	= radial direction in the real plane	$L*$
RE, Re_n	= numeric Reynolds number on the stream and vorticity function plots $\bar{V}_{\text{ref}}\bar{R}/\bar{\nu}$	none
Re_d, Re_β	= orifice plate Reynolds number $4\bar{Q}/(\pi\bar{\nu}\,\overline{D1})$	none
$\Delta\bar{R}_\beta$	= radial length of the bevel of the orifice plate	$L*$
ST, St_n	= numeric Strouhal number on the stream and vorticity function plots $2\pi\bar{f}\,\bar{R}/\bar{V}_{\text{ref}}$	none
St	= pipe Strouhal number $2\pi\,\bar{f}\,\bar{D}/\bar{V}_1$	none
St_d, St_β	= orifice plate Strouhal number $2\pi\,\bar{f}\,\overline{D1}/\bar{V}_2$	none

$$v(r,t) = \frac{-i(KAA)}{ST} e^{it} \left[1 - \frac{J_0(r\sqrt{-i\ Re_n St_n})}{J_0(\sqrt{i\ Re_n St_n})} \right] \quad (12)$$

The values of the stream and vorticity functions are determined from this equation. Since the boundary corresponds to fully developed oscillating flow, the value of the radial velocity vector is zero.

The boundary conditions described above are presented in Table 1. The boundary condition not defined thus far is the value of the vorticity at a solid boundary. This cannot be specified a priori. It is obtained by iterating the solution of the equations.

The fluid is assumed to be incompressible, and thus the speed of sound in the fluid is infinite. An infinite sound speed implies that a pressure pulse propagates in the fluid instantly. Therefore, the stream function and velocity profiles at the inflow and outflow boundaries are set equal at each time step.

Transformations

Placing of the inflow and outflow at infinity is computationally desirable and permits specification of fully developed flow boundary conditions. However, an infinite number of grid points would be required to obtain a solution for equally spaced grid points. Therefore, a mathematical transformation, shown by equation (13), was used to map infinity into ± 1 for the axial coordinate. The radial coordinate was transformed using equation (14) in order to increase the density of the points near the orifice bore.

$$z = \tanh(ax); \quad a = \frac{1}{T} \ln \left(\frac{m+j}{m-j} \right);$$

j = number of lines from center to edge of plate   (13)

$$r = Cg^3 + Eg^2 + Fg + H \quad (14)$$

The constant, a, in equation (13) is determined by setting the distance to the second axial grid line equal to half the orifice plate thickness. The radial transformation is forced to line up with the bore of the orifice meter and the intersection of the bevel and the downstream side of the plate. In total, 5 points, having a spacing of 1/4 the plate thickness in the axial direction, were located on the bore of the orifice plate. The point halfway along the 45 degree bevel was subject to a slight

Table 1 Boundary Conditions

Variable	Centerline	Solid boundary	$\pm \infty$
v_z	$\dfrac{\partial v_z}{\partial r} = 0$	$v_z = 0$	$v_z = f(r,t)$
v_r	$v_r = 0$	$v_r = 0$	$v_r = 0$
ξ	0	Unknown	$-\dfrac{\partial v_z}{\partial r}$
ψ	0	$\int_0^R v_z r\,dr \big|_{z = \pm 1}$	$\int_0^r v_z r\,dr$

positioning error which is approximately equal to the surface finish of an orifice plate.

Application of these transformations to equation (8) through (11) yields equations (15) through (18). The transformation applied to these equations have also allowed the specification of a uniform grid spacing in the transformed plane coordinates, z and g.

$$St \frac{\partial \xi}{\partial t} + \frac{\partial g}{\partial r} \frac{\partial(v_r \xi)}{\partial g} + \frac{\partial z}{\partial x} \frac{\partial(v_z \xi)}{\partial z}$$

$$= \frac{1}{Re_n} \left[\frac{\partial^2 \xi}{\partial g^2} \left(\frac{\partial g}{\partial r} \right)^2 + \frac{\partial \xi}{\partial g} \frac{\partial^2 g}{\partial r^2} \right.$$

$$\left. + \frac{1}{f(g)} \frac{\partial \xi}{\partial g} \frac{\partial g}{\partial r} + \frac{\partial^2 \xi}{\partial z^2} \left(\frac{\partial z}{\partial x} \right)^2 + \frac{\partial \xi}{\partial z} \frac{\partial^2 z}{\partial x^2} - \frac{\xi}{f(g)^2} \right] \quad (15)$$

$$v_r = -\frac{1}{f(g)} \frac{\partial \psi}{\partial z} \frac{\partial z}{\partial x} \quad (16)$$

$$v_z = +\frac{1}{f(g)} \frac{\partial \psi}{\partial g} \frac{\partial g}{\partial r} \quad (17)$$

$$\xi = \frac{1}{f(g)} \left[-\frac{\partial^2 \psi}{\partial g^2} \left(\frac{\partial g}{\partial r} \right)^2 + \frac{\partial \psi}{\partial g} \left[-\frac{\partial^2 g}{\partial r^2} + \frac{\partial g / \partial r}{f(g)} \right] \right.$$

$$\left. - \frac{\partial \psi}{\partial z} \frac{\partial^2 z}{\partial x^2} - \frac{\partial^2 \psi}{\partial z^2} \left(\frac{\partial z}{\partial x} \right)^2 \right] \quad (18)$$

Finite Difference Approximations

The finite difference approximations for equations (15) through (18) are shown in equations (19) through (22).

Nomenclature (cont.)

$\overline{T}$ =	orifice plate thickness	L*
$\overline{t}$ =	time	T*
$\overline{V}_1$ =	average velocity for the pipe flow	LT^{-1}*
$\overline{V}_2$ =	average velocity for the orifice flow	LT^{-1}*
$\overline{v}_x(r,t)$ =	pulsating axial velocity at infinity	LT^{-1}*
$\overline{V}_{ref}$ =	refernce velocity $\overline{V}_1/2$	LT^{-1}*
v =	velocity in a direction determined by its subscript	LT^{-1}*
$\overline{x}$ =	axial direction in the real plane	L*
x_r =	downstream reattachment distance	none
z =	transformed coordinate in the axial direction	none
β =	beta ratio- the ratio of the orifice diameter to the pipe diameter	none
Θ =	a variable	none
θ =	cylindrical coordinate angle	radians
ν =	kinematic viscosity	L^{2}T^{-1}
ξ =	vorticity defined by equation 4	T^{-1}*

$\overline{\rho}$ =	density	ML^{-3}*
$\overline{\psi}$ =	stream function defined by equations (5) and (6)	LT^{-1}*

Subscripts

d, β =	taken at the orifice plate	
r =	radial direction or component	
wall =	wall value	
x =	axial direction or component	
z =	transformed axial direction	

Superscripts

$\overline{}$ =	as an overbar denotes a dimensional value	
n =	time step	

Notes

* =	without an overbar this symbol is dimensionless	
+ =	units cited are the fundamental units of mass (M) length (L) and time (T)	

Table 2 Quasi-steady state discharge coefficients

Beta ratio	Re_d***	Experimental Johansen*	Turve and Sprinkle*	Keith*	Theoretical This work
0.5	.8	---	---	---	0.129
0.5	8	0.398	0.408	---	0.391
0.5	40	0.649	0.638	0.683**	0.643
0.5	64	0.700	0.672	---	0.698
0.2	.8	---	---	---	0.124
0.2	20	0.555	---	---	0.545
0.2	40	0.638	---	---	0.652
0.2	64	0.660	---	---	0.731

*Values obtained by interpolating from data shown in Coder (1973).
**Highest value shown.

***Bore Reynolds number $\dfrac{4Q}{\pi d \bar{\nu}}$

$$\frac{\partial \Theta}{\partial t} = \frac{\Theta_{i,j}^{n+1} - \Theta_{i,j}^{n}}{\Delta t} \tag{19}$$

$$\frac{\partial^2 \Theta}{\partial r^2} = \frac{\Theta_{i+1,j}^{n} + \Theta_{i-1,j}^{n} - 2\Theta_{i,j}^{n}}{2\Delta r} \tag{20}$$

$$\frac{\partial \Theta}{\partial r} = \frac{\Theta_{i+1,j}^{n} - \Theta_{i-1,j}^{n}}{2\Delta r} \tag{21}$$

$$\xi_{wall}^{n+1} = \frac{2(g')^2(\psi_{i,j+1}^{n+1}\psi_{i,j}^{n+1})}{f(g)\Delta g^2}$$
$$- \frac{2(z')^2(\psi_{i+1,j}^{n+1} - \psi_{i,j}^{n+1})}{f(g)\Delta z^2} \tag{22}$$

Equations (19) through (21) are five-point central differences in space with forward time differences for the temporal terms. Equation (22) is the wall vorticity formulation used on the pipe wall and the orifice plate. This formulation is obtained from equations (4) through (6) and the no-slip condition at the wall (see Jones (1984)). Applying these formulations yields equations (23) through (26), which are the formulations used in the computer code. The method solves the flow equations implicitly by computing the solution to each time step simultaneously.

$$\xi_{ij}^{n} = KVT_1\xi_{i,j}^{n+1} + KVT_2\xi_{i+1,j}^{n+1} + KVT_3\xi_{i-1,j}^{n+1}$$
$$+ KVT_4\xi_{i,j+1}^{n+1} + KVT_5\xi_{i,j-1}^{n+1} \tag{23}[1]$$

$$v_r = \frac{-z'}{2f(g)\Delta z}\psi_{i,j+1}^{n+1} + \frac{z'}{2f(g)\Delta z}\psi_{i,j-1}^{n+1} \tag{24}$$

$$v_z = \frac{g'}{2f(g)\Delta g}\psi_{i+j,I}^{n+1} - \frac{g'}{2f(g)\Delta g}\psi_{i-j,I}^{n+1} \tag{25}$$

$$\xi_{i,j}^{n+1} = \psi_{i+1,j}^{n+1}[CSF_1] + \psi_{i-1,j}^{n+1}[CSF_2]$$
$$+ \psi_{i,j+1}^{n+1}[CSF_3] + \psi_{i,j-1}^{n+1}[CSF_4]$$
$$+ \psi_{i,j}^{n+1}[CSF_5] \tag{26}[1]$$

Model Verification

In order to validate the numerical scheme, steady flow solutions as well as the time-average values of some of the slowly varying pulsating flow solutions were compared to experimental and other analytical data as presented in Table 2. The discharge coefficient of the orifice is computed by employing equation (27).

$$C_D = \frac{V_1}{\sqrt{2\Delta p}}\left\{\frac{(1-\beta^4)}{\beta^4}\right\}^{0.5} \tag{27}$$

In this equation, all variables are known from the geometry and defined flow rate except for the pressure differential across the orifice plate. The pressure differential is computed by a

___
[1]See Appendix 1 for the definitions of the constants is these equations.
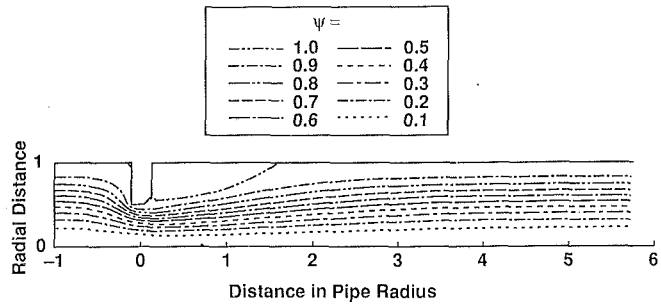
Fig. 2 Steady-state stream lines for an orifice bore Reynolds number of 40

Legend: Z

······ 0   – – – 32   –·–· 2   —·— 4   —··— 6   ——— 16
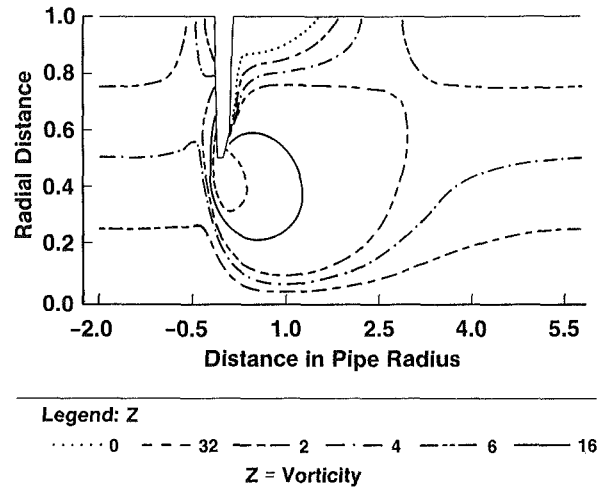
Z = Vorticity

Fig. 3 Steady-state vorticity lines for an orifice bore Reynolds number of 40

method similar to that in Coder (1973). Starting upstream from the orifice, the pressure is calculated along the pipe wall to a distance far upstream where the pipe wall and centerline pressures are equal. The pressure is then calculated downstream along the centerline to a distance far from the plate when the pipe wall and centerline pressures are again equal. The pressure is then calculated upstream to the location of the orifice. This path is shown on Fig. 1 by moving from point 1 to point 6 in sequence. Using this method the pressure differential is determined, without the need to compute the pressure at the sides and sharp edges of the orifice plate.

The code computes the pressure as described above, as well as the velocity vectors, stream function, and vorticity function at every point in the flow field. Plots of the stream and vorticity function for the steady flow case with an orifice bore Reynolds number of 40 (equivalent to a pipe Reynolds number of 20) and a beta ratio of 1/2 are shown in Fig. 2 and 3. This Reynolds number falls in the experimental range covered by Johansen (1930) and Turve (1933). Figures 2 and 3 show that the stream and vorticity functions converge smoothly to the fully developed value at approximately 5 pipe radii downstream of the plate. Figures 2 and 3 also show the recirculation region downstream of the orifice plate. The reattachment point occurs at the location where the stream line ($\psi = 1$) or the vorticity line ($\xi = 0$) intersects the pipe wall. General information about the flow can be obtained from plots of the stream and vorticity functions. The pressure profile and in turn the discharge coefficient are thus calculated. As shown in Table 2, the predicted discharge coefficient for this case agrees well with the experimental data. The table shows good agreement with the work of Johansen (1930). Other references (Nigro, 1978; Alvi, 1978; and McGreehan, 1985) provide generally useful information about these types of flows but are not as directly comparable as the data presented in Table 2. The deviation of the numerical

solutions from the experimental data did not become large until the orifice bore Reynolds number reached a value of 64 with a 0.2 beta ratio orifice. The computer solution's sensitivity was determined by testing the computational scheme for its grid spacing dependency. In the axial direction 50 grid lines were located on either side of the center of the orifice and one at its center for a total of 101 lines. In the radial direction a total of 21 lines were used with 10 points on either side of the orifice bore. For the time dependent pulsating flow studies a total of 8 time steps were used. No effect on the solutions shown was evident if the number of axial grid lines was increased to 151. However, instability did occur if the spacing among grid lines was increased near the orifice. For an orifice plate Reynolds number of 100 and with pulsation flow the numerical solution would not converge. Convergence did not occur for this case even if the number of axial grid lines was increased to 151. A steady-state solution for this Reynolds number was obtained without difficulty.

Results

Tables 3 and 4 present a summary of the computational results for the various flow conditions studied for orifices with beta ratios of 0.5 and 0.2, respectively. Further subdivision is done on the basis of the Reynolds and Strouhal numbers of the flow. Notice that there are two different Reynolds numbers and two different Strouhal numbers used in these tables as well as some of the figures presented. The orifice bore Reynolds number is four times the numeric Reynolds number divided by the beta ratio. Thus, for a beta ratio of one-half the orifice bore Reynolds number is eight times the numeric Reynolds number. The equations relating the two Reynolds and Strouhal numbers give by equations (28) and (29), respectively.

$$Re_d = Re_n \left(\frac{4}{\beta}\right) \qquad (28)$$

Table 3 Discharge coefficients and pulsation product for a beta ratio of 0.5

$\beta = 0.5$

	0.1	1.0	Re_n 5	8	St_n
C_D	0.1308	0.3957	0.6570	0.6973	10^{-5}
$Re_\beta St_\beta$	1×10^{-6}	1×10^{-5}	5×10^{-5}	8×10^{-5}	
C_D	0.1305	0.3937	0.6259	0.6571	10^{-1}
$Re_\beta St_\beta$	0.01	0.1	0.5	0.8	
C_D	0.1293	0.3481	0.4387	0.4185	1
$Re_\beta St_\beta$	0.1	1	5	8*	
C_D	---	0.2387	---	---	5
$Re_\beta St_\beta$	---	5	---	---	
C_D	0.1147	0.1650	---	---	10
$Re_\beta St_\beta$	1	10	---	---	
C_D	0.0549	---	---	---	100
$Re_\beta St_\beta$	10	---	---	---	

*Solution Questionable.

Table 4 Discharge coefficients and pulsation product for a beta ratio of 0.2

$\beta = 0.2$

	0.04	1	Re_n 2	3.2	St_n
C_D	0.1257	0.5543	0.6673	0.7438	10^{-5}
$Re_\beta St_\beta$	6.4×10^{-8}	1.6×10^{-6}	3.2×10^{-6}	5.12×10^{-6}	
C_D	0.1258	0.5535	0.6654	0.7406	10^{-1}
$Re_\beta St_\beta$	6.4×10^{-4}	1.6×10^{-2}	3.2×10^{-2}	5.12×10^{-2}	
C_D	0.1259	0.5464	0.6471	0.7062	1
$Re_\beta St_\beta$	6.4×10^{-3}	1.6×10^{-1}	0.32	0.512	
C_D	---	---	---	---	5
$Re_\beta St_\beta$	---	---	---	---	
C_D	0.1255	0.4647	---	---	10
$Re_\beta St_\beta$	6.4×10^{-1}	1.6	---	---	
C_D	0.1204	---	---	---	100
$Re_\beta St_\beta$	0.64	---	---	---	

$$St_\beta = St_n (\beta^3) \qquad (29)$$

Solutions were obtained at each 45 deg increment in a pulsation cycle, or eight times per cycle. The time step referred to in the text and figures is 1/8 of a cycle. No solutions were obtained for flows with both a high Reynolds number and a high Strouhal number; as the product of these two numbers increased, the numerical solution became unstable. The discharge coefficients shown in Tables 3 and 4 are the time averages of the instantaneous discharge coefficients computed at each time interval. The effect of increasing the pulsating frequency (higher Strouhal number) at a given Reynolds number results in a decrease in discharge coefficient. This occurs because the calculated pressure differential across the orifice plate increases as the frequency of flow pulsation increases.

The effects of pulsation on the flow field are also evident by comparing the stream function plots of various solutions. Figure 4 shows the odd number time step solutions for the stream function for the case of an orifice bore Reynolds number of 40, beta ratio of 0.5, and a Strouhal number of 1.0. The effects of the changing flow rate are evident from the change in position of the reattachment and separation points as well as other variations in the stream lines. In comparing these solutions with different Strouhal number cases for the same Reynolds number, it was observed that the average position of the reattachment point moves further away from the orifice as the Strouhal number is increased. These data are summarized in Table 5. The reattachment point moves from about 1.58 radii for either a steady state or a very low Strouhal number flow to about 2.49 radii for a flow with a Strouhal number of 1.0. For comparison purposes, it is noted that the reattachment point for the steady state solution for an orifice bore Reynolds number of 80 was 2.9 radii. This location of the reattachment point is near the instantaneous value of the third time step for the Strouhal-number-1.0 solution shown for the orifice bore Reynolds number 40 solution. The separation point is also affected by the flow pulsation. The steady-state solution Fig. 2 for a Reynolds number of 5 shows the separation point at the sharp edge of the bevel of the plate. The separation point moves down the bevel when pulsation is
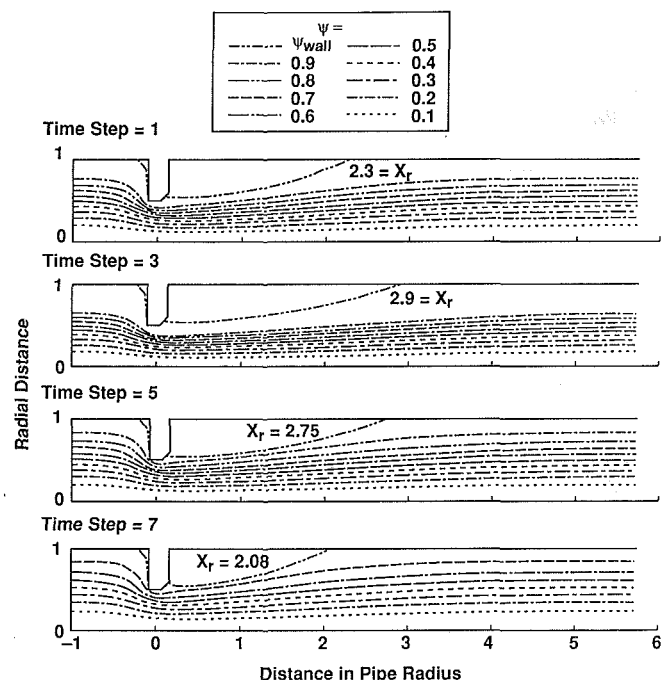

Fig. 4 Stream function plot $Re_d = 40$, amplitude ratio = 1, and ST = 1.0 ($St_\beta = 0.125$)

Table 5 Reattachment points for a Reynolds number of 5 (see Jones (1984) p. 84)

	$St = 10^{-5}$		$St = 0.1$		$St = 1.0$	
Time step	ψ wall	Reattachment point x_r	ψ wall	Reattachment point x_r	ψ wall	Reattachment point x_r
1	0.999	1.60	1.0014	1.63	1.0387	2.30
2	1.1767	1.83	1.1766	1.85	1.2075	2.65
3	1.2499	1.90	1.2469	1.90	1.2547	2.90
4	1.1767	1.81	1.1711	1.85	1.1527	2.87
5	0.9999	1.60	0.9936	1.67	0.9612	2.75
6	0.8232	1.34	0.8184	1.40	0.7925	2.38
7	0.7499	1.26	0.7481	1.35	0.7453	2.08
8	0.8232	1.30	0.8239	1.40	0.8473	2.00
Ave	0.9999	1.58	0.9975	1.63	0.9999	2.49

NOTES: (1) All distances are in pipe radii.
(2) The steady state value of ψ_{wall} is 1.000.
(3) The reattachment point distance, x_r, for steady-state flow and a Reynolds number of 5 is 1.60.
(4) The reattachment point distance, x_r, for steady-state flow and a Reynolds number of 10 is 2.9.
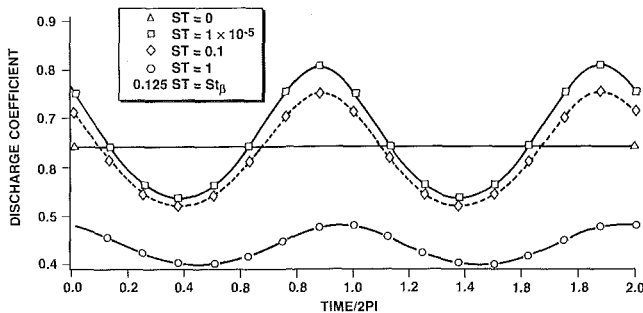
Fig. 5 Discharge coefficient plot for pulsating flow with beta ratio = 0.5, amplitude ratio = 1.0, orifice Re = 40 (ST of 0 is from Johansen's experimental work.)

Fig. 6 Normalized discharged coefficient as a function of the pulsation product (RE and ST are evaluated at the orifice)

introduced, Fig. 4. However, the location is not constant, it varies with the time step and the Stouhal number.

The effects of pulsation on the instantaneous discharge coefficient are shown in Fig. 5. Shown are two time cycles of the computed discharge coefficients for the orifice bore Reynolds number 40, beta ratio 0.5 cases studied. Notice that as the flow rate increases, the discharge coefficient decreases, because of an increase in the pressure differential due to the corresponding acceleration pressure drop. As the flow is decreased, the discharge coefficient increases due to the pressure recovery resulting from flow deceleration. The maximum variation in the flow rate is approximately 25 percent of the mean flow for all the curves shown in Fig. 5. This flow rate variation corresponds to an amplitude ratio, KAA/St, in equation (12) of 1. The amplitude ratio was varied to determine its effect. In cases where both a 0.1 and a 1.0 amplitude ratio were used, there was only a minor difference, approximately 1.5 percent, in the computed average discharge coefficient. The instantaneous values of the discharge coefficient were, however, quite different. It was also observed that smaller values of the amplitude ratio required fewer iterations to converge for the high Reynolds numbers cases.

There is a marked difference in the performance of the orifice meter as the Strouhal number is increased from the low value of 0.0001 to 1.0. Not only has the mean value of the discharge coefficient decreased, but the amplitude of variation of the discharge coefficient also decreased even though the flow rate variation is constant.

The effect of the Reynolds number and beta ratio on the discharge coefficient was eliminated, to determine the pulsation effect, by plotting the normalized discharge coefficient against the product of the Reynolds and Strouhal numbers evaluated at the bore of the orifice. This product is defined by equation (30) and is denoted the Pulsation Product.
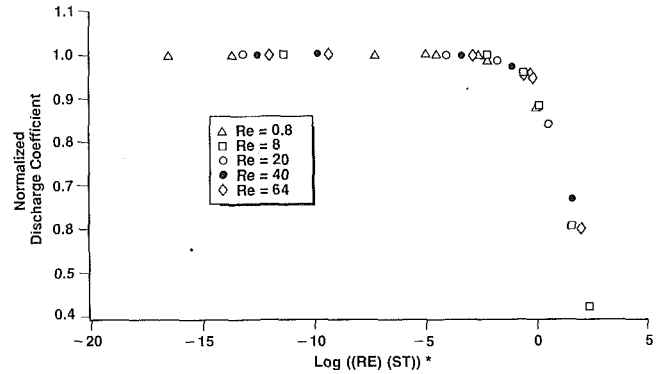
$$p_p = Re_\beta St_\beta = (2\pi\overline{fR}^2/\overline{\nu}) \, (\beta^2) \qquad (30)$$

This product may be interpreted from dimensional consideration as the ratio of an oscillating velocity to a viscous velocity. Figure 6 presents the result of the correlation for all the cases shown in Tables 3 and 4. The normalized discharge coefficient is obtained by dividing the mean discharge coefficient of each case by the steady flow coefficient for that Reynolds number and beta ratio. Figure 6 shows that there is little effect due to pulsation until the natural log of the Pulsation Product is about -2.5. At this point, the discharge coefficient begins to decrease rapidly in value, and reaches 40 percent of the steady state value when the natural log of the Pulsation Product is near 2.5.

Conclusions

Flow rate pulsation through an orifice meter causes more energy to be dissipated across the orifice plate. This result is evident from the increase in pressure dissipation, decrease in discharge coefficient, and from the changes in the vorticity and stream function plots for the cases studied. As the pulsation frequency is increased, the recirculation region downstream of the orifice is altered. The point of reattachment moves further downstream at higher pulsation frequencies, and the location and angle of departure of the wall stream line changes on the downstream side of the orifice plate.

The Pulsation Product is a useful tool in determining the effect of pulsation on the flow. It provides an indication of when the frequency of pulsation is sufficient to cause significant changes in the performance of the orifice meter. An estimation of the discharge coefficient can be obtained by using Fig. 6. The product of the normalized and steady-state discharge coefficient with pulsating flow.

References

Alvi, S. H., Sridharan, K., and Lakshmana Rao, N. S., 1978, "Loss Characteristics of Orifice and Nozzles," *Journal of Fluids Engineering*, Vol. 100, pp. 299–307.

Coder, D. W., 1973, "Implicit Solutions of the Unsteady Navier–Stokes Equation for Laminar Flow Through an Orifice," Ph.D. dissertation, University of Maryland.

Johansen, F. C., 1930, "Flow through Pipe Orifices at Low Reynolds Number," *Proceedings of the Royal Society*, London, Vol. 126, Series A.

Jones, Jr., E. H., 1984, "A Numerical Study of Laminar Pulsating Flow Through A Pipe Orifice," West Virginia University.

Keith, Jr., T. G., 1971, "Finite Difference Solution of Steady Laminar Flow Through a Pipe Orifice," University of Maryland.

McGreehan, W. F., Ghia, U., and Osswald, G. A., 1985, "Analysis of Separated Flow in a Pipe Orifice Using Unsteady Navier–Stokes Equations," Lecture Notes in Physics, 9th International Conference on Numerical Methods in Fluid Dynamics.

Nigro, F. E. B., Strong, A. B., and Alpay, S. A., 1978, "A Numerical Study of the Laminar Viscous Imcompressible Flow Through a Pipe Orifice," ASME JOURNAL OF FLUIDS ENGINEERING, Vol. 100, pp. 467–472.

Roache, P. J., 1976, *Computational Fluid Dynamics*, Hermosa Publishers, Albuquerque, N.M.

Schlichting, H., 1968, *Boundary-Layer Theory*, McGraw-Hill Company, New York, Sixth Edition.

Tuve, G. L., and R. E. Sprinkle, 1933, "Orifice Discharge Coefficients for Viscous Liquids," *Instruments*, Vol. 6, pp. 201–206.

APPENDIX 1

Coefficients Used in Equations (23) and (26)

$$KVT_1 = \frac{\Delta t}{St_n}\left[\frac{St_n}{\Delta t}\frac{v_r}{f(g)} + \frac{2g'^2}{\Delta g^2 Re_n} + \frac{2z'^2}{\Delta z^2 Re_n} + \frac{1}{f(g)^2 Re_n}\right]$$

$$KVT_2 = \frac{\Delta t}{St_n}\left[\frac{v_r g'}{2\Delta g} - \frac{g'^2}{Re_n \Delta g^2} - \frac{1}{2\Delta g Re_n}\left(\frac{g'}{f(g)} + g''\right)\right]$$

$$KVT_3 = \frac{\Delta t}{St_n}\left[\frac{v_r g'}{2\Delta g} - \frac{g'^2}{\Delta g^2 Re_n} - \frac{g'/f(g) + g''}{2\Delta g\ Re_n}\right]$$

$$KVT_4 = \frac{\Delta t}{St_n}\left[\frac{v_z z'}{2\Delta z} - \frac{z'^2}{\Delta z^2 Re_n} - \frac{z''}{2(\Delta z)Re_n}\right]$$

$$KVT_5 = \frac{\Delta t}{St_n}\left[\frac{v_z z'}{2\Delta z} - \frac{z'^2}{\Delta z^2 Re_n} + \frac{z''}{2(\Delta z)Re_n}\right]$$

$$CSF_1 = \frac{-g'^2}{f(g)\Delta g^2} - \frac{g''}{2f(g)\Delta g} + \frac{g'}{2\Delta f(g)^2}$$

$$CSF_2 = \frac{-g'^2}{f(g)\Delta g^2} + \frac{g''}{2f(g)\Delta g} - \frac{g'}{2\Delta g f(g)^2}$$

$$CSF_3 = \frac{-z''}{2\Delta z(f)g} + \frac{z'^2}{\Delta z^2 f(g)}$$

$$CSF_4 = \frac{z''}{2\Delta z(f)} - \frac{z'^2}{\Delta z^2 f(g)}$$

$$CSF_5 = \frac{+2g'^2}{\Delta g^2 f(g)} + \frac{2z'^2}{f(g)\Delta z^2}$$

Intermittent Phenomena in the Flow Over a Rib Roughened Surface

T. Mullin

The Clarendon Laboratory,
Oxford, United Kingdom

S. R. Martin

AEA Technology, Harwell Laboratory,
Oxfordshire, United Kingdom

Laser Doppler anemometry has been used to make measurements of a small recirculation bubble in a turbulent water flow over a rib roughened surface. The bubble occurs near the leading edge of a transverse rib which is a model of the ribbed surface used to enhance cooling on nuclear reactor fuel pins. The bubble is transient, and spectral and correlation measurements were made to investigate any periodicity. It was found that the bubble itself did not show any periodicity but there was evidence for fluctuations in the main stream with a Strouhal number of 0.1.

1 Introduction

The turbulent flow over a rib roughened surface has been investigated in two extensive studies using very different approaches. Martin and Drain (1988) used LDV to obtain high quality measurements of the mean and fluctuating velocity components in a nominally two dimensional water channel. Attached to one wall of the channel were square ribs which protruded 0.2 channel widths into the flow and were spaced at 7.2 heights. This configuration is a model of an advanced gas cooled reactor heat exchange device. The experimental results obtained were compared with numerical calculations. In general, there is good agreement between calculations and experiments for the mean velocity components but the results for the fluctuating components appear to highlight deficiencies in the numerical turbulence models.

The general problem of heat transfer enhancement by the action of flow over ribbed or grooved surfaces is of considerable practical interest, for example see the review of Incropera (1988) for discussion of this problem in the electronics industry. The basic flow phenomena have been investigated by numerical means by Ghaddar et al. (1986) and Ghaddar et al. (1986). These studies were restricted to Reynolds number regimes where the flow is laminar. However, an interesting heat transfer enhancement effect is predicted when the flow is pulsed (Ghaddar et al., 1986). At present it is not clear if this enhancement will occur in the common practical situation of turbulent flow.

The problem of turbulent flow over periodic disturbances was studied experimentally by Hanjalic and Launder (1972) who used hot wire techniques in two different planar channel sections of a wind tunnel where one wall was roughened by square ribs spaced at 10 rib heights. The two channels had rib height protrusions of 0.06 and 0.11 channel widths, respectively. The motivation for their work was to investigate the turbulent energy transfer processes in channels with asymmetric boundaries and to compare the results with those obtained in plane walled channels. Most of the detailed measurements were obtained at one particular value of the Reynolds number where they measured one-dimensional frequency spectra for all the velocity components and their combinations. One observation they made is that there appeared to be reasonably well correlated eddy structures near the roughened surface although their measuring techniques did not allow them to obtain results adjacent to the ribs.

More recently, Fujita et al. (1988) investigated the enhancement of secondary flow of Prandtl's second kind by the presence of periodic roughness elements on one wall of a rectangular duct. They found a pronounced effect and attributed this to the anisotropy of the shear stress produced by the roughness.

Laminar flow over arrays of cavities are known to produce strongly correlated motions which are manifested as time periodic phenomena in the flow. Binnie (1960) observed strong cross waves in the free surface along channels with corrugated sides. In a later paper, Binnie (1961), he reported similar phenomena in the sound generation by the flow of air along corrugated and fixed tubes. However, in both these studies he found that turbulence tended to destroy the resonant phenomena or at the very least minimized the effect.

More recently, Stepanhoff (1986) has observed the selective amplification of oscillatory modes in laminar air flow through a periodic array of cavities. She has shown that temporal bimodal behavior may occur with two frequencies being amplified in some ranges of Reynolds number. The argument is given that there is an interaction between the free shear layers over each cavity and the cavity edges. This mechanism has been discussed at length by Rockwell (1983) who also points out that shallow cavities, such as the ones used in our present study, are less likely to produce sustained oscillations. Szczepura (1986) has also carried out an extensive investigation of "bimodal" behavior in the turbulent flow through an axisymmetric expansion.

The principal aim of the present study is to investigate in detail the intermittent formation of a separation bubble near the leading edge of each rib. This phenomenon appears to be related to a shear layer reattachment effect in turbulent flow

over bluff bodies as pointed out by Castro (1981), Castro and Dianat (1983), Dianat and Castro (1984). Their work is concerned with the shear layer reattachment to the surface of square and rectangular bodies in a simulated atmospheric turbulent boundary layer. They found evidence for the intermittent reattachment of the shear layer when $\frac{\delta}{H} \gg 1$ where δ is the boundary layer thickness and H is the body height. Moreover, they found no reattachment for square sectioned blocks for large Reynolds numbers. A further feature they found was a low frequency oscillation in the flow downstream of the obstacle which they attribute to "flapping" of the shear layer.

Work of a similar nature is reported in Melbourne and Saathoff (1986) who observed the formation of a three-dimensional separation bubble on the leading edge of a bluff body in a nominally two-dimensional flow. In addition, they found that the bubble would "burst" intermittently causing sudden pressure changes on the top surface of the body. In the present study we investigate the turbulent flow over a periodic array of ribs in which one would also expect these bubble features to exist.

We also investigate the extent to which the formation and collapse of he bubble affects the free stream flow. Finally we use power spectral analysis to see whether the turbulent flow over the periodic array of ribs gives rise to periodic flow phenomena.

A brief description of the apparatus and measuring techniques used is given in Section 2. The main results are presented and discussed in Section 3 and some conclusions are drawn in Section 4.

2 Apparatus and Measuring Techniques

The working section of the flow channel is 25 mm high and 200 mm wide giving an aspect ratio of 8:1. One wall of the channel has 5 mm high square sectioned ribs attached to it which span the full 200 mm. They are spaced at a rib center to center distance of 36 mm. The flow is provided by a constant head source as shown schematically in Fig. 1 and all measurements are taken at a fixed Reynolds number of 21,250. (Here we define Reynolds number not be $U_{mean} d/\nu$ where d is the half height of the channel).

Measurements are made using a DANTEC differential Doppler LDV system with frequency shift for directional discrimination. The system uses three He - Ne beams, two of which are polarized in orthogonal planes so that two different velocity components can be measured simultaneously. The scattered laser light is separated by a polarization beam splitter into two photomultipliers whose outputs are fed into two tracking filters. The velocity components measured are at + and − 45 deg to the U vector and are denoted A and B. The U and V velocity components are obtained by summing and differencing the A and B components and are then fed to an fm tape recorder.

The positioning system could be moved in increments of 1.25μm. Positioning accuracy was approximately ±5μm in the
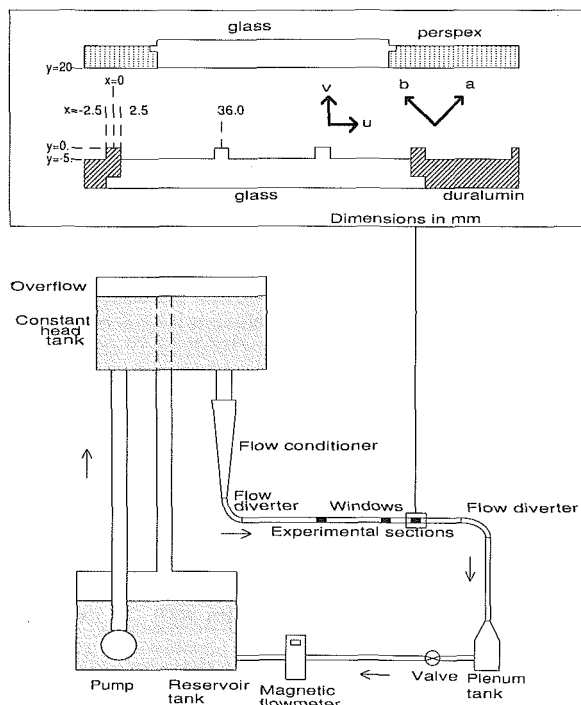

Fig. 1 Schematic diagram of the water channel flow system

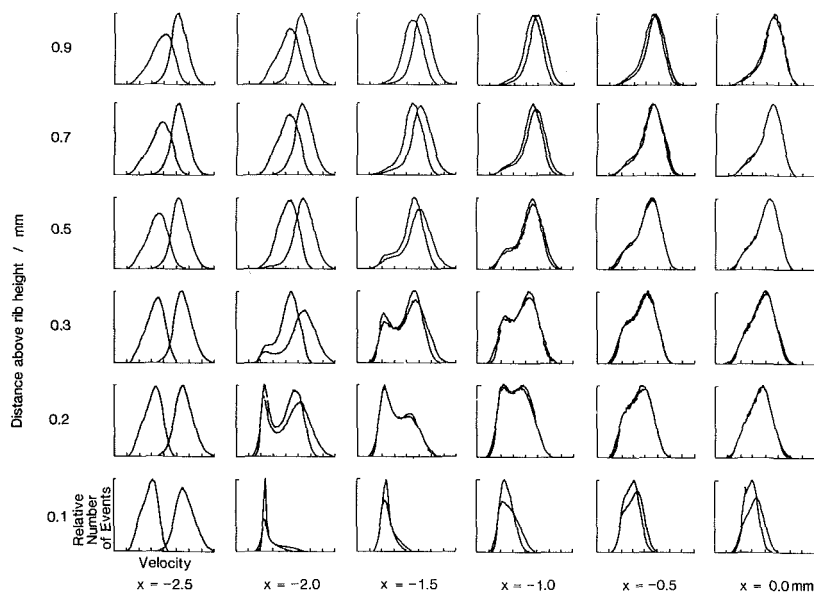Fig. 2 Probability distributions of the A and B components of velocity taken at the indicated positions over the front portion of the rib. The velocities are accurate to 1 part in 128 of the total range of the horizontal scale. The sample was large enough so that the accuracy is better than 1 percent on the vertical scale.
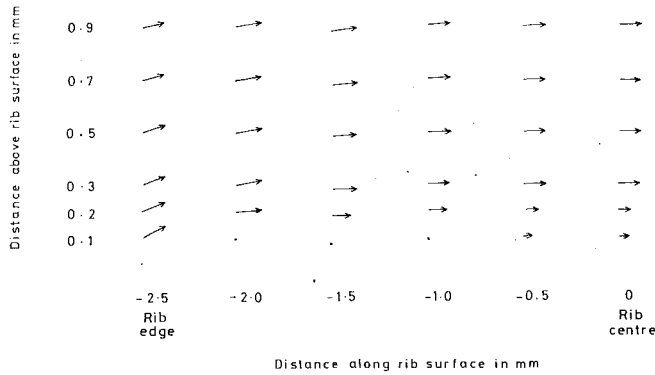
Fig. 3(a) Velocity vector field over the leading edge of the rib for the "high" flow state of the probability distributions of Fig. 2.
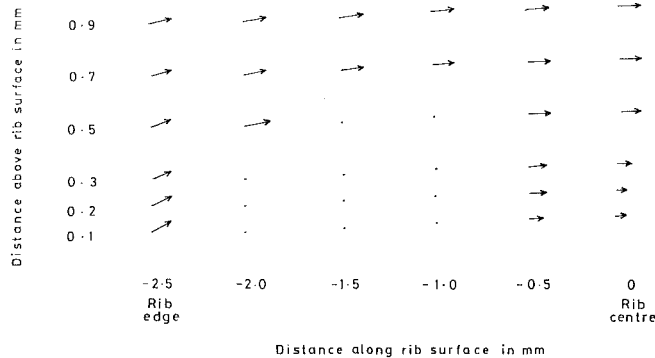

Fig. 3(b) Velocity vector field of the "low" flow state. The lengths of the vectors are accurate to ± 5 percent.

Fig. 4(a) The power spectrum of U taken in the bimodal region at $(-1.75, 0.2)$.
  (b) The spectrum of V taken in the bimodal region at $(-1.75, 0.2)$.
  (c) The cross spectrum of U, V taken in the bimodal region at $(-1.75, 0.2)$. The spectra were averaged over 4 hours so that the maximum error at the low frequency end is ± 2 percent.

y direction (relative to the top surface of the rib) and ± 50μm in the x direction (relative to the rib sides).

The tape recorded signals were then analyzed in a MAS-SCOMP 5600 computer system based at Oxford University where the power spectrum can be calculated. Full details of the flow channel and measuring system are presented in Martin and Drain (1988) where details of the flow velocity profile and LDV system are given.

3 Results

The majority of the measurements were taken around rib number 29 at which station previous work (Bates et al, 1983) had established that the flow is fully developed. The first set of results to be discussed is shown in Fig. 2 as velocity probability distributions measured over an array of spatial positions covering the front half of the top of the rib and up to 0.9 mm into the free stream. The optical configuration limited the closest approach to the rib surface to 0.1 mm since the measuring volume dimensions were 70 μm diameter by 0.81 mm long. Each individual plot is a graph of the probability of a particular velocity versus velocity for both trackers. It should be noted that the spatial scale of the y-axis has been contracted for the bottom rows to enable all the distributions to be drawn to the same size. The velocity scale is presented in arbitrary units and includes an offset from zero produced by frequency shifting.

An apparent feature of the distributions is the bimodal nature of those near the leading edge of the rib, i.e., in the range $-2. < x < -0.5$, $0.2 < y < 0.5$. This indicates that the flow in the region has two states whereas the distributions outside have two distinctive normal distributions for V and U. One of the states corresponds to a situation where the mean flow is around zero and the other where there is a strong positive component. We will refer to the former as the low flow state and the latter as the high flow state.
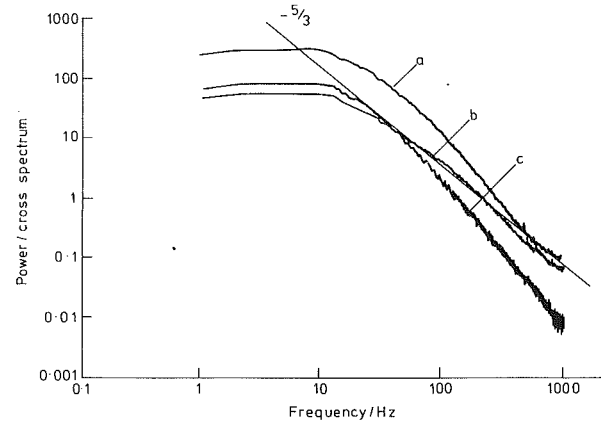
The bimodal effect is localized and its influence does not

appear to spread far into the main flow as the distributions at 0.9 mm above the surface are near normal. This could either be due to the turbulence of the free stream (typically ~ 20 percent of the mean) or could indicate that the bubble is strongly three dimensional. This latter conclusion is in accord with the observations of Castro and Dianat (1983) and Melbourne and Saathoff (1986). A further feature of Fig. 2 which is in good agreement with Dianat and Castro (1984) is the sharpness of the velocity probability distribution at station $x = -2.0$, $y = 0.1$. Dianat and Castro found a similar sharpening in the probability distributions of the fluctuating surface shear stress near the leading edge of their bluff body. This they interpreted as the flow spending most of the time at a well defined mean with only occasional explosive bursts away from it. Further, they found generally skewed distributions along the middle portion of the body which also agrees with the present case along stations at heights $y = 0.1$.

Finally we would like to emphasize that similar probability distributions have been observed on other ribs in the flow rig and using a different LDV system (Martin, 1990). The ribs have been machined square but inevitably a certain rounding of the sharpness of corners has occurred over a period of years. However, the bubble features are robust and do not depend on the detailed sharpness of the corners.

A more useful way of visualizing the bubble is shown in Fig. 3. The velocity vectors draw here have been reconstructed from the peaks of the velocity distributions and the two states of the flow are represented in Figs. 3(a) and 3(b). In each case the diagram is drawn to scale and the nature of the separation bubble is clearly evident. There is also some evidence that there is a negative mean flow in a thin layer adjacent to the rib surface near the leading edge, but this occurs on the limit of resolution of the LDV arrangement.

A series of one-dimensional frequency spectra were taken in this region to see if any time periodic phenomena were associated with the growth and collapse of the bubble. A set of spectra for U, V and UV are presented in Fig. 4 which were recorded in the centre of the bimodal region. It may be seen that the spectra do not show any periodic features indicating that the flipping between states is irregular. Indeed, the velocity time series taken in this region appear to be completely irregular.

The spectra shown in Fig. 4 are qualitatively similar to those found for flat plates (Klebanoff, 1955) with the $-5/3$ law being followed over the high frequency range of the spectra. In addition, the cross spectrum decays more rapidly than the individual spectra showing that there is some local isotropy of the small scale turbulence. Similar sets of spectra were found
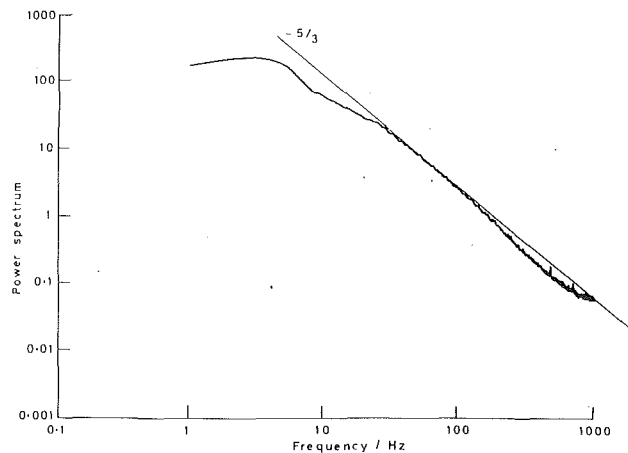
Fig. 5 The power spectrum of U taken in the free stream at (1.75,5.0). The maximum error in the spectrum is ± 2 percent.
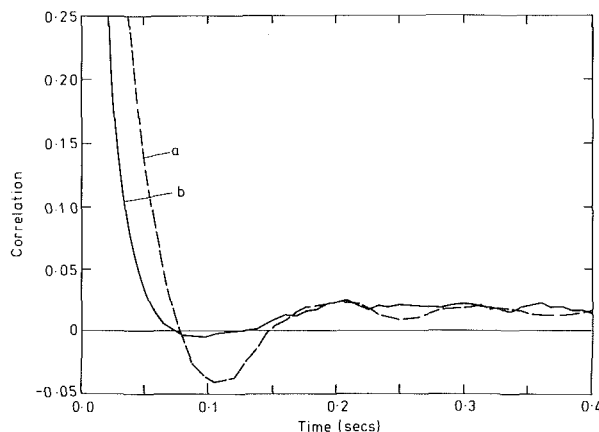

Fig. 6(a) The autocorrelation function of U taken in the free stream at (−1.75,5.0).

6(b) The autocorrelation function of U taken in the bimodal region at (−1.75,0.2). The maximum error in the autocorrelation function is ±1 percent at the longest time scales.

at other positions near the rib surface both inside and outside of the separation region.

Spectra taken in the free stream revealed evidence for an almost periodic component with a mean frequency of 5 Hz. One such spectrum is shown in Figure 5 which was taken at one rib height above the rear section of rib number 29. Another representation of the component is given by the auto-correlation functions shown in Fig. 6. Figure 6(a) shows the auto-correlation functions for the U-component one rib height above the rib and near the leading edge. The flow is highly turbulent but a damped oscillation with a period of 0.2 s is visible. The corresponding auto-correlation in the bubble region, Fig. 6(b), does not show any oscillatory behavior.

The oscillating component has been detected at a variety of different spatial locations in the free stream flow. It has not been observed, however, in spectra taken near the rib surfaces or in the cavities between ribs. A similar low frequency oscillation was found by Castro (1981) and he attributed it to a "flapping" of the shear layer. We were unable to confirm this conjecture although one might expect a similar phenomenon to occur.

4 Conclusions

The main conclusions to be drawn from this study are that a small recirculation bubble is formed along the leading edge

of each rib and subsequently collapses at irregular intervals. This could be of practical significance in the operation of a heat exchanger as it may give rise to local hot spots. It is also interesting to note that there is no evidence for this phenomenon in the numerical studies of Ghaddar et al. This could suggest that it is a feature of turbulent flow although the numerical resolution would presumably have to be increased before a definite statement could be made.

Further, we found evidence for some temporally correlated flow behavior centered around 5 Hz. This corresponds to a Strouhal number ($f L/U_{mean}$ where f is the frequency and L is the cavity length) of 0.1 which is in accord with the laminar flow results of Stephanoff (1986). Thus resonant phenomena could be induced if the flow were externally excited at this frequency.

References

Bates, C. J., Yeoman, M. L., and Wilkes, N. S., 1983, "Non-Intrusive Measurements and Numerical Comparison of the Axial Velocity Components in a Two-Dimensional Flow Channel for a Backward Facing Step and a Rib Roughened Surface", AERE R10787.

Binnie, A. M., 1960, "Self-Induced Waves in a Conduit with Corrugated Walls. I) Experiments with Water in an Open Horizontal Channel with Vertically Corrugated Sides," *Proc. Roy Soc.*, Series A, Vol. 259, pp. 18–27.

Binnie, A. M., 1961, "Self-Induced Waves in a Conduit with Corrugated Walls. II) Experiments with Air in Corrugated and Fixed Tubes," *Proc. Roy Soc.* Series A, Vol. 261, pp. 179–191.

Castro, I. P. , 1981, "Turbulent Flow over a Square Sectioned 2-Dimensional Block," *J. of Wind Engineering and Industrial Aerodynamics*, Vol. 7, pp. 253–272.

Castro, I. P., and Dianat, M., 1983, "Surface Flow Patterns on Rectangular Bodies in Thick Boundary Layers," *J. of Wind Engineering and Industrial Aerodynamics*, Vol. 11, pp. 107–119.

Dianat, M., and Castro, I. P., 1984, "Fluctuating Surface Shear Stresses on Bluff Bodies," *J. of Wind Engineering and Industrial Aerodynamics*, Vol. 17, pp. 133–146.

Fujita, H., Yokosawa, H., and Hirota, M., 1989, "Secondary Flow of the Second Kind in Rectangular Ducts with One Rough Wall," *Experimental Thermal and Fluid Science*, Vol. 2, pp. 72–80.

Ghaddar, N. K., Karniadakis, G. E., and Patera, A. T., 1986, "A Conservative Isoparametric Spectral Element Method for Forced Convection; Application to Fully Developed Flow in Periodic Geometries," *Numerical Heat Transfer*, Vol. 9, pp. 277–300.

Ghaddar, N. K., Korczak, K. Z., Mikic, B. B., and Patera, A. T., 1986, "Numerical Investigation of Incompressible Flow in Grooved Channels. Part 1; Stability and Self-Sustained Oscillations," *J. Fluid Mechanics*, Vol. 163, pp. 99–127.

Ghaddar, N. K., Magen, M., Mikic, B. B., and Patera, A. T., 1986, "Numerical Investigation of Incompressible Flow in Grooved Channels. Part 2: Resonance and Oscillatory Heat-Transfer Enhancement," *Journal of Fluid Mech.*, Vol. 168, pp. 541–567.

Hanjalic, K., and Launder, B. E., 1972, "Fully Developed Asymmetric Flow in a Plane Channel," *J. Fluid Mech.*, Vol. 51, pp. 301–335.

Incropera, F. P., "Convective Heat Transfer in Electronic Equipment Cooling," ASME *Journal of Heat Transfer*, Vol. 110, pp. 1097–1111.

Klebanoff, P. S., 1955, "Characteristics of Turbulence in a Boundary Layer with Zero Pressure Gradient," NACA Rep 1247.

Martin, S. R., and Drain, L. E., 1988, "Extensive Measurements of Turbulent Flow in a Ribbed Wall Water Channel Using Laser Doppler Anemometry" AERE R 12911.

Martin, S. R., 1990, "Laser Doppler Measurements of Turbulent Water Flow and Comparisons with a k-ε Turbulence Model," PhD thesis University of Wales.

Melbourne, W. H., and Saathoff, P. J., 1986, "Under the Reattaching Shear Layer," *Proceedings of the Ninth Australian Fluid Mechanics Conference.*

Rockwell, D., 1983, "Oscillations of Impinging Shear Layers," *AIAAJ*, Vol. 21, pp. 645–664.

Stephanoff, K. D., 1986, "Self-Excited Shear-Layer Oscillations in a Multi-Cavity Channel with Steady Mean Velocity," ASME JOURNAL OF FLUIDS ENGINEERING, Vol. 108, 1986, pp. 338–342.

Szczepura, R. T., "Flow Characteristics of an Axisymmetric Sudden Pipe Expansion; Results Obtained From the Turbulence Studies Rig Part 2: Spectral Measurements CEGB TPRD/B/0703/R86.

Mingshun Yuan

Post Doctoral Fellow,
Department of Hydraulic Engineering,
Tsinghua University, Beijing,
People's Republic of China

Charles C. S. Song

Professor.

Jianming He

Research Assistant.

St. Anthony Falls Hydraulic Laboratory,
Department of Civil and
Mineral Engineering,
University of Minnesota,
Minn. MN 55414

Numerical Analysis of Turbulent Flow in a Two-Dimensional Nonsymmetric Plane-Wall Diffuser

By solving weakly compressible flow equations with application of Smogrinsky's subgrid-scale turbulent model and partial-slip condition at the wall, a two-dimensional analysis is made on the flow of Re = 1.2 × 10⁶ in a nonsymmetric plane-wall diffuser. The calculated velocity profiles are compared with the measured data, and the effect of inlet and outlet conditions on diffuser performance is evaluated. Comparison is also made between the symmetric and non-symmetric plane-wall diffusers.

Introduction

The great majority of diffusers in use are symmetrical and designed to optimize the pressure recovery and minimize the over all energy loss. Various numerical methods available to design two-dimensional diffusers are based on the equations of boundary layer integral developed by Ghose and Kline (1978). Much experimental work has also been carried out for two-dimensional and symmetrical diffusers (Waitman et al., 1961; Wolf and Johnston, 1969; Hoffman and Gonzalez, 1984). Various flow regimes are known to exist depending on the diffuser angle and length. It is also well known that the flow in a diffuser is very sensitive to the inflow velocity distribution.

For special applications to water tunnels for which low cavitation number is desirable at the test section, nonsymmetrical diffusers with horizontal ceiling have been designed (Song et al., 1987; Song, et al. 1988). Very little is known about the performance of two or three-dimensional diffusers. For this reason, a fairly extensive experimental and numerical programs has been carried out at the St. Anthony Falls Hydraulic Laboratory to help the design process. Physical modelings were carried out and the data were used to validate the mathematical modeling works. The mathematical model was then used to predict the prototype flow conditions.

In the present paper, only the calculations based on a two-dimensional model and the comparison with experimental data will be presented. Some comparisons with the performance of the equivalent symmetrical diffuser will also be presented. More complex three-dimensional aspects of diffuser flows will be referred to in later papers.

Governing Equations and Numerical Scheme

The numerical model is based on solving the equations of

weakly compressible flow (Song and Yuan, 1988; Yuan, 1988; Song and Yuan, 1990),

$$\frac{\partial p}{\partial t} + \nabla \cdot (K\mathbf{u}) = 0 \tag{1}$$

$$\frac{\partial \mathbf{u}}{\partial t} + \mathbf{u} \cdot \nabla \mathbf{u} + \frac{1}{\rho} \nabla p = \nu \nabla^2 \mathbf{u} \tag{2}$$

Where ρ, ν, and K are the density, kinematic viscosity and bulk modulus of elasticity of fluid, and p and $\mathbf{u}$ represent pressure and velocity vector.

When turbulent flow is modeled, p and $\mathbf{u}$ may be considered as the resolvable components. In this case, the subgrid scale (SGS) turbulences are accounted for by adding the SGS term $-\overline{u_i' u_j'}$ to the right-hand side of equation (2). Smagerinsky's model (1963) is selected to calculate the SGS stress,

$$\overline{u_i' u_j'} = \nu_t \left(\frac{\partial u_i}{\partial x_j} + \frac{\partial u_j}{\partial x_i} \right) \tag{3}$$

and

$$\nu_t = (C\Delta)^2 \overline{S_{ij} S_{ij}} \tag{4}$$

Where $S_{ij} = (\partial u_i/\partial x_i + \partial u_j/\partial x_i)/2$ is the resolvable strain rate, Δ is the grid size, C is the SGS coefficient, and ν_t is the SGS diffusivity. Such a model is widely used in large eddy simulation (Roggallo and Moin, 1984). Although the SGS model is originally intended for three-dimensional flows, the same equations are used herein for two-dimensional flow computation.

Equations (1) and (2) are solved numerically by finite volume approach for spacial discretization (Jococks and Kneile, 1981). The quantities p and $\mathbf{u}$ are stored at the cell center, and ν_t is calculated for the cell faces. The finite volume approach is based on an integral form of the governing equations. For numerical convenience equations (1) and (2) are written in a conservation form after ignoring a high order Mach number

term. The resulting equation with the SGS turbulence term included is

$$\frac{\partial G}{\partial t} + \nabla \cdot F = 0 \qquad (5)$$

where

$$G = [P \ u \ v]^t \qquad (6)$$

$$F = \begin{bmatrix} Ku & Kv \\ uu + \dfrac{P}{\rho} - \nu \dfrac{\partial u}{\partial x} - 2\nu_t \dfrac{\partial u}{\partial x} & uv - \nu \dfrac{\partial u}{\partial y} - \nu_t \left(\dfrac{\partial u}{\partial y} + \dfrac{\partial v}{\partial x} \right) \\ uv - \nu \dfrac{\partial v}{\partial y} - \nu_t \left(\dfrac{\partial v}{\partial x} + \dfrac{\partial u}{\partial y} \right) & vv + \dfrac{P}{\rho} - \nu \dfrac{\partial v}{\partial y} - 2\nu_t \dfrac{\partial v}{\partial y} \end{bmatrix} \qquad (7)$$

By integrating over a specific control volume $\forall$ and invoking the divergence theorem, equation (7) becomes

$$\frac{\partial G_m}{\partial t} = -\frac{1}{\forall} \int_S n \cdot F \, ds \qquad (8)$$

where G_m represents a mean quantity referred to the center of the volume and n is the normal vector of the volume surface S. For temporal integral, MacCormack's explicit predictor-corrector scheme (1969) is used as

predictor:

$$\overline{G}(t + \Delta t) = G(t) - \frac{\Delta t}{\forall} \left(\sum_k F \cdot S_k^+ + \sum_k F^- \cdot S_k^- \right) \qquad (9)$$

corrector:

$$G(t + \Delta t) = \frac{1}{2} [G(t) + \overline{G}(t + \Delta t)]$$
$$- \frac{\Delta t}{2\forall} \left(\sum_k \overline{F}^+ \cdot S_k^+ + \sum_k \overline{F} \cdot S_k^- \right) \qquad (10)$$

where the bar represents the predicted values; S_k^+ and S_k^- denote the backward and forward surfaces of a control volume respectively; F^+ and F^- correspond the flux vector evaluated at the center of the backward and forward control volumes respectively; and subscript k is an index of cell surfaces. MacCormack (1969) also showed that the two step scheme is second-order accurate in time and in space. The finite volume method has been chosen for the following reasons: 1. The
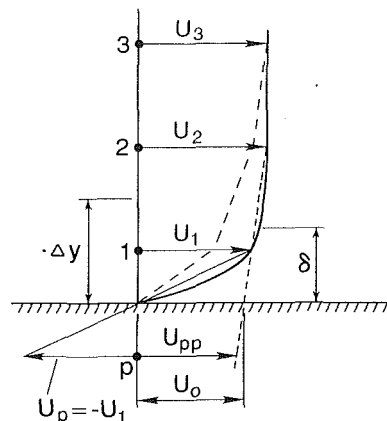
Fig. 1 Schematic of partial slip boundary condition

integral form of the governing equation (equation (8)) is valid for any finite volume regardless of its shape; 2. Since the governing equation is in cell averaged form, it is a nutural form for the large eddy simulation approach; 3. Since all equations (continuity and momentum) are written in the same form, it is relatively simple to code.

Boundary Conditions

When Reynolds number is large, a complete resolution of the thin wall layer of high velocity gradient would lead to a prohibitively high cost. Therefore, in turbulent flow calculation, it is a common practice to assume the existence of a layer near the wall, where the mean velocity distribution follows the wall law such as the logarithmic law (Ferziger, 1987). The measured data of diffuser flow (Ashjaee et al., 1980) showed that such an assumption is suitable for the symmetric diffuser with considerably large diverging angle.

Figure 1 is a schematic diagram showing a velocity profile near a wall. Let Δy be the grid size that is larger than the thickness of the near-wall layer of large $\partial u / \partial y$. Then a good approximation of the velocity profile should be u_1, u_2 and u_3 at the center of the grids. If the no-slip condition is enforced at the wall, the broken line would be the profile typically

---

Nomenclature

A_f = boundary layer thickness ratio = δ_T / δ_B
A_{fc} = critical value of A_f
B = inlet blockage = $(\delta_T + \delta_B) / m(1 + H_i)$
C = subgrid scale coefficient
C_p = pressure recovery = $(p - p_i) / \left(\frac{1}{2} \rho V_i^2 \right)$
F = flux vector
G = variable matrix
$\overline{G}$ = mean value of G on a cell
H = diffuser height
K = bulk modulus of fluid elasticity
L = diffuser length
m = power law exponent at inlet
n = unit outwards norm of cell surface
P_d = section-averaged pressure at downstream

p = pressure
Re = inlet Reynolds number = $H_i V_i / \nu$
RQ = discharge ratio divided by diffuser center line
RQ_e = discharge ratio at diffuser exit
$R\alpha$ = diverging angle ratio = α_T / α_B
$R_{\Delta y}$ = vertical mash ratio = $\max(\Delta y) / \min(\Delta y)$
U_o = u_o = velocity at wall boundary
U_p = velocity at phantom cell
U_{pe} = perturbation velocity at inlet
u = x component velocity
$\mathbf{u}$ = velocity vector
u^* = shear velocity
V_i = section-averaged velocity at inlet
v = y component velocity
x = horizontal coordinate
Y^+ = $(\Delta y / 2) u^* / \nu$

α = bottom wall diverging angle
Δy = vertical cell space
δ = boundary layer thickness
ϵ = velocity perturbation coefficient
ϵ_p = pressure perturbation coefficient
μ = molecular viscosity
ν = kinematic viscosity
ρ = density
τ = shear stress

Subscripts

B = bottom wall
d = downstream
i = inlet and variable index
j = variable index
k = cell surface index
T = top wall
t = turbulent
w = wall

---

calculated. To avoid such an unrealistic result, the velocity U_0 > 0 at the wall should be assumed, instead of $U_0 = 0$. In order to specify U_0, the relationship

$$\frac{\partial u}{\partial y} = f(u) \quad \text{at } y = \frac{\Delta y}{2} \tag{11}$$

is needed since u is stored at $y = \Delta y/2$.

Let $\overline{(\cdot)}$ represent the long time average of the resolvable quantities, τ the shear stress and τ_w the shear stress at the wall. Then the logarithmic law may be written as

$$\frac{\overline{u}}{u^*} = 2.5 \ln \left(9.0 \frac{u^* y}{\nu} \right) \tag{12}$$

for hydraulically smooth wall, where $u^* = (\overline{\tau}_w/\rho)^{1/2}$ is the shear velocity. From (3), we have

$$\tau = (\mu + \mu_t) \frac{\partial u}{\partial y} \tag{13}$$

To obtain (11), a relationship between u and τ must be established. Similar to Schumann's assumption (1978), it is assumed that

$$\frac{\tau}{\overline{\tau}} = \frac{u}{\overline{u}} \tag{14}$$

and

$$\overline{\tau} = \overline{\tau}_w \tag{15}$$

The above two assumptions associate the wall stress with the streamwise velocity at $\Delta y/2$. Experiments showed that such a $u - \tau_w$ correlation improves with increasing Reynolds number and decreasing Δy (Roggallo and Moin, 1984).

The computational procedure is as following.

(a) Calculate $\overline{u}$ using calculated historical data of u at $y = \Delta y/2$,

(b) Solve equation (12) for $\overline{u}$ or $\overline{\tau}_w$,

(c) Calculate τ, using (14) and (15),

(d) Using ν_t of previous step, $\partial u/\partial y$ is obtained from (13).

(e) The partial slip velocity U_0 for the next time step is calculated using the values of u and $\partial u/\partial y$ just calculated.

An additional condition is needed for pressure on the wall. In the present study, we use

$$\frac{\partial p}{\partial n} = \pm \rho \frac{u_0^2}{R} \tag{16}$$

where n and R are the unit outwards norm and the radius of curvature of the wall. At the inlet,

$$u = u_i, \quad v = 0, \quad \frac{\partial p}{\partial x} = 0 \tag{17}$$

are the boundary condition used, where u_i is the measured streamwise velocity. At the outlet,

$$\frac{\partial \mathbf{u}}{\partial x} = 0, \quad p = p_d \tag{18}$$

where p_d is given.

Model Validation

Figure 2 shows the three-dimensional HYKAT diffuser that has a 5.4 deg diverging angle at the bottom wall and a 0.73 deg angle at the side walls. This diffuser is symmetrical with respect to the vertical center plane but diffuses only downward in the vertical direction. Measurements were taken in a 1:5; scale model using air rather than water as the working fluid. Velocity measurements were taken along vertical center lines located at three cross sections located at the inlet, middle, and the exit of the diffuser as shown. The model was operated with an average test section velocity of $V_i = 15$ m/s giving the Reynolds number $H_i V_i/\nu = 1.2 \times 10^6$.
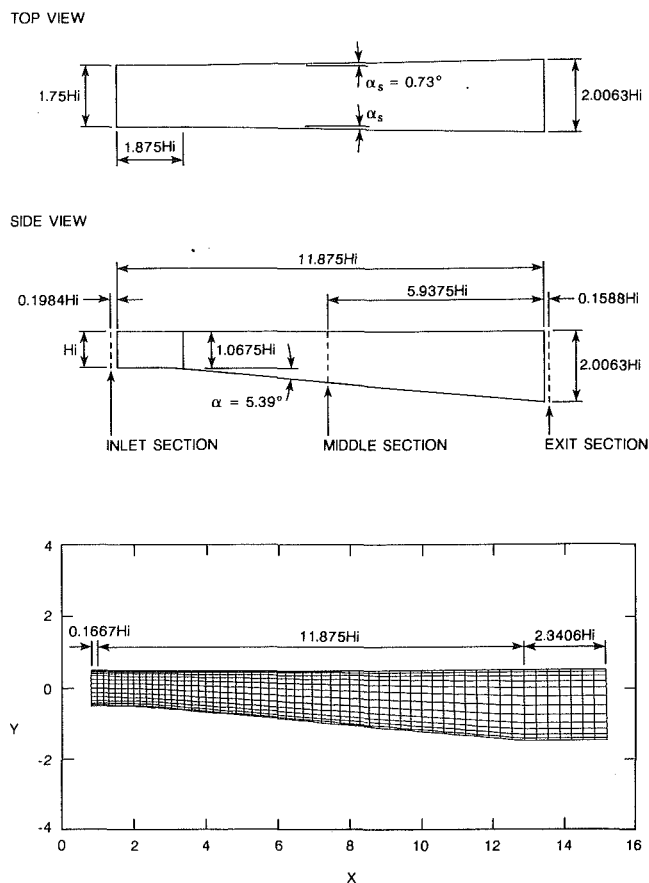
Considering the practical difficulty in modeling three-di-

Fig. 2 HYKAT diffuser and computational coarse mesh

mensional flow and the small diverging angles of side walls, a two-dimensional analysis of the flow on the vertical plane of symmetry was carried out. Several mesh sizes were tried to test the accuracy of the numerical scheme and look for an accurate and economical grid system. Finally it is found that a relatively coarse mesh of 58 × 12 cells shown in Fig. 2 is good enough to resolve the unseparated diffuser flow without causing a significant numerical error. Therefore, most of the results presented here are based on the coarse mesh. For comparison, however, the velocity profiles based on a fine mesh of 116 × 24 cells are also displayed, which will be shown later. The grid size Δy is so distributed that the ratio $R_{\Delta y} = \max(\Delta y)/\min(\Delta y) = 4.0$ for any given cross section. At the inlet, $\min(\Delta y)/H_i = .033$.

The degree of symmetry of the velocity profile is of most interest in the present study, for which the discharge ratio

$$RQ = \frac{Q_T}{Q_B} \tag{19}$$

is used to represent the quality of the flow, where Q_T and Q_B are the discharges of flow through the top and bottom halves of a given cross section, respectively. The discharge ratio defined above reflects the relative thickness of the boundary layers at the top and bottom walls. Its variation in the streamwise direction gives the relative growth rate of the two boundary layers.

For convenience, all the velocity profiles to be presented are normalized so that their means are unity. Normalization of velocity profiles partially compensates for the effect of small lateral diffusion. Figure 3 shows the measured inflow, whose boundary layers may be represented by the 5th power law. The inlet blockage is about .045 which is quite large. The measured velocity profiles at the middle section and the exit of the diffuser are also shown in Fig. 3.
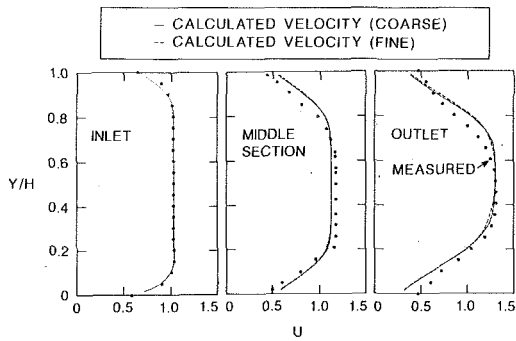
Fig. 3 Comparison of measured (Song et al., 1988) and calculated velocity profiles without inflow perturbation ($\epsilon = 0.0$), based on coarse mesh (58 × 12 cells) and fine mesh (116 × 24 cells)

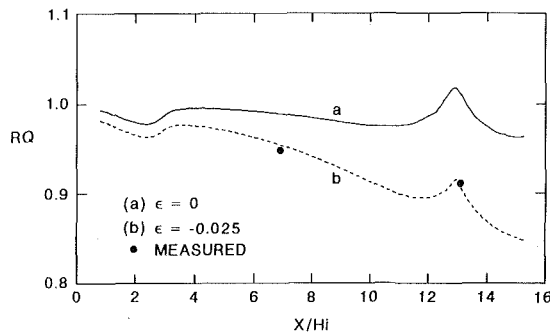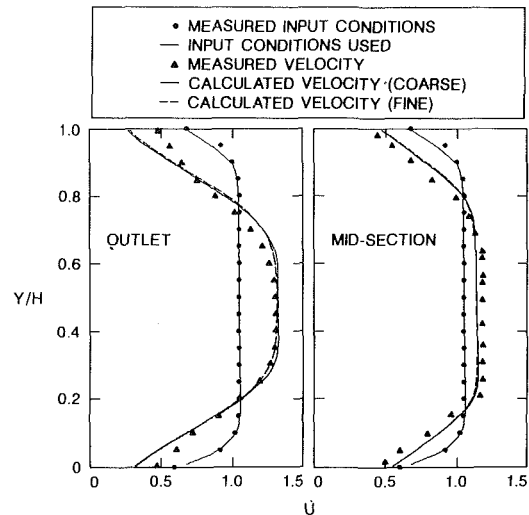Fig. 5 Comparison of measured (Song et al., 1988) and calculated velocity profiles with 2.5 percent inflow perturbation ($\epsilon = -0.025$), based on the coarse and fine meshes

Fig. 4 Distribution of discharge ratio (RQ) along diffuser; solid line: no inflow perturbation ($\epsilon = 0.0$); dash line: 2.5 percent inflow perturbation ($\epsilon = -0.025$)

Using the measured inflow and the two grid systems described before, velocity profiles at the other two cross sections can be calculated, for which the SGS coefficient $C = 0.15$ for coarse mesh and 0.3 for fine mesh were used. The comparison in Fig. 3 shows fairly good agreement between the calculated and measured profiles. The calculated discharge ratio is plotted in Fig. 4 (curve a). The difference between the values on this curve and the measured two points indicates that the boundary layer at the bottom wall grows too fast. Since the flow is very sensitive to the inflow, which will be shown later, such a difference may be caused by the allowable error of the measurement at the inlet. To obtain a good agreement of RQ, the measured inflow is adjusted by superimposing a perturbation velocity

$$U_{pe} = \epsilon V_i \left(\frac{y}{H_i} - 0.5 \right) \qquad (20)$$

where y is the distance from the bottom wall. The curve b in Fig. 4 was obtained by using $\epsilon = -.025$, which agrees with the measured points very well. The computed and measured velocity profiles for this case are shown in Fig. 5. Fairly good agreements are obtained.

Figures 3 and 4 also indicate that the differences between the results based on the two grid systems are quite small. The maximum error which occurs in outlet section in Fig. 5 is only three percent. This amount of difference is within the range of experimental accuracy. Therefore, it should be feasible to use the coarse mesh for validating the diffuser performance in the following section. It should be mentioned, that the calculated value of $Y^+ = (\Delta y/2) u^*/\nu$ at the wall is maximum near the inlet. The calculated maximum values are approximately $Y^+_{max} = 500$ by the coarse mesh and $Y^+_{max} = 250$ by

the fine mesh. It is encouraging to notice the fact that although Y^+_{max} is quite large for these two meshes, they produced almost the same results.

More measured data have been compared with the calculations. For example, when $RQ_i = 1.0065$ at inlet, the measured velocity profile at exit shows $RQ_e = 1.114$. By using the measured inflow for the numerical model, we obtained $RQ_e = 1.134$. Due to space limitation, the plots would not be presented here.

Figure 6 gives the comparison of the measured and computed pressure recovery for a symmetric diffuser. Generally, the results of present calculation are very close to the experimental data (Ashjaee et al., 1980).

Diffuser Performance

The results to be presented in this section were obtained by using the coarse mesh given previously.

Effect of Inflow With Constant Vorticity in the Core Region. Diffuser response was evaluated by the numerical model, for which the inflow has various values of discharge ratio RQ. The type of inflow is determined by equation (20) with ϵ varying from -0.1 to 0.1, which adds a constant vorticity to the core region equal to $\omega = \epsilon(V_i/H_i)$.

From the calculated RQ (x/H_i, ϵ) chart in Fig. 7, it can be seen that the inflow non-symmetry is greatly amplified by the diffuser. Due to the nonsymmetry of the diffuser, such an amplification is also nonsymmetric. For the same value of $|\omega|$, the flow is more unstable in the case that at the inlet more flow goes through the top half than the bottom half. For a two-dimensional diffuser that has different diverging angles at both walls, flow is less stable to the inflow with more flow at the side of smaller diverging angle.

To compare the performance of the nonsymmetric diffuser with the symmetric one, inflow of $\epsilon = -0.025$ is used while the ratio $R\alpha = \alpha_T/\alpha$ is varied, where $\alpha = 5.4$ deg is the total angle and α_T is the angle at the top wall. The chart RQ (x/H_i, $R\alpha$) is shown in Fig. 8. It can be seen that the symmetric diffuser ($R\alpha = 0.5$) has a better performance than the nonsymmetric one when at the inlet, there is more flow going through the half cross section at the side of smaller angle. Therefore, whether a nonsymmetric diffuser gives a better performance than the symmetric one really depends on the type of inflow.
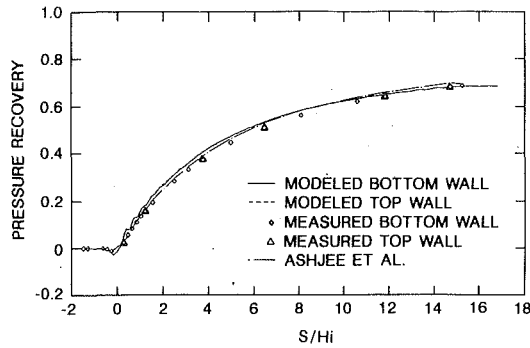
Fig. 6 Comparison of measured (Ashjaee et al., 1980) and modeled pressure recovery $C_p = (p - p_i)/(1/2\,\rho V_i^2)$ for a symmetric diffuser $L/H_i = 15$ with 6 deg total diffusion angle
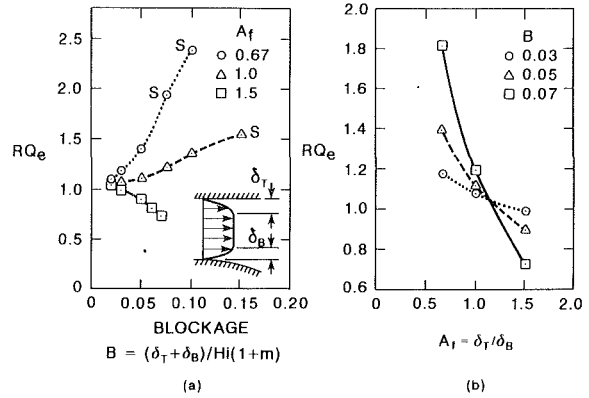

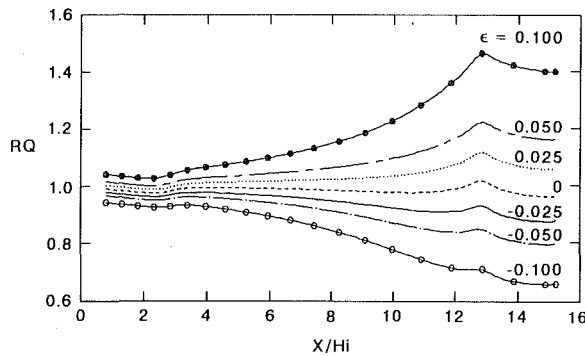Fig. 9 Effect of inflow boundary layer thickness on exit discharge ratio (RQ_e)

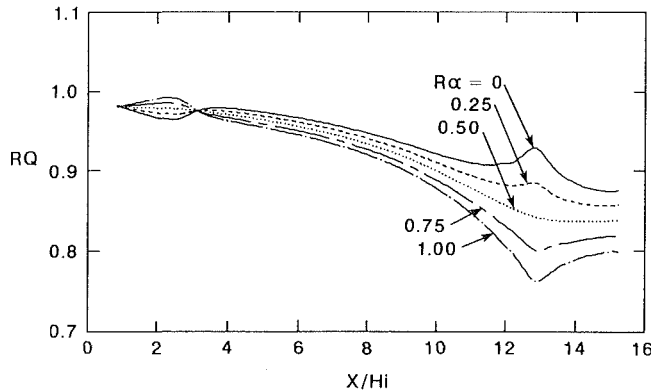Fig. 7 Effect of inflow perturbation (ϵ) on the distribution of discharge ratio (RQ) along diffuser

Fig. 8 Effect of top wall diverging angle ($R\alpha = \alpha_T/\alpha$) on the distribution of discharge ratio (RQ) along diffuser

Effect of Inflow With Potential Core. Let δ_T and δ_B represent the thickness of the top and bottom boundary layers at the inlet. By using the power law with exponent m for the velocity distribution in the boundary layers, the inlet blockage B is

$$B = \frac{\delta_T + \delta_B}{H_i}\frac{1}{1+m} \tag{21}$$

where $m = 5.125$ from the measured data. The ratio

$$A_f = \frac{\delta_T}{\delta_B} \tag{22}$$

may be used as a parameter to indicate the nonsymmetry of inflow with a potential core.

The computed RQ distributions along the diffuser for fixed B and A_f look much like those shown in Figs. 7 and 8. In Fig. 9(a), the discharge ratio at the exit, RQ_e, is plotted as a function of B for three fixed values of A_f. The three curves starts from a point with very small B and diverge as B increases. The curve for $A_f = 1.0$ indicates that the outflow can be very skewed when the inflow is symmetric on account of the diffuser asymmetry. There is a critical value of inflow assymmetry, $A_{fc} = 1.12$ (not shown in the figure) which produces a symmetric outflow. The critical value A_{fc} is equal to 1 for a symmetrical diffuser. The points marked by S are from the runs for which the calculated flow has a separation bubble on the bottom wall near the diffuser exit, indicating that stall could occur in the real case.

The same set of calculated RQ_e is plotted in Fig. 9(b) as a function of A_f for three selected values of B. Note that the three curves intersect at the point ($A_f = 1.12$, $RQ_e = 1.04$) indicating that the initial value A_{fc} is practically independent of the blockage B.

Effect of Pressure Nonuniformity at Diffuser Exit. For the previous calculations, a short straight channel was added to the diffuser exit, to make it easier to apply the downstream boundary condition: recall that the pressure was assumed to be constant at the downstream end. However, the actual HY-KAT diffuser is connected to a vaned elbow at the downstream of its outlet. Due to the centrifugal force, nonuniform pressure distribution could occur at the downstream of diffuser. Therefore, the effect of pressure nonuniformity should be evaluated.

The inflow used for this case is the one from equation (20) at $\epsilon = -.025$. According to the calculation of the flow in the vaned elbow (Song et al., 1987) a 3rd-order polynomial pressure distribution,

$$p_d = P_d + \epsilon_p\left(\frac{1}{2}\rho V_i^2\right)\left[3\left(\frac{y}{H_d}\right)^2 - 2\left(\frac{y}{H_d}\right)^3\right] \tag{23}$$

should be a reasonable first approximation. In the above equation, P_d is the given mean pressure, H_d is the height of the outlet cross section, and y is the distance measured from the bottom wall. The parameter ϵ_p represents the maximum dimensionless pressure difference $(p_T - p_B)/(1/2\,\rho V_i^2)$.

Figure 10 shows the chart of RQ distribution along the diffuser for seven different values of ϵ_p ranging from -0.1 to 0.1. Note that the nonuniform back pressure distribution affects the flow only within a fairly short distance, especially the straight portion, upstream of the boundary. The calculation of the flow in the elbow shows that the value of ϵ_p between 0.025 and 0.05 is appropriate for the HYKAT diffuser.

Conclusions

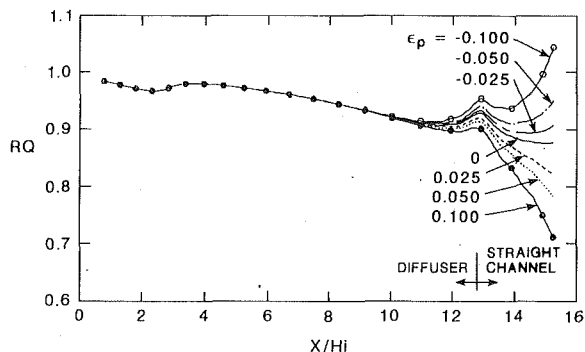The two-dimensional model presented can give mean velocity

Fig. 10 Effect of outlet pressure nonuniformity (ϵ_p) on the distribution of discharge ratio (RQ) along diffuser

profile and pressure recovery that are generally in good agreement with the measured data. Such a numerical model is useful in the design of diffusers being operated at high Reynolds numbers, especially when the details of the velocity profile are of concern.

Effects of inlet and outlet condition on the diffuser performance are evaluated in terms of flow symmetry. Among the parameters studied, the inlet blockage should be considered as the most important parameter. The influence of the inflow asymmetry including the core flow and the boundary layer is also considerable. Compared with the symmetric diffuser, the advantage and disadvantage of using an asymmetric diffuser depend on the inflow profile. The effect of nonuniform back pressure distribution on the diffuser flow is limited to fairly small region close to the boundary.

Comparison of results between the fine (116 × 24) and coarse (58 × 12) meshes indicates that the model results are almost mesh-size independent if the subgrid model coefficient is adjusted properly. The subgrid model is at its developing stage for turbulence flow simulation. In the present study of two-dimensional flow, it was noticed that the calculated turbulence intensity is too small, due to the improper resolution of eddies by the current meshes and the absence of three-dimensional mechanism of generating eddies.

References

Ashjaee, J., Johnston, J. P., and Kline, S. J., 1980, "Subsonic Turbulent Flow in a Plane-Wall Diffuser: Peak Pressure Recovery and Transitory Stall," Report PD-21, Dept. of Mech. Eng., Stanford University.

Ferziger, J. H., 1987, "Simulation of Incompressible Turbulent Flows," *J. Comp. Phys.*, Vol. 69, pp. 1–48.

Ghose, S., and Kline, S. J., 1978, "The Computation of Optimum Pressure Recovery in Two-Dimensional Diffusers," ASME JOURNAL OF FLUIDS ENGINEERING, Vol. 100, pp. 419–426.

Hoffman, J. A., and Gonzalez, G., 1984, "Effects of Small-Scale, High Intensity Inlet Turbulence on Flow in a Two-Dimensional Diffuser," *J. Fluids Eng.*, Vol. 106, pp. 121–124.

Jacocks, J. L., and Kneile, K. R., 1981, "Computation of Three-Dimensional Time-Dependent Flow Using the Euler Equations," AEDC-TR-80-49.

MacCormack, R. W., 1969, "The Effect of Viscosity in Hypervelocity Impact Cratering," AIAA Paper, No. 69-354.

Roggallo, R. S. and Moin, P., 1984, "Numerical Simulation of Turbulent Flow," *Ann. Rev. of Fluid Mech.*, Vol. 16, pp. 99–137.

Schumann, U., 1978, "Subgrid-Scale Model for Finite Difference Simulations of Turbulent Flows in Plane Channels and Annuli," *J. Comp. Phys.*, Vol. 18, pp. 376–404.

Smagorinsky, J., 1963, "General Circulation Experiments with the Primitive Equations," Mon. Weath. Rev., Vol. 91, No. 3, pp. 99–164.

Song, C. C. S. and Yuan, M., 1988, "A Weakly Compressible Flow Model and Rapid Convergence Method," ASME JOURNAL OF FLUIDS ENGINEERING, Vol. 110, pp. 441–445.

Song, C. C. S. and Yuan, M., 1990, "Simulations of Vortex-Shedding Flow about a Circular Cylinder at High Reynolds Numbers," ASME JOURNAL OF FLUID ENGINEERING, Vol. 112, pp. 155–161.

Song, C. C. S., Wetzel, J. M., Killen, J. M., and Arndt, R. E. A., 1988, "Physical and Mathematical Modeling of the HYKAT," Project Report No. 282, St. Anthony Falls Hydraulic Lab., University of Minnesota.

Song, C. C. S., Wetzel, J. M., Yuan, M., Arndt, R. E. A., and Killen, J. M., 1987, "Hydrodynamic Analysis of the HYKAT," Project Report No. 261, St. Anthony Falls Hydraulic Lab., University of Minnesota.

Yuan, M., 1988, "Weakly Compressible Flow Model and Simulations of Vortex-Shedding Flow About a Circular Cylinder," Ph.D. thesis, University of Minnesota.

Waitman, B. A., Reneau, L. R., and Kline, S. J., 1961, "Effects of Inlet Conditions on Performance of Two-Dimensional Sonic Diffusers," JOURNAL OF FLUIDS ENGINEERING, pp. 349–360.

Wolf, S. and Johnston, J. P., 1969, "Effects of Non-Uniform Inlet Velocity Profiles on Flow Regimes and Performance in Two-Dimensional Diffusers," ASME JOURNAL OF FLUIDS ENGINEERING, pp. 462–474.

A Numerical Investigation of the Turbulent Flow Field Generated by a Stationary Cube

R. Raul
Research Associate,
Applied Physics Laboratory,
Johns Hopkins University,
Laurel, MD 20707

P. S. Bernard
Associate Professor,
Department of Mechanical Engineering,
The University of Maryland,
College Park, MD 20742

The turbulent flow field generated by a stationary cube at Reynolds numbers 2000 and 14,000 is investigated numerically. A vorticity-vector potential formulation of the equations of motion is employed. Turbulence effects are accounted for through the use of a vorticity transport closure scheme in which dynamical equations for vorticity mean and covariance are supplemented by a kinematic equation for turbulent kinetic energy. Semi-implicit finite difference approximations to the equations of motion are solved iteratively by a vectorizable 8-color SOR algorithm. The numerical mesh is designed so that the turbulent flow field can be computed down to solid surfaces without the use of wall functions. The properties of the computed flow field, including drag, axial velocity, separation points, and three-dimensional flow structure show good agreement with experimental observations of similar bluff body flows.

Introduction

The prediction and analysis of three-dimensional turbulent bluff body flow fields is often times a necessary component in the design of a wide range of structures including ground vehicles, aircraft fuselages, submarines, tall buildings and so on. The capability of numerically treating such flows can enhance the efficiency with which three-dimensional objects can be designed for optimal drag, stability, and wake structure. Following the recent proliferation of supercomputers, with their high speed and large memories, an increasing number of numerical studies have been concerned with the prediction of turbulent bluff body flows. Among these, several investigations have considered the flow field generated by complex automotive shapes (Gooding et al., 1988; Markatos, 1983; Laurence, 1986; Demuren and Rodi, 1982) and the flow past bluff obstacles fixed to the ground (Han, 1989; Murakami and Mochida, 1988; Murakami, 1990). While these studies have had some success in predicting the gross features of the fluid motion, it has proven to be more difficult to capture the detailed properties of the flow separation and wake structures. Consequently, considerable interest remains in developing and exploring the properties of new methods for treating the flows associated with bluff bodies. Areas where improvements can be made include turbulence closure schemes, numerical methods and the treatment of turbulent boundary conditions.

Previous computations of turbulent bluff body flows have generally relied on the widely used algebraic eddy viscosity and $k - \epsilon$ closures. In view of the well documented inadequacy of these models in the context of complex flow fields (Lakshminarayana, 1986) it is likely that their unmodified use in computing bluff body flows is a major source of errors in predictions. In addition, these models are generally applied

with insufficient grid resolution in the boundary region to accurately resolve the wall flow. Partly as a consequence, wall function boundary conditions are usually applied which introduce errors into the prediction of separation points and thus distort the entire computed flow field.

The present paper describes the results of calculations of the three-dimensional flow past a fixed cube based on the application of a vorticity transport closure scheme (Bernard and Berger, 1982; Bernard, 1990a). In this approach, the presence of turbulence in the flow field is accounted for by solving dynamical equations for the ensemble averaged vorticity mean and covariance. The turbulent kinetic energy, k, is computed kinematically from the vorticity covariance, an idea first suggested by Chorin (1974), so that the considerable difficulties inherent in modeling the k equation, (Mansour et al., 1989), are avoided. By directly approximating the processes affecting the vorticity field, namely, vorticity transport and stretching, the method attempts to take advantage of the importance which vorticity dynamics has to understanding the nature of complex turbulent flows. The capacity of the approach to successfully model a range of complex engineering flows has been demonstrated in previous studies of an internal combustion engine flow field (Bernard, 1981), the edgetone flow field generated by the impingement of a jet on a sharp-edged wedge (Bernard, 1990b) and the flow past a squared cylinder with periodic vortex shedding (Raul and Bernard, 1990).

The present calculations consider the turbulent flow around a cube at the Reynolds numbers of 2000 and 14000. These results extend a previous investigation (Raul et al., 1990) of the equivalent laminar flow field using a vorticity-vector potential method. The cube flow field is considered, apart from its intrinsic interest, so as to maximize the possible grid resolution. In particular, the simplicity of the cube geometry permits the calculation of all fields down to the solid boundary without the use of wall functions. The computations to be

described below appear to demonstrate the capacity of the current method to predict the mean properties of the cube flow over a range of Reynolds numbers. The predicted drag is shown to be in good agreement with experimental results, and the computed three-dimensional flow structure compares favorably with many of the observed attributes of similar bluff body flow fields.

The turbulence closure scheme used in the present study is described in the next section. Following this, a brief description of the numerical approach is given and then the results of the calculations are described. Finally, some conclusions are given in the last section.

Turbulence Equations

Implementation of the most general form of the vorticity transport closure scheme in the context of turbulent cube flow requires the solution of dynamical equations for the three components of the vorticity mean, $\overline{\Omega}_i$ and six components of the vorticity covariance $\zeta_{ij} \equiv \overline{\omega_i \omega_j}$ (Bernard and Berger, 1982). Coupled to this system of equations are several kinematic relations in which the mean velocity field is determined from $\overline{\Omega}_i$ and the Reynolds stresses $\overline{u_i u_j}$ are obtained from ζ_{ij}. Here, u_i is the velocity and ω_i the vorticity fluctuation vectors. Following the approach of Richardson and Cornish (1977), $\overline{U}_i$ is obtained from scalar and vector potentials which are determined kinematically from $\overline{\Omega}_i$. In view of the extreme computational requirements of the present simulation, the expediency is taken of solving a single equation for the trace $\zeta \equiv \zeta_{ii}$ of ζ_{ij} instead of separate relations for each of the components of ζ_{ij}. In this case, the kinematic problem of calculating $\overline{u_i u_j}$ from ζ_{ij} is reduced to one of computing just the turbulent kinetic energy, k, from ζ.

After some simplifications warranted by the replacement of ζ_{ij} by ζ, it follows that the dynamical equations for $\overline{\Omega}_i$ and ζ are, respectively,

$$\frac{\partial \overline{\Omega}_i}{\partial t} = -\overline{U}_j \frac{\partial \overline{\Omega}_i}{\partial x_j} + \frac{\partial}{\partial x_j} \left(\left(\nu + \frac{2}{3} kT \right) \frac{\partial \overline{\Omega}_i}{\partial x_j} \right)$$
$$+ \frac{\partial}{\partial x_j} \left(\frac{\frac{2}{3} Q_1 \left(\overline{\Omega}_i \frac{\partial k}{\partial x_j} - \overline{\Omega}_j \frac{\partial k}{\partial x_i} \right)}{1 + Q_1 Q_2 \overline{\Omega}_k^2} \right) + \overline{\Omega}_j \frac{\partial \overline{U}_i}{\partial x_j} \quad (1)$$

and

$$\frac{\partial \zeta}{\partial t} = -\overline{U}_j \frac{\partial \zeta}{\partial x_j} + \frac{\partial}{\partial x_j} \left(\left(\nu + \frac{2}{3} kT \right) \frac{\partial \zeta}{\partial x_j} \right) + \frac{4}{3} kT \frac{\partial \overline{\Omega}_i}{\partial x_j} \frac{\partial \overline{\Omega}_i}{\partial x_j}$$
$$+ 2S\overline{\Omega}_i^2 \Gamma_1 + 2S\zeta \Gamma_1 + 4S\Gamma_1 \Gamma_2 - \frac{14\nu\zeta}{\lambda^2}. \quad (2)$$

Here T, S, Q_1, and Q_2 are Lagrangian integral time scales, $\Gamma_1 = 4k/\lambda^2$ and $\Gamma_2 = (\zeta - 3\Gamma_1)/2$. A discussion of the derivation of (1) and (2) may be found, for example, in the thesis by Raul (1989). The first and second terms on the right-hand sides of these equations represent advection and diffusion processes, respectively. Note that the total (viscous + turbulent) diffusivity in each equation is given by $\nu + 2/3kT$. The last two terms in equation (1) account for vortex stretching and shearing phenomena. Production of turbulence from the mean flow is represented in the ζ equation by the third and fourth terms on the right-hand side. The fifth and sixth terms account for turbulence self-production effects while the last term represents dissipation.

The mean velocity vector $\overline{U}_i$ can be determined from scalar and vector potentials ϕ and $\overline{\psi}_i$, respectively, by the decomposition

$$\overline{U}_i = \frac{\partial \phi}{\partial x_i} + \epsilon_{ijk} \frac{\partial \overline{\psi}_k}{\partial x_j} \quad (3)$$

where ϵ_{ijk} is the alternating tensor. As shown by Richardson and Cornish (1977), ϕ is obtained as a solution to the Laplace equation

$$\nabla^2 \phi = 0 \quad (4)$$

while $\overline{\psi}_i$ satisfies the Poisson equation

$$\nabla^2 \overline{\psi}_i = -\overline{\Omega}_i. \quad (5)$$

At solid surfaces ϕ satisfies the non-penetration condition $\partial\phi/\partial n = 0$, where n is the outward normal coordinate. In the present study the condition $\partial\phi/\partial n = u_n$ is used at the far field boundary, where u_n is the outflow velocity. As in the earlier laminar flow calculations, u_n is set equal to the value appropriate to the flow past a sphere with volume equivalent to that of the cube. At fixed surfaces the vector potential, $\overline{\psi}_i$, satisfies the condition that both of the tangential components and the normal derivative of the normal component are zero. At the far field boundaries a soft condition is imposed to the effect that the second normal derivative of $\overline{\psi}_i$ vanishes.

A general kinematic relationship between ζ and k consists of

$$\zeta = \frac{12k}{\lambda^2} + \frac{1}{2k} \nabla k \cdot \nabla k \quad (6)$$

which may be derived, after some simplification, from the defining equations for the microscales associated with the two point Eulerian velocity correlation coefficient

$$R(r) = \frac{\overline{\mathbf{u}(\mathbf{x}) \cdot \mathbf{u}(\mathbf{x} + r\mathbf{n})}}{\overline{\mathbf{u}(\mathbf{x}) \cdot \mathbf{u}(\mathbf{x})}^{\frac{1}{2}} \overline{\mathbf{u}(\mathbf{x} + r\mathbf{n}) \cdot \mathbf{u}(\mathbf{x} + r\mathbf{n})}^{\frac{1}{2}}} \quad (7)$$

where $\mathbf{n}$ is an arbitrary unit vector. Equation (7) always has a microscale (Bernard and Berger, 1983) so that (6) is well defined. Note that expressed in terms of Γ_1 and Γ_2, (6) becomes $\zeta = 3\Gamma_1 + 2\Gamma_2$.

It is evident from equations (2) and (6) that a separate relation giving λ in terms of $\overline{\Omega}_i$ and ζ is needed in the present approach. This may be found in a family of solutions for the decay of isotropic turbulence first described by Sedov (1944). One aspect of this is the scale equation

$$\frac{d\lambda}{dt} = -\frac{\delta}{2} \sqrt{\zeta} \lambda + \frac{2\nu}{\lambda} \quad (8)$$

Nomenclature

a	=	cube dimension	T	=	Lagrangian time scale	
C_D	=	drag coefficient $(2D/\rho U_0^2 a^2)$	u_i	=	fluctuating velocity component	
C_s	=	constant				
D	=	drag	U_0	=	free-stream velocity	
k	=	turbulent kinetic energy	$\overline{U}_i$	=	mean velocity	
Q_1, Q_2	=	Lagrangian time scales	ω_i	=	fluctuating vorticity component	
Re	=	Reynolds number				
$R(r)$	=	two point Eulerian velocity correlation coefficient	x, y, z	=	Cartesian coordinates	
			ϵ	=	turbulent dissipation	
S	=	Lagrangian time scale	ϵ_{ijk}	=	alternating tensor	
t	=	time	Ω	=	mean vorticity component	

ϕ	=	scalar potential
ψ_i	=	vector potential
δ	=	constant proportional to skewness factor of the velocity derivative fluctuation
λ	=	microscale
ζ_{ij}	=	vorticity covariance $(\overline{\omega_i \omega_j})$
ζ	=	trace of ζ_{ij}
ν	=	kinematic viscosity
ρ	=	density

where δ is a constant proportional to the skewness factor of the velocity derivative fluctuations. Equation (8) governs the change in λ during decay from its initial value. The effect of the first term on the right-hand side is to reduce λ by vortex stretching while the second causes an increase in λ due to viscous spreading of eddies. While λ will change in time during turbulent decay, it may be hypothesized that in flows with a source of turbulence due to a mean shear, the opposing processes of vortex stretching and viscous spreading will be in balance, and that this equilibrium will be maintained despite changes in the mean flow field. Consequently, it is assumed that

$$\lambda^2 = \frac{4\nu}{\delta\sqrt{\zeta}}. \tag{9}$$

It should be remarked that it is common practice in many other closures to determine λ implicitly through its defining equation, i.e., a relation such as (6), as one aspect of modeling the dynamical k equation. The very different use to which (6) is made here (as a source of k) necessitates the inclusion of a separate relation for λ. Besides the advantage (9) has of bringing some of the physics of the dissipation scale into the closure scheme, the present methodology avoids the formidable difficulties entailed in modeling the k equation (Mansour et al., 1989).

For the present study, T, Q_1, Q_2, and S were computed as in earlier applications of the approach. T, Q_1, and Q_2 were set to constants while the scale S was given by

$$S = \frac{C_s k}{\nu \zeta^*} \tag{10}$$

where C_s is a constant and $\zeta^* \equiv 12k/\lambda^2$. This expression is suggested by dimensional arguments (Hinze, 1975, p. 394). An attractive feature of equation (10) is that its use provides a means of insuring that the turbulence self-production terms in equation (2) are always bounded by the dissipation term, a necessary condition for stability. Thus, equations (6), (9), and (10) imply that

$$2S\zeta\Gamma_1 + 4S\Gamma_1\Gamma_2 - \frac{14\nu\zeta}{\lambda^2} \le 2S\zeta^2 - \frac{14\nu\zeta}{\lambda^2} = -\zeta^{3/2}\left(\frac{7}{2}\delta - \frac{2}{9}\frac{C_s}{\delta}\right),$$

so that as long as

$$\frac{7}{2}\delta - \frac{2}{9}\frac{C_s}{\delta} > 0 \tag{11}$$

finite solutions to equation (2) may exist. Equation (11) acts as a constraint on the selection of C_s and δ which must always be satisfied.

To summarize, the complete set of equations forming the vorticity transport model consists of equations (1) and (2) accounting for the dynamics of $\bar{\Omega}_i$ and ζ, respectively, and the kinematical relationships given by (4) for ϕ, (5) for ψ_i and (6) for k. Finally, λ^2 is computed via equation (9) and S by (10). The externally supplied quantities to the system of equations consist of the five constants $T, Q_1, Q_2, C_s,$ and δ.

For the computation of the cube flow at Re = 2000 described below, the values of the constants appearing in the turbulent equations were $\delta = 0.037$, $C_s = 0.007$, $T = 0.25$, $Q_1 = 0.1$ and $Q_2 = 0.01$. In the case when Re = 14,000 the values $\delta = 0.01$, $C_s = 0.001$, $T = 0.25$, $Q_1 = 0.1$ and $Q_2 = 0.01$ were used. The selection of parameters was based on previous studies of channel and jet flow fields in which allowance was made for the differing Reynolds numbers. The approximate Reynolds number dependence of the constants can be deduced from an analysis of the governing equations (Raul, 1989). The numerical solutions to the system of equations were found to be relatively insensitive to the particular values chosen for the scales. In particular, variations by ± 15 percent of the principle scales T, δ, and C_s were found to cause a change in the drag of less
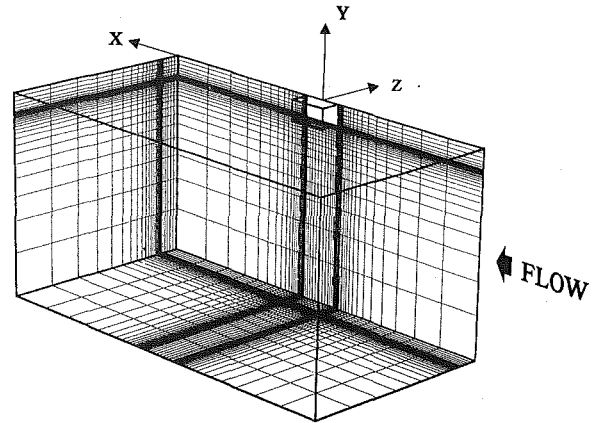

Fig. 1 Numerical mesh in quarter domain

than .4 percent, and no qualitative effect on the visualized flow fields. In addition, the possibility of having converged solutions was not dependent on a precise selection of the parameter values.

Numerical Scheme

The present simulation capitalizes on the symmetries of the cube flow field by considering just a quarter of the flow domain. Besides reducing the expense of the computations, this allows for enhanced resolution of the boundary layers. Since experiments (Bearman, 1978; Nakaguchi, 1978) indicate that periodic vortex shedding from alternate sides of the cube is not expected, no loss of generality is imposed by this limitation. The finite difference mesh incorporated in the quarter domain is shown in Fig. 1. The cube occupies the region $-.5$ to $+.5$ in all three directions. Grid points are exponentially stretched in each direction with allowance for greatest densities on the surfaces, edges and corners of the cube. The complete storage requirement of the mesh is limited to several one dimensional arrays of positions and scale factors.

As in the previous laminar flow study, semi-implicit second order spatial finite difference approximations were applied to the equations of motion transformed into the numerical coordinate system. The details of these formulas may be found elsewhere (Raul, 1989). The coupled algebraic equations were solved using an 8 color SOR algorithm in which 8 passes are made through the mesh, on each of which relaxation occurs only on every other mesh point in the three directions. In this way, no two adjacent points are updated together so that a fully vectorizable calculation is possible.

The numerical solution of equation (6) is complicated somewhat in that the term containing gradients, which is the highest differentiated term, is negligible compared to the other term at points sufficiently far from boundaries. For the present study this difficulty was avoided by calculating k outward from the solid surfaces assuming an inconsequential variation of k parallel to the surface. From the location near the wall where k achieved a peak and beyond, the entire gradient term in equation (6) was set to zero and k was computed from

$$k = \frac{\lambda^2 \zeta}{12}.$$

Tests of this procedure in a channel flow demonstrate it to be highly accurate. By this technique, a good approximate solution to equation (6) was obtained with minimal numerical difficulties.

The outer boundaries of the computed domain were assumed to be in the far field of the cube flow. For the calculations reported here the computational box extended 10 cube diameters in the streamwise, i.e., x direction, and 8 diameters in the two spanwise directions, y and z, while the numerical
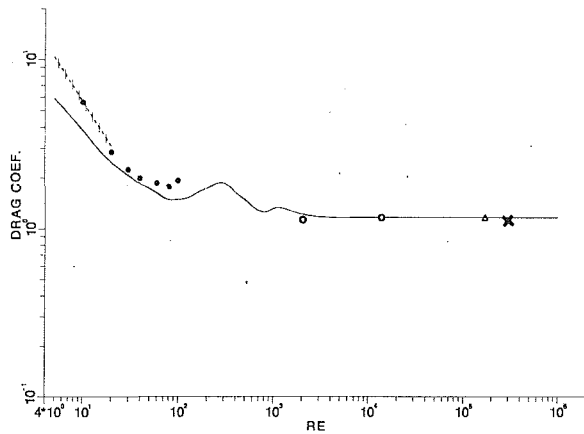
Fig. 2 Drag versus Reynolds number. o, present calculations; •, laminar flow calculations (Raul et al., 1990); Δ, Nakaguchi data; ×, Anderson data; —, Flat plates normal to the flow; ·····, cube drop experiments.

Fig. 3   Velocity vectors, Re = 2000, on z = 0.0 plane

Fig. 4   Velocity vectors, Re = 2000, on z = −0.43 plane

grid contained $69 \times 31 \times 31$ points in the x, y, and z directions, respectively. The computations on this grid were carried out on the SDSC Cray XMP/48 supercomputer. To test the dependence of the primary calculation on the grid density, several additional simulations at Re = 2000 and 14,000 were performed on the NCSA Cray 2 using a mesh with $99 \times 50 \times 50$ points and the identical computational box size. The results of these secondary calculations revealed the presence of a relatively insignificant dependence of the computed flow field on the numerical parameters. In particular, the differences between the solutions computed on the two grids would not be evident in the plots of the velocity field and other quantities to be shown below. In the case of the drag at Re = 2000 a 2 percent change was observed and at Re = 14,000 this difference was 3 percent. Part of these changes may be attributed to the fact that the test computations were not run to as high a degree of convergence as were the primary calculations, since the trend was toward reducing the differences in drag at the end of the test simulations.

The extent to which the numerical solution depended on the domain size was also tested. In particular, a calculation was made on the SDSC Cray XMP in an extended domain of 15 × 12 × 12 cube diameters. This used a mesh containing a few extra points in each direction so as to accommodate the larger domain without altering the density of points in the vicinity of the cube surface. As before, only a minor change in the computed solution was observed. In this case a less than 1 percent change in drag occurred suggesting that the procedures for taking into account the far field conditions were adequate.

The solution at Re = 2000 was computed using a converged solution at Re = 100 as initial condition. The ζ field was given an initial value in the form of a large constant near the cube, and a small constant value elsewhere. In view of the absence of a good initial guess for ζ it was necessary to integrate approximately 20,000 time steps, with integration intervals Δt varying from .00002 to .00005, until the global L_2 norm of the change in the mean vorticity, i.e., $\|\overline{\Omega}_i^{n+1} - \overline{\Omega}_i^n\|_2 < 3 \times 10^{-4}$. At this point the change in the drag value was less than 1×10^{-5} and the solution was assumed to have converged and the calculation was stopped. It should be noted that even after the flow in the vicinity of the cube reached steady state, the wake continued to develop in the far field. The small time step used in the calculation was necessary to prevent non-linear instabilities in the coupled equations. The flow field at Re = 14000 was started from the solution at 2000 so that in this case, convergence to a steady solution was much more rapid.

Results and Discussion

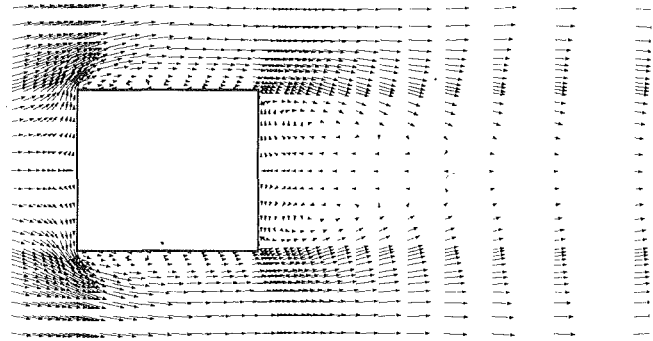A principal quantity of interest in regards to the cube flow
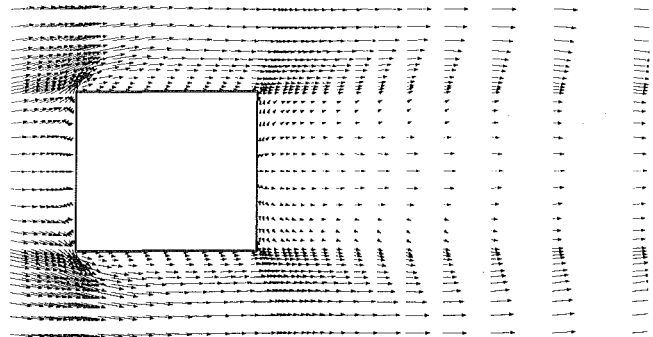
is the drag coefficient. For the converged numerical solution at Re = 2000 this was computed to be 1.23 while at Re = 14000 it was 1.17. A comparison of these values with experimental data is shown in Fig. 2. Included in the latter is a point which is obtained from extrapolation of the drag coefficients measured by Nakaguchi (1978) for the flow past bars of square cross section aligned with the flow. In particular, it is found that C_D for a cube is 1.17 at Re = 1.7×10^5. These experiments also suggest that the drag coefficient does not change appreciably for Re between $.77 \times 10^5$ and 2.3×10^5. An additional data point in Fig. 2 is due to Anderson (1977) who reported that $C_D = 1.09$ for the cube flow at Re = 3×10^5. To give an idea of what is to be expected at other Reynolds numbers, the drag due to a square flat plat held normal to the flow (Hoerner, 1965) is also shown, as well as some results for laminar flows reported earlier (Raul et al., 1990).

The character of the computed flow field may be deduced from the series of velocity vector plots contained in Figs. 3–10 for the Re = 2000 solutions. The flow at Re = 14000 shows many of the same features. A view of the cube flow in the $x-y$ plane through its midpoint is shown in Fig. 3. The wake is much longer here as compared to the laminar case (Raul et al., 1990). In particular, the point of flow reversal on the central axis behind the cube extends 1.12 cube diameters, versus .52 for the Re = 100 case. Along the side surfaces of the cube a zone of relatively stationary fluid exists. In contrast to the laminar solution, a region of reverse flow occurs which extends approximately half way along the sides of the cube. Flow separation begins a little aft of the front edge, and not exactly at it, as has been observed in earlier studies of two-dimensional bluff body flows (Ghia and Davis, 1974; Lane and Loehrke, 1980). These general attributes of the computed flow field agree with experimental observations at Re = 3×10^5 by Anderson (1977), who observed that dye placed on the side surfaces of the cube did not show significant motion.

At points closer to the edge, as depicted in Fig. 4 on the plane $z = -.43$, the boundary layer stays attached. A three-dimensional view of velocity vectors just off the surface, given in Fig. 5, shows the complete separation zone. Flow reversal
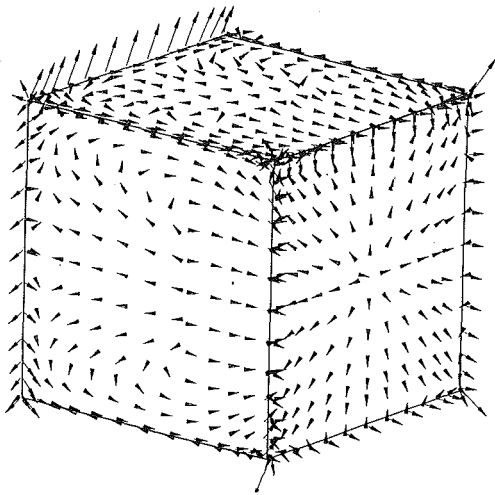
Fig. 5 Velocity vectors just off the cube surface, Re = 2000, three-dimensional view from rear
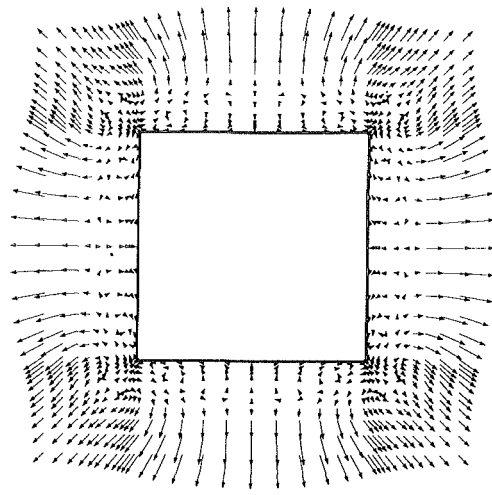

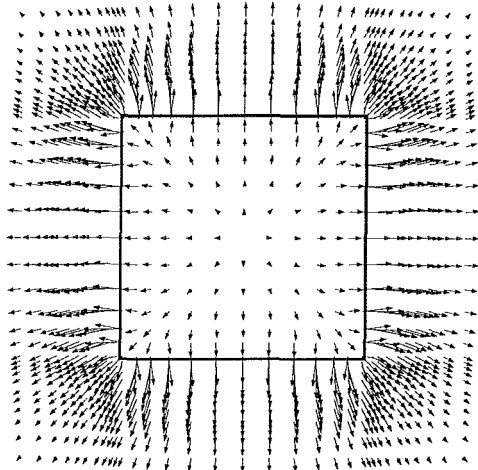
Fig. 8 Velocity vectors, Re = 2000, on $x = 0.0$ plane

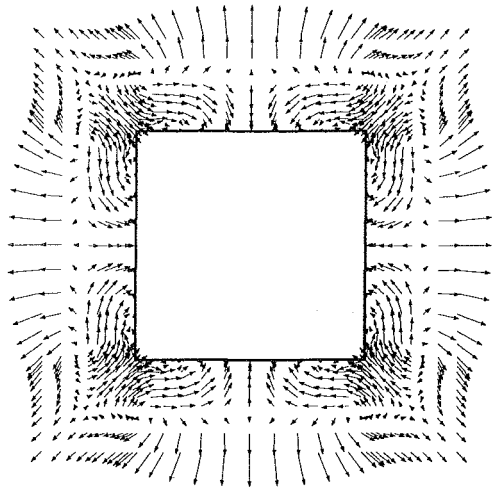**Fig. 6** Velocity vectors, Re = 2000, on $x = -0.51$ plane

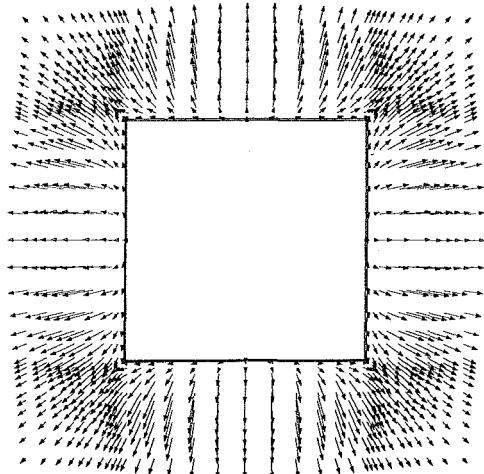**Fig. 9** Velocity vectors, Re = 2000, on $x = 0.11$ plane

Fig. 7 Velocity vectors, Re = 2000, on $x = -0.43$ plane

is observed to reach a maximum at a point along the mid-line of the sides, while none occurs near the edges. An interesting vortical circulation pattern is also evident as the flow negotiates past the front corners. Near the rear edges of the cube the flow is away from the corners. In the wake behind the cube this causes the velocity defect distribution to acquire a double ex-

tremum as is visible in Fig. 4. In contrast, at the mid point of the cube, as may be seen in Fig. 3, a single minimum velocity defect exists.

Further insight into the field may be gained from Figs. 6–10 which display the velocity vectors on planes normal to the main flow direction. In Fig. 6 the view is just ahead of the cube at $x = -.51$. The flow is outward from the stagnation point at the center. The fluid tends to slip around the corners, first traveling away from the diagonal line between the center and corner of the front cube face, and then toward it at points beyond the plane of the cube. At the location $x = -.43$ in Fig. 7, the flow has a sizable component distinctly toward the edge. The flow here is uniformly away from the cube surface. This changes by the plane $x = 0$ in Fig. 8, which is through the center of the cube. Here, the flow near the cube is toward it and in a direction away from the edges. A clear line demarcating the flow toward and away from the cube is also visible. The most intense outward movement appears to be at points furthest from the streamwise edges of the cube.

At the location $x = .11$ shown in Fig. 9 there is an increase in the magnitude of the fluid movement away from the edges in comparison to Fig. 8, while the line separating inward from outward flow has moved further from the cube. The motion away from the cube is also less significant than previously. Figure 10 is a view in the wake of the cube at $x = .64$. Here the flow is now entirely towards the cube. The motion on the rear face is toward the edges as a manifestation of the presence
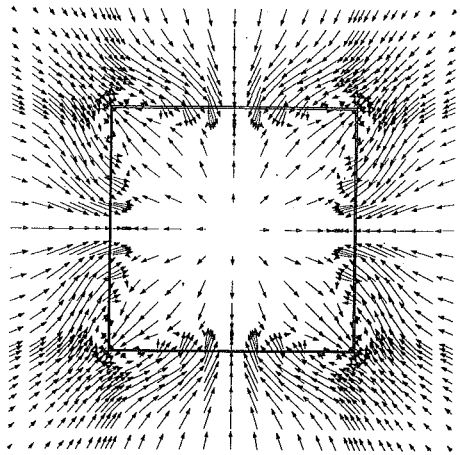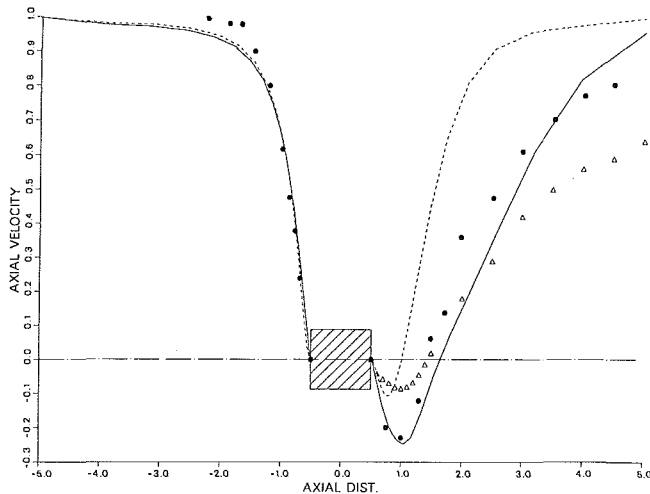
Fig. 10   Velocity vectors, Re = 2000, on x = 0.64 plane

Fig. 11   Mean axial velocity on central line, $y = 0$, $z = 0$. —, cube calculation Re = 14000; · · · · ·, cube calculation Re = 100; ●, data for square bars from Durao et al. (1988); △, result from calculation using $k - \epsilon$ closure Durao et al. (1987).

Fig. 12   Contours of ζ on plane $z = 0.0$, Re = 2000

Fig. 13   Cross sections of turbulent kinetic energy k/U_0^2 for Re = 14000 solution

of counter-rotating vortical pairs formed around each corner. This motion accounts for the influx of high speed fluid toward the center of the rear edges of the cube, thereby leading to the double velocity defect observed previously in Fig. 4.

An important characteristic of the computed solution is the nondimensional mean axial velocity, $\overline{U}_1/U_0$, along the centerline. Here, U_0 denotes the undisturbed free-stream velocity. While such data appears to be unavailable for cube flow, some measurements of this for the case of the flow past a square bar has been reported by Durao et al. (1988). A comparison of the cube results with these experiments is shown in Fig. 11 for Re = 14000. Also included is the axial velocity computed in the laminar flow at Re = 100 as well as a curve computed by Durao et al. (1987) using the $k - \epsilon$ closure. This particular curve is one in which the parameters of the model were adjusted to get a good prediction of the size of the separated region in the rear, though in fact for this solution no separation occurred at the sides. It is also evident that the velocity defect for this curve is greatly underpredicted.

Figure 11 shows only a minor difference in the computed axial velocity ahead of the cube for the Re = 100 and 14,000 flow fields, with the latter slightly steeper, as may be expected. The calculated axial velocity displays a more gradual reduction toward the front face than is evident from the experiments. This may be due to a potential blockage effect resulting from
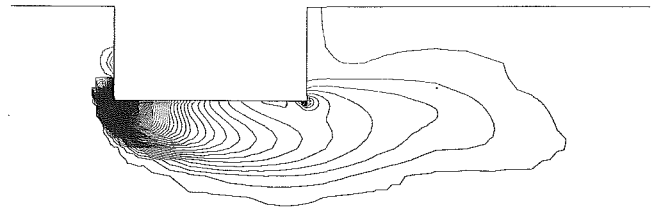
the use of a finite computational box, or, perhaps, due to the differences between the cube and square bar flow fields.

In the wake behind the cube a very significant difference exists between the laminar and turbulent axial velocities, with the latter showing close agreement with the data. The relatively rapid recovery of the computed solution toward the free stream value, which is visible in the figure, may be due to the fact that the wake is still developing in the present calculation.

Experimental or numerical predictions of turbulence levels in the cube flow with which the present results may be compared appear to be unavailable. Nonetheless, to give some idea of the turbulent field computed in the present case, contours of ζ in the central plane $z = 0$ are shown in Fig. 12. Extremely high levels of turbulence are evident along the front edge of the cube with the greatest concentration at the sharp corner. The turbulence produced here is unable to convect or diffuse very far upstream of the cube so that a relatively sharp interface between the turbulence and upstream potential regions of the flow is evident. The turbulence generated at the front face convects outward and downstream forming a decaying turbulent wake. Some additional turbulence is generated as the fluid passes by the rear edge of the cube.

Further insight into the computed turbulent field may be obtained from Fig. 13 showing profiles of the scaled turbulent kinetic energy, k/U_0^2, for the Re = 14000 solution, at several stations along and behind the cube. The highest level of k is observed to occur just off the front edge of the cube on the line which is flush with the front face. The region of significant turbulent activity is seen to broaden outward along the sides of the cube and into the wake. A slight narrowing of the wake may also be observed, as well as the convection and diffusion of turbulence into the region directly behind the cube. Turbulence generated at the rear edge of the cube is responsible for the secondary peak in k at this location. The magnitude of the computed k field compares favorably with that measured in related flows including that of square bars (Durao et al., 1987) and circular disks (Taylor and Whitelaw, 1984).

Conclusions

The turbulent flow field generated by the movement of fluid past a stationary cube has been calculated at two Reynolds numbers in the turbulent regime. The present approach implements a vorticity transport closure scheme depending on the solution of closed dynamical equations for the vorticity mean and covariance. The need to model the dynamical equa-

tion for turbulent kinetic energy is circumvented by instead obtaining k kinematically. The possibility of such a development rests on the opportunity to calculate the dissipation length scale λ from a relation expressing a balance of vortex stretching and diffusion processes.

Special provision was taken to supply sufficient grid resolution near boundaries so that wall function boundary conditions and all the uncertainties associated with them could be avoided. It is likely that this step contributed significantly to the success of the present calculations. Converged solutions for the cube flow proved to be attainable for a wide range of the input constants as long as equation (11) was satisfied and the integration time step was kept small enough.

The computed flow field appeared to have physical characteristics in keeping with the observed properties of similar bluff body flow fields. In particular, the separated region on the side and wake appeared to be well accounted for as well as the predicted drag. The numerical solutions also revealed a number of interesting features of the cube flow, such as the presence of streamwise vortex pairs formed at each rear corner. The indication from these results is that the vorticity transport closure scheme, in combination with a numerical grid allowing for adequate resolution of the flow in the wall region, should be capable of providing converged solutions to a wide range of bluff body flow fields. Future work will consider flows past more complex bodies such as a cube extended in the streamwise direction, and, as a step toward consideration of a real automotive shape, the flow past a rectangular prism with a rear base slant.

Acknowledgments

References

Anderson, H. L., 1977, "Investigation of the Forces on Bluff Bodies Near the Ground," M. Sc. dissertation, University of London.

Bearman, P. W., 1978, "Some Effects of Free-Stream Turbulence and the Presence of the Ground on the Flow Around Bluff Bodies," *Aerodynamic Drag Mechanisms of Bluff Bodies and Road Vehicles*, Sovran, G., et al. (eds.), Plenum Press, New York.

Bernard, P. S., 1981, "Computation of the Turbulent Flow in an Internal Combustion Engine During Compression," ASME JOURNAL OF FLUIDS ENGINEERING, Vol. 103, pp. 75-81.

Bernard, P. S., 1990a, "Turbulent Vorticity Transport in Three Dimensions," *Theoretical and Computational Fluid Dynamics*, Vol. 2, pp. 165-183.

Bernard, P. S., 1990b, "Turbulence Effects in the Edgetone Flowfield," *Journal of Fluids and Structures*, Vol. 4, pp. 449-470.

Bernard, P. S., and Berger, B. S., 1982, "A Method for Computing Three-Dimensional Turbulent Flows," *SIAM Journal on Applied Mathematics*, Vol. 42, pp. 453-470.

Bernard, P. S., and Berger, B. S, 1983, "Microscales and Correlation Tensors in the Viscous Turbulent Sublayer," ASME *Journal of Applied Mechanics*, Vol. 105, pp. 455-456.

Chorin, A. J., 1974, "An Analysis of Turbulent Flow with Shear," Report FM-74-9, College of Engineering, University of California, Berkeley.

Demuren, A. O., and Rodi, W., 1982, "Calculation of Three-Dimensional Flow Around Car Bodies," *Int. Symposium, Vehicle Aerodynamics*, Wolfsburg.

Durao, D. F. G., Heitor, M. V., and Pereira, J. C. F., 1988, "Measurements of Turbulent and Periodic Flows around a Square Cross-Section Cylinder," *Experiments in Fluids*, Vol. 6, pp. 298-304.

Durao, D. F. G., Heitor, M. V., and Pereira, J. C. F., 1987, "The Turbulent Flow in the Near Wake of a Squared Obstacle," *Forum on Turbulent Flows*, Bower, W. W., (ed.), FED-Vol. 51, pp. 45-50.

Gooding, A., Engelman, M. S., and Haroutunian, V., 1988, "Simulation of Transient Turbulent Flow Past a Bluff Body," *Proceedings of The Second FIDAP Users Conference*, Evanston, Ill., Oct. 2-4.

Ghia, U., and Davis, T., 1974, "Navier–Stokes Solutions for Flow Past a Class of Two-Dimensional Semi-Infinite Bodies," *AIAA Journal*, Vol. 12, pp. 1659-1665.

Han, T., 1989, "Computational Analysis of Three-Dimensional Turbulent Flow Around a Bluff Body in Ground Proximity," *AIAA Journal*, Vol. 27, No. 9, pp. 1213-1219.

Hinze, J. O., 1975, *Turbulence*, 2nd ed. McGraw-Hill, New York.

Hoerner, S. F., 1965, *Fluid Dynamic Drag*, Sec. 3, Published by Author, Brick Town, N. J.

Lakshminarayana, B., 1986, "Turbulence Modeling for Complex Shear Flows," *AIAA Journal*, Vol. 24, No. 12, pp. 1900-1917.

Lane, J. C., and Loehrke, R. I., 1980, "Leading Edge Separation From a Blunt Plate at Low Reynolds Numbers," *Momentum and Heat Transfer Processes in Recirculating Flows*, ASME publication HTD, Vol. 13, pp. 45-48.

Laurence, D., 1986, "A Computational Method for the Determination of the Flow Field Around Vehicles," von Karman Institute for Fluid Dynamics Lecture Series 1986-05.

Mansour, N. N., Kim, J., and Moin, P., 1989, "Near-Wall $k-\epsilon$ Turbulence Modeling," *AIAA Journal*, Vol. 27, pp. 1068-1073.

Markatos, N. G., 1983, "The Theoretical Prediction of External Aerodynamics of Road Vehicles," *International Journal of Vehicle Design*, Technological Advances in Vehicle Design Series, SP3, Impact of Aerodynamics on Vehicle Design, pp. 387-400.

Murakami, S., 1990, "Numerical Simulation of Turbulent Flowfield Around Cubic Model: Current Status and Applications of the $k-\epsilon$ Model and LES," *Journal of Wind Engineering and Industrial Aerodynamics*, Vol. 33, pp. 139-152.

Murakami, S., and Mochida, A., 1988, "3-D Numerical Simulation of Airflow Around a Cubic Model By Means of the $k-\epsilon$ Model," *Journal of Wind Engineering and Industrial Aerodynamics*, Vol. 31, pp. 283-303.

Nakaguchi, H., 1978, "Recent Japanese Research on Three-Dimensional Bluff Body Flows Relevant to Road Vehicle Aerodynamics," *Aerodynamic Drag Mechanisms of Bluff Bodies and Road Vehicles*, Sovran, G. S., et. al. (eds.), Plenum Press, New York.

Raul, R., 1989, "A Numerical Investigation of Laminar and Turbulent Flow Past a Cube," Ph.D. thesis, University of Maryland.

Raul, R., and Bernard, P. S., 1990, "Numerical Simulation of Unsteady Forces on a Square Prism in Turbulent Flow," *Proc. AIAA Aerosciences Meeting*, Reno, Nevada, Paper AIAA-90-0582.

Raul, R., Bernard, P. S., and Buckley, F. T., 1990, "An Application of the Vorticity-Vector Potential Method to Laminar Cube Flow," *International Journal of Numerical Methods in Fluid Dynamics*, Vol. 10, pp. 875-888.

Richardson, S. M., and Cornish, A. R. H., 1977, "Solution of Three-Dimensional Incompressible Flow Problems," *Journal of Fluid Mechanics*, Vol. 82, pp. 309-319.

Sedov, L. I., 1944, "Decay of Isotropic Turbulent Motions of Incompressible Fluids," *Doklady Akademie Nauk*, SSSR, Vol. 42, pp. 116-119.

Taylor, A. M. K. P., and Whitelaw, J. H., 1984, "Velocity Characteristics in the Turbulent Near Wakes of Confined Axisymmetric Bluff Bodies," *Journal of Fluid Mechanics*, Vol. 139, pp. 391-416.

P. J. Lefebvre

Naval Underwater Systems Center,
Newport, RI 02841
Mem. ASME

F. M. White

University of Rhode Island,
Kingston, RI 02881
Mem. ASME

Further Experiments on Transition to Turbulence in Constant-Acceleration Pipe Flow

A second series of experiments was conducted to extend and validate recently reported data by the present authors on transition to turbulence in pipe flows started from rest under constant acceleration. The test section diameter was increased from the 5 cm of the previous experiment to 9 cm for the present study. The low end of the acceleration range was also extended by an order of magnitude from 1.8 m/s^2 down to 0.2 m/s^2. The highest acceleration was 11.2 m/s^2. Pipe Reynolds number at transition was observed to be as high as 1.1×10^6. The present results are shown to validate the previously suggested transition correlation parameters. An analysis based on an empirical equation for transition in convectively accelerated flows is extended and applied to the current experimental data.

Introduction

In a previous paper, Lefebvre and White (1989) presented data on a unique series of experiments on transition to turbulence in pipe flows started from rest under approximately constant acceleration. In the remainder of this paper that study will be identified as the "previous study." Those experiments were conducted on a 5-cm (2-in.) diameter circular test section with accelerations ranging from 2 to 12 m/s^2. The test section was 30-m long with an internal surface machined to tight tolerances and honed to a 0.4 micron finish. Instrumentation to detect laminar to turbulent transition included six hot-film surface shear stress sensors equally distributed along the test section length and a laser Doppler velocimeter (LDV) with its measuring volume positioned at the test section centerline.

Transition from laminar to turbulent flow was shown to be considerably delayed when compared to that expected from a quasi-steady analysis; transition pipe Reynolds numbers ranged between 2×10^5 and 5×10^5. Several dimensionless transition correlation parameters were suggested and shown to be reasonably representative of the data. Those experiments were a subset of a larger project which included transient velocity profile, turbulence and surface shear stress measurements; results are presented in Lefebvre (1987).

The present paper reports on a subsequent series of similar transition experiments conducted on a larger 9-cm (3.57-in.) diameter circular test section. This new series of experiments further extends the data base at the lower portion of the acceleration range, thus more closely approaching steady-state conditions. The new data provide further validation of the dimensionless transition correlation parameters previously presented. The present paper also compares the experimental data

with a simplified analysis based on an empirical equation for transition in convectively accelerated external flows.

Experimental Procedure

As in the previous study, the present experiment was performed in the Unsteady Flow Loop Facility at the Naval Underwater Systems Center (NUSC), Newport, RI. This facility is capable of providing user-programmed acceleration of the mean flow over a large range of velocities and accelerations through transient control of a flow control valve. A detailed description of the facility design and operation is provided in Lefebvre (1986).

Facility modifications that were incorporated for the present study consisted mainly of changing the test section to one with the larger 9-cm diameter and replacing the 7.6-cm control valve with a 15.2-cm valve to accommodate the higher flow rates through the larger test section.

As shown in Fig. 1, the new 9-cm-diameter test section consists of a 24.4-m-long section of PVC pipe followed by a 6.0-m-long cast acrylic section where LDV measurements are made. At each flanged junction, care was taken to minimize any step at the interface between adjacent pipe sections. This test section was built specifically for only this one series of tests aimed at extending the laminar-turbulent transition data base to a larger diameter. Consequently, unlike the extensively machined 5-cm diameter test section, the internal surface of the 9-cm diameter test section was used as purchased with no subsequent machining to improve the constancy of the diameter or the roundness. Since PVC pipe may be slightly out-of-round, the flange connections in Fig. 1 are possible sources of flow disturbances in this new experiment.

As was done in the previous study, the time of transition to turbulence was monitored by the LDV positioned at the cen-

---

Fig. 1 Test section (9-cm diameter)
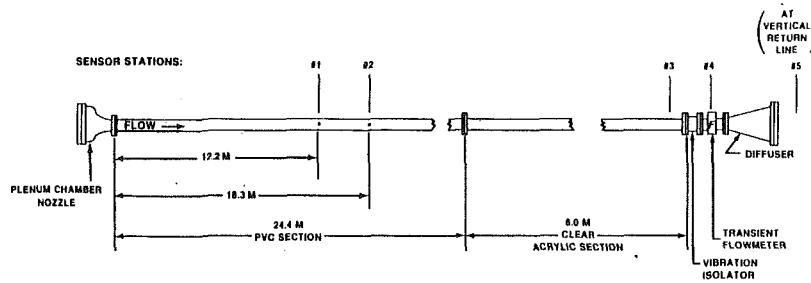
STATION	INSTRUMENTATION
1-2	SURFACE SHEAR STRESS SENSOR
3	LASER DOPPLER VELOCIMETER
4	TRANSIENT FLOWMETER
5	TEMPERATURE PROBE

terline of the pipe and by hot-film surface shear stress sensors. Since the results of the previous study exhibited essentially the same time of transition at each of the six shear stress sensors, for the present study only two shear stress sensors were used and located in the PVC section at 12.2 m and 18.3 m from the entrance to the test section. All other aspects of testing including instrumentation, instrumentation setup, data acquisition and facility operation are identical to those of Lefebvre and White (1989).

For each test run, the control system was programmed to provide constant acceleration from rest, leveling off to a final mean velocity that was sufficiently above the transition velocity so as not to affect transition itself. Mean flow accelerations ranged from 0.2 to 11.2 m/s². Final mean velocity ranged from 2.4 to 11.2 m/s, depending on acceleration.

Simplified Stability Analysis

As in the previous study, Lefebvre and White (1989), the classic analytic solution given by Szymanski (1932) for the startup of laminar pipe flow subject to a suddenly applied constant pressure gradient forms the basis of the present analysis.

From small nondimensional times, $t^* = \nu t/R^2 < 0.05$, Szymanski's solution gives a centerline velocity that increases linearly with time, approximating a constant-acceleration startup. This solution is assumed to hold as long as the flow is laminar, i.e., from the start of the transient to the time of transition to turbulence. The values of t^* at transition for the combined 5- and 9-cm experiments ranged from 0.00045 to 0.0036, well within the applicable range for the constant-acceleration approximation.

Figure 2 shows LDV centerline velocity data, u_0, plotted against t^* for a typical pipe startup test on each of the test
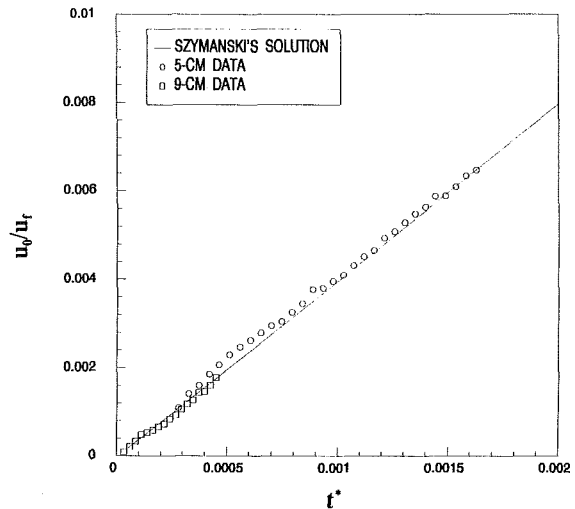

Fig. 2 LDV centerline velocity data (Uncertainty in $u_0/u_f = \pm 3$ percent, in $t^* = \pm 2$ percent)

sections. Velocity data are non-dimensionalized with u_f, Szymanski's final centerline velocity or the Poiseuille maximum velocity at steady state. The value of u_f for each run was calculated by applying Szymanski's equation for nondimensional velocity at the transition values of t^* and u_0.

The 5-cm data in Fig. 2 were at an acceleration of 6 m/s², while those for the 9-cm section were at 4.5 m/s². Even though the times of transition for both sets of data are approximately equal, the 9-cm data do not cover as wide a t^* range due to the larger diameter. The data are shown to compare well with

─────── Nomenclature ───────

a = acceleration
D = pipe diameter
D^* = dimensionless parameter, equation (10)
R = pipe radius
Re_D = pipe Reynolds number, UD/ν
R_x = distance Reynolds number, Ux/ν
Re_δ = boundary layer Reynolds number, $U\delta/\nu$

t = time
t^* = dimensionless time, $\nu t/R^2$
T^* = dimensionless parameter, equation (9)
U = instantaneous mean axial velocity
u_f = Poiseuille maximum velocity, $R^2(-dp/dx)/4\mu$
u_0 = axial velocity at pipe centerline
x = axial displacement of bulk fluid

δ = boundary layer thickness (99 percent)
δ^* = displacement thickness
θ = momentum thickness
μ = viscosity
ν = kinematic viscosity

Subscript
tr = at the transition point
crit = at the critical point

Szymanski's solution, thus validating the appropriateness of basing the current analysis on that solution.

As shown in the previous paper, Szymanski's solution can be used to obtain the boundary layer parameters:

$$\delta_{99\%} \sim 2.9(\nu t)^{1/2} \tag{1}$$

$$\delta^* \sim 0.77(\nu t)^{1/2} \tag{2}$$

$$\theta \sim 0.35(\nu t)^{1/2}. \tag{3}$$

For transition values of these parameters, t was taken as the time from the start of the transition to the time at which transition occurred.

To estimate the time of transition for the case of constant-acceleration pipe flow, the assumption is made that transition occurs because the velocity profile becomes unstable. The mechanisms and events leading to the initiation of this instability and transition are assumed to be similar to those which are responsible for instability and transition in steady external flows with pressure gradients. This appears to be a reasonable first-order approximation considering that the maximum boundary layer thickness at transition, $\delta_{99\%,\mathrm{tr}}$, in both the 5- and 9-cm experiments ranged between $0.06R$ and $0.17R$ which resulted in sufficiently small pipe curvature effects.

A reasonable criterion for estimating transition to turbulence in external flows under a large range of pressure gradients (convective acceleration or deceleration) was given by Michel in 1952 (White, 1974) as

$$(U\theta/\nu)_{\mathrm{tr}} \sim 2.9(Ux/\nu)^{0.4}. \tag{4}$$

To apply this equation to the present case of constant acceleration a, the instantaneous mean axial velocity can be taken as $U = at$. Likewise, the mean displacement of the bulk fluid since the start of the acceleration is estimated to be $x = at^2/2$. Combining these along with equation (3) into equation (4) leads to an equation for the time of transition:

$$t_{\mathrm{tr}} \sim 450(\nu/a^2)^{1/3}. \tag{5}$$

This simple expression is in better agreement with the present experiments than any of the many other transition-prediction schemes reviewed by White (1974) and Arnal (1984). Apparently, most transition correlations are keyed toward adverse pressure gradients.

Theoretical Values of Proposed Correlations Groups

The results from the above analysis can be incorporated into the equations of the various transition correlation parameters presented in the previous study. The resulting theoretical values for the more pertinent correlation parameters, those of which will be used in this paper, are:

$$\mathrm{Re}_{D,\mathrm{tr}} = DU/\nu \sim 450\, D(a/\nu^2)^{1/3} \tag{6}$$

$$\mathrm{Re}_{\delta,\mathrm{tr}} = \delta U/\nu \sim 28{,}200 \tag{7}$$

$$t_{\mathrm{tr}}^* = \nu\, t_{\mathrm{tr}}/R^2 \sim 3.65 \times 10^8/\mathrm{Re}_{D,\mathrm{tr}}^2 = 1800/D_{\mathrm{tr}}^{*2} \tag{8}$$

$$T_{\mathrm{tr}}^* = t_{\mathrm{tr}}(a^2/\nu)^{1/3} \sim 450 \tag{9}$$

$$D_{\mathrm{tr}}^* = D(a/\nu^2)^{1/3} \sim \mathrm{Re}_{D,\mathrm{tr}}/450. \tag{10}$$

As noted in Lefebvre and White (1989), these parameters are not independent, e.g., $\mathrm{Re}_D = T^*D^*$. Equations (7) and (9) are the simplest predictions, with the latter having the smallest experimental scatter.

Results

Thirty-two test runs were conducted on the 9-cm-diameter test section. As in the study of Lefebvre and White (1989) and shown in their Fig. 4, all of the surface shear stress sensors and the LDV indicate transition to turbulence at nearly the same time. Among the measurements, the maximum deviation in transition time was similar to that observed during the pre-

vious test series, that is, within 50 milliseconds or 3 percent of the total time to transition. This further supports the conclusion that for constant-acceleration pipe startup flow, the entire flow in the test section undergoes a kind of global instability, with transition being essentially independent of axial position.

During all the previous 5-cm and most of the 9-cm test runs, the flow, as observed at the three measurement stations, remained laminar until final transition to turbulence occurred. However, during several of the 9-cm test runs, what appeared to be a turbulent slug preceded final transition. This slug was a localized, short duration region of turbulence thought to arise from a natural occurrence and was observable only at the surface shear stress sensor and not at the LDV. The presence of the slug was identified by an abrupt laminar to turbulent transition followed by a brief duration of sustained turbulence and subsequently a reversion back to laminar flow.

Figure 3 shows the uncalibrated voltage output signal from the two surface shear stress sensors for two different runs; the upper frame at an acceleration of 7.1 m/s^2 and the lower at 5.65 m/s^2. In both cases, the time of final transition, as noted on the figure, is apparent by the abrupt and persistent increase in the magnitude of both the signal level and the fluctuations. Final transition is seen to occur at the same time at each of the sensor locations. The sensitivity for sensor number 2 was not set as high as that for sensor number 1 and therefore the fluctuations in the signal due to turbulence were not as large.

The turbulent slug that precedes the time of final transition is clearly identifiable in Fig. 3, the flow on both sides of the turbulent slug being laminar. In the upper frame ($a = 7.1$ m/s^2), the slug was observed at sensor location 2; in the lower frame ($a = 5.65$ m/s^2), the slug appeared at sensor location 1. Based on a constant acceleration of the mean flow and assuming that the slug traveled at the bulk flow velocity, it is estimated that the slug's length was 2.0 m for the 7.1 m/s^2 case and 1.2 m for the 5.65 m/s^2 case. The Reynolds number at the start of the slug was 6.0×10^5 and 5.6×10^5 for the 7.1 m/s^2 and 5.65 m/s^2 cases, respectively.

The signals of Fig. 3 are similar to those observed by Moss (1989) in his constant-head facility, where the quick opening of a valve provided an approximate step increase in flow rate. Moss also classified the phenomenon as a turbulent slug being generated by either of two modes. Mode I was a slug generated at a disturbance in the pipe (such as at the entrance to the test
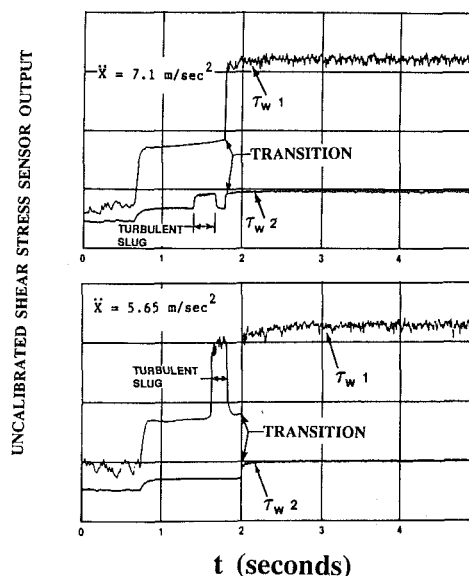

Fig. 3 Surface shear stress sensor output exhibiting a turbulent slug

section) that then propagates downstream; mode II was a natural occurrence of transition within the temporally and spatially developing flow.

Unlike the present study, Moss observed continued turbulence (no slugs) after the initial transition for flows above a relatively low Reynolds number, $Re_D > 11,000$. In the present study, the substantially higher values of Reynolds number at which turbulent slugs were observed is expected because Moss's test condition did not maintain acceleration of the mean flow at the times when the slugs were observed. The present facility, being able to maintain constant acceleration over a large Reynolds number range, provides the stabilizing effect of acceleration at the higher flows, thus tending to delay transition or the generation of turbulent slugs.

In the present study, the length of the test section precluded either the entrance flow or flow that started at a flanged junction from reaching any of the sensor locations at either the time of the slug or the time of final transition. Therefore, a slug originating at any of the known geometric disturbances is ruled out. Because the slug appeared only during a few test runs, and even then at different sensor locations, it is believed that the cause of the slug is more likely a relatively small disturbance within the test section or a natural instability in the velocity profile. Furthermore, the observance of a slug was believed to be intermittent because, under the accelerations tested, the flow tends to become unstable at even slight disturbances, including vibrations, which can occur randomly.

Because a surface shear stress sensor monitors the flow at only one spatial location, it is possible that the turbulence observed during what is classified here as a turbulent slug, may in fact be turbulence confined to the near wall region and then only in the immediate vicinity of the sensor. More sensors at one axial location including LDV measurements and flow visualization are recommended in order to draw a definitive conclusion.

For the calculation of transition correlation parameters, the turbulent slug was ignored and the time of final transition taken as shown on Fig. 3. The remaining figures of this paper present the correlation parameters based on the 32 data points for the present 9-cm tests along with the 37 values of the 5-cm tests and the theoretical predictions.

Figure 4 presents transition Reynolds number, $Re_{D,tr}$, as a function of acceleration a. The Re_D values increase with acceleration, with the 9-cm data having values ranging from 1.31×10^5 to 1.1×10^6. Both sets of data approximately follow the prediction of equation (6) that transition Reynolds number is proportional to the cube root of the acceleration.

Figure 5 shows that the boundary layer thickness Reynolds number at transition rises slowly with pipe Reynolds number. The simple prediction of equation (7) is a good average value.

Dimensionless time t^* is plotted in Fig. 6 and, as expected from equation (8), is shown to decrease with nondimensional acceleration D^*. The correlation of Fig. 6 appears reasonable because both the 5- and 9-cm data collapse nicely onto a single curve. It should be pointed out, however, that data scatter is somewhat hidden as $t^* \alpha (D^*)^3$ and therefore t^* is relatively insensitive to acceleration. The solid curve from equation (8) is again a reasonable approximation of the experimental data predicting the trend and approximate values of the data.

Data in the form of the second dimensionless time parameter T^* are presented in Fig. 7. The combined data of both experiments fall approximately evenly distributed about the theoretical value of 450, with the combined data having a value of $T^* = 420 \pm 30$ percent. The data show a gradual increase of T^* with D^*.

The above simplified stability analysis is only a first step toward an understanding of the effects of acceleration in pipe startup flows. The relatively close agreement between the theory and the experimental data warrant further theoretical investigations based on fundamental principles as is done with
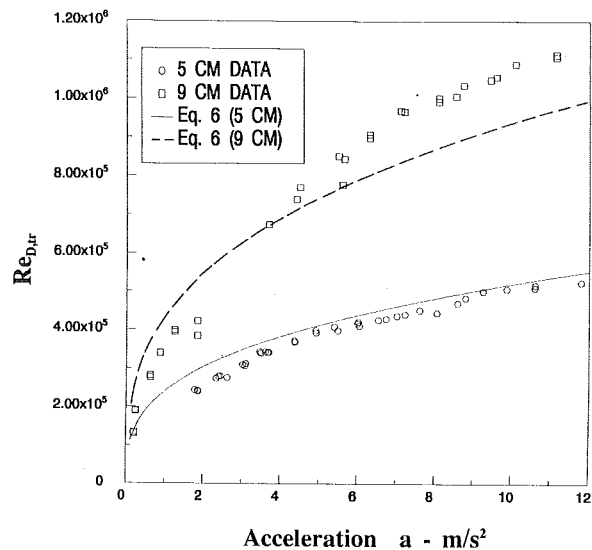

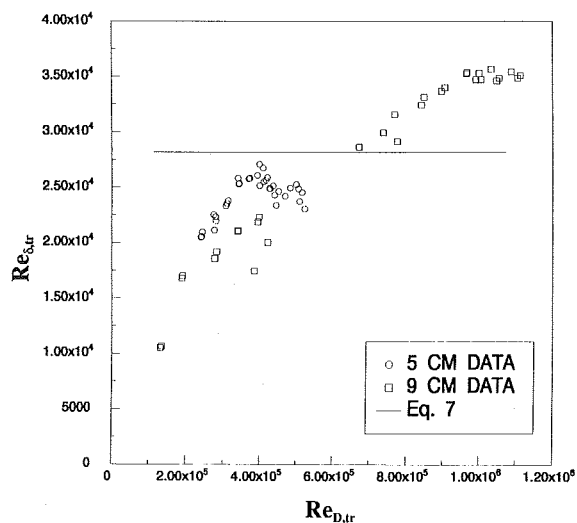Fig. 4 Pipe transition Reynolds number (Uncertainty in $Re_D = \pm 1.1$ percent, in $a = \pm 3$ percent)

Fig. 5 Boundary layer thickness Reynolds number versus pipe Reynolds number at transition (Uncertainty in $Re_\delta = \pm 10$ percent, in $Re_D = \pm 1.1$ percent)

external convectively accelerated flows by using the Orr-Sommerfeld equation.

Conclusions

Constant-acceleration pipe startup flow experiments were conducted in the NUSC Unsteady Flow Loop Facility fitted with a 9-cm-diameter test section. This set of experiments generated 32 data points for transition to turbulence under mean flow accelerations ranging from 0.2 to 11.2 m/s². These data complemented and extended the data base of a previously reported set of similar experiments conducted on a 5-cm-diameter test section.

Both series of experiments experienced global transition over the length of the test section. For several of the tests conducted on the 9-cm test section, what was believed to be a turbulent slug was observed for pipe Reynolds numbers as high as 600,000, considerably higher than previously observed by others. It was conjectured that maintaining the stabilizing effect of acceleration up to the high Reynolds numbers tested allowed the flow to remain laminar behind the slug.
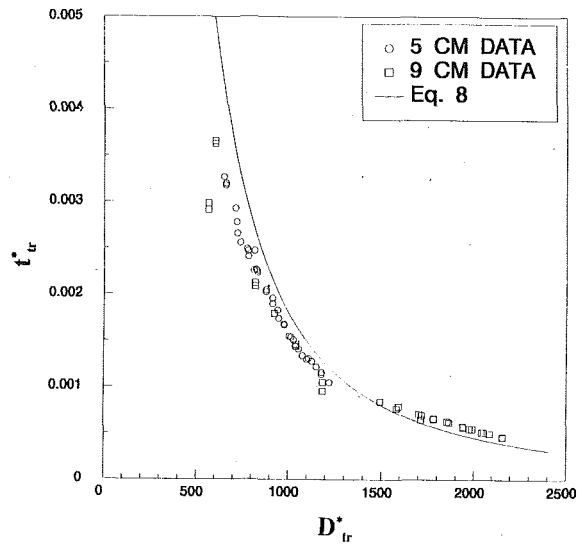
Fig. 6 Szymanski time at transition (Uncertainty in $t^* = \pm 2$ percent, in $D^* = \pm 1.5$ percent)
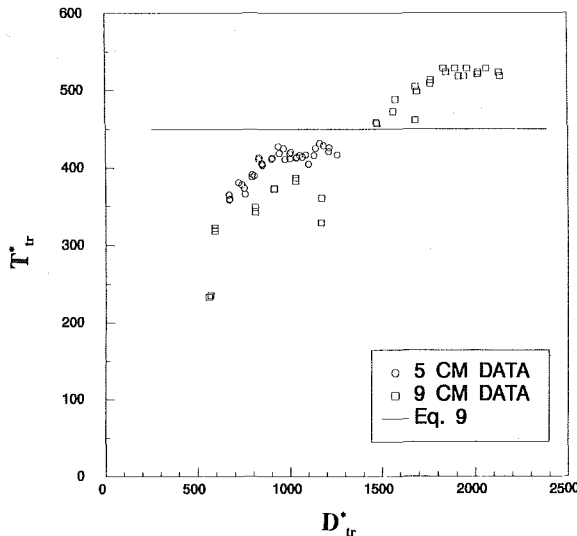

Fig. 7 Transition time T^* versus nondimensional acceleration D^* (Uncertainty in $T^* = \pm 2$ percent, in $D^* = \pm 1.5$ percent)

The experiments show that pipe Reynolds number at transition, $Re_{D,tr}$ is dependent not only upon acceleration but also upon pipe diameter. Moreover, $Re_{D,tr}$ increases with both these parameters. Values of $Re_{D,tr}$ ranged from 1.3×10^5 to 1.1×10^6 for the combined 5- and 9-cm data. Boundary layer thickness Reynolds number at transition, $Re_{\delta,tr}$, another useful parameter, rises slowly with pipe Reynolds number.

The final correlation parameter, T^*, showed more promise in that its value at transition was approximately constant. The recommended value is

$$T_{tr}^* = t_{tr}(a^2/\nu)^{1/3} \sim 420 \pm 30\%.$$

A simplified stability analysis was developed, based on Michel's empirical correlation for convectively accelerated external flows combined with Szymanski's solution for the time-dependent flow field. Predicted values for the various transition parameters compared reasonably well with the experimental data in both the absolute values and the trends exhibited.

The experimental and theoretical results are valid only for constant-acceleration pipe flow. Future experiments are planned to investigate: the effect of disturbances; the effect of general time-varying accelerations; and further detail of the turbulent slugs by incorporating flow visualization.

Acknowledgment

References

Arnal, D., 1984, "Description and Prediction of Transition in Two-Dimensional Incompressible Flow," AGARD Report No. 709, pp. 2-1 to 2-71.

Lefebvre, P. J., 1986, "Design and Evaluation of NUSC's Flow Loop Facility," Technical Document 6512, NUSC, Newport, RI.

Lefebvre, P. J., 1987, "Characterization of Accelerating Pipe Flow," Ph.D. thesis, University of Rhode Island.

Lefebvre, P. J., and White, F. M., 1989, "Experiments on Transition to Turbulence in a Constant-Acceleration Pipe Flow," ASME JOURNAL OF FLUIDS ENGINEERING, Vol. 111, No. 4, pp. 428–432.

Moss, E. A., 1989, "The Identification of Two Distinct Laminar to Turbulent Transition Modes in Pipe Flows Accelerated From Rest," Experiments in Fluids, Vol. 7, pp. 271–274.

Szymanski, P., 1932, "Some Exact Solutions of the Hydrodynamic Equations of a Viscous Fluid in a Cylindrical Tube," J. Math. Pure et Appliquées, Vol. 11, pp. 67–107.

White, F. M., 1974, Viscous Fluid Flow, Mc-Graw-Hill, p. 442.

A Multizone Time-Marching Technique for Unsteady Separating Three-Dimensional Boundary Layers and Its Application to the Symmetry-Plane Solution of an Impulsively Started Prolate Spheroid

Tzuyin Wu
Graduate Research Assistant.

Shan-Fu Shen
John Edson Sweet
Professor of Engineering.

Sibley School of Mechanical and Aerospace
Engineering,
Cornell University,
Ithaca, NY 14853

Recent interest in unsteady separation and separated flows brings up the need of an accurate and efficient computational scheme for general unsteady three-dimensional boundary-layer flows. Resolution of the singular behavior at separation is a delicate problem. The task is further complicated by the geometrical singularity and the nonstationary stagnation point. The present paper proposes a numerical scheme to sidestep these difficulties. At the first stage of development, the simpler problem of the symmetry-plane solution of the laminar boundary-layer over an impulsively-started prolate spheroid is calculated. Results show that the present Eulerian calculation satisfactorily captures the singular behavior of the boundary layer when separation is approached. Comparison with Xu and Wang's recent results and those for the two-dimensional elliptic cylinder calculated by the Lagrangian method are also made. Discussions of the results for unsteady separation at zero, small and large incidences are presented.

Introduction

The separation of three-dimensional laminar boundary layer has long been an intriguing subject of both basic and practical interest. Even in the steady case, the separation "pattern" on the body surface, as observed in the experiments, takes a variety of forms. Recent progress in the qualitative theory and the actual computations have greatly improved our understanding of the complex phenomena. See, for example, the analytic studies of Maskell (1955), Lighthill (1963), Chapman (1986), Perry and Chong (1986); the experimental observations of Werle (1962) and Chanetz (1986); and the numerical calculations of Wang (1970, 1974a, 1975), Cebeci et al. (1981), Cebeci and Su (1988). In the steady flow, zero wall shear signifies separation and the breakdown of the boundary-layer equations. The usual analysis of steady separation is to focus on the limiting streamlines at the wall. For the unsteady case, it is now well-known that separation starts "off" the wall and neither the wall shear nor the wall streamlines can serve as reliable indicators of separation. But very little is known about

the details of the phenomenon. Even numerical examples are hard to come by, since efficient and reliable computational schemes for calculating the general unsteady three-dimensional boundary-layer flows still are not well developed.

In steady flow, the separation of the boundary layer over a prolate spheroid at various incidence angles has been the subject of several computational studies due to Wang (1970, 1972, 1974a, 1974b, 1975). Two different types of separation, "open" and "closed", based on the limiting-streamlines analysis are proposed. In his terminology, the convergence of the limiting streamlines defines the separation line on the body. At small incidence, a closed type separation prevails where the separation line completely separates the limiting streamlines originating from different stagnation points. At moderate incidence, the separation line is approached on two sides by limiting streamlines originating from the same stagnation point. This type of separation is then classified as open separation, since two separation lines, one on each side of the spheroid are formed and are not connected on the lee-side symmetry plane. In a recent paper of Xu and Wang (1988), the evolution of the skin friction on the symmetry plane of an impulsively-started spheroid is studied. They suggest an unsteady analogy

of the above open and closed separations, the term "separation" used in their study referring to vanishing skin-friction in the streamwise direction. An off-symmetry-plane calculation of the above problem has been performed by Ragab (1986). Focus of his work is on the crosswise separation at high incidence. The computational domain covers only the front quarter of the prolate spheroid. His results of skin friction lines support the open type separation advocated by Wang for unsteady three-dimensional flows. Following van Dommelen and Shen (1980), unsteady boundary-layer separation is better defined by the termination of the boundary-layer solution in a singularity. In the two-dimensional problem, the occurrence of a singularity and its structure have been well established (e.g., van Dommelen, 1981; Cowley, 1983; Ingham, 1984). In the three-dimensional case, this singularity may form a curve whose projection on the wall can then be properly defined as the 'separation line' (Shen, 1978). The concept is consistent with that of van Dommelen and Cowley (1990), in which the authors examine the asymptotic structure of the unsteady three-dimensional separation in a Lagrangian coordinates system. In fact, the structure of separation is found to be quasi two-dimensional.

Confirmation of this singularity at separation was not part of Xu and Wang's calculation, but is the focal point of the present paper. In order to do so, the numerical scheme has been modified. It is noticed, for instance, that no details of the flow near the rear end of the spheroid were included in their results. As pointed out in Cebeci et al. (1980, 1981), a "geometrical singularity" is present at both ends of the prolate spheroid when a single body-oriented coordinates system is used. In Xu and Wang (1988), no provision was made for the singularities, and their method might lead to local difficulty and inaccuracy, particularly for a slender spheroid. Another problem of the space-marching schemes usually adopted in solving a boundary-layer type equation is associated with the stability consideration. In the unsteady case, the grid size in the reversed flow region is limited by the domain-of-dependence rule (CFL criterion). In particular, the restriction on the time step can become so stringent that the calculation is practically prevented from proceeding further (Cebeci, 1986). Still another technical difficulty of the space-marching method is the requirement of a starting profile to initiate the spatial integration. This is not available in the general case involving arbitrary body motion for which the stagnation point is non-stationary.

The present paper is actually the first phase of a more ambitious research program dealing with general three-dimensional unsteady separation over an arbitrarily moving body. In developing a solution scheme, we abandon the conventional space-marching technique and choose instead a more classical initial-value approach. That is, the solution is advanced in the time direction only. This allows the calculation of more general unsteady flows 'as it does not require a fixed stagnation-point to construct the flow downstream. In conjunction with an implicit time-marching scheme, a flow-dependent, one-sided spatial difference is applied to discretize the convection terms in accordance with the CFL criterion. The severe restriction on the time step is thus relieved. Finally, to overcome the difficulty of the aforementioned "geometrical singularity," we propose a multidomain attack. Suitable transformation which removes the singularity is applied at both nose and tail regions. Calculations are performed separately in each region, and the solutions are patched on the interfaces by interpolation procedure.

For an orderly development, we limit ourselves first to redo the case of a prolate spheroid, following Xu and Wang (1988). The following presents mainly the boundary-layer development in the symmetrical plane of an impulsively started prolate spheroid. The governing equations and the relevant coordinates transformation are given in the next section. Details of the numerical scheme and the solution procedure are also described. Calculations are performed for three different angles of attack: 0, 6, and 50 deg. Comparison with Xu and Wang (1988) are made. In addition, the results are compared with those for the two-dimensional elliptic cylinder calculated by the Lagrangian method. The significance of the findings of the first occurrence of three-dimensional separation on lee side and wind side, at small and large angles of incidence is discussed. If and when and how different unsteady three-dimensional separation patterns are generated and developed can only be answered by computation of the flow off the symmetry plane. Much more remains to be done.

Formulation of the Problem

The geometry and the boundary-layer coordinate system of a prolate spheroid, following Xu and Wang (1988), are spec-

---

Nomenclature

D_1, D_2 = mapping constants in β-direction
e = eccentricity of spheroid
h_1, h_2, h_3 = metric coefficients
p = pressure
S = transformed coordinate defined in equation (4)
t = time
t/c = axes ratio
u = velocity component in x-direction
U_e = value of u at edge of boundary layer
v = velocity component in y-direction
V_e = value of v at edge of boundary layer
v_y = derivative of v in y-direction
V_{ye} = value of v_y at edge of boundary layer

V_0, V_{90} = constants in the velocity distribution at edge of boundary layer
w = velocity component in z-direction
x = streamwise coordinate along the major axis of prolate spheroid
y = circumferential coordinate
z = boundary-layer coordinate normal to x and y direction
$\hat{\alpha}$ = angle of attack
α, β = computational coordinates
δ = difference operator in finite-difference equations
Δ = indicating difference; also, displacement thickness

ϵ = stretching factor of the mapping in α-direction
μ = average operator in finite-difference equations
ρ = density
τ = wall shear

Subscripts

o = stagnation
s = separation
x, y, z = components in x, y, and z directions, respectively
$,$ = indicating derivatives

Superscripts

n = nth time level in finite-difference equations
$(\bar{\ })$ = quantities in nose region
$(\tilde{\ })$ = quantities in tail region

ified in Fig. 1. The metric coefficients h_1, h_2, and h_3 are defined as

$$h_1 = \sqrt{\frac{1 - e^2 x^2}{1 - x^2}}, \quad h_2 = \sqrt{(1 - e^2)(1 - x^2)}, \quad h_3$$

$$= 1; \quad e = \sqrt{1 - (t/c)^2}$$

where t/c denotes the ratio of minor to major axis (axes ratio). After a proper scaling with the free stream velocity and the half-chord length of the prolate spheroid, the nondimensional forms of the boundary-layer equations on the symmetry plane are, in conventional notation,

$$h_2 \frac{\partial u}{\partial x} + h_1 v_y + h_1 h_2 \frac{\partial w}{\partial z} + u \frac{\partial h_2}{\partial x} = 0 \qquad (1)$$

$$\frac{\partial u}{\partial t} + \frac{u}{h_1} \frac{\partial u}{\partial x} + w \frac{\partial u}{\partial z} = \frac{-1}{\rho h_1} \frac{\partial p}{\partial x} + \frac{\partial^2 u}{\partial z^2} \qquad (2)$$

Crosswise momentum equation is identically zero on the symmetry plane. A supplementary equation can be obtained by differentiating it with respect to the circumferential coordinate y:

$$\frac{\partial v_y}{\partial t} + \frac{u}{h_1} \frac{\partial v_y}{\partial x} + w \frac{\partial v_y}{\partial z} + \frac{v_y^2}{h_2} + \frac{u v_y}{h_1 h_2} \frac{\partial h_2}{\partial x} = \frac{-1}{\rho h_2} \frac{\partial^2 p}{\partial y^2} + \frac{\partial^2 v_y}{\partial z^2} \qquad (3)$$

where v_y stands for $\partial v / \partial y$. Based on the velocity profiles u and v_y, the skin friction and the displacement thickness are defined by

$$\tau_x = \left(\frac{\partial u}{\partial z} \right)_{z=0}, \quad \tau_{y,y} = \left(\frac{\partial v_y}{\partial z} \right)_{z=0}, \quad \Delta_x = \int_0^\infty \left(1 - \frac{u}{U_e} \right) dz.$$

The above governing equations are then subject to a Rayleigh-type initial condition for an impulsively-started motion. As usual, no-slip boundary conditions are imposed on the wall, and the velocities at the outer edge of the boundary layer must approach the values specified by the inviscid potential flow:

$$u = v_y = 0 \quad \text{at } z = 0$$

$$u = U_e$$
$$= \frac{1}{(1 - e^2 x^2)^{1/2}} [V_0 (1 - x^2)^{1/2} \cos \hat{\alpha} + V_{90} \frac{t}{c} x \sin \hat{\alpha} \cos y]$$

$$v_y = V_{ye} = V_{90} \sin \hat{\alpha} \cos y \quad \text{at } z = \infty$$

where $\hat{\alpha}$ = angle of attack,

$$V_0 = \frac{e^2}{1 - \frac{1 - e^2}{2e} \ln \frac{1 + e}{1 - e}}, \quad V_{90} = \frac{2 V_0}{2 V_0 - 1}$$

As already mentioned in the introduction, a difficulty of the present spherical coordinates system is that the metric coefficients h_1, h_2 become singular at both $x = -1$ and $x = +1$. A transformation which removes this geometric singularity was proposed by Cebeci et al. (1980, 1981). Define

$$\frac{d\overline{S}}{\overline{S}} = \frac{h_1 dx}{h_2} = \frac{\sqrt{1 - e^2 x^2} dx}{\sqrt{1 - e^2 (1 - x^2)}} \quad \text{with } \overline{S} = 0 \text{ at } x = -1$$

it follows

$$\overline{S} = B \exp \left[\frac{e}{\sqrt{1 - e^2}} \sin^{-1}(ex) + A \right]$$

$$\times \left[\frac{\sqrt{1 - e^2} \sqrt{1 - e^2 x^2} - e^2 x + 1}{\sqrt{1 - e^2} \sqrt{1 - e^2 x^2} + e^2 x + 1} \right]^{1/2} \sqrt{\frac{1 + x}{1 - x}} \qquad (4)$$

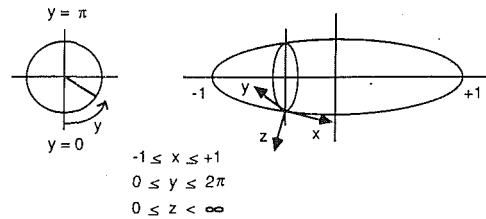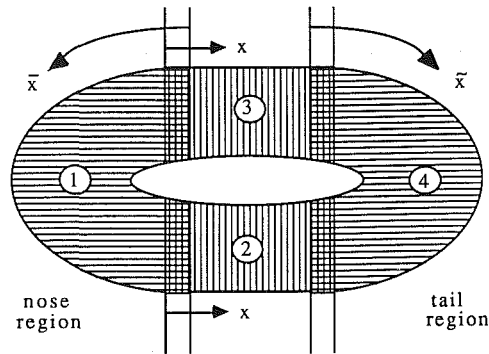Fig. 1 Geometry and coordinates system

Fig. 2 Multiple zones

where A and B are mapping constants. With transformation (4), and further let

$$\overline{x} = \overline{S} \cos y \qquad u = \overline{u} \cos y + \overline{v} \sin y$$
$$\overline{y} = \overline{S} \sin y \qquad v = -\overline{u} \sin y + \overline{v} \cos y$$
$$\overline{z} = z \qquad w = \overline{w}$$

Equations (1), (2), and (3) then become

$$\frac{1}{\overline{h}} \left(\frac{\partial \overline{u}}{\partial \overline{x}} + \overline{v}_{\overline{y}} \right) + \frac{\partial \overline{w}}{\partial \overline{z}} - \overline{R} \overline{x} \overline{u} = 0 \qquad (5)$$

$$\frac{\partial \overline{u}}{\partial t} + \frac{\overline{u}}{\overline{h}} \frac{\partial \overline{u}}{\partial \overline{x}} + \overline{w} \frac{\partial \overline{u}}{\partial \overline{z}} = \frac{-1}{\rho \overline{h}} \frac{\partial p}{\partial \overline{x}} + \frac{\partial^2 \overline{u}}{\partial \overline{z}^2} \qquad (6)$$

$$\frac{\partial \overline{v}_{\overline{y}}}{\partial t} + \frac{1}{\overline{h}} \left(\overline{u} \frac{\partial \overline{v}_{\overline{y}}}{\partial \overline{x}} + \overline{v}_{\overline{y}}^2 \right) + \overline{w} \frac{\partial \overline{v}_{\overline{y}}}{\partial \overline{z}}$$
$$- \overline{R} \overline{u} (\overline{x} \overline{v}_{\overline{y}} - \overline{u}) = \frac{-1}{\rho \overline{h}} \frac{\partial^2 p}{\partial \overline{y}^2} + \frac{\partial^2 \overline{v}_{\overline{y}}}{\partial \overline{z}^2} \qquad (7)$$

where $\overline{h} = \frac{h_2}{\overline{S}}$, $\overline{R} = \frac{1}{\overline{S}} \left(\frac{1}{h_2} - \frac{1}{h_1 h_2} \frac{\partial h_2}{\partial x} \right)$

Equations (5), (6), and (7) are now regular at $x = -1$. Similar treatment can be applied to remove the singularity at the rear end $x = +1$ and we shall not restate the derivation here. In the following context, quantities in the tail region of the prolate spheroid will be denoted by ($\tilde{\ }$).

Solution Method

The solution domain is decomposed into four regions as shown in Fig. 2. The transformed coordinate system described in the last section is used in the nose and tail regions to remove the geometry singularity. Each region is overlapped with the adjacent ones. Calculations are performed separately in different regions, the required boundary conditions on the interface of one region are then obtained from interpolating the values at the interior points of the other region. Successful results where similar composite-grid techniques have been applied were reported in several previous investigations of Navier-Stokes flows (Rai, 1987; Chesshire and Henshaw, 1989), transonic flows (Atta and Vadyak, 1982; Flores et al., 1986), Euler equations (Allmaras and Baron, 1986), and the combined Navier-Stokes, Euler, and boundary-layer equations (Schmatz

and Hirschel, 1986). The principal advantages of composite-grid are the generation of grids for regions of complicated geometry, and an easier implementation of different formulations in different regions. However, the "patching" of the solutions between different regions needs attention. Care must be taken so that the interpolation procedure on the interface will not destroy the stability and accuracy of the interior solution. See, e.g., Chesshire and Henshaw (1989). In the following calculations, a cubic Lagrangian interpolation formula was used. No apparent error and instability were observed in this particular numerical example.

The physical domain is more conveniently transformed into a finite computational region (α, β) by using appropriate mapping functions. In the main region, for example,

$$x = (x_2 - x_1)[(1-\epsilon)(3-2\alpha)\alpha^2 + \epsilon\alpha)] + x_1 \qquad 0 \le \alpha \le 1$$

$$z = D_2 \sqrt{\frac{t}{t+D_1}} \tan \frac{\pi\beta}{2} \qquad 0 \le \beta \le 1$$

where x_1, x_2 and D_1, D_2 are constants, ϵ is a small number which controls the stretching in the streamwise coordinate x. The mapping in the α-direction gives the mesh clustering effect near the front and rear ends where the pressure gradient varies rapidly. The time-like β coordinate removes the singular behavior in the flow at impulsive start-up. A uniform grid is drawn in the α-β plane, and the governing equations are discretized in terms of these computational coordinates.

In contrast to the conventional space-marching technique in solving the boundary-layer type equation, we next formulate strictly an initial-value problem in which the flow variables in each region are advanced in the time-direction only. A similar approach was already carried out in Van Dalsem and Steger (1987) who used a time-relaxation scheme in their calculations. We seek to reduce the computation effort at each time step by adopting a noniterative predictor-corrector formulation, Douglas and Jones (1963). That is, in advancing the time step from n to $n + 1$, a predicted value is first evaluated at $n + 1/2$ where all the nonlinear coefficients in the momentum equations are linearized by using the values frozen from the previous time n. Thus the governing equations are decoupled in the predictor step. A backward Euler differencing in time is preferred in solving the predictor value for the purpose of damping out the numerical error. Second order accuracy of temporal difference can be restored by following a Crank-Nicolson like correction step.

In both the predictor and the corrector steps, a flow-dependent, one-sided spatial difference is applied to the convection term in accordance with its hyperbolic character (i.e., backward difference is used if $u > 0$, and forward difference for $u < 0$). In the usual marching scheme, flow quantities needed to account for the backflow influence are grabbed from the previous time level. By appealing to the CFL criterion, this explicit formulation will then restrain the time step used in the discretization procedure. This is particularly important as the restriction on the step size can be very stringent when separation is approached (Cebeci, 1986). In the present scheme, an implicit time-advancing approach is used, and upwind differences are performed at the current time level throughout the whole do-

main. The CFL condition is satisfied automatically, allowing us to relax the time-step limitation.

The formulation is very similar in both the predictor and corrector steps. By applying the above discretization procedures to (2) and (3), the following are the resulting finite difference equations in the computational plane-(α, β) for the corrector step:

$$\left\{ 1 + \frac{\Delta t \alpha_{,x} u}{2 h_1 \Delta \alpha} \delta_\alpha^\pm - \frac{\Delta t \beta_{,z}^2}{2\Delta\beta^2} \delta_\beta^2 \right.$$
$$\left. - \frac{\Delta t (\beta_{,zz} - \beta_{,t} - \beta_{,z} w)}{4\Delta\beta} (2\mu\delta)_\beta \right\}^{n+1/2} \Delta q^{n+1}$$
$$= \frac{-\Delta t}{\rho h_1} \frac{\partial p}{\partial x} + \Delta t \left\{ \frac{-\alpha_{,x} u}{h_1 \Delta\alpha} \delta_\alpha^\pm + \frac{\beta_{,z}^2}{\Delta\beta^2} \delta_\beta^2 \right.$$
$$\left. + \frac{(\beta_{,zz} - \beta_{,t} - \beta_{,z} w)}{2\Delta\beta} (2\mu\delta)_\beta \right\}^{n+1/2} u^n \quad (8)$$

$$\left\{ 1 + \frac{\Delta t \alpha_{,x} u}{2 h_1 \Delta \alpha} \delta_\alpha^\pm - \frac{\Delta t \beta_{,z}^2}{2\Delta\beta^2} \delta_\beta^2 - \frac{\Delta t (\beta_{,zz} - \beta_{,t} - \beta_{,z} w)}{4\Delta\beta} (2\mu\delta)_\beta \right\}^{n+1/2} \Delta q_y^{n+1}$$
$$= \frac{-\Delta t}{\rho h_2} \frac{\partial^2 p}{\partial y^2} - \frac{\Delta t (v_y^2)^{n+1/2}}{h_2} - \frac{\Delta t u^{n+1/2} v_y^{n+1/2}}{h_1 h_2} \frac{\partial h_2}{\partial x}$$
$$+ \Delta t \left\{ \frac{-\alpha_{,x} u}{h_1 \Delta\alpha} \delta_\alpha^\pm + \frac{\beta_{,z}^2}{\Delta\beta^2} \delta_\beta^2 + \frac{(\beta_{,zz} - \beta_{,t} - \beta_{,z} w)}{2\Delta\beta} (2\mu\delta)_\beta \right\}^{n+1/2} v_y^n \quad (9)$$

where $\Delta q^{n+1} = u^{n+1} - u^n$
$$\Delta q_y^{n+1} = v_y^{n+1} - v_y^n$$

$\alpha_{,x}$, $\beta_{,t}$, $\beta_{,z}$ and $\beta_{,zz}$ denote the derivatives of the corresponding mapping functions. The difference operators used follows those defined in Warming and Beam (1978):

$$\delta = (\cdot)_{i+1/2} - (\cdot)_{i-1/2} \quad \delta^+ = (\cdot)_{i+1} - (\cdot)_i \quad \delta^- = (\cdot)_i - (\cdot)_{i-1}$$
$$\delta^2 = (\cdot)_{i+1} - 2(\cdot)_i + (\cdot)_{i-1} \quad \mu = 1/2[(\cdot)_{i+1/2} + (\cdot)_{i-1/2}]$$

Equations (8) and (9) are then factored into two sweeps by the approximate factorization procedure of Warming and Beam (1978). Each sweep involves solving a system of algebraic equations with a scalar tri-diagonal coefficient matrix:

$$\left\{ 1 - \frac{\Delta t \beta_{,z}^2}{2\Delta\beta^2} \delta_\beta^2 - \frac{\Delta t (\beta_{,zz} - \beta_{,t} - \beta_{,z} w)}{4\Delta\beta} (2\mu\delta)_\beta \right\}^{n+1/2} \Delta q'^{n+1}$$
$$= \text{RHS of (8)}$$

$$\left\{ 1 + \frac{\Delta t \alpha_{,x} u}{2 h_1 \Delta\alpha} \delta_\alpha^\pm \right\}^{n+1/2} \Delta q^{n+1} = \Delta q'^{n+1}$$

Having solved u and v_y, the transverse velocity w can be updated from integrating the continuity equation (1) by trapezoidal rule.

Similar difference schemes are applied to the equations in the transformed coordinates systems for the nose and tail regions. Their final forms are omitted here for brevity.

The accuracy of the predictor-corrector method used has been studied by Douglas and Jones (1963) on one-dimensional model equations. The results show that for a transient problem, the overall accuracy in time is of second order. Linearized von Neumann stability analysis of the corrector step predicts the scheme to be unconditionally stable if the one-side difference conforms with the flow direction. In the following numerical examples, no instability was encountered in the calculations. Furthermore, in order to preserve second order accuracy in the spatial direction, the convection terms were discretized by a three-point upwind-difference formula. This will result in a penta-diagonal matrix in the α-sweep rather than tri-diagonal

during the factorization procedure. Both matrices were solved using well vectorized penta- and tri-diagonal solvers.

Results and Discussion

Calculations were done for the symmetry plane of a prolate spheroid with axes ratio 1/4 and various angles of attack which typify the axisymmetry (0 deg), low incidence (6 deg) and high incidence (50 deg) categories. To assure the convergence of the solution, a numerical test on the effects of grid refinement was performed first and the results are included in the appendix. At each different incidence, the skin friction and displacement thickness are presented and discussed in the following subsections. The focus will be on the initiation of separation evidenced by the emergence of a Lagrangian singularity in the flow. Because of the similarity between the flow in the symmetry plane and the two-dimensional cylinder case, comparison with the results obtained from the two-dimensional elliptic cylinder with the same axes ratio is made, and certain analogy between the two flows is shown.

All the numerical computations were performed on the Cornell National Supercomputer Facility. For a typical 30,000 grid points (including all four regions) used in each of the present examples, the required CPU time in advancing one time step was around 2 seconds on IBM 3090-600E. About 45 percent of the job was executed under the vector mode, and the measured vector speed-up was 3. More effort is being made to improve the percentage of vectorization of the program.

0 Deg Incidence. The zero degree incidence case was not included in Xu and Wang's calculation. It is given here as a bench test of the present numerical scheme. Calculated wall shear and displacement thickness are shown in Figs. 3 to 8. In the nose region, the skin friction $\bar{\tau}_{\bar{x}}$ quickly approaches a steady value (Fig. 3) while in the tail region, Fig. 4, a reversed-flow region is seen to form shortly after the impulsive start and spread subsequently toward the front. Also notice that due to the small axes ratio, the reversed flow is confined in a narrow region near the rear end, and the skin friction does not vary much along most part of the body (Fig. 5). Figure 6 plots the distribution of crosswise skin-friction $\tau_{y,y}$. Owing to the axisymmetry property of the flow at 0° incidence, the value of $\tau_{y,y}$ is zero in this particular case. However, as pointed out in the previous section, quantities on the left and right interfaces of the main region are obtained from interpolating the flow variables in the nose and tail regions respectively. Specifically, the crosswise skin-friction in the main region is related to that in the nose through the transformation

$$\tau_{y,y} = -\bar{\tau}_{\bar{x}} \cos y + \bar{\tau}_{\bar{y},\bar{y}} \, \bar{S} \cos^2 y.$$

In general, terms on the right-hand side of the above transformation do not sum up to zero due to discretization and hence introducing error on the interface. It can be seen from Fig. 6 that this error on the left interface is quickly damped out after few nodal points, while the error on the downstream interface does not propagate back into the domain because of the upwind differencing. The accuracy of the solution at the interior points is found to be essentially unaffected.

The displacement thickness Δ_x is given in Fig. 7 and Fig. 8. In the main region (Fig. 7), the flow changes slowly over a large part of the body except very close to the rear end where the boundary layer increases drastically. Figure 8 shows the details just ahead of the end point. A "spike"-like structure similar to that discovered in the Lagrangian computations of two-dimensional problems (van Dommelen, 1981; Wu, 1985) is observed near $\bar{x} = -0.08$. In order to be convinced that it is not created by numerical stability, the calculation was carried out again in several refined meshes and reduced time steps. Results show only a "sharper" spike and the overall picture does not change. Formerly, this spike-like behavior has only
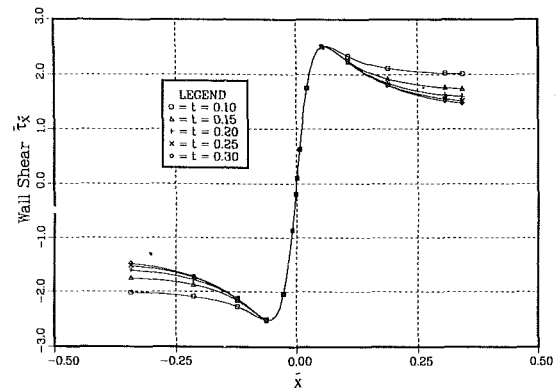

Fig. 3 Skin friction $\bar{\tau}_{\bar{x}}$ in nose region ($\hat{\alpha} = 0$ deg)
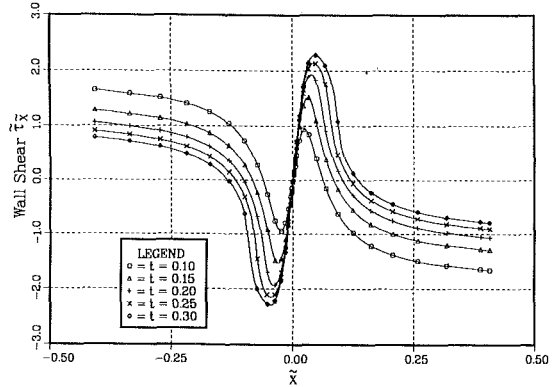

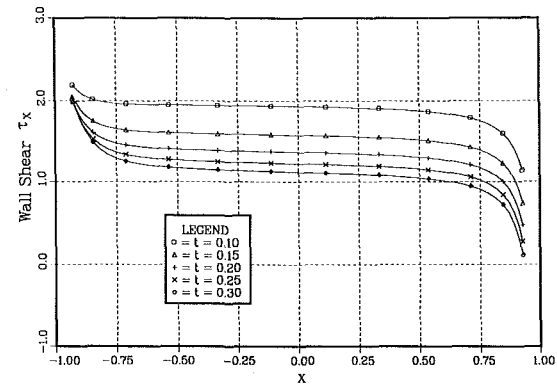Fig. 4 Skin friction $\bar{\tau}_{\bar{x}}$ in tail region ($\hat{\alpha} = 0$ deg)

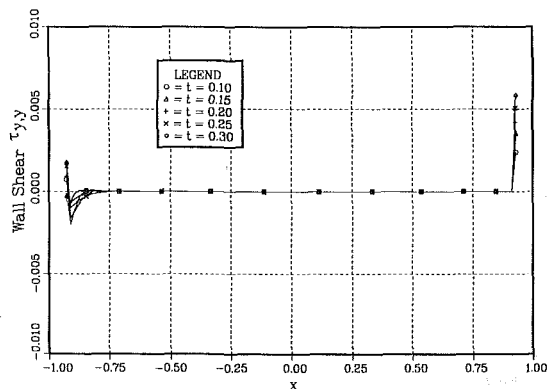Fig. 5 Lee-side skin friction τ_x ($\hat{\alpha} = 0$ deg)

Fig. 6 Lee-side crosswise skin-friction $\tau_{y,y}$ ($\hat{\alpha} = 0$ deg)
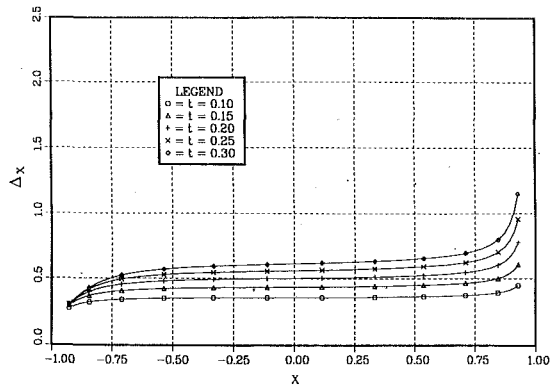
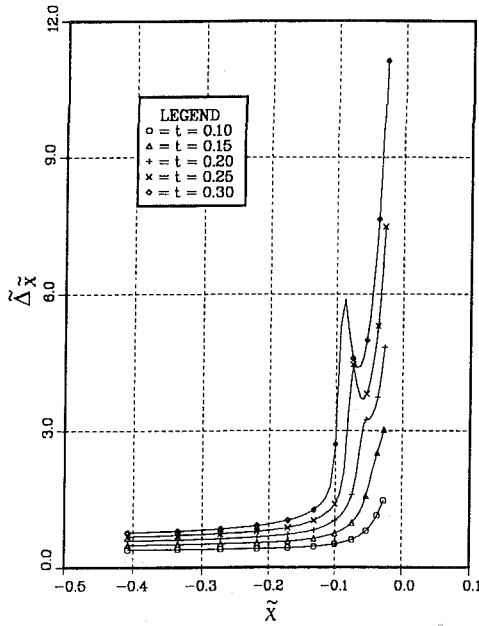Fig. 7   Lee-side displacement thickness Δ_x ($\hat{\alpha}$ = 0 deg)

been found in Lagrangian computations. Most of the previous two-dimensional boundary-layer results calculated by the Eulerian formulation encountered difficulty near separation and consequently did not give a conclusive displacement thickness variation at this point (e.g., Cebeci, 1982; Wang, 1982; Kim and Chang, 1988). Failure to obtain a converged and stable solution in these calculations upon approaching separation may be attributed to the aforementioned severe limitation on the step size needed in the conventional space-marching technique. The present time-marching Eulerian scheme proves to be not only stable but also capable of confirming the critical features near separation which were previously obtained by the Lagrangian computation.

The behavior of the displacement thickness reflects the behavior of the velocity profile $\tilde{u}$. Shown in Fig. 9 is the velocity

Fig. 8   Displacement thickness $\tilde{\Delta}_{\tilde{x}}$ in tail region ($\hat{\alpha}$ = 0 deg)
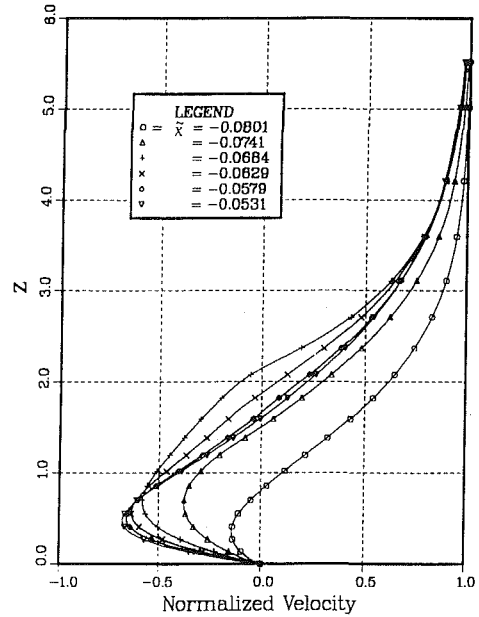
Fig. 9(b)
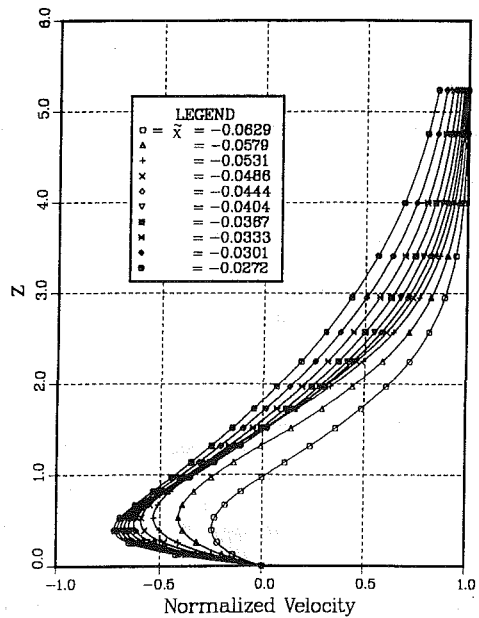
Fig. 9(a)
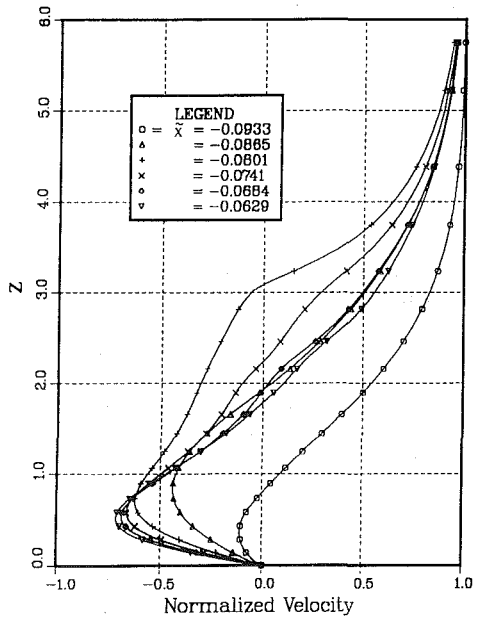
Fig. 9(c)

Fig. 9   Velocity profiles at $\hat{\alpha}$ = 0 deg; (a) t = 0.19, (b) t = 0.23, (c) t = 0.27

profile at several $\tilde{x}$ locations. It is found that starting from $t = 0.19$, there is an unusual "clustering" of the velocity profiles around $\tilde{x} = -0.045$. The same phenomenon was reported in Cebeci (1982). The clustering of the velocity profiles results in a "kink" in the $\tilde{\Delta}_{\tilde{x}}$ distribution at $t = 0.20$, Fig. 8. Beyond $t = 0.20$, there is a sudden thickening in some of the velocity profiles (Figs. 9b, c) which in turn leads to a fast increase in the displacement thickness at such locations. The peculiar velocity profiles are only found to occur in a very narrow region of $\tilde{x}$. Further into the reversed flow regime, the velocity profiles look normal again. The formation of the sharp "spike" and "valley" immediately following in the displacement thicknesses for $t > 0.20$, Fig. 8, are thus explained.

Accompanying this thickening of the displacement thickness is the sudden growth in the transverse velocity $\tilde{w}$. From the Lagrangian view point (van Dommelen, 1981; Shen and Wu, 1988), the thickening happens because a certain fluid "packet" gets squeezed in the streamwise direction and must expand laterally in order to preserve the volume. Since in the axisymmetry case every meridian plane that cuts through the prolate spheroid is a symmetry plane, the critical fluid packets form a front that has no choice but to explode in the direction normal to the wall. The projection of this front onto the wall encircles the spheroid, and is the logical generalization of the separation point for two-dimensional flows. It unequivocally defines the separation line for unsteady three-dimensional separation.

The singular behavior of the boundary layer at separation is also seen from the continuously increasing $\partial \tilde{u}/\partial \tilde{x}$ near separation. According to the two-dimensional Lagrangian computation of van Dommelen (1981), $\partial \tilde{u}/\partial \tilde{x}$ should blow up at separation. Moreover, the velocity profile near separation would exhibit a very "flat" front corresponding to a large inviscid region that splits the boundary-layer into two vorticity layers. The present Eulerian calculation did find a thickening of some velocity profiles as was shown in Fig. 9, but none of the profiles are very "flat." Now, given a grid size, a simple estimation based on the Taylor series expansion would suggest an upper bound of the value $\partial \tilde{u}/\partial \tilde{x}$ that can be determined by differencing. Specifically, when the term $(\Delta \tilde{u}/\Delta \tilde{x})$ $(\Delta \tilde{x})$ becomes order 1, the finite difference formula ceases to be meaningful. In other words, if the mesh $\Delta \tilde{x} = 0.007$, which was the grid size near separation in this case, the maximum $\Delta \tilde{u}/\Delta \tilde{x}$ we can get is roughly 150. Indeed in the calculation, it is found that the maximum value of $\Delta \tilde{u}/\Delta \tilde{x}$ hardly exceeded this order. As such a maximum is reached, the singularity is smeared out by the numerical diffusion, and the legitimacy of continuing the calculation becomes questionable. Higher resolution thus is needed to obtain more accurate velocity profiles near separation. Further discussion about this will be given in the subsequent sections.

6 Deg Incidence. This can be considered as an axisymmetry flow perturbed by a small angle of attack. It is expected that most of the features will be similar to those in the 0 deg incidence. Figure 10 shows the lee-side skin friction, also superimposed is the result by Xu and Wang (1988). The two results do agree in the general trend but not in the values. The skin friction in the tail region is plotted in Fig. 11 where details of a small region of reversed flow near the rear end are revealed. (This was not available in Xu and Wang's result.) Again, no anomalous phenomenon is found in the wall shear, and the whole picture looks almost the same with the one in the previous case (Fig. 4) except now the rear stagnation point has shifted upstream a little bit from the rear end. In the present numerical scheme, the velocity profile at the stagnation point is not needed to construct the flow as normally done in a space-marching technique. The stagnation flow evolves by itself. From Fig. 11, it is seen that both the stagnation point and the asymmetry of the flow due to the small angle of attack are well captured in the calculation.
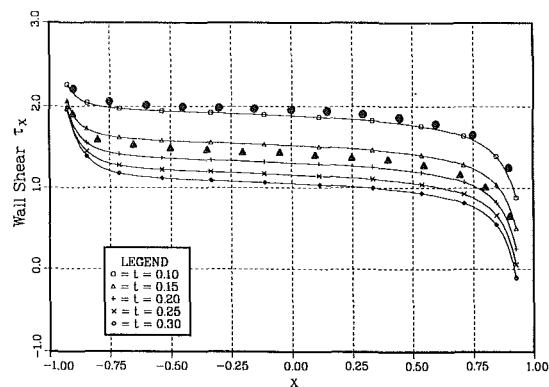

Fig. 10 Lee-side skin friction τ_x ($\tilde{\alpha} = 6$ deg); $\bullet - t = 0.1$, $\blacktriangle - t = 0.2$, Xu and Wang (1988)
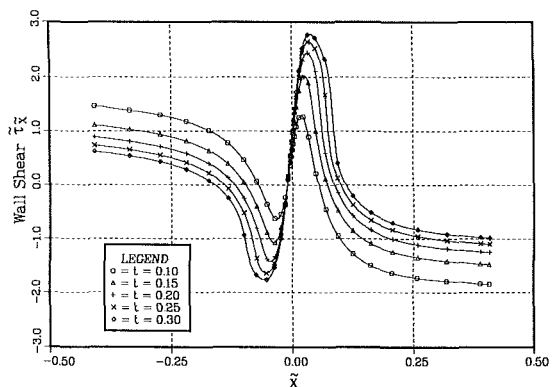

Fig. 11 Skin friction $\tilde{\tau}_{\tilde{x}}$ in tail region ($\tilde{\alpha} = 6$ deg)

Figure 12 exhibits a nonzero distribution of crosswise skin-friction $\tau_{y,y}$ at lee side. At small times, $\tau_{y,y}$ remains negative which indicates that the circumferential velocity v near the symmetry plane is pointing toward the plane of symmetry. As time increases, a region of positive $\tau_{y,y}$ begins to develop near the end point. In other words, a small crosswise reversed flow is formed at the rear end. This reversed flow region will then extend gradually toward the forward direction with increasing time. The present results are consistent with those described in Xu and Wang (1988).

Both the lee-side and wind-side displacement thicknesses in the tail region are shown in Figs. 13 and 14. (Details of the displacement thickness near the rear end were left out in Xu and Wang (1988), therefore no comparison is made.) By examining Fig. 13, it is observed that a spike appears first in the wind-side displacement thickness at $t = 0.25$. If we accept the assumption that the initial separation does not substantially alter the flow over the lee side and simply proceed with the calculation, a similar spike-like structure is also found to occur on the lee side at a somewhat later time (Fig. 14). Without the benefit of off-symmetry-plane solution, it may be conjectured here that the separation is likely to occur first as a point on the wind-side symmetry plane and then spread with increasing time in both circumferential directions, and finally, meet on the lee-side symmetry plane to form a closed curve. Turning to the Lagrangian interpretation, because of the presence of a small incidence, fluid packets on each different meridian plane will now deform differently. The time at which these packets might get squeezed into zero thickness would also differ. Besides, the three-dimensional geometry offers the fluid packets a chance to expand in the crosswise direction. The details of how the separation, after its initiation from the wind-side symmetry plane, propagates along the circumferential di-
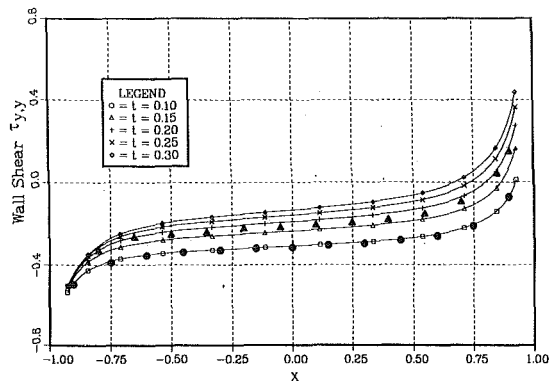
Fig. 12 Lee-side crosswise skin-friction $\tau_{y,y}$ ($\hat{\alpha}$ = 6 deg); • – t = 0.1, ▲ – t = 0.2, Xu and Wang (1988)
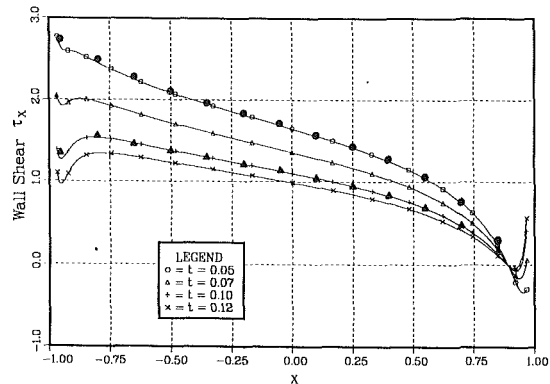

Fig. 15 Lee-side skin friction τ_x ($\hat{\alpha}$ = 50 deg); • – t = 0.05, ▲ – t = 0.1, Xu and Wang (1988)
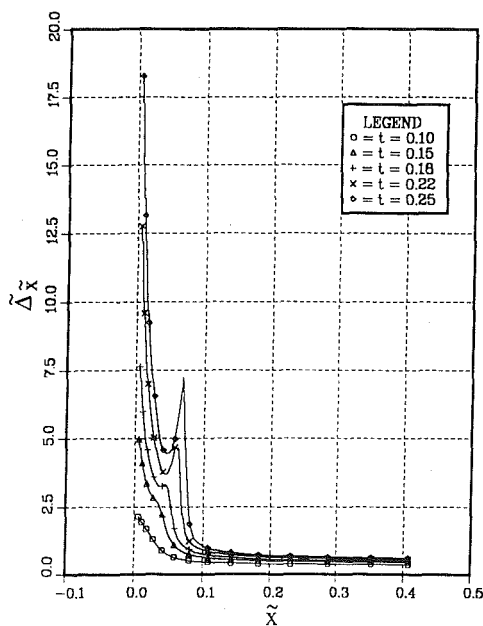

Fig. 13 Displacement thickness $\tilde{\Delta}_{\tilde{x}}$ in tail region, wind side ($\hat{\alpha}$ = 6 deg)
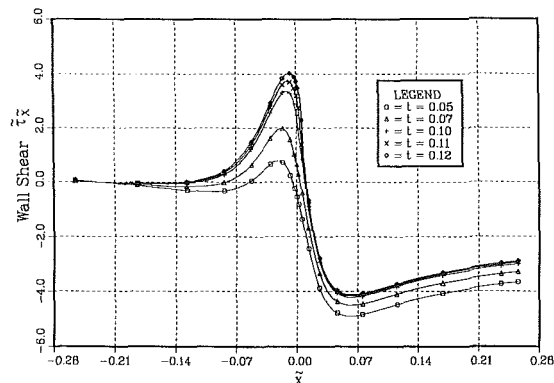

Fig. 16 Skin friction $\tilde{\tau}_{\tilde{x}}$ in tail region ($\hat{\alpha}$ = 50 deg)
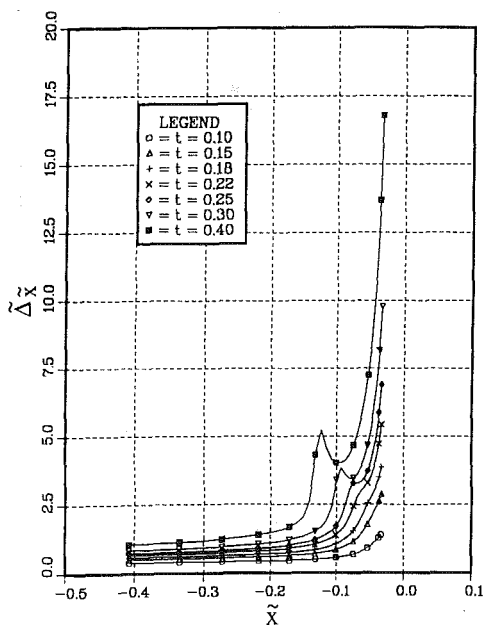
Fig. 14 Displacement thickness $\tilde{\Delta}_{\tilde{x}}$ in tail region, lee side ($\hat{\alpha}$ = 6 deg)

rection is a question that can only be answered after a fully three-dimensional calculation over the entire prolate spheroid is made.

50 Deg Incidence. After the impulsive start-up, the lee-side skin-friction decreases from a maximum value at the front vertex to zero at the rear stagnation point (Fig. 15). However, beginning from t = 0.05, a dip near the front vertex is found, and the value of τ_x at the dip drops quickly thereafter. According to the large time calculation of Xu and Wang (1988), this value will eventually become negative as a small recirculating bubble is established. A similar situation was found in a high-incidence elliptic cylinder (Wu, 1985) where a reversed flow appears at early time near the leading edge. The skin friction in the tail region is presented in Fig. 16. In this picture, the rear stagnation point is located at $\tilde{x}$ = –0.23. By the definition of the coordinate transformation, positive $\tilde{x}$ points to wind-side direction. Therefore, positive wall shear around $\tilde{x}$ = 0 in this plot actually corresponds to a recirculating flow near the rear end. The recirculation region first occurs just shortly above the end point and then expands in both directions. The zero $\tilde{\tau}_{\tilde{x}}$ point moving toward the wind-side direction appears to stop at $\tilde{x}$ = 0.01, and the recirculation region does not penetrate further upstream. In fact, the skin friction at the wind side seems to have already reached a steady value at t = 0.12. The same trend was also found in the previous two-dimensional calculation (Wu, 1985).

An interesting behavior in the lee-side crosswise skin-friction is demonstrated in Fig. 17. The reversal of circumferential velocity v (positive $\tau_{y,y}$) first occurs at the rear end and the zero $\tau_{y,y}$ point quickly moves upstream. At t = 0.08, another region of reversed v appears at the front and grows in the downstream direction. These two regions coalesce at approximately t = 0.11 which means the flow near the symmetry
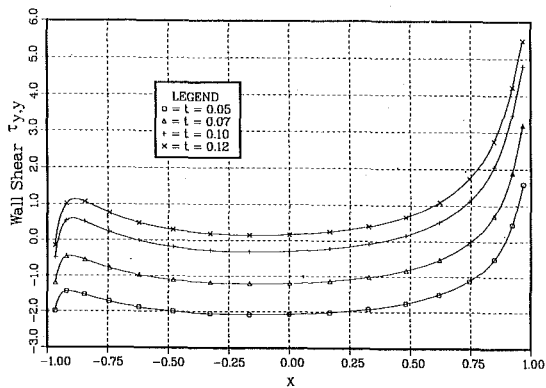
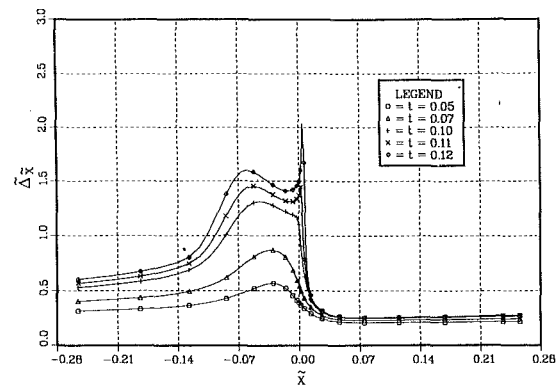Fig. 17 Lee-side crosswise skin-friction $\tau_{y,y}$ ($\hat{\alpha} = 50$ deg)

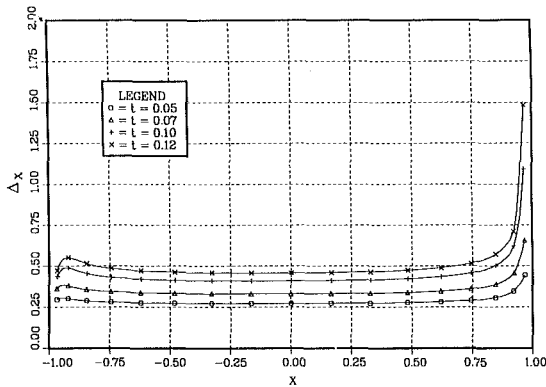Fig. 19 Displacement thickness $\tilde{\Delta}_{\tilde{x}}$ in tail region ($\hat{\alpha} = 50$ deg)

Fig. 18 Lee-side displacement thickness Δ_x ($\hat{\alpha} = 50$ deg)

Fig. 20(a)

Fig. 20(b)

Fig. 20 Velocity profiles at $\hat{\alpha} = 50$ deg; (a) $t = 0.12$, (b) $t = 0.122$.

plane is moving away from the plane over the entire lee side except for a small part close to the front vertex. It is believed that the reversal of the crosswise velocity v will have an important influence on the off-symmetry-plane separation.

At such a high angle of attack, the lee-side displacement thickness at small time still remains essentially constant along most part of the body (Fig. 18). Yet a "hump" resulting from the "dip" in the skin friction (Fig. 15) is evolved at $t = 0.05$. Near the rear end, the displacement thickness shows a sharp increase and forms a spike almost right at the rear end-point (Fig. 19). This fact suggests a possible difficulty of the method used by Xu and Wang (1988) in obtaining accurate results near the rear end, because they did not remove the geometrical singularity there. The reason that the spike at $t = 0.12$ appears to be sharper than those presented in the previous cases of this paper is due to a somewhat higher resolution in the present case. The grid size $\Delta \tilde{x}$ near the rear end is approximately 0.001 here. According to the argument stated at the end of the first subsection, the maximum $\Delta \tilde{u}/\Delta \tilde{x}$ that can be obtained here is around 1000, which is an order larger than that in the zero incidence case. Associated with this result is a "flatter" velocity profile near separation (Figs. 20a, b). Although the relevant profiles are not too smooth, the trend is clear. Shown in Fig. 21 is one of the corresponding vorticity profiles. The splitting of the boundary-layer into two vorticity layers is apparent.

The calculation was terminated at $t = 0.12$ after the presence of a singularity on the wind side. Whether or not another singularity may appear at the lee side near the front vertex can not be answered at this moment. However, suggested by the large time calculation of Xu and Wang (1988) and the former results on the elliptic cylinder, Wu (1985), it is likely that another singularity would develop at later time near the front end, and afterwards the separation would probably be of the closed type at this high incidence.
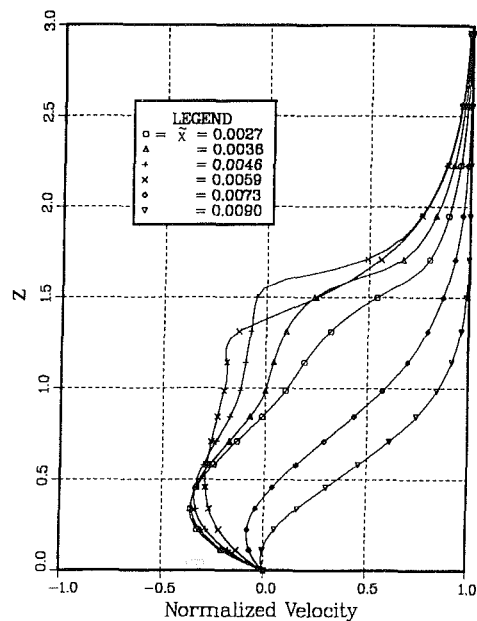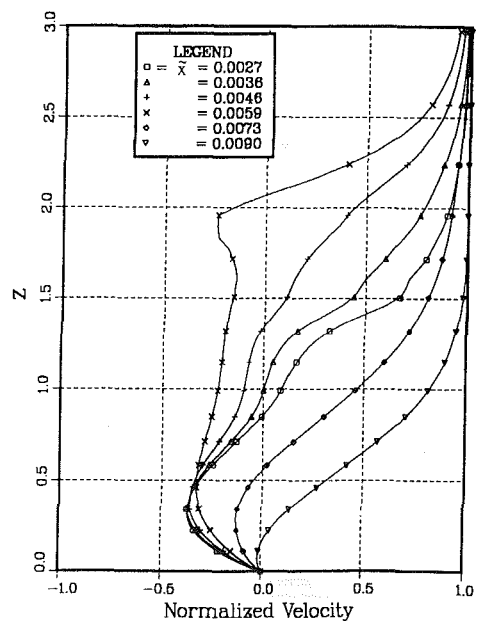
Comparison With Two-Dimensional Results. The results of an unsteady boundary-layer over an impulsively started elliptic cylinder with axes ratio 1/4, calculated by the Lagrangian method described in Wu (1985), are presented here for comparison. Shown in Figs. 22a, b, c are the displacement thicknesses at 0 deg, 6 deg, and 50 deg incidence. In these plots, the time t has been converted to conform with the present time scale. Here, ξ denotes the streamwise boundary-layer coordinate measured along the body from the leading edge in the clockwise direction. Resemblance between the two cases is clear (cf. Figs. 8, 14, 19) except that in the Lagrangian result, the spike is steeper and more pronounced. This is due to the high resolution of the Lagrangian grid near separation (van Dommelen, 1981). Besides, the displacement thickness in the Lagrangian calculation is obtained by integrating the continuity equation which turns singular as the separation is appoached.
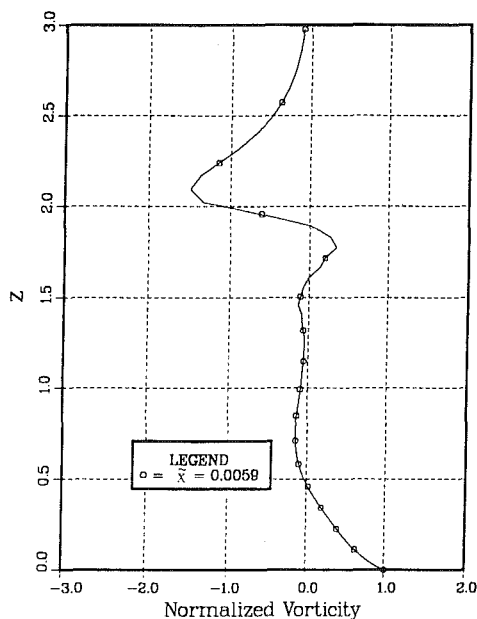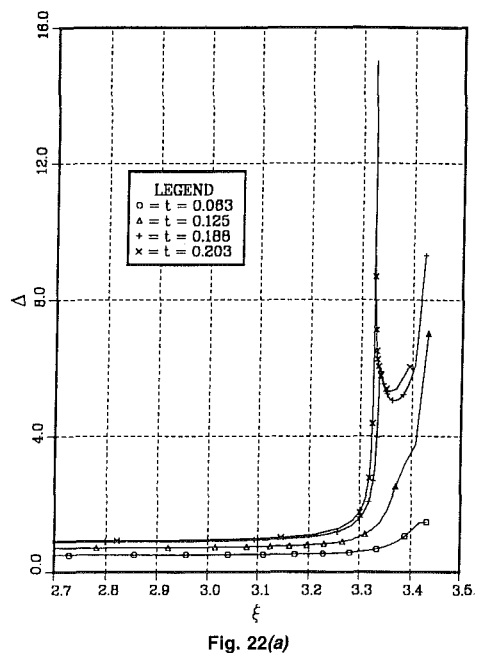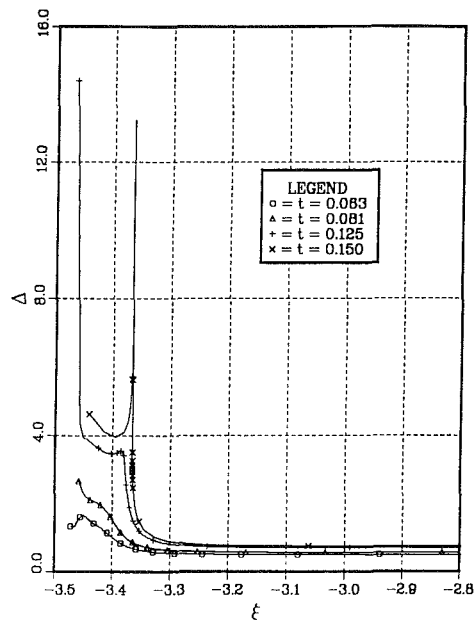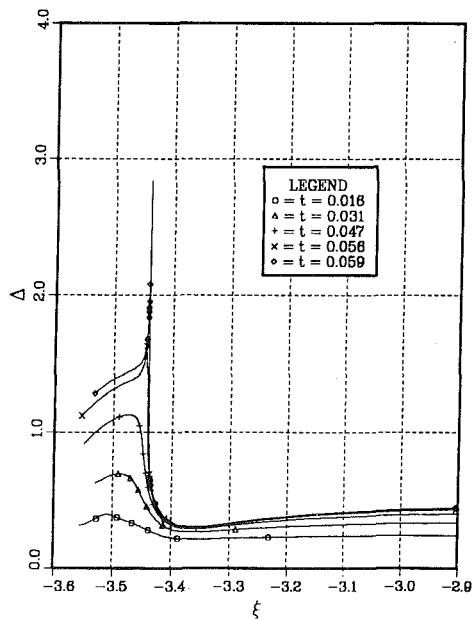
It is noticed that for all three incidences calculated here, separation occurs earlier in time in the two-dimensional case. This can be attributed to the curvature effect as well as the non-zero crosswise velocity v_y in the present three-dimensional calculation.

In Fig. 23 we plot the maximum $\partial \tilde{u}/(\tilde{h}\partial \tilde{x})$ in the present symmetry plane calculation against $(t_s - t)$, t_s being the separation time when the solution turns singular. At t_s, the maximum $\partial \tilde{u}/(\tilde{h}\partial \tilde{x})$ goes to infinity theoretically. We obtain an approximate t_s by extrapolating the zero point of $1/(\partial \tilde{u}/(\tilde{h}\partial \tilde{x}))$ from the available data. In the 50 deg incidence case, least-square fittings with models from quadratic to 4th-order polynomial gives almost the same value of t_s, namely, $t_s =$

Fig. 21   Vorticity profile near separation, $t = 0.122$ ($\hat{\alpha} = 50$ deg)

Fig. 22(b)

Fig. 22(c)

Fig. 22(a)

Fig. 22   Displacement thickness of an impulsively-started elliptic cylinder calculated by the Lagrangian method; (a) $\hat{\alpha} = 0$ deg, (b) $\hat{\alpha} = 6$ deg, (c) $\hat{\alpha} = 50$ deg
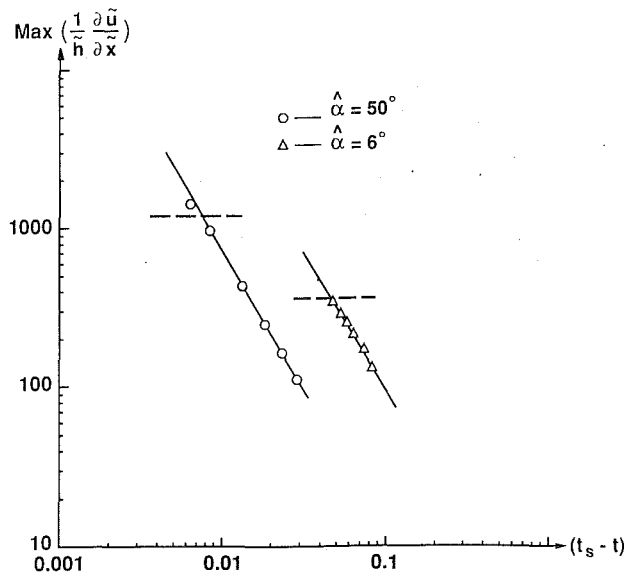
Fig. 23 Blow-up of Max $(1/\bar{h})(\partial\tilde{u}/\partial\tilde{x})$ as calculated by the present Eulerian scheme, ———— straight line of slope 7/4 predicted in the two-dimensional case

0.123. The result for the 6 deg incidence is less certain because of the scattering and relatively low value of maximum $\partial\tilde{u}/(\bar{h}\partial\tilde{x})$, a quadratic polynomial was used to obtain t_s in this case. Also shown in Fig. 23 are the straightlines of slope $-7/4$ predicted by van Dommelen (1981) from the asymptotic structure of the two-dimensional singularity. The dotted line indicates the limiting value of $\partial\tilde{u}/(\bar{h}\partial\tilde{x})$ beyond which the calculated result is unreliable. The blow-up of maximum $\partial\tilde{u}/(\bar{h}\partial\tilde{x})$ appears to follow the 7/4 line. This suggests that the structure of the separation on the symmetry plane is similar to that for the two-dimensional case.

Summary

The subject of unsteady three-dimensional boundary-layer separation is of growing importance. Recent understanding about the unsteady separation mechanism reveals that the usual wall shear and limiting streamlines analysis are not strictly applicable to the separation in an unsteady flow. An accurate and efficient computation scheme for a general three-dimensional boundary-layer flow is needed. The present paper is a progress report of a broader research program for this difficult problem.

We propose a noniterative, time-advancing numerical scheme along with a multiple-zone strategy to solve the unsteady three-dimensional boundary-layer equations. As a preliminary study, the problem of Xu and Wang (1988), i.e., the symmetry-plane solution of an impulsively-started prolate spheroid with axes ratio 1/4 has been redone. Calculations have been performed for three different incidences, 0, 6, and 50 deg. Results from the examples indicate that the algorithm produces accurate results over the entire symmetrical plane, including certain Lagrangian features near separation found in the two-dimensional case. For the 0 deg incidence, projection of the separation locus off the wall on the body forms a closed curve encircling the spheroid owing to the axisymmetry. For non-zero incidence, separation could conceivably start as a point on the wind-side symmetry plane and then propagate toward the lee side in the crossflow directions. Whether or not the curve will become closed on reaching the lee-side symmetry plane may depend on the angle of attack. Based on the behavior of the maximum $\partial\tilde{u}/(\bar{h}\partial\tilde{x})$, the structure of the three-dimen-
sional singularity on the symmetry plane seems to be similar to that for the two-dimensional case.

By using the time-advancing scheme and a flow-dependent one-sided spatial difference, the domain-of-dependence rule is satisfied. No instability was experienced in the calculations. The accuracy of the solution near separation was found to be limited by the requirement of increasing spatial resolution, not by the stability consideration as was inherent in a space-marching technique. Besides, the present time-advancing scheme allows more general flow motions to be calculated while the conventional space-marching scheme has the difficulty of defining a starting profile to initiate the spatial integration.

The primary concern of adopting a multi-zone approach hear is to remove the geometrical singularity presented on the prolate spheroid. Since the calculation task in each region is essentially independent, possible implementation of a parallel processing on these multiple regions is therefore worth studying.

Acknowledgment

References

Allmaras, S. R., and Baron, J. R., 1986, "Embedded Mesh Solutions of the 2-D Euler Equations: Evaluation of Interface Formulations," AIAA Paper 86-0509.

Atta, E. H., and Vadyak, J., 1982, "A Grid Interfacing Zonal Algorithm for Three Dimensional Transonic Flows About Aircraft Configurations," AIAA Paper 82-1017.

Cebeci, T., 1982, "Unsteady Separation," Numerical and Physical Aspects of Aerodynamic Flows, ed. T. Cebeci, Springer-Verlag, New York, pp. 265–278.

Cebeci, T., 1986, "Unsteady Boundary Layers with an Intelligent Numerical Scheme," Journal of Fluid Mechanics, Vol. 163, pp. 129–140.

Cebeci, T., and Su, W., 1988, "Separation of Three-Dimensional Laminar Boundary Layers on a Prolate Spheroid," Journal of Fluid Mechanics, Vol. 191, pp. 47–77.

Cebeci, T., Khattab, A. A., and Stewartson, K., 1980, "On Nose Separation," Journal of Fluid Mechanics, Vol. 97, p. 435–454.

Cebeci, T., Khattab, A. A., and Stewartson, K., 1981, "Three-Dimensional Laminar Boundary Layers and OK of Accessibility," Journal of Fluid Mechanics, Vol. 107, pp. 57–87.

Chanetz, B., 1986, "Experimental Investigation of Three-Dimensional Separation on Ellipsoid Bodies at Incidence," Boundary-Layer Separation, ed. F. T. Smith and S. N. Brown, Springer-Verlag, pp. 383–385.

Chapman, G. T., 1986, "Topological Classification of Flow Separation on Three-Dimensional Bodies," AIAA Paper 86-0485.

Chesshire, G., and Henshaw, W. D., 1989, "Composite Overlapping Meshes for the Solution of Partial Differential Equations," IBM Research Report, RC 14355.

Cowley, S. J., 1983, "Computer Extension and Analytic Continuation of Blasius' Expansion for Impulsively Flow Past a Circular Cylinder," Journal of Fluid Mechanics, Vol. 135, pp. 389–405.

Douglas, J., and Jones, B. F., 1963, "On Predictor-Corrector Methods for Non Linear Parabolic Differential Equations," SIAM Journal, Vol. 11, pp. 195–204.

Flores, J., Holst, T. L., Kaynak, U., Gundy, K., and Thomas, S. D., 1986, "Transonic Navier-Stokes Wing Solution Using A Zonal Approach: Part 1. Solution Methodology and Code Validation," AGARD-CP-412, Paper No. 30A.

Howarth, L., 1951, "The Boundary Layer in Three Dimensional Flow—Part 2. The Flow Near a Stagnation Point," Philosophical Magazine Series 7, Vol. 42, No. 335, pp. 1433–1440.

Ingham, D. B., 1984, "Unsteady Separation," Journal of Computational Physics, Vol. 53, pp. 90–99.

Kim, J.-S., and Chang, K.-S., 1988, "Unsteady Boundary Layer and Its Separation over a Heated Circular Cylinder," International Journal of Numerical Methods in Fluids, Vol. 8, pp. 165–179.

Lighthill, M. J., 1963, Laminar Boundary Layers, ed. L. Rosenhead, Chapter 2, Oxford University Press, Oxford.

Maskell, E. C., 1955, "Flow Separation in Three Dimension," RAE Rep. Aero. 2565.

Perry, A. E., and Chong, M. S., 1986, "A Series-Expansion Study of the Navier-Stokes Equations with Application to Three-Dimensional Separation Patterns," *Journal of Fluid Mechanics*, Vol. 173, pp. 207–223.

Ragab, S. A., 1986, "The Laminar Boundary Layer on a Prolate Spheroid Started Impulsively from Rest at High Incidence," AIAA Paper 86-1109.

Rai, M. M., 1987, "Navier-Stokes Simulation of Rotor/Stator Interaction Using Patched and Overlaid Grids," *Journal of Propulsion*, Vol. 3, pp. 387–396.

Schmatz, M. A., and Hirschel, E. H., 1986, "Zonal Solutions for Airfoil Using Euler, Boundary-Layer and Navier-Stokes Equations," AGARD-CP-412, Paper No. 20.

Shen, S. F., 1978, "Unsteady Separation of Three-Dimensional Boundary Layers from the Lagrangian Viewpoint," *Nonsteady Fluid Dynamics*, eds. D. E. Crow and J. A. Miller, ASME, pp. 47–51.

Shen, S. F., and Wu, T., 1988, "Unsteady Separation Over Maneuvering Bodies," AIAA Paper 88-3542.

Van Dalsem, W. R., and Steger, J. L., 1987, "Efficient Simulation of Separated Three-Dimensional Viscous Flows Using the Boundary-Layer Equations," *AIAA Journal*, Vol. 25, pp. 395–400.

van Dommelen, L. L., 1981, "Unsteady Boundary-Layer Separation," Ph.D. thesis, Cornell University, Ithaca, New York.

van Dommelen, L. L., and Cowley, S. J., 1990, "On the Lagrangian Description of Unsteady Boundary-Layer Separation. Part I. General Theory," *Journal of Fluid Mechanics*, Vol. 210, pp. 593–626.

van Dommelen, L. L., and Shen, S. F., 1980, "The Spontaneous Generation of the Singularity in a Separating Laminar Boundary Layer," *Journal of Computational Physics*, Vol. 38, pp. 125–140.

Wang, K. C., 1970, "Three-Dimensional Boundary Layer Near the Plane of Symmetry of a Spheroid at Incidence," *Journal of Fluid Mechanics*, Vol. 43, pp. 187–209.

Wang, K. C., 1972, "Separation Patterns of Boundary Layer over an Inclined Body of Revolution," *AIAA Journal*, Vol. 10, pp. 1044–1050.

Wang, K. C., 1974a, "Boundary Layer Over a Blunt Body at High Incidence With an Open-Type of Separation," *Proceedings Royal Society of London*, Series A, Vol. 340, pp. 33–55.

Wang, K. C., 1974b, "Laminar Boundary Layer over a Body of Revolution at Extremely High Incidence," *Physics of Fluid*, Vol. 17, pp. 1381–1385.

Wang, K. C., 1975, "Boundary Layer Over a Blunt Body at Low Incidence With Circumferential Reversed Flow," *Journal of Fluid Mechanics*, Vol. 72, pp. 49–65.

Wang, K. C., 1982, "On the Current Controversy about Unsteady Separation," *Numerical and Physical Aspects of Aerodynamic Flows*, ed. T. Cebeci, Springer-Verlag, New York, pp. 279–292.

Warming, R. F., and Beam, R. M., 1978, "On the Construction and Application of Implicit Factored Schemes for Conservation Laws," *SIAM-AMS Proceedings*, Vol. 11, pp. 85–125.

Werle, H., 1962, "Separation on Axisymmetrical Bodies at Low Speed," *La Recherche Aeronautique*, No. 90, pp. 3–14.

Wu, T., 1985, "Unsteady Incompressible Boundary-Layer Separation Over a Two Dimensional Impulsively Started Elliptic Cylinder Calculated by Lagrangian Method," MS thesis, Cornell University, Ithaca, New York.

Xu, W. C., and Wang, K. C., 1988, "Unsteady Laminar Boundary Layer Along the Symmetry Plane of an Impulsively Started Prolate Spheroid," *Journal of Fluid Mechanics*, Vol. 195, pp. 413–435.

APPENDIX

In this appendix, accuracy of the present numerical calculations is estimated by studying the effect of grid refinement on the value of skin friction at the front stagnation point. On the stagnation line, the velocity component u is identically zero. The derivative of the skin friction at stagnation is obtained by

$$\bar{\tau}_o = (\bar{\tau}_{\bar{x},\bar{x}}/\bar{h})/(\bar{U}_{e,\bar{x}}/\bar{h})^{3/2}.$$

The scaling factor $(\bar{U}_{e,\bar{x}}/\bar{h})^{3/2}$ is introduced here for the purpose of comparison with Howarth's (1951) steady state result. At steady state, $\bar{\tau}_o$ is equivalent to $f''(0)$ defined in Howarth (1951). For the axisymmetrical case, $f''(0) = 1.312$.

Table 1 lists $\bar{\tau}_o$ at $t = 0.2$ calculated at three different mesh sizes with time step Δt equals 0.02, 0.01 and 0.005 respectively. All three values appear to approach the steady state result 1.312 given by Howarth. The last row of the table is the Richardson extrapolation of the above three meshes. Using this value as a reference 'exact' solution, errors in $\bar{\tau}_o$ obtained from each grid size are listed in the second column. Quadratic convergence of the result is apparent.

Table 1   Effects of grid refinement on the value of skin friction at stagnation point

grid size	$\bar{\tau}_o$	error
30 × 31	1.305591	0.006341
60 × 61	1.310520	0.001412
120 × 121	1.311590	0.000342
RE	1.311932	- - -

Experimental Study of Casing Boundary Layers in a Multistage Axial Compressor

S. Venkateswaran

Principal Engineer,
Fluid/Thermal Research
Lockheed Engineering and Science Co.,
Hampton, VA 23666

Measurements of the casing boundary layers were obtained in a four-stage, low speed axial flow compressor, to verify the 'law of the wall' applicability to these complex flows. Some of the available shear stress models of the two-dimensional flows have been examined towards the quantitative assessment of skin friction. The shear stress prediction obtained from the Ludwieg-Tillmann relation applied to the streamwise or untwisted profile agreed closely with the measured shear stress by the hot wire. The skin friction was fairly constant for rotor and stator flows and was close to the flat plate values. The boundary layer profiles exhibited a well pronounced semi-logarithmic region with the universal constants of the law of the wall far removed from the standard two dimensional values, especially for rotor flows. Stator flows showed signs of similarity to two dimensional flows.

Introduction

The flow in the wall regions of an axial compressor, both at the hub and casing, is extremely complex. However complex may be the end wall flow, there is evidence that the flow could be considered as a conventional boundary layer and its behavior calculated on that premise (Smith, 1969, and Horlock et al., 1974). The boundary layer that is chopped up by a rotating blade row reforms as a shear layer, the mean flow of which possess many of the characteristics of a boundary layer such as a well defined and linear semi-logarithmic region (Prasad, 1981; Papailiou et al, 1977; and Bhowmik, 1979). On the basis of this assumption that the wall shear layer can be treated as a conventional boundary layer, several calculation methods have been proposed to calculate its growth and predict its behavior. (Horlock and Perkins, 1974; Railly and Howard, 1962; Gregory, 1970; Mellor and Wood, 1971; and De Ruyck et al., 1979). The momentum integral methods have been used in computational schemes to predict boundary layer along the end walls and to relate it to the variation of efficiency and initiation of stall. None of the methods are equally successful for all flow configurations. Several assumptions have to be made in the computational schemes regarding velocity profile models, magnitude of blade force differences, apparent stresses, skin friction, etc.

There is a lot of uncertainty, especially, regarding the magnitude of the skin friction in the skewed boundary layers. Papailiou et al., (1977) carried out extensive experimental and computational studies in stationary cascades to check the basic assumptions of the theories of Mellor and Wood (1971). They found that, in spite of the large variation of the shape factor, the value of C_f did not change appreciably along the blade passage. This result supported the assumption of Mellor and

Wood that C_f was invariant along the blade passage. Hirsch (1974) estimated the value of C_f using the momentum integral equation and experimental data of Nguyen (1971). The mean C_f for the hub boundary layer was about 0.003 which is about the same as that for a nominal two-dimensional boundary layer. However, for the casing boundary layers (with tip clearance), the value of C_f was as high as 0.025. Balsa and Mellor (1974) assumed C_f values of 0.011, both for the hub and tip to get their computations to agree with overall efficiency of unshrouded machines. However, for shrouded blade ends they reported values of C_f to be 0.003. Railly and Sharma (1976) used the measured turbulent and mean flow quantities, with arrays of hot wires downstream of an isolated rotor, in the momentum integral equations. The evaluated C_f was compared with that of Hirsch (1974). The trend was found to be opposite, where the tip values were lower, of the order of 0.002 compared to that of hub, which was of the order of 0.023. Measurements by Bhowmik (1979) and Prasad (1981), behind single rotor, showed values of C_f consonant with flat plate results (about 0.003) at hub and tip.

Thus the ambiguity in the C_f values in a complex flow situation is evident. Further, there is a scarcity in the experimental data from a multi-stage machine to examine the end wall flows towards validating computational schemes. In the present work, extensive experiments have been done in a 4-stage axial flow compressor that has been built to form a general aerodynamic test bed and only typical results have been presented in the light of the above requirement.

Description of Experiment

Research Compressor. The results presented here are from a low speed, four-stage axial compressor, the schematic of which is given in Fig. 1. The compressor was driven by a 100

R - Rotors
S - Stators
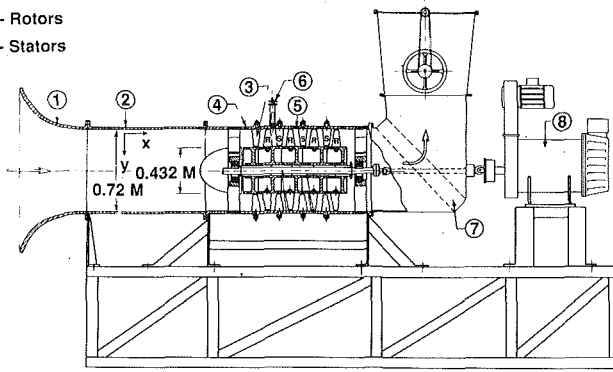
① Bell mouth ② Inlet duct ③ Inlet guide vanes
④ Upstream measuring station ⑤ Measuring station at downstream of rotor
⑥ Traverse gear ⑦ Elbow with deflecting vanes ⑧ 100 h.p d.c. motor

Fig. 1 Schematic of the four-stage low speed axial compressor

H.P. variable speed dc motor and had a maximum speed of 2000 rpm. The blade tip diameter was 720 mm with a hub to tip ratio of 0.6. The work coefficient, Ψ_t, and the flow coefficient, Φ_t, both based on the blade tip, were 0.4 and 0.47, respectively. A combined vortex design was adopted to have a constant potential flow static pressure rise, along the annulus, from hub to tip. The C.4 compressor aerofoil base profile, which has been given by Howell (1945), was chosen for the blading of rotor, stator, and the inlet guide vanes. The detailed design procedure of the compressor is given by Venkateswaran (1983).

Instrumentation. The velocities and the flow angles were measured with a single hot wire in conjunction with a compact combination yaw-pitot probe of low frontal area similar to that used by Bitterlich and Kummel (1977). The hot wire probe introduces a difficulty when the probe is retracted to allow for measurements close to the casing. The retraction exposes a cavity which would disturb the flow near the wall. To mitigate this difficulty a technique similar to that of Rogers and Head (1969) was employed. A separate attachment was made so that at any traverse location of the hot wire, a perspex bush was always in flush with the inner surface of the casing. The maximum step introduced by the bush at its worst angular position was 0.056 mm. Fluid stresses were measured by the use of single straight and rotated slanted wires adopted from the

technique of Fugita and Kovaznay (1968). The closest measurements to the wall were 0.5 mm and 2.0 mm with the straight and inclined wires, respectively.

Experimental Accuracy. The angle measurements by the single hot wire and yaw probe agreed very well away from the wall region with a maximum deviation of 0.5 deg. However, very close to the wall, the difference in the angle was about 3 deg. This difference was attributed to the interference effects of the combination probe near the wall. In the near wall region hot wire angle measurements were accepted as being the true values. Near the wall, the heat conduction effect in the overall estimation of the velocity becomes significant for distances y from the wall given by $yU^*/\nu < 5$ (Oka and Kostic, 1972). In the present case, this gives a lower limit of $y = 0.084$ mm. The closest measurement made in the present experiments was for $y = 0.5$ mm. Therefore, the heat conduction to the wall is not expected to affect the results.

The velocity fluctuations in the wakes would be expected to affect the mean velocity measurements by hot wire. At the measuring stations the estimated decrease in the wake was about 15 percent. The error in mean velocity would be of the order of 2 percent in isotropic turbulence and about 5 percent in non-isotropic turbulence (Oka and Kostic, 1972). The likely error in the present measurements due to fluctuations in the relatively spaced out wakes would be less than this. As an overall indication of measurement accuracy, the integrated axial velocity to give the flow rate agreed within 1 percent (with a single exception where the agreement was within 2.5 percent) compared with the flow measured by the calibrated bell mouth flow meter.

Results and Discussions

Experimental data were obtained in each of the blade row gap of the compressor for four flow rates. Only typical results are presented for discussion. The measuring probes were held stationary with reference to the stator and the measured quantities are with reference to an absolute frame of reference.

Flow at Inlet to the Compressor. Wall static pressure measurements at four equally spaced circumferential positions at the inlet traversing station 4 (Fig. 1) showed a maximum static pressure variation of 0.66 percent of the inlet dynamic pressure based on the axial velocity. This was taken as a measure of the inlet flow uniformity and the flow was treated as axisymmetric. The boundary layer at the inlet was found to be turbulent from the measured $\sqrt{\overline{u'^2}}/U$ which was about 13 percent close to the wall. This was slightly higher than the flat plate

---

Nomenclature

A = universal constant, equation (1)
B = universal constant, equation (1)
C_f = skin friction coefficient, $\tau_w/(1/2\rho U^2)$
H = shape factor, δ^*/θ
r = radial distance from compressor center line
u = local absolute velocity vector
U = absolute velocity vector at boundary layer edge
U_t = blade tip velocity
U^* = friction velocity, τ_w/ρ
U^+ = inner variable, u/U^*
V = relative velocity vector at boundary layer edge

x, y, z = axial, normal, and tangential directions
y = distance from the casing wall
Y^+ = inner variable, yU^*/ν
α = relative flow angle to rotor
β = absolute flow angle to rotor
δ = boundary layer thickness
δ^* = boundary layer displacement thickness
ϵ = skew angle
Φ = flow coefficient, $\overline{U}_x/U_t$
ν = kinematic viscosity
θ = momentum thickness
ρ = density
τ = shear stress

Ω = rotational speed
Ψ = work coefficient, $\rho U_t(U_{z,2} - U_{z,1})/(1/2 \, \rho U_t^2)$

Subscripts

e = boundary layer edge
n = normal component
s = streamwise component
w = wall
x, z = axial and tangential components
1 = rotor inlet condition
2 = rotor exit condition

Superscripts

$'$ = fluctuating quantity
$-$ = mean quantity

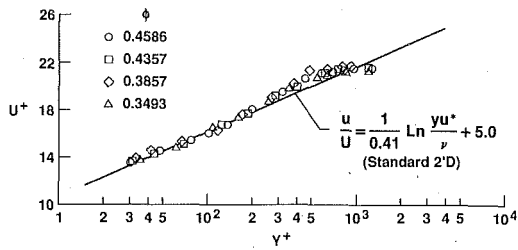Fig. 2 Plot of the inner variables at inlet to the compressor

Fig. 3 Plot of the streamwise profile; second rotor exit

Fig. 4 Velocity triangles for rotor flows

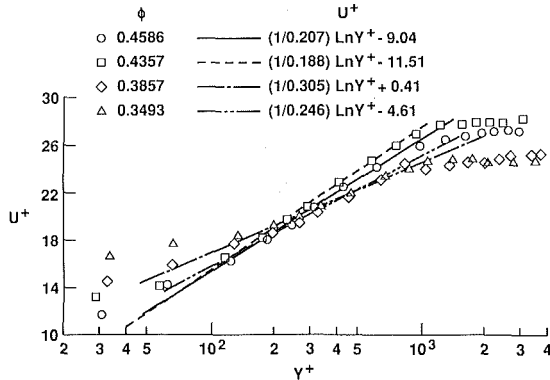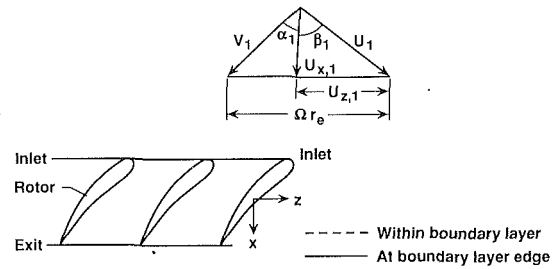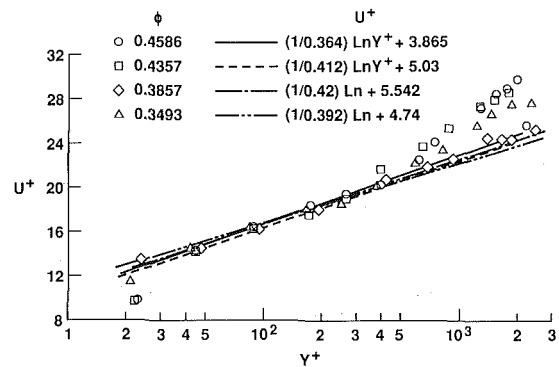Fig. 5 Plot of the streamwise profile; second stator exit

Fig. 6 Plot of the untwisted profile; C_f from equation (2)

value of about 9 percent, at zero pressure gradient (Klebanoff, 1955). This higher level of inlet turbulence level is considered due to the inlet flow acceleration in the bell mouth. Also, the calculated shape factor hovers around 1.4 indicating that the flow is turbulent. These results showed a good agreement with the measurements of Bhowmik (1979) and Prasad (1981) in similar situations.

Fig. 2 shows a good comparison of the plot of the inner variables U^+ and Y^+ of the boundary layer at inlet to the inlet guide vanes with the standard two-dimensional flat plate result in the form:

$$u_s/U^* = 1/A \ \text{Ln} \ (yU^*/\nu) + B \qquad (1)$$

where the universal constants, A and B, are 0.41 and 5.0 or 5.5, respectively. However, the wake region is not as pronounced as for the flat plate flows, with the velocity distribution levelling off rapidly in the wake region. This is due to the acceleration of flow at entry which is also reflected in the increased inlet turbulence level. The C_f values used to plot Fig. 2 were obtained from Clauser (1954) plots.

Flow Behind Rotors and Stators. A typical plot of the streamwise velocities for the rotor flows is shown in Fig. 3. The C_f values for the plots were obtained from the Ludwieg-Tillmann (1949) empirical relation given by:

$$C_f = 0.246 \, (U\theta/\nu)^{-0.268} e^{-1.56H} \qquad (2)$$

where, θ and H are calculated from the streamwise profile. The profiles exhibit a well pronounced linear semi-logarithmic region, typical of a normal turbulent boundary layer, but with the universal constants "A" and "B" very different from the standard values. The same observations were reported for flows behind an isolated rotor by Bhowmik (1979) and Prasad (1981). In the wake region (Fig. 3), the velocity profiles show signs of acceleration. The reason for this is evident from the velocity triangles at the boundary layer edge for inlet and outlet rotor flows illustrated in Fig. 4 (a). The flow relative to the rotor is turned towards the axial direction through the blade passage,
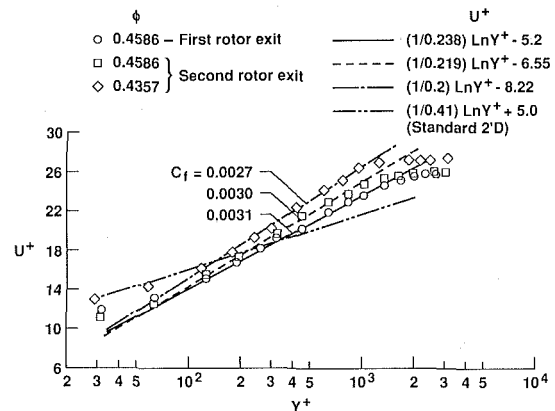
resulting in $\alpha_2 < \alpha_1$ and a decrease in the relative velocity, V_2. For a same blade velocity, Ωr_e, at the inlet and outlet of the rotor, the decrement in the relative velocity results in the increase in the absolute velocity. Also for values Y^+ about 10^2 and smaller, we get a large local velocity (Fig. 3). The reason for this is that, within the boundary layer, there is a large increase in the absolute tangential velocity, $u_{z,2}$ due to the axial velocity reduction (Fig. 4 (b)). Toward the casing wall the blade speed, Ωr increases. These effects result in the increase of the local streamwise velocity vector such that it is more than the boundary layer edge value. This overshoot of the near wall velocity is seen in the Fig. 3.

Boundary layers behind stators (Fig. 5) seems to approximate

Table 1 Comparison of C_f obtained from various methods

	First rotor exit		Second rotor exit		Third rotor exit	Fourth rotor exit
$\phi =$	0.4586	0.3493	0.4586	0.4357	0.4357	0.4586
C_f obtained from L. T. formula applied to streamwise profile	0.0027	0.0025	0.0027	0.0026	0.0028	0.0022
C_f obtained from equation 3 and $A = 1/0.41$ applied to streamwise profile	0.009	0.006	0.0094	0.0115	0.0103	0.0082
As second case but applied to untwisted profile	—	—	—	0.0101	0.008	—
As first case but applied to untwisted profile	0.0031	0.0024	0.003	0.0027	0.0029	0.0024
From the extrapolated measured values of $\overline{u_s' u_y'}$ to the wall	0.0024	0.0036	0.0034	0.0032	0.0032	0.002
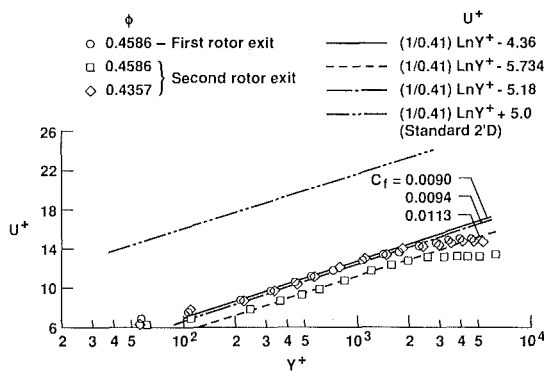
Fig. 7 Plot of the streamwise profile; C_f from equation (3)
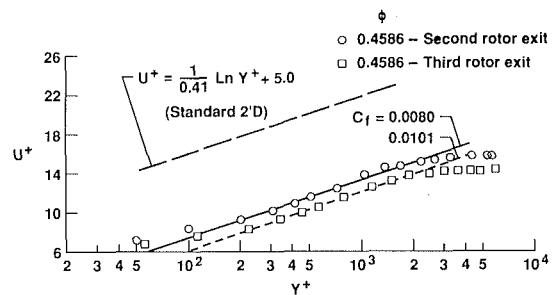

Fig. 8 Plot of the untwisted profile; C_f from equation (3)

to the two-dimensional standard profiles. It appears that the turbulent structure of the boundary layer is different for a shear layer immediately downstream of a rotating blade row due to the complexity of the flow than a naturally developing one, as in the flow past flat plate, resulting in the non-standard values of A and B. The structure of the turbulence seems to revert fairly quickly to its normal boundary layer form as it moves across the stators, the distance being 2 to 2.5 times the physical thickness of the boundary layer. Similar plot of the velocity profiles was attempted for the measured untwisted profiles (i.e., only magnitude of the total velocity vector is considered and not their streamwise components). This method of representation brings them no closer to the standard semi-log plot and the values of A and B are almost the same as before.

An attempt was made to obtain C_f from the slope of the law of the wall relation using the standard values of A. The law of the wall can be rewritten in the form:

$$u_s/U_s = A\sqrt{C_f/2}\ \mathrm{Ln}(y/\delta) + B\sqrt{C_f/2} \\ + A\sqrt{C_f/2}\ \mathrm{Ln}[(U_s\sqrt{C_f/2}\delta)/\nu] \quad (3)$$

The slope of the plot u_s/U_s versus y/δ and the corresponding C_f was used to replot the rotar streamwise profiles of Fig. 7. Because A has been forced to be equal to $1/0.41$, it is not surprising that the slopes correspond to the standard value. However, the plots lie well below the standard one. The same is true for the stator untwisted profiles (Fig. 8). The C_f values are very large and are about three times the Ludwieg-Tillmann value. Table 1 compares the values of C_f obtained from different methods. The measured values of $\overline{u_s' u_y'}$ when extrapolated to the wall gave C_f close to Ludwieg-Tillmann formula applied to the streamwise profile. Although extrapolation to the wall is not exact, the data support the conclusion that
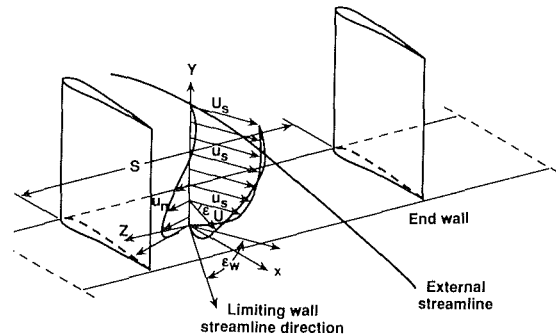
Fig. 9 Nomenclature of three-dimensional boundary layer
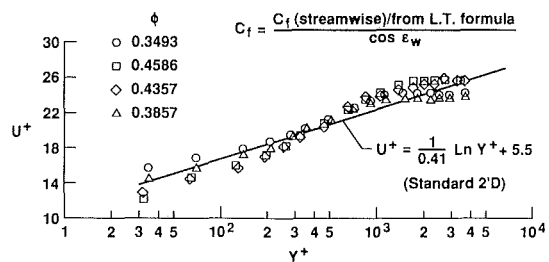
Fig. 10 Plot of the untwisted profile; third rotor exit

Ludwieg-Tillmann formula can be applied to the streamwise component of C_f with reasonable accuracy. The full value of C_f would then be the streamwise value divided by $\cos \epsilon_w$ and act in the limiting streamline direction (Fig. 9). When the untwisted profiles of the rotor flows with C_f values corresponding to the limiting streamline direction were plotted (Fig. 10), by and large there was a bunching of the profiles around the standard two-dimensional plot. Plot of the stator untwisted
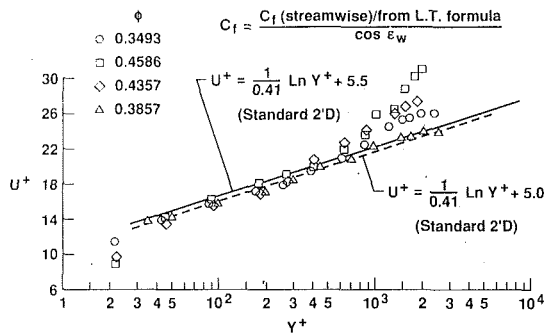
Fig. 11 Plot of the untwisted profile; second stator exit

profiles using the above procedure showed similar results (Fig. 11). In all of the plots the logarithmic scale corresponds to log base 10. However, the values of the constants quoted against each plot are computed with reference to natural logarithm.

Concluding Remarks

An experimental investigation was conducted into the flow in the casing wall region of a 4-stage, low speed axial compressor to verify the 'law of the wall' applicability to these complex flows. Some of the available shear stress models of the two-dimensional flows have been examined to quantitatively assess the skin friction.

When the casing boundary layer profiles are examined for agreement with the 'law of the wall', a semi-logarithmic region is seen to exist for both the stator and rotor flows. However, the universal constants 'A' and 'B' of the 'law of the wall' seem to be widely removed from the standard values, especially, for rotor flows. However, the situation changes for most of the stator flows where the velocity plots tend to approximate to the standard two-dimensional plot.

The skin friction, C_f, obtained from hot wire measurements extrapolated to the wall, give values close to the flat plate results. The C_f obtained from the Ludwieg-Tillmann formula applied to the streamwise or untwisted velocity profiles agrees closely with the hot wire results. When the measured profiles are forced to conform to the standard slope of the 'law of the wall', the resultant value of the C_f is three times higher than the above value.

Acknowledgments

References

Balsa, T. F., and Mellor, G. L., 1974, "The Simulation of Axial Compressor Performance Using Annulus Wall Boundary Layer Theory," ASME Paper No. 74-GT-56.

Bhowmik, S. K., 1979, "Hub Boundary Layer Development in Axial Impellers," Ph.D thesis, Department of Mechanical Engineering, Indian Institute of Science, Bangalore, India.

Bitterlich, W., and Kummel, W., 1977, "Zum Problem der Messung der Stromungegrossen mit Zweiloch-TotaldruckSonden bei Periodisch Instationarer Stromung in Axialen Turbomaschinen," *VDI-Z*, Vol. 119, No. 1-2, pp. 98–106.

Clauser, F. H., 1954, "Turbulent Boundary Layers in Adverse Pressure Gradients," *Journal of Aeronautical Sciences*, Vol. 21, pp. 91–108.

De Ruyck, J., Hirsch, C., and Kool, P., 1979, "An Axial Compressor End-Wall Boundary Layer Calculation Method," ASME *Journal of Engineering for Power*, Vol. 101, pp. 233–249.

Fugita, H., and Kovasznay, L. S. G., 1968, "Measurement of Reynolds Stress by a Single Rotated Hot Wire Anemometer," *Rev. Scientific Instruments*, Vol. 39, No. 9, pp. 1351–1355.

Gregory-Smith, D. G., 1970, "An Investigation of Annulus Wall Boundary Layer in Axial Flow Turbomachines," ASME *Journal of Engineering for Power*, Vol. 92, No. 4, pp. 369–376.

Hirsch, C. R., 1974, "End Wall Boundary Layers in Axial Compressors," ASME Paper No. 74-GT-72.

Horlock, J. H., and Perkins, H. J., 1974, "Annulus Wall Boundary Layers in Turbomachines," AGARDograph-No-185.

Howell, A. R., 1945, "Fluid Dynamics of Axial Compressors," *Proc. of Institution of Mechanical Engineers* (London), Vol. 153, pp. 441–452.

Klebanoff, P. S., 1955, "Characteristics of Turbulence in a Boundary Layer with Zero Pressure Gradient," NACA Report 1247.

Ludwieg, H., and Tillmann, W., 1950, "Investigation of the Wall Shearing Stress in Turbulent Boundary Layers," NACA TM-1285.

Mellor, G. L., and Wood, G. M., 1971, "An Axial Compressor End-Wall Boundary Layer Theory," ASME *Journal of Basic Engineering*, Vol. 93, pp. 300–316.

Oka, S., and Kostic, Z., 1972, "Influence of Wall Proximity on Hot Wire Velocity Measurements" DISA-Information, Vol. 5, pp. 29–33.

Nguyen, D. T., 1971, "Contribution a l'Etude de l'Ecoulement au Voisinage de l'EExtremite des Pales d'un Rotor," *Revue Thermique et Aeraulique*, Vol. 5, pp. 449–502.

Papailiou, K., Flot, R., and Mathieu, J., 1977, "Secondary Flows in Compressor Bladings," ASME *Journal of Engineering for Power*, Vol. 99, pp. 211–224.

Prasad, C. R. K., 1981, "Casing Boundary Layer Development in Axial Impellers with Tip Clearance," Ph.D. thesis, Dept. of Mechanical Engineering, Indian Institute of Science, Bangalore, India.

Railly, J. W., and Howard, J. H. G., 1962, "Velocity Profile Development in Axial Flow Compressors," *Journal of Mechanical Engineering Science*, Vol. 4, No. 2, pp. 166–176.

Railly, J. W., and Sharma, P. R., 1976, "Treatment of the Annulus Wall Boundary Layer Using a Secondary Flow Approach," ASME Paper No. 76-GT-52.

Rogers, B. K., and Head, M. R., 1969, "Measurement of Three-Dimensional Boundary Layers," *The Aeronautical J. of the Royal Aeronautical Society*, Vol. 73, pp. 796–798.

Smith, L. H., Jr., 1969, "Casing Boundary Layers in Multi-Stage Axial-Flow Compressors," Brown Boveri Symposium, *Flow Research on Blading*, Amsterdam.

Venkateswaran, S., 1983, "Casing Boundary Layers in Multi-Stage Axial Compressor," Ph.D. thesis, Dept. of Mechanical Engineering, Indian Institute of Science, Bangalore, India.

Experimental Investigation of the Flow With a Free Surface in an Impulsively Rotating Cylinder

Sangmin Choi

Department of Mechanical Engineering,
Korea Advanced Institute Science &
Technology,
Taejon 305-701, Korea

Jae Won Kim

Jae Min Hyun

Department of Mechanical Engineering,
Korea Advanced Institute Science &
Technology,
Seoul, Korea

An experimental investigation was made of the impulsive spin-up from rest of a liquid in a partially filled cylindrical container. The main impetus was placed on delineating the effects of the presence of a free surface on the transient development of flow. Of particular interest were the situations in which the free surface intersected either or both of the endwall disks during the course of spin-up. Extensive flow visualizations were carried out by using suspended metal particles. An image processing technique was utilized to determine accurately the propagating velocity shear front as well as the time-dependent free surface contour. Precise measurements of the fluids velocities were obtained by using a laser Doppler velocimeter. The transient velocity profiles were mapped out, and they were found to be in satisfactory agreement with the predictions based on the simplified analysis. The radial location, Rs(t), of the propagating shear front was measured by applying the image processing technique to the visualized azimuthal flow field. The experimental data were found to be consistent with the numerical predictions.

1 Introduction

One problem of central importance in modern rotating fluid dynamics is the issue of spin-up from rest (e.g., Wedemeyer, 1964; Homicz and Gerber, 1987). Let us consider a viscous incompressible fluid in a vertically mounted circular cylinder at rest. At a certain instant $t = 0$, the container is impulsively started spinning about its longitudinal axis, aligned parallel to gravity, at a finite constant angular speed Ω. The subsequent transient motions of the fluids, in response to the impulsive initiation of the rotation of the container, constitute the essence of the problem at hand. Here, the main interest is confined to the classes of flow for which the rotational Reynolds number $\mathrm{Re} \equiv \Omega R^2 / \nu$ (where R denotes the radius of a rotating cylinder and ν the kinematic viscosity) is sufficiently large. The transient fluid motions will persist until the entire body of the liquid acquires the same angular speed as that of the solid boundaries of the container. This time-dependent fluid flow poses a canonical problem of intrinsic significance to the basic fluid dynamics. The subject is highly relevant to such practical engineering applications as chemical mixers, centrifuges, and fluid machinery, etc.

The bulk of the previous studies on spin-up was concerned with the situations in which the cylindrical container was filled completely with a liquid (e.g., Wedemeyer, 1964; Weidman, 1976; Kitchens, 1980; Hyun et al., 1983). These prior accounts, encompassing elaborate analytical modeling efforts (Wedemeyer, 1964) as well as extensive and systematic laboratory and numerical experiments (Weidman, 1976; Watkins and Hussey, 1977; Hyun et al., 1983), have measurably deepened

our understanding of the principal dynamic ingredients involved in the process.

Recently, the question of spin-up of a liquid in a partially-filled cylindrical cavity has emerged to be of considerable concern. This has been motivated by the desire to acquire a clear understanding of the transient flow process affected by the presence of a free surface. Knowledge of such internal liquid flows is of direct relevance for the analyses of a liquid propellant rocket or a shell containing a liquid-filled cavity, to name a few. Also, the problem is of interest in its own right; this entails complex dynamical interactions between the Coriolis force, the pressure gradient and the viscous actions, and the additional effects due to the free surface deformation.

The earlier study of Goller and Ranov (1968) laid the groundwork to tackle the spin-up with a free surface. Utilizing the extended Wedemeyer-Goller-Ranov model, Homicz and Gerber (1986, 1987) gave a relatively simple numerical formula to properly depict the transient free surface shape as well as the dominant azimuthal velocity structure. An extensive experimental verification on the deformation of the free surface was recently performed by Choi et al. (1989).

The primary purpose of this study is to develop a carefully controlled experimental research program to undertake laboratory measurements of the unsteady flows in spin-up from rest in a cylinder. Considerable efforts have been expended to fabricate the experimental apparatus and install measurement systems. As asserted earlier, the objective here is to validate experimentally the predictions of the preceding numerical models, with particular reference given to the model of Homicz and Gerber, to deal with the cases when the free surface intersects either or both of the endwall disks.

It should be mentioned that a preliminary account of the present experiments was prepared recently (Choi et al., 1989). This previous experimental report illustrated only the transient contour of the free surface, which was shown to be in accord with the predictions of Homicz and Gerber's model (hereafter referred to as H&G model), including the cases when the free surface intersected the end walls. A major element of this paper is an experimental determination of the propagating velocity shear front and of the azimuthal flow characteristics. The experimental data will be thoroughly cross-checked against the available predictions, and critical appraisals will be made of the existing analytical models.

2 Overall Description of the Flow

Before proceeding to the details, it is useful to give an overall illustration of the outstanding features of the flow. Since the Wedemeyer model contributes the basic building block for the general theory of spin-up from rest, the highlights of the original Wedemeyer model, for a completely-filled cylinder, are briefly reviewed.

Taking cognizance of the axial uniformity of the dominant flow in the interior region for $Re \gg 1$, Wedemeyer (1964) proposed a greatly simplified differential equation. The radial (u) and azimuthal (v) velocities are taken to be functions of the radial coordinate (r) and time (t) only. In order to close the formulation, a functional form relating u and v, i.e., $u = f(r,v)$, has been postulated. After several physically insightful steps, the azimuthal flow field can be expressed as

$$v/R\Omega = (r/R \exp(2T) - R/r)/(\exp(2T) - 1.0),$$

$$\text{for } r/R > \exp(-T)$$

$$v/R\Omega = 0, \text{ for } r/R < \exp(-T),$$

where T is the characteristic time scale and depicted as

$$T = \left(0.886 \frac{R}{H}\right) Re^{-\frac{1}{2}} \Omega t.$$

The above results, commonly referred to as the Wedemeyer solution, clearly state that the azimuthal flow field can be divided into a nonrotating region for $r/R < \exp(-T)$ and a rotating region for $r/R > \exp(-T)$. The interface, $r/R = \exp(-T)$, represents a velocity shear front, which is seen to propagate radially inward from the cylinder sidewall to the central axis. These eminent features of the evolving velocity field have been qualitatively verified by the previous numerical as well as laboratory studies for a completely filled cylinder (e.g., Weidman, 1976; Watkins and Hussey, 1977; Kitchens, 1980; Hyun et al. 1983).

3 Experiments

The major components of the experimental apparatus are a high-quality rotating turntable, cylindrical containers, visualization and photographing systems, an image processing system and a flow velocity measuring device.

The rotating turntable was built with a precision-controlled AC-servo motor (0.4kW rating). The rotational speed of the turntable was controlled by varying the frequency of the input pulse signal. The speed was checked continuously by digital tachometer (ONO SOKKI, HT441) which received the reflection-light from a reflector on the rotating cylinder and by
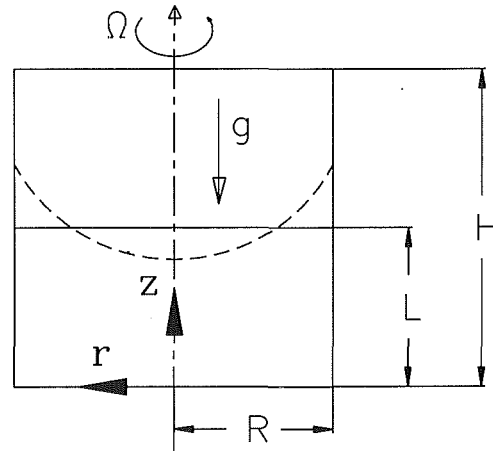

Fig. 1 Schematic diagram of the flow system

monitoring the signal from the servo unit. The turntable was capable of reaching the steady rotation within 0.05 ± 0.01 seconds measured from the voltage signal to the servo unit. The variation of the rotational speed was found to be less than ± 0.1 percent under the typical operational condition of 200 rpm. A series of cylindrical containers was fabricated with plexiglass. The cylindrical container was securely attached to the turntable; extreme care was exercised to ensure the upright configuration of the apparatus. The usual working fluid was pure water at $18 \pm 0.5°C$.

The general experimental techniques, together with the preliminary results displaying the transient free surface contour, have been described in the prior report (Choi et al., 1989).

One of the elementary, yet highly versatile, visualization techniques is by using aluminum powder suspended in the fluid. As is well-known, the disk-like particles are randomly oriented in the region where the fluid is nonrotating; however, a shearing motion tends to align these metallic particles in the primary direction of shear. The cylindrical tank was illuminated from the side by using a vertical sheet light beam. A 35 mm still camera and a video camera were used to record the visual images of light scattered by particles from a direction perpendicular to the slit beam. The intensity of the scattered light is a function of the number density of the suspended particles. As demonstrated in the representative photograph of Greenspan (see Fig. 1.4 of Greenspan, 1968), the shear front is clearly observable in the visualized picture as a demarcation of the bright and dark regions. Quantitative determination of the location of the shear front was made possible by employing an image processing technique. A digital image was enhanced by undergoing a filtering process and the image was converted into a set of binary data by prescribing a suitably-chosen threshold value to a plug-in type image processor (PC-Vision +, Imaging Technologies, Inc.). The digital image had a total of 256 gray levels. After undergoing a series of trial and error, the threshold value was selected to be customarily around the level 175. By this method, two distinct regions were identified; the bright area represented the nonrotating core region ahead of the front, and the dark area corresponded to the rotating region behind the front. The above-stated experi-

---

Nomenclature

Fr = Froude number = $(\Omega R)^2/gh$
g = gravitational acceleration
H = height of the container
L = initial depth of fluid in the container
r,θ,z = cylindrical coordinates
R = radius of the endwall disk

Re = Reynolds number
Rs = radial location of shear front
t = physical time
T = dimensionless time = 0.886 $(R/H)t/Re^{\frac{1}{2}}\Omega^{-1}$

u, v, w = velocity components in the $r-$, $\theta-$, and z-directions
κ, γ = exponents of numerical formula
ν = kinematic viscosity of fluid
Ω = angular speed

mental method, in conjunction with the image-enhancing technique, produced a clear-cut depiction of the shear front as a sharp demarcation between the bright and dark areas in the visualized plot. However, it should be emphasized again that, in reality, as can easily be deduced, the shear front represents a narrow zone in which the azimuthal velocity varies continuously with great rapidity. A more realistic description of the shear front, therefore, could be made in terms of a very thin band in which substantial flow gradients are concentrated.

Another concern of considerable practical implications is the optical distortion or the lens effect. This stems from the fact that the diametrical sections are viewed through a cylindrical volume of the fluid plus the plexiglass sidewall of the container. Consequently, the radial distance from the central axis, as viewed in the experiments, had to be corrected for the optical distortion. By conducting extensive test runs to calibrate the apparent radial distances against the known lengths, a relatively simple geometrical optical model was devised; this model accounted for the difference in the refractive indices of water and air. This optical correction model was incorporated in the quantifications of the cross-sectional image data. Combining these preliminary steps, the propagation of the shear front as well as the deformation of the free surface were examined by analyzing the sequential pictures obtained primarily for the visualized azimuthal flows.

For the velocity measurements, the laser Doppler velocimeter is an important and well-established experimental technique. This device was used in the present experiments to complement and cross-check the observations made by the flow visualizations. In a manner similar to the preceding work for a completely filled cylinder (e.g., Watkins and Hussey, 1977; Kawashima and Yang, 1988), extensive use was made of a laser Doppler velocimeter (TSI model 1990) together with a timer/counter unit interfaced to a personal computer. Care was taken to make an accurate determination of the location of the focal point (see the discussion of the correction method by Watkins and Hussey, 1977). The water inside the cylinder was seeded with a small amount of milk. An optimum seeding was found to be 1 to 2000 in volume ratio. A frequency shifter (TSI model 1980) was employed to remove noise signals from the irregular surface of the rotating container. This noisy signal can mainly be attributed to the non-uniform thickness of the rotating cylindrical sidewall. Typically, the velocity data were constructed by sampling 512 velocity measurements at an interval of 100 microsecond. This gives an averaging time of approximately 0.05 second.

Measurement uncertainties associated with the present experiments were evaluated according to the procedure of Moffat (1988) in terms of root-sum-square combination. Here, the measurement uncertainty was classified in the following three categories: 1) the one-dimensional determination of the location of the velocity shear front, 2) the errors in measuring the propagating distances of the velocity shear front from the consecutive images, 3) the lens distortion effects due to the difference in the refractive indices of water and air. The inherent errors of the measurement systems were corrected by repeating measurements and calibration. The uncertainty related with the effect of lens distortion was excluded by employing a geometric optics model. The one-dimensional reading of the shear front location was considered to be the most significant source of uncertainty. In the experiments, the boundary between the bright and dark area regions from the visualized photographs was defined as the location of the velocity shear front. The boundary was determined by assigning a proper threshold gray level for the light front. Since the image processing system handled 641×480 pixels, and the diametric cross-section of the rotating cylinder was typically 100 mm by 200 mm, the measurement volume had a resolution of 0.16 mm per pixel in the radial direction. At a typical rotating speed, the buoyant particle moved 0.66 mm in the axial di-
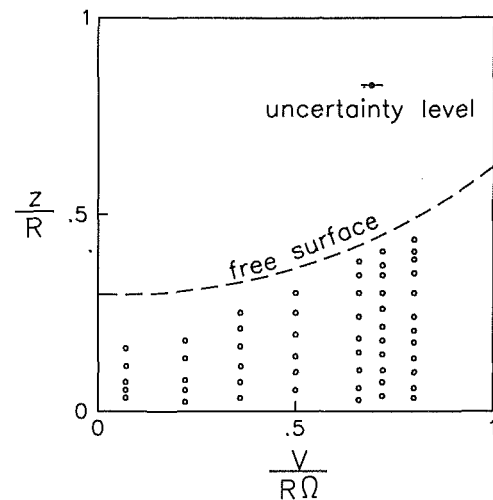

Fig. 2 Typical profiles of the azimuthal velocity field v and transient free surface shape. The radial positions are, from left to right, r/R = 0.07, 0.22, 0.36, 0.50, 0.66, 0.72, 0.80. Re = 1.13 × 10⁵, Fr = 0.4, L/H = 0.5, H/R = 3.0.
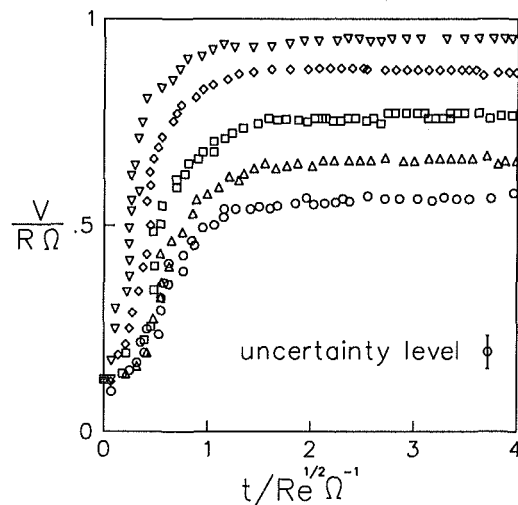

Fig. 3 Typical time—histories of the azimuthal velocity v

rection over a time period of two consecutive images; hence, the bias limit caused by this finite time difference between the two images was considered to be 0.66 mm. As a result, it can be asserted that the uncertainty in determining the location from the two consecutive images was 0.73 mm. In the present experiment, the average distance of the propagating velocity shear front over a time period of two consecutive images was approximately 9 mm. Therefore, the uncertainty in measuring the location of the velocity shear front was estimated to be 8 percent.

4 Results and Discussions

As remarked earlier, the experimental determination of the transient free surface contour and the attendant comparisons with the analytical predictions have been contained in the previous account (Choi et al., 1989). The present exposition, therefore, intends to highlight the salient experimental observations related to the velocity fields in the interior. These include the columnar nature of the dominant flows, the transient azimuthal velocity structure, and the propagating shear front.

4.1 Columnar Nature of the Flow. One essential building block of the existing models has been the assumption of the columnar flow in the interior. This implies that the horizontal velocities (u, v) are substantially uniform in the axial direction
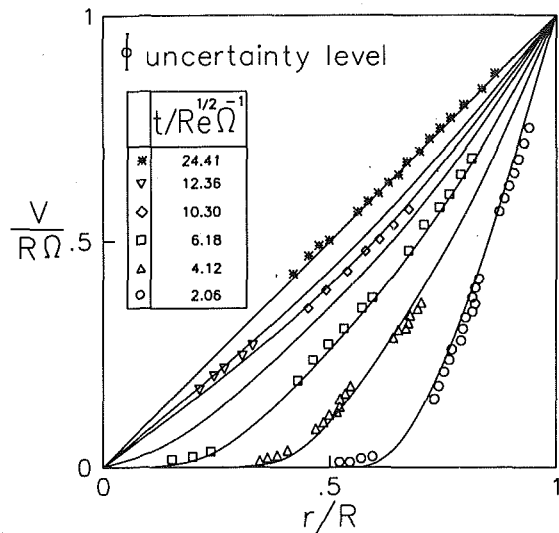
Fig. 4 Evolution of the azimuthal flow field. Times, $t\mathrm{Re}^{-1/2}\,\Omega$ are: *, 24.41; $\triangledown$, 12.36; $\diamond$, 10.30; $\square$, 6.18; $\triangle$, 4.12; $\circ$, 2.06. The symbols denote the present experimental measurements, and the solid lines the analytical predictions based on the model of Homicz and Gerber. $\mathrm{Re} = 3.4\times10^5$, $\mathrm{Fr} = 3.36$, $L/H = 0.5$, $H/R = 3.0$.

Fig. 6 Radial location of the propagating shear front, R_s. The final-state free surface intersects only the top endwall disk. $\mathrm{Re} = 2.3\times10^5$, $\mathrm{Fr} = 1.5$, $L/H = 0.7$, $H/R = 3.0$.
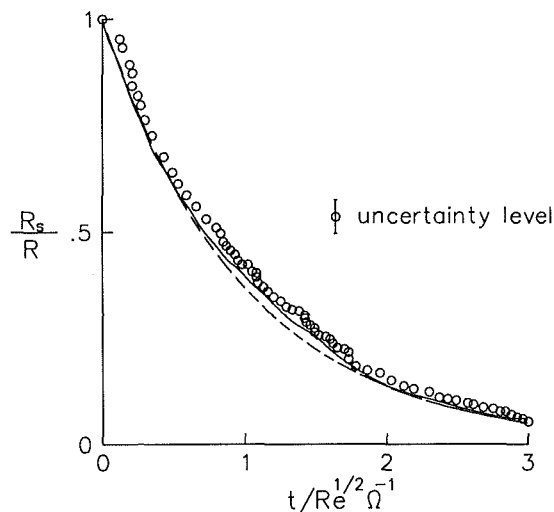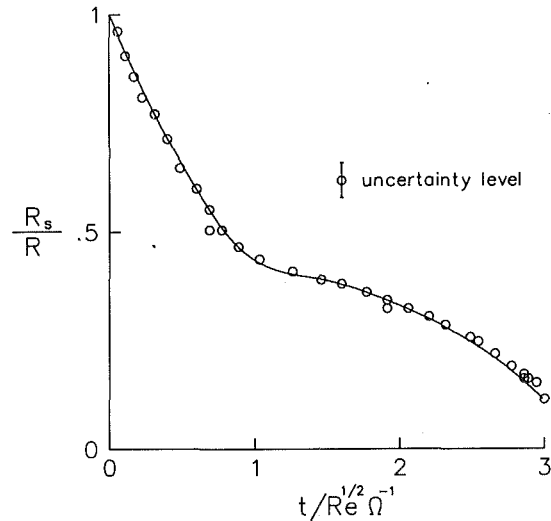

Fig. 5 Radial location of the propagating shear front, R_s. The final-state free surface intersects neither of the endwall disks. $\mathrm{Re} = 1.13\times10^5$, $\mathrm{Fr} = 0.4$, $L/H = 0.5$, $H/R = 3.0$.

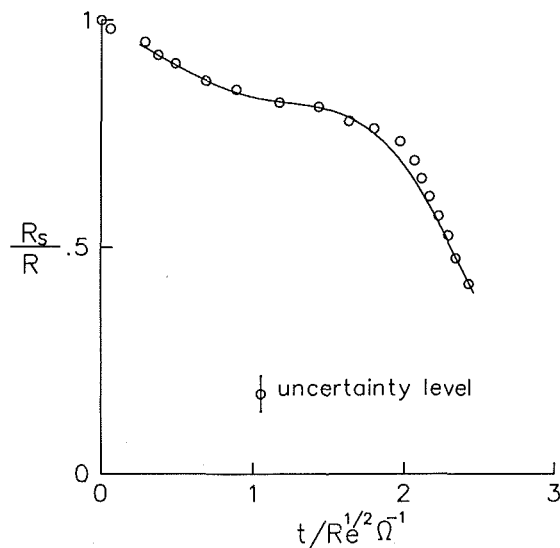**Fig. 7 Radial location of the propagating shear front R_s. The final-state free surface intersects both the top and bottom endwall disks. $\mathrm{Re} = 3.4\times10^5$, $\mathrm{Fr} = 3.36$, $L/H = 0.5$, $H/R = 3.0$.**

in the region far away from the boundary layers. Figure 2 gives a representative plot based on the LDV measurements. It is intended here to demonstrate the validity of the assumption used in the subsequent experiments.

The fluid is in a solid-body rotation when spin-up has been completed. This figure, however, plots normalized azimuthal velocities at several radial positions when the flow with a free surface displayed in this figure as a dotted line, is in a transient state ($t = 0.7T$). The characteristic of "columnar flow" is displayed even in the case of the rotating flow with a free surface. It can be concluded from this result that there is no need to try LDV measurements at the different axial positions because the propagating azimuthal velocity shear front poses a straight band in the meridional plane of a cylindrical container.

4.2 Transient Azimuthal Velocity. Figure 3 displays a comprehensive set of the LDV measurements of the transient azimuthal velocities at several radial locations along the same height of the container ($z/R = 0.25$). The radial position of LDV measurements is selected at an irregular interval from the sidewall of the container to the central axis. The measured

velocities at the corresponding radial locations are shown with symbols (O, $r/R = 0.55$;$\triangle$, 0.64; $\square$, 0.75; $\diamond$, 0.87; $\triangledown$, 0.93). The time histories shown here are corroborative of the basic theoretical contentions that the substantial flow transiency persists over a time span $O(\mathrm{Re}^{1/2}\,\Omega^{-1})$. This spin-up time scale, originally derived for the cases of a completely-filled container, is seen to be equally applicable to the flows with a free surface. Figure 3 also indicates that the gross pattern of transient evolution of the flows during $t \sim O(\mathrm{Re}^{1/2}\,\Omega^{-1})$ can be described to be approximately exponential; this behavior is qualitatively similar to the velocity evolution of Wedemeyer as summarized in the previous section, which is portrayed by the classical model for a filled cylinder.

Figure 4 gives the comparisons of the experimental data of the azimuthal velocities in the interior and the theoretical predictions due to H&G model. The solid lines in the figure denote the predictions and the symbols show the experimental results of the LDV measurements. Notice that, for the parameter values of Fig. 4, the free surface intersects the bottom end wall disk and the inner core becomes dry when $t/\mathrm{Re}^{1/2}\,\Omega^{-1}$ reaches somewhere around 10.3.

As is evident in the figure, the consistency between the experimental observations and the numerical predictions is highly encouraging. This close agreement is a clear manifestation in support of the numerical predictions. It should be mentioned that the model of Homicz and Gerber contains several heuristic, although physically plausible, approximations to arrive at a relatively simple expression for the Ekman pumping effects. When the free surface intersected the end walls, the experiments verified that the model was capable of predicting the transient free surface contour with a reasonable accuracy, as illustrated in our previous report. These critical assessments, with respect to both the transient free surface contour and the azimuthal velocity evolutions in the interior, provide concrete bases of credence to the main contentions of the H&G model due to Homicz and Gerber (1987).

4.3 Propagating Shear Front.

One significant dynamical element of the spin-up process is the presence of the radially-inward propagating azimuthal velocity shear front. As stated earlier, the classical solution of Wedemeyer for a completely filled cylinder gives the location of this front as $r/R = \exp(-T)$. No systematic experimental verifications have appeared in the literature regarding a precise depiction of the radial propagation of this front for the cases of partially filled cylinder as well as completely filled cylinder.

Figure 5 shows the radial location of the azimuthal velocity shear front, when the final state free surface does not intersect any one of the endwalls. There are three sets of results in this figure for comparison. The experimental results are displayed with circular symbols (o), the prediction as a solid line, using $\kappa = 1.0$, $\gamma = 1.01$, in accordance with the suggestion of H&G model. For comparison, the analytical solution by Wedemeyer is shown as a dotted line. Since the final-state shape of the free surface does not touch either of the endwall disks, only one Ekman layer at the bottom endwall disk is present. Therefore, for an effective cross-comparison, the curve representing the Wedemeyer solution, $r/R = \exp(-T)$, was constructed for a filled cylinder with the height twice the water level of the present experiment, i.e., $H = 2L$. As is discernible in Fig. 5, the agreement among the predictions and the experimental findings is satisfactory.

Figure 6 illustrates the results when the final-state free surface intersects only the top endwall disk. The symbols denote the experimental measurements, and the solid line represents the prediction due to the H&G model (using $\kappa = 1.0$, $\gamma = 1.01$). It is obvious that the propagation speed of the shear front for this case is lower than for the case displayed in Fig. 5. Obviously, the top endwall disk is only partially wet during the course of spin-up. This implies that the contribution of the Ekman layer at the top endwall disk is reduced. Consequently, the propagation of the shear front is retarded.

Figure 7 demonstrates the results when the final-state free surface intersects both the top and bottom endwall disks. The retardation of the propagation of the shear front is clearly discernible.

The comparisons shown above manifest close consistency between the predictions of Homicz and Gerber's model and the present experimental measurements. The validations exhibited in Figs. 5, 6, and 7 provide strong support to the adequacy and accuracy of the H&G model in portraying the propagation of the azimuthal velocity shear front.

In the present work, the values of the model constants, κ and γ in the model of Homicz and Gerber (see equations (10) and (15) of Homicz and Gerber, 1986), were fixed at $\kappa = 1.0$ and $\gamma = 1.01$. These are the values suggested in the orginial model development by Homicz and Gerber. At this point, a remark is in order. The experimental results seem to indicate that, for very high values of Fr, i.e., $Fr \geq 10.0$, closer agreement was attained between the measurements and the predictions when these model constants κ and γ were slightly adjusted to

higher values. The insights gained in the selection of the model constants will be addressed in detail in a subsequent paper.

5 Conclusions

Comprehensive laboratory experimental investigations have been undertaken with a view toward verifying the previous numerical models. Both the flow visualization studies and the laser Doppler measurements were performed to obtain quantitative data.

The assumption of the columnar flow, which is well accepted for the cases of rotating flow in a completely filled cylinder, is also found to be valid when there is a free surface, for the parameter values considered.

Transient development of the azimuthal velocity has been measured by using the LDV. The predictions of the model of Homicz and Gerber have been shown to be consistent with the experimental data for the azimuthal velocity field. The azimuthal velocities in the interior as well as the free surface contour are well represented by the numerical procedures for all possible cases of the final-state shape of the free surface.

The radially inward propagating azimuthal velocity shear front has been captured by flow visualizations. The location of the shear front has been determined by the image processing of experimental data. Although limited by an error bound restricted by the uncertainty analysis, the results indicate broad agreement between the experimental findings and the previous model predictions. The present experiments give strong support to the adequacy of the numerical model in predicting transient free surface contour and the evolutions of the velocity fields in the interior. The overall adjustment time is found to be comparable with the conventional spin-up time scale $Re^{1/2} \Omega^{-1}$.

References

Choi, Sangmin, Kim, J. W., and Hyun, J. M., 1989, "Transient Free Surface Shape in an Abruptly-Rotating, Partially-Filled Cylinder," ASME JOURNAL OF FLUIDS ENGINEERING, Vol. 111, pp. 439–442.

Gerber, N., 1975, "Properties of Rigidly Rotating Liquids in Closed Partially Filled Cylinders," ASME Journal of Applied Mechanics, Vol. 97, pp. 734–735.

Goller, H., and Ranov, T., 1968, "Unsteady Rotating Flow in a Cylinder with a Free Surface," ASME Journal of Basic Engineering, Vol. 90, No. 4, pp. 445–454.

Greenspan, H. P., 1968, The Theory of Rotating Fluids, Cambridge University Press, Cambridge.

Greenspan, H. P., and Howard, L. N., 1963, "On a Time Dependent Motion of a Rotating Fluid," Journal of Fluid Mechanics, Vol. 17, Part 3, pp. 385–404.

Homicz, G. F., and Gerber, N., 1986, "Numerical Model for Fluid Spin-Up from Rest in a Partially Filled Cylinder," AIAA paper AIAA–86—1121, pp. 1–9.

Homicz, G. F., and Gerber, N., 1987, "Numerical Model for Fluid Spin-Up from Rest in a Partially Filled Cylinder," ASME JOURNAL OF FLUIDS ENGINEERING, Vol. 109, pp. 195–197.

Hyun, J. M., Leslie, F., Fowlis, W. W., and Warn-Varnas, A., 1983, "Numerical Solutions for Spin-Up from Rest in a Cylinder," Journal of Fluid Mechanics, Vol. 127, pp. 263–281.

Kawashima, G., and Yang, W. J., 1988, "Unsteady Flow in Rotating Drums Using Laser Doppler Velocimetry," Experiments in Fluids, Vol. 6, pp. 165–171.

Kitchens, C. W. Jr., 1980, "Navier–Stokes Equations for Spin-Up in a Filled Cylinder," AIAA Journal, Vol. 18, No. 8, pp. 929–934.

Moffat, R. J., 1988, "Describing the Uncertainties in Experimental Results," Experimental Thermal and Fluid Science, Vol. 1, pp. 3–17.

Watkins, W. B., and Hussey, R. G., 1977, "Spin-Up from Rest in a Cylinder," Physics of Fluids, Vol. 20, No. 10, pp. 1596–1604.

Wedemeyer, E. H., 1964, "The Unsteady Flow within a Spinning Cylinder," Journal of Fluid Mechanics, Vol. 20, Part 3, pp. 383–399.

Weidman, P. D., 1976, "On the Spin-Up and Spin-Down of a Rotating Fluid. Part I: Extending the Wedemeyer Model. Part II: Measurements and Stability," Journal of Fluid Mechanics, Vol. 77, Part 4, pp. 685–735.

Velocity Bias Associated With Laser Doppler Anemometer Controlled Processors

A. R. Winter
Post-Graduate Student.

L. J. W. Graham
Post-Graduate Student.

K. Bremhorst
Associate Professor.

Department of Mechanical Engineering,
The University of Queensland,
Queensland 4072
Australia

The controlled processor has been proposed as a means of avoiding velocity bias in laser Doppler anemometry. A theoretical model is presented to show that results free of bias can be obtained if both the ratio of integral time scale to measurement time scale (integral scale data density) and the ratio of sampling time to the measurement time scale (normalized sample interval) are greater than five. Further, by separation of the integral scale data density and normalized sample interval parameters, it is shown that at any integral scale data density the controlled processor will not produce any less bias than a sample and hold processor and no more bias than the free running (unweighted) processor. In some situations it may be considered superior to the sample and hold processor as the data processing and hardware requirements are reduced without any loss of measurement accuracy. Experimental data confirming the theoretical results are also shown. Some of these data are contrary to at least one model available in the literature.

Introduction

Laser Doppler anemometry (LDA) has become widespread because of the nonintrusive nature of the measurements as well as its versatility of application in highly turbulent reversing flows and hostile environments. Its potential to provide highly accurate measurements in turbulent flows is, however, not often realized because of the problem of velocity bias. Velocity bias occurs because the LDA approximates the statistics of the flow by the sample statistics of the measured particle realizations. When the velocity fluctuates, the volume flow rate through the measuring volume varies with the velocity magnitude and direction. The rate of particle arrivals in the measuring volume is, therefore, strongly correlated with the fluctuations in the fluid velocity. Arithmetic averaging of the resultant velocity realizations (free running processor) will thus often produce a velocity result biased to a higher value than the actual flow velocity. McLaughlin and Tiederman (1973) predicted a bias equal to the square of the turbulence intensity for flows which are essentially one dimensional in nature with a turbulence intensity of less than 30 percent in the major flow direction.

The controlled processor (Stevenson et al., 1982; Erdmann and Tropea, 1981, 1984; and Edwards, 1981, 1987) has been put forward as a method of sampling LDA signals to reduce velocity bias. Its principle of operation is illustrated in Fig. 1. The validated particles, N_2, are all those particles with sufficient signal amplitude and quality to trigger the processor and not be rejected by the validation circuits. After the start of the measurement, the first particle to arrive is labelled $i = 1$ through

to the last particle labelled $i = N_2$, ($= 11$ in Fig. 1). The controlled processor, starting at a time ΔT_s from the start of the measurement, samples the validated data at equally spaced intervals of duration, T_s, rejecting all but the first particle signal to arrive in each interval. The accepted signals, N_3, are then averaged to give the required statistical quantities. This method of data processing has a distinct advantage over other correction schemes such as sample and hold processing and residence time weighting, Edwards (1987), as these require the time between particle arrivals and the particle residence time respectively. They also have more complicated algorithms than the controlled processor.

Edwards (1981) examined the velocity bias of a controlled processor for $T_s/\tau_c \ll 1$ over a range of ratios of T_s/τ_m. τ_c was defined, without further qualification, as the velocity fluc-
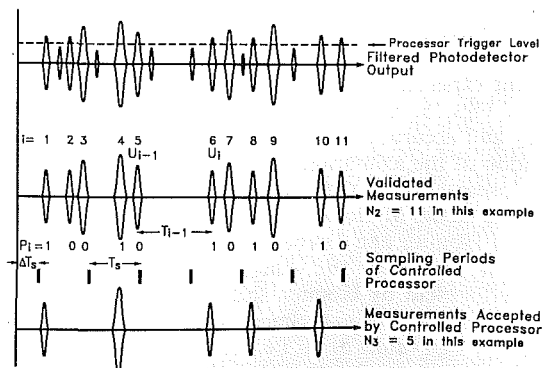

Fig. 1 Operation of the controlled processor - extension of Erdmann and Tropea (1981, 1984) representation.

tuation correlation time and τ_m the inverse of the validation rate. The results showed that the bias would be a minimum when a measurement is taken every sample period. No results were shown for larger values of T_s/τ_c. Much of the work was, however, on the effects of T_s being smaller than the residence time of the particle in the measuring volume. That aspect will not be examined in this paper.

Erdmann and Tropea (1981, 1984) produced a theoretical model which showed that given a sufficiently high particle rate and for $T_s/T_u \geq 1$, where T_u is the integral time scale of the flow, an unbiased velocity measurement is achieved. Their model also showed that if $T_s/T_u \rightarrow \infty$ velocity bias would disappear as the integral scale data density approaches zero. The case when $T_s/T_u \rightarrow \infty$ was defined as the one-shot processor. However, Edwards (1987) cast some doubt on the derivation by Erdmann and Tropea (1981, 1984) and recommended that further work was required on bias at low and intermediate data densities. Furthermore, there is a lack of published experimental data to verify the above claims.

A different approach to analyzing the velocity bias associated with a controlled processor has been taken in this paper. The effect on the velocity bias of the integral scale data density, T_u/τ_m, is treated separately to the effect of the normalized sample interval length, T_s/τ_m, rather than using T_s/T_u as done by Erdmann and Tropea (1981, 1984). This allows a direct comparison with the velocity bias associated with the sample and hold processor, which is widely accepted (Dimotakis, 1976; Edwards and Jensen, 1983; Edwards, 1987) as producing unbiased velocity results at a sufficiently high data density. A number of authors, Edwards and Jensen (1983) and Adrian and Yao (1987) have defined the data density as the ratio of the Taylor microscale and the inverse of the validation rate. To avoid confusion T_u/τ_m will be defined as the integral scale data density.

Theory

The controlled processor can best be analyzed by considering two modes of operation. The first is when the normalized sample interval is long, $(T_s \gg \tau_m)$, and the second is for all other sample interval lengths.

In the first case every sample interval of a controlled processor will contain at least one realization of which the first will be accepted and the remainder rejected. Thus, the probability of acceptance of a realization must be considered. Because T_s is constant, no correlation can exist between the interval starting times and particle arrival times or velocities. Since no correlation exists, the expected acceptance, $\langle P_i \rangle$, of a realization, i, is directly proportional to the interarrival time, T_{i-1}, between i and the previous realization, $i-1$. This is given by:

$$\langle P_i \rangle = T_{i-1}/T_s \qquad (1)$$

where $P_i = 1$ if the realization is accepted and $P_i = 0$ if it is rejected.

For a given value of ΔT_s, the mean output of a controlled processor for long normalized sample intervals is given by equation (2).

$$\overline{U}_{CP} = \Sigma\, U_i P_i / \sum P_i \qquad (2)$$

where $\Sigma\, P_i = N_3$, the number of points accepted, which is also given by $\Sigma\, T_{i-1}/T_s$. The summations in equation (2) are taken over the total number, N_2, of validated realizations in a measurement.

The expected value of $\overline{U}_{CP}$ taken for $0 \leq \Delta T_s < T_s$ is given by:

$$\langle \overline{U}_{CP} \rangle = \langle \Sigma\, U_i P_i / \Sigma\, P_i \rangle \qquad (3)$$

$$= \Sigma(U_i \cdot \langle P_i | U = U_i \rangle) \cdot T_s / \Sigma\, T_{i-1} \qquad (4)$$

where $\langle P_i | U = U_i \rangle$ is the expected value of P_i, $\langle P_i \rangle$ of equation (1), if the velocity is equal to U_i. Thus,

$$\langle P_i | U = U_i \rangle = \langle T_{i-1} | U = U_i \rangle / T_s \qquad (5)$$

and

$$\langle \overline{U}_{CP} \rangle = \Sigma\, U_i \langle T_{i-1} | U = U_i \rangle / \Sigma\, T_{i-1} \qquad (6)$$

The expected value of $\overline{U}_{CP}$ is, therefore, identical to that which would be achieved by a processor weighting each of the N_2 realizations by T_{i-1}. This is defined as arrival time weighting.

Nomenclature

$g_{SH}(U)$ = probability density function of velocity of a sample and hold processor

$\dot{N}_2$ = validation rate. The rate at which a signal processor with no dead time (e.g., processing time) would produce valid measurements or velocity realizations. N_2 is the total number of validated measurements, Fig. 1.

$\dot{N}_3$ = stored data rate. The rate at which the measurements are accepted by a controlled processor for averaging. N_3 is total number accepted.

$\dot{N}_{3max}$ = maximum rate of storage of measured velocities

P_i = acceptance of a particle, i, by a controlled processor. $P_i = 1$ indicates acceptance, $P_i = 0$ indicates rejection

$p(U)$ = probability density function of velocity

R_{uu} = normalized autocorrelation function

σ_m = standard deviation of the measured value of the mean velocity

σ_U = true rms of the flow velocity in the measuring volume

τ_c = velocity fluctuation correlation time, Edwards (1981)

T_i = time between the arrival in the measuring volume of particle i and particle $i+1$

τ_m = measurement time scale. Inverse of validation rate $(\dot{N}_2^{-1})$

T = total sample length of signal

T_s = sample interval time. Time between sampling intervals for a controlled processor. This may be hardware controlled at the signal processor or computer interface or software controlled.

T_s/τ_m = normalized sample interval

T_u = integral time scale of the flow defined by
$$T_u = \int_0^\infty R_{uu}(\tau)d\tau$$

T_u/τ_m = integral scale data density

ΔT_s = time period from start of LDA measurement to the start of the first sample interval

U = flow velocity under consideration

$\overline{U}$ = true mean flow velocity in the measuring volume

$\overline{U}_{CP}$ = mean velocity calculated by a controlled processor for a random value of ΔT_s

U_i = velocity of particle i

$\overline{U}_M$ = measured mean velocity

$\overline{U}_{SH}$ = mean velocity calculated by a sample and hold processor

$\overline{U}_{UNW}$ = mean velocity calculated by a free running processor

x/d = axial distance from jet exit normalized on the exit diameter

$\langle...\rangle$ = indicates expected value

At this stage, a comparison between the results of a sample and hold processor and the arrival time weighting processor is required. The mean velocity of a sample and hold processor as given by equation (7) has been shown by Winter et al. (1990), to produce results free of velocity bias if $N_2 T_u \geq 5$ where all validated data are accepted by the sample and hold processor. In calculating the flow statistics, each realization U_i is weighted with the interarrival time, T_i.

$$\overline{U}_{SH} = \Sigma \ U_i T_i / \Sigma \ T_i \qquad (7)$$

Winter et al. (1990) modelled the fluid flow with a variable speed "conveyor belt" type model. The seed particles are placed on the conveyor belt with a Poisson spatial distribution which is independent of the velocity of the particles. Therefore, the arrival probability per unit time is proportional to the instantaneous velocity magnitude of the particle. The movement of the flow is modelled as having a velocity persistence time which is the period of time after the arrival of a particle that the flow velocity may be considered, on average, to remain perfectly correlated. This was shown to be T_u, the integral time scale of the flow.

The interarrival time of two consecutive particles with a given spacing and velocity, U_i, of the first particle, is calculated by assuming the flow to have a velocity U_i for a period T_u after the arrival of the particle in the measuring volume, and the mean velocity of the flow, $\overline{U}$, for the remaining distance between the particles. This is integrated over all particle spacings in the Poisson distribution to determine the expected time between particles for a given velocity of the first particle. From this, equation (8), which gives the effect on the probability density function of velocity, $p(U)$, may be found, Winter et al. (1990).

$$\langle g_{SH}(U) \rangle = p(U)[1 - (1 - |U|/|\overline{U}|)\exp(-T_u/\tau_m \cdot |U|/|\overline{U}|)] \qquad (8)$$

where $p(U)$ is the probability density of U as measured by an instrument free of velocity bias or error. The measured mean velocity is given by integration of equation (8) over all values of U, just as the true mean velocity is obtained by integration of $p(U)$ over all U.

Using the above model based on weighting U_i by T_i, and given that the autocorrelation function used to determine T_u must be symmetrical about $\tau = 0$, the model may, without any changes, be used to model the arrival time weighted processor. Here, the interarrival time of two particles with a given spacing and given velocity, U_i, of the second particle, is calculated by assuming the flow takes on the velocity $\overline{U}$, for the time greater than T_u before the ith particle arrives in the measuring volume and a value U_i for the time less than T_u before arrival of the ith particle. As the model is the same for both cases, the expected statistics of the two methods of interarrival time weighting should, therefore, be the same. As it has already been shown that the expected statistics of a controlled processor with long normalized sample intervals are identical to those of an arrival time weighted processor, it follows from the above that they are also identical to the expected statistics of a sample and hold processor.

In the second case, $T_s \gg \tau_m$ is no longer true and, therefore, some sample intervals do not contain a measurement. As each particle can be accepted no more than once, the expected acceptance of P_i, where $T_{i-1} > T_s$, is no longer proportional to T_{i-1} as in equation (1) so that equation (9) holds.

$$\langle P_i \rangle = T_{i-1}/T_s \qquad (T_s > T_{i-1})$$
$$= 1 \qquad (T_s \leq T_{i-1}) \qquad (9)$$

Therefore, the results of a controlled processor become different to those of a sample and hold processor.

Again using the model of Winter et al. (1990), the effect the limit of $\langle P_i \rangle$ has on the controlled processor results may be
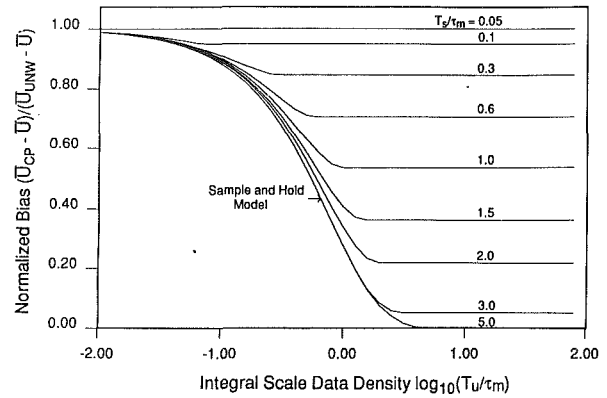

Fig. 2   Effect of normalized sample interval time on velocity bias

determined. When the model is slightly modified to put a limit of T_s on the maximum weighting time that can be applied to each particle, the weighting time is once again proportional to $\langle P_i \rangle$ and the bias produced by a controlled processor may be simulated.

By using a Gaussian velocity distribution in these calculations, the effect the normalized sample interval has on velocity bias can be shown, Fig. 2. For long normalized sample intervals ($T_s/\tau_m > 5$) there is no change to the original sample and hold model results over the range of data densities, while for short normalized sample intervals ($T_s/\tau_m < 0.05$) the bias remains at the maximum bias value for all data densities, the same as a free running processor.

From these results it is clear that the controlled processor cannot provide less velocity bias than the sample and hold processor for any normalized sample interval. When $T_s/\tau_m > 5$ both processors produce identical statistics. There is a smooth transition of the results to those of a free running processor which may now be defined as a controlled processor with $T_s/\tau_m < 0.05$. The bias produced by the controlled processor does not exceed that of a free running processor for any normalized sample interval.

Another result of interest is the effect of limited system speed on the velocity bias produced by a sample and hold processor. When the system speed is such that some realizations are not accepted, the data processing will be the same as with a controlled processor with T_s set by the system speed, followed by a sample and hold processor.

For the case where $T_s/\tau_m > 5$ the data to the sample and hold processor will be essentially equispaced and, therefore, each realization will be equally weighted. The result will then be the same as for a controlled processor which is seen from Fig. 2 to be equivalent to a sample and hold processor with no limitation in system speed. When $T_s/\tau_m < 5$, not all sample intervals will contain a measurement. Therefore, the next particle, U_i, to be measured after a blank interval will have $T_{i-1} > T_s$ and as mentioned previously, equation (1) will no longer hold. If, however, the particle is, in addition, accepted once for every blank interval of duration T_s before it, equation (1) would hold. It can be shown that this is achieved when either arrival time weighting or the sample and hold processor is applied to the output of the controlled processor. Therefore the resultant statistics are again equivalent to a sample and hold processor without system speed limitations. The results of a sample and hold processor should, therefore, be unaffected by the controlled processor effect of a system with a limited sampling speed.

Equipment and Instrumentation

LDA measurements were made in a 15.79 mm diameter axisymmetric steady air jet at a distance of $x/d = 30$ from the

exit plane on the centre line. The LDA used was a TSI system measuring one velocity component in the streamwise flow direction with an effective frequency shift of 5 MHz and counting eight cycles per burst. Measurements were taken at integral scale data densities from $T_u/\tau_m = 56$ to $T_u/\tau_m = 0.1$.

The output of the processor was sampled by the computer interface at 10.417 kHz, with the computer recording the velocity of the first particle to arrive in the previous 96 μs and its arrival time to a 6 μs resolution. The low integral scale data density measurements consisted of a minimum of approximately 10 000 stored realizations while up to 300 000 points were stored for the higher integral scale data density measurements with record lengths being 180 s and 30 s, respectively.

The data were subsequently processed using a computer to simulate the controlled processor. T_s could be varied within the sampling software to be any multiple of 96 μs. By using this method of sampling, the first validated realization after the beginning of a sample interval is always accepted, giving statistics identical to a typical controlled processor with hardware controlled sampling periods. Further, direct comparisons could be made with the sample and hold, arrival time, and free running processors by applying them to the identical raw data.

The controlled processor, particularly at long normalized sample intervals, accepts only a small percentage of the available measurements requiring very long signals to produce good statistical averages. The amount of data required was reduced by processing the available data a number of times for different values of ΔT_s. As the expected statistics are the same for all values of ΔT_s this does not affect the expected result other than to reduce the statistical scatter.

Because of the limited sampling rate of the processor/computer interface it was not possible to simulate a perfect free running processor. At higher data rates some measurements would be lost in the interface. Only when $T_s/\tau_m < 0.05$, where $T_s = 1/N_{3max}$, are the results identical to an infinitely fast, free running processor. It is clear that the free running processor used with this system is in fact a controlled processor with $T_s = 96\mu$s.

Error Analysis

Experimental errors in the LDA measurements have been quantified in three parts. The first part is due to fluctuations in the mass flow rate. The flow was regulated by monitoring the static pressure upstream of the nozzle contraction and manually adjusting a flow regulator valve. Including the effects of calibration drift of the manometer, this allowed an accuracy of ± 4 Pa in the static pressure giving an error of ± 0.25 percent in the velocity. The second error source to be investigated was the error in the individual burst measurements which can be attributed mainly to the limited digital resolutions of the signal processors. This resolution is typically less than 0.5 percent of the measured velocity. Since a large number of samples are used, any effect on the mean velocity will be the same for each data set and is, therefore, not relevant.

The third error source is introduced by the limited number of independent samples of the velocity. This can be brought about by too few LDA realizations or by too short a sample time. George (1979) showed that a time spacing of $2T_u$ is required between measurements for the samples to be independent and produced an equation for the variance of the estimated mean which incorporates both the signal length and number of samples:

$$\sigma_m^2/\overline{U}^2 = 2T_u/T(1 + 1/(2T_u\dot{N}_3))(\sigma_U/\overline{U})^2 \qquad (10)$$

where T is the total sample length of the signal, σ_U is the true rms of the velocity signal, and σ_m is the standard deviation of the measured value of the mean velocity. Therefore, for a given sample length, decreasing $\dot{N}_3^{-1}$ below $2T_u$ does not decrease
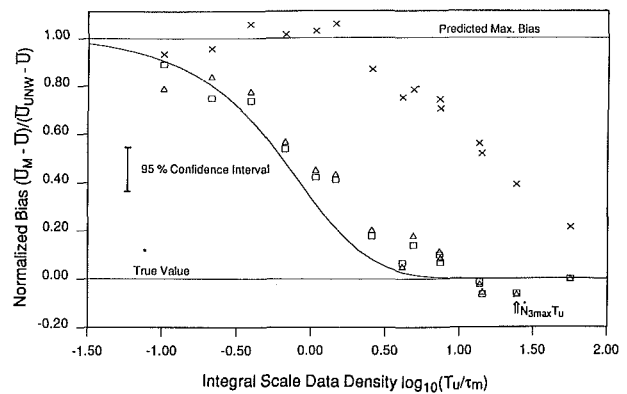

Fig. 3 Comparison of predicted bias with experimental data.
□ - sample and hold processor; △ - arrival time weighting processor; × - controlled processor, $T_s/\tau_m = 0.043$; ———— sample and hold model (from Fig. 2)

the statistical scatter. Similarly, for a fixed number of velocity realizations, increasing the length of a sample such that $\tau_m \gg 2T_u$ will not significantly improve statistical scatter. When the experimental data were inserted into equation (10), the standard deviation of the estimated mean velocity ranged from 0.17 to 0.35 percent of the mean. The total error for the measurements was determined by the root mean square of the individual errors and the 95 percent confidence interval. This produced an experimental uncertainty ranging from ± 0.45 to ± 0.7 percent of the mean velocity with an average of ± 0.52 percent. This error is shown on the figures.

Results and Discussion

The integral time scale of the flow was determined using the slotted time approach, Adrian and Yao (1987). This was determined to be 2.3 ms which agreed closely with T_u determined using a hot-wire velocity trace from the same flow.

Figure 3 shows normalized errors in the mean velocities for a range of integral scale data densities. The rate corresponding to the maximum interface rate, $N_{3max}T_u$, is also shown. The sample and hold and arrival time weighting results show no significant differences and compare well with the bias predicted with the model. As expected, the results of the free running processor show a constant value up to $T_u/\tau_m = 1.65$ corresponding to a data rate of approximately 720 samples/s and a normalized sample period of $T_s/\tau_m = 0.07$. Above this data rate, the normalized sample period increases and the velocity bias drops, approaching the unbiased limit. For $T_s/\tau_m > 5$ and all integral scale data densities, the controlled processor, when averaged over all ΔT_s gave results identical to the arrival time weighted results and are not shown separately on Fig. 3.

The effect of the normalized sample interval on velocity bias at fixed data density can be seen in a plot of measured mean velocity, Fig. 4. The raw data from a measurement with an integral scale data density of 0.75 shown in Fig. 3, were processed with a controlled processor for a range of normalized sample periods. These were plotted together with the sample and hold and arrival time weighting results from Fig. 3. As the sample interval increases the controlled processor results drop from a maximum value to become identical to the arrival time weighting. There is very little scatter in these results as they all originate from the same raw data and have been averaged over a range of values of ΔT_s.

The highest integral scale data density sample and hold measurement of Fig. 3 was considered to give the actual mean and rms of the flow and was used in the controlled processor model together with an assumed Gaussian velocity distribution to predict the results of the controlled processor for the range of normalized sample intervals presented in Fig. 4. The models
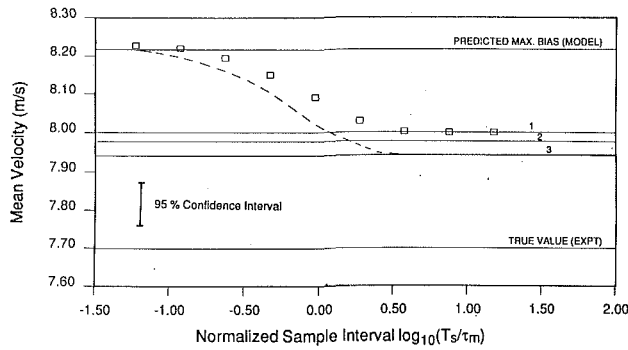
Fig. 4 Comparison of predicted controlled processor bias with exper-
imental data for integral scale data density = 0.75
□   controlled processor (expt.)
- - - - controlled processor (model)
——1—— arrival time weighting (expt.)
——2—— sample and hold processor (expt.)
——3—— sample and hold processor (model)

Fig. 5 Comparison of new model with Erdmann and Tropea (1981, 1984)
model.
- - - - - - - Erdmann and Tropea
————————— new controlled processor model

◇ experimental data $T_s/T_u = 0.043$
× experimental data $T_s/T_u = 0.17$
▽ experimental data $T_s/T_u = 10$

show a smooth transition of the controlled processor results
from the free running to the sample and hold processor results
as the normalized sample interval is increased. The theoretical
predictions for the sample and hold bias and maximum bias
compare well with the experimental results and are within the
uncertainty limits. Similarly, the controlled processor model
and experimental results compare well, verifying the smooth
transition of controlled processor results from sample and hold
results for $T_s/\tau_m > 5$ to free running processor results for $T_s/\tau_m < 0.05$. Due to the small error in the sample and hold result
from Fig. 3, a corresponding offset in the experimental con-
trolled processor results compared with the predicted results
is evident in Fig. 4.

The above results and discussion lead to the conclusion that
the bias mechanism associated with the integral scale data
density is completely independent of the mechanism associated
with the normalized sample interval. The former mechanism
is the real statistical velocity bias and is dependent on the
integral scale data density while the latter mechanism is purely
a sampling phenomenon and can be completely avoided by
sampling at the correct rate. This would indicate that the ratio
T_s/T_u used by previous authors, Edwards (1981) and Erdmann
and Tropea (1981, 1984), is not a fundamental independent
parameter in determining bias. If both $T_s/\tau_m > 5$ and $T_u/\tau_m > 5$, no velocity bias will exist whatever the ratio of T_s/T_u.
That is, neither the case of $T_s/\tau_m \gg 5$ and $T_u/\tau_m > 5$ nor
$T_s/\tau_m > 5$ and $T_u/\tau_m \gg 5$ would produce bias.

In Fig. 5 the results of the controlled processor model have
been replotted to show the normalized velocity bias parameter
as defined by Erdmann and Tropea (1981, 1984) and used in
their theoretical analysis of the controlled processor. These are
compared with the results of the Erdmann and Tropea (1981,
1984) model and three sets of the present experimental results
at different values of T_s/T_u. There is good agreement between
the two models at $T_s/T_u = 0.1$ although the Erdmann and Tro-
pea model does not quite reach a value of unity at a data
density approaching zero as the new model does. Experimental
results for ratios of $T_s/T_u = 0.043$ and 0.17 follow both models
well although scatter prevents firm conclusions to be drawn
regarding the limiting value of bias at low T_u/τ_m. However,
at $T_s/T_u = 10$, the experimental results and the prediction of
the model proposed in this paper agree well but diverge sig-
nificantly from the result of the model proposed by Erdmann
and Tropea (1981, 1984). The latter model predicts that bias
for $T_u/\tau_m \to 0$ will be small and will approach zero if the ratio
T_s/T_u approaches infinity. The new model and the experi-
mental results would indicate that for $T_u/\tau_m \to 0$ the normalized
bias approaches unity for all values of T_s/T_u. Although the
maximum ratio of T_s/T_u reached was over 300, no evidence
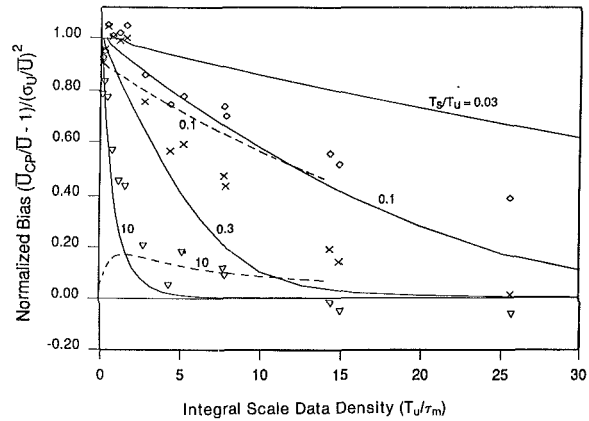
could be found to substantiate the conclusion reached by Erd-
mann and Tropea (1981, 1984) that large T_s and low data
density (one shot processor) will produce no bias.

Having an understanding of the velocity bias characteristics
of the controlled processor in relation to the sample and hold
processor allows a correct decision to be made regarding which
processor is most suited for a particular application. Whereas
the sample and hold processor allows a higher rate of meas-
urement, useful for spectral analysis, Adrian and Yao (1987),
and producing lower statistical scatter in measurements of
limited sample time, the controlled processor (with $T_s/\tau_m > 5$) which does not require as sophisticated a data processing
system, will not produce a larger velocity bias for a given data
density. The controlled processor has a simpler algorithm and
does not require any interarrival time information. By match-
ing the sample interval time to the speed of the data reduction
system used, measurements may be made in real time, avoiding
the necessity to store the raw data and reprocess it.

Conclusions

This work has shown that the velocity bias of a controlled
processor can be comprehensively modelled using the model
for the sample and hold processor, Winter et al. (1991). A new
approach was taken in that the bias effects of the integral scale
data density were separated from the bias effects of the nor-
malized sample interval. These were found to be independent
mechanisms of bias.

For a controlled processor to produce results free of velocity
bias, two criteria must be met:

1. $T_u/\tau_m > 5$

2. $T_s/\tau_m > 5$

For the case when $T_u/\tau_m > 5$ the controlled processor pro-
duces no bias when $T_s/\tau_m > 5$. It produces a maximum bias
when $T_s/\tau_m < 0.05$ which is the same as that produced by a
free running processor. Given that the two criteria stated above
are met, there will be no velocity bias regardless of the ratio
of T_s/T_u.

It was found that for a given integral scale data density,
velocity bias reaches a minimum when $T_s/\tau_m > 5$. This value
is identical to the bias associated with a sample and hold pro-
cessor at the same data density. A practical consequence of
this is that the sampling rate of the velocity realizations may

be reduced to match the data processing system speed without sacrificing accuracy. Also, the maximum bias is identical to the bias produced by a free running processor and is reached when $T_s/\tau_m < 0.05$. Therefore, a free running processor may be defined as a controlled processor with a normalized sample interval less than 0.05.

Acknowledgments

References

Adrian, R. J., and Yao, C. S., 1987, "Power Spectra of Fluid Velocities Measured by Laser Doppler Velocimetry," *Exp Fluids*, Vol. 5, pp. 17–28.

Dimotakis, P. E., 1976, "Single Scattering Particle Laser Doppler Measurements of Turbulence," *Appl. of Non-Intrusive Instrumentation in Flow Research*, AGARD CP-193, pp. 10.1–10.14.

Edwards, R. V., 1981, "A New Look at Particle Statistics in Laser-Anemometer Measurements," *J. Fluid Mech.*, Vol. 105, pp. 317–325.

Edwards, R. V., (Ed.) 1987, "Report of the Special Panel on Statistical Particle Bias Problems in Laser Anemometry," ASME JOURNAL OF FLUIDS ENGINEERING, Vol. 109, pp. 89–93.

Edwards, R. V., and Jensen, A. S., 1983, "Particle-Sampling Statistics in Laser Anemometers: Sample-and-Hold Systems and Saturable Systems," *J. Fluid Mech.*, Vol. 133, pp. 397–411.

Erdmann, J. C., and Tropea, C., 1981, "Statistical Bias in Laser Anemometry," SBF 80/ET/198, Aug. 1981, Sonderforschungsbereich 80, "Ausbreitungs- und Transportvorgänge in Strömungen," Universität Karlsruhe, FRG.

Erdmann, J. C., and Tropea, C., 1984, "Statistical Bias of the Velocity Distribution Function in Laser Anemometry," *Laser Anemometry in Fluid Mechanics*, Lisbon, Ladoan, pp. 393–403.

George, W. K., 1979, "Processing of Random Signals," *Dynamic Meas. in Unsteady Flows, Proceedings of the Dynamic Flow Conference*, Skovlunde, Denmark, pp. 757–800.

McLaughlin, D. K., and Tiederman, W. G. Jr., 1973, "Biasing Correction for Individual Realization of Laser Anemometer Measurement in Turbulent Flow," *Phys Fluids*, Vol. 16, pp. 2082–2088.

Stevenson, W. H., Thompson, H. D., and Roesler, T. C., 1982, "Direct Measurement of Laser Velocimeter Bias Errors in a Turbulent Flow," *AIAA Journal*, Vol. 20, pp. 1720–1723.

Winter, A. R., Graham, L. J. W., and Bremhorst, K., 1991, "The Effects of Time Scales in LDA Measurements Using Sample and Hold Processing," In press, *Exp. Fluids*, Springer.

A Method for Correcting Wall Pressure Measurements in Subsonic Compressible Flow

C. Ducruet

Institut de Mecanique des Fluides,
59000-Lille, France

A theoretical and experimental investigation has been made of the static pressure hole problem in subsonic flow. Thanks to a linearization, the effects of the boundary layer, of the velocity gradient and of the wall curvature could be separated so that a formula of correction containing three influence functions has been obtained. These functions were determined in the case of practical requirements by means of experiments made on appropriate models for two values of the depth-to-diameter ratio and for at least three values of the Mach number. Then, the method of correction has been applied to the flow around an airfoil at zero angle of attack.

1 Introduction

The wall pressure in a flow is usually obtained by means of a hole drilled in the wall and connected to a manometer. The presence of a hole, however small, disturbs the local flow and thus the registered pressure is not the true static pressure. The magnitude of the error is small but it can have important consequences: that is the case when the pressure distribution is used to determine a small quantity such as the drag coefficient of a slender body.

This problem has already been investigated on several occasions, mainly in turbulent pipe flow (Franklin and Wallace, 1970; Livesey et al., 1962; Myadzu, 1936; Ray, 1956; Shaw, 1960). Some experiments have also been made in high speed flow (Flack, 1978; Morrisson et al., 1966; Moulden et al., 1977; Pugh et al., 1970; Rainbird, 1967; Rayle, 1949).

As there are many discrepancies between these various results and the empirical correction formulae which are proposed are only valid under particular circumstances, one may consider the problem as still unsolved. Therefore, a research supported by the French Ministry of Defense has been undertaken, so as to provide a universal method of correction.

In 1984, the case of steady incompressible flow has entirely been solved for some values of the depth to diameter ratio h/d (Ducruet, 1983; Ducruet and Dyment, 1984). The aim of the present research is to extend the universal method of correction previously presented to subsonic compressible flow.

2 The Theoretical Approach in Subsonic Compressible Flow

We recall here the principle of the method of correction which has been presented in a previous paper (Ducruet and Dyment, 1986). As the properties of the fluid in the vicinity of the orifice can result from different flows, we have to consider the problem from a local point of view.

Let p_d be the pressure measured at the orifice of diameter d and p_0 the true pressure corresponding to $d = 0$. The flow is assumed to be steady, two dimensional, and adiabatic. Let x be the curvilinear abscissa along the wall, h the depth of the orifice, d_c the diameter of the cylindrical cavity located behind the orifice, u_e, ρ_e, p_e, ν_e, and M_e the velocity, density, pressure, kinematic viscosity, and Mach number outside the boundary layer, u_{e_x} the external velocity gradient, θ the momentum thickness of the boundary layer and γ the specific heats ratio.

A dimensional analysis shows that the error $\dfrac{p_d - p_0}{\frac{1}{2}\rho_e u_e^2}$ is a function of $\dfrac{u_e d}{\nu_e}$, $\dfrac{u_{e_x} d}{u_e}$, $\dfrac{d}{D}$, $\dfrac{d}{\theta}$, $\dfrac{h}{d}$, $\dfrac{d_c}{d}$, M_e and γ, both in laminar and in turbulent flow.

A more detailed analysis of the phenomenon and some experimental results have shown that the hole Reynolds number can be disregarded (Ducruet, 1983; Ducruet and Dyment, 1984). If it is assumed that the specific heats ratio γ is constant, one obtains for geometrically similar orifices $\left(\dfrac{h}{d} \text{ and } \dfrac{d_c}{d} \text{ constant}\right)$:

$$\frac{p_d - p_0}{\frac{1}{2}\rho_e u_e^2} = \psi\left(\frac{u_{e_x} d}{u_e}, \frac{d}{D}, \frac{d}{\theta}, M_e\right). \tag{1}$$

As the dimensionless parameters $\dfrac{u_{e_x} d}{u_e}$ and $\dfrac{d}{D}$ are generally small, we can do a partial linearization, so that

$$\frac{p_d - p_0}{\frac{1}{2}\rho_e u_e^2} = F + G_v \frac{u_{e_x} d}{u_e} + G_c \frac{d}{D} \tag{2}$$

where F, G_v, and G_c depend on $\dfrac{d}{\theta}$, on the nature of the boundary layer, whether laminar or turbulent, and also on the local Mach number M_e.

For $d \ll \theta$, F can be expanded and the previous formula can be written:

$$\frac{p_d - p_0}{\frac{1}{2}\rho_e u_e^2} = I_\theta \frac{d}{\theta} + I_v \frac{u_{e_x} d}{u_e} + I_c \frac{d}{D}. \qquad (3)$$

On the other hand, for $d \gg \theta$, the function F can be restricted to its asymptotic value, say F_1, so that we obtain:

$$\frac{p_d - p_0}{\frac{1}{2}\rho_e u_e^2} = F_1 + J_v \frac{u_{e_x} d}{u_e} + J_c \frac{d}{D}. \qquad (4)$$

Thanks to the linearization, all the coefficients I_θ, F_1, I_v, I_c, J_v, and J_c depend on the Mach number, but only I_θ and F_1 depend on the nature of the boundary layer.

3 Experimental Methods

3.1 The functions F, G_v, and G_c can only be determined experimentally. From a practical standpoint, for an airfoil, the velocity gradient and the wall curvature interfere only in the vicinity of the leading edge where the boundary layer is generally laminar and where θ is not large in comparison with d. On the other portion, which is the major part of the airfoil, only the influence of the boundary layer has to be taken into account. As a consequence, the knowledge of the asymptotic values J_v and J_c is sufficient to determine the effect of the velocity gradient and of the wall curvature. The function F has to be determined both in laminar and turbulent flows, but there is no need to determine the coefficient I_θ, because the case $d \ll \theta$ is rarely met on an airfoil in compressible flow.

3.2 The experiments have been conducted in a continuous-running wind tunnel of section 150×200 mm². All the models are equipped with holes of depth to diameter ratio equal to 1 or 3. The cavity behind the pressure hole is cylindrical and the diameter d_c is much larger than d in order to eliminate the influence of $\dfrac{d_c}{d}$. The holes have their axis normal to the wall

and the quality of the boring was carefully examined using a microscope magnifying 50 times and providing d with an accuracy of 10^{-2} mm.

The values of the diameter d have been selected so that a large range of the dimensionless parameters could be covered.

As the pressure error to be detected is very small, it must be estimated by differential measurements between a reference hole and other ones situated on the same generatrix of the model. These differential readings have been achieved with an accuracy of 2×10^{-2} mm of water by "Debro Miniscope" manometers. The reference pressure is measured using a mercury manometer and a cathetometer. In that way, we obtain $\dfrac{p_d}{p_i}$ for each value of the diameter, p_i being the stagnation pressure. Then, the extrapolation to $d = 0$ of the plots of $\dfrac{p_d}{p_i}$ versus d provides the true value $\dfrac{p_0}{p_i}$. As the two curves corresponding to $\dfrac{h}{d} = 1$ and $\dfrac{h}{d} = 3$ must give the same extrapolated value, the process is quite accurate. Next, the measurement of the stagnation temperature T_i allows the calculation of ρ_e and u_e so that we obtain the dimensionless error $\dfrac{p_d - p_0}{\frac{1}{2}\rho_e u_e^2}$ for each value of M_e.

4 Influence of the Boundary Layer

The function F must be determined in a flow without any velocity gradient or curvature. The chosen model was a flat plat at zero angle of attack, 500 mm long and 18 mm thick; its leading edge is such that the velocity gradient is positive and vanishes after a distance of about 100 mm. A housing is hollowed in the central part in order to receive elements equipped with 6 rows of orifices located between abscissae $\xi = 115$ mm and $\xi = 310$ mm.

The tests were realized at M_e equal to 0.44, 0.68 and 0.85. The boundary layer was tested using a small total-pressure probe.

The final results, including the incompressible case, are summarized in Figs. 1 and 2. These results have already been given by Ducruet and Dyment (1986).

Nomenclature

C_D = section drag coefficient, $\left(= \displaystyle\int_{\text{profile}} C_p \frac{d\eta}{l} \right)$

d = diameter of an orifice

d_c = diameter of the cavity at the back of the orifice

$D/2$ = radius of curvature of the wall

F = influence function of the boundary layer

G_v = influence function of the velocity gradient

G_c = influence function of the wall curvature

h = depth of an orifice

$I_\theta, I_v, I_c, F_1, J_v, J_c$ = particular values of the influence functions

C_p = pressure coefficient $\left(= \dfrac{p - p_\infty}{\frac{1}{2}\rho_\infty u_\infty^2} \right)$

l = model chord

M = Mach number

p = pressure

u = velocity

x = curvilinear abscissa along the streamline at the wall

θ = boundary layer momentum thickness

μ = viscosity

ξ, η = distances from the leading edge in the body fixed axis system

ρ = fluid density

Subscripts

d = referring to the hole of diameter d

0 = referring to the flow in the absence of the hole ($d = 0$)

e = referring to the local flow outside the boundary layer

∞ = referring to the upstream conditions

i = referring to the stagnation conditions

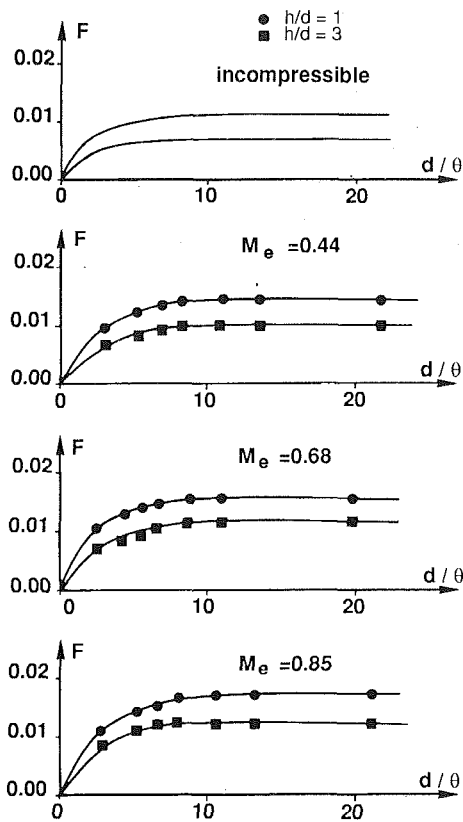x = derivative with respect to the curvilinear abscissa

Journal of Fluids Engineering

JUNE 1991, Vol. 113 / 257

Downloaded 02 Jun 2010 to 171.66.16.104. Redistribution subject to ASME license or copyright; see http://www.asme.org/terms/Terms_Use.cfm
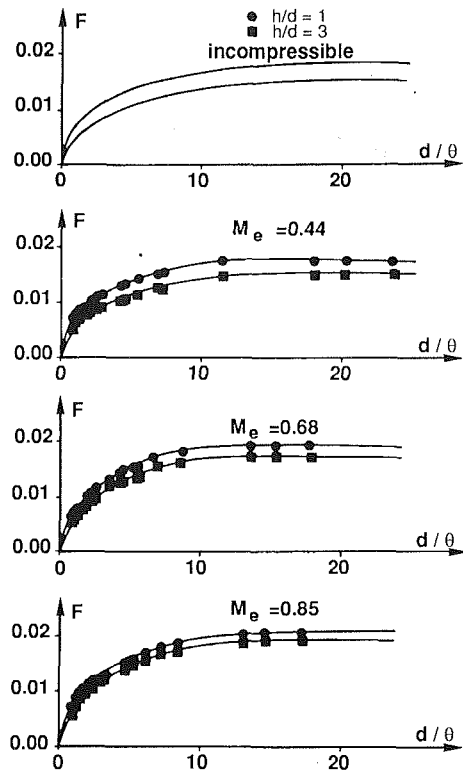
Fig. 1 Influence of the laminar boundary layer

Fig. 2 Influence of the turbulent boundary layer
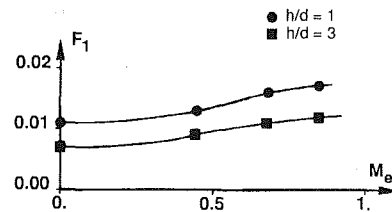
Fig. 3 F_1 in laminar flow

Fig. 4 F_1 in turbulent flow

It appears that F is an increasing function both of $\frac{d}{\theta}$ and M_e. The error is larger in the case of the turbulent boundary layer and it is more important for $\frac{h}{d} = 1$ than for $\frac{h}{d} = 3$.

The effect of M_e is more important in laminar than in turbulent flow.

For all the values of M_e and for the two ratios h/d, the asymptotic value F_1 is reached for $d \approx 8\theta$ in the laminar case and $d \approx 15\theta$ in the turbulent case. Figures 3 and 4 give F_1 as a function of the Mach number M_e.

A comparison may be made to some tests reported by Moulden et al. (1977), which have given $F_1 = 0.020$ for $\frac{h}{d} = 2.8$ and $M_e = 0.8$ in turbulent flow.

5 Influence of the Velocity Gradient and of the Wall Curvature

5.1 The coefficient J_v has been estimated on wedges in order to cancel the curvature effects. Measurements give access to $F_1 + J_v \frac{u_{e_x}d}{u_e}$ and, as F_1 is already known, J_v can easily be deduced.

Two wedges of angle 60 and 90 deg have been tested in order to cover a large range of variation of $\frac{u_{e_x}d}{u_e}$.

On one side the models are hollowed to receive interchangeable elements containing two rows of orifices located at the stations $x = 18$ mm and $x = 30$ mm. On the other side they are equipped with some holes used to determine the velocity gradient and the parameter θ. Several pairs of identical pressure taps located on either sides are used to check the symmetry of the flow.

The Mach numbers we have tested were 0.40, 0.50 and 0.65;

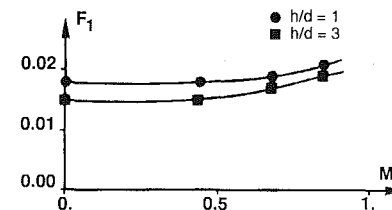the last one is the largest value which can be realized in our wind tunnel because of the blockage.

The results are gathered in Figs. 5 and 6.

As we can see, the linear formula is quite appropriate: straight lines are obtained with a slope J_v intersecting the $d = 0$ axis at the laminar value F_1 previously determined.

The values of J_v are given later.

5.2 As for the influence of the wall curvature, two cylinders of diameter 20 mm and span 150 mm were used. Four orifices are drilled on a generatrix of each cylinder. Experiments were made for azimuths between 20 and 50 deg.

As $\frac{d}{\theta}$ is always large, the measurements provide the complete formula (4).
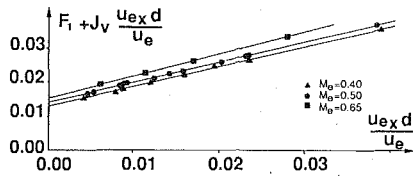
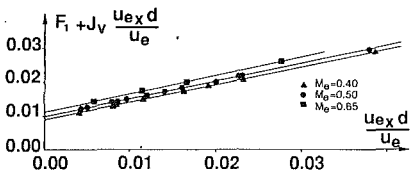Fig. 5   Influence of the velocity gradient $h/d = 1$

Fig. 6   Influence of the velocity gradient $h/d = 3$
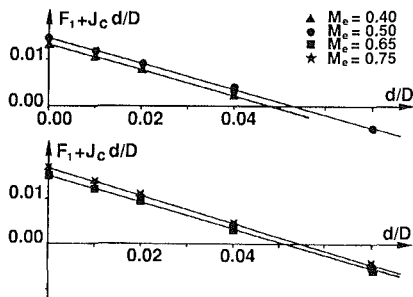

Fig. 7   Influence of the wall curvature $h/d = 1$
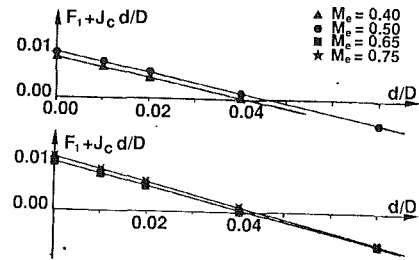

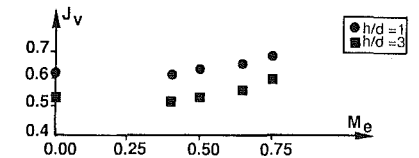Fig. 8   Influence of the wall curvature $h/d = 3$
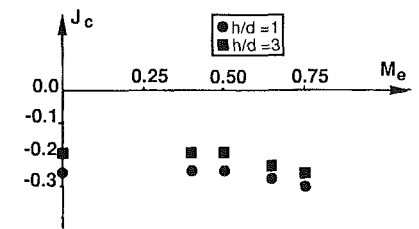

Fig. 9   Influence of M_e on J_v

Fig. 10   Influence of M_e on J_c

For M_e lying between 0.40 and 0.65, F_1 and J_v are known, so that J_c can be obtained by subtraction. For $M_e = 0.75$, only F_1 is known; J_v and J_c can be considered as unknowns in equation (4) and their values can be deduced from experiments. Finally, J_c can be calculated from Figs. 7 and 8, where $F_1 + J_c \dfrac{d}{D}$ is represented versus $\dfrac{d}{D}$.

It can be seen that J_c has negative values.

Figures 9 and 10 show the dependence of J_v and J_c on M_e. The value corresponding to $M_e = 0$ is reported from a previous work (Ducruet, 1983).

On the whole, it appears from these tests that the differences with the incompressible flow become significant only when approaching the transonic regime.

It must be noticed that experimental verifications have shown the linearized formulae to be valid for $\dfrac{u_{e_x} d}{u_e} \le 0.15$ and $\dfrac{d}{D} \le 0.10$.

6   Application to an Airfoil

In order to illustrate the magnitude of the error, the previous method has been applied to the flow around a NACA 0012 airfoil at zero angle of attack and Reynolds number based on the chord equal to $1.1 \cdot 10^6$. For that, we have used experimental results already obtained by Dyment and Gryson (1971) on a model of chord 80 mm equipped with 36 orifices and at an upstream Mach number of 0.6. The holes are 0.2 mm in diameter, but the ratio $\dfrac{h}{d}$ is not known precisely; its value lies between 1 and 3.

The radius of curvature, the boundary layer and the velocity gradient have been calculated. The results indicate that up to $\dfrac{x}{l} \approx 20$ percent the boundary layer is laminar and $\dfrac{d}{\theta}$ is always larger than 8.

On the remaining of the model, $\dfrac{d}{\theta}$ decreases and becomes equal to 0.9 at the trailing edge.

The velocity gradient and the wall curvature interfere up to $\dfrac{x}{l} \approx 6$ percent. Moreover, the parameter $\dfrac{u_{e_x} d}{u_e}$ is always smaller than 0.17 which represents the limit of validity of the linearized formula (Ducruet, 1983).

As a consequence, the full formula (4) has to be applied from the leading edge to $\dfrac{x}{l} \approx 6$ percent. On the remaining part of the airfoil, the error is reduced to F. As h/d is uncertain, we have calculated the correction both with $h/d = 3$ and $h/d = 1$.

The knowledge of the nondimensional error leads to the true pressure coefficient $C_{p0} = \dfrac{p_0 - p_\infty}{\dfrac{1}{2}\rho_\infty u_\infty^2}$. Afterwards, the actual pressure drag coefficient C_{D0} is calculated by integration of C_{p0} and then compared with the drag C_D deduced from the measured pressures: it has been found that C_D is about 8 percent larger than C_{D0} for $h/d = 3$ and 11 percent for $h/d = 1$. It can be anticipated that the correction will be more severe with nonzero angle of attack.

7   Conclusion

The present study furnishes a complete knowledge of the hole-pressure error for values of local Mach numbers up to 0.75, whereas the effect of the boundary layer has been evaluated up to $M_e = 0.85$. These results allow the correction of numerous experiments on airfoils in subsonic flow.

As for the influence of compressibility, the experiments indicate that the results obtained in incompressible flow are still valid as long as the local Mach number remains lower than

about 0.40. However the effects of the Mach number become significant when approaching the transonic regime.

It must be noticed that the method of correction is not very easy to use because it requires the calculation of D, u_e, u_{e_x}, θ, and M_e. In wind tunnel experiments, the velocity u_e is obtained with sufficient accuracy from the local pressure measurement and the stagnation conditions, under the assumption of isentropic flow. The values of the radius of curvature and of the velocity gradient may easily be calculated by a least squares fit of some appropriate spline function to the body coordinates and to the measured external velocity. The boundary layer momentum thickness θ may be obtained with a good enough precision by an integral method, using the measured pressure distribution. It is obvious that the major difficulty is the determination of the location of an eventual transition. However the interest of the method is well exemplified by the results for an airfoil where the pressure drag magnitudes obtained by integrating the raw and the corrected pressures are significantly different.

Finally, it must be emphasized that this method is to be applied only when measurements are accurate enough for the experimental uncertainty to be smaller than the error!

References

Ducruet, C., 1983, "Détermination exacte de la pression pariétale dans un écoulement," Thèse de doctorat d'état, Université de Lille.

Ducruet, C., and Dyment, A., 1984, "The Pressure Hole Problem," *J. Fluid Mech.*, Vol. 142, pp. 251-267.

Ducruet, C., and Dyment, A., 1986, "A Method for Correcting Wall Pressure Measurements in a Flow," ASME Winter Annual Meeting, Anaheim, Ca., Nov.

Dyment, A., and Gryson, P., 1971, "Etude en écoulement plan subsonique et transsonique du profil," NACA 0012-Transition libre, Rapport IMFL n° 1046 SR.

Flack, R. D., 1978, "Static Pressure Hole Errors in Transonic Flow with Pressure Gradient," *ISA Trans.*, Vol. 17, pp. 89-95.

Franklin, R. E., and Wallace, J. M., 1970, "Absolute Measurement of Static Hole Error Using Flush Transducers," *J. Fluid Mech.*, Vol. 42, pp. 33-48.

Livesey, J. L., Jackson, J. D., and Southern, C. J., 1962, "The Static Hole Error Problem," *Aircraft Engng*, Vol. 34, pp. 43-47.

Morrisson, D. F., Sheppard, L. M., and Williams, M. J., 1966, "Hole Size Effect on Hemisphere Pressure Distributions," *J. R. Aero Soc.*, Vol. 71, pp. 317-319.

Moulden, T. H., Wu, J. M., Collins, F. G., and Ramon, H. J., 1977, "Experimental Study of Static Pressure Orifice Interference," Arnold Eng. Dev. Center Tr 77,57.

Myadzu, A., 1936, "Über den Einfluß der Bohrungen auf die Druckanzeige.," *Ing. Arch.*, Vol. 7, pp. 35-41.

Pugh, P. G., Peto, J. W., and Ward, L. C., 1970, "Experimental Verification of Predicted Static Hole Size Effects on a Model With Large Streamwise Pressure Gradients," NPL Aero Rep. 1313 ARC 31, 900.

Rainbird, W. J., 1967, "Errors in Measurement of Mean Static Pressure of a Moving Fluid Due to Pressure Holes," *DME/NAE Q. Bull.*, Vol. 3, pp. 55-89.

Ray, A. K., 1956, "On the Effect of Orifice Size on Static Pressure Reading at Different Reynolds," Transl. in ARC Rep. TP 498.

Rayle, R. E., 1949, "An Investigation of the Influence of Orifice Geometry on Static Pressure Measurement," M.S. thesis MIT.

Shaw, R., 1960, "The Influence of Hole Dimensions on Static Pressure Measurements," *J. Fluid Mech.*, Vol. 7, pp. 550-563.

A Cavitation Susceptibility Meter With Optical Cavitation Monitoring—Part One: Design Concepts

L. d'Agostino[1]

A. J. Acosta

California Institute of Technology,
Pasadena, Calif. 91125

This work is concerned with the design of a Cavitation Susceptibility Meter based on the use of a venturi tube for the measurement of the active cavitation nuclei concentration in water samples as a function of the applied tension. The operation of the Cavitation Susceptibility Meter is analyzed and the main considerations leading to the proposed design are illustrated and critically discussed. The results of this analysis indicate that the operational range is mainly limited by nuclei interference, flow separation and saturation (choking), and suggest to develop a Cavitation Susceptibility Meter where: (a) the flow possesses a laminar potential core throughout the venturi throat section in all operational conditions; (b) the pressure at the venturi throat is determined from the upstream pressure and the local flow velocity; (c) the detection of cavitation and the measurement of the flow velocity are carried out optically by means of a Laser Doppler Velocimeter; (d) a custom-made electronic Signal Processor incorporating a frequency counter is used for real time data generation and temporary storage; (e) a computerized system performs the final acquisition and reduction of the data.

1 Introduction

It has long been recognized (Knapp et al., 1970) that the occurrence of cavitation is controlled by weak spots, generically called "nuclei", which act as preferential points for the onset of liquid rupture and significantly reduce the tensile strength of the liquid. The inception, development, and scaling of cavitation are greatly influenced by the concentration of cavitation nuclei which become active at a given pressure level. The problem of cavitation nuclei detection has received considerable attention in view of the importance of cavitation in a wide variety of technical applications (Billet, 1986; Billet, 1985). Photography, holography, acoustical and optical scattering, Coulter Counters and acoustical attenuation have all been used in the past to detect cavitation nuclei and measure their size concentration distribution. However, the tensile strength of all kinds of nuclei except microbubbles is not directly related to their size and therefore little quantitative information can be obtained from the above methods on the critical tension which makes each nucleus unstable, as required for cavitation studies. This limitation is overcome in Cavitation Susceptibility Meters (CSM), instruments first proposed by Oldenziel (Oldenziel, 1982a; Oldenziel, 1982b), where cavitation occurring in the internal flow through a venturi tube is directly monitored. Ideally, if the size of the venturi throat region and the nuclei concentration are sufficiently small, each

nucleus can cavitate individually in carefully controlled conditions and the concentration of active cavitation nuclei at any given pressure can be directly measured. In the CSM developed by Oldenziel cavitation takes place in a glass venturi and is detected optically, while in other applications (Lecoffre and Bonnin, 1979; Le Goff and Lecoffre, 1983; Shen et al., 1984) stainless-steel venturi tubes are used and cavitation bubbles are recognized acoustically from the noise generated by their collapse.

Mutual interference between cavitation nuclei and saturation (chocking) in the venturi throat at high nuclei concentration modify the pressure with respect to its steady noncavitating value and limit the useful operational range of CSM's. Flow separation in the diffuser and the occurrence of sheet cavitation in the throat section of the venturi tube due to the higher susceptibility of surface nuclei with respect to free stream ones also represent possible causes of malfunction in CSM's. As shown later in this paper, these difficulties are quite severe and must be carefully controlled by proper design of the CSM. On the other hand, the main advantages of CSM' consist in the capability of measuring the nuclei critical tension and concentration directly (thus eliminating the problem of the uncertain behavior of particles as cavitation nuclei), in the relative speed and convenience of data analysis and in the absence of limitations on the minimum size of cavitation nuclei that can be detected. These distinct advantages make CSM's an attractive alternative to other nuclei detection techniques for the purpose of cavitation research. The present study is part of our current work on this subject (d'Agostino, 1987; d'Agostino et al., 1989)
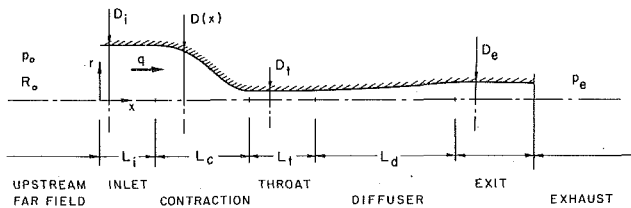
Fig. 1 Geometry and nomenclature of axisymmetric CSM venturi duct

and reports the main considerations leading to the design of the CSM recently developed at the California Institute of Technology. For conciseness the implementation and operation of the whole system are described in detail in a companion paper (d'Agostino and Acosta, 1991).

2 Bubble Dynamics and Venturi Geometry

The configuration of the axisymmetric CSM venturi pipe considered in the present study in shown in Fig. 1. The flow originates from the far field on the left (subscript 0), representing the sampled liquid, passes through the venturi and finally reaches the exhaust region on the right. Both the upstream and downstream conditions are supposed to be independent on time t. Let x be the space coordinate along the venturi centerline. A volume flux $q(t)$ of liquid with density ρ and kinematic viscosity ν flows with average axial velocity $u(x, t)$ through the venturi of local diameter $D(x)$ and cross-sectional area $A(x) = \pi D^2(x)/4$. The venturi duct is divided in five segments: a cylindrical inlet (subscript i), a contraction (subscript c), a cylindrical throat (subscript t), a diffuser (subscript d), and a cylindrical exhaust (subscript e). The length L of each segment of the duct is shown in the same figure; the inlet contraction area ratio is: $C_c = A_t/A_i$ and the diffuser expansion area ratio is: $C_e = A_e/A_t$.

By means of various assumptions and approximations, a simplified model can be derived which adequately represents the operation of CSM's in terms of a limited number of relevant parameters (see Fig. 2). The investigation of their mutual relations leads to a functional description of CSM operation which enables one to address the problem of their design in a systematic and organic way.

In cavitation research literature the liquid quality of a sample is usually expressed by means of the nuclei number concentration density distribution: $N(R_0) = -dn(R_0)/dR_0$, where
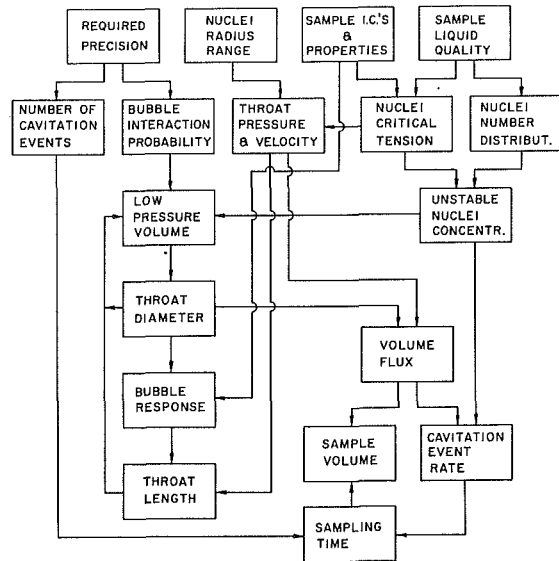

Fig. 2 Block diagram of CSM parameters

$n(R_0)$ is the number concentration of nuclei whose equilibrium radius is not smaller than R_0. The nuclei number distributions of water samples of technological interest spread in practice over a very large range and in most cases approximately follow a hypergeometric distribution (Bader, 1970). Here, for simplicity, we assume $N(R_0) = K_N/R_0^3$ and therefore $n(R_0) = K_N/2R_0^2$, with $K_N = 10^{-1}$ m^{-1}. This value is generally representative of the data from technical waters reported in the literature for the radius range from 10 to 100 μm considered in this analysis (O'Hern et al., 1988). However, errors by an order of magnitude on both sides are quite possible in practice because of the large dispersion of liquid quality data reported in the literature.

Bubble dynamics closely models cavitation from any kind of nuclei as the cavity grows bigger than the original nuclei size. We thus assume for simplicity that all the nuclei consist of equilibrium gas bubbles, whose critical tension with respect to quasi-static mechanical stability (Knapp et al., 1970) is expressed by:

$$(p_v - p)_{cr} = \frac{4S}{3R_0}\left[3\left(1 + \frac{p_0 - p_v}{2S/R_0}\right)\right]^{-1/2} \tag{1}$$

———— **Nomenclature** ————

A = cross-sectional area
C_c = venturi contraction coefficient
C_e = venturi expansion coefficient
C_{p_e} = exhaust pressure coefficient
D = venturi diameter
d_x, d_y, d_z = principal axes of the LDV focal ellipsoid
f = frequency, focal length, probability density distribution
f_D = Doppler frequency or its data value
K_N = nuclei number distribution parameter
L = length
L_f = detection length of a bubble or cavitation nucleus

m = index of refraction
$n(p_t)$ = concentration of nuclei with critical pressure not smaller than p_t
$n(R_0)$ = concentration of nuclei with equilibrium radius not smaller than R_0
N = integer number
$N(R_0)$ = nuclei number concentration density distribution
p = pressure
p_b = bubble external far field pressure
p_g = bubble noncondensable gas pressure
p_t = venturi throat pressure
p_u = venturi upstream pressure
Pr = probability
q = volume flux, Gaussian beam complex parameter

R = radius, bubble or cavitation nucleus radius
$1/R$ = laser beam wave front curvature
R_f = detection radius of a bubble or cavitation nucleus
$1/R_f$ = laser beam wave front curvature at the LDV focal point
Re = Reynolds number
s = LDV beam semi-separation
s_{fr} = fringe spacing
S = surface tension
t = time
t_f = detection time of a bubble or cavitation nucleus
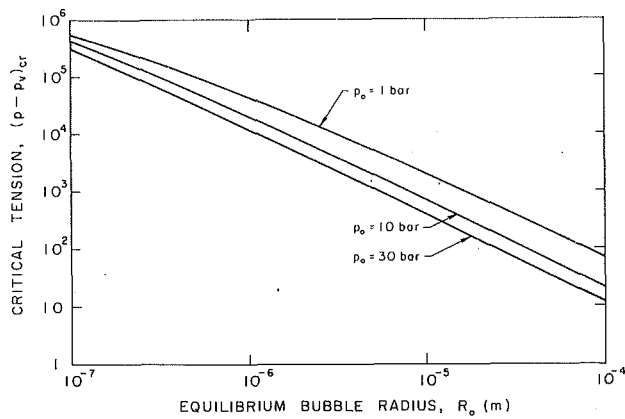T = temperature
T_g = Doppler gate time
u = velocity

Fig. 3   Critical tension $(p - p_v)_{cr}$ of a spherical air bubble v/s its equilibrium radius R_0 in water at various pressures $p_0 = 1$, 10 and 30 bar and $T = 20°C$ (surface tension $S = 0.073$ N/m, vapor pressure $p_v = 1919$ Pa, water density $\rho = 1000$ kg/m³).
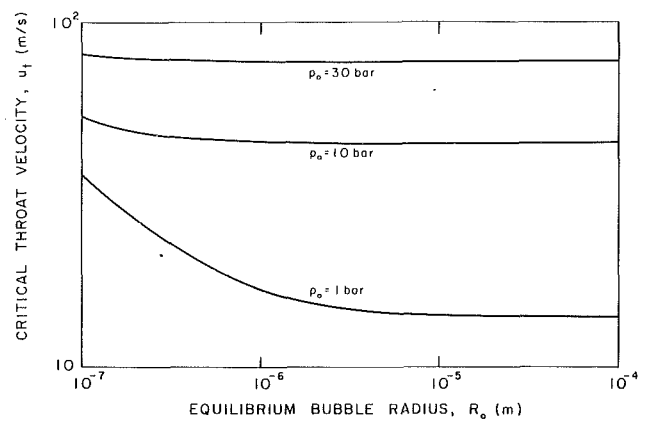

Fig. 4   Throat velocity u_t v/s equilibrium bubble radius R_0 in water at various pressures $p_0 = 1$, 10 and 30 bar and $T = 20°C$

Here p_0 and R_0 are the equilibrium pressure and radius of the bubble, p_v is the vapor pressure and S is the surface tension (see Fig. 3). The corresponding "critical" velocity at the venturi throat deduced from ideal, incompressible, one-dimensional, steady flow calculations is shown in Fig. 4. Similarly, the exhaust pressure coefficient $C_{p_e} = (p_e - p_v)/(p_0 - p_v)$ is plotted in Fig. 5 for the case $p_0 = 1$ bar and various expansion ratios. When the equilibrium pressure p_0 increases, the C_{p_e} curves shift to the left in the diagram. Note that, since the critical tensions of bubbles in the radius range of interest (from 10 to 100 μm) are quite small, the radius of marginally stable bubbles (critical radius) is a very sensitive function of the applied tension. If, in first approximation, dynamic effects are neglected, the above critical pressure would be representative of the cavitation pressure in the venturi throat, with several important (and unfortunate) implications for the design of CSM's. The first is that it would be virtually impossible to measure these small pressures at the throat because of inadequate sensitivity and, if done intrusively, separation and/or cavitation would surely be induced in such an extremely unstable flow. The second is that the throat pressure should be evaluated accurately to avoid large errors in the determination of the nuclei number distribution. A third consequence has to do with the problem of regulating the flow. Since the pressure
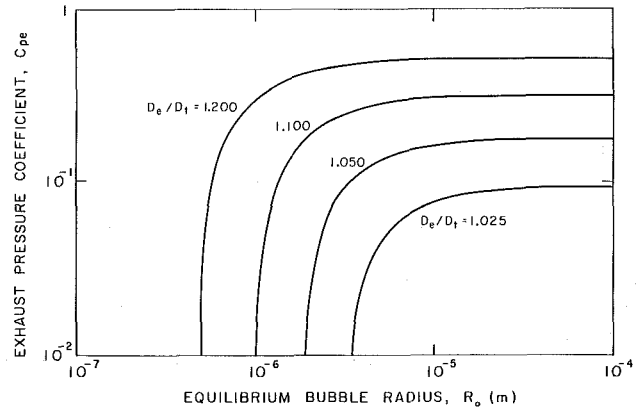

Fig. 5   Exhaust pressure coefficient $C_{p_e} = (p_e - p_v)/(p_0 - p_v)$ v/s equilibrium bubble radius R_0 in water at $p_0 = 1$ bar and $T = 20°C$ for various values of the diffuser's exhaust to throat diameter ratio $D_e/D_t = 1.025$, 1.050, 1.100, and 1.200

upstream cannot be changed without seriously affecting the sample and therefore interfering with the liquid quality measurement, this must be done by varying the exhaust pressure. The curves of Fig. 5 for $p_0 = 1$ bar show that very low sensitivity

<hr/>

Nomenclature (cont.)

u_t =	venturi throat velocity	
U =	velocity component measured by the LDV	
V =	volume	
w =	laser beam radius	
w_f =	laser beam radius at the LDV focal point	
w_0 =	laser beam waist radius	
x =	venturi axial coordinate	
y =	coordinate in the direction of the LDV optical axis	
z =	vertical coordinate normal to x and y	
β =	nuclei interference probability	
β_d =	semi-aperture angle of the venturi diffuser	
δ^* =	displacement boundary layer thickness	
ϵ =	error	

θ =	momentum boundary layer thickness	
λ =	boundary layer correlation parameter	
λ_0 =	wave length of LDV laser beams in air	
ν =	water kinematic viscosity	
$\bar{\nu}_b$ =	average cavitation event rate	
ρ =	water density	
σ =	standard deviation	
σ^2 =	variance	
φ =	semi-aperture angle of the LDV beams in air	
ξ =	Poisson distribution parameter	

Subscripts

b =	bubble or cavitation event	
c =	venturi tube contraction	

cr =	critical
d =	venturi tube diffuser
e =	venturi tube exhaust
fr =	fringe
i =	venturi tube inlet
0 =	reference equilibrium conditions
p =	particle or velocity tracer
s =	sample
t =	venturi tube throat
u =	upstream
v =	vapor
zc =	zero crossing

Acronyms

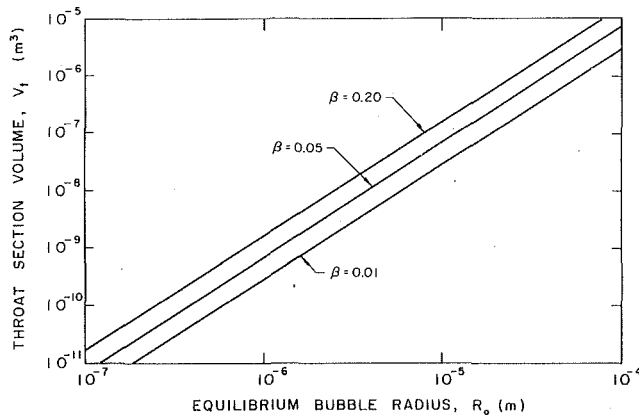|	
CSM =	Cavitation Susceptibility Meter
LDV =	Laser Doppler Velocimeter

Fig. 6 CSM venturi throat section volume V_t v/s equilibrium bubble radius R_0 for $K_N = 0.001 \text{ m}^{-1}$ (nuclei number distribution parameter) and various values of the bubble interference probability $\beta = 0.01$, 0.05 and 0.20

Fig. 7 Bubble detection length L_f necessary for a bubble to reach a detectable radius $R_f = 150 \,\mu\text{m}$ v/s equilibrium bubble radius R_0 at various initial pressures $p_0 = 1$ bar (squares), 10 bar (upward triangles) and 30 bar (downward triangles) for $T = 20°C$ (water temperature) and $D_t = 1$ mm (throat diameter)

would be obtained, unless diffusers with a very small expansion ratio were used. In practice the highly dynamic nature of cavitation in the CSM throat significantly decreases the cavitation pressure (d'Agostino et al., 1989) with respect to the value indicated by (1), but the above considerations still remain valid in a qualitative sense.

As pointed out briefly in the introduction, the problem of saturation poses a significant limitation to the operation of CSM's. It also introduces a systematic error, since the unsteady pressure perturbations due to the presence of a growing or collapsing bubble in the cavitation region of the CSM can prevent the normal growth of other neighboring nuclei. To control such an error the probability of finding more than one unstable nucleus in the throat volume V_t of the CSM must be minimized. When the nuclei concentration is uniform, the occurrence of N_b unstable nuclei in V_t is expected to follow the Poisson distribution $Pr(N_b) = \xi^{N_b}/N_b!e^{\xi}$, where $\xi = n(R_0)V_t$ is the average number of unstable nuclei in V_t. Hence, the cumulative probability of observing two or more unstable nuclei in V_t (bubble interference probability) is: $\beta = 1 - Pr(0) - Pr(1) = 1 - (1 + \xi)e^{-\xi}$. It is therefore possible to express the throat volume of the CSM as a function of the equilibrium bubble radius and of the bubble interference probability. The results of Fig. 6 show that in the radius range from 10 to 100 μm the volume of the throat section of the CSM should not exceed about 100 mm³ if the interference error is to be reduced to an acceptable level, say less than 20 percent. In this respect a throat diameter of 1 mm ca. appears to be both feasible and adequate, therefore further considerations are based on such a choice.

The problem of the response of an isolated bubble in the throat of the CSM is now approached. The solution of such a problem is expressed in terms of the detection time t_f and detection length L_f, respectively defined as the time and the length necessary for the bubble to grow from its initial size R_0 to a final detectable radius R_f. The choice of the final radius R_f is somewhat arbitrary, since it clearly depends on the sensitivity of the method used to detect cavitation. The solution of the above problem provides a way to estimate the minimum necessary length of the throat volume, thus completing its geometrical definition. A number of assumptions are made in order to construct a simplified set of equations which nevertheless models the interactions between the bubble and the liquid. First the flow is supposed to be one-dimensional, ideal, incompressible and the relative motion of the bubble with respect to the surrounding liquid is neglected. The bubble, moving along the centerline of the duct with instantaneous position $x_b(t)$, remains spherical and its radius $R(t)$ is determined by the Rayleigh-Plesset equation (Plesset and Prosperetti, 1977; Knapp et al., 1970):
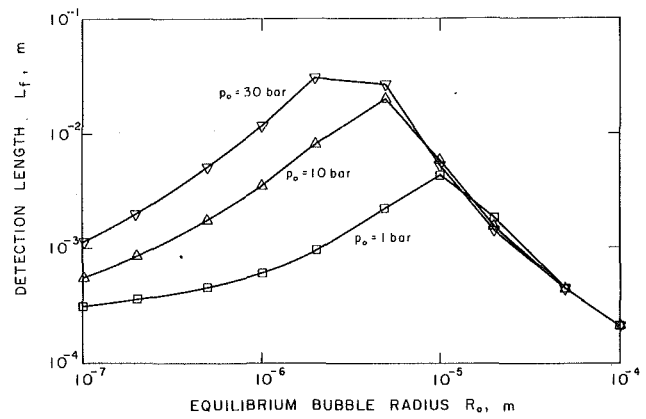
$$p_v - p_b = \rho \left[R \frac{d^2R}{dt^2} + \frac{3}{2} \left(\frac{dR}{dt} \right)^2 \right] - p_g \left(\frac{R_0}{R} \right)^3 + \frac{2S}{R}$$

where S is the surface tension and diffusive and thermal effects are neglected, i.e., p_v and p_g are constant. Here p_b is the external pressure driving the bubble volume changes and it is assumed to be equal to the pressure of the liquid in the proximity of the bubble. Then, from the continuity and unsteady Bernoulli's equations for the inlet flow upstream of the bubble (subscript i) and the exit flow downstream of the bubble (subscript e):

$$q_i - q_b + 2\pi R^2 \frac{dR}{dt} = 0 \qquad (2)$$

$$q_e - q_b - 2\pi R^2 \frac{dR}{dt} = 0 \qquad (3)$$

$$-I_i \frac{dq_i}{dt} + \frac{p_i - p_b}{\rho} - \frac{1}{2} \frac{q_b^2}{A_b^2} = 0 \qquad (4)$$

$$-I_e \frac{dq_e}{dt} + \frac{p_b - p_e}{\rho} + \frac{1}{2} \frac{q_b^2}{A_b^2} - \frac{q_e^2}{A_e^2} = 0 \qquad (5)$$

where $A_b = A(x_b)$, p_i and p_e are constant and:

$$I_i \simeq \int_{x_i}^{x_b} \frac{dx}{A(x)}; \quad I_e \simeq \int_{x_b}^{x_e} \frac{dx}{A(x)}$$

Equations (2) through (5) are then transformed by introducing perturbation quantities with respect to the steady-state solution and linearized for small changes in the volume fluxes. Finally, if $I_i \simeq x_b/A_b = u_t t/A_t \ll I_i + I_e$, which is essentially equivalent to consider the dynamics of a bubble entering a semi-infinite pipe of constant cross-sectional area A_t, the perturbation and Rayleigh-Plesset equations can be reduced to the following second order differential equation for the bubble radius $R(t)$:

$$\frac{2\pi\rho u_t}{A_t} \left[2tR^2 \frac{d^2R}{dt^2} + 4tR \left(\frac{dR}{dt} \right)^2 + R^2 \frac{dR}{dt} \right] +$$
$$+ \rho R \frac{d^2R}{d^2t} + \frac{3}{2} \rho \left(\frac{dR}{dt} \right)^2 - p_v - p_g \left(\frac{R_0}{R} \right)^3 + \frac{2S}{R} + p_t = 0$$

where p_t and u_t are the steady-state pressure and velocity at the throat. Note that the solution of the above equation depends on A_t, the throat cross-sectional area. The detection length $L_f = u_t t_f$, computed for a final detection radius $R_f = 150 \,\mu$m and a throat diameter $D_t = 1$ mm by numerically integrating the above equation, is shown in Fig. 7. The maximum in the results separates two regimes: in the upper radius range the inertial effects of the displaced liquid dominate, while
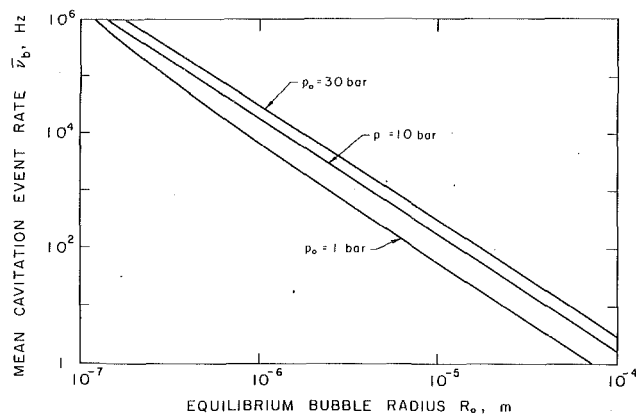
264 / Vol. 113, JUNE 1991

Transactions of the ASME

Fig. 8 Average cavitation event rate $\bar{\nu}_b$ v/s equilibrium bubble radius R_0 in water at various pressures $p_0 = 1, 10$ and 30 bar for $D_t = 1$ mm (throat diameter), $K_N = 0.001$ m^{-1} (nuclei number distribution parameter) and $T = 20°$C (water temperature)

in the lower one the effects of surface tension and bubble gas content prevail, therefore accelerating the bubble dynamic response to a change of the external pressure. Note that, in the radius range of interest, the detection length is almost independent of the equilibrium bubble pressure and that the length of the throat section should not be shorter than 5 to 10 mm. Given the throat diameter initially assumed, this choice is compatible with the need to control the bubble interference error over the nuclei radius range in consideration.

3 Unstable Nuclei Concentration and Throat Pressure Measurements

Once the throat cross-sectional area has been determined, the volume flux $q = u_t A_t$ and the mean cavitation event rate $\bar{\nu}_b = qn(R_0)$ can be computed. Results of Fig. 8 for a throat diameter $D_t = 1$ mm indicate that in the radius range from 10 to 100 μm as many as maybe a thousand cavitation events per second are to be expected. In steady-state conditions, if the liquid quality of the sample is constant and the cavities do not appreciably interfere with each other, the occurrence of cavitation at the venturi throat is described by a Poisson process with average arrival time $1/\bar{\nu}_b$. Then, the probability of observing N_b cavities during the time t is expressed by $Pr(N_b) = (\bar{\nu}_b t)^{N_b}/N_b!e^{\bar{\nu}_b t}$ and the probability density distribution of the time interval t between successive cavitation events follows the exponential distribution $f(t) = \bar{\nu}_b e^{-\bar{\nu}_b t}$. The agreement of the observed distribution of cavitation delay times with the above theoretical one provides a rational and quantitative way to assess the importance of interference effects among the cavities in the CSM venturi flow and to introduce corrections when appropriate (d'Agostino and Acosta, 1991). Note that a large portion of cavitation events will occur with a separation in time considerably smaller than the average arrival time $1/\bar{\nu}_b$. Therefore the CSM data acquisition system must be designed to handle as many as, say, order of ten thousand cavitation events per second for a reliable measurement of the water quality to be made. In addition, it also must record the arrival times with comparable precision, if the importance of cavitation interference effects is to be assessed from consideration of the delay time statistics.

For a given pressure at the throat, the corresponding concentration of unstable nuclei can be estimated from the count N_b of the cavitation bubbles observed during the sampling time t_s. Since t_s can be conveniently measured, the problem of estimating $\bar{\nu}_b$ now reduces to the estimation of the Poisson parameter $\xi = \bar{\nu}_b t_s$. It is known from the theory of probability distributions, (Browlee, 1960), that the best estimator of the Poisson parameter ξ is the observed frequency N_b, whose ex-

pected value and variance are respectively: $\overline{N}_b = \sigma^2_{N_b} = \xi$. Thus, the estimated root mean square relative error in the measurement of ξ and of any other linearly related quantity such as $\bar{\nu}_b$, $n(R_0)$ and $N(R_0)$ is $\epsilon = 1/\sqrt{N_b}$. The sampling time $t_s = 1/\bar{\nu}_b \epsilon^2$ and liquid sample volume $V_s = A_t u_t t_s$ necessary for one single measurement of unstable nuclei concentration of acceptable precision (say, $\epsilon = 0.20$) are found to be at most of the order of 10 dm^3 and 10 s, respectively. Clearly, the overall sampling time and volume of liquid necessary for the evaluation of the nuclei number distribution will depend on the total number of points where the measurement of the unstable nuclei concentration is carried out. Finally, the unstable nuclei concentration is estimated as $n(R_0) = N_b/V_s$, with standard deviation $\sigma_n = \sqrt{N_b}/V_s$.

In existing CSM's cavitation detection has been made either optically (Oldenziel, 1982a; Oldenziel, 1982b; Oldenziel et al., 1982; Ito and Oba, 1980) or acoustically (Lecoffre and Bonnin, 1979; Le Goff and Lecoffre, 1983; Shen et al., 1984) from the noise generated by the rapid volume changes of the cavities and in particular by their collapses. Acoustical detection is relatively simple and has the distinct advantage of not requiring optical access to the cavitation region. However, rebounds frequently occur in practice during the collapse of cavitation bubbles, possibly leading to spurious counts due to multiple acoustical signals from the same original cavity. Optical detection is clearly preferable whenever feasible because it safely locates the occurrence of cavitation in space, thus eliminating the possibility of spurious multiple counts, and preserves the information on the arrival time of cavitation events, which represents a powerful diagnostic tool in monitoring the operation of CSM's. In addition, the possibility of direct optical observation of cavitation in the venturi is an important advantage of optical methods for cavitation detection.

It was previously mentioned that one of the most difficult problems of CSM's consists in measuring the throat pressure with the required precision. Since direct methods appear to be impossible, indirect methods must be used. Most naturally a representative value of the inception pressure at the venturi throat may be deduced from the measurements of the upstream pressure and of the throat velocity using Bernoulli's equation for ideal, incompressible, steady flow:

$$p_t = p_u - \frac{1}{2}\rho u_t^2 (1 - C_c^2) \qquad (6)$$

An unavoidable problem associated with this technique is that the throat pressure, being inherently small compared to the inlet pressure and kinetic pressure drop, is expressed as the difference of two almost equal quantities. Thus, small relative errors in the evaluation of these quantities lead to a much larger relative error for the throat pressure.

In existing CSM's, (Oldenziel, 1982a; Oldenziel, 1982b; Oldenziel et al., 1982; Godefroy et al., 1981; Le Goff and Lecoffre, 1983; Shen et al., 1984) the velocity measurement was carried out either in the upstream or downstream sections of the duct, relatively far from the venturi throat. This method appears to be rather unsatisfactory for various reasons. First, any intrinsic error in the measurement of the velocity or due to inaccurate estimate of boundary layer effects is amplified proportionally to the reciprocal of the venturi contraction ratio when the throat velocity is derived by means of continuity arguments. This limitation is particularly severe since in CSM's the contraction ratio should be as small as possible in order not to appreciably affect the conditions of the sampled liquid during its flow to the test section. Moreover, it is generally necessary to make the inlet line longer, which is also likely to affect the conditions of the sampled liquid, especially when a second venturi of smaller contraction ratio is used to monitor the velocity. These difficulties are overcome if the velocity measurement is carried out at the throat. In consideration of the

extreme instability of the flow, the use of a Laser Doppler Velocimeter (LDV) seems to be the best solution.

The error analysis of this measurement can be easily developed if the two independent variables p_u and u_t are assumed to be normally distributed about their expected values $\bar{p}_u$ and $\bar{u}_t$ with variances $\sigma^2_{p_u}$ and $\sigma^2_{u_t}$. Standardizing p_u and u_t and using the properties of the moments of the standard normal distribution (Browlee, 1960), one obtains the following expressions for the expected value and the variance of p_t:

$$\bar{p}_t = \bar{p}_u - \frac{1}{2}\rho(1 - C_c^2)(\bar{u}_t^2 + \sigma^2_{u_t})$$

$$\sigma^2_{p_t} = \sigma^2_{p_u} + \rho^2(1 - C_c^2)^2\sigma^2_{u_t}\left(\bar{u}_t^2 + \frac{\sigma^2_{u_t}}{2}\right)$$

Note the "shift" due to the dispersion of the measured velocity together with the quadratic nature of equation (6).

4 Viscous Effects

For the pressure to be correctly deduced from velocity measurements, the presence of a laminar potential core at the CSM throat must be demonstrated. Viscous effects have therefore been estimated by matching an axisymmetric laminar boundary layer (White, 1974) to the quasi one-dimensional ideal flow solution based on the duct geometry. The assumption of laminar flow in the venturi is justified by the low value of the Reynolds number at the inlet (Re$_i$ = $u_iD_i/\nu \simeq 1500$) and, further downstream where the Reynolds number increases beyond the transition value, by the effect of the steep contraction which tends to laminarize the flow by drastically reducing pre-existing velocity fluctuations. The turbulent transition length for a flat plate with equal free stream velocity is of the order of 20 cm and it seems likely that it would not be shorter for the guided flow in the CSM venturi. Thus there is strong reason to believe that at least the noncavitating flow remains laminar throughout the whole venturi. In the boundary layer computation the duct profile has been assumed to be continuous with continuous first and second derivatives, as required from fluid mechanical considerations to avoid separation. In the contraction and the transitions at the inlet and outlet of the diffuser the duct radius was supposed to have sinusoidal second derivative in the streamwise direction. The inlet and throat sections were taken to be cylindrical and the center part of the diffuser to be conical, of given semi-aperture angle β_d. The boundary layer displacement and momentum thicknesses δ^* and θ for a typical venturi with inlet Reynolds Re$_i$ = 1400 (the lowest expected value during operation) are summarized in Fig. 9, where they are normalized with respect to the local duct radius. They clearly demonstrate the presence of a potential core in the throat section of the CSM, corresponding to normalized axial coordinates ranging from 4 to 6.

Another effect of the boundary layer is the reduction of the flux-averaged cross-sectional area of the venturi with respect to its geometrical area. This effect is particularly important in the diffuser, whose performance is very sensitive to even very small changes of the expansion ratio (see Figure 5). In theory it would be possible to compute the boundary layer displacement thickness for the assigned, nominal profile of the potential core velocity and to correct accordingly the venturi geometry. In practice this possibility should be regarded with some skepticism because boundary layer computations for flows with a highly unfavorable pressure gradient as the one in the diffuser are rather imprecise. Furthermore, it is questionable that their results could be accurately implemented in the manufacturing of small size venturis. However, if the results of these computations are to be trusted, in a venturi equal to the one previously considered but with a 20 mm long diffuser the presence of the boundary layer would, for example, increase the expansion ratio from its nominal value of 1.10 to a geometric value of 1.37.
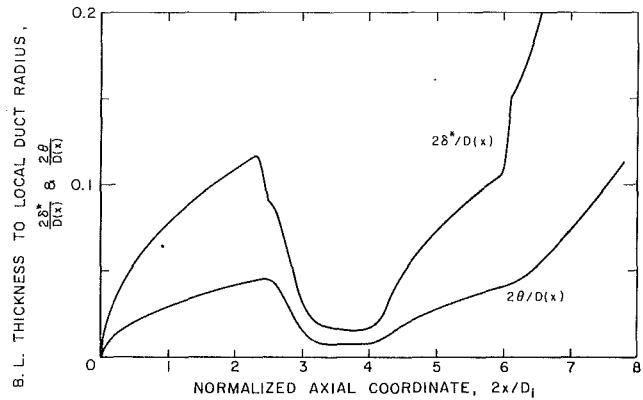

Fig. 9 Relative displacement thickness, $2\delta^*/D(x)$, and momentum thickness, $2\theta/D(x)$, v/s normalized axial coordinate $2x/D_i$ in a typical CSM venturi with D_t = 1 mm (throat diameter), C_c = 1/100 (contraction ratio), β_d = 0.76 deg (diffuser semi-aperture angle) and Re$_i$ = 1400 (inlet Reynolds number). The lengths of the various sections are: L_i = 11.4 mm (inlet), L_c = 10.4 mm (contraction), L_t = 7.7 mm (throat), L_d = 10.4 mm (diffuser).
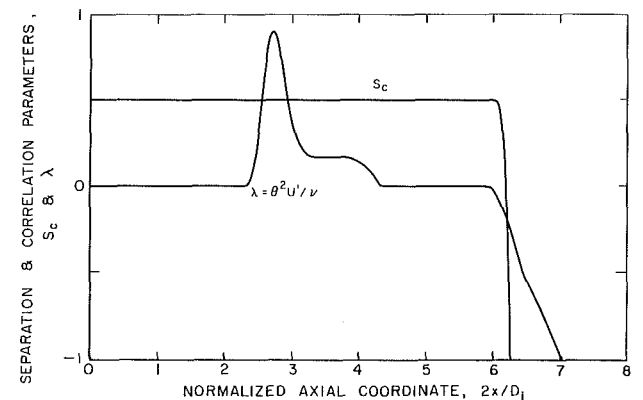

Fig. 10 Stratford's laminar separation criterion S_c and Thwaites' shear and shape correlation parameter $\lambda = \theta^2 U'/\nu$ v/s normalized axial coordinate $2x/D_h$ for the venturi of Fig. 9. Laminar separation is predicted when S_c drops to zero or $\lambda \simeq -0.09$.

Another problem to be expected in the venturi as a consequence of viscous effects is the occurrence of laminar separation in the diffuser when too large negative pressure gradients are present. If laminar separation takes place, cavitation nuclei from the main flow are likely to be trapped in the recirculation region, where they eventually grow and possibly develop into an attached cavity, whose unsteady behavior greatly disturbs the rest of the flow. The situation is further worsened if this cavity propagates downstream and reaches the exit. In this case the exhaust pressure is established throughout the cavity and the useful portion of the diffuser is proportionally shortened. A cylindrical section of appropriate length downstream of the diffuser promotes the stability of the exhaust flow and usually prevents the separation-cavitation from extending to the exit.

Preliminary tests on a prototype venturi and later experience with operational ones showed that steady or intermittent separation in the diffuser can indeed occur, a problem also reported by previous investigators (Oldenziel, 1982a; Shen et al., 1984). In view of this, the boundary layer correlation parameter $\lambda = \theta^2 U'/\nu$ (where U' is the streamwise derivative of the flow velocity at the boundary layer edge) and the Stratford laminar boundary layer separation criterion S_c (Stratford, 1954) have been plotted in Fig. 10. Separation is predicted when $\lambda = -0.09$ or $S_c = 0$. The two methods agree well with each other and also with the observed location of separation in the prototype venturi, thus indicating that less steep diffusers should be used, significantly limiting the minimum attainable throat pressure in the CSM venturi tube.

In view of the above considerations it was decided to develop a CSM with a transparent venturi tube where the throat velocity is measured by a LDV and the upstream pressure by an absolute pressure transducer. At the same time the LDV signal will also be used to detect the occurrence of cavitation at the throat of the venturi tube. The analysis of the signals from the LDV and the upstream pressure transducer will be carried out by an especially designed electronic Signal Processor for real time generation and temporary storage of the relevant data. Finally, the final acquisition and reduction of the data will be performed by a microcomputer.

5 LDV Optical Analysis and Signal Processing

In this section the main considerations and electro-optical analysis are presented which led to the design of the LDV used in the CSM. These considerations mostly concern the choice of the optical configuration and the connected problem of the LDV signal processing. Basic principles of operation of LDV's are recalled as required for clarity of the presentation, but for more details the reader is referred to the vast literature available on this complex field (see, for example, Durst et al. 1981).

The typical optical properties of the LDV scatterers naturally present in the CSM flow cannot be anticipated with any degree of accuracy, since they depend on the individual characteristics of the sampled water and no artificial seeding can be used without greatly interfering with the water quality measurement. However, cavities will clearly be present at the end of the venturi throat section as long as measurements with the CSM can be made. Since the pressure gradient in the venturi throat is ideally zero, it can be shown that the slip velocity of the two phases nearly vanishes at the end of the throat section and the cavities themselves can therefore be safely used as velocity tracers. The possibility of recording the velocity of cavities in the flow also provides useful information on their origin. In fact, since the typical cavity size is much larger than the boundary layer thickness at the CSM throat, the cavities generated by free stream nuclei mostly travel at the potential core speed, while those just released by nearby surface nuclei are significantly slower. A dual beam back-scattering LDV focused at the end of the venturi test section that uses the cavities themselves as tracers has therefore been selected for measuring the CSM throat velocity. The back-scattering configuration combines the advantages of greater simplicity with superior optical efficiency when operating in the scattering regime expected from cavities whose average size clearly much exceeds the wave length of the illuminating laser beams.

For this arrangement the Doppler frequency of the LDV signal, the fringe spacing and the number of fringes are respectively expressed by:

$$f_D = \frac{2Um\sin\varphi}{\lambda_0}; \quad s_{fr} = \frac{\lambda_0}{2m\,\sin\varphi}; \quad N_{fr} = \frac{d_x}{s_{fr}} = \frac{d_x f_D}{U}$$

where φ is the semi-aperture angle of the two intersecting beams, λ_0 is the wave length of the beams in air, m is the index of refraction of the optical medium, U is the velocity component perpendicular to the optical axis in the plane of the two beams, and d_x is the size of the LDV probe volume in the flow direction.

The Doppler frequency and the fringe spacing are not affected by the refraction of the two beams through a plane interface separating two optical media with index of refraction m and m', because in this case from Snell's law: $m\,\sin\varphi = m'\sin\varphi'$, where φ' is the beam semi-aperture angle in the second medium. This result can be easily generalized to the case of a sequence of planar, parallel interfaces. Also note that the Doppler frequency is only sensitive to the orientation of the impinging radiation in the plane of the two beams, which coincides with the meridional plane of the CSM venturi. Within the limits of Gaussian or paraxial optics the effects due to the
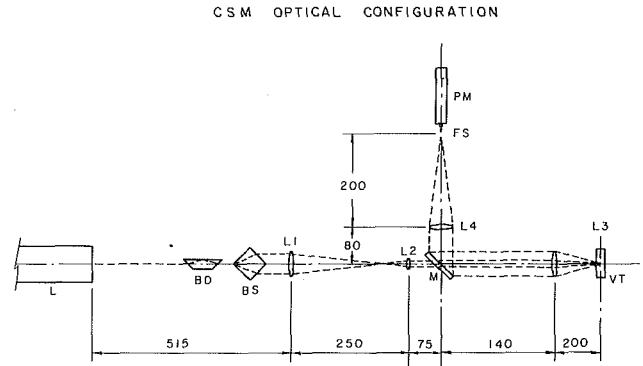
Fig. 11 Schematic for the CSM optical components (dimensions in mm): continuous wave laser (L), beam displacer (BD), beamsplitter cube (BS), telescopic relay lenses (L1 and L2), focusing and receiving lens (L3), venturi tube (V), front surface mirror (M) with slit for transmission of laser beams, photomultiplier collimating lens (L4), field stop aperture (FS), photomultiplier tube (PM).

cylindrical geometry of the venturi optical interfaces can be separately analyzed in the meridional and cross-sectional planes. The curvature of these interfaces in the cross-sectional plane therefore refracts the impinging beams in the same plane, but has no effect on the direction of the beam propagation in the meridional plane. The above considerations imply that the LDV Doppler frequency only depends on the venturi geometry in the meridional plane and that its relation to the velocity is the same in air and in the CSM flow, provided that the walls of the venturi are parallel. This is a very fortunate situation, since it implies that the calibration of the LDV can be carried out in air and that its results can be directly extended to the flow in the CSM venturi.

As mentioned earlier, in the CSM it is highly advisable to preserve the information on the occurrence time of individual cavitation events. In addition, the drop-out rate and the signal level are expected to be high, since the cavities used as velocity tracers are relatively sparse and large. Therefore frequency counters, which operate in the time domain, are the most suitable solution for measuring the LDV Doppler frequency. Each burst is recognized, isolated, and its Doppler frequency is counted by comparing the LDV signal to properly adjusted threshold levels. On the other hand, with respect to alternative methods, in frequency counters the maximum measurable frequency is more severely limited by the speed of the processing electronics and therefore the LDV optics must be designed accordingly.

The best LDV signal quality is obtained when the fringe spacing is of the same order of magnitude as the size of the scatterer, whose characteristic dimensions cannot be safely anticipated. It seems therefore advisable to keep the beam separation adjustable within a relatively large range. The above consideration and the need to limit the Doppler frequency below about 1 MHz in order to simplify the LDV processing electronics led to the arrangement schematically shown in Fig. 11. The laser beam, generated by a 5 mw He-Ne continuous wave laser (L), goes through a beam displacer (dove prism, BD) and a metal-coated beamsplitter cube (BS). The separation of the two outcoming beams can be widely adjusted (2 to 17 mm ca.) using the beam displacer to change the transversal position of the beam entering the beamsplitter. In order to reduce the Doppler frequency of the LDV signal and consequently simplify the processing electronics, the beam separation is then four times reduced by a telescopic lens relay (L1 and L2). After passing through a slit in the front surface mirror (M), the two beams are finally focused by the lens (L3) to the test section of the CSM venturi tube (VT). The back-scattered light is then collected by the whole aperture of the same lens (L3) and mostly reflected by the front surface mirror (M)

toward the photomultiplier collimating lens (L4). The resulting image of the test section is filtered by a field stop aperture (FS) to reduce the optical background noise and finally reaches the photomultiplier tube (PM), where it is converted into an electric signal. All lenses have a back focal length of 200 mm, except the second lens (L2) of the telescopic relay, whose focal length is 50 mm.

Since the deviation of the laser beams from the optical axis is small, the theory of propagation of paraxial Gaussian beams can now be used to analyze the optical system in order to deduce the focal volume and the expected number of fringes of the LDV signal. Then, for the system of thin lenses of Fig. 11, the ray transfer matrices (Kogelnik and Li, 1966) of the focusing optics from the laser window to the LDV focal point and of receiving optics from the LDV focal point to the photomultiplier are respectively:

$$\underline{A}_F = \begin{bmatrix} 0 & -0.8 \\ 1.250 & -0.3063 \end{bmatrix}; \quad \underline{A}_R = \begin{bmatrix} -1 & 0 \\ -4.5 & -1 \end{bmatrix}$$

where the optical lengths are in meters. The elements a_{11} and $-a_{21}$ of these matrices are, respectively, the magnification and the reciprocal of the back focal length of the optical system. As expected, the magnification of the receiving optics is equal to -1. Furthermore, the ray transfer matrix of the focusing optics shows that, for the flow velocity expected at the venturi throat ($U \simeq 15$ m/s), the Doppler frequency can be decreased to less than 250 kHz with a beam separation of a few millimeters, still large enough to be achieved with a cube beamsplitter.

In the theory of paraxial optics the propagation of a Gaussian beam is expressed in terms of the complex beam parameter (Kogelnik and Li, 1966):

$$\frac{1}{q} = \frac{1}{R} - i \frac{\lambda}{\pi w^2}$$

where $1/R$ is the beam wave front curvature and w is the beam radius, defined as the distance from the beam axis where the electromagnetic field amplitude drops to $1/e$ times its maximum value. At the beam waist the wave front curvature is zero and the beam radius is minimum. The size and location of the beam waist depend on the internal geometry of the laser optics. In the Spectra Physics He-Ne gas laser model Stabilite 120 to be used in the CSM the beam waist radius is $w_0 = 0.325$ mm and coincides with the output window of the laser. In the propagation of a Gaussian beam through an optical system with ray transfer matrix $\underline{A}$ the complex beam parameter at the output q_2 is related to the input value q_1 by (Kogelnik and Li, 1966):

$$q_2 = \frac{a_{11}q_1 + a_{12}}{a_{21}q_1 + a_{22}}$$

From this equation and the above results the beam radius and the curvature of the wave front at the LDV focal point are: $1/R_f = 0.383$ m^{-1} and $w_f = 0.496$ mm. In the final operational configuration of the LDV the beam angular semi-separation is $\varphi = 5.27 \cdot 10^{-3}$ rad and the fringe spacing $s_{fr} = 60$ μm, which experience has shown to give the best results. With this choice the axes of the LDV focal ellipsoid are: $d_x = 2w_f/\cos\varphi = 0.992$ mm in the flow direction, $d_y = 2w_f/\sin\varphi = 188$ mm in the direction of the optical axis, $d_z = 2w_f = 0.992$ mm in the vertical direction. Then the number of fringes and the duration (gate time) of a typical Doppler burst can be estimated to be $N_{fr} = d_x/s_{fr} \simeq 17$ and $T_g = d_x/U \simeq 66$ μs. Clearly the fringe spacing must be as uniform as possible throughout the LDV focal volume in order to obtain consistent velocity readings regardless of the location of the scatterer trajectory. For this to happen the beam divergence angle $w_f/R_f = 1.90 \cdot 10^{-4}$ rad must be much smaller than the angular semi-separation φ between the two beams. This condition is indeed satisfied in the configuration examined here. Finally, the magnification

of the receiving optics is equal to -1 in the meridional plane and slightly larger in the cross-sectional plane as a consequence of the curvature of the venturi tube interfaces. Thus, the optimum diameter of the photomultiplier field stop aperture should be about 1 mm or a bit larger, as confirmed in practice.

Note that for a throat diameter $D_t = 1$ mm the LDV focal volume extends far across the venturi walls in the direction of the optical axis and also covers the whole throat in the vertical direction. Therefore the LDV signal can effectively monitor the occurrence of cavitation, but at the same time velocity readings in the boundary layer are likely to occur. This situation must be taken into account in the reduction of the LDV data in order to introduce the appropriate corrections when necessary. The occurrence of velocity readings in the boundary layer also provides a direct way to check for the presence of a potential core in the flow at the venturi throat, which is essential for the correct deduction of the throat pressure.

In theory the intensity of the LDV output signal could now be estimated from the laser power, the transmittance of the optical system, the focal point dimensions and the photomultiplier's sensitivity. However, in practice the scattering and collecting efficiencies are too uncertain for a useful estimate to be made because they depend in a very complex way on the optical and geometrical properties of both the tracer itself and of the collecting optics.

6 Summary and Conclusions

The results of design analysis of the CSM operation can be summarized as follows:

• the flow is likely to remain laminar throughout the venturi's throat section and the first portion of the diffuser;

• the existence of a potential core at the throat has been demonstrated in venturi tubes of proper geometry by estimating the boundary layer thickness;

• the pressure in the CSM cavitation region is an extremely sensitive parameter and cannot be measured directly with the necessary accuracy;

• the indirect measurement of the pressure in the cavitation region appears to be best accomplished by measuring the upstream pressure with an absolute pressure transducer and the potential core velocity at the CSM throat with non-intrusive direct methods such as a LDV;

• the detection of cavitation at the venturi throat is best accomplished optically by the same LDV signal used to measure the flow velocity;

• it is clearly advantageous for the purpose of monitoring the flow to preserve the optical access to the cavitation region whenever possible;

• the errors and limitations due to nuclei interference effects can be effectively controlled by decreasing the volume of the cavitation region to less than ten cubic millimeters;

• for a throat diameter of 1 mm the time response of the cavitating nuclei imposes a lower bound of about 5 to 10 mm to the length of the CSM throat section;

• the flow is extremely sensitive to laminar separation in the diffuser, which limits the maximum achievable expansion ratio to less than 1.1;

• the acquisition system must be designed to handle up to ten thousand events per second, recording for each of them the occurrence time, the Doppler frequency and the upstream pressure;

• a dual-beam back-scattering LDV seems to be the most suitable solution for measuring the CSM throat velocity and monitoring the occurrence of cavitation;

• it is advisable to keep the fringe spacing widely adjustable in order to optimize the LDV signal visibility and Doppler frequency depending on the operational conditions;

- the Doppler frequency must be measured in the time domain with a frequency counter in order to record both the velocity and the occurrence time of individual cavitation events;
- the Doppler frequency should not exceed about 1 or 2 MHz due to likely limitations of the processing electronics;
- spurious velocity readings from scatterers convected in the boundary layers must be eliminated in the reduction of the data.

In conclusion, the above analysis provides a rational basis and strong indications for CSM design orientation. It clearly shows that proper CSM operation poses a relatively complex technological problem, where a number of critical factors are involved. In the proposed configuration, the solution of this problem requires the integration of both fluid dynamic and electro-optical aspects. The above analysis indicates that, by careful consideration of these aspects, a CSM capable of measuring the concentration of active cavitation nuclei as a function of the throat pressure can be successfully developed according to the proposed design. As mentioned in the introduction, the implementation and operation of this system are described and discussed in a companion publication (d'Agostino and Acosta, 1991).

Acknowledgments

References

Bader, H., 1970, "The Hyperbolic Distribution of Particle Sizes," *Journal of Geophysical Research*, Vol. 75, No. 15, pp. 2822-2830.

Billet, M., 1986a, "The Importance and Measurement of Cavitation Nuclei," *Advancements in Aerodynamics, Fluid Mechanics and Hydraulics*, Minneapolis, Minn., pp. 967-989.

Billet, M., 1985, "Cavitation Nuclei Measurement—A Review," *ASME Cavitation and Multiphase Flow Forum*, Albuquerque, N.M., pp. 31-38.

Browlee, K. A., 1960, *Statistical Theory and Methodology in Science and Engineering*, Wiley, NY.

Chahine, G. L., and Shen, Y. T., 1986, "Bubble Dynamics and Cavitation Inception in Cavitation Susceptibility Meters," ASME JOURNAL OF FLUIDS ENGINEERING, Vol. 108, pp. 444-452.

d'Agostino, L., 1987, "Experimental and Theoretical Study on Cavitation Inception and Bubbly Flow Dynamics," Ph.D. thesis, Report No. Eng. 183.16, California Institute of Technology, Pasadena, Calif.

d'Agostino, L., and Acosta, A. J., 1991, "A Cavitation Susceptibility Meter with Optical Cavitation Monitoring—Part Two: Experimental Apparatus and Results," published in this issue pp. 270-277.

d'Agostino, L., Thai Pham, and Green, S., 1989, "Comparison of a Cavitation Susceptibility Meter and Holographic Observation for Nuclei Detection in Liquids," ASME JOURNAL OF FLUIDS ENGINEERING, Vol. 111, No. 2, pp. 197-203.

Durst, F., Melling, A., and Whitelaw, J. H., 1981, *Principles and Practice of Laser-Doppler Anemometry*, Academic Press, 2nd edition.

Godefroy, H. W. H. E., Jansen, R. H. J., Keller, A. P., and van Renesse, R. L., 1981, "Comparison of Measuring and Control Methods of the Water Quality with Respect to Cavitation Behaviour," Delft Hydraulics Laboratory Publication.

Ito, Y., and Oba, R., 1980, "Cavitation Observations through a Fine Laser-Beam Technique," Report No. 337, Institute of High Speed Mechanics, Tohoku University.

Knapp, R. T., Daily, J. W., and Hammitt, F. G., 1970, *Cavitation*, McGraw-Hill, New York.

Kogelnik, H., and Li, T., 1966, "Laser Beams and Resonators," *Applied Optics*, Vol. 5, No. 10, pp. 1550-1567.

Lecoffre, Y., and Bonnin, J., 1979, "Cavitation Tests and Nucleation Control," *International Symposium on Cavitation Inception*, New York, New York, pp. 141-145.

Le Goff, J. P., and Lecoffre, Y., 1983, "Nuclei and Cavitation," *14th Symposium on Naval Hydrodynamics*, National Academy Press, pp. 215-242.

Oba, R., Ikohagi, T., and Kim, K. T., 1979, "Cavitation in an Extremely Limited Flow through Very Small Orifices," *International Symposium on Cavitation Inception*, ASME, New York, N.Y., pp. 147-152.

Oldenziel, D. M., 1982a, "A New Instrument in Cavitation Research: the Cavitation Susceptibility Meter," ASME JOURNAL OF FLUIDS ENGINEERING, Vol. 104, pp. 136-142.

Oldenziel, D. M., 1982b, "Utility of Available Instruments during Cavitation Tests," *Proceedings of Symposium on Operating Problems of Pump Stations and Power Plants*, IAHR, Amsterdam.

Oldenziel, D. M., 1979, "New Instruments in Cavitation Research," *International Symposium on Cavitation Inception*, New York, N.Y., pp. 111-124.

Oldenziel, D. M., Jansen, R. H. J., Keller, A. P., Lecoffre, Y., and van Renesse, R. L., 1982, "Comparison of Instruments for Detection of Particles and Bubbles in Water during Cavitation Studies," *Proceedings of Symposium on Operating Problems of Pump Stations and Power Plants*, IAHR, Amsterdam.

O'Hern, T. J., d'Agostino, L., and Acosta, A. J., 1988, "Comparison of Holographic and Coulter Counter Measurements of Cavitation Nuclei in the Ocean," ASME JOURNAL OF FLUIDS ENGINEERING, Vol. 110, pp. 200-207.

Plesset, M. S., and Prosperetti, A., 1977, "Bubble Dynamics and Cavitation," *Ann. Rev. Fluid Mech.*, Vol. 9, pp. 145-85.

Shen, Y. T., Gowing, S., and Pierce, R., 1984, "Cavitation Susceptibility Meters by a Venturi," *International Symposium on Cavitation Inception*, ASME Winter Annual Meeting, pp. 9-18.

Shen, Y. T., and Gowing, S., 1985, "Scale Effects on Bubble Growth and Cavitation Inception in Cavitation Susceptibility Meters," *ASME Cavitation and Multiphase Flow Forum*, Albuquerque, New Mexico, pp. 14-16.

Shen, Y. T., Gowing, S., and Eckstein, B., 1986, "Cavitation Susceptibility Measurements of Ocean Lake and Laboratory Waters," David W. Taylor Naval Ship Research and Development Center, Report DTNSRDC-86/D19.

Stratford, B. S., 1954, "Flow in Laminar Boundary Layer near Separation," Aeronautical Research Council, R&M 3002.

White, F. M., 1974, *Viscous Fluid Flow*, McGraw Hill, New York.

A Cavitation Susceptibility Meter With Optical Cavitation Monitoring—Part Two: Experimental Apparatus and Results

L. d'Agostino[1]

A. J. Acosta

California Institute of Technology,
Pasadena, CA 91125

This work is concerned with the development and operation of a Cavitation Susceptibility Meter based on the use of a venturi tube for the measurement of the active cavitation nuclei concentration in water samples as a function of the applied tension. The pressure at the venturi throat is determined from the upstream pressure and the local flow velocity without corrections for viscous effects because the flow possesses a laminar potential core in all operational conditions. The detection of cavitation and the measurement of the flow velocity are carried out optically by means of a Laser Doppler Velocimeter. A custom-made electronic Signal Processor is used for real time data generation and temporary storage and a computerized system for final data acquisition and reduction. The implementation of the whole system is described and the results of the application of the Cavitation Susceptibility Meter to the measurement of the water quality of tap water samples are presented and critically discussed with reference to the current state of knowledge on cavitation inception.

1 Introduction

Experience shows (Knapp et al., 1970) that the maximum tensile stress that liquids can theoretically sustain according to thermodynamic considerations is much larger than observed in practice. It has therefore been postulated that the tensile strength of liquids is considerably reduced by the presence of weak spots, generically called "nuclei," which act as preferential points for the onset of liquid rupture. The concentration and susceptibility of nuclei profoundly affect the inception, development, and scaling of cavitation in a wide variety of technically important applications. Therefore significant efforts have been made to develop effective cavitation nuclei detection methods (Billet, 1986; Billet, 1985; Oldenziel et al., 1982; Godefroy et al., 1981). Commonly used techniques, like Coulter counters, acoustical attenuation, acoustical and optical scattering, photography and holography, monitor noncavitating liquids and therefore cannot provide reliable information on cavitation nuclei susceptibility. Cavitation Susceptibility Meters (CSM's) are intended to overcome this limitation by directly measuring the active nuclei concentration as a function

of the applied tension in a flow through a small venturi tube, where cavitation is induced under carefully controlled conditions. In the original design by Oldenziel (Oldenziel, 1982a; Oldenziel 1982b) a glass venturi is used and cavitation is detected optically. Later applications employ stainless steel venturi tubes, where cavitation bubbles are detected acoustically (Lecoffre and Bonnin, 1979; Le Goff and Lecoffre, 1983; Shen et al., 1984). Among the advantages of CSM's over alternative techniques are the absence of resolution limitations in the minimum size of nuclei they can detect and the relative convenience of data analysis. On the other hand, CSM's are subject to a number of unwanted phenomena, like flow separation, nuclei interference, choking and surface nuclei effects, which severely limit their performance. This paper is part of a systematic investigation of CSM's and critically describes the implementation and operation of the CSM recently developed at the California Institute of Technology (d'Agostino and Acosta, 1983; d'Agostino, 1987; d'Agostino et al., 1989). The principles of operation and the main considerations leading to the current design have been reported in a companion publication (d'Agostino and Acosta, 1991).

2 Experimental Apparatus

The design of the CSM described herein is based on the indications of a detailed operational analysis previously re-
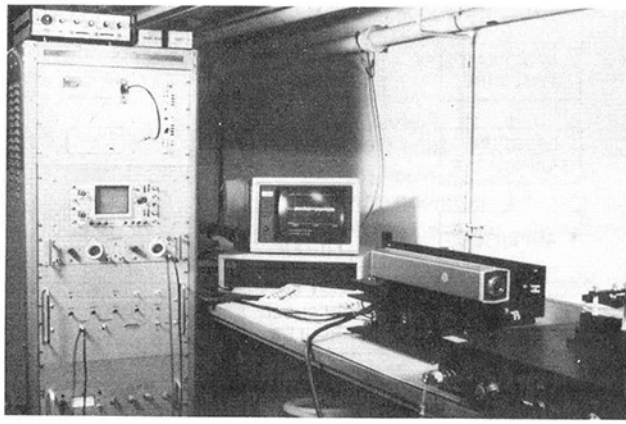

Fig. 1 General view of the CSM experimental apparatus. In the fore-ground on the right: the I-beams supporting the laser and the baseplate where most of the optical and fluidic components are mounted. In the background: the electronic instrumentation rack (left) and the data ac-quisition computer (center).
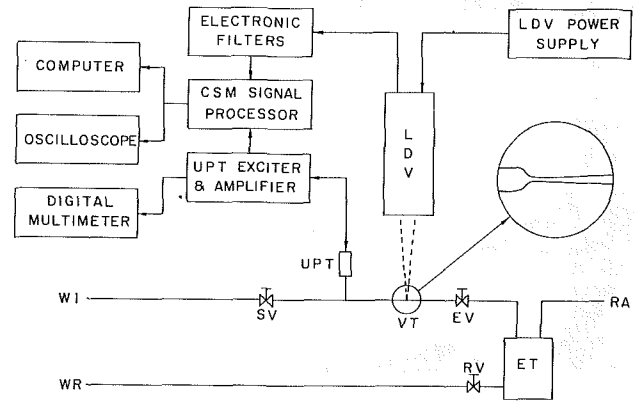
Fig. 2 Schematic of the various components of the CSM experimental apparatus: water inlet (WI), sampling valve (SV), upstream pressure trans-ducer (UPT), venturi tube (VT), exhaust valve (EV), exhaust tank (ET), regulated air pressure line (RA), return valve (RV), water return (WR), laser Doppler velocimeter (LDV).

ported in earlier works (d'Agostino and Acosta, 1983; d'Agostino, 1987) and more recently summarized in a com-panion paper (d'Agostino and Acosta, 1991). The results of this analysis suggested to develop a CSM where cavitation occurs in the restricted section of a transparent venturi tube. The throat velocity is measured by a back-scattering Laser Doppler Velocity (LDV) and the upstream pressure by an ab-solute pressure transducer. The LDV signal is also used to detect the occurrence of cavitation at the throat of the venturi tube. The pressure gradient in the venturi throat is ideally zero and thus the slip velocity between the bubbles and the liquid is also zero. Cavitating bubbles are, therefore, accurate velocity indicators. The throat pressure is controlled by adjusting the exhaust pressure and is calculated from the throat velocity and the upstream pressure using Bernoulli's equation for ideal, incompressible, steady, fully-wetted flow, without corrections for viscous effects because the flow possesses a laminar po-tential core in all operational conditions. The dependence of the active nuclei concentration on throat pressure is measured by repeating the procedure at different exhaust pressures.

A general view of the experimental apparatus is shown in Fig. 1. The electronic instrumentation rack is on the left, the data acquisition and reduction computer is in the center and the optical and fluidic components of the CSM are in the foreground on the right. The connections of the various parts comprising the CSM are illustrated in Fig. 2. The water from

the water inlet (WI) passes through the sampling valve (SV), the venturi tube (VT), the exhaust valve (EV) and is finally collected in the exhaust tank (ET). The pressure in the exhaust tank is kept constant by the regulated air pressure line (RA), which is used to control the flow rate and therefore the pressure generated at the throat of the venturi. The static pressure of the sampled water is measured by a pressure transducer (UPT) located upstream of the test venturi. Periodically the sampled water is removed from the exhaust tank through the return valve (RV) and the water return line (WR) by increasing the regulated air pressure. During test runs the dual beam back-scattering Laser Doppler Velocimeter (LDV) monitors the oc-currence of cavitation and the flow velocity at the throat of the transparent venturi (VT). The analysis of the signals from the LDV and the upstream pressure transducer is carried out by an especially designed electronic Signal Processor for real time generation and temporary storage of the relevant data. The LDV generates a burst when an inhomogeneity such as a cavity or a suspended particle scatters light during its motion through the focal point. After band-pass filtering this burst ideally consists of a Doppler carrier frequency modulated by a Gaussian-shaped envelope. The Doppler frequency is pro-portional to the velocity of the scatterer. The amplitude of the burst's envelope is instead mostly related to the scatterer size, although it also depends in a complex way on its shape, optical

─────────── Nomenclature ───────────

A = cross-sectional area
C_c = venturi contraction coeffi-cient
C_e = venturi expansion coefficient
D = venturi diameter
f = probability density distribu-tion
L = length
M = number of data groups
$n(p_t)$ = concentration of nuclei with critical pressure not smaller than p_t
N = integer number
N_b = number of cavitation events or bubbles
N_{zc} = number of zero crossings
p = pressure

p_t = venturi throat pressure
p_u = venturi upstream pressure
q = volume flux
R = venturi radius
t = time
t_s = sampling time
T = temperature
T_b = arrival time of a cavitation event or bubble
T_g = Doppler gate time
T_p = arrival time of a velocity tracer or particle
u = velocity
u_t = venturi throat velocity
α = air content
δ = boundary layer thickness
ϵ = error
$\bar{\nu}_b$ = average cavitation event rate

σ = standard deviation
σ^2 = variance

Subscripts

b = bubble or cavitation event
c = venturi tub contraction
e = venturi tube exhaust
o = reference conditions
p = particle or velocity tracer
s = sample
t = venturi tube throat
u = upstream
zc = zero crossing

Acronyms

CSM = Cavitation Susceptibility Meter
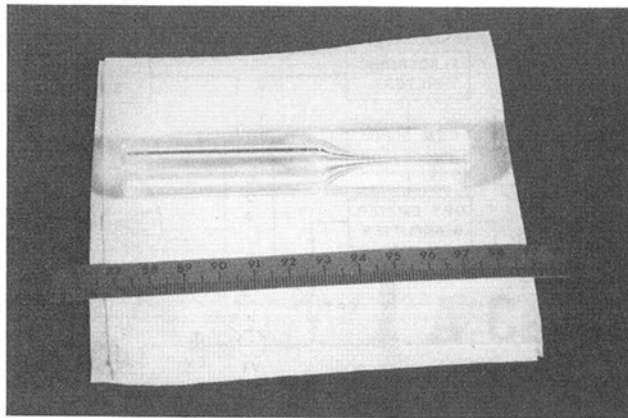LDV = Laser Doppler Velocimeter

Fig. 3 Close-up view of the CSM venturi tube No. 1. A cylindrical shell of cast transparent resin contains the glass blown venturi tube for mechanical protection and easy installation. The contraction ratio of the tube is about 1/100, the throat diameter is about 1 mm and the exit diameter is about 1.2 mm.
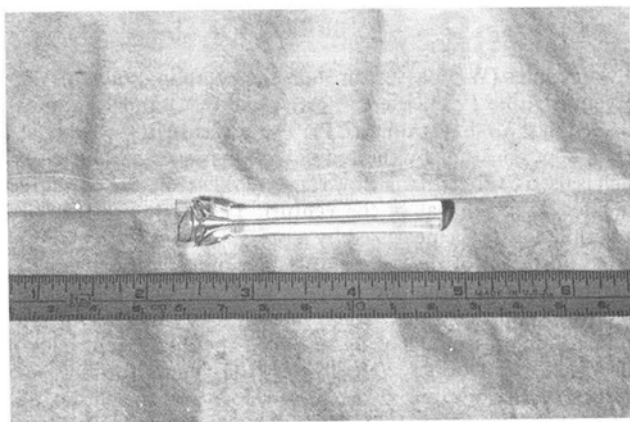

Fig. 4 Close-up view of the CSM venturi tube No. 2. This blown glass venturi has thicker walls, a contraction ratio of about 1/100, a throat diameter of about 1 mm, a long straight section after the diffuser and an exhaust diameter of about 1.2 mm.

properties and on the location of its trajectory through the LDV focal point. The CSM Signal Processor uses the intensity and the Doppler modulated frequency of the LDV bursts to respectively monitor the occurrence of cavitation and to measure the flow velocity. The instantaneous upstream pressure of the water is provided by the output of the pressure transducer. At the conclusion of each run the data are transferred to the minicomputer for final acquisition, storage and reduction. The LDV signal is normally monitored by an oscilloscope and the signal of the upstream pressure transducer by a digital multimeter.

Two types of glass venturi tubes have actually been used. The first type, indicated as tube No. 1, is an extremely fragile blown glass venturi contained in a cylindrical shell of transparent acrylic resin (see Fig. 3) for mechanical protection and connection to the hydraulic lines. The second type of glass venturi, indicated as tube No. 2, has much thicker walls and can therefore be directly connected to the hydraulic lines without mechanical protection. It is shown in detail in Fig. 4. These two venturi tubes have very similar fluid mechanical characteristics. They both have about the same throat diameter ($D_t \simeq 1$ mm), the same throat section length ($L_t \simeq 5$ mm) and the same geometrical contraction and expansion ratios ($C_c \simeq 1/100$ and $C_e \simeq 1.44$, respectively). Hence, the velocity profile determined from fully wetted flow measurements with artificial seeding using the LDV is also very similar in the two venturis and the corresponding minimum pressure developed is in both cases $p_{t_{min}} \simeq -35$ kPa. The most important fluid mechanical

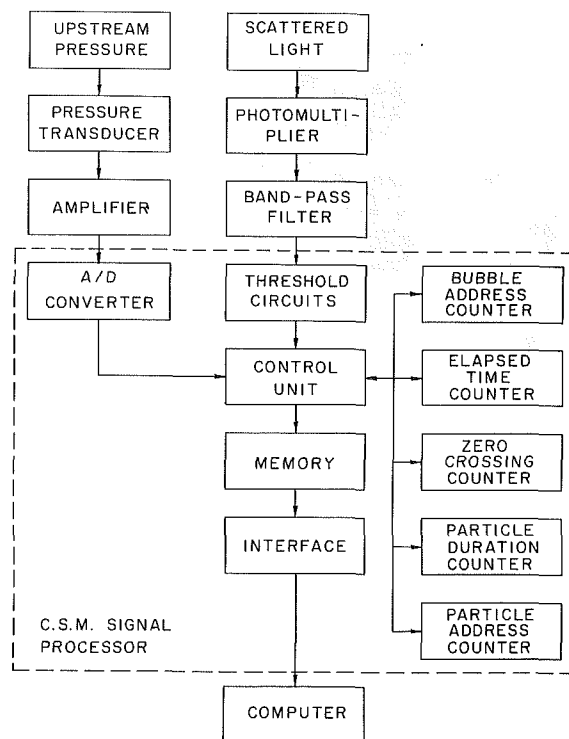BLOCK DIAGRAM OF C.S.M. INFORMATION FLOW

Fig. 5 Block diagram of the information flow in the CSM Signal Processor

difference between the two venturi tubes is the different length of the exit section, much shorter in the venturi No. 1 (only a few mm) than in the venturi No. 2 (about 3 cm). As a consequence, the flow in the second venturi is considerably more stable with respect to the insurgence of cavitation-separation.

3 Data Acquisition and Reduction

A simplified block diagram of the CSM signal processing and data acquisition is shown in Fig. 5. The output of the photomultiplier is band-pass filtered for separating the Doppler frequency from the electronic noise and sent to the CSM Signal Processor, where it is amplified before entering the threshold circuits. Here a zero level and two couples of adjustable, symmetric threshold levels are used to reject the residual noise and to discriminate valid Doppler bursts coming from a velocity tracer from the ones coming from a cavitation event. For simplicity cavitation events will be indicated as bubbles and velocity tracers as particles, although in practice smaller cavities probably represent the majority of the velocity tracers recognized by the CSM Signal Processor during a typical CSM run. The information from the threshold circuits is used by the Signal Processor to control five counters and to generate, collect and temporarily store in real time the following data:

* when a cavitation event (bubble) is recognized:
  1 the occurrence time measured from the beginning of the run (bubble elapsed time, T_b);
* when a velocity tracer (particle) is recognized:
  1 the occurrence time measured from the beginning of the run (particle elapsed time, T_p);
  2 the duration of the Doppler burst (particle gate time, T_g);
  3 the number of zero crossings of the Doppler burst N_{zc};
  4 the upstream water pressure p_u;

A maximum of 1024 cavitation bubbles and velocity tracers can be independently recorded at a maximum acquisition rate

of about 10000 events per second. At the conclusion of each run the data collected by the CSM Signal Processor are serially transferred to the microcomputer for final acquisition, storage on a magnetic disk and reduction.

The data reduction develops through the following steps:

1 zero crossing validation and statistical filtering of the Doppler frequency and upstream pressure data;
2 computation of the average potential core velocity, of the potential core velocity data standard deviation and of the boundary layer thickness;
3 computation of the average throat pressure and of the throat pressure data standard deviation;
4 validation of the arrival times of cavitation events and velocity tracers;
5 computation of the observed and expected occurrence frequency distributions of the delay times between cavitation events;
6 computation of the unstable nuclei concentration and of its standard deviation.

During the first step Doppler frequency data are computed by dividing the number of zero crossings of each burst by twice its duration. To reject spurious bursts, only counts with a preselected minimum number of zero crossings are used (zero crossing validation). Both the Doppler frequency data and the upstream pressure data contain a relatively small number of outliers due to various noise sources in the electronics. In addition, the Doppler frequency data may sometimes contain a significant number of low frequency readings from scatterers deep inside the venturi boundary layers. To eliminate the noise and to isolate the velocity information primarily coming from the venturi's potential core the Doppler frequency data are statistically filtered by only retaining those readings whose deviation from their average values does not exceed a preset multiple of their standard deviation (usually three standard deviations). The same procedure is also applied to the upstream pressure data, leading to the determination of the average upstream pressure $\bar{p}_u$ and of the upstream pressure data standard deviation σ_{p_u}.

The computation of the average potential core velocity, of the potential core velocity data standard deviation and of the boundary layer thickness (step 2) is carried out as follows. First the observed occurrence frequency distribution of the measured velocity data is calculated in the form of a histogram chart. When boundary layer effects are important and their role is not masked by other factors, this distribution is negatively skewed and therefore its third central moment is negative. If this is not the case the expected value and the standard deviation of the observed distribution are simply used to compute the average potential core velocity $\bar{u}_t$ and the standard deviation of the potential core velocity data σ_{u_t}, while the boundary layer thickness δ is taken to be zero. Otherwise, assuming uniformly distributed scatterers throughout the venturi cross-section, a theoretical probability distribution of the measured velocity is derived that parametrically depends on $\bar{u}_t$, σ_{u_t} and the ratio of the boundary layer thickness to the local duct radius δ/R_t. These parameters are then determined by fitting the theoretical distribution to the observed one. This process results in a slightly higher estimate of the average throat velocity and in a small reduction of the standard deviation of the throat velocity data depending on the value of the parameter δ/R_t.

The venturi throat pressure p_t (step 3) is deduced from the measurements of the upstream pressure p_u and of the throat velocity u_t using Bernoulli's equation for ideal, incompressible, steady, fully wetted flow. An unavoidable problem associated with this technique is that the throat pressure, being inherently small compared to the upstream pressure and the kinetic pressure drop, is expressed as the difference of two almost equal quantities. Thus, small relative errors in the evaluation of these quantities lead to a much larger relative error for the throat pressure. The statistical analysis for the determination of the average value $\bar{p}_t$ and the standard deviation σ_{p_t} of the throat pressure data p_t is carried out assuming that the two independent data populations p_u and u_t are normally distributed about their average values $\bar{p}_u$ and $\bar{u}_t$, with variances $\sigma_{p_u}^2$ and $\sigma_{u_t}^2$, respectively.

Clearly, the arrival times of LDV bursts are monotonically increasing and, in steady conditions, approximately proportional to their index. These properties are used to validate the data and to assess the uniformity of both the sample and the test conditions. First, the linear regression curve of the arrival times as a function of their index is calculated. Then, the data which are not in monotonically increasing order and whose deviation from the regression line is the largest are eliminated, in order to eliminate spurious readings (step 4).

The observed frequency distribution of the time t between successive cavitation events is calculated and a histogram chart is constructed by sorting the N_b data in, say, M groups equally spaced in time for comparison with the expected Poissonian exponential distribution $f(t) = N_b \bar{\nu}_b e^{-\bar{\nu}_b t}$, where $\bar{\nu}_b = N_b/t_s$ is the average arrival rate of cavitation events during the sampling time t_s (step 5). Finally, the volume flow rate $q = A_t \bar{u}_t$ is used to estimate the unstable nuclei concentration $n(p_t) = N_b/t_s q$ and its standard deviation $\sigma_n = \sqrt{N_b}/t_s q$ (step 6).

4 Experimental Procedure, Results, and Discussion

The calibration of the CSM system has been carried out using a mercury barometer for the upstream absolute pressure transducer and a rotating disk in air as a source of a finely controlled velocity field for the LDV. The overall accuracy (linearity plus repeatability) of the calibrations was better than 200 Pa for the upstream pressure transducer over the range 20 to 160 kPa, and 0.05 m/s for the LDV over the range 9 to 22 m/s. Thus, in general, the CSM instrumentation error was always negligible with respect to the inherent dispersion of the measured quantities.

The experimental procedure for measuring the water quality with the CSM is relatively simple. The water source is connected to the CSM test section with the shortest possible tubing, taking care to avoid abrupt changes of the duct internal section. An overflow line is also used to reduce as much as possible the transfer time of the sample to the CSM. The temperature of the sampled water is measured with a thermometer and its air content with a manometric van Slyke meter before each CSM run.

The location of the LDV focal point is very important for obtaining high quality repeatable results from the CSM. Experience showed that the best location is at the end of the venturi throat section. This choice provides better LDV signal strength, due to the larger size of the scattering bubbles, with acceptable dispersion of the velocity data. The electronic settings also are of crucial importance for the operation of the CSM, since they determine the number of LDV bursts recognized and counted as cavitation events. Proper choice of these settings depends on the correlation of the scatterer size to its LDV signature and on the definition of a general criterion for discriminating in dynamic conditions unstable cavitating nuclei from stable ones. This first aspect can be partially addressed by calibrating the LDV signal from cavities of known sizes, for example by monitoring the sampled water with holographic methods (d'Agostino et al., 1989; d'Agostino and Green, 1989). The discrimination of unstable cavitating nuclei, however, is essentially equivalent to the definition of the cavitation inception conditions, which is still an open problem in cavitation research. Until these two problems are satisfactorily solved, the selection of the electronic settings of the CSM remains, at least to some extent, arbitrary. In the present case the electronic settings were chosen trying to optimize the re-
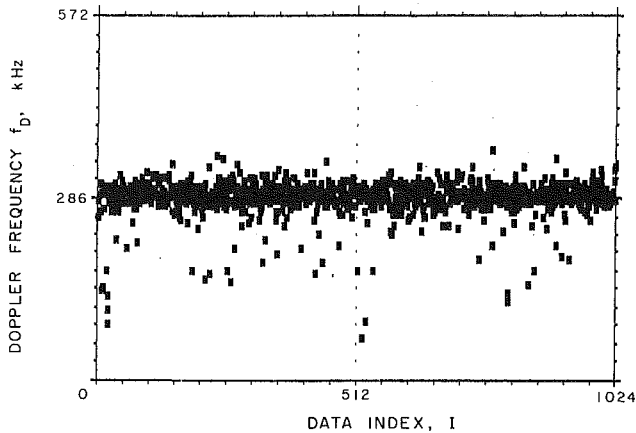
Fig. 6 Doppler frequency data f_D as a function of the data index I in a typical CSM run. The data refer to a tap water sample with initial pressure p_o = 1 atm, temperature T = 21°C, air content α = 20.5 ppm, throat pressure p_t = −15 kPa and velocity u_t = 14.8 m/s.
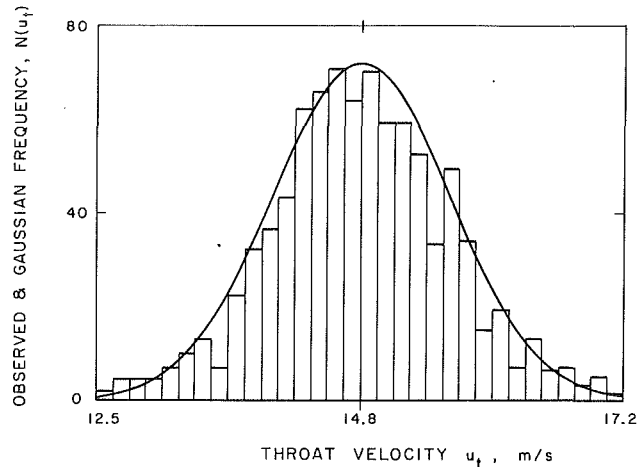

Fig. 7 Observed distribution of filtered throat velocity data (histograms) compared to the Gaussian distribution (solid line) of equal mean and standard deviation for the data sample of Fig. 6
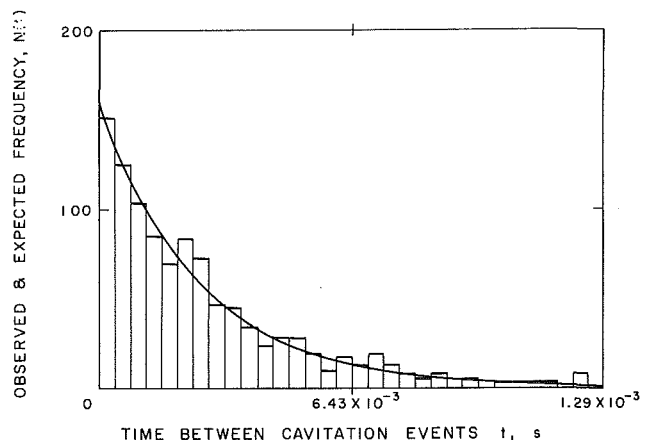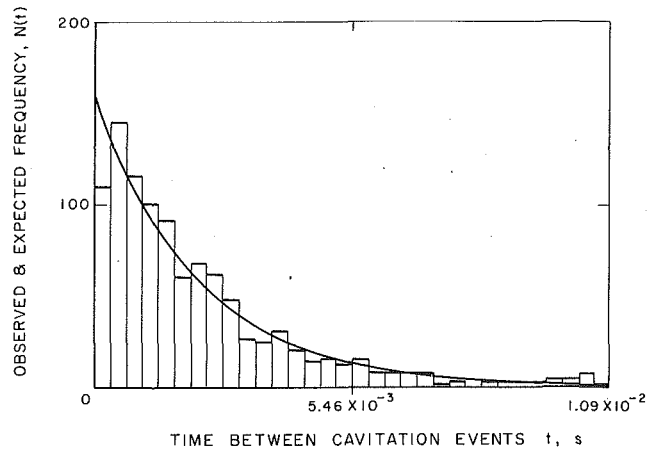

Fig. 8 Observed distribution of time intervals between cavitation events (histograms) in a typical CSM run compared to the theoretical exponential distribution (solid line) of equal average arrival rate. The data refer to the tap water sample of Fig. 6

sponse of the electronics and to ensure the applicability of the same settings to the whole range of the expected operational conditions.

The results reported in this section have been obtained testing tap water in the venturi tubes No. 1 and No. 2 briefly described in the previous section. Three different flow regimes have been observed:

- travelling bubble cavitation;
- cavitation-separation and sheet cavitation;
- spot and resonant cavitation.

Clearly only the first one is the nominal operational regime of the CSM where meaningful water quality measurements can be made. The others involve unwanted phenomena, which often perturb the flow conditions in an uncontrollable way and prevent the possibility of reliably measuring the active cavitation nuclei concentration in the sampled water. Therefore, for conciseness, they will not be examined here.

The traveling bubble flow regime is characterized by the random occurrence of cavitation bubbles in the CSM venturi and has been observed in both venturi tubes No. 1 and No. 2. The bubbles start to develop in the bulk of the liquid in the upstream region of the venturi's throat section, travel downstream reaching their maximum size somewhere in the diffuser or sometimes in the exit section, and later collapse. Under stroboscopic light the bubbles appear approximately spherical, at least during their growth phase. The length of the region where cavitation bubbles can be observed, their maximum size and occurrence rate depend on the flow conditions, clearly increasing with the throat tension and the velocity of the flow. In the venturi tube No. 2 (the only one where the entire life cycle of the cavitation bubbles can be observed) the length of the cavitation region ranges from about 5 to 25 mm. The maximum size of the bubbles varies greatly and can even be comparable to the local diameter of the venturi. Optical observation also indicates that larger bubbles occur when the cavitation event rate is relatively low. This behavior suggests the possible presence of significant interactive effects among the bubbles at high concentrations and is directly related to the general problem of flow saturation, which will be discussed later.

Some of the physical raw data and of the reduced data from a typical CSM run of a tap water sample with an air content of 20.5 ppm at 21°C are shown in Fig. 6 through Fig. 8. The water sample, initially at atmospheric pressure, was tested in the venturi tube No. 2 at a throat pressure of −15 kPa corresponding to a velocity of 14.8 m/s.

The Doppler frequency data in the first plot of Fig. 6 are centered about their average value indicated on the scale. The

dispersion of the data is mainly due to the intrinsic slightly unsteady nature of the flow and to the non-uniformity of the velocity profile in the venturi. However, this data set also contains a small but significant number of low frequency readings. Some of these readings do not appear to be randomly distributed during the run, but rather seem to occur sequentially in small groups. Experience with the operation of the CSM indicates that they are probably coming from cavities rather than, for example, from small particles normally present in the boundary layer. Most likely they are due to bubbles originating from the disintegration of small attached cavities from surface nuclei under the action of the incoming flow and later swept downstream through the LDV probe volume before they had time to accelerate to the surrounding flow velocity. This conclusion is also supported by the observation that cavitation events occasionally occur in clusters, which correspond to short, almost horizontal stretches in the plot of the bubble arrival time data.

In the second plot (Fig. 7) the histogram chart representing the velocity data distribution is compared to the Gaussian curve of equal average value and standard deviation. Readings deviating from the mean more than three standard deviations have been eliminated. Note that the observed distribution of velocity data seems to follow rather closely a normal distribution and does not display any appreciable skewness which could be attributed for example to the effects of the boundary layers, as previously mentioned. Experience from other runs

274 / Vol. 113, JUNE 1991

Transactions of the ASME

Fig. 9 Observed distribution of time intervals between cavitation events (histograms) slightly deviating from the theoretical exponential distribution (solid line) as a consequence of short range bubble interference effects


Fig. 10 Cavitating nuclei concentration $n(p_t)$ measured by the CSM as a function of the venturi throat pressure p_t in a sample of tap water with temperature $T = 21°C$ and air content $\alpha = 20.5$ ppm

Fig. 11 Standard deviation of the throat velocity data σ_{u_t} as a function of the throat pressure p_t in the tap water sample of Fig. 10

showed that the skewness of velocity distributions is usually small in both directions and probably statistically insignificant, as if the biasing effects of the boundary layer were unimportant or masked by some other phenomenon. Therefore the estimates of the ratio of the boundary layer thickness computed from the observed negative skewness of the velocity data distribution should be regarded with some skepticism, despite the fact that they never gave unrealistic results.

In the last plot (Fig. 8) the histogram chart representing the distribution of the observed time intervals between cavitation events is compared to the Poissonian exponential distribution expected to describe the occurrence of cavitation when the flow conditions are constant and the cavitation events are uncorrelated. This comparison provides a way to assess the importance of short range nuclei interference effects at the throat of the CSM venturi due to the inhibiting action that the pressure perturbations from a growing cavity can exert on the growth of neighboring nuclei. Clearly, this kind of interaction especially penalizes the occurrence of the shortest time intervals between successive cavitation events with respect to the theoretical Poissonian distribution. The data from Fig. 8 do not show any evidence of important short range bubble interference. For comparison, an example of a distribution deviating from the expected exponential behavior as a consequence of nuclei interference effects is shown in Fig. 9 for a different CSM run. In general these effects in CSM flows are not large. At most they affect a few percent of the total number of cavities and only tend to appear at heavier cavitation rates, when the separation between cavitating nuclei is proportionally reduced. This is not surprising when considering that the minimum average separation of cavitation bubbles is comparable to the length of the CSM venturi tube even at the highest cavitation rates. Clearly, more cavities are actually present in the flow whose LDV signatures are not large enough for them to be recognized as cavitation events by the CSM Signal Processor. For these cavities short range interference effects are likely to be more significant.

When a large number of cavities is continuously present in the cavitation region of the CSM venturi the collective effects of the bubble volume changes produce a global, permanent increase of the pressure throughout the venturi test section (choked flow conditions). In this situation the tube is saturated and the maximum tension that venturi tube can develop at any given flow rate is reduced, as it will be shown later in this section. However, the pressure experienced by any one bubble is not appreciably modified by the presence of the neighboring ones, since saturation is a large scale effect due to the collective contribution of many cavities widely distributed in the flow.
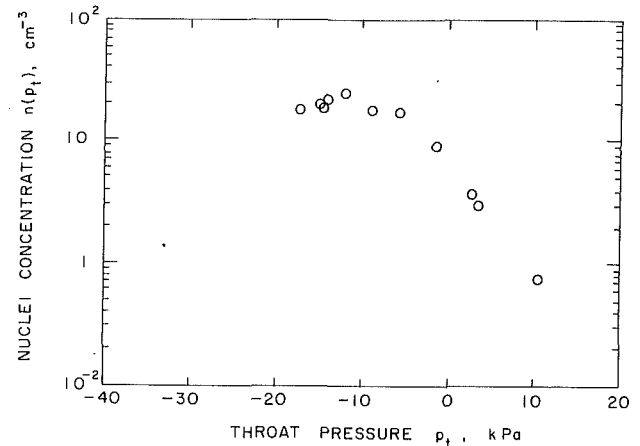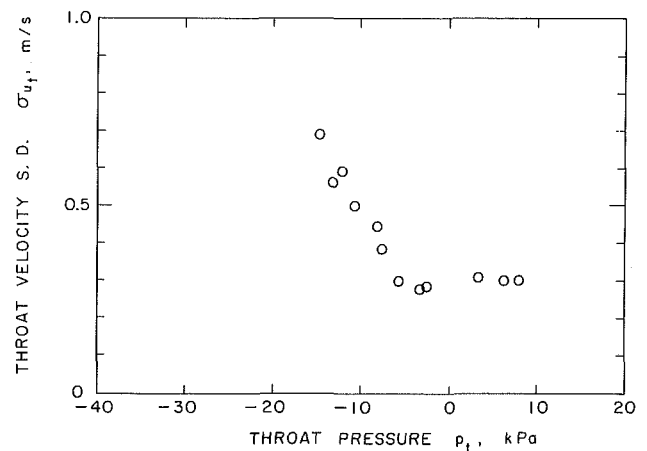
Therefore this kind of bubble interference will affect the average cavitation rate but will not be reflected in an anomalous distortion of the observed distribution of the time intervals between cavitation events. Clearly, saturation phenomena tend to increase with the concentration of unstable cavitation nuclei in the water sample and with the tension they are exposed to and impose limitations to the range of liquid quality measurements which can be carried out with the CSM.

An example of the application of the CSM to the measurement of the cavitation nuclei concentration as a function of the venturi throat pressure by means of repeated runs on a sample of tap water at 21°C with a dissolved air content of 20.8 ppm is shown in Fig. 10 and Fig. 11. These results are generally representative of CSM water quality measurements on other tap water samples in similar conditions. At first the concentration of cavitation nuclei increases about exponentially with the applied tension, as also reported by other investigators (Oldenziel, 1982a; Shen and Gowing, 1985; Shen et al., 1986). When the throat pressure is further reduced below about −7 kPa the concentration of cavitation nuclei reaches a maximum ranging from 20 to 40 cm^{-3} and remains nearly constant thereafter. The observed behavior of the concentration of cavitation nuclei probably reflects the actual lack of cavitation nuclei which become active when the throat pressure is lowered below about −7 kPa. In this case a further decrease of the throat pressure would simply produce a more violent growth and collapse of the available population of active nuclei. Larger perturbations would then be induced in the flow,

thus generating the parallel increase of the velocity data standard deviation from a previously constant value that is clearly apparent in Fig. 11. This interpretation has also been favorably tested by comparison of CSM results with holographically determined nuclei concentration density distributions (d'Agostino et al., 1989; d'Agostino and Green, 1989). Finally, note that, assuming in first approximation that the throat pressure is correctly measured also in the presence of heavy cavitation, the minimum pressure generated by the CSM venturi in the run of Fig. 10 is of the order of -15 kPa and therefore considerably higher than the venturi can develop in the absence of extensive cavitation. It appears that saturation phenomena are responsible for the observed decrease of the maximum achievable tension in the venturi and the consequent performance limitations.

At given settings of the CSM the accuracy in the determination of the water quality is due to the errors in the measurement of the cavitating nuclei concentration and of the average throat pressure. With good approximation the throat pressure data are normally distributed and the occurrence of cavitating nuclei is a Poisson process, provided that the flow conditions are constant during the run. Then, both the above errors are inversely proportional to the square root of the size of the data sample (Browlee, 1960) and therefore can be significantly reduced by averaging the measured quantities on a sufficiently large number of data. Since the number of filtered data is usually close to 900, the relative r.m.s. error of the measurement of the cavitating nuclei concentration is rather small, of the order of a few percent. The standard deviation of the throat pressure data is quite large in relative sense due to the inherent dispersion of the throat velocity data and to the small value of the pressure at the CSM venturi throat. Values of about 5 to 10 kPa for the standard deviation of the throat pressure data are representative of the results usually obtained from CSM runs. As mentioned earlier, this value must be divided by the square root of the sample size in order to obtain the standard deviation of the average throat pressure. With the same size of data sample as previously assumed the corresponding error in the determination of the average throat pressure is therefore of the order of a few hundred Pascals. The above expected errors are both relatively small, but it should be born in mind that they strictly refer to the measurement process alone. In a broader sense the indetermination in the measurement of the water quality also includes the effects of the uncertainties in the relationship between the LDV signal intensity and the size of cavitating bubbles and in the discrimination of unstable nuclei from the stable ones. The former of these effects is related to the specific nuclei detection technique used in the CSM and could presumably be resolved to some extent by calibrating the instrument response with cavities of known sizes, as previously suggested. The latter is instead shared by all currently devised techniques of cavitation nuclei detection. The inclusion of all error sources involved makes the measurement of the liquid quality with CSM's (and with other alternative methods) considerably more uncertain than it would first appear from the above considerations.

5 Conclusions

The following conclusions can be drawn from the available experience on the CSM system at the present stage of the project:
- three different flow regimes have been observed in the CSM venturi tube:
  1 travelling bubble cavitation (during normal operation);
  2 cavitation-separation and sheet cavitation;
  3 spot and resonant cavitation.
- the proposed design concept has been successfully demonstrated in all its components;
- the CSM is able to measure the concentration of active

cavitation nuclei as a function of the throat pressure over an extended range of applied tensions;
- the maximum value of the tension currently attainable (-35 kPa) is often insufficient for cavitating waters with relatively low nuclei content;
- at high nuclei concentrations flow saturation produces a generalized increase of the pressure and a parallel decrease of the velocity throughout the venturi throat section and therefore limits the performance of the CSM by reducing the maximum value of the tension exerted on the liquid;
- contrary to preliminary expectations, the arrival of cavitation events remains nearly Poissonian also at high cavitation results. Therefore saturation does not produce important short range interference effects between cavitating nuclei nor, consequently, poses significant limitations to the measurement of the concentration of active cavitation nuclei other than those due to the reduction of the maximum tension applied to the liquid;
- the maximum measurable concentration of active cavitation nuclei in the water samples tested so far appears to be limited by the available supply of nuclei in the samples rather than by the occurrence of saturation;
- active cavitation nuclei concentrations up to about 40 cm^{-3} have been recorded with little evidence of short range interference effects between cavitating bubbles;
- the flow is very sensitive to laminar separation in the diffuser, which limits the minimum throat pressure currently attainable to about -35 kPa;
- cavitation-separation and sheet cavitation frequently interfere with the normal operation of the CSM;
- the possibility of measuring the velocity of individual cavities at the venturi throat represents a powerful and unique mean for discriminating the cavities produced by free-stream nuclei from the ones originated from surface nuclei and for introducing corrections to the CSM measurements when necessary;
- the possibility of recording the transit time of cavitating bubbles is extremely useful to assess the importance of short range interference effects from the statistical properties of the cavitation process;
- the measurements of the cavitation nuclei number concentration density distributions in tap water samples obtained using the CSM show little dispersion and good repeatability;
- comparison of the CSM with a reliable nuclei detection method (holography) is indispensable in order to "properly" choose the electronic thresholds for the discrimination of cavitation events and in order to correctly interpret some of the observed results.

References

Billet, M., 1986, "The Importance and Measurement of Cavitation Nuclei," *Advancements in Aerodynamics, Fluid Mechanics and Hydraulics*, Minneapolis, Minn., pp. 967–989.

Billet, M., 1985, "Cavitation Nuclei Measurement—A Review," *ASME Cavitation and Multiphase Flow Forum*, Albuquerque, N.M., pp. 31–38.

Browlee, K. A., 1960, *Statistical Theory and Methodology in Science and Engineering*, Wiley.

Chahine, G. L., and Shen, Y. T., 1986, "Bubble Dynamics and Cavitation Inception in Cavitation Susceptibility Meters," ASME JOURNAL OF FLUIDS ENGINEERING, Vol. 108, pp. 444–452.

d'Agostino, L., 1987, "Experimental and Theoretical Study on Cavitation Inception and Bubbly Flow Dynamics," Ph.D. thesis, Report No. Eng. 183.16, California Institute of Technology, Pasadena, Calif.

d'Agostino, L., and Acosta, A. J., 1983, "On the Design of Cavitation Susceptibility Meters," *American Towing Tank Conference*, Hoboken, N.J.

d'Agostino, L., and Acosta, A. J., 1991, "A Cavitation Susceptibility Meter With Optical Cavitation Monitoring—Part One: Design Concepts," published in this issue pp. 261–269

d'Agostino, L., Thai Pham and Green, S., 1989, "Comparison of a Cavitation Susceptibility Meter and Holographic Observation for Nuclei Detection in Liquids," ASME JOURNAL OF FLUIDS ENGINEERING, Vol. 111, No. 2, pp. 197–203.

d'Agostino, L., and Green, S. I., 1989, "Simultaneous Cavitation Susceptibility Meter and Holographic Measurements of Nuclei in Liquids," *ASME Cavitation and Multiphase Flow Forum*, San Diego, California, USA.

Godefroy, H. W. H. E., Jansen, R. H. J., Keller, A. P., and van Renesse, R. L., 1981, "Comparison of Measuring and Control Methods of the Water Quality with Respect to Cavitation Behavior," Delft Hydraulics Laboratory Publication.

Ito, Y., and Oba, R., 1980, "Cavitation Observations through a Fine Laser Beam Technique," Report No. 337, Institute of High Speed Mechanics, Tohoku University.

Knapp, R. T., Daily, J. W., and Hammitt, F. G., 1970, *Cavitation*, McGraw Hill, N.Y.

Lecoffre, Y., and Bonnin, J., 1979, "Cavitation Tests and Nucleation Control," *International Symposium on Cavitation Inception*, New York, N.Y., pp. 141–145.

Le Goff, J. P., and Lecoffre, Y., 1983, "Nuclei and Cavitation," *14th Symposium on Naval Hydrodynamics*, National Academy Press, pp. 215–242.

Oldenziel, D. M., 1982a, "A New Instrument in Cavitation Research: the Cavitation Susceptibility Meter," ASME JOURNAL OF FLUIDS ENGINEERING, Vol. 104, pp. 136–142.

Oldenziel, D. M., 1982b, "Utility of Available Instruments during Cavitation Tests," *Proceedings of Symposium on Operating Problems of Pump Stations and Power Plants*, IAHR, Amsterdam.

Oldenziel, D. M., 1979, "New Instruments in Cavitation Research," *International Symposium on Cavitation Inception*, New York, N.Y., pp. 111–124.

Oldenziel, D. M., Jansen, R. H. J., Keller, A. P., Lecoffre, Y., and van Renesse, R. L., 1982, "Comparison of Instruments for Detection of Particles and Bubbles in Water during Cavitation Studies," *Proceedings of Symposium on Operating Problems of Pump Stations and Power Plants*, IAHR, Amsterdam.

Shen, Y. T., Gowing, S., and Pierce, R., 1984, "Cavitation Susceptibility Meters by a Venturi," *International Symposium on Cavitation Inception*, ASME Winter Annual Meeting, pp. 9/18.

Shen, Y. T., and Gowing, S., 1985, "Scale Effects on Bubble Growth and Cavitation Inception in Cavitation Susceptibility Meters," *ASME Cavitation and Multiphase Flow Forum*, Albuquerque, New Mexico, pp. 14–16.

Shen, Y. T., Gowing, S., and Eckstein, B., 1986, "Cavitation Susceptibility Measurements of Ocean Lake and Laboratory Waters," David W. Taylor Naval Ship Research and Development Center, Report DTNSRDC-86/D19.

A. S. Ramamurthy[1]
Professor, Department of
Civil Engineering,
Mem. ASME,

R. Balachandar[2]
Research Associate, Faculty
of Engineering and Computer Science.
Assoc. Mem. ASME

H. S. Govinda Ram
Visiting Scientist, Department
of Civil Engineering.

Concordia University,
Montreal, Canada

Some Characteristics of Flow Past Backward Facing Steps Including Cavitation Effects

Backward facing steps were used to study experimentally the effects of expansion ratio and Reynolds numbers on the incipient cavitation indices. For small changes in the expansion ratio, significant changes in incipient cavitation index were observed. The effect of cavitation and expansion ratio on the frequency of vortex shedding and pressure distribution downstream of flow separation were also obtained. The dependence of the flow characteristics like the reattachment length, the frequency of vortex shedding and the pressure distribution downstream of the step were obtained under noncavitating conditions. In the present study, the range of Reynolds numbers has been extended to values which are normally encountered in prototype installations.

General Remarks

Separated flows associated with boundary discontinuity result in highly turbulent recirculating flows and are of considerable interest in many branches of engineering. Examples include, flow over surface discontinuities such as slots and steps, flow along the walls of rapidly expanding diffusers, and flow past blunt structures. Flow separation can cause significant energy losses. In fact, sudden enlargements in flow systems have been effectively used as energy dissipators. The optimum performance of fluid machinery can be predicted by a better understanding of the characteristics of flow separation. Further, flow separation occurs just prior to or at maximum loading conditions (Chang, 1970). Flow past backward facing steps exhibit well defined regions of flow separation and reattachment. The resulting complex turbulent flow field can significantly change the local wall pressure field besides exhibiting unsteady low frequency behavior. The intense vortical action present may lead to inception of cavitation. Hence, the flow field generated can be a major source of flow induced vibration, noise, and cavitation.

Previous Studies

Noncavitating Flows. Numerous studies dealing with noncavitating flow past backward facing steps have been reported. Extensive reviews like those of Bradshaw and Wong (1972), Eaton and Johnston (1981) and Simpson (1989) are available in literature. With the advent of the Laser Doppler velocimeter system, the problems associated with measurements in the reversed flow region have been effectively overcome. This has resulted in the availability of some new experimental information related to the behavior of separated flows (Adams,

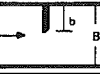1988; Durst and Tropea, 1982; Etheridge and Kemp, 1978, Isomoto and Honami, 1989; and Stevenson, 1984).

Kim (1980), Moss and Baker (1978), Narayanan (1974), Tani (1961), and Westphal (1984) have presented the pressure distribution downstream of a backward facing step. Adams (1988) studied the effect of the separating shear layer thickness on the structure of the flow in the reattachment region downstream of a backward facing step and found that the wall pressure profiles were insensitive to the nature of the boundary layer. The pressure profiles depended only on the parameter δ/h, where δ is the boundary layer thickness ahead of separation and h is the height of the step. Based on δ/h, Bradshaw and Wong (1972) have suggested a "strength of perturbation" criterion for classifying flows with separated regions.
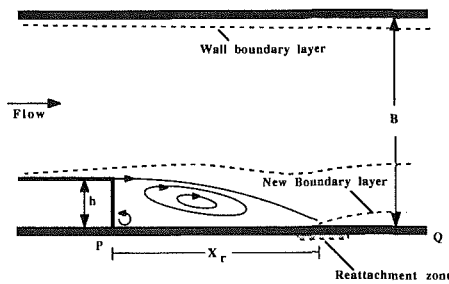
Driver (1987), Eaton (1982), Farabee (1984), Greshilov (1969), Katz (1982), and Rockwell (1979) studied the effects of flow past backward facing steps on the downstream wall pressure fluctuations. Eaton (1982) reports that Tani (1961) did not observe low frequency motions for flow past backward facing steps. Driver (1987) noted a global flapping of the shear layer which appeared to contribute little to the fluctuating energy. He also observed a second type of fluctuating vortical motion and found that a major portion of the energy in the flow resides in the frequencies characteristic of roll-up and pairing of vortical structure. Rockwell (1979) has suggested that the low frequency motions may be a result of the oscillations of the shear layer induced by the feed back of the disturbance from the impingement point to the separation point. For a small range of expansion ratios, Mabey (1972) formed a modified Strouhal number based on the length of the separation bubble and the free stream velocity, which appeared to display an almost universal trend. The effect of Reynolds number on the values of Strouhal number $S = fh/U$ at various expansion ratios have not been obtained.

Table 1 Summary of some previous studies involving cavitation in separated flows

Reference	Flow type	Remarks	Reference	Flow type	Remarks
Shalnev 1977 Varga 1966 Oba 1981		Characteristics of cavitating flow past circular cylinders	Narayanan 1984		Flow past a normal wall Limited studies related to inception
Ramamurthy 1977 1990		Flow past wedges. Damage and noise characteristics were also obtained. Partially cavitating conditions.	Ball 1974		Flow past sudden enlargements
Young et al., 1966		Flow past symmetric wedges	Katz 1982		Flow past blunt axisymmetric bluff body
Sarpkaya 1961		Flow past butterfly valves. Limited studies related to cavitation characteristics.	Arakeri 1981		Flow past axisymmetric backward facing step
Holl 1965		Flow past roughness elements.	Vigander 1965		Flow past boundary discontinuities

Fig. 1 Flow past a backward facing step

Fig. 2 Step models

STEP 1
Aspect ratio = 8.0
Expansion ratio = 1.07
h = 0.635 cms
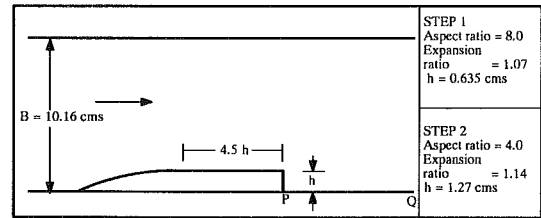
STEP 2
Aspect ratio = 4.0
Expansion ratio = 1.14
h = 1.27 cms

Several methods have been used to obtain the reattachment lengths X_r (Fig. 1) behind backward facing steps. Narayanan (1974) used a surface-oil flow observation and reports that X_r varied from 5.8–6.4 step heights for $1.01 < ER < 1.14$. Based on surface-oil flow visualization, Baker (1978) reports a value of $X_r/h = 5.8$ for $ER = 1.1$. Westphal (1984), Adams (1988), Driver (1987) used a thermal tuft probe to determine the near-wall instantaneous flow direction. This device was used to determine X_r based on the assumption that reattachment occurs at the point where the flow direction is downstream 50 percent of the time. Using a Laser Doppler anemometer, Durst and Tropea (1982) obtained X_r for a range of expansion ratios by extrapolating the line of zero velocity to the wall. With the help of a special skin friction probe, Westphal (1984) also determined X_r by finding the position where the skin friction coefficient was zero. These values of X_r compare favorably with the reattachment lengths obtained by the thermal tuft probe and pulsed wire anemometer.

Cavitating Flows. Literature dealing with cavitation in separated flows associated with boundary discontinuities are limited. Table 1 gives a summary of some of the existing results related to cavitation in separated flow regions. Vigander (1965) and Appel (1961) studied cavitation along the surface of separation in two-dimensional sudden expansions and found that cavitation stabilizes the vortices formed against further breakup. Lush (1975) studied the sound generated by cavitating flows past a backward facing step. Arakeri (1981) investigated the inception of cavitation downstream of an axisymmetric backward facing step having an hemispherical forebody. For a similar model, Katz (1982) observed that cavitation appeared in the form of a ring that surrounded the body. He also obtained the incipient indices over a range of Reynolds numbers. Ball (1974) studied the incipient cavitation damage in sudden expansions ($2 \leq ER \leq 6$) using orifices in pipelines. Several studies have been reported on the characteristics of flow past cavitating bluff bodies (Balachandar, 1990; Shalnev, 1977; Varga, 1966; Oba, 1981; Ramamurthy, 1977; Young, 1966; Narayanan, 1984). In the case of sharp edged bluff bodies, it

─────── **Nomenclature** ───────

B = test section width
C_p = $(P - P_{ref})/0.5 \rho U_{ref}^2$, pressure coefficient
C_{pmin} = minimum value of pressure coefficient along PQ (Fig. 1)
C_p^* = modified pressure coefficient (equation (1))
ER = expansion ratio
f = frequency of pressure pulsations
h = height of step
P = free-stream pressure

P_v = vapor pressure
P_x = pressure along PQ (Fig. 1)
Re = Reynolds number ($= U_{ref}h/\nu$)
S = Strouhal number ($= fh/U$)
P_{ref} = pressure upstream of step
U_{ref} = mean velocity ahead of the step ($X = 0$)
U_{max} = maximum velocity at a particular section
u' = turbulent component in the flow direction
X = distance from step edge along separation bubble

X_r = reattachment length
X^* = $(X - X_r)/X_r$
y = ordinate measured from the step
δ = boundary layer thickness
δ_1 = displacement thickness
δ_2 = momentum thickness
Ψ = stream function
ρ = density of fluid
σ = $(P - P_v)/0.5 \rho U_{ref}^2$, cavitation number
σ_i = Inception cavitation number
ν = kinematic viscosity

Fig. 3(a) Water tunnel
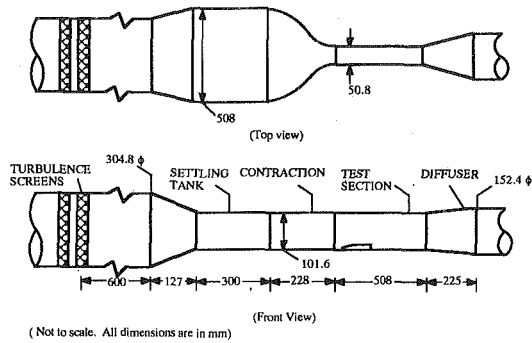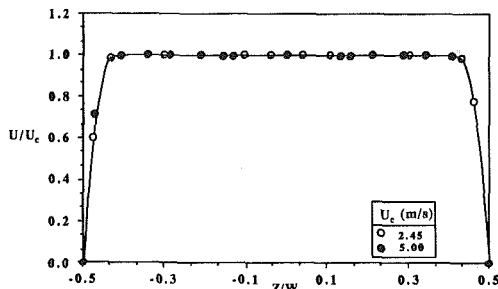

Fig. 3(b) Typical span-wise velocity measurements

Fig. 4 Typical cavitation nuclei measurements

was observed that cavitation produces negligible effects on the vortex shedding frequency with decreasing cavitation number σ down to as low as half the incipient value. At very low values of σ, vortex shedding was found to be random and highly intermittent. At choking conditions, no distinct vortex shedding frequency could be discerned from the power spectra of the pressure fluctuations. Recent visual observations in the wake of bluff bodies also indicate that the vortex appeared to be stabilized from breaking up in the partially cavitating regime of flow (Ramamurthy, 1990).

In the present study, two background facing steps (Fig. 2) were used to study the effect of expansion ratio (ER) on incipient cavitation indices σ_i at various Reynolds numbers. The effect of cavitation on the frequency of vortex shedding and pressure distribution downstream of separation was also obtained and in these tests, the Reynolds number of the flow was maintained constant at 1.28×10^5 and 0.77×10^5 for ER = 1.14 and 1.07, respectively. The corresponding ratio of the boundary layer thickness to the step height were of the order of 0.15 and 0.20. The dependence of the flow characteristics like the reattachment length, the frequency of vortex shedding, and the pressure distribution downstream of the step was also obtained under noncavitating conditions. In the present study, the range of Reynolds numbers has been extended to values which are normally encountered in prototype installations.

Experimental Setup and Procedures

Water Tunnel and Test Models. A schematic of the water tunnel used is shown in Fig. 3(a). A ten to one contraction was provided to obtain a uniform flow at the test section. The test section was 101.6 mm high, 50.8 mm wide, and 508 mm long. Wall static pressures were measured with 0.5 mm diameter pressure taps, typically spaced 1.27 cm apart located on the floor of the test section. The test section side walls were fitted with plexiglas windows. Preliminary experiments were made to check the quality of flow in the test section in the absence of the test model. Figure 3(b) shows typical Laser Doppler Velocimeter (LDV) measured span-wise velocity distributions. The velocities were uniform over the mid 80 percent of the span and the ratio of the centerline velocity to the average velocity was of the order of 0.94. This is a good indication of
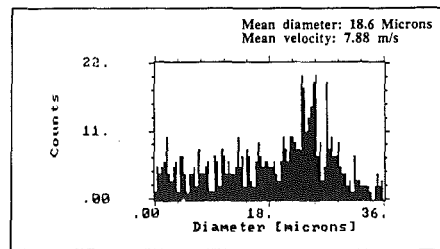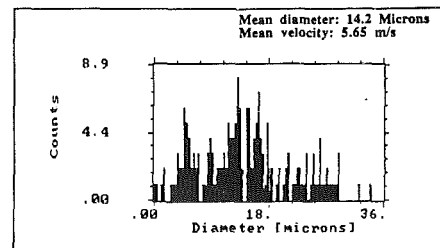
the two-dimensionality of the flow in the test section. The turbulence level in the test section varied from 1 to 3.5 percent. The higher values of turbulence intensities occurred only in a few tests, when the pressures in the test section were very low and were generally associated with very low values of σ.

The backward facing step models used in the present study are indicated in Fig. 2. Machined steps of heights 0.635 cm and 1.270 cm resulting in expansion ratios ER of 1.07 and 1.14 were used. The models were placed on the floor of the test section and spanned its entire width. Several pressure taps were provided along PQ (Fig. 2) to obtain the pressure distribution in the separated bubble region.

Pressure Pulsation Measurements. The frequency of pressure pulsations in the cavity was obtained with the help of pressure transducers located close to the edge of free shear layer and along the bottom wall of the separated region. The pressure signals were fed to a Fast Fourier Transform Analyser (Wavetek, 5830-A) to carry out the spectral analysis. A stroboscope (Bruel and Kjaer, Type 4912) and a battery of powerful lights were used to aid visual observation.

Velocity Measurements. Use was made of a TSI Laser Doppler Velocimeter (LDV) system in the forward scatter mode to obtain the velocity distributions in the test section. The system includes a 15mW He-Ne laser having a wavelength of 632.8 nm, a system of transmitting and receiving optics, a photodetector, and a signal processor (IFA 550) interfaced to a personal computer. To measure the reverse velocities in the separated regions behind the backward facing steps, a standard frequency downshift of 2 MHz was used. The LDV system and the data analysis software were also calibrated directly using a specially fabricated nozzle unit (Balachandar, 1990). The reference mean velocity U_{ref}, ahead of the step was obtained from the discharge measurements and verified by LDV measurements.

Cavitation Nuclei Measurements. The presence of imperfections or weak spots in liquids, commonly denoted as "cavitation nuclei" influences the scaling laws. The weak spots prevent the liquid from supporting higher tensions. Studies indicate that two forms of cavitation nuclei i.e., stream nuclei and surface nuclei influence the cavitation process. The cavitation nuclei measurements were made with a Laser Particle Dynamics Analyser (PDA). The PDA system (DANTEC Inc.) is an extension of the LDV system. The transmitting optics essentially resembles that of the LDV system with the 40 MHz Bragg cell being an essential part of the optic train. The re-
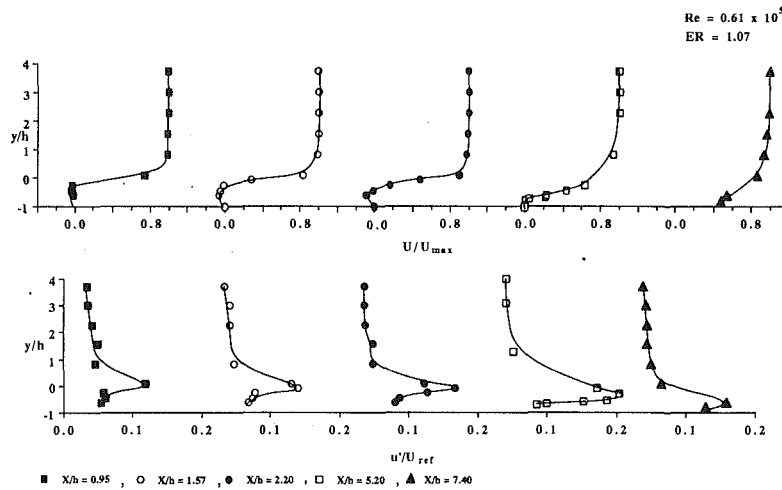
Fig. 5 Streamwise mean and fluctuating velocity measurement (ER = 1.07)

ceiving optics includes a system of 3 photomultiplier tubes (PM tubes) located at different scattering angles. The signals received at the PM tubes have a phase difference which is linearly dependent on the particle diameter. The system of 3 PM tubes assist in data validation checks and aid in the discrimination of spherical particles from other particulates. The mean diameter of the spherical particles ranges from 14 to 20 micrometers and does not vary over the range of velocities covered by the tests (Fig. 4). Qualitative relationships between cavitation inception and nuclei have been developed by Holl (1970) and Gates et al. (1979). As rightly pointed out by Blake (1986), beyond a rather notional relationship between nucleus population and cavitation, there is no rigorous theory in hydrodynamic cavitation that satisfactorily explains or accounts for the influence of nuclei in a quantitative sense.

Cavitation Inception Detection. Cavitation inception was detected visually by noting the occurrence of a few minute bubbles. In the present study, no significant cavitation hysteresis was distinguishable. The incipient condition was obtained at each velocity by reducing the free stream pressure until cavitation began to occur in the wake and then increasing the pressure until cavitation just disappeared or occurred intermittently. This state of cavitation was generally accompanied by the intermittent presence of a sharp crackling noise which was detected with the help of a stethoscope placed on the plexiglas window close to the free shear layer.

Other Measurements. During each test, the water temperature was noted to the nearest 0.25°C. The air content ranged from 11 to 17 ppm. The air content was estimated by obtaining the dissolved oxygen content using a YSI-57 D.O. meter (Morgan, 1972). During any specific run, the change in air content was negligibly small. The rate of flow was measured with the help of a calibrated venturimeter or a V-notch. The depth of flow over the notch was measured to the nearest 0.1 mm. The accuracy of discharge measurement is estimated to be 3 percent. Based on a 20:1 odds, the maximum uncertainties in the reported values of the cavitation number and the pressure coefficients are estimated to be 3.5 percent (Kline, 1985). The maximum uncertainties associated with the Strouhal number are of the order of 2 percent.

Analysis of Results

Velocity Measurements and Reattachment Length. Figure 5 shows the LDV measurements related to the streamwise mean velocity distribution, downstream of the backward facing step at ER = 1.07. The Reynolds number Re = $U_{ref}h/\nu$ was 0.61
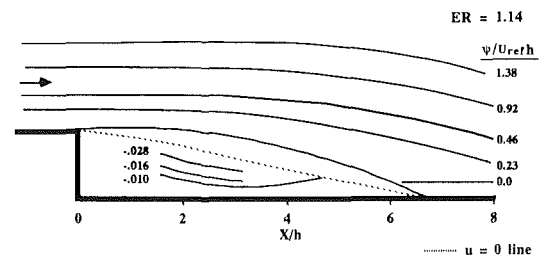

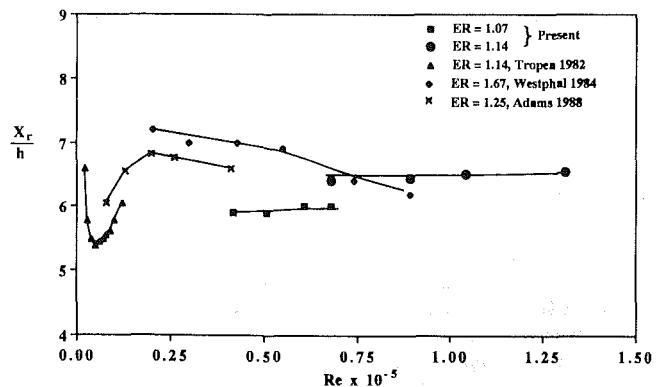Fig. 6 Typical streamline plot behind backward facing steps

Fig. 7 Variation of reattachment length with Re

× 10^5. In Fig. 5, at any location, the velocities were normalized by the maximum velocity U_{max} measured at that particular section. The velocity distribution typically resembles the measurements reported in previous studies (Eaton et al., 1988). As observed in other studies, the maximum reverse velocities were of the order of 0.2 U_{ref}. Furthermore, at the Reynolds number indicated in Fig. 5, the boundary layer shape parameter $H = \delta_1/\delta_2$ slightly ahead of separation was 2.2. However, the Clauser parameter G at $X/h = 7.4$ had a value of 19.6. This indicates that the recovery of the shape parameters of the reattached layer to that of a flatplate boundary layer does not occur immediately. In fact, Bradshaw and Wong (1972) report that the recovery was not complete even at 52 step heights downstream of separation. Figure 5 also shows the streamwise fluctuating components u' measured at Re = 0.61 × 10^5. The maximum value of u' increased with increasing X/h up to reattachment beyond which it decreased. Similar streamwise
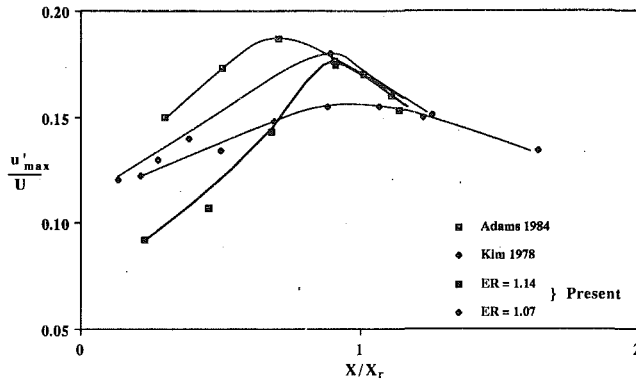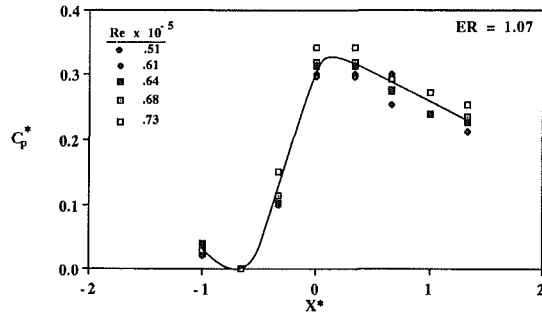
Fig. 8 Variation of (u'_{max}/U) with X/X_r.

Fig. 9 Variation of C_p^* with X^* (ER = 1.07)

Fig. 10 Variation of C_p^* with X^* at different expansion ratios

Fig. 11 Variation of C_p with X/h (ER = 1.14)

mean and fluctuating velocity distributions were also obtained at an expansion ratio of 1.14.

Using sketches such as Fig. 5, the loci of the streamwise zero mean velocity line were obtained and extrapolated to the wall to obtain the reattachment lengths. Figure 6 shows a typical loci of the zero mean velocity line. Also shown in Fig. 6 are a plot of the streamlines behind the backward facing step at ER = 1.14. Here, the stream function Ψ is normalised by $U_{ref}h$. In many cases, the value of X_r was also confirmed by obtaining the streamwise velocity measurements in the neighborhood of the reattachment zone and locating the section where the velocity was almost zero most of the time. To this end, the probability density functions of the velocity measurements were obtained by operating the signal analyser (IFA 550-TSI Inc.) in a real time mode. Figure 7 shows the variation of X_r with Re. As one would expect, Fig. 7 shows that X_r has a very minor dependence on Re for the higher ranges of Re tested. It may be added that, in the present study, the range of Re has been extended to larger values. Also shown in Fig. 7 are the values of X_r obtained from several other previous studies. At lower Reynolds numbers (Re $< 0.5 \times 10^5$) parameters such as the shape factor can have a dominant influence on the characteristics of separated flows and render the value of X_r/h to be highly dependent on Re. Fortunately, in field applications, the Reynolds number of the flow will be high and its influence on X_r is marginal. Hence, one can predict the value of X_r with a higher degree of confidence.

Figure 8 shows the relation between the maximum values of $(u'/U)_{max}$ with X/X_r through the reattachment zone. Inspite of the varying trends displayed by these relationships ahead of the reattachment, the data seem to collapse to a single curve downstream of reattachment ($X/X_r > 1.0$).

Mean Pressure Distribution. Figure 9 shows the static pressure distribution along the floor of the separated flow region. In an attempt to obtain a universal distribution (Roshko and Lau, 1965), the abscissa is represented as $X^* = (X - X_r)/X_r$ and the ordinate is represented as C_p^*. Here, C_p^* is defined as

$$C_p^* = \frac{C_p - C_{p\,min}}{1 - C_{p\,min}} \qquad (1)$$

where, C_p is the pressure coefficient ($= (P - P_{ref})/0.5\rho U_{ref}^2$) normalized by the upstream dynamic head and $C_{p\,min}$ is the minimum value of C_p occurring along PQ in Fig. 1. For the range of Re covered, it is clear from Fig. 9 that Re does not appear to have a dominant effect on C_p^*, especially ahead of reattachment. A similar behavior was also noticed at ER = 1.14.

Figure 10 shows a similar pressure distribution obtained from several previous studies which indicates that there are distinct trends downstream of reattachment. There are several parameters affecting the flow and as noted by Adams (1988), "the concept of a universal pressure rise curve for the entire region of reattachment region is valid only in the limit as $\delta/h \rightarrow 0$." Further the data of Adams (1988) also indicate that the larger the value of δ/h, the earlier the pressure curve departs from the suggested "universal" curve.

Figure 11 shows the variation of C_p with X/h, at Re = 1.28 $\times 10^5$ and different degrees of cavitation. The mean pressure distribution curve obtained from noncavitating flow conditions is also shown in Fig. 11. In general, the values of C_p obtained under cavitating conditions are slighty lower than those obtained under non-cavitating conditions. From previous studies related to cavitating flow past bluff bodies (Streeter, 1961), one notes that as σ ($= (P - P_v)/0.5 \rho U_{ref}^2$) is decreased to very low values ($\sigma \rightarrow 0$), the cavity formed by the separating streamline tends to be longer. Consequently, for step flows, the rate at which the flow expands downstream of the step is expected to be lower, at lower values of σ ($\sigma \ll \sigma_i$). As a result of this, the pressures in the expanding flow will be lower for $\sigma < \sigma_i$ than for the case $\sigma \gg \sigma_i$. The pressure being continuous across the separating streamline, the cavity pressures are expected to be lower for $\sigma < \sigma_i$ than for the case $\sigma \gg \sigma_i$ which
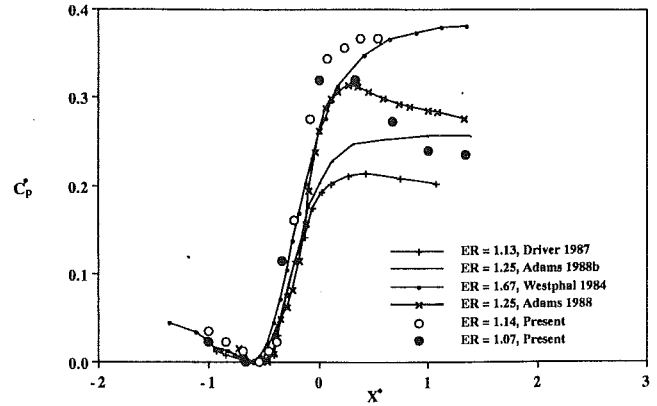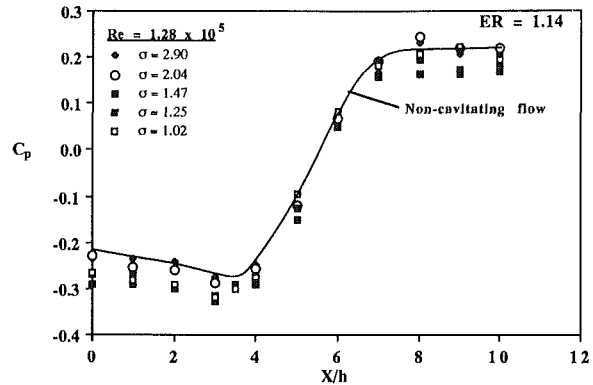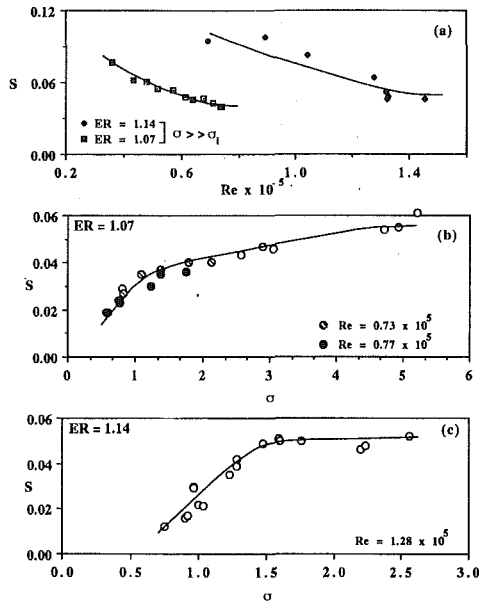
Fig. 12   *(a)* Variation of S with Re *(b)* Variation of S with σ (ER = 1.07)
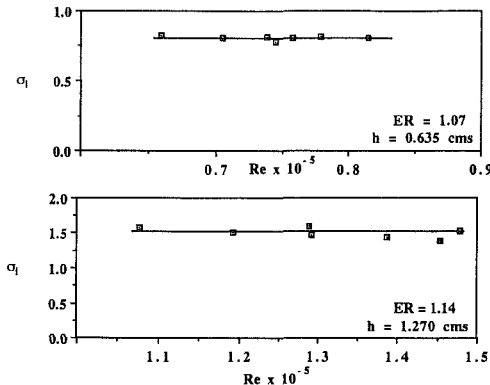*(c)* Variation of S with σ (ER = 1.14)

Fig. 13   Variation of σ_i with Re

inturn renders the wall pressures to be lower for cavitating flows than for non-cavitating flows. A similar behavior is also found to occur at the ER 1.07.

Figure 12(*a*) shows the variation of Strouhal number S with Re for the two expansion ratios under noncavitating conditions. For a single value of Re = 37,000 and an expansion ratio of 1.13, Driver (1987) obtained a Strouhal number of 0.098. This appears to qualitatively follow the trend obtained in the present study. Figure 12(*a*) indicates a decreasing trend with increasing Re. This is in contrast to flow past sharp-edged bluff bodies where the Strouhal number is almost independent of Re. The flow pattern in the separated region is quite different in the two situations. In the case of bluff bodies, the flow contracts immediately after separation while the flow expands after separating at the step edge. More significantly, there is a considerable interaction between the two separating shear layers and there is an effective organization of the flow pattern behind bluff bodies, resulting in an alternate vortex shedding mechanism and the formation of the well known Karman vortex street. Similar organization mechanisms are absent in the case of flow past a backward facing step. However, in the case of backward facing steps, it has been suggested by Rockwell (1979) that due to impingement of the shear layer resulting in a feed back mechanism, a possible organization of flow could result in low frequency oscillations.

Figures 12(*b*) and 12(*c*) show the variation of Strouhal number S with σ for the two expansion ratios. With decreasing σ, the value of S decreases. Comparing with cavitating flow past sharp-edged bluff bodies, the value of S does not remain constant at the noncavitating value for $\sigma > 0.5\,\sigma_i$ (Balachandar, 1990). In the case of backward facing steps, the values of S begin to decrease slightly ahead of inception. Beyond inception, the value of S drops rapidly. The differences in the dependence of S on σ, between a bluff body and a backward facing step are a consequence of the difference in the nature of vortex shedding stated earlier.

With the onset of cavitation, the presence of vapor in the core of the vortices aided visual observation. These observations indicate that the visible portion of the vortices appear closer and closer to the step edge with decreasing σ. At very low values of σ, cavitation bubbles are visible at the step edge and further decrease in σ results in the separating region presenting a foamy appearance. The flow is essentially choked at this stage and there is the absence of a dominant frequency in the pressure records. A similar trend has also been noticed in the case of flow past sharp-edged bluff bodies (Ramamurthy, 1990).

Figure 13 shows inception cavitation indices σ_i for the backward facing steps (h = 0.635 and 1.27 cms) obtained at various Reynolds numbers for the two expansion ratios. The values of σ_i are essentially constant for the range of Re tested. As in the case of flow past bluff bodies, inception of cavitation is accompanied by the presence of a sharp crackling noise. Some remarks regarding inception behind backward facing steps are in order. At inception, span-wise vortex like filaments were visible in the shear layer at about 3 or 4 step heights downstream of separation. With increasing Re, these vortex like filaments appeared closer to the step edge, though the value of σ_i remained the same. Previous visual observations (Durst, 1982) with the use of a dye in non-cavitating flow indicate that the shear layer rolled up into vortices and this location of the initial formation of the vortices moved upstream with increasing Re. From the studies of Driver (1987), one notes that the streamwise velocity fluctuations near the wall correlate negatively with the velocity fluctuations in the outer part of the boundary layer. This is clearly a characteristic of clockwise rotating flow. It is conjectured that as the location of the initial formation of the vortices move toward the edge of the step, the vortices rotating in clockwise direction become smaller in diameter and hence have higher rotational speeds. This inturn causes the vortex core pressure to reach the vapor pressure value earlier along the shear layer and consequently account for the inception of cavitation at more upstream locations closer to the step edge at higher values of Re.

Summary and Conclusions

Under noncavitating conditions, at fairly large Reynolds numbers, the reattachment length for the backward facing step is found not to be significantly affected by the Reynolds number and is found to be dependent on the expansion ratio. Under noncavitating conditions, the Strouhal number of the flow is found to be dependent on the Reynolds number. Under cavitating conditions, the wall static pressure coefficients in the separated region are slightly lower than those found under noncavitating conditions. The frequency of vortex shedding is severely influenced by the cavitation number of the flow and at very low values of σ, vortex shedding ceases. Inception cavitation indices are independent of Re and are found to be strongly dependent on the expansion ratio. At inception, spanwise vortex like filaments are visible in the shear layer at about 3 or 4 step heights downstream of separation. With increasing Re, these vortex like filaments appear closer to the step edge, though the value of σ_i remained the same.

References

Adams, E. W., and Johnston, J. P., 1988a, "Effects of Separating Shear Layer on the Reattachment Flow Structure," Part 1—Pressure and Turbulence Quantities," *Experiments in Fluids*, Vol. 6, pp. 400–408, "Part 2—Reattachment Length and Wall Shear Stress," *Experiments in Fluids*, Vol. 6, pp. 493–499.

Adams, E. W., and Eaton, J. K., 1988b, "An LDA Study of Backward Facing Step Flow, Including the Effects of Velocity Bias," ASME JOURNAL OF FLUIDS ENGINEERING, Vol. 110, pp. 275–282.

Arakeri, V. H., and Ramarajan, V., 1981, "Inception of Cavitation From a Backward Facing Step," ASME JOURNAL OF FLUIDS ENGINEERING, Vol. 103, pp. 288–293.

Appel, D. W., "Cavitation Along Surfaces of Separation," ASME paper No. 60-WA-205.

Balachandar, R., 1990, "Characteristics of Separated Flows Including Cavitation Effects," Ph.D. thesis, Concordia University, Montreal, Canada, Mar.

Ball, J. W., and Sweeney, C. W., 1974, "Incipient Cavitation Damage in Sudden Enlargement Energy Dissipations," Cavitation—Fluid Machinery Group of the Inst. of Mech. Enggs., Edinburgh, Sept. 1986, pp. 73–79.

Blake, W. K., 1986, *Flow Induced Sound and Vibration*, Vol. 1, Academic Press.

Bradshaw, P., and Wong, F. Y. F., 1972, "The Reattachment and Relaxation of a Turbulent Shear Layer," *J. Fluid Mechanics*, Vol. 52, Part 1, pp. 113–135.

Chang, P., 1970, *Separation of Flow*, Pergamon Press, New York.

Driver, M. David, Seegmiller, H. L., and Marvin, G. J., 1987, "Time-Dependent Behavior of a Reattaching Shear Layer," *AIAA Journal*, July, pp. 914–919.

Durst, F., and Tropea, C., 1982, "Flows Over Two-Dimensional Backward Facing Steps," *Structure of Complex Turbulent Shear Flows*, IUTAM symposium, Marseille, pp. 41–52.

Eaton, J. K, and Johnston, J. P., 1982, "Low Frequency Unsteadyness of a Reattaching Turbulent Shear Layer," *Third Intl. Symposium on Turbulent Shear Flows*, Springer-Verlag, Berlin, pp. 162–170.

Eaton, J. K., and Johnston, J. P., 1981, "A Review of Research on Subsonic Turbulent Flow Reattachment," *AIAA Journal*, pp. 1093–1100.

Etheridge, D. W., and Kemp, P. H., 1978, "Measurements of Turbulent Flow Downstream of Rearward Facing Step," *J. Fluid Mechanics*, Vol. 86, Part 3, pp. 545–566.

Farabee, T. M., and Casarella, M. J., 1984, "Effects of Surface Irregularity on Turbulent Boundary Layer Wall Pressure Fluctuations," ASME *J. Vib., Acoustics, Stress and Reliability in Design*, Vol. 106, pp. 343–350.

Gates, E. M., Billet, M. L., Katz, J., and et al., 1979, "Cavitation and Nuclei Distributions, Joint ARL/CIT Experiments," Report No. 244.1, California Institute of Technology, Sept.

Greshilov, E. M., Evtushenko, A. V., and Lyamshev, L. M., 1969, "Spectral Characteristics of the Wall Pressure Fluctuations Associated with Boundary Layer Separation Behind a Projection on a Smooth Wall," *Soviet Physics—Acoustics*, Vol. 15, No. 1, pp. 29–34.

Holl, J. W., 1970, "Nuclei and Cavitation," ASME *Journal of Basic Engineering.*, Dec., pp. 681–688.

Holl, J. W., 1965, "The Estimation of the Effect of Surface Irregularities on the Inception of Cavitation," *Symp. Cavitation in Fluid Machinery*, ASME, pp. 3–15.

Isomoto, K., and Honami, S., 1989, "The Effect of Inlet Turbulence Intensity on the Reattachment Process Over a Backward Facing Step," ASME *Journal Fluids Engineering.*, Vol. 111, pp. 87–92.

Katz, J., 1982, "Cavitation Inception in Separated Flows," Ph.D. thesis, California Inst. of Tech.

Kim, J., 1978, "Investigation of Separation and Reattachment of a Turbulent Shear Layer: Flow Over a Backward Facing Step," Ph.D. thesis, Stanford University.

Kim, J., Kline, S. J., and Johnston, J. P., 1980, "Investigation of a Reattaching Turbulent Shear Layer: Flow Over a Backward Facing Step," ASME JOURNAL OF FLUIDS ENGINEERING, Vol. 102, pp. 302–308.

Kline, S. J., 1985, "The Purpose of Uncertainty Analysis," ASME JOURNAL OF FLUIDS ENGINEERING, Vol. 107, pp. 153–160.

Knapp, R. T., Daily, J. W., and Hammitt, F. G., 1970, *Cavitation*, McGraw-Hill, New York.

Lush, P. A., 1975, "Sound Generated by Cavitating Flows in a Duct," Dept. of Mechanical Engineering, University of Southampton.

Mabey, D. G., 1972, "Analysis and Correlation of Data on Pressure Fluctuations in Separated Flow," *J. Aircraft*, Vol. 9, No. 9, pp. 642–645.

Morgan, W. B., 1972, "Air Content and Nuclei Measurement," Appendix I—Report of Cavitation committee, 13th Intl. Towing Tank Conference, pp. 657–674.

Moss, W. D., Baker, S., and Bradbury, J., 1977, "Measurements of Mean Velocity and Reynolds Stresses in Some Regions of Recirculating Flows," *First International Symposium on Turbulent Shear Flows*, The Penn. State Univ., Apr. pp. 198–207.

Narayanan, M. A. B., Khadgi, Y. N., and Vishwanath, P. R., 1974, "Similarities in Pressure Distribution in Separated Flow Behind Backward-Facing Steps," *Aeronautical Qtly.*, pp. 305–312.

Narayanan, R., 1984, "The Role of Pressure Fluctuations in Hydraulic Modelling," *Symposium on Scale Effects in Modelling Hydraulic Structures*, IAHR, Esslingen am Neckar, Germany, Sept.

Oba, R., Ikohagi, T., and Yasu, S., 1980, "Supercavitating Cavity Observations by Means of Laser Velocimeter," ASME JOURNAL OF FLUIDS ENGINEERING, Vol. 102, pp. 433–440.

Ramamurthy, A. S., and Balachandar, R., 1990, "The Near Wake Characteristics of Cavitating Bluff Sources," Accepted for publication in the ASME JOURNAL OF FLUIDS ENGINEERING, Dec.

Ramamurthy, A. S., and Bhaskaran, P., 1977, "Constrained Flow Past Cavitating Bluff Bodies," ASME JOURNAL OF FLUIDS ENGINEERING, Vol. 99, No. 4, pp. 717–726.

Rockwell, D., and Knisely, C., 1979, "The Organized Nature of Flow Impingement Upon a Corner," *J. Fluid Mechanics*, Vol. 93, pp. 413–432.

Roshko, A., and Lau, J. C., 1965, "Some Observations on Transitions and Reattachment of a Free Shear Layer in Incompressible Flow," *Proc. Heat Transfer and Fluid Mech. Inst.*, Stanford University Press, pp. 157–167.

Sarpkaya, T., 1961, "Torque and Cavitation Characteristics of Butterfly Valves," ASME *Journal Applied Mech.*, pp. 511–518.

Shalnev, K. K., and Shapoval, I. F., 1977, "The Growth of Cavitation in Restricted Flow," *Soviet Physics Dokl.*, Vol. 22 (12), Dec.

Simpson, R. L., 1989, "Turbulent Boundary-Layer Separation," *Ann. Review of Fluid Mech.*, Vol. 21, pp. 205–234.

Stevenson, W. H., Thompson, H. D., and Craig, R. R., 1984, "Laser Velocimeter Measurements in Highly Recirculating Flows," ASME JOURNAL OF FLUIDS ENGINEERING, Vol. 106, p. 173.

Streeter, V. L., (ed), 1961, *Handbook of Fluid Dynamics*, McGraw-Hill, New York.

Tani, I., Iuchi, M., and Komoda, H., 1961, "Experimental Investigation of Flow Separation Associated With a Step or a Groove," Aero. Res. Inst., Report No. 364, Apr.

Tropea, C., 1982, "Die Turbulente Stufestromung in Flachkanalen und Offenen Gerinnen," Ph.D. thesis, Univ. of Karlsruhe, FRG.

Varga, J., and Sebsteyen, G. Y., 1966, "Determination of the Frequencies of Wakes Shedding from Circular Cylinder," *Acta Technicia Academiae Scient. Hungaricae*, Vol. 53, pp. 91–108.

Vigander, S., 1965, "An Experimental Study of Wall Pressure Fluctuations in a Cavitating Turbulent Shear Flow," *Studies in Engineering Mechanics*, Report No. 41, University of Kansas, 1965.

Westphal, R. V., Johnston, P. J., and Eaton, J. K., 1984, "Experimental Study of Flow Reattachment in a Single Sided Sudden Expansion," NASA CR 3765.

Young, J. O., and Holl, J. W., 1966, "Effects of Cavitation on Periodic Wakes Behind Symmetric Wedges," ASME Journal Basic Engineering, Vol. 88, pp. 163–176.

Convective Gaseous Diffusion in Steady Axisymetric Cavity Flows

B. Parkin
Professor Emeritus, Applied Research
Laboratory and Aerospace Engineering,
The Pennsylvania State University,
State College, PA 16804

K. Ravindra
Assistant Professor,
Department of Aerospace Engineering,
Parks College, Saint Louis University,
Cahokia, Ill 62206

Theoretical results on gaseous convective turbulent diffusion in steady axisymmetric flows are found to compare well with experimental results already in the literature. The investigation starts with the formulation of a highly idealized "slug-flow" model of the process for a quick estimate of the importance of turbulent boundary layer convection and for a comparison of previously published experimental and analytical results which had revealed order-of-magnitude discrepancies between calculated and measured air diffusion rates. Next, an existing two-dimensional convective diffusion model is adapted to axisymmetric cavity flow. Good agreement between experimental and calculated mass flow rates is found with a proper choice of turbulent diffusively from a Launder-Spaulding mixing-length model. The adapted "wrap around" model predicts a concentration boundary-layer thickness of the order of the cavity radius at the cavity terminus. Consequently, an axisymeetric analysis is also presented. From this it is found that the important part of the gaseous mass flow into the cavity occurs near the very front of the cavity where the concentration gradients are most severe. Downstream flow regions near the cavity are thereby depleted of dissolved air and the resulting concentration gradients are greatly reduced. Therefore the mass flow rate through downstream cavity surfaces are relatively unimportant and the simpler wrap around calculation can give useful engineering estimates of total mass flow rates.

Introduction

Gaseous diffusion across a cavity surface has long been recognized as being fundamental to the understanding of both natural vaporous and ventilated full cavity flows because diffusion into or out of the liquid can influence the cavity pressure, the cavity geometry, the cavitation number and the hydrodynamic forces experienced by the traveling body which creates the cavity. Moreover, it is generally thought that the main source of air in a natural vaporous cavity is diffusion from the surrounding supersaturated water. The reentrant jet and turbulent mixing at the cavity terminus is mainly responsible for air entrainment from the cavity into the wake. Thus, for estimates of cavity air mass balance and entrainment rates the engineer needs a way to calculate the air mass-flow rate through the cavity walls and a number of investigators have already given thought to this convective diffusion problem.

For example, the steady convective diffusion of gases across a two-dimensional cavity surface has been used with molecular diffusivity by Parkin and Kermeen (1963) to approximate the rate of convective air diffusion into a microbubble in a laminar boundary layer. Brennen (1969) considered turbulent gaseous diffusion into a large two-dimensional cavity using a model which accounts for the enhanced diffusivity associated with the turbulent shear layer on the cavity surface. Billet and Weir (1975) used Brennen's model to calculate the rate of diffusion across axisymmetric surfaces. They extended Brennen's two-dimensional solution to the axisymmetric case by wrapping the

two-dimensional solution around the cavity and they found their observed diffusion rates to exceed the calculated rates by an order of magnitude. They overcame this difficulty by choosing a constant multiplicative factor for use with Brennen's model.

Brennen's solution holds that diffusion is augmented by intense turbulent mixing within the bounding shear layer on the cavity and it is supposed that the turbulence extends all along the cavity starting at the separation point, because in most practical high Reynolds number cases the extent of laminar flow on the cavity surface will be negligible. The solution is strictly applicable when the boundary layer on the upstream wetted surface has adequate time to grow as, for example, behind the trailing edge of a fully cavitated hydrofoil. In other cases as when the cavity springs from the sharp leading edge of a hydrofoil at small attack angles or as in the Billet-Wier experiments on zero-caliber ogives the free shear layer will at first be laminar with a small growth rate in the laminar region. In these flows of limited extent, convective diffusion with molecular diffusivity seems to offer a more realistic model of the process. But as we have noted, the laminar shear layer will often be of short streamwise extent with the shear layer being turbulent thereafter. Consequently, we too shall assume completely turbulent shear layers.

In order to gain some understanding of the discrepancies between analytical and observed mass flow rates discovered by Billet and Weir (1975), we first consider a highly idealized version of Brennen's model in which we assume that the shear layer turbulence causes diffusion to be instantaneous and only the dissolved air in the shear layer diffuses into the cavity in

Table 1 Comparison of mass flow rates, ṁ, gm/s

Cavitation number	$U_\infty = 1839$ cm/s			$U_\infty = 910$ cm/s		
	Slug-flow model	Billet and Weir (1975)	Brennen (1969)	Slug-flow model	Billet and Weir (1975)	Brennen (1969)
0.15	0.0036	0.032	0.0040	0.0018	0.024	0.0050
0.20	0.0033	0.024	0.0030	0.0016	0.018	0.0038
0.25	0.0030	0.019	0.0023	0.0015	0.014	0.0031
0.30	0.0029	0.016	0.0021	0.0014	0.012	0.0026
0.35	0.0027	0.014	0.0018	0.0013	0.010	0.0023

order to see if convective transport dominates the effect to diffusion from the outer flow. Since this idealization excludes diffusion from the outer flow, we shall characterize the thickness of the entire shear layer by its thickness at the cavity terminus. Only the air in a volume of water occupied by this moving shear layer enters the cavity. Results from this simple "slug-flow" model are then compared with calculations from Brennen's theory and experimental data from Billet and Weir in order to judge the relative importance of convection in the mass flow estimates.

Second, in order to consider the added influence of convective turbulent diffusion in an infinite fluid volume having a turbulent diffusivity representative of free shear flows is used instead of a molecular diffusivity in Parkin's model. The two-dimensional calculation is wrapped around the axisymmetric cavity in order to permit comparisons with experimental data.

Third, because of the fundamental difference in the geometry of planar and axisymmetrical flows, we formulate an approach and solve for the convective gaseous diffusion across an axisymmetric cavity surface. This solution is then compared with results from the wrap around model to test the usefulness of the simpler result.

Convective Slug-Flow Model

Having described the purpose and assumptions of the slug-flow model we turn to its implementation. Since we assume that the quantity of gas available for diffusion into the cavity is contained in a tubular slug of fluid we first calculate its volume. Let the mean radius of the hollow fluid cylinder be a, its length equal to the cavity length, L, and its thickness, δ, equal to the shear layer thickness at the end of the cavity as shown in Fig. 1. This volume is $2\pi aL\delta$ and it is swept downstream with a velocity U_∞, so that a fresh supply of dissolved gas becomes available for diffusion into the cavity every L/U_∞ seconds.

If we denote by c_0, the dissolved air concentration difference across the cavity surface, and the water solute density by ρ, the resulting diffusion gas mass flow rate is

$$\dot{m} = (2\pi a\rho L\delta)c_0 \left(\frac{U_\infty}{L}\right) = 2\pi a\rho U_\infty \delta c_0. \qquad (1)$$

Mass flow rates calculated from equation (1) are given in Table 1 for cavities behind zero-caliber ogives. Also tabulated are
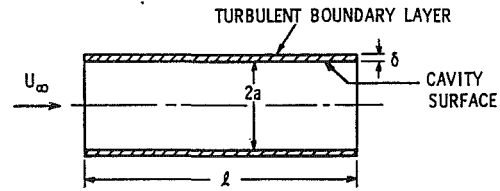
Fig. 1 Slug flow model for estimating the gaseous diffusion across an axisymmetric cavity

diffusion rates from the Billet-Weir experiments and calculated mass flow rates from Brennen's model. The value of the concentration difference is $c_0 = 14.5$ molar parts per million and the ogive diameter is 0.635 cm. The calculations and data pertain to the free-stream velocities of 1839 and 910 cm/s and five cavitation numbers as shown in the table. The tabulation shows that the convective diffusion rates from the slug-flow model are nearly an order of magnitude less that those observed and that the slug-flow rates, which slightly over emphasize convective effects, do show some resemblance to calculated values from Brennen's model. The Billet-Weir correlating constant is not used in these calculations. Evidently the observed diffusion rates may be due to convection and also due to diffusion from the entire flow field.

Wrap-Around Diffusion Model

The first step in the development of this simple model is to replace the molecular diffusivity, κ, with a turbulent diffusivity, ν_t, in the two-dimensional result from Parkin and Kermeen (1963). Then the air mass-flow rate per unit width of cavity surface is

$$\dot{M}_{2D} = \frac{4\rho\nu_t c_0}{\sqrt{\pi}} \left[\sqrt{2\lambda l} - \frac{\sqrt{\pi}}{2} \right], \qquad (2)$$

where again, ρ is the water density, ν_t is the turbulent diffusivity, c_0 is the concentration difference between the free-stream and the saturation concentration on the cavity surface. The dimensionless cavity length is $l = L/a$, where a is the mean cavity radius. The diffusive Reynolds number, λ, is given by $\lambda = U_\infty a/2\nu_t$. Wrapping this two-dimensional solution around an axisymmetric cavity of mean radius a, we get the total air mass-flow rate through the axisymmetric cavity surface to be

---

Nomenclature

a = cavity radius, cm

A = a constant, see equation (18)

c = dissolved-air concentration difference

C = molar concentration, parts per million

C_0 = concentration on cavity surface

C_∞ = free-stream concentration

D = ogive-body diameter, cm

$f(x)$ = mass flux per unit cavity length

l = non dimensional cavity length

$\dot{m}$ = total mass flow rate across axisymmetric cavity, gr/s

$\dot{M}_{2D}$ = mass flow per unit width on two-dimensional cavity

P_{FS} = free-stream saturation dissolved-gas pressure

q = source strength

r = radius, dimensionless

R = radius, dimensional

U_∞ = free-stream velocity

x, y, z = dimensionless Cartesian coordinates

α_1 = free-stream saturation dissolved gas content, ppm

β = Henry's law constant

γ = constant of proportionality, equation (7)

δ = free shear layer thickness

κ = molecular diffusivity

λ = diffusive Reynold's number

ν_t = turbulent diffusivity

π = 3.1415...

ρ = liquid density

σ = cavitation number

$$\dot{m} = 8\sqrt{\pi}\,\rho \nu_t a c_0 \left[\sqrt{2\lambda l} - \frac{\sqrt{\pi}}{2}\right]. \qquad (3)$$

For a zero-caliber ogive, the nondimensional cavity length, l, and cavity radius are related to the cavitation number, σ, according to Billet, Holl and Weir (1974) by

$$l = 0.955/\sigma, \qquad (4a)$$

and

$$a = 0.715 D/\sigma^{0.34}. \qquad (4b)$$

In equation (4b), D is the diameter of the axisymmetric ogive body. When these two equations are substituted into equation (3), one finds that

$$\dot{m} = 10.14\rho c_0 D\nu_t \sigma^{0.34}[1.382(\lambda/\sigma)^{1/2} - 0.886]. \qquad (5)$$

For the turbulent diffusivity we use a simple Launder-Spaulding (1959) mixing length model in which

$$\nu_t = l_m[\overline{v^2}]^{1/2} \qquad (6)$$

and the mixing length is $l_m \sim 0.07\delta$, the rms turbulence level is $[\overline{v^2}]^{1/2} \sim 0.09 U_\infty$ and the shear layer thickness is δ. From these planar mixing layer relationships we get

$$\nu_t = 0.0063\delta U_\infty\gamma. \qquad (7)$$

In the following comparisons the constant of proportionality, γ, is taken to be unity. Figures 2 and 3 show the variation of volume flow rates predicted by equations (5) and (7) and the corresponding values observed by Billet and Weir (1975). The calculated and experimental trends agree rather well. Of course, the present approach applies turbulent mixing which is characteristic of the free shear layer to the entire field of flow. This fact would enhance the role of diffusion. On the other hand, we have found that the present selection of the proportionality factor, γ, tends to compensate for this and permits the agreement shown for a range of flow parameters. We suggest therefore that the present analytical approximation may be a useful estimating formula.

Strictly speaking one can expect a wraparound convective diffusion model to be useful only if the concentration boundary layer is thin. In the present instance one should require the concentration layer thickness to be smaller than the cavity radius. In order to examine this point, the concentration distribution normal to the flow direction has been calculated using the two-dimensional theory at the end of the cavity. Calculated results are plotted in Fig. 4 for flow conditions representative of the Billet-Weir (1975) experiments. Figure 4 shows that the concentration layer thickness is comparable to the cavity radius. Therefore we expect a wraparound solution to be valid for only a short distance downstream of the cavity separation point. Fortunately for mass diffusion estimates, it is in this region where the diffusion rate is highest so that errors in regions downstream of this critical zone may have little influence on the over-all result. Nevertheless, a truly axisymmetric solution will have contributing terms which are not found in a two-dimensional calculation and one needs to determine their importance to the overall diffusion rates.

An Axisymmetric Model

Gaseous diffusion across a cavity surface occurs when there is a dissolved gas concentration gradient between the free stream and the liquid on the cavity surface. If α_1 is the measured dissolved air content in molar parts per million (ppm), then by Henry's law, the saturation partial pressure of the gas in the free stream is given by

$$P_{FS} = \alpha_1\beta, \qquad (8)$$

where β is the value of the Henry's law constant at the water temperature. Then the mean concentration difference in molar parts per million is
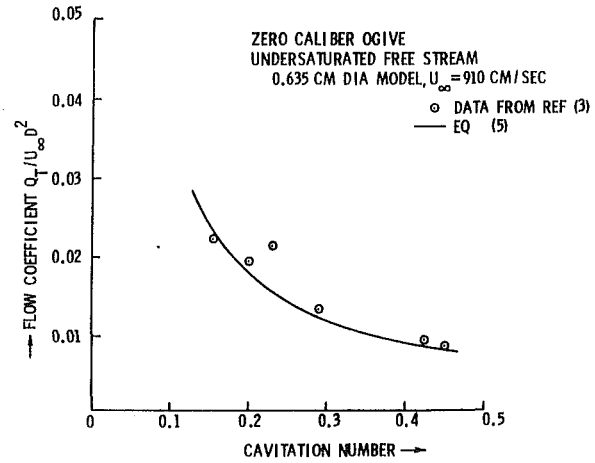

Fig. 2   Flow coefficient versus cavitation number, $U_\infty = 910$ cm/s
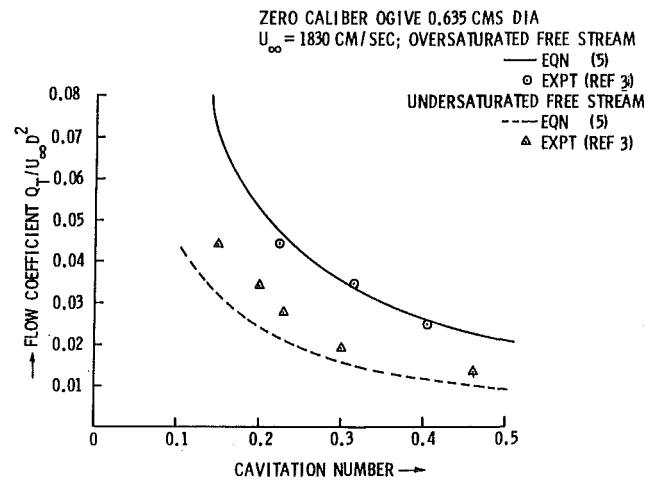

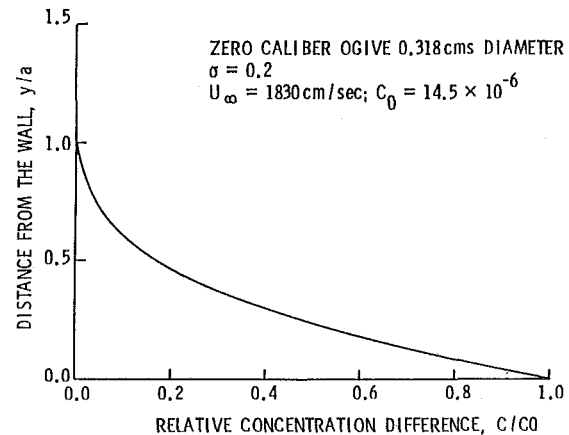Fig. 3   Flow coefficient versus cavitation number, $U_\infty = 1830$ cm/s

Fig. 4   Concentration layer profile over a two-dimensional cavity

$$c = \alpha_1 - \frac{P_G}{\beta}. \qquad (9)$$

Consider an axisymmetric flow of water containing dissolved gases which has the concentration $C(X,R)$ ppm at any point in the region $R \geq a$, where a is the mean cavity radius. Let the undisturbed flow have the velocity U_∞ in the X direction. In the interest of simplicity, all momentum shear layer perturbation velocities, u and v in the X and R directions, respectively, are neglected. The free-stream velocity and diffusivity then apply to the entire flow field. The mass diffusion of gases through the constant radius, permeable axisymmetric cavity
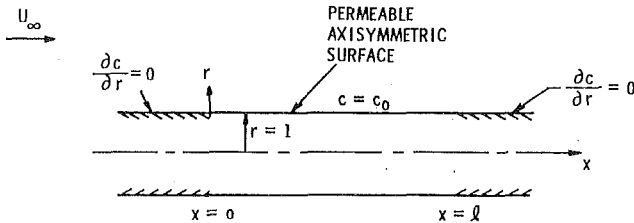
Fig. 5 Idealized cavity geometry and boundary conditions

Fig. 6 Ring source geometry

surface occurs between $X = 0$ and $X = L$ as shown in Fig. 5. The remaining portions of the cylindrical surface along the X axis are supposed to be impermeable to diffusion. On the permeable surface let the concentration have a constant value, C_0, and let the dissolved gas in the water far from the permeable surface have a concentration C_∞. Then the concentration difference $c(X,R)$ is defined as

$$c(X,R) = C(X,R) - C_\infty. \qquad (10)$$

Without identifying it as molecular or turbulent diffusivity, let κ be the mass diffusivity coefficient. In either case the governing differential equation for the concentration difference has the elliptic form, Carslaw and Jaeger (1959),

$$U_\infty \frac{\partial c}{\partial X} = \kappa \nabla^2 c, \qquad (11)$$

where ∇^2 is the Laplacian operator. By introducing the normalized coordinates $x = X/a$, $y = Y/a$ and $z = Z/a$, we can write a nondimensional form of equation (11) as

$$\frac{\partial c}{\partial x} = (\kappa/aU_\infty)\nabla^2 c. \qquad (12)$$

In order to find the solution to equation (12) subject to the prescribed boundary conditions, we first write a solution of equation (12) when a source of strength "q" in the moving fluid is located at the fixed point (ξ,η,ζ) as

$$c(x,y,z; \xi,\eta,\zeta) = \frac{q}{4\pi k r' a} e^{-\lambda[r' - (x-\xi)]}, \qquad (13)$$

where $r' = \sqrt{(x-\xi)^2 + (y+\eta)^2 + (z-\zeta)^2}$, is the distance between the field point (x,y,z) and the source point (ξ,η,ζ), q is the mass flux of gas from the source, k is the mass conductivity $= \kappa\rho$, ρ is the liquid density and λ is a diffusive Reynolds number, $U_\infty a/2\kappa$.

Consider next a ring source of unit radius and unit strength centered at $x = \xi$ with the plane of the ring perpendicular to the x axis. Take a segment of the ring of length $d\theta$, as shown in Fig. 6. The incremental strength, dq, of this element will be $d\theta/2\pi$ and from equation (13), the concentration at a point (x,r) due to an incremental flux, $d\theta/2\pi$, at $(\xi,1,\theta)$ will be

$$\delta c(x,r'; \xi,1,\theta) = \frac{d\theta}{8\pi^2 k r' a} e^{-\lambda[r' - (x-\xi)]}. \qquad (14)$$

Integrating this equation between $\theta = 0$ and 2π, we have

$$c(x,r; \xi) = \frac{e^{\lambda(x-\xi)}}{8\pi^2 k a} \int_0^{2\pi} \frac{e^{-\lambda r'}}{r'} d\theta. \qquad (15)$$

The integral in equation (15) can be evaluated for large values of λ (of the order of 2000) with the help of Laplace's method, Erdelyi (1961). The asymptotic evaluation for the concentration is

$$c(x,r; \xi) = \frac{e^{\lambda(x-\xi)}}{8(\pi a)^{3/2}\rho\sqrt{\kappa r U_\infty}} \frac{e^{-\lambda\sqrt{(x-\xi)^2 + (r-1)^2}}}{[(x-\xi)^2 + (r-1)^2]^{1/4}}. \qquad (16)$$

equation (16) satisfies two boundary conditions, namely: $c \to 0$ as $x \to -\infty$ and that $c \to 0$ as $r \to \infty$.

Now suppose that the mass flux per unit length between
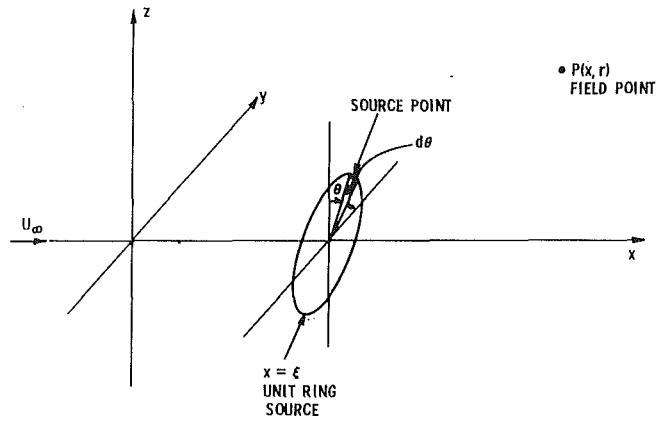
$x = -\infty$ and $x = +\infty$ is given by the function $f(x)$. Then the function $c(x,r)$ can be expressed in terms of this source distribution as

$$c(x,r) = \frac{A}{\sqrt{r}} \int_{-\infty}^{+\infty} f(\xi)e^{\lambda(x-\xi)} \left[\frac{e^{-\lambda\sqrt{(x-\xi)^2 + (r-1)^2}}}{[(x-\xi)^2 + (r-1)^2]^{1/4}} \right] d\xi, \qquad (17)$$

where

$$A = \frac{1}{8(\pi a)^{3/2}\rho\sqrt{\kappa U_\infty}}. \qquad (18)$$

In the integral of equation (17), the infinite limits are used because the unit ring source does not satisfy the boundary conditions on the impermeable surfaces upstream and downstream of the cavity where we must have for $r = 1$, $dc/dr|_{x \neq \xi} = 0$ and therefore these conditions must be used in the determination of $f(x)$. Moreover we must also require that $c(x,1) = C_0 - C_\infty = c_0$, in the interval, $0 \leq x \leq l$, as well as the impermeability conditions that require $dc(x,1)/dx = 0$ in the intervals $-\infty < x < 0$ and $l < x < +\infty$. Therefore on $r = 1$ we can write three integral equations for the determination of $f(x)$:

$$\frac{c_0}{A} = \int_{-\infty}^0 \frac{f_1(\xi)}{\sqrt{x_2-\xi}} d\xi + \int_0^{x_2} \frac{f_2(\xi)}{\sqrt{x_2-\xi}} d\xi$$
$$+ \int_{x_2}^l \frac{f_2(\xi)e^{-2\lambda(\xi-x_2)}}{\sqrt{\xi-x_2}} d\xi + \int_l^{+\infty} \frac{f_3(\xi)e^{-2\lambda(\xi-x_2)}}{\sqrt{\xi-x_2}} d\xi, \qquad (19)$$

$$0 = \int_{-\infty}^{x_1} \frac{f_1(\xi)}{\sqrt{x_1-\xi}} d\xi + \int_{x_1}^0 \frac{f_1(\xi)e^{-2\lambda(\xi-x_1)}}{\sqrt{\xi-x_1}} d\xi$$
$$+ \int_0^l \frac{f_2(\xi)e^{-2\lambda(\xi-x_2)}}{\sqrt{\xi-x_1}} d\xi + \int_l^{+\infty} \frac{f_3(\xi)e^{-2\lambda(\xi-x_1)}}{\sqrt{\xi-x_1}} d\xi, \qquad (20)$$

$$0 = \int_{-\infty}^0 \frac{f_1(\xi)}{\sqrt{x_3-\xi}} d\xi + \int_0^l \frac{f_2(\xi)}{\sqrt{x_3-\xi}} d\xi$$
$$+ \int_l^{x_3} \frac{f_3(\xi)}{\sqrt{x_3-\xi}} d\xi + \int_{x_3}^{+\infty} \frac{f_3(\xi)e^{-2\lambda(\xi-x_3)}}{\sqrt{\xi-x_3}} d\xi, \qquad (21)$$

where the positive branch of all square roots has been taken. The functions f_1, f_2, and f_3 are the source distributions in the intervals $-\infty < x_1 < 0$, $0 \leq x_2 \leq l$ and $l < x_3 < +\infty$, respectively. These distributions are naught outside of their specified intervals.

The coupled integral equations, (19) to (21), can be simplified further by using the fact that in certain of the individual integrands the exponential factors are appreciable only when $x = x_1$, x_2, or x_3 because λ is very large. The simplified equations become

$$\frac{c_0}{A} = \int_{-\infty}^0 \frac{f_1(\xi)}{\sqrt{x_2-\xi}} d\xi + \int_0^{x_2} \frac{f_2(\xi)}{\sqrt{x_2-\xi}} d\xi + \frac{\pi}{2\lambda} f_2(x_2), \qquad (19a)$$

$$0 = \int_{-\infty}^{x_1} \frac{f_1(\xi)}{\sqrt{x_1 - \xi}} \, d\xi + \frac{\pi}{2\lambda} f_1(x_1), \qquad (20a)$$

and

$$0 = \int_{-\infty}^{0} \frac{f_1(\xi)}{\sqrt{x_3 - \xi}} \, d\xi + \int_{0}^{l} \frac{f_2(\xi)}{\sqrt{x_3 - \xi}} \, d\xi + \int_{l}^{x_3} \frac{f_3(\xi)}{\sqrt{x_3 - \xi}} \, d\xi$$

$$+ \frac{\pi}{2\lambda} f_3(x_3). \qquad (21a)$$

equation (20a) can be solved by Picards's method, Hildebrand (1965) and the resulting expression for f_1 is

$$f_1(x_1) = c_1 e^{2\lambda x_1}, \qquad (22)$$

where $x_1 < 0$ and c_1 is an arbitrary constant. The function $f_1(x_1)$ can now be substituted into equation (19a) and then the function $f_2(x_2)$ may be found by the use of Laplace transforms (Ravindra and Parkin, 1987). The solution is

$$f_2(x_2) = \left[\frac{c_0}{A} \sqrt{\frac{2\lambda}{\pi}} + c_1 \right] e^{2\lambda x_2} \text{erfc} \sqrt{2\lambda x_2} - \frac{c_1}{\sqrt{2\pi\lambda x_2}}, \qquad (23)$$

where the diffusive Reynold's number, λ, is defined following equation (13) above, where the quantity A is given by equation (18) and where erfc(t) denotes the complementary error function. Having found f_1 and f_2, one can find the function f_3 from equation (23a). The function $f_2(x_2)$ governs the diffusion across the cavity wall, however, so we have not found it necessary to obtain $f_3(x_3)$. We note that the source strength f_2 is greatest at the separation point. Evidently, most of the mass flux will occur near the start of the cavity. Down-stream areas will contribute relatively less to the total air diffusion into or out of the cavity in agreement with the wrap around solution.

The rate at which mass is diffused along the entire length of the axisymmetric cavity is

$$\dot{m} = \int_{0}^{l} \frac{dM}{dt} \, dx = \int_{0}^{l} f_2(x_2) dx_2, \qquad (26)$$

from whence

$$\dot{m} = 4\pi a^2 U c_0 \left[\frac{e^{2\lambda l} \text{erfc}\sqrt{2\lambda l}}{2\lambda} + \sqrt{\frac{2l}{\pi\lambda}} - \frac{1}{2\lambda} \right]$$

$$+ c_1 \left[\frac{e^{2\lambda l} \text{erfc}\sqrt{2\lambda l}}{2\lambda} - \frac{1}{2\lambda} \right]. \qquad (27)$$

The first term of equation (27) closely resembles the wrap around solution of equation (3) and the second term involving c_1, gives the correction to the air mass-flow rate due to axial symmetry. In order to show this we employ the asymptotic representation for the expression $e^{2\lambda l} \text{erfc}\sqrt{2\lambda l}$, so that equation (27) can be written as

$$\dot{m} = 8 \sqrt{\pi} \, \kappa c_0 a \left[\sqrt{2\lambda l} - \frac{\sqrt{\pi}}{2} + \frac{1}{2\sqrt{2\lambda l}} - \frac{1}{4[2\lambda l]^{3/2}} + \cdots \right]$$

$$+ \frac{c_1}{2\lambda\sqrt{\pi}} \left[-\sqrt{\pi} + \frac{1}{2\lambda l} - \frac{1}{2[2\lambda l]^{3/2}} \cdots \right],$$

where now $k = \rho \nu_t$ is the turbulent mass conductivity and we have carried a few more terms than are given in equation (3). Equation (28) enables us to compare the magnitudes of the wraparound and correction terms. If we suppose that $c_1 = O(8\sqrt{\pi}\kappa c_0 a)$, we see that the leading term in the wraparound expression is of order $\sqrt{\lambda}$ while the leading correction term is of order $1/\lambda$. This makes the ratio of the correction term to the wrap around term roughly equal to $1/(8 \times 10^4)$ for a λ of the order of 2000. Consequently, we have considered the wrap around solution as being adequate for most purposes and therefore we have not continued the analysis. On the other hand, if one espouses a semiempirical approach as we do, the undetermined constant c_1 offers an opportunity to fit the analytical expression over a somewhat broader range of parameters than might otherwise be possible, or at least improve the correlations with the experimental data now available.

Conclusions

This investigation has explored some aspects of convective gaseous diffusion in steady axisymmetric cavity flows. One of its objectives which has been achieved is the semiemperical determination of a Launder-Spaudling type turbulent diffusivity for use in the analysis of convective diffusion in other cavity flows. This choice is essential for most cavity flow studies in which mass diffusion across cavity surfaces is not measured and it must be calculated from estimates or measurements of the overall flow parameters. The use of a single diffusivity for the entire flow field does not change the fact that the only two basic physical processes at work are diffusion and convection. The choice of a turbulent diffusivity tends to balance one process with respect to the other and the use of experimental results to strike this balance seems to offer hope that the balance is approximately correct.

It has been found that a modified planar convective diffusion model, using a wraparound approach, can give satisfactory estimates of dissolved air mass-flow rates across a cavity surface. The good agreement might be explained by the fact that both axisymmetric and wraparound models show the most intense mass flux across a cavity surface to be in the vicinity of the separation point. There the concentration boundary layer is thin and the wraparound approach closely approximates the axisymmetrical solution. Downstream flow regions, where the concentration layer is no longer thin, will have suffered a depletion of dissolved air as a result of the intense upstream diffusion and they will contribute a lesser amount to the total diffusion rate.

Acknowledgment

References

Billet, M. L., Holl, J. W., and Weir, D. S., 1974, "Geometric Description of Developed Cavities on Zero and Quarter Caliber Ogive Bodies," *Applied Research Laboratory Technical Memorandum*, File No. 74-136, The Pennsylvania State University, pp. 5–6.

Billet, M. L., and Weir, D. S., 1975, "The Effect of Gas Diffusion on the Flow Coefficient for a Ventilated Cavity," ASME JOURNAL OF FLUIDS ENGINEERING, Vol. 97, pp. 501–506.

Brennen, C., 1969, "The Dynamic Balances of Air and Heat in Natural Cavity Flows," *Journal of Fluid Mechanics*, Vol. 37, No. 1, pp. 115–127.

Carslaw, H. S., and Jaeger, J. C., 1959, *Conduction of Heat in Solids*, Second Edition, Oxford University Press, New York, p 267.

Erdelyi, A., 1961, *Asymptotic Expansions*, Dover Publications, New York, pp. 29–34.

Hildebrand, F. B., 1965, *Methods of Applied Mathematics, Second Edition*, Prentice Hall, New York, pp. 435–438.

Launder, B. E., and Spaulding, B., 1959, *Lectures in Mathematical Models for Turbulence*, Academic Press, New York, pp. 23–27.

Parkin, B. R., and Kermeen, W. R., 1963, "The Roles of Convective Air Diffusion and Tensile Stresses During Cavitation Inception," *Proceedings of the IAHR Symposium on Cavitation and Hydraulic Machinery*, Sendai, Japan, pp. 21–24.

Ravindra, K., and Parkin, B. R., 1987, "Gas Diffusion Studies in Steady and Nonsteady Cavities," *Technical Report No. TR-87-003*, Applied Research Laboratory, The Pennsylvania State University, University Park, pp. 107–117.

K. Ravindra
Department of Aerospace Engineering and
Engineering Sciences,
Parks College, Saint Louis University,
Cahokia, Ill. 62206

B. R. Parkin
Applied Research Laboratory and Aerospace
Engineering Department,
The Pennsylvania State University,
State College, PA 16804

Unsteady Gaseous Diffusion Associated With a Fully Cavitating Oscillating Flat-Plate Hydrofoil[1]

This paper gives an analysis of convective gaseous diffusion into a full cavity behind an oscillating flat-plate hydrofoil in a turbulent flow. The unsteady diffusion theory accounts for fluctuations of cavity gas pressure and length which are assumed to be harmonic oscillations but are not necessarily in phase with the hydrofoil motion. A diffusive lag function is found which, for a given reduced frequency, determines the instantaneous diffusion rate as a product of the lag function and the quasisteady mass diffusion. The present results can be used to study the rate of gas entrainment from the cavity into the wake behind the oscillating cavity.

Introduction

Previous studies of cavity pressure fluctuations in fully cavitating flows behind oscillating hydrofoils by Jiang and Leehey (1977) and the two-dimensional experimental investigations of Ravindra and Parkin (1987), indicate, for unsteady cavity flows, that these internal pressure fluctuations can affect the hydrofoil lift and drag. Such fluctuations result from noncondensable gas (air) which, in naturally occurring vapor cavities, generally diffuses from the supersaturated liquid flow into the cavity.

When hydrofoil oscillations are absent and the cavity flow is said to be steady, the effect of air diffusion is well known. In naturally occurring vapor cavities if the water is supersaturated, diffusion into the cavity increases the cavity pressure. Or in the case of ventilated cavities when the cavity air pressure is greater than the saturation pressure in the liquid at the cavity wall, air diffuses through the cavity wall into the outer flow.

Of course, for either steady or unsteady fully cavitating flows, the overall mass balance of condensable and noncondensable gases in the cavity is affected by the processes of convective diffusion discussed above and by turbulent entrainment at the cavity terminus. The study of this complicated process requires reasonably accurate engineering estimates of mass diffusion rate if one wishes to measure the turbulent entrainment of noncondensable gas from the cavity terminus. For this reason it is important to have a realiable method of calculating the convective diffusion for both steady and non-steady supercavitating flows in order to estimate steady and nonsteady hydrodynamic forces and for cavity attrition rate in water entry problems. Finally we note that lifting surface (Jiang and Leehey, 1977) or gravitational effects (Swanson and O'Neill, 1951, Cox and Clayden, 1955) can create a flow having hollow vortex cores which act as conduits for the entrained

gases. Such phenomena are excluded here and we also rule out cavity pulsations of the kind first studied by Song (1977). The present study deals only with the rate at which gas can diffuse in or out of the cavity walls behind an oscillating profile. This is the primary source of gas which becomes available for entrainment at the cavity terminus. Events in the downstream wake, such as the possibility of further out gassing into traveling vortex cores behind the cavity is ignored.

The purpose of this paper is to review briefly a previous experimental and analytical investigation of convective diffusion into an axisymmetric cavity (Billet and Weir, 1975; Ravindra and Parkin, 1987; Parkin and Ravindra, 1991), and to apply key findings from that study, such as an appropriate value of a turbulent diffusivity for use in a Fickian diffusion theory, to the analysis of steady and nonsteady convective diffusion in the two-dimensional flow around a supercavitating flat-plate hydrofoil. The authors are not aware of any similar analysis of convective diffusion for nonsteady flow. The present investigation, however, is an idealized beginning compared to future experimental and analytical developments needed if the applications noted above are to be addressed realistically.

Specific Background

We can now turn our attention to those facts from previous investigations bearing most directly upon important aspects of the present study. Our chief concern is that of turbulence in the free stream because most hydrofoils and propulsor blades find themselves in a turbulent flow. The question of turbulent mass transport has been addressed by Brennen (1969) who analyzed the gaseous diffusion into a large two-dimensional cavity by considering the mass flux into the cavity associated primarily with convection from a turbulent shear layer on the cavity free surface. Brennen's approach shows an enhanced mass flux across the cavity surface compared to the two-dimensional diffusive calculation of Parkin and Kermeen (1963) which was designed for a laminar outer flow with only molecular diffusion providing the driving mechanism.

Billet and Weir (1975) extended Brennen's model by wrapping his two-dimensional solution around an axisymmetrical cavity surface in order to calculate the mass diffusion rate across axisymmetric cavity surfaces. Their observed diffusion rates were found to exceed the calculated rates by nearly one order of magnitude. In order to circumvent this discrepancy they used their experimental data to choose a constant multiplicative factor in Brennen's model.

As a result of these facts the present authors examined an alternative approach to the steady axisymmetric convective diffusion problem (Ravindra and Parkin, 1987; Parkin and Ravindra, 1991) which does not use Brennen's model nor the Billet-Weir factor. Here we assume the entire outer flow field to be turbulent in spite of the fact that the most intense mixing is restricted to the cavity free-shear layer as Brennen indicates. Even so, one can use a diffusive theory along the lines of Parkin and Kermeen (1963). But for axiymmetric flow, one might be able to use the Billet-Weir data to determine an effective turbulent diffusivity, ν_t and this value can then be used to provide some confidence in the engineering estimates for the two-dimensional nonsteady mass diffusion calculations of interest here.

The reason that such an approximate calculation might be useful is due to the fact that the concentration gradients are extremely large in the vicinity of the free-surface separation point for both axiymmetric and two-dimensional flow geometries. Therefore if one selects the eddy diffusivity on the basis of the free-shear layer properties, it seems that the most important physical aspects of the flow will be modeled.

In order to arrive at a value for ν_t, we first write the dissolved air concentration in terms of the concentration difference, c, where

$$c(x,y,z,\text{t}) = C(x,y,z,t) - C_\infty. \tag{1}$$

The concentration at any point in the flow is $C(x,y,zt)$ and C_∞ is the free-stream concentration as might be measured with a van Slyke apparatus. In the Fickian diffusion equation the partials of the difference concentration are decomposed into time-averaged parts, $\partial \bar{c}/\partial (\ )$ and turbulent components, $\partial c'/\partial (\ )$, as is the customary practice. The problem is linearized by writing the velocity components as $(U + u')$, v', w' in which primes denote turbulent fluctuations. We have used G.I. Taylor's statistical theory of turbulence, Goldstein (1961), coupled with Boussinesq's hypothesis, Schlichting (1979). In this way we can write the gradients of the time averaged concentration difference in two dimensions as

$$-\overline{\rho u' c'} = A_T \frac{\partial \bar{c}}{\partial x} \text{ and } -\overline{\rho v' c'} = A_T \frac{\partial \bar{c}}{\partial y}, \tag{2}$$

where only the eddy transport terms, being much larger than the molecular transport terms, are retained, and the factor of proportionality A_T is the exchange coefficient. The eddy diffusivity is then defined as

$$\nu_t = A_T/\rho. \tag{3}$$

We now write the turbulent diffusivity for a free-shear layer as

$$\nu_t \approx \ell_m \sqrt{\overline{v^2}}, \tag{4}$$

where $\sqrt{\overline{v^2}}$ is the r.m.s turbulence level and ℓ_m is the mixing length. For a planar mixing layer Launder and Spaulding (1959) give

$$\ell_m \approx 0.07\delta \text{ and } \sqrt{\overline{v^2}} \approx 0.09U, \tag{5}$$

where δ is the free-shear layer thickness. Therefore, introducing a constant of proportionality, γ, we can combine equations (4) and (5) and write

$$\nu_t = 0.0063\delta U \gamma. \tag{6}$$

For axisymmetric flow (Parkin and Ravindra, 1991), the best agreement between calculations and experiment was found when $\gamma = 1$.

Finally, from the standard procedures sketched above, we see that the time-averaged two-dimensional form of Fick's diffusion equation is

$$\frac{\partial \bar{c}}{\partial t} + U \frac{\partial \bar{c}}{\partial x} = \nu_t \nabla^2 \bar{c}. \tag{7}$$

The Boundary Value Problem

In linearizing equation (7) we have considered $\bar{u}(x,y,z)$ and $\bar{v}(x,y,z)$ and their gradients to be much smaller than U. Thus we have supposed that for any cavitation number, σ, much less than unity, one can replace the cavity-wall speed, $U\sqrt{1+\sigma}$, with the free-stream velocity, U. We also suppose that the foil experiences steady pitching oscillations of circular frequency, ω, about a small fixed angle, α_0. The dimensionless oscillation amplitude is $\Delta \alpha$, and $\Delta \alpha \ll 1$. Therefore one can write

$$\alpha(t) = \alpha_0(1 + \Delta \alpha e^{j\omega t}), \tag{8}$$

where $j = \sqrt{-1}$. Equation (8) will be refined further below. As a consequence of these linearizing assumptions we can represent the profile and its cavity as a cut of length $\ell(t)$ along the x axis in the $x-y$ plane as shown in Fig. 1. Thus one sees that the boundary conditions for this linearized problem can be applied on the x axis instead of on the cavity or hydrofoil surfaces.

─────────── **Nomenclature** ───────────────────────

A_T = turbulent exchange coefficient	ℓ_0 = steady cavity length	
a = complex or real constant	ℓ_u = unsteady cavity length	α_0 = steady or mean attack angle
b = complex or real constant	$\bar{\ell}$ = normalized cavity length	β = Henry's law constant
$\bar{b}$ = profile chord length	ℓ_m = mixing length	γ = proportionality constant
C = concentration	**Subscripts**	$\Delta \alpha$ = foil oscillation amplitude
c = concentration difference	∞ = in the free stream	δ = free shear layer thickness
$f(x)$ = source-strength distribution	c = on or in the cavity	$\bar{\delta}$ = unsteady concentration amplitude
$g(k')$ = spectral function, cavity length	s = steady	ϵ = unsteady normalized cavity length amplitude
$h(k')$ = spectral function, concentration	u = unsteady	ν_t = effective turbulent diffusivity
$j = \sqrt{-1}$	M = air mass flow rate	ξ = dummy variable along x axis
K_0 = modified Bessel's function of the second kind	p_G = cavity partial gas pressure	ρ = liquid density
k' = modified reduced frequency	R = diffusive Reynolds number	σ = cavitation number
ℓ = cavity length	t = time	ϕ = cavity to foil phase lag angle
	U = free-stream velocity	ω = circular frequency
	α = angle of attack	
	$\bar{\alpha}$ = complex constant	
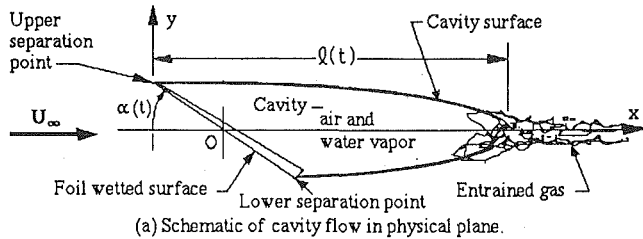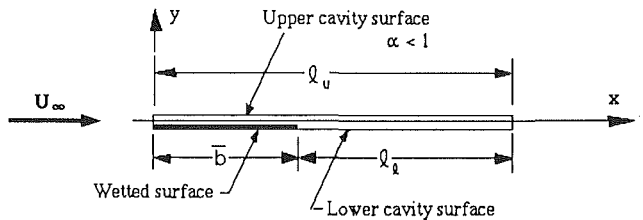
Fig. 1 Cavity flow about an oscillating hydrofoil

Fig. 2 Boundary conditions
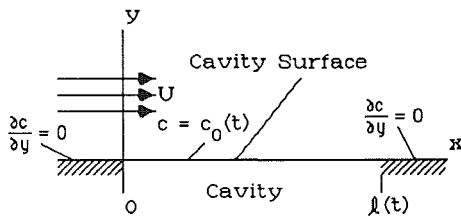

Fig. 3 Comparison of experimental data with a simple amplitude formula

The geometry of Fig. 1 suggests a corresponding linearization for the present diffusion problem. For example, suppose we consider the upper surface of the cavity. The applicable geometry is illustrated in Fig. 2. Note that for simplicity we have dropped the over bars used previously, as in equation (7), for example. This abbreviation will be adopted in the following.

Let C_∞ be the free-stream concentration of dissolved air in molar parts per million. Suppose the partial pressure of air in the cavity is $p_G(t)$ at any instant. Then if the Henry's law constant is β, the equilibrium concentration on the cavity surface is $C_c(t) = p_G(t)/\beta$ and on the cavity surface the concentration difference of equation (1) becomes

$$c_c(x,0,t) = [p_G(t)/\beta] - C_\infty. \qquad (9)$$

We shall split this concentration difference into steady, c_s, and unsteady, c_u, parts. That is,

$$c_c(x,y,t) = c_s(x,y) + c_u(x,y,t), \qquad (9a)$$

where now $c_s(x,0) = c_0$ is a constant when $0 \leq x \leq \ell(t)$. Since the air pressure, once the air has reached the cavity, is independent of turbulence level we can regard this concentration difference as a time-averaged quantity although it is an instantaneous concentration with respect to diffusion. When $y = 0$ equation (9) governs the diffusion in or out of the permeable cavity surface. Referring to Fig. 1 we see that up stream and down stream of the foil and cavity there will be little or no diffusion so that on the x axis the condition,

$$\frac{\partial c}{\partial y} = 0, \qquad (10)$$

will hold when $0 \geq x \geq \ell(t)$. These conditions are illustrated in Fig. 2. Not shown in Fig. 2 is the fact that at all points far from the origin,
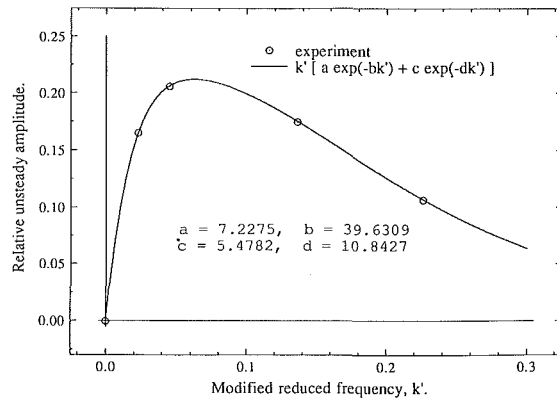
$$c(\infty, t) = 0. \qquad (11)$$

As noted at the outset, the foil oscillates steadily in pitch with circular frequency ω, or reduced frequency, $k = \dfrac{\omega b}{U}$. Therefore we expect that the cavity length will also be in steady oscillation, but out of phase with the foil. If we let the unsteady cavity length about the steady terminus at $x = \ell_0(\sigma)$, the fluctuating length will be $\ell_u = \epsilon \ell_0 \, g(k') \, e^{j(\omega t + \phi)}$, where ϵ depends on the amplitude of the pitching oscillations and $k' = \dfrac{k}{\sqrt{1 + \sigma}}$ is the modified reduced frequency. We cannot give a theoretical evaluation of ϵ and $g(k')$. Instead, we use the experimental results from Ravindra and Parkin (1987) for their determination. Therefore we will write

$$\ell(t) = \ell_0[1 + \epsilon g(k')e^{j(\omega t + \phi)}], \qquad (12)$$

where ϵ is much less than ℓ_0 and ϕ is the phase-angle lag between cavity and foil oscillations. Next we shall rewrite equation (12) as the sum of steady, ℓ_0, and unsteady, ℓ_u, terms. In particular, we shall write the normalized expression for the unsteady part as,

$$\frac{\ell_u}{b} = \frac{\epsilon \ell_0}{b} \, (k' \, [a \exp(b k') + c \exp(d k')])e^{j(\omega t + \phi)}. \qquad (13)$$

Equation (13) is determined by the values of the constants a, b, c and d, as shown in Fig. 3, and which were obtained by curve fitting data from Ravindra and Parkin (1987). When $\omega = 0$, equation (13) shows that $\ell_u = 0$ because the experimentally based (Ravindra and Parkin, 1987) function, $g(k')$, is designed in accordance with that fact. Moreover the added empirical relationships, $\ell_0 = \sqrt{\dfrac{2\alpha_0}{\sigma}}$ and $\epsilon = .85 \dfrac{\Delta \alpha}{\alpha_0}$, complete the determination of the unsteady cavity fluctuations, ℓ_u. The factor, ℓ_u/ℓ_0, in equation (12) has its peak value of 0.211 at $k' = .06$, in agreement with experimental data. It also vanishes as $k' \to \infty$. Figure 3 compares calculated and experimental values of the relative amplitude, ℓ_u/ℓ_0, for a range of modified reduced frequencies. The experimental points were obtained for a cavitation number, σ, of 0.48, a steady attack angle, α_0, of 10 deg, and a pitching angle amplitude, $\Delta \alpha$, of 4 deg. From the experiments, $\epsilon = .34$ in this case, so that $\epsilon \times 1.24 = .422$ is the factor used for the calculations leading to the curve shown in Fig. 3.

We shall also assume that harmonic cavity air pressure oscillations lag the hydrofoil oscillations by a phase angle ϕ_a. Then following the pattern of equations (12) and (13), we shall write

$$c_u(x,y,t) = \bar{\delta}\,[c_s(x,y)h(k')e^{(j\phi_a)}]e^{j\omega t}, \qquad (14)$$

where the terms in brackets will now be denoted by $c_u(x,y,k')$ and the nonsteady amplitude, $\bar{\delta}$, is small. Thus we will abbreviate equation (14) by writing

$$c_u(x',y',t) = \bar{\delta}c_u(x',y',k')e^{j\omega t}. \qquad (14a)$$

The conditions to be satisfied by (14a) follow from equations (9), (10), and (11) and may be given explicitly as

$$c_u(x',0,k') = \bar{\delta}\,[c_0 h(k')e^{(j\phi_a)}] \text{ for } 0 \le x' \le \ell_u(k')/\bar{b}, \qquad (15)$$

$$\frac{\partial c_u(x',0,k')}{\partial y'} = 0 \text{ for } 0 > x' > \ell_u(k')/\bar{b}, \qquad (16)$$

and

$$c_u(\infty) = 0, \qquad (17)$$

where $x' = x/\bar{b}$ and $y' = y/\bar{b}$. These boundary conditions apply only to nonsteady diffusion. In order to complete the solution the steady solution must be combined as stated by equation (9a). As in the case of equation (13), the *function $h(k')$ must vanish when $k' = 0$.* Further progress in the determination of $h(k')$, $\phi(k')$ and $\phi_a(k')$ must await resolution of the nonsteady closure condition which involves the unsteady cavity length of equation (13). This lengthy aspect of the theory is given by Ravindra and Parkin (1987). But now, we must solve equation (7) subject to the mixed boundary conditions of equations (15), (16), and (17).

The Solution

We can find the solution if we use the symmetry of the fundamental solution of equation (7). Thus we start by finding the solution for an oscillating source at the origin using separation of variables (Ravindra and Parkin, 1987). First one separates the time dependent terms by writing $c_u(x,y,t) = c(x,y,k)e^{j\omega t}$ and $x' = x/\bar{b}$ and $y' = y/\bar{b}$. These quantities can be substituted into equation (7) and the common factor, $e^{j\omega t}$, the subscript u and the primes can be dropped. Moreover, we can also drop the common factor, $e^{j\omega t}$, appearing in equations (15), (16), and (17). Next, the reduced frequency, $k = \omega\bar{b}/U$, is introduced. The transformed equation is

$$2\left(jkc + \frac{\partial c}{\partial x}\right) = \frac{1}{R}\,\nabla^2 c, \qquad (18)$$

where R is a diffusive Reynolds number,

$$R = \frac{U\bar{b}}{2\nu_t}. \qquad (19)$$

We seek a solution of (18) which depends on x and $r = \sqrt{x^2 + y^2}$ only. For a unit source at the origin one finds that

$$c(x,r) = \frac{1}{2\pi\rho\nu_t}\,e^{-jkx}e^{Rx}K_0(Rr), \qquad (20)$$

where $K_0(Rr)$ is a modified Bessel's function of the second kind. Suppose now that we consider a source of strength $f(\xi;k)$ at the point ξ on the x axis. Then the distance between the source point and a field point (x,y) is $\sqrt{(x-\xi)^2 + y^2}$. If the field point is on the x axis, $y = 0$ and equation (20) becomes

$$c(x;\xi) = \frac{f(\xi;k)}{2\pi\rho\nu_t}\,e^{-jkx}e^{Rx}K_0[R(x-\xi)]. \qquad (21)$$

By differentiating equation (20) with respect to y and then letting $y = 0$, it is found that $\frac{\partial c}{\partial y} = 0$, as required by equation (16). Being the mass flux per unit length, the source strength, $f(\xi;k)$, in equation (21) is independent of y and equation (16) continues to be satisfied. We note also that if $k = 0$, equation (20) reduces to the steady fundamental solution of Parkin and Kermeen (1963). But source superposition in the interval $0 \ge \xi \ge \bar{\ell}$ on the cavity surface will lead to a solution which contains only the nonsteady solution because of equations (15), (16), and (17).

Before superposing these sources we normalize $\ell_u(t)$ as we did above and write the unsteady cavity length as

$$\tilde{\ell} = \ell_u(k')/\bar{b}. \qquad (22)$$

Then for a typical field point (x,y), we have

$$c(x,y;k') = \frac{1}{2\pi A_T}\int_0^{\tilde{\ell}} f(\xi,k)e^{(R-jk)(x-\xi)}$$
$$\times K_0[R\sqrt{(x-\xi)^2 + y^2}]\,d\xi. \qquad (23)$$

Formally, equation (23) is the general solution, but we do not yet know $f(\xi,k)$. According to equation (15), however, on the cavity surface $y = 0$ and $c(x,0,k') = \bar{\delta}\,[c_0 h(k')e^{(j\phi_a)}]$. Therefore we find $f(\xi,k)$ to be given by the integral equation,

$$[\bar{\delta}c_0 h(k')e^{(j\phi_a)}] = \frac{1}{2\pi A_T}\int_0^{\tilde{\ell}} f(\xi,k)$$
$$\times e^{(R-jk)(x-\xi)}K_0[R\sqrt{(x-\xi)^2}]\,d\xi. \qquad (24)$$

We restrict the argument of K_0 in equation (24) to positive values and since both ξ and x are within the range of integration, equation (24) must be broken into two parts. Moreover R is a large number and K_0 can be replaced by the first term of its asymptotic expansion. Therefore

$$\bar{\delta}c_0 h(k')e^{(j\phi_a)} = \frac{1}{2\pi A_T}\sqrt{\frac{\pi}{2R_0}}\int_0^x \frac{f(\xi,k)e^{-jk(x-\xi)}}{\sqrt{x-\xi}}\,d\xi$$
$$+ \frac{1}{2\pi A_T}\sqrt{\frac{\pi}{2R}}\int_x^{\tilde{\ell}} \frac{f(\xi,k)e^{-(2R-jk)(x-\xi)}}{\sqrt{\xi-x}}\,d\xi. \qquad (25)$$

The first integral is a convolution integral. Because R is large, the second integrand contains a sharp exponential cut off and $f(\xi,k)$ varies slowly with ξ compared to the negative exponential. Therefore $f(\xi,k)$ contributes to the integrand only very near $\xi = x$ and $f(x,k)$ can be taken out of the integral. Then we see that, if we ignore the upper limit, the resulting integral can be expressed as a Laplace transform giving $\sqrt{\pi/(2R+jk)}$. Therefore, with small error the transformed integral equation is

$$[(\bar{\delta})c_0 h(k')e^{(j\phi_a)}] = \frac{1}{2\pi A_T}\sqrt{\frac{\pi}{2R}}$$
$$\times \left\{\int_0^x \frac{f(\xi,k)e^{-jk(x-\xi)}}{\sqrt{x-\xi}}\,d\xi + f(x,k)\sqrt{\frac{\pi}{2R+jk}}\right\} \qquad (26)$$

Equation (26) can be solved for $f(x,k)$ by Laplace transforms. The result is

$$f(x,k) = 2A_T[\bar{\delta}c_0 h(k')e^{(j\phi_a)}]\sqrt{2R(2R-jk)}$$
$$\times \left\{(a/\bar{\alpha}) - (b^2/\bar{\alpha})e^{-\alpha x}\mathrm{erfc}(b\sqrt{x}) - \frac{b\sqrt{a}}{\bar{\alpha}}\,\mathrm{erf}\,\sqrt{ax}\right\}, \qquad (27)$$

where $a = jk$, $b = \sqrt{2R-jk}$, and $\bar{\alpha} = 2(jk-R)$. In principle, equation (27) completes the general solution of equation (23) for the nonsteady concentration, $c(x,y,t)$.

Mass Flow Rates

Equation (27) gives the mass flow rate per unit length along a two-dimensional cavity surface. Therefore the instantaneous total mass flow rate can be found by integrating $f(x,k)$ over the surface length. On the upper surface the normalized length is $\tilde{\ell}$ and on the lower cavity surface it is $\tilde{\ell} - 1$. Then if the total unsteady flow rate is M_u, we have

Journal of Fluids Engineering

$$\dot{M}_u = \int_0^{\tilde{\ell}} f(x,k)dx + \int_0^{\tilde{\ell}-1} f(x,k)dx. \qquad (28)$$

The integrations of equation (28) have been given by Ravindra and Parkin (1987). The result is

$$\dot{M}_u = 2A_T[\tilde{\delta}c_0 h(k)e^{(j\phi_a)}]\sqrt{2R(2R-jk)}$$
$$\times \{a[2\tilde{\ell}-1]+(b^2/\tilde{\alpha})[e^{-\tilde{\alpha}\tilde{\ell}}\text{erfc}(b\sqrt{\tilde{\ell}})+e^{-\tilde{\alpha}(\tilde{\ell}-1)}$$
$$\text{erfc}(b\sqrt{\tilde{\ell}-1})]+(b^3/\tilde{\alpha}\sqrt{a})[\text{erf}\sqrt{a\tilde{\ell}}+\text{erf}\sqrt{a(\tilde{\ell}-1)}]$$
$$-(b^2/\tilde{\alpha})-b[\sqrt{a\tilde{\ell}}\,\text{erf}\sqrt{a\tilde{\ell}}+\sqrt{a(\tilde{\ell}-1)}$$
$$\text{erf}\sqrt{a(\tilde{\ell}-1)}]-b[\sqrt{\tilde{\ell}/\pi}\,e^{-a\tilde{\ell}}+\sqrt{(\tilde{\ell}-1)/\pi}$$
$$e^{-a(\tilde{\ell}-1)}]+(b/2\sqrt{a})\,[\text{erf}\sqrt{a\tilde{\ell}}+\text{erf}\sqrt{a(\tilde{\ell}-1)}]\} \quad (29)$$

The steady mass flow rate predicted by Parkin and Kermeen (1963) is

$$\dot{M}_s = 2A_T c_0 \{e^{2R\tilde{\ell}_0}\text{erfc}\sqrt{2R\tilde{\ell}_0}+e^{2R(\tilde{\ell}_0-1)}$$
$$\times \text{erfc}\sqrt{2R(\tilde{\ell}_0-1)}+2[\sqrt{2R\tilde{\ell}_0/\pi}$$
$$+\sqrt{2R(\tilde{\ell}_0-1)/\pi}-1]\}, \quad (30)$$

where $\tilde{\ell}_0=\tilde{\ell}(k')$ from equation (22). The total instantaneous mass flow is the sum of the steady and unsteady contributions. Therefore

$$\dot{M}=\dot{M}_s\left\{1+\frac{\dot{M}_u}{\dot{M}_s}\right\}. \qquad (31)$$

The fraction in equation (31) can be expressed as $r(k)e^{j\psi(k')}$, where $r(k')$ is the absolute value of the quotient and $\psi(k')$ is the unsteady phase angle. Of course this quotient, or lag function, will vanish in the limit as $k'\to 0$.

We note again that the nonsteady effects in equation (31) are caused by fluctuations in concentration at the cavity wall and by fluctuations in cavity length. Although quantitative evaluation of their effects on the mass flow rate into the cavity must await the cavity closure analysis, we can use the steady flow result of equation (30) to evaluate their relative importance. This approximate evaluation is facilitated if one replaces the complementary error function term by the first term of its asymptotic expansion for large arguments. Then for the upper surface only, the important terms in the steady mass flow rate are

$$\dot{M}_s=\frac{4A_T c_0}{\sqrt{\pi}}\left\{\sqrt{2R\tilde{\ell}_0}-\frac{\sqrt{\pi}}{2}+\ldots\right\}.$$

From the logarithmic derivative of this expansion we find that

$$\frac{\Delta\dot{M}}{\dot{M}_s}=\frac{\Delta c}{c_0}+\frac{\Delta\tilde{\ell}}{2\tilde{\ell}_0}.$$

The experimental observations of Ravindra and Parkin (1987) show maximum relative concentration variations of the order of 5 percent and maximum length variations of about 20 per-

cent. Thus one sees that cavity length and concentration variations are equally significant and one might expect to see mass flow fluctuations in the order of 10 or 15 per cent.

Conclusions

This paper gives a linearized theory for gaseous convective diffusion across two-dimensional steady and unsteady cavity surfaces. Changes in cavity length and gas pressure are accounted for. The theory applies to steady and nonsteady supercavitating hydrofoils undergoing steady harmonic pitching oscillations. Expressions are given for mass flow rate across the permeable cavity surface for any reduced frequency. It appears that the analysis can be extended to nonsinusoidal hydrofoil pitching motions by superposing the Fourier components of the more general motion, provided that nonsteady closure, as well as the Fourier components of pressure and cavity length are accounted for. For the pitching oscillations of present interest, it remains to give the nonsteady closure and mass balance calculations before specific nonsteady lag function data can be presented. We plan to give those added results in the future. It is hoped that the present work will encourage more comprehensive experimental investigations in order that the present approach can be validated. The experimental basis now available suggests that perhaps the present analytical approach may be useful.

References

Brennen, C., 1969, "The Dynamic Balances of Air and Heat in Natural Cavity Flows," J. Fluid Mechs., Vol. 37, No. 1, pp. 115-127.

Billet, M. L., and Weir, D. S., 1975, "The Effect of Gas Diffusion on the Flow Coefficient for a Ventilated Cavity," ASME JOURNAL OF FLUIDS ENGINEERING, Vol. 97, pp. 501-506.

Cox, R. N., and Clayden, W. A., 1955, "Air Entrainment at the Rear of a Steady State Cavity," Report No. 12 in Cavitation in Hydrodynamics, Proceedings of an NPL Conference, H. M. Stationary Office.

Goldstein, S. (Ed.), 1961, Modern Developments in Fluid Dynamics, Vol. 2, Dover Publications, New York, p. 647.

Jiang, C. W., and Leehey, P., 1977, "Experimental and Theoretical Investigation of Unsteady Supercavitating Hydrofoils of Finite Span," Report No. 83481-4, Massachusetts Institute of Technology, pp. 72-75.

Launder, B. E., and Spaulding, D. B., 1959, Lectures in Mathematical Models for Turbulence, Academic Press, New York, pp. 23-27.

Parkin, B. R., and Kermeen, R. W., 1963, "The Roles of Convective Air Diffusion and Tensile Stresses During Cavitation Inception," Proc. IHAR Symposium in Cavitation and Hydraulic Machinery, Sendai, Japan, pp. 21-24.

Parkin, B. R., and Ravindra, K., 1991, Convective Gaseous Diffusion in Steady Axisymetric Cavity Flows," to appear in ASME JOURNAL OF FLUIDS ENGINEERING.

Ravindra, K., and Parkin, B. R., 1987, "Gas Diffusion Studies in Steady and Nonsteady Cavities," Applied Research Laboratory, Technical Report No. TR-87-003 (1987), The Pennsylvania State University, pp. 23-46.

Schlichting, H., 1979, Boundary Layer Theory, 7th Edition, McGraw-Hill, New York, p. 753.

Song, C. S., 1977, "Pulsation of Ventilated Cavities," Technical Paper No. 32, Serial B., Saint Anthony Falls Hydraulic Laboratory, The University of Minnesota.

Swanson, W. M., and O'Neill, J. P., 1951, "The Stability of an Air Maintained Cavity Behind a Stationary Object in Flowing Water," Report No. M24.3, Hydrodynamics Laboratory, California Institute of Technology.

M. Lance

J. L. Marié

J. Bataille

Laboratoire de Mécanique des Fluides et
d'Acoustique,
URA CNRS 263-Ecole Centrale de Lyon,
Ecully Cedex, France

Homogeneous Turbulence in Bubbly Flows

The present study is devoted to the interaction between a swarm of bubbles and a turbulent field in a linear shear flow. The transversal and longitudinal evolutions of the void fraction and of the Reynolds stress tensor have been measured. When the air bubbles are blown uniformly into the shear, the void fraction profiles exhibit a strong gradient which can be explained by kinematical effects. No void migration has been observed. The behavior of the Reynolds tensor indicates that the nonisotropy induced by the mean velocity gradient decreases when the void fraction increases. A simple mechanism is proposed to interpret this fact, and a turbulence model based on one-point closures is compared to the experimental data.

1 Introduction

The physical understanding of the mechanisms involved in any local transfer process taking place in the bulk of a turbulent dispersed two-phase flow requires the knowledge of the behavior of the Reynolds stress tensor in the continuous phase. On the other hand, the closure of the local time averaged equations (Ishii, 1975) necessitates a modeling of this quantity if a numerical treatment is attempted. Very few papers devoted to the theoretical or experimental determination of turbulent parameters have been published: Serizawa et al. (1975), Theofanous and Sullivan (1982), Sato and Sekoguchi (1975), Ohba et al. (1977), Lance (1979), Lance and Bataille (1982), Lahey (1987). The most commonly studied geometry is the pipe flow. Unfortunately, despite its practical importance, such a situation makes it difficult to interpret the experimental results. Therefore, it appears necessary to reconsider the whole problem in much simpler configurations. The investigation of turbulence in single phase flows shows that the basic mechanisms have been understood owing to the study of the so-called homogeneous turbulence. It is our intention here to transpose this approach to turbulent bubbly flows. The simplest case— a uniform bubbly flow—has been described in a previous work (Lance and Bataille, 1982). The next step consists in superimposing on this experiment a linear velocity gradient while keeping the homogeneity of the statistical moments of the fluctuating velocity. This configuration makes it possible to examine the influence of the air bubbles on the turbulence production by the mean velocity gradient, which is one of the most important mechanisms in turbulent shear flows. It is expected that these experimental informations can be used in the numerical modeling of the Reynolds tensor. In particular, an attempt has been made to adapt the single phase flow model of Launder et al. (1975) to our bubbly shear flow.

2 Description of the Experiment

The measurements have been performed in a hydrodynamic

tunnel described in details in Lance et al. (1980) (Fig.1). Its test section is a 2 m long square channel (450×450 mm) and it is operated at atmospheric pressure and ambient temperature, at mean liquid velocities smaller than 1.20 m/s. The linear shear flow is produced by means of a device very similar to that used by Champagne et al. (1970). The shear-turbulence generator consists of a row of ten parallel, equal width channels having adjustable head losses (bronze screens have been used for this purpose). Linear velocity profiles are rather easily obtained, but due to the instabilities of such a system, the homogeneity of turbulent field proved to be very sensitive to the arrangement of the screens. A turbulence grid has been inserted between the shear generator and the test section, in order to improve this homogeneity and to blow the air bubbles through 256 equally spaced injectors. The void fraction ranges from 0 to 5 percent.

The velocity and turbulence measurements have been obtained by Laser Doppler Anemometry, using the signal processing technique developed by Marié (1983). The Reynolds stress tensor components are calculated from the projections of the velocity fluctuation on three directions: 0, 45, and -45 deg from the vertical axis, with:

$$\overline{uv}^x = \frac{1}{2}\left(\overline{u_{45}^2}^x - \overline{u_{-45}^2}^x\right)$$
$$\overline{v^2}^x = \overline{u_{45}^2}^x + \overline{u_{-45}^2}^x - \overline{u_o^2}^x \tag{1}$$

the symbol $\overline{}^x$ denoting the phase average in the liquid(Ishii, 1975; Delhaye and Achard, 1976). The $\overline{w^2}^x$ component cannot be measured with the present device. Now, as the initial total turbulent kinetic energy is required for the modeling, we estimate this quantity by assuming equality between transverse components of the Reynolds stress tensor, that is:

$$k = \frac{1}{2}\left(\overline{u^2}^x + 2\overline{v^2}^x\right)$$

which is a reasonable approximation at the beginning of the test section. The initial dissipation rate, at the first measure-
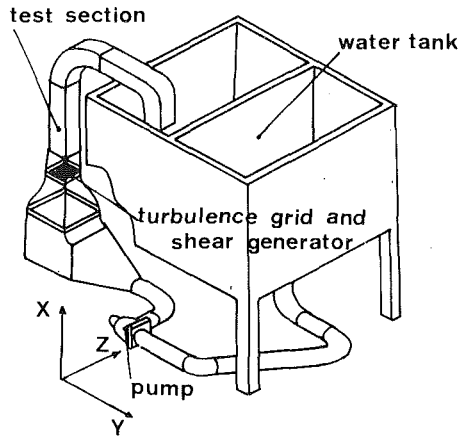
Fig. 1 Experimental device

Fig. 2 Mean velocity profiles in the absence of air bubbles for different locations from the grid. Volumetric flow rate:
$Q_L = 0.17$ m³/s;
Mean shear rate $= 2.9$ s⁻¹

ment station, is estimated from the balance of kinetic energy. The accuracy of these measurements is estimated from the experimental scattering, the main source of error coming from the rejection of the noise due to light scattering by the bubbles. The estimated uncertainty on

$$\overline{u_o^2}^x, \ \overline{u_{45}^2}^x, \ \overline{u_{-45}^2}^x$$

does not exceed 10 percent, which is consistent with the comparison between hot film anemometry and LDA in bubbly flows performed by Marié (1983). In order to reduce cumulative errors, the evolution of the previous quantities has been smoothed before calculating the Reynolds tensor. The mean equivalent diameter D of the bubbles and their mean relative rise velocity, as measured photographically, proved to be approximately constant and, respectively, equal to 5 mm, with a standard deviation ± 1 mm, and to .24 $\pm$ 0.02m/s.

The local void fraction α is measured with an AID7401 optical probe. The probe diameter is 200μ, which is very small compared to the bubble diameter. The accuracy is estimated to ± 5 percent, by comparison with the gas volumetric flow rate obtained by integration of the void fraction profiles.

3 Qualification of the Flow

(a) **Mean Velocity.** The mean velocity profiles in the absence of air bubbles are presented on Fig. 2, for three longitudinal stations. The maximum value of the shear rate $S = dU/dY$ reaches $3s^{-1}$, and is constant along the test section. Figure 3 shows that the injection of the bubbles does not modify significantly the linear transversal distribution of the mean liquid velocity.

(b) **Turbulent Intensity Profiles.** The transversal homogeneity of the single phase turbulent field is insured within 10
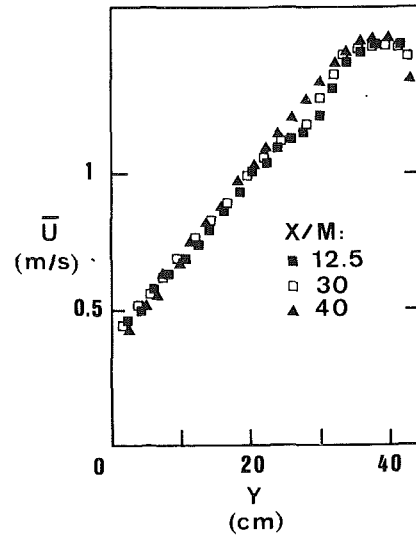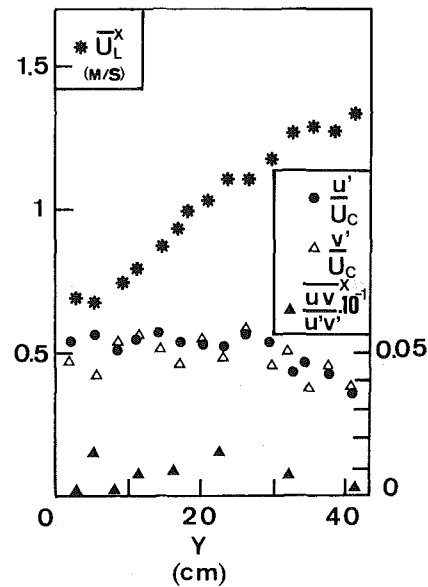

Fig. 3 Reynolds stress tensor and mean velocity profiles at the first measurement section $X/M = 12.5$.
Liquid flow rate: $Q_L = 0.18$m³/s;
Gas flow rate: $Q_G = 1.9.10^{-3}$m³/s;
Void fraction: $\alpha = 1.5$ percent;
Uncertainty in mean liquid velocity: ± 5 percent
Uncertainty in Reynolds stress tensor: ± 10 percent

─────── Nomenclature ───────

──	= time average	S = shear intensity dU/dY
──x	= local phase average	T = convection time:
A	= cross area of the test section	$\quad T = X/U$
C_i	= constants of the model	$\overline{U_G}^x$ = mean gas velocity
D	= bubble diameter	U_c = mean liquid velocity at the center of the pipe
H	= channel width (45 cm)	$\overline{U_L}^x$ = mean liquid velocity
M	= mesh of the grid (4 cm)	$\overline{U_R}^x$ = slip velocity:
P_{ij}	= interfacial production term	$\quad \overline{U_R}^x = \overline{U_G}^x - \overline{U_L}^x$
Q_G	= volumetric gas flow rate	u_i = liquid velocity fluctuation
k	= total turbulent kinetic energy	$u, v, w,$ = liquid velocity fluctua-

tion in the (X, Y, Z) coordinates
u', v', w' = r.m.s. values of the fluctuation components
V_T = terminal velocity of a single bubble
X, Y, Z = coordinates system
α = local void fraction
ϵ = total dissipation rate
τ_D = characteristic time
$\phi_{ij,1}$ = non-linear part of the pressure-strain correlation
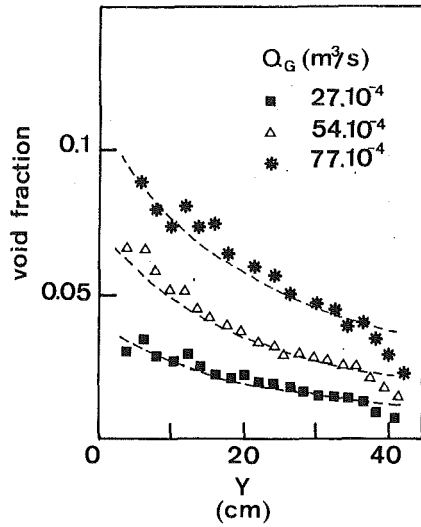$\phi_{ij,2}$ = rapid part of the pressure-strain correlation

Fig. 4 Void fraction profiles for three different air flow rates at the section X/M = 38, without correction for the pressure injection. Uncertainty in α: $\pm$ 5 percent; Dashed line: correlation (2).

Fig. 5 Longitudinal evolution of the Reynolds stress tensor. $S = 2.9 \, s^{-1}$; $Y = 27$ cm; $\overline{U_L}^x = 1$ m/s; $Q_L = 0.17$ m^3/s; $Q_G = 0$; $\alpha = 0$. Uncertainty in Reynolds stress components: ± 10 percent.

percent. When the air bubbles are injected, the profiles of the Reynolds tensor components proved to be flat within 20 percent over a large part of the section (Fig. 3).

4 Void Fraction Profiles

The appearance of maxima of void fraction near the wall in pipes has been reported by several authors (Serizawa et al., 1975); Herringe and Davis, 1976; Zun, 1985). Among various explanations for such an effect, a void migration due to the velocity gradient has been proposed. In order to estimate this effect, we first inject a single bubble in the shear flow. No significant deviation of the trajectory has been observed for the range of bubble diameters considered here (1 to 5 mm). This fact is not surprising, since the expected deviation due to the lift effect, calculated from the expression proposed by Auton et al. (1988), is of the order of 8 mm at the top of the test section. Such a value is comparable with the turbulent dispersion of the bubbles. It must be emphasized that the intensity of the shear is one order of magnitude lower than the one usually encountered in developed pipe flows.

In another experiment, the air bubbles (5 mm diameter) are blown uniformly in the flow. The void fraction profiles (Fig. 4) exhibit a strong transversal gradient, which does not vary with the longitudinal location. This phenomenon, reminiscent of the above mentioned "void migration," can nevertheless be explained by a simple kinematical argument. As a matter of fact, due to the width of the test section, the mean flow is completely controlled by the entrance conditions. The longitudinal development is only due to the hydrostatic pressure gradient, which has a small effect on the velocity or void fraction profiles, as it is confirmed experimentally. Therefore, the quantities describing the mean motion are with a good approximation function of the transverse position Y only. The transverse homogeneity of the local gas flux yields:

$$\frac{d}{dY}\alpha(Y)\overline{U_G}^x(Y) = 0, \text{ or } \alpha(Y)\overline{U_G}^x(Y) = cte.$$

As the air bubbles are blown uniformly through the grid, the constant is given by the ratio of the volumetric flow rate Q_G to the cross section A. For a dilute bubbly flow, $\overline{U_G}^x$ can be approximated by the sum of the liquid velocity in the absence of gas bubbles of the terminal velocity of a single bubble (neglecting lift and turbulence effects).
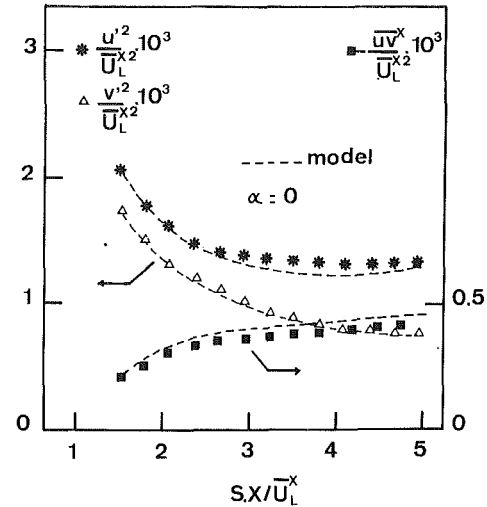
Therefore,

$$\alpha(Y)\overline{U_G}^x(Y) = \alpha_c(U_c + V_T),$$

where α_c is the void fraction at the center of the pipe, and finally:

$$\alpha = \alpha_c / \left(1 + S\left(Y - \frac{H}{2}\right)/(U_c + V_T)\right) \qquad (2)$$

The good agreement between (2) and the measured void fraction profile (Fig. 4) indicates that no migration effect occurs in the present experiment. In the following measurements, the pressure injection has been adjusted for each row of injectors, in order to correct this effect and to obtain flat void fraction profiles.

5 Turbulence Measurement

(a) Longitudinal Evolution of the Reynolds Stress Tensor-Single Phase Case. The components $\overline{u^2}, \overline{v^2}$ and $\overline{uv}$ of the Reynolds tensor were first obtained without air bubbles, in order to compare our results with previous experiments, especially those of Champagne et al. The quantities, normalized by the squared mean velocity at the center of the section, are shown in Fig. 5, versus the parameter: $S.T = (d\overline{U_L}/dY).X/\overline{U_L}$. This nondimensional variable is the product of the shear intensity and the time during which a fluid particle is subjected to the action of the shear. Our results are quite similar to those of Champagne et al. The components of the Reynolds stress tensor reach an asymptotic state, but due to the feeding by the mean velocity gradient, the longitudinal component $\overline{u^2}$ decreases less rapidly than $\overline{v^2}$.

(b) Longitudinal Evolution of the Reynolds Stress-Tensor-Two-Phase Case. As previously, the $\overline{u^2}^x$, $\overline{v^2}^x$, $\overline{uv}^x$ components are shown as functions of S. T for different values of the local void fraction (1, 1.4, 2 percent) and of the shear intensity (Figs. 6–9). These curves, compared to Fig. 5, exhibit a smaller difference between $\overline{u^2}^x$ and $\overline{v^2}^x$, associated with an apparently reduced production by the mean shear. The component $\overline{uv}^x$ remains approximately constant along the duct, with a slight decreasing trend.

Figures 8 and 9 are relative to two situations for which the inlet conditions give a nonisotropic turbulent field at the beginning of the duct. In the first case, $\overline{v^2}^x$ is greater than $\overline{u^2}^x$.
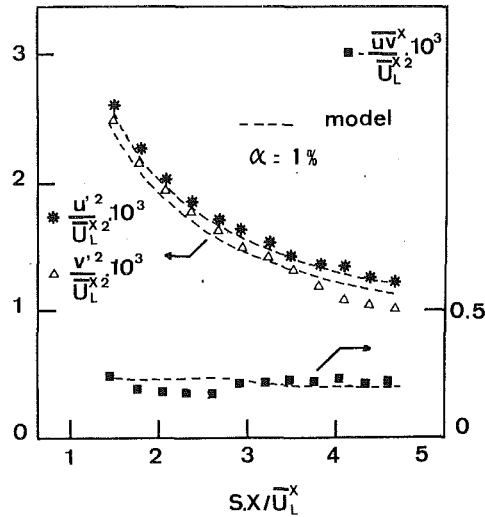
Fig. 6 Longitudinal evolution of the Reynolds stress tensor.

$S = 2.4 \text{ s}^{-1}$; $Y = 27$ cm; $\overline{U_L}^x = 1$ m/s; $Q_L = 0.18$ m³/s; $Q_G = 1.3.10^{-3}$ m³/s; $\alpha = 1$ percent.
Uncertainty in Reynolds stress components: ±10 percent.

Fig. 8 Longitudinal evolution of the Reynolds stress tensor.

$S = 2.9$; $Y = 27$ cm; $\overline{U_L}^x = 1$ m/s; $Q_L = 0.17$ m³/s; $Q_G = 1.25.10^{-3}$ m³/s; $\alpha = 1$ percent.
Uncertainty: ±10 percent.

Fig. 7 longitudinal evolution of the Reynolds stress tensor.

$S = 2.9 \text{ s}^{-1}$; $Y = 27$ cm; $\overline{U_L}^x = 1$ m/s; $Q_L = 0.17$ m³/s; $Q_G = 1.75.10^{-3}$ m³/s; $\alpha = 1.4$ percent
Uncertainty: ±10 percent.

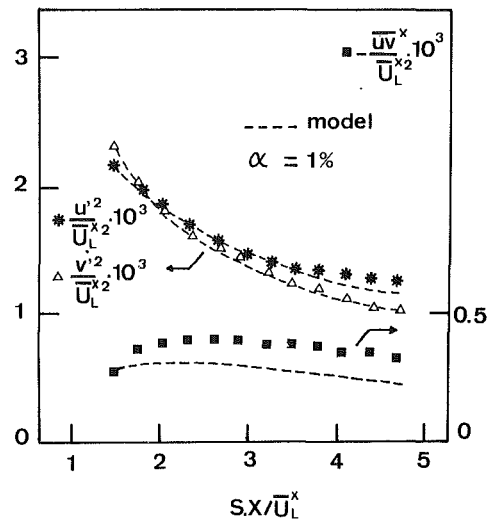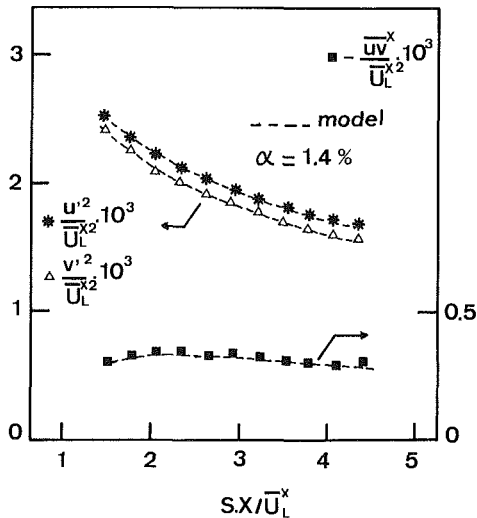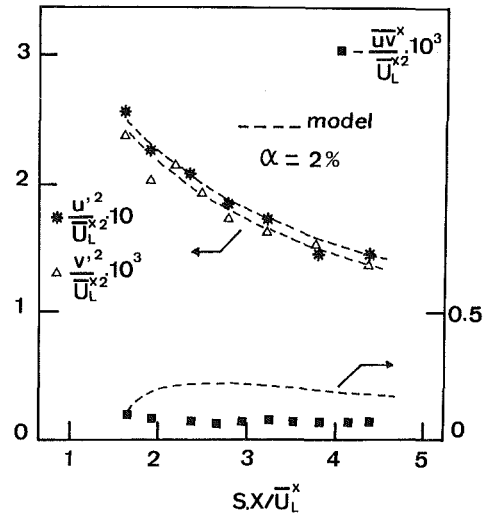**Fig. 9 Longitudinal evolution of the Reynolds stress tensor.**

$S = 2.9$; $Y = 27$ cm; $\overline{U_L}^x = 1$ m/s; $Q_L = 0.17$ m³/s; $Q_G = 2.5.10^{-3}$ m³/s; $\alpha = 2$ percent.
Uncertainty: ±10 percent.

We then observe a rapid decay of the transversal component, whereas the longitudinal component becomes stable. This point brings out the influence of the velocity gradient, as in a single phase flow. In the second case, $\overline{u^2}^x$ is much higher than $\overline{v^2}^x$. The latter decreases slowly, in order to minimize the anisotropy.

We can summarize the influence of the air bubbles on the sheared turbulent field by two effects:

• Decrease of the production of longitudinal kinetic energy of a mean velocity gradient.
• Tendency toward isotropy.

6 Discussion and Modeling

As indicated in the introduction, an attempt was made at modeling the unknown terms in the balance equation for the Reynolds stress tensor in the liquid. When the flow is homogeneous, the equations read: (Lance, 1979)

$$\frac{1}{2}\frac{d}{dt}\overline{u^2}^x = -\overline{uv}^x S + \frac{1}{\rho}\overline{p\frac{\partial u}{\partial x}}^x - \frac{\epsilon}{3} + \frac{1}{2}P_{11}$$

$$\frac{1}{2}\frac{d}{dt}\overline{v^2}^x = \frac{1}{\rho}\overline{p\frac{\partial v}{\partial y}}^x - \frac{\epsilon}{3} + \frac{1}{2}P_{22}$$

$$\frac{d}{dt}\overline{uv}^x = -\overline{v^2}^x S + \frac{1}{\rho}\overline{p\left(\frac{\partial u}{\partial y}+\frac{\partial v}{\partial x}\right)}^x + P_{12}$$

$$\frac{d}{dt}k = -\overline{uv}^x S - \epsilon + \frac{1}{2}P_{ii}, \quad k = \frac{1}{2}\left(\overline{u^2}^x + \overline{v^2}^x + \overline{w^2}^x\right) \quad (3)$$

The viscous dissipation rate ϵ, arises from the hypothesis of isotropy of the smallest turbulent structures. The tensor P_{ij} which vanishes when $\alpha = 0$ describes the interfacial transfer.

The numerical exploitation of this system requires the knowledge of ϵ, P_{ij} and of the terms due to the coupling between pressure and strain. Various closure methods have been de-

Table 1   Initial values taken for the calculation, at the first measurement section $X/M = 12.5$ MKSA units

Fig.	α	$\overline{u^2}^x$	$\overline{v^2}^x$	$\overline{uv}^x$	k	ϵ_0
5	0	$2.1.10^{-3}$	$1.75.10^{-3}$	$-.23.10^{-3}$	$2.8.10^{-3}$	$5.4.10^{-3}$
6	1%	$2.6.10^{-3}$	$2.5.10^{-3}$	$-.25.10^{-3}$	$3.8.10^{-3}$	6.10^{-3}
7	1.4%	$2.54.10^{-3}$	$2.4.10^{-3}$	-3.10^{-3}	$3.65.10^{-3}$	$3.5.10^{-3}$
8	1%	$2.2.10^{-3}$	$2.35.10^{-3}$	$-.28.10^{-3}$	$3.45.10^{-3}$	$5.5.10^{-3}$
9	2%	$2.55.10^{-3}$	$2.4.10^{-3}$	$-.1.10^{-3}$	$3.85.10^{-3}$	6.10^{-3}

veloped in single phase turbulent flows in order to provide suitable expressions for the dissipation rate and the pressure-strain correlations (Launder, et al. 1975; Lumley, 1975). It is worth recalling that the latter can be split into two terms, $\phi_{ij,1}$ and $\phi_{ij,2}$. The first one contains only correlations of the velocity fluctuations and is responsible for the return to isotropy when the mean shear is suppressed. The second one describes the linear coupling between the mean flow and the Reynolds stress (so-called rapid term). Closures laws for these terms have been proposed by the above mentioned authors. We chose the model proposed by Launder et al. (1975) as a starting point for the modeling of the turbulent field in the bubbly flow. We refer the reader to this paper for a more detailed discussion of the closure method for single phase flows, and will discuss how this model can be modified to take the presence of air bubbles into account.

The first problem to solve is the evaluation of the interfacial production term P_{ij} and the dissipation rate ϵ. It is important to notice that the fluctuating kinetic energy k results from three different contributions: the first one is the kinetic energy associated with the velocity perturbations induced by the relative motion of the bubbles with respect to the liquid. As the motion of the bubble is random, these velocity fluctuations are taken into account in the definition of k. However, they are not turbulent in the usual sense. We shall call pseudo-turbulence these random fluctuations due to the flow around the bubbles. The second contribution stems from the wakes behind the bubbles, which produce small scales turbulent structures. The last contribution is the kinetic energy of the turbulence generated by the grid.

Now, as the pseudo-turbulent fluctuations are basically inviscid, the dissipation rate ϵ can be split into two parts $\epsilon = \epsilon_0 + \epsilon_w$, where ϵ_w is the dissipation rate in the wakes of the bubbles, and ϵ_0 is the dissipation rate associated with the energy flux from large scale structures to small scale structures. Such a decomposition assumes that both contributions are statistically independent. The contribution ϵ_0 can be calculated from the widely used equation for the dissipation rate in single phase flows:

$$\frac{d}{dt}\epsilon_0 = -C_{\epsilon 1}\frac{\epsilon_0}{k}\overline{uv}^x S - C_{\epsilon 2}\frac{\epsilon_0^2}{k}, \qquad (4)$$

where $C_{\epsilon 1} = 1.44$ and $C_{\epsilon 2} = 1.9$. It is worth remarking that a better estimation for the time scale of the turbulent stretching k/ϵ_0 would be obtained by removing the pseudo-turbulent contribution from k. However, due to the uncertainty on this quantity, this splitting did not lead to better predictions here.

Now, when the bubbles have reached their mean terminal velocity, the energy production term $P_{ii}/2$ is equal to the rate of work of the drag force exerted by the bubbles on the liquid, assuming that the gas velocity fluctuations are small compared to the mean relative velocity. According to the procedure adopted in single phase turbulence modeling, we can connect ϵ_w to the energy production by:

$$\frac{d}{dt}\epsilon = \frac{1}{\tau}\left(\frac{P_{ii}}{2} - \epsilon_w\right)$$

where τ is the characteristic time of eddy generation in the

wake, which is usually very short compared to the turbulence time scale k/ϵ_0. We can therefore assume that $\epsilon_w = P_{ii}/2$, which is confirmed experimentally for a uniform grid turbulence perturbed by air bubbles (Lance and Bataille, 1982). Therefore, the only required quantity is ϵ_0, which is given by equation (4).

The second mechanism to examine is the interaction between the mean and the fluctuating field, which is described in equation (3) by the production terms $\overline{u_i u_j}^x S$ and by the contribution $\phi_{ij,2}$ to the pressure-strain correlation. The mean velocity gradient acts upon the stretching of the turbulent eddies, on the flow around the bubbles and on their wakes which contributes to the fluctuating kinetic energy. The possible effect of the bubble motion on the stretching of the turbulent structures is not relevant of $\phi_{ij,2}$ and shall be discussed later. According to Launder et al., the tensor $\phi_{ij,2}$ is approximated by a linear combination of Reynolds stresses:

$$\phi_{ij,2} + \phi_{ji,2} = -\frac{C_2+8}{12}\left(\Pi_{ij} - \frac{2}{3}\Pi\delta_{ij}\right) - \frac{30C_2-2}{55}k$$
$$\times\left(\frac{\partial\overline{U_i}^x}{\partial x_j} + \frac{\partial\overline{U_j}^x}{\partial x_i}\right) - \frac{3C_2-2}{11}\left(D_{ij} - \frac{2}{3}\Pi\delta_{ij}\right) \qquad (5)$$

where

$$\Pi_{ij} = -\left(\overline{u_i u_k}^x\frac{\partial\overline{U_j}^x}{\partial x_k} + \overline{u_j u_k}^x\frac{\partial\overline{U_i}^x}{\partial x_k}\right),$$

$$D_{ij} = -\left(\overline{u_i u_k}^x\frac{\partial\overline{U_k}^x}{\partial x_j} + \overline{yu_k}^x\frac{\partial\overline{U_k}^x}{\partial_{ij}}\right)$$

$$\Pi = tr\Pi_{ij}, C_2 = 0.55.$$

We shall make the assumption that this functional form is still valid for a low void fraction bubbly flow and that the empirical constant C_2 is unchanged.

A last important mechanism is the interaction of the fluctuating field with itself. Roughly speaking, we can distinguish three contributions: the nonlinear coupling between turbulent eddies, the distortion of the turbulent eddies by the flow around the bubbles, and the hydrodynamic interaction between the bubbles. The second effect deserves special interest. As a matter of fact, due to the relative motion of the bubbles, the turbulent structures are stretched and distorted by the hydrodynamic fields around the bubbles, the time scale of this interaction being given by the residence time of a turbulent eddy in the vicinity of a bubble $\tau_D = D/\overline{U_R}^x$.

The interaction between the turbulent field and the hydrodynamic fields around the bubbles causes a random distortion of the turbulent structures. This mechanism competes with the action of the mean shear flow which imposes a well-defined deformation of the turbulent eddies. Therefore we can consider that these random stretchings tend to restore the isotropy of the flow, which is consistent with the experimental observations. Mathematically, we can model this phenomenon by adding to Launder's expression for the non-linear part of the pressure-strain correlation, $\phi_{ij,1}$, an extra term:

$$C_3 \alpha \frac{\overline{U}_R^x}{D} \left(\overline{u_i u_j}^x - \frac{2}{3} k \delta_{ij} \right) \qquad (6)$$

That is, for bubbly flows:

$$\phi_{ij,1} + \phi_{ji,1} = - \left(\overline{u_i u_j}^x - \frac{2}{3} k \delta_{ij} \right) \left(C_1 \frac{\epsilon_0}{k} + C_3 \alpha \frac{\overline{U}_R^x}{D} \right), \quad C_1 = 2.2 \qquad (7)$$

The additional constant C_3 has to be determined empirically in order to obtain the best fitting with the experimental longitudinal evolution of the Reynolds stress tensor. It is found here to be equal to 8.

The system of equation (3) can then be written:

$$\frac{\lambda}{2} \frac{d}{dt} \overline{u^2}^x = - \overline{uv}^x S + \phi_{11,1} + \phi_{11,2} - \frac{\epsilon_0}{3}$$

$$\frac{\lambda}{2} \frac{d}{dt} \overline{v^2}^x = \phi_{22,1} + \phi_{22,2} - \frac{\epsilon_0}{3}$$

$$\frac{d}{dt} \overline{uv}^x = - \overline{v^2}^x S + (\phi_{12,1} + \phi_{21,1}) + (\phi_{12,2} + \phi_{21,2})$$

$$\frac{d}{dt} k = - \overline{uv}^x S - \epsilon_0$$

$$\frac{d}{dt} \epsilon_0 = - C_{\epsilon 1} \epsilon_0 \frac{\overline{uv}^x}{k} S - C_{\epsilon 2} \frac{\epsilon_0^2}{k}$$

$$(8)$$

The comparison between our experimental data and the numerical predictions of the model is shown in Figs. 5 to 9. The initial values taken for the calculation are given for each case. The very simple modeling of the "two-phase terms" adopted here reproduces very well all the observed behaviors. Due to the lack of experimental information, it is difficult to estimate the range of validity of such a model. Nevertheless we can expect it to be suitable for low values of α (in order to prevent bubble coalescences) and for weak shear intensity (in order to avoid bubble break-up).

References

Auton, T. R., Hunt, J. C. R., and Prud'homme, M., 1988, "The Force Exerted on a Body in Inviscid Unsteady Non-Uniform Rotational Flow," *J. Fluid Mech.*, Vol. 197, pp. 241–257.

Champagne, F. H., Harris, V. G., and Corrsin, S., 1970, "Experiments on Nearly Homogeneous Turbulent Shear Flows," *Journal of Fluid Mechanics*, Vol. 41, Part 1, p. 81.

Delhaye, J. M., and Achard, J. L., 1976, "On the Averaging Operators Introduced in Two-Phase Flow Modeling," *Specialist's Meeting on Transient Two-phase Flows*, OCDE report, Toronto, Canada.

Drew, D., and Lahey, R. T., 1982, "Phase Distribution Mechanisms in Turbulent Low-Quality Flow in a Circular Pipe," *Journal of Fluid Mechanics*, Vol. 117, p. 91.

Herringe, M. A., and Davis, M. R., 1976, "Structural Development of Gas-Liquid Mixture Flows," *Journal of Fluid Mechanics*, Vol. 73, Part 1, p. 97.

Ishii, M., 1975, *Thermo-Fluid Dynamics of Two-Phase Flow*, Eyrolles.

Lahey, R. T., 1987, "Turbulence and Phase Distribution Phenomena in Two-Phase Flow," *Proceedings of the Conference on Transient Phenomena in Multiphase Flow*, Dubrovnik, Yugoslavia, May 24–30.

Lance, M., 1979, "Contribution à l'Etude de la Turbulence dans la Phase Liquide des Ecoulements à Bulles," Thèse de Docteur-Ingénieur, Université de Lyon.

Lance, M., Marié, J. L., Charnay, G., and Bataille, J., 1980, "Turbulence Structure of a Co-Current Air-Water Bubbly Flow," *Proceedings of the ANS/ASME/NRC International Topical Meeting on Nuclear Thermal Hydraulics*, NUREG/CP-0014, Vol. 3, p. 1363.

Lance, M., and Bataille, J., 1982, "Turbulence in the Liquid Phase of a Bubbly Air-Water Flow," Nato Specialist's Meeting, Spitzingsee, Martinus Nijhoff Publishers, The Netherlands.

Launder, B. E., Reece, G. J., and Rodi, W., 1975, "Progress in the Development of a Reynolds-Stress Turbulence Closure," *Journal of Fluid Mechanics*, Vol. 68, p. 537.

Lighthill, J., 1956, "Drift," *Journal of Fluid Mechanics*, Vol. 1, p. 31.

Lumley, J., 1975, "Prediction Methods for Turbulent Flows," I.V.K. Lecture series, 76.

Marié, J. L., 1983, "Investigation of Two-Phase Bubbly Flows Using LDA," *Physical Chemical Hydrodynamics*, Vol. 4, pp. 103–118.

Ohba, K., Kishimoto, I., and Ogasawara, M., 1977, "Simultaneous Measurement of Local Liquid Velocity and Void Fraction in Bubbly Flows Using a Gas Laser," Technology report of the Osaka University, Vol. 27, No. 1358.

Sato, Y., and Sekoguchi, K., 1975, "Liquid Velocity Distribution in Two-Phase Bubble Flow," *International Journal of Multiphase Flow*, Vol. 2, p. 79.

Serizawa, A., Kataoka, I., and Mishigoshi, I., 1975, "Turbulence Structure of Air-Water Bubbly Flow," *International Journal of Multiphase Flow*, Vol. 2, No. 3, p. 221.

Theofanous, T. G., and Sullivan, J., 1982, "Turbulence in Two-Phase Dispersed Flows," *Journal of Fluid Mechanics*, Vol. 116, p. 343.

Zun, I., 1985, "The Role of Void Peaking in a Vertical Two-Phase Bubbly Flow," *Proceedings of 2nd International Conference on Multi-phase Flow*, London, England, June 19–21.

Nonideal Gas Effects for the Venturi Meter

W. Bober[1] and W. L. Chow[2]

A method for treating nonideal gas flows through a venturi meter is described. The method is an extension of a previous study reported in an earlier paper. The method involves the determination of the expansion factor which may then be used to determine the mass flow rate through the venturi meter. The method also provides the means for determining the critical pressure ratio as well as the maximum flow rate per unit throat area. The Redlich-Kwong equation of state is used, which allows for closed form expressions for the specific heat at constant volume and the change in entropy. The Newton-Raphson method is used to determine the temperature and specific volume at the throat. It is assumed that the following items are known: the upstream temperature and pressure and the ratio of the throat pressure to the upstream pressure. Results were obtained for methane gas. These results indicate that for the cases considered, the use of the ideal gas expression for the expansion factor would lead to an error in the determination of the mass flow rate; the error increases as the throat to inlet pressure ratio decreases. For the example reported in this study, the maximum percent difference in the critical pressure ratio between the ideal and nonideal gases was 5.81 percent, while the maximum percent difference in the maximum flow rate per unit throat area was 7.62 percent.

Introduction

In a recent paper (Bober and Chow, 1991) the effects of nonideal gas behavior on flows through converging-diverging nozzles were investigated. The authors demonstrated that for reservoir conditions that lead to a fluid property path that comes close to the critical point, nonideal gas effects are very significant. Interest in this topic was motivated by the fact that in recent times, there has been a significant increase in the operating pressures of power plants, gas fields and transmission lines (Fagerlund and Winkler, 1982). These high pressure operations have resulted in a need for a more accurate means for metering the discharge of gas flows from reservoirs and transmission lines. Two common instruments for metering such flows are the venturi and orifice meters. In this paper, which is an extension of a previous study (Bober and Chow, 1991),

[1] Associate Professor, Mem. ASME.
[2] Professor, Fellow ASME. Department of Mechanical Engineering, Florida Atlantic University, Boca Raton, FL 33431.

the effects of nonideal gas behavior on the expansion factor for the venturi meter are examined.

Technical Discussion

The formula that is commonly used to determine the gas mass flow rate, $\dot{m}$, through a venturi meter (Miller, 1983) is:

$$\dot{m} = \frac{C_d A_2 Y \sqrt{2\tilde{v}_1 (p_1 - p_2)}}{\tilde{v}_1 \sqrt{1 - (A_2/A_1)^2}} \tag{1}$$

where A is the cross-sectional area, p is the pressure, $\tilde{v}$ is the specific volume, C_d is the discharge coefficient, Y is the expansion factor and the subscripts 1 and 2 refer to points at the inlet and throat sections of the venturi, respectively. For an ideal gas, the expansion factor, Y_I, is

$$Y_I = \left[\left(\frac{p_2}{p_1}\right)^{2/k} \left(\frac{k}{k-1}\right) \left[\frac{1 - (p_2/p_1)^{(k-1)/k}}{1 - p_2/p_1} \right] \right.$$
$$\left. \times \left[\frac{1 - (A_2/A_1)^2}{1 - (A_2/A_1)^2 (p_2/p_1)^{2/k}} \right] \right]^{1/2} \tag{2}$$

where k is the ratio of specific heats. Equations (1) and (2) are derived from the one-dimensional momentum equation assuming ideal isentropic inviscid flow with constant specific heats. The term, C_d, in equation (1) is an empirical factor which depends mainly on the Reynolds number of the flow and is thus a correction factor for viscous effects. An empirical curve giving C_D versus the Reynolds number, Re, can be found in Miller, 1983. With $Y = 1.0$, equation (1) gives $\dot{m}$ for an incompressible fluid; thus Y accounts for compressibility effects when the fluid is a gas. From the work described in Bober and Chow, 1991, one must question the accuracy of the expansion factor when the fluid property path comes close to the critical point. For such a case, the expansion factor, Y, will differ from the ideal value, Y_I. A method for evaluating Y for a nonideal gas follows.

The mass conservation and energy equations for frictionless, isentropic flow are:

$$\dot{m} = \frac{A_1 V_1}{\tilde{v}_1} = \frac{A_2 V_2}{\tilde{v}_2} \tag{3}$$

$$h_1 + \frac{V_1^2}{2} = h_2 + \frac{V_2^2}{2} \tag{4}$$

where V is the section fluid velocity and h is the enthalpy per unit mass. Combining equations (3) and (4) and rearranging gives:

$$V_2^2 = \frac{2(h_1 - h_2)}{1 - (A_2 \tilde{v}_1 / A_1 \tilde{v}_2)^2} \tag{5}$$

The factor that accounts for the compressibility of a fluid may be obtained from equation (1) with $C_D = 1$, i.e.,

$$Y = \frac{\dot{m}\tilde{v}_1\sqrt{1-(A_2/A_1)^2}}{A_2\sqrt{2\tilde{v}_1(p_1-p_2)}} \qquad (6)$$

To account for nonideal gas behavior, an equation of state must be introduced. To obtain analytical expressions for the specific heat at constant volume, $c_{\tilde{v}}$, the specific heat at constant pressure, c_p, and entropy, s, the equation of state should be reducible to the form (see·Vinokur's discussion following article by Bober and Chow, 1991).

$$p = \sum_n f_n(T)g_n(\tilde{v}) \qquad (7)$$

where $f_n(T)$ are twice differentiable analytic functions of T and $g_n(\tilde{v})$ are differentiable and also integrable in closed form.

Two commonly used equations of state are the Redlich-Kwong equation and the Hall-Yarborough equation (Miller, 1983). For natural gas at high reduced pressures and reduced temperatures above 1.05, the compressibility coefficient, Z, computed by the Hall-Yarborough equation has an accuracy of ± 0.3 percent (Miller, 1983). For Methane gas, at a reduced temperature of 1.6 and a reduced pressure between 3.2 and 8.5, the error in the compressibility coefficient computed by the Redlich-Kwong equation (as compared to the true value) is between 1 and 2 percent (Miller, 1983). However, the Redlich-Kwong equation fits the form of equation (7) and the Hall-Yarborough equation does not (one term in that equation cannot be expressed as $f_n(T) g_n(\tilde{v})$). Since the method described in this paper requires analytical expressions for $c_{\tilde{v}}$ and s, the Redlich-Kwong equation was used. However, it should be realized that the error in the compressibility coefficient resulting from the use of the Redlich-Kwong equation is far less than that obtained by assuming the gas to be ideal.

The Redlich-Kwong equation of state is given by (Miller, 1983)

$$p = \frac{RT}{\tilde{v}-b} - \frac{a}{T^{0.5}\tilde{v}(\tilde{v}+b)} = \frac{\rho RT}{1-b\rho} - \frac{a\rho^2}{T^{0.5}(1+b\rho)} \qquad (8)$$

where T is the temperature, R is the gas constant, ρ is the mass density and

$$a = 0.42748\frac{R^2 T_c^{2.5}}{p_c} \text{ and } b = 0.08664\frac{RT_c}{p_c}$$

In the above equations, (p_c, T_c) are, respectively, the critical pressure and temperature of the gas. Then the ratio p_2/p_1 can be expressed as

$$\frac{p_2}{p_1} = \frac{\dfrac{RT_2}{\tilde{v}_2-b} - \dfrac{a}{T_2^{0.5}\tilde{v}_2(\tilde{v}_2+b)}}{\dfrac{RT_1}{\tilde{v}_1-b} - \dfrac{a}{T_1^{0.5}\tilde{v}_1(\tilde{v}_1+b)}}$$

This provides an equation for $(T_2, \tilde{v}_2)$ assuming that p_2/p_1, T_1 and $\tilde{v}_1$, are known; i.e.,

$$F_1(T_2,\tilde{v}_2;\frac{p_2}{p_1},\tilde{v}_1,T_1) = \frac{RT_2}{\tilde{v}_2-b} - \frac{a}{T_2^{0.5}\tilde{v}_2(\tilde{v}_2+b)}$$

$$- \frac{p_2}{p_1}\left[\frac{RT_1}{\tilde{v}_1-b} - \frac{a}{T_1^{0.5}\tilde{v}_1(\tilde{v}_1+b)}\right] = 0 \qquad (9)$$

An expression for the entropy change, s_2-s_1, can be obtained by integrating the differential equation for entropy (Wark, 1988); i.e.,

$$ds = c_{\tilde{v}}\frac{dT}{T} + \left(\frac{\partial p}{\partial T}\right)_{\tilde{v}}d\tilde{v} \qquad (10)$$

The term $(\partial p/\partial T)_{\tilde{v}}$ can be obtained from equation (8). It is

$$\left(\frac{\partial p}{\partial T}\right)_{\tilde{v}} = \frac{R}{\tilde{v}-b} + \frac{a}{2T^{3/2}\tilde{v}(\tilde{v}+b)} \qquad (11)$$

An expression for the specific heat at constant volume, $c_{\tilde{v}}$, can also readily be obtained (Bober and Chow, 1991). It is

$$c_{\tilde{v}} = c_{\tilde{v}}^+(T) + \frac{3a}{4bT^{3/2}}\ln\left(1+\frac{b}{\tilde{v}}\right) \qquad (12)$$

where

$$c_{\tilde{v}}^+ = c_p^+ - R \qquad (13)$$

In the above equations, $c_{\tilde{v}}^+$ and c_p^+ are the zero pressure specific heats at constant volume and constant pressure, respectively. The term c_p^+ can be determined by

$$\frac{c_p^+}{R} = A_0 + A_1 T + A_2 T^2 + A_3 T^3 + A_4 T^4 \qquad (14)$$

The coefficients A_0 through A_4 and the gas constant R for various gases can be found in Wark, 1988.

Since entropy is a property, equation (10) can be integrated along any path from state 1 to state 2. A convenient path is to integrate from $(T_1, \tilde{v}_1)$ to $(T_2, \tilde{v}_1)$, holding $\tilde{v}$ constant, and then from $(T_2, \tilde{v}_1)$ to $(T_2, \tilde{v}_2)$, holding T constant. This gives:

$$s_2 - s_1 = R\left[(A_0-1)\ln\left(\frac{T_2}{T_1}\right) + A_1(T_2-T_1) + \frac{A_2}{2}(T_2^2-T_1^2)\right.$$

$$\left. + \frac{A_3}{3}(T_2^3-T_1^3) + \frac{A_4}{4}(T_2^4-T_1^4)\right]$$

$$- \frac{a}{2b}\ln\left[1+\frac{b}{\tilde{v}_1}\right]\left[\frac{1}{T_2^{1.5}} - \frac{1}{T_1^{1.5}}\right]$$

$$+ R[\ln(v_2-b) - \ln(\tilde{v}_1-b)]$$

$$- \frac{a}{2bT_2^{1.5}}\left[\ln\left(\frac{\tilde{v}_2+b}{\tilde{v}_2}\right) - \ln\left(\frac{\tilde{v}_1+b}{\tilde{v}_1}\right)\right] = F_2(T_2,\tilde{v}_2;T_1,\tilde{v}_1) \qquad (15)$$

For isentropic flow, $s_2 - s_1 = 0$ and thus

$$F_2(T_2,\tilde{v}_2;T_1,\tilde{v}_1) = 0 \qquad (16)$$

Equations (9) and (16) provide two algebraic equations for the two unknowns $(T_2, \tilde{v}_2)$ assuming that $(T_1, \tilde{v}_1)$ and p_2/p_1 are known. Since these equations are nonlinear, an iterative method of solution, such as the Newton-Raphson method is appropriate. The $(i+1)$ iteration for T_2 and $\tilde{v}_2$ is given by (Chapra and Canale, 1988):

$$T_2^{i+1} = T_2^i - \frac{F_1^i\left(\frac{\partial F_2}{\partial \tilde{v}_2}\right)^i - F_2^i\left(\frac{\partial F_1}{\partial \tilde{v}_2}\right)^i}{\left(\frac{\partial F_1}{\partial T_2}\right)^i\left(\frac{\partial F_2}{\partial \tilde{v}_2}\right)^i - \left(\frac{\partial F_1}{\partial \tilde{v}_2}\right)^i\left(\frac{\partial F_2}{\partial T_2}\right)^i} \qquad (17)$$

and

$$\tilde{v}_2^{i+1} = \tilde{v}_2^i + \frac{F_1^i\left(\frac{\partial F_2}{\partial T_2}\right)^i - F_2^i\left(\frac{\partial F_1}{\partial T_2}\right)^i}{\left(\frac{\partial F_1}{\partial T_2}\right)^i\left(\frac{\partial F_2}{\partial \tilde{v}_2}\right)^i - \left(\frac{\partial F_1}{\partial \tilde{v}_2}\right)^i\left(\frac{\partial F_2}{\partial T_2}\right)^i} \qquad (18)$$

The derivatives $\partial F_1/\partial T_2$, $\partial F_1/\partial \tilde{v}_2$, $\partial F_2/\partial T_2$, and $\partial F_2/\partial \tilde{v}_2$ can readily be obtained from equations (9) and (15).

To start the iteration, it is convenient to select values for T_2 and $\tilde{v}_2$ equal to those corresponding values that would be obtained by assuming the gas to be ideal.

The formulation has assumed that the values T_1, $\tilde{v}_1$ and p_2/p_1 are known. However, $\tilde{v}_1$ is not a readily measurable term, and thus it must be determined indirectly from pressure and temperature measurements, i.e., p_1 and T_1 respectively. As a

matter of convenience, the compressibility factor, Z, is introduced; where

$$Z = \frac{p\tilde{v}}{RT} \qquad (19)$$

Equations (8) and (19) may be combined to give

$$Z^3 - Z^2 + \left[\frac{ap}{R^2 T^{2.5}} - \frac{b^2 p^2}{R^2 T^2} - \frac{bp}{RT}\right] Z - \frac{abp^2}{R^3 T^{3.5}} = 0 \qquad (20)$$

For given values of p and T (in the range where equation (8) is valid), equation (20) may readily be solved and the proper root selected (Bober and Chow, 1991). Having p_1, T_1 and Z_1, equation (19) gives $\tilde{v}_1$.

To complete the formulation, an equation for the enthalpy, h, must be introduced. It is

$$h = u + p\tilde{v} \qquad (21)$$

where u is the internal energy per unit mass.

An expression for the internal energy, u, that is compatible with the Redlich-Kwong equation of state and the fourth degree polynomial expression for the zero pressure specific heat at constant pressure is given in Bober and Chow, 1991. It is:

$$u(T, \tilde{v}) = u^+(T) - \frac{3a}{2bT^{0.5}} \ln\left(1 + \frac{b}{\tilde{v}}\right) \qquad (22)$$

where u^+ is the zero pressure internal energy which is given by

$$u^+(T) = R\left[(A_0 - 1)T + \frac{A_1}{2}T^2 + \frac{A_2}{3}T^3 + \frac{A_3}{4}T^4 + \frac{A_4}{5}T^5\right] \qquad (23)$$

The formulation is now complete. The procedure for obtaining a solution is as follows: Given p_1, T_1, and p_2/p_1, first determine Z_1 from equation (20), followed by $\tilde{v}_1$, from equation (19). Then, utilizing equations (9), (15)–(18), determine T_2 and $\tilde{v}_2$. Next, determine u_2 and h_2 from equations (22), (23) and (21). The velocity, V_2, may then be calculated from equation (5), followed by $\dot{m}$ from equation (3) and Y from equation (6). The expansion factor, Y, may then be compared with the ideal value, Y_I, which is given by equation (2).

One additional item of interest is to determine the critical pressure ratio, $(p_2/p_1)_c$. For fixed values of p_1, T_1 and d_2/d_1, there exists a p_2/p_1 ratio that gives the maximum possible flow rate per unit throat area that can pass through the venturi. At this condition, the venturi is said to be choked and the pressure ratio at which this occurs is designated as the critical pressure ratio. When the venturi is choked the Mach Number, M_2, at the throat equals 1.0. An expression for the speed of sound, c, consistent with the Redlich-Kwong equation is given in Bober and Chow (1991). It is

$$c^2 = \frac{RT}{(1-b\rho)^2}\left[1 + \frac{R}{c_{\tilde{v}}}\right] + \frac{aR\rho}{c_{\tilde{v}}T^{1/2}(1-b^2\rho^2)} + \frac{a^2\rho^2}{4c_{\tilde{v}}T^2(1+b\rho)^2}$$
$$- \frac{a(2+b\rho)\rho}{T^{1/2}(1+b\rho)^2} \qquad (24)$$

The Mach number is given by

$$M = \frac{V}{c} \qquad (25)$$

The procedure for determining the critical pressure ratio is to hold p_1, T_1 and d_2/d_1 constant and successively decrease p_2/p_1. At each step T_2, $\tilde{v}_2$ (or ρ_2) and V_2 are determined as indicated earlier; then the Mach Number, M_2, is determined by equations (24), (25), (12), (13), and (14). The value of p_2/p_1 that results in $M_2 = 1.0$ is the critical pressure ratio. The maximum flow rate per unit throat area, $(\dot{m})_{max}/A^*$, can then be determined by equation (3).

A formula for determining the critical pressure ratio for an ideal gas with constant specific heats is given in Bean, 1971. It is

$$r_c^{(1-k)/k} + \frac{k-1}{2}\beta^4 r_c^{2/k} - \frac{k+1}{2} = 0 \qquad (26)$$

where $r_c = (p_2/p_1)_c$ and $\beta = d_2/d_1$. The ideal gas critical pressure ratio may then be compared to the corresponding value obtained by the method described in the previous paragraph.

A formula for determining the maximum possible flow rate per unit throat area for a real gas is also given in Bean, 1971. The formula is based on a polytrope model; i.e., $p/\rho^\Gamma = $ constant. As stated in the above reference, Γ is not a constant and not equal to $c_p/c_{\tilde{v}}$, but is a function of the stagnation temperature and pressure. However, a method for determining Γ is not given. As a result one cannot readily compute $(\dot{m})_{max}/A^*$ by the given formula. Therefore only ideal gas values for this term are compared to the corresponding values obtained by the method described in this paper. The method for determining $(\dot{m})_{max}/A^*$ for an ideal gas is to determine the ideal gas critical pressure ratio, r_c, by equation (26), then evaluate Y_I by equation (2) and $(\dot{m})_{max}/A^*$ by equation (1) with $C_d = 1.0$. For cases where $\dot{m}/A_2$ is not a maximum, Bean (1971) recommends the use of equations (1) and (2), and evaluating $\tilde{v}$, by equation (19). Thus, nonideal gas effects are only applied at the inlet and not throughout the entire flow field as is done in this paper.

Results

A computer program was developed to solve the system of equations outlined in the previous section. Several runs were made for Methane gas at different values for p_1, T_1, p_2/p_1 and throat to inlet diameter ratios, d_2/d_1. Values of p_1 and T_1 were selected that result in the gas being far from ideal and with a ratio of specific heats far from its value at standard temperature and pressure. The program produced tables containing Y, Y_I, V_2, V_1, $\dot{m}_I/A_1$ and $\dot{m}/A_1$, versus p_2/p_1, where $\dot{m}_I$ is the mass flow rate evaluated by equation (1) with $C_D = 1.0$. Figure 1 is a plot of Y versus p_2/p_1 for several different values of d_2/d_1 at an inlet reduced pressure and temperature, $(p_r)_1$, $(T_r)_1$, equal to 4.5 and 1.4, respectively, where $(p_r)_1 = p_1/p_c$ and $(T_r)_1 = T_1/T_c$. As it is for an ideal gas, for a fixed p_2/p_1 ratio, Y decreases as d_2/d_1 increases. Furthermore, for $d_2/d_1 << 1$, Y exhibits the same limiting behavior as Y_I. As can be seen from equation (2), for $d_2/d_1 << 1$,

$$Y_I \rightarrow \left[\left(\frac{p_2}{p_1}\right)^{2/k}\left(\frac{k}{k-1}\right)\left(\frac{1 - (p_2/p_1)^{k-1/k}}{1 - p_2/p_1}\right)\right]^{1/2}$$

which is independent of d_2/d_1.

A plot of the percent relative error in Y_I versus p_2/p_1 is given in Fig. 2. From this figure it can be seen that for all d_2/d_1
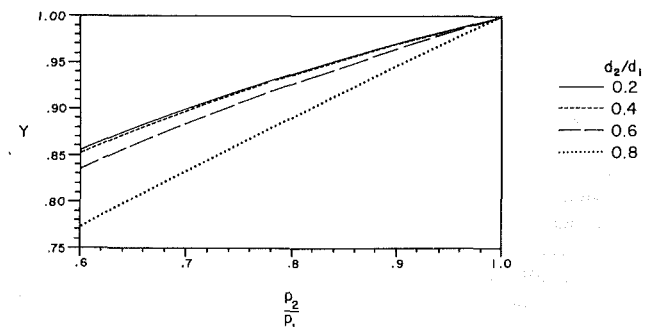

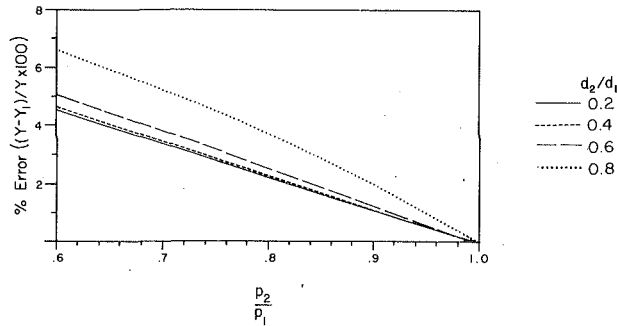Fig. 1 Expansion factor versus p_2/p_1 ($(p_r)_1 = 4.5, (T_r)_1 = 1.4, k_1 = 1.938, Z_1 = 0.774$)

Fig. 2 Percent error versus p_2/p_1 ($(p_r)_1 = 4.5$, $(T_r)_1 = 1.4$, $k_1 = 1.938$, $Z_1 = 0.774$)

Table 1* Critical pressure ratios and maximum flow rates per unit throat area

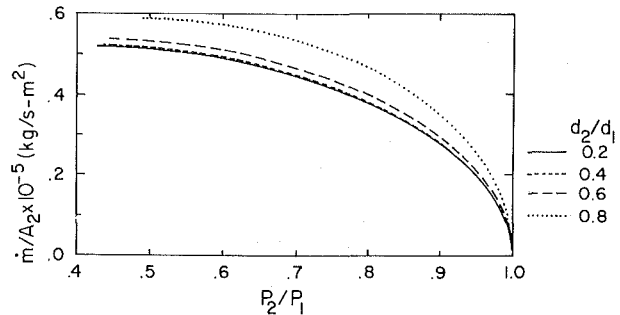|	Nonideal gas		Ideal gas	
d_2/d_1	$(p_2/p_1)_c$	$(\dot{m})_{max}/A^*$	$(p_2/p_1)_c$	$(\dot{m})_{max}/A^*$
0.8	0.49304	5.8649×10^4	0.52107	5.4181×10^4
0.6	0.44422	5.3669×10^4	0.47003	5.0109×10^4
0.4	0.43020	5.2214×10^4	0.45519	4.8905×10^4
0.2	0.42719	5.1900×10^4	0.45199	4.8644×10^4

* $(p_r)_1 = 4.5$, $(T_r)_1 = 1.4$, $k_1 = 1.938$, $Z_1 = 0.774$.

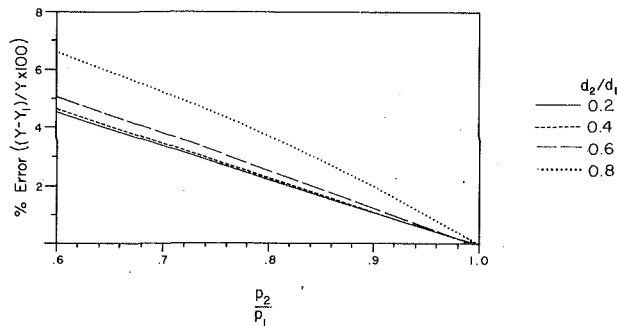Fig. 3 Mass flow rate per unit throat area versus p_2/p_1 ($(p_r)_1 = 4.5$, $(T_r)_1 = 1.4$, $k_1 = 1.938$, $Z_1 = 0.774$)

cases, the percent relative error in Y_I increases as p_2/p_1 decreases. For all cases considered Y_I drops faster than Y as p_2/p_1 decreases. For the range of values tried, the maximum relative error is 6.58 percent at $p_2/p_1 = 0.6$ and $d_2/d_1 = 0.8$. Note that the Z value at the inlet as determined by equations (8) and (19) is 0.774. This results in a 29.2 percent error in the Z value for the ideal gas, which is much larger than the relative error in Y_I. This leads one to believe that any small error in the Z value that results from the use of the Redlich-Kwong equation (as compared to the true value for Z) would have a minimal effect on the determination of Y.

To make sure that the difference between Y_I and Y was not caused by a computer error, the constants a and b in equation (8), and A_1 through A_4 in equation (14) were all set to zero. This reduced the gas to an ideal gas with constant specific heats. The program was then run at the same p_1, T_1 and p_2/p_1 values as those given in Fig. 2, and the difference between Y and Y_I disappeared.

Table 1 gives $(p_2/p_1)_c$ and $(\dot{m})_{max}/A^*$ for both ideal and nonideal gases. As can be seen from this table, the nonideal critical pressure ratios are less than the corresponding ideal gas values, the maximum percent difference being 5.81 percent. However, the nonideal maximum flow rates per unit throat area are greater than the corresponding ideal gas values, the maximum percent difference being 7.62 percent.

Figure 3 is a plot of $\dot{m}/A_2$ versus p_2/p_1. As can be seen from this figure, $\dot{m}/A_2$ increases as p_2/p_1 decreases. As expected, these curves exhibit the same asymptotic behavior as the Y curves in Fig. 1. That is, for small d_2/d_1 values, the curves nearly coincide. Also notice that the tangents to the curves at their corresponding critical points are parallel to the p_2/p_1 axis, indicating that at the critical points $d(\dot{m}/A_2)/d(p_2/p_1)$ equals zero.

In conclusion, a program has been developed to determine the expansion factor of a nonideal gas through a venturi meter. The program accounts for nonideal gas behavior as described by the Redlich-Kwong equation of state. For gas flows that are nonideal, the use of the ideal expansion factor in determining $\dot{m}$, underestimates the true value. For the example given in this paper, a relative error as much as 6.58 percent was obtained when $p_2/p_1 = 0.6$ and $d_2/d_1 = 0.8$. The program also provides the means for determining the critical pressure ratio as well as the maximum flow rate per unit throat area. For the example given in this paper the maximum percent difference in the critical pressure ratio between the nonideal and ideal gases was 5.81 percent while the maximum percent difference in the maximum flow rate per unit throat area was 7.62 percent. An important aspect of the venturi flow problem that has not been treated in this paper is the nonideal gas effects on the discharge coefficient, C_D. If these effects are minimal, then the procedure outlined in this paper would provide an accurate method for determining the mass flow rate of a nonideal gas through a venturi meter.

References

Bean, H. S., Ed., 1971, *Fluid Meters*, ASME, 6th Ed.

Bober, W., and Chow, W. L., 1991, "Non-Ideal Isentropic Gas Flow Through Converging-Diverging Nozzles," ASME JOURNAL OF FLUIDS ENGINEERING, Vol. 112, No. 4, pp. 455–461.

Chapra, S. C., and Canale, R. P., 1988, *Numerical Methods for Engineers*, McGraw-Hill, New York.

Fagerlund, A. C., and Winkler, R. J., 1982, "The Effect of Non-Ideal Gases on Valve Sizing," *Adv. Instrum.*, Vol. 37, No. 3, pp. 1323–1333.

Miller, R. W., 1983, *Flow Measurement Engineering Handbook*, McGraw-Hill, New York.

Wark, K., Jr., 1988, *Thermodynamics*, McGraw-Hill, New York.

Modulation of Turbulence by a Dispersed Phase

R. A. Gore[1] and C. T. Crowe[1]

The results of an earlier investigation that demonstrated the significance of the particle diameter/fluid length scale ratio in determining whether or not the addition of a dispersed phase would cause an increase or decrease in the carrier phase turbulent intensity are extended to radial locations other than the centerline. Presently, it is shown that similar trends are valid except the results become less correlated approaching the wall for the case of pipe flows. The results for jets are independent of radial location. It is also shown that other possible nondimensional parameters do not correlate the data as well.

[1]Department of Mechanical and Materials Engineering, Washington State University, Pullman, WA 99164-2920. Dr. Gore is currently at Los Alamos National Laboratory, Group T-3, Los Alamos, NM 87545.

Fig. 2 Percent error versus p_2/p_1 ($(p_r)_1 = 4.5$, $(T_r)_1 = 1.4$, $k_1 = 1.938$, $Z_1 = 0.774$)

d_2/d_1	Nonideal gas		Ideal gas	
	$(p_2/p_1)_c$	$(\dot{m})_{max}/A^*$	$(p_2/p_1)_c$	$(\dot{m})_{max}/A^*$
0.8	0.49304	5.8649×10^4	0.52107	5.4181×10^4
0.6	0.44422	5.3669×10^4	0.47003	5.0109×10^4
0.4	0.43020	5.2214×10^4	0.45519	4.8905×10^4
0.2	0.42719	5.1900×10^4	0.45199	4.8644×10^4

* $(p_r)_1 = 4.5$, $(T_r)_1 = 1.4$, $k_1 = 1.938$, $Z_1 = 0.774$.

cases, the percent relative error in Y_I increases as p_2/p_1 decreases. For all cases considered Y_I drops faster than Y as p_2/p_1 decreases. For the range of values tried, the maximum relative error is 6.58 percent at $p_2/p_1 = 0.6$ and $d_2/d_1 = 0.8$. Note that the Z value at the inlet as determined by equations (8) and (19) is 0.774. This results in a 29.2 percent error in the Z value for the ideal gas, which is much larger than the relative error in Y_I. This leads one to believe that any small error in the Z value that results from the use of the Redlich-Kwong equation (as compared to the true value for Z) would have a minimal effect on the determination of Y.

To make sure that the difference between Y_I and Y was not caused by a computer error, the constants a and b in equation (8), and A_1 through A_4 in equation (14) were all set to zero. This reduced the gas to an ideal gas with constant specific heats. The program was then run at the same p_1, T_1 and p_2/p_1 values as those given in Fig. 2, and the difference between Y and Y_I disappeared.

Table 1 gives $(p_2/p_1)_c$ and $(\dot{m})_{max}/A^*$ for both ideal and nonideal gases. As can be seen from this table, the nonideal critical pressure ratios are less than the corresponding ideal gas values, the maximum percent difference being 5.81 percent. However, the nonideal maximum flow rates per unit throat area are greater than the corresponding ideal gas values, the maximum percent difference being 7.62 percent.

Figure 3 is a plot of $\dot{m}/A_2$ versus p_2/p_1. As can be seen from this figure, $\dot{m}/A_2$ increases as p_2/p_1 decreases. As expected, these curves exhibit the same asymptotic behavior as the Y curves in Fig. 1. That is, for small d_2/d_1 values, the curves nearly coincide. Also notice that the tangents to the curves at their corresponding critical points are parallel to the p_2/p_1 axis, indicating that at the critical points $d(\dot{m}/A_2)/d(p_2/p_1)$ equals zero.

In conclusion, a program has been developed to determine the expansion factor of a nonideal gas through a venturi meter. The program accounts for nonideal gas behavior as described by the Redlich-Kwong equation of state. For gas flows that are nonideal, the use of the ideal expansion factor in determining $\dot{m}$, underestimates the true value. For the example given in this paper, a relative error as much as 6.58 percent was obtained when $p_2/p_1 = 0.6$ and $d_2/d_1 = 0.8$. The program also provides the means for determining the critical pressure ratio as well as the maximum flow rate per unit throat area. For the example given in this paper the maximum percent difference in the critical pressure ratio between the nonideal and ideal gases was 5.81 percent while the maximum percent difference in the maximum flow rate per unit throat area was 7.62 percent. An important aspect of the venturi flow problem that has not been treated in this paper is the nonideal gas effects on the discharge coefficient, C_D. If these effects are minimal, then the procedure outlined in this paper would provide an accurate method for determining the mass flow rate of a nonideal gas through a venturi meter.
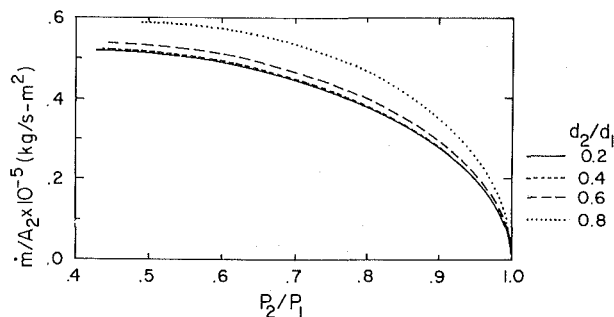

Fig. 3 Mass flow rate per unit throat area versus p_2/p_1 ($(p_r)_1 = 4.5$, $(T_r)_1 = 1.4$, $k_1 = 1.938$, $Z_1 = 0.774$)

References

Bean, H. S., Ed., 1971, *Fluid Meters*, ASME, 6th Ed.

Bober, W., and Chow, W. L., 1991, "Non-Ideal Isentropic Gas Flow Through Converging-Diverging Nozzles," ASME JOURNAL OF FLUIDS ENGINEERING, Vol. 112, No. 4, pp. 455–461.

Chapra, S. C., and Canale, R. P., 1988, *Numerical Methods for Engineers*, McGraw-Hill, New York.

Fagerlund, A. C., and Winkler, R. J., 1982, "The Effect of Non-Ideal Gases on Valve Sizing," *Adv. Instrum.*, Vol. 37, No. 3, pp. 1323–1333.

Miller, R. W., 1983, *Flow Measurement Engineering Handbook*, McGraw-Hill, New York.

Wark, K., Jr., 1988, *Thermodynamics*, McGraw-Hill, New York.

Modulation of Turbulence by a Dispersed Phase

R. A. Gore[1] and C. T. Crowe[1]

The results of an earlier investigation that demonstrated the significance of the particle diameter/fluid length scale ratio in determining whether or not the addition of a dispersed phase would cause an increase or decrease in the carrier phase turbulent intensity are extended to radial locations other than the centerline. Presently, it is shown that similar trends are valid except the results become less correlated approaching the wall for the case of pipe flows. The results for jets are independent of radial location. It is also shown that other possible nondimensional parameters do not correlate the data as well.

[1]Department of Mechanical and Materials Engineering, Washington State University, Pullman, WA 99164-2920. Dr. Gore is currently at Los Alamos National Laboratory, Group T-3, Los Alamos, NM 87545.

Nomenclature

d_p = particle diameter
l_e = characteristic length of the most energetic eddy
R = pipe radius
$\bar{U}$ = mean flow velocity
U_M = local time averaged velocity
U_R = local mean relative velocity
ϕ = volume concentration
ρ = fluid density
ρ_P = particle density

Introduction

This paper is an extension of an earlier work (Gore and Crowe, 1989) in which numerous investigations were compiled to show the effect of particles size on modulating turbulent intensity. Here as in that work, particles are defined as any dispersed entity, whether liquid, solid or gas. It was shown that the particle size/fluid length scale ratio was an important parameter in determining whether the addition of a dispersed phase would cause an increase or decrease in the carrier phase turbulent intensity. The significant result of that investigation is presented in Fig. 1. In this figure the percent change in turbulent intensity is defined as $(\sigma_{TP} - \sigma_F)/\sigma_F \times 100$ where

$\sigma = \sqrt{\overline{u'^2}}/U_M$ is measured along the centerline and the subscripts TP and F refer to the fluid flow field with and without the dispersed phase, respectively. As can be seen from the figure, a value of $d_P/l_e \simeq 0.1$ represents a demarcation point where at larger values of d_P/l_e the addition of particles will increase the carrier phase turbulent intensity and at lower values cause a decrease. This point will henceforth be referred to as the critical length scale ratio. It is to be noted that l_e is the fluid length scale taken from the works of Wygnanski and Fiedler (1969) for single phase jet flows and Hutchinson et al. (1971) for single phase pipe flows. The fluid length scale, l_e, is a measure of the size of the most energetic eddy. The results shown in Fig. 1 include both pipe and jet flows with gas-solid, gas-liquid, liquid-solid and liquid-gas phases, over a large range of density ratio, concentration and flow Reynolds number. It should be noted that Fig. 1 presented here contains both additions and corrections to the original figure of Gore and Crowe (1989).
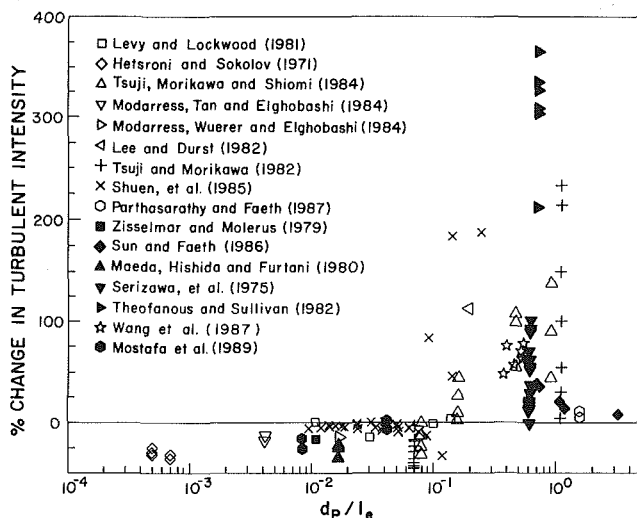

Fig. 1 Change in turbulent intensity as a function of length scale ratio. It is estimated that the percent precision error is the same or smaller than the size of the data symbols. It is assumed that the bias error is the same for flows with and without the dispersed phase and therefore cancels out.

The proposed explanation for the trend depicted in Fig. 1 is as follows. The small particles, which are much smaller than the most energetic eddy, will follow the eddy for at least part of its lifetime. Part of the eddy's energy will be imparted to the particle since the eddy, through the drag force, will be moving the particle. The turbulent energy of the eddy is therefore transformed into the kinetic energy of the particle and the turbulent intensity will be reduced. The larger particles will tend to create turbulence (in its wake) near the scale of the most energetic eddy, thus increasing the turbulent intensity of the fluid. In this case energy is transformed from the mean flow, which is moving the particles, to the turbulent kinetic energy of the fluid.

The present investigation extends the original study (Gore and Crowe, 1989) by examining the influence of the particles on the turbulence intensity at radial locations other than the centerline and examines the effect of other nondimensional parameters.

Results

To examine the effect of radial distributions one must separate the two different flows. That is, one must examine the results for free jets alone and the results for pipes alone. As will be shown the two flows exhibit different trends.

The results for pipe flows at radial locations of $r/R = 0.25$, 0.50, 0.75 and 0.90 are presented in Figs. 2(a)-2(d). From careful examination of the figures the following general trends can be inferred. First, it appears that the critical value of d_P/l_e is increased as one nears the pipe wall. At the centerline the critical ratio is approximately 0.1 but increases to 0.30 at $r/R = 0.90$. Also, it appears that if $d_p/l_e < d_P/l_e|_{crit}$ at the centerline, thus showing a decrease in turbulent intensity, the percent change remains at approximately the same level throughout the pipe with a few data points showing an increase of the fluid phase turbulent intensity at $r/R = 0.75$ and 0.9. But, if on the centerline $d_P/l_e < d_P/l_e|_{crit}$ and thus the turbulent intensity of the carrier phase is increased, there is a general decrease in the level of the percent change in turbulent intensity as one approaches the pipe wall.

Even though the number of data points that do not fall in the proposed quadrant increases approaching the wall, the approximation is still quite reasonable across most of the pipe. This is demonstrated by the fact that at the centerline 100 percent of the data points fall into the proposed quadrant, at $r/R = .25$, 98 percent; at $r/R = .5$, 95 percent; at $r/R = .75$, 84 percent; and at $r/R = .9$, 72 percent. Considering the large differences in flow situations this is still quite acceptable. Later, some explanation will be given as to the effect of the pipe wall.

Some observations can be made for the data points that fall outside the proposed quadrants. All the points that show an increase in turbulent intensity for d_P/l_e less than $d_P/l_e|_{crit}$ are from the work of Tsuji and Morikawa (1982) for horizontal pipe flows. All the points correspond to data obtained near the upper surface of the pipe. A further observation is that the lower the Reynolds number the more likely it is for a data point to fall outside the proposed quadrant.

The vast majority of data points that show a decrease in turbulent intensity with the addition of a second phase for d_P/l_e greater than $d_P/l_e|_{crit}$ are those from Serizawa et al. (1975) and Wang et al. (1987). Both of these investigations are for gas bubbles in a liquid. The Reynolds number effect in these investigations is opposite that shown in Tsuji and Morikawa (1982). It was found that a data point is more likely to fall outside the proposed quadrant the higher the Reynolds number. The reason for these trends is not clear to the authors.

The results for jets are shown in Fig. 3. In this figure the data at different radial positions ($r/x = 0, 0.03, 0.06, 0.10$) are all plotted on one graph. As can be seen there is little or no effect of radial position in sharp contrast to that found in
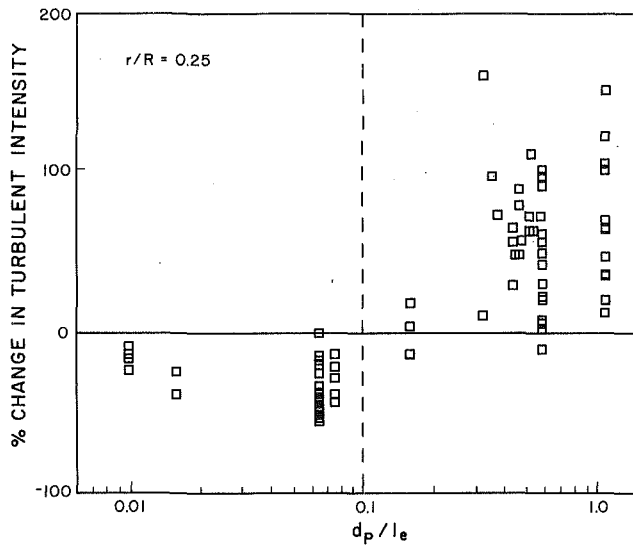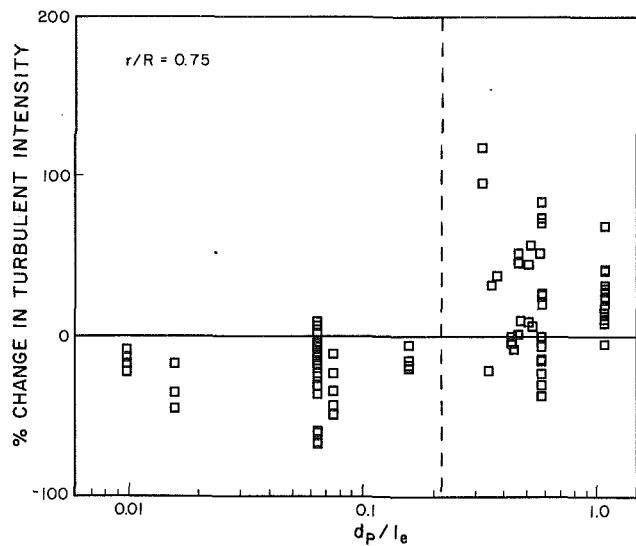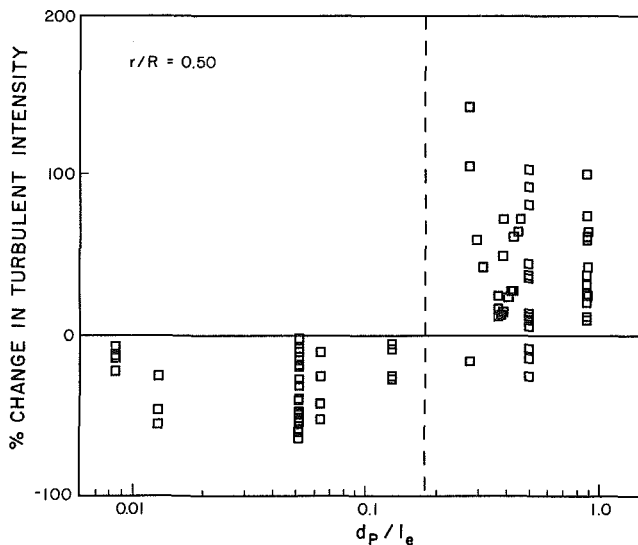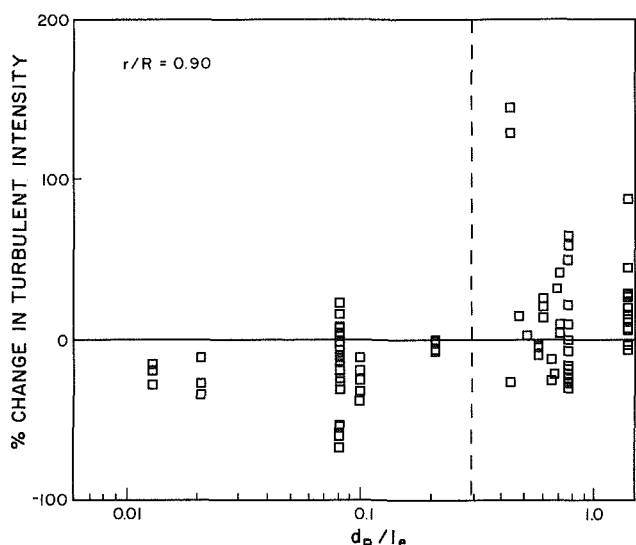
Fig. 2(a)

Fig. 2(b)

Fig. 2(c)

Fig. 2(d)

Fig. 2 Change in turbulent intensity in pipe flows at various radial locations. (a) r/R = 0.25, (b) r/R = 50, (c) r/R = 0.75, and (d) r/R = 0.90.

pipe flows. The majority of the points that fall outside the proposed quadrant are those from the investigations of Parthasarathy and Faeth (1987) and Sun and Faeth (1986) at an axial distance of $x/D = 8.0$. It may be that at this location the correlation given by Wygnanski and Fiedler (1969) is not valid. In any case, 92 percent of all data points fall inside the proposed quadrants for all radial locations.

Discussion

As noted earlier, the data for multiphase pipe and jet flows exhibit very different trends. The data for jets show that radial locations have little or no effect on the critical value for d_P/l_e or the magnitude of the percent change in turbulent intensity. Flows in pipes exhibit different trends for different radial locations. Approaching the pipe wall, the percentage of data points in the proposed region reduces from 100 percent on the centerline to 72 percent at $r/R = 0.9$. It is hypothesized that this is due to the anisotropic nature of turbulence in the vicinity of the pipe wall. The anisotropic nature of the flow would result in different l_e in different directions (each l_e would also be a function of radial location). This would reduce the likelihood of a single length scale correlating the effects of the particles.
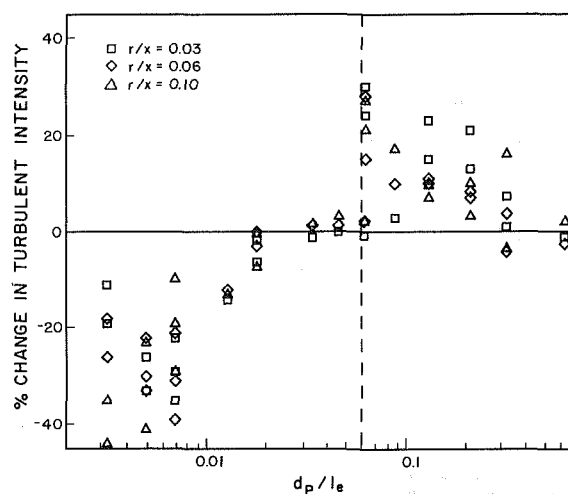

Fig. 3 Change in turbulent intensity in jets at various radial locations

The change in turbulent intensity with the addition of a second phase can be a function of various parameters of the flow system. These parameters are: particle size, particle density, concentration, relative velocity between the dispersed and continuous phases, fluid phase velocity, fluid density, fluid viscosity, fluid turbulent velocity scale, and fluid turbulent length scale. Application of the Buckingham Pi theorem results in:

$$\% \text{change} = f\left(\frac{\rho_P}{\rho}, \frac{\rho L \bar{U}}{\mu}, \frac{\rho U_R d_P}{\mu}, \frac{l_e}{d_P}, \frac{\sqrt{\overline{u'^2}}}{U_R}, \phi\right)$$

where L (characteristic length of the geometry) is used in place of l_e in defining the flow Reynolds number. The effect of the length scale ratio is the subject of this paper and has been discussed in depth. In examining the effect of other nondimensional parameters it will be shown that these parameters do not correlate the data as well.

There is no correlation between the density ratio, flow Reynolds number or concentration on whether the addition of a second phase causes an increase or decrease in the fluid turbulent intensity. This is shown by the various investigations examined here in which these parameters were kept at approximately the same value but the experiments showed both increases and decreases in fluid turbulence levels with various sized particles. This only refers to the question of increasing or decreasing fluid turbulent intensity with the addition of another phase, not by how much.

Unfortunately the adequacy of the other two parameters, particle Reynolds number and velocity scale ratio, to correlate the data is not as easy to evaluate. This is due to the fact that many of the investigations do not contain the information needed to compare turbulent intensity changes with relative velocity. Many of the investigations either reported velocity and turbulent intensity profiles at different flow parameters (i.e. concentration and flow velocity) or they presented the data in nondimensional form such that it was impossible to obtain the relative velocity. For the limited amount of data presented it is possible to make a few conclusions (although these conclusions are far from complete). First examining the velocity scale ratio, an increase in turbulent intensity with the addition of a second phase is found in Levy and Lockwood

(1981) at a velocity ratio, $\sqrt{\overline{u'^2}}/U_R$, of 1.26 and an increase is found in Lee and Durst (1982) at a velocity ratio of .087. The rest of the available data show a decrease in turbulent intensity but have a velocity scale ratio somewhere between these two limits. This suggests that the velocity ratio will not be sufficient to correlate the data. As to the Reynolds number, Levy and Lockwood found that the one particle size which corresponded to an increase in turbulent intensity had a relative Reynolds number between the Reynolds number of those particles sizes that decreased the turbulent intensity. Again, based on this limited data, it appears that the Reynolds number will not be sufficient to correlate the data.

Another nondimensional parameters important in dispersed flows which does not follow directly from the dimensional analysis is the Stokes number as defined by the ratio of the aerodynamic response time of the particle to the characteristic time of the fluid:

$$St = \frac{t_P}{t_f} = \frac{\rho_P d_p^2 \bar{U}}{18 \mu l_e}$$

The presentation of the change in turbulent intensity as a function of the Stokes number is given in Fig. 4. One notes that the data is not as well correlated as with the length scale ratio.
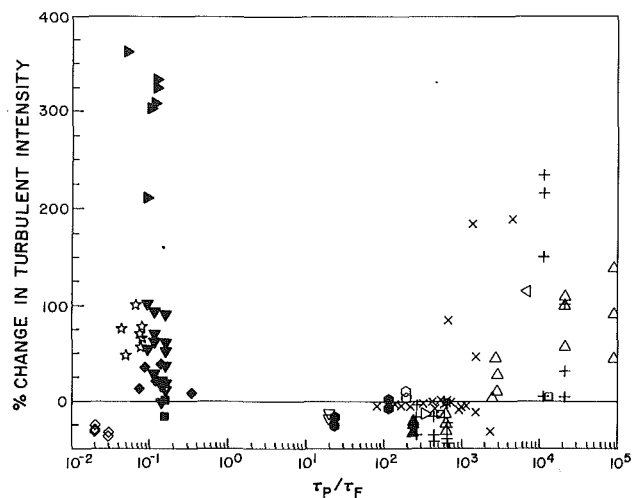

Fig. 4 Change in turbulent intensity as a function of time scale ratio

Conclusions

Available data indicates that the ratio of particle diameter to turbulent length scale is the most appropriate parameter to correlate the increase or decrease in turbulent intensity due to the addition of a second phase. It is stressed that this ratio is used only to determine whether the turbulence level is increased or decreased not by how much. The magnitude of the change will likely be a function of all the parameters listed above.

Although the exclusion of other parameters, i.e. particle Reynolds number and velocity scale ratio, is premature at this point, the length scale ratio does have an advantage. The value chosen for l_e, namely the single phase value, is generally known. This value is selected more out of necessity, since rarely is data presented that allows the determination after the addition of particles. Use of this definition of l_e allows a prediction of the effect of a dispersed phase. The other two parameters contain the relative velocity between the phases. This can only be determined accurately by experimentation and once this is performed presumably the change in turbulent intensity is known as well.

References

Gore, R. A., and Crowe, C. T., 1989, "Effect of Particle Size on Modulating Turbulent Intensity," Int. J. Multiphase Flow, Vol. 15, pp. 279–285.

Hutchinson, P., Hewitt, G., and Dukler, A. E., 1971, "Deposition of Liquid or Solid Dispersion From Turbulent Gas Streams: A Stochastic Model," Chem. Eng. Sci., Vol. 26, pp. 419–439.

Lee, S. L., and Durst, F., 1982, "On the Motion of Particles in Turbulent Duct Flows," Int. J. Multiphase Flow, Vol. 8, pp. 125–146.

Levy, Y., and Lockwood, F. C., 1981, "Velocity Measurements in a Particle Laden Turbulent Free Jet," Comb. and Flame, Vol. 40, pp. 333–339.

Parthasarathy, R. N., and Faeth, G. M., 1987, "Structure of Particle–Laden Turbulent Water Jets in Still Water," Int. J. Multiphase Flow, Vol. 13, pp. 699–716.

Serizawa, A., Kataoka, I., and Michigoshi, I., 1975, "Turbulence Structure of Air-Water Bubbly Flow–II. Local Properties," Int. J. Multiphase Flow, Vol. 12, pp. 235–246.

Sun, T-Y., and Faeth, G. M., 1986, "Structure of Turbulent Bubbly Jets-I. Methods and Centerline Properties," Int. J. Multiphase Flow, Vol. 12, pp. 99–114.

Tsuji, Y., and Morikawa, Y., 1982, "LDV Measurements of an Air–Solid Two-Phase Flow in a Horizontal Pipe," J. Fluid Mech., Vol. 120, pp. 385–409.

Wang, S. K., Lee, S. J., Jones, O. C., and Lahey, R. T., 1987, "3-D Turbulence Structure and Phase Distribution Measurements in Bubbly Two–Phase Flows," Int. J. Multiphase Flow, Vol. 13, pp. 327–343.

Wygnanski, I., and Fiedler, H., 1969, "Some Measurements in the Self-Preserving Jet," J. Fluid Mech., Vol. 38, pp. 577–612.

Nonideal Isentropic Gas Flow Through Converging-Diverging Nozzles[1]

J. C. Leung[2] and M. Epstein.[2] In their recent paper the authors gave a numerical method of treating nonideal gas flows through converging-diverging nozzles based on the Redlich-Kwong (R-K) equation of state (EOS). Though they present a case where nonideal gas effects are important, they did not provide the range of inlet conditions where this nonideality is significant. The present writers had published a nonideal gas flow paper (Leung and Epstein, 1988) earlier. This paper treats only the critical flow through convergent nozzles and not the divergent section where supersonic flow prevails. Using also the R-K EOS, generalized solutions in terms of reduced pressure, reduced temperature and the specific heat ratio at zero pressure (ideal gas specific heat ratio k^+ or $\gamma = C_p^+/C_v^+$) were presented. Moreover, these were algebraic equations from which maximum flow and throat conditions can be easily obtained. Generalized charts, such as Fig. 1 for γ of 1.2, were most useful in displaying the conditions under which large departures from the ideal gas solution can be expected. We should point out that a constant C_p^+ has been assumed, as is common practice in ideal gas treatment and which allows the simplicity in results. The success of such a generalized treatment, admittedly less precise than the subject paper, was demonstrated by comparison with both experimental data (Hendricks, 1974), and critical flow data (calculated with very complex virial-type EOS) published by Johnson (1964, 1965, 1968, 1970, 1972, 1974) at NASA Lewis Research Center. To provide a further comparison, we take the two cases discussed in the subject paper for methane gas and tabulate the following results based on our generalized solution approach as well as the interpolated results from the Johnson's publication (1972). For the nonideal case (Case I), our solution is in good agreement with the subject paper, and our mass flux is only 4 percent lower than Johnson's data which were calculated using NASA's extensive computer program (Johnson, 1971). As for the near-ideal case (Case II), our generalized chart of Fig. 1 clearly demonstrates that nonideal gas effects are unimportant for the given reservoir conditions.
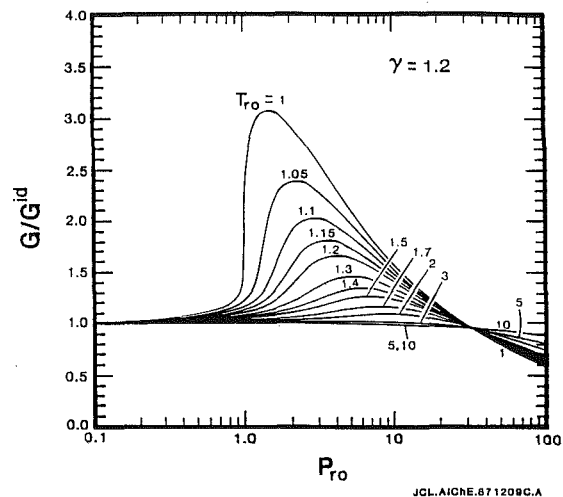

Fig. 1 Generalized chart for $\gamma = 1.2$ (G^{id} denotes ideal gas mass flux based on γ)

Table 1

Critical flow parameters	$\dfrac{\dot{m}\sqrt{RT_0}}{A\,P_0}$	$\dfrac{P_t}{P_0}$	$\dfrac{T_t}{T_0}$
Case I (Nonideal condition) $P_{r0}=5.0 \quad T_{r0}=1.4$ $C_p^+=2124$ J/kg-K $\quad k^+=1.32$			
Bober and Chow (1990)	0.93[a]	0.406	0.85[b]
Leung and Epstein (1988)	0.926	0.418	0.846
Johnson (1972)	0.964	0.416	0.843
Case II (Near ideal condition) $P_{r0}=0.8 \quad T_{r0}=3.0$ C_p+3150 J/kg-K $k^+=1.20$			
Bober and Chow (1990)	0.650[a]	0.463[c]	0.905[c]
Leung and Epstein (1988)	0.6505	0.560	0.907
Johnson (1972)	0.6506	0.560	0.905

[a]From Fig. 14 of Bober and Chow.
[b]From Fig. 1 of Bober and Chow.
[c]From ideal gas evaluation using $k = 1.209$.

Additional References

Hendricks, R. C., 1974, "Normalized Parameters for the Critical Flow Rate of Simple Fluids Through Nozzles," Papers J10, Int. Cryog. Eng. Conf., ed. K. Mendelssohn, IPC Science and Technology Press, 278.

Johnson, R. C., 1964, "Calculations of Real-Gas Effects in Flow Through Critical-Flow Nozzles," ASME *Journal of Basic Engineering*, Vol. 86, p. 519.

_____, 1965, "Real-Gas Effects in Critical-Flow-Through Nozzles and Tabulated Thermodynamic Properties," NASA TN D-2565.

_____, 1968, "Real-Gas Effects in Critical Flow Through Nozzles and Thermodynamic Properties of Nitrogen and Helium at Pressures to 300×10^5 N/m² (Approx. 300 atm)," NASA SP-3046.

_____, 1970, "Calculations of the Flow of Natural Gas Through Critical Flow Nozzles," ASME *Journal of Basic Engineering*, Vol. 92, p. 580.

_____, 1971, "A Set of Fortran IV Routines Used to Calculate the Mass Flow Rate of Natural Gas Through Nozzles," NASA TM X-2240.

_____, 1972, "Tables of Critical-Flow Functions and Thermodynamic Properties for Methane and Computational Procedures for Both Methane and Natural Gas," NASA SP-3074.

_____, 1974, "Real-Gas Effects in Flow Metering," *Flow-Its Measurement and Control in Science and Industry*, Vol. I, R. B. Dowdell editor-in-chief, pp. 269–278.

Leung, J. C., and M. Epstein, 1988, "A Generalized Critical Flow Model for Nonideal Gases," *AIChE Journal*, Vol. 34, pp. 1568–1572.

G. Emanuel.[3] The authors utilize the Redlich-Kwong (R-K) thermal equation of state and a polynomial in temperature T for the zero-pressure specific heat c_p^+ to examine nonideal behavior of methane for isentropic nozzle flow. Nonideal behavior occurs as the state of the gas approaches the coexistence curve, particularly in the vicinity of the critical point. At the end of the paper, there is a useful discussion by M. Vinokur. Additional comments are presented here.

The R-K state equation may be superior to van der Waals' equation, but is also subject to the same criticisms (Emanuel, 1987). For example, one can show that the compressibility factor at the critical point, Z_c, equals 1/3 for the R−K equation, whereas the experimental methane value is 0.28631 (Friend et al., 1989) This agreement is not good and would be worse for the many polyatomic gases whose Z_c value is below that of methane. As with the van der Walls equation (Emanuel, 1987), there is a multiplicity of critical-point solutions for the two free parameters, a and b, in the R-K equation. Bober and Chow utilize the form

$$a = \frac{\alpha R^2 T_c^{5/2}}{9 p_c}, \quad b = \frac{RT_c}{3\alpha p_c}$$

where it can be shown that

$$\alpha = 1 + 2^{1/3} + 2^{2/3} = 3.8473$$

An alternative solution would be

$$a = \frac{1}{3} \alpha R T_c^{3/2} v_c, \quad b = \frac{v_c}{\alpha}$$

With either set, the R-K equation is

$$p_r = \frac{3\alpha T_r}{\alpha v_r - 1} - \frac{\alpha^2}{T_r^{1/2} v_r (\alpha v_r + 1)}$$

in reduced variables. The equation for the entropy is also readily written in terms of reduced variables. The isentrope solution is then independent of the choice made for a and b. However, when reverting back to dimensional variables, there is a difference, and it is uncertain which a, b set provides the most realistic isentrope.

While a paper by Tsien is referenced, readers should be alerted to its errors, listed in Tsien (1947).

As noted, the zero-pressure specific heat c_p^+ is represented by a polynomial in T, as is frequently done. An alternative approach is to utilize an harmonic oscillator approximation for the vibrational modes of a polyatomic molecule (Emanuel, 1987). In terms of the constant volume, zero-pressure, specific heat c_v^+, this also yields closed-form results for both the $\int c_v^+ dT$ and $\int (c_v^+ / T) dT$ integrals that appear in the internal energy, entropy fundamental equations.

Evaluation of nonideal gas flows, isentropic or otherwise,

is most accurately achieved with computerized thermodynamic properties. (An introductory presentation, along with additional references, can be found in Emanuel (1987) and Stewart et al. (1986).) One reason for this is that no state equation, such as van der Waals or the R-K equation, can represent the non-analytic critical-point behavior of real fluids (Emanuel, 1987). This is true even though all free parameters in the state equation are evaluated using critical point properties. Consequently, the nonideal trend exhibited by Bober and Chow in Fig. 12 for the polytropic exponent n may not be appropriate for methane.

A more important reason is that the computerized approach is based on extensive experimental data, including coexistence curve data and data in the vicinity of the critical point. Methane has been treated in this manner by Friend et al. (1989).

Additional References

Emanuel, G., 1987, *Advanced Classical Thermodynamics*, AIAA Education Series, Wash. D.C., (a) Chap. 8, (b) Chap. 9.

Friend, D. G., Ely, J. F., and Ingham, H., 1989, "Thermophysical Properties of Methane," *J. Phys. Chem. Ref. Data*, Vol. 18, pp. 583–638.

Tsien, H.-S., 'Corrections on the Paper, 1947, "One Dimensional Flows of a Gas Characterized by van der Waal's Equation of State,"' *J. Math. and Phys.*, Vol. 26, pp. 76–77.

Stewart, R. B., Jacobsen, R. T., and Pennoncello, S. G., 1986, "Thermodynamic Property Formulation for Design and Analysis of Engineering Systems," *Cryogenic Properties, Processes and Applications*, ed. by A. J. Kidnay and M. J. Hiza, AIChE 251, Vol. 82, pp. 52–62.

Authors' Closure

The authors would like to thank Dr. Leung for pointing out his previous work on the subject of nonideal gas flows. As he mentioned in his discussion, our analysis of nonideal gas flows through converging-diverging nozzles was more extensive than the work of Leung and Epstein. We were also pleased to see that for the critical flow parameters cited in his discussion, our work is in good agreement with theirs as well, as the experimental work of Johnson. However, it should be noted that their generalized charts of G/G^{id} versus $P_{r,0}$ for various values of $T_{r,0}$ do not account for the possibility that the flow may become two-phase before critical flow conditions are reached. For example, when stagnation conditions for methane at a $(T_{r,0}, P_{r,0}) = (1.1, 2.0)$ were used in our program, the liquid state was reached at a Mach number equal to 0.675. Therefore, the Redlich-Kwong equation was not valid all the way to the choked nozzle condition. The curves for $T_{r,0}$ of 1.05 and 1.0 are even less likely to be valid.

The authors would also like to thank Dr. Emanuel for providing additional useful information regarding the behavior of nonideal gas flows, especially near the critical point. For such cases, the use of computerized thermodynamic properties, as suggested by Dr. Emanuel, is an alternative which one may choose when a high degree of accuracy is required.

---

[3] Department of Aerospace and Mechanical Engineering, University of Oklahoma, Norman, OK, 73019.